UNIVERSITÀ DEGLI STUDI DI MILANO
FACOLTÀ DI SCIENZE E TECNOLOGIE

Dipartimento di Chimica

PhD School in Chemistry

Cycle XXXIV

Hydrogen Production from Chemical Hydrogen Storage Materials Using Carbon-Based Catalysts

Supervisor of the Thesis: Prof. Alberto VILLA

Co-Supervisor of the Thesis: Dr. Alberto ROLDAN MARTINEZ

Director of the School: Prof. Daniele PASSARELLA

PhD Student:

Ilaria BARLOCCO

Academic Year 2020-2021

“I'll be the spark if you'll be the flame
Start a reaction that can't be contained
Balance your pH by sharing my base
I'll be your star if you'll be my space
'Cause there is no distance that I wouldn't go
To space time and wormholes my matter would flow
To the edge of the universe
I'll be your G if you will be C
Or I can be A if you will be T
If there's a mutation I'll fix every base
Work as yours zinc finger nuclease

Just like an atom
Don't rip us apart
Unless you want a big boom in my heart

We can take it fast, or really slow
But we can't know in certainty where we'll go
If at first we don't succeed
We'll try two more times
So our failure's a statistically significant try
Like an equation
It all works out
If we balance the size
There's no need to dial”

Science Love Song

“Humans! They lived in a world where the grass continued to be green and the sun rose every day and flowers regularly turned into fruit, and what impressed them? Weeping statues. And wine made out of water! A mere quantum-mechanistic tunnel effect, that'd happen anyway if you were prepared to wait zillions of years. As if the turning of sunlight into wine, by means of vines and grapes and time and enzymes, wasn't a thousand times more impressive and happened all the time”

Terry Pratchett, Small Gods

“Wizards don't believe in gods in the same way that most people don't find it necessary to believe in, say, tables. They know they're there, they know they're there for a purpose, they'd probably agree that they have a place in a well-organised universe, but they wouldn't see the point of believing, of going around saying "O great table, without whom we are as naught." Anyway, either the gods are there whether you believe in them or not, or exist only as a function of the belief, so either way you might as well ignore the whole business and, as it were, eat off your knees.”

Terry Pratchett, Reaper Man

ABSTRACT

The aim of this thesis is to design new catalytic systems in order to improve the performances of the existing catalysts to convert formic acid (FA) and hydrazine ($N_2H_4 \cdot H_2O$) into ultra-pure hydrogen in order to be effective in the future hydrogen economy. Different are the issues to solve in order to efficiently employ these chemicals in our energy transition. In particular, efficient carbon-based heterogeneous systems can effectively make enormous difference in the production of hydrogen from liquid carriers. Indeed, metal-based catalysts and especially Pd-based ones offer enhanced activity also at room temperature, but selectivity and stability need to be improved to be industrially applicable. In addition, carbon materials have the advantage of being easily tuned through variation in their structure, for example, changing the surface area and porosity and adding functional groups or generating topological defects. Moreover, their stability in liquid phase reactions makes them auspicious candidates in catalytic processes.

For these reasons, the first part of this thesis is dedicated to the design of new catalytic materials with the aim to improve the catalytic behaviour compared to existing Pd-based catalysts for the selective decomposition of FA at mild reaction conditions. In particular, the effect of the metal-support interaction and the geometrical and electronic effect in alloyed catalysts play a fundamental role to enhance the catalytic performance (Chapter 3-5).

Chapter 3 is devoted to study the metal-support interaction by doping with O and P functionalities the carbonaceous support. In order to establish the presence of functional groups in the support and their effect on Pd nanoparticles, the obtained samples were then, characterised by Transmission Electron Microscopy (HR-TEM, STEM-HAADF and STEM-EDS) and X-ray photoelectron spectroscopy (XPS). Density functional theory (DFT) simulations provided further insights in the interaction of Pd_{15} cluster with different support surfaces, i.e. pristine graphene (PG), carboxyl doped graphene (G_COOH), hydroxyl doped graphene (G_OH), carbonyl doped graphene (G_CO) and phosphate doped graphene (G_PO_3H).

The effect of the addition of a second metal to Pd is considered (Rh in Chapter 4 and Au in Chapter 5). In particular, in ***Chapter 4*** the synthesis of PdRh nanoparticles with different Pd:Rh molar ratios was studied. The obtained catalysts were characterised by Transmission Electron Microscopy (TEM) and Inductively coupled plasma optical emission spectroscopy (ICP-OES). For bimetallic catalysts, EDX-STEM analysis of individual nanoparticles was employed to investigate the presence of random-alloyed nanoparticles. Finally, PdRh catalysts were tested in the liquid-phase hydrogenation of muconic acid using formic acid as hydrogen donor.

Chapter 5 combines DFT and experimental data to disclose the role of gold in enhancing activity, selectivity and stability of palladium catalyst during the formic acid decomposition. PdAu bimetallic nanoparticles with different Pd:Au molar ratio were synthesised and the obtained catalysts were characterised by using Transmission Electron Microscopy (TEM), X-ray photoelectron spectroscopy (XPS) and inductively coupled plasma optical emission spectroscopy (ICP - OES). Finally, Density functional theory (DFT) calculations on Pd_{15}, Au_{15} and Pd_9Au_6 clusters supported on a carbon sheet were then simulated to provide atomic level understanding to the beneficial effect of gold observed in the experimental results.

In addition, in order to decrease the cost and increase the environmental benignity of the catalyst, the application of metal-free carbon materials in the formic acid dehydrogenation is investigated (***Chapter 6***). Indeed, Commercial graphite (GP), graphite oxide (GO), and two carbon nanofibers (CNF-PR24-PS and CNF-PR24-LHT) were used as catalysts for the metal-free dehydrogenation reaction of formic acid (FA) in liquid phase. Raman and XPS spectroscopies were employed to characterize the materials and Density Functional Theory (DFT) calculations were utilized to study the role of defects in this reaction.

In the final results chapter (***Chapter 7***), the above reported metal-free carbocatalysts are employed for the hydrazine hydrate dehydrogenation reaction, in order to produce H_2 without the presence of CO_2. A combination of DFT and experimental studies were used to unravelling the hydrazine hydrate decomposition reaction on metal-free catalysts. The study focuses on commercial graphite and two different carbon nanofibers, Pyrolytically Stripped (CNF-PS) and High Heat-Treated (CNF-HHT), respectively treated at 700 and 3000 °C to increase their intrinsic defects.

Finally, ***Chapter 8*** presents a summary of the main findings of this work and different possibilities to continue this research study.

TABLE OF CONTENTS

1. INTRODUCTION

1.1. Renewable Energy

In this century, energy plays a key role in our society. Our interaction with Earth resources intensifies in the last eras due to an accelerated socio-economic development including in particular technological progress, trade and the increasing in goods demand. Nowadays, constant energy supply is indispensable for maintaining our living standards. In fact, the 2020 IEA (International Energy Agency) Key World Energy Statistics states that in 2018 the World total final energy consumption was 9938 Mtoe (Million Tonnes of Oil Equivalent)[1]. Moreover, the International Energy Outlook 2019 (IEO2019) of U.S. EIA (Energy Information Administration) projects that global energy consumption will increase by nearly 50% by 2050[2]. In the present time, energy demand is fulfilled by petroleum-based fuels and electricity by fossil fuels. These sources have a significant negative impact on the environment, especially on global climate change. Greenhouse effect is the major responsible of climate change and humankind is increasing the concentration of greenhouse gasses in the atmosphere, i.e. carbon dioxide, methane, nitrous oxide and fluorinated gasses[3,4]. Nonetheless, carbon dioxide is the main by-product in the use of fossil fuels and the largest supplier to global warming, which contributes at almost 80 % of the greenhouse gasses[5]. Indeed by 2020, CO_2 concentration in the atmosphere had increased to 48 % up to its pre-industrial level[6]. In addition, they are not equally distributed on the globe, but the major resources are ruled by the Organization of the Petroleum Exporting Countries (OPEC)[7], questioning the security of supply and their distribution.

In this scenario, ruled by the depletion of fossil fuels, global warming and the growth of energy demand, renewable energy can be a solution. In addition, the Covid-19 crisis largely affects global economy and energy use. In 2020 mid-April full lockdown countries experienced an average 25 % decline in energy demand per week. On the contrary, in both 2020 and 2021 a growth in renewable energy demand (in particular wind and photovoltaic) was registered by the IEA Global Energy Review[8,9] expressing a change of route in the energy supply. Indeed, in 2020 the share of renewable energy sources (RES) in electricity generation covered the 29 % of the global demand[9] (Figure 1).

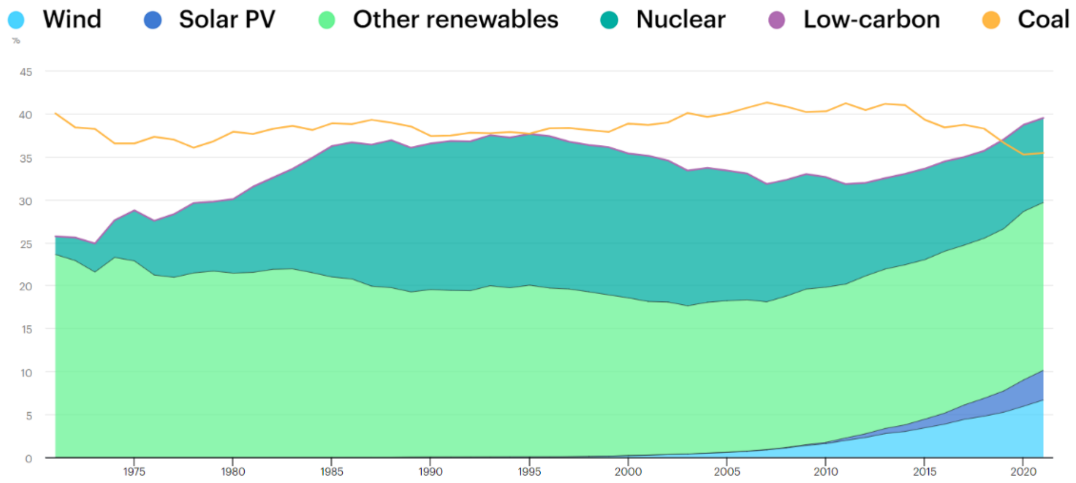

Figure 1: Share of low-carbon sources and coal in world electricity generation from 1971 to 2021. Adapted from Source: IEA (2021), Global Energy Review 2021, All rights reserved. (https://www.iea.org/data-and-statistics/charts/share-of-low-carbon-sources-and-coal-in-world-electricity-generation-1971-2021)

Renewable energy sources are, by definition, resources which can be continuously replenished, e.g. geothermal energy, hydropower, solar energy, wind energy and bioenergy[10,11].

Hydropower concerns the utilization of rapidly flowing water (kinetic energy) to generate electrical or mechanical energy[12]. Differently from other RES, hydroelectric power has achieved high level of technological development[13]. On the contrary, the construction of dams is expensive and it brings geological changes affecting the ecology of the environment. In 2019, the 58 % of the renewable energy share of global electricity production was covered by this source (Figure 2)[14].

The second most used RES based technology applied to electricity generation is wind power. By using wind turbines, the motion of the wind is convert into rotational energy and transferred to a generator obtaining electricity or mechanical power[15]. Nevertheless, this clean energy source is practical for minor power needs but in combination with other technologies can ensure continuity and flexibility of power generation[10]. Nearly 20 % of the electricity generated by renewable sources was produced by wind (Figure 2).

Solar energy is categorized as the best free and infinite renewable energy source. Direct solar energy conversion to electricity can be obtained employing photovoltaic cells and concentrators, which are based on photovoltaic effect[16]. The materials employed in this technology interact with photons with energy equal or superior than their band-gap[17]. Despite the free nature of sunlight, the photovoltaic materials are expensive and solar energy possesses low energy density[10]. In addition, the intake of solar energy depends on the location and the season of maximum exposure to the sun. Hydropower, solar and wind energy together cover the 90 % of global electricity production from clean energy.

The remaining 10 % is accounted mainly to bioenergy, a form of renewable energy derived from biomass, which is plant or animal material employed as fuel to obtain heat or electricity. It is classified into three categories: first, second and third generation[18,19]. The first one mainly consists in triglycerides which can be found in vegetable oils and agricultural crops and waste grease[20]. Second-generation of biomass is based on non-food derived lignocellulose, i.e. municipal solid waste, agricultural residues and wood[21]. Finally, the third and last generation derives from microalgae, which are more abundant than other sources[22]. Biomass can be converted into biofuels, obtaining energy for transportation but also it can also be converted into heat and electricity lowering the overall carbon intensity[23].

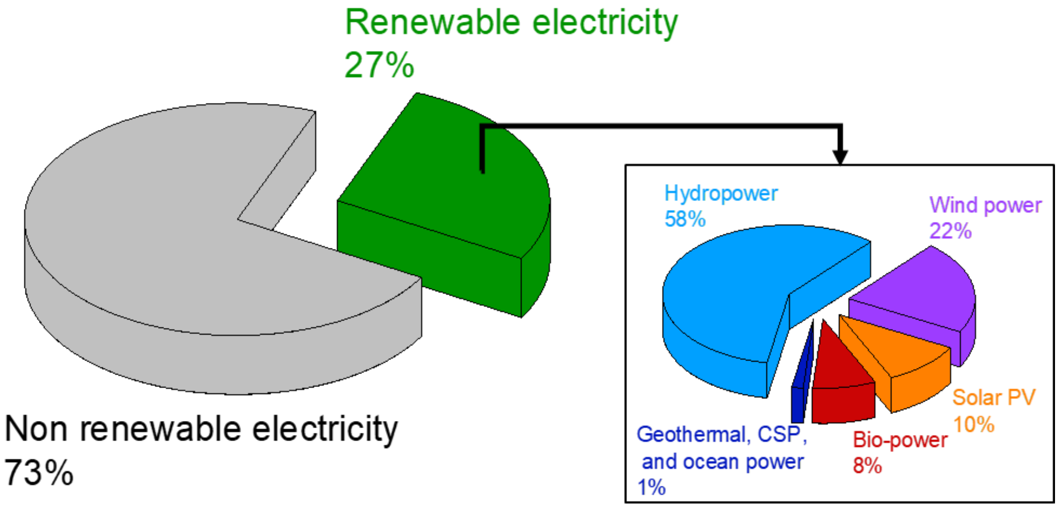

Figure 2: Estimated Renewable Energy Share of Global Electricity Production, End-2019

Different types of biofuels are available nowadays, such as straight vegetable oil (SVO), hydrogenated vegetable oil (HVO or green diesel), biogas, biodiesel, bioethanol and algal biofuel[24,25]. There are different techniques to produce them: for example, SVO can be obtained by direct extraction methods and biodiesel from transesterification of oils. Finally, HVO and algal biofuels can be produced from hydrogenation[24]. Hydrogenation increases the value of biofuels by removing heteroatoms such as, sulphur, oxygen and nitrogen, which reduce their heating value and promotes the formation of sulphur dioxide. This process consist of two steps: i) saturation of the unsaturated fat and ii) isomerization forming branched chains[26]. This hydrogen-based upgrading process needs to be consider in the utilization of biomass with improved economic value and broadened applications[27]. The development of a green method for hydrogen production can expand the application of biofuels.

Clean energy sources have the potential to meet future needs. Nevertheless, the technology related to them need to be implemented in order to eliminate the limitation discussed before. In this scenario, there is an urge to identify new clean energy sources in order to maximize energy extraction and hydrogen appear to be the ideal energy carrier which can be generated, transported and stored until its utilization.

1.1.1. Hydrogen as a renewable energy carrier

Hydrogen is the most abundant and lightest element in the universe. In addition, its availability is expected to endure as long as the human race[28]. Differently from petroleum-based fuels or natural gas products, this element possesses a very simple structure. Even though its simplicity, it is found in nature combined to other elements, e.g. O, C and metals[11,29].

In 1992 under the U.S. Energy policy Act[30] and in 1995 in the Green Energy Report[31], hydrogen was identified as a valuable clean source to decarbonize our energy system. After that, hydrogen stopped to gain attention of energy leaders[32]. Nowadays, this energy vector starts again to play a central role in the prospective of a low-carbon future[33], in fact the global annual demand of this molecule is rising rapidly (Figure 3). This renewed interest in H_2 as energy source is due to the skyrocketing number of applications of fuel cells on numerous areas, i.e. electricity, transport, industry and heat[34]. Moreover, different studies have assessed that hydrogen can penetrate the future energy system, providing significant benefits, although only reaching certain level of technological maturity, i.e. improving its transportation, production and storage[35,36].

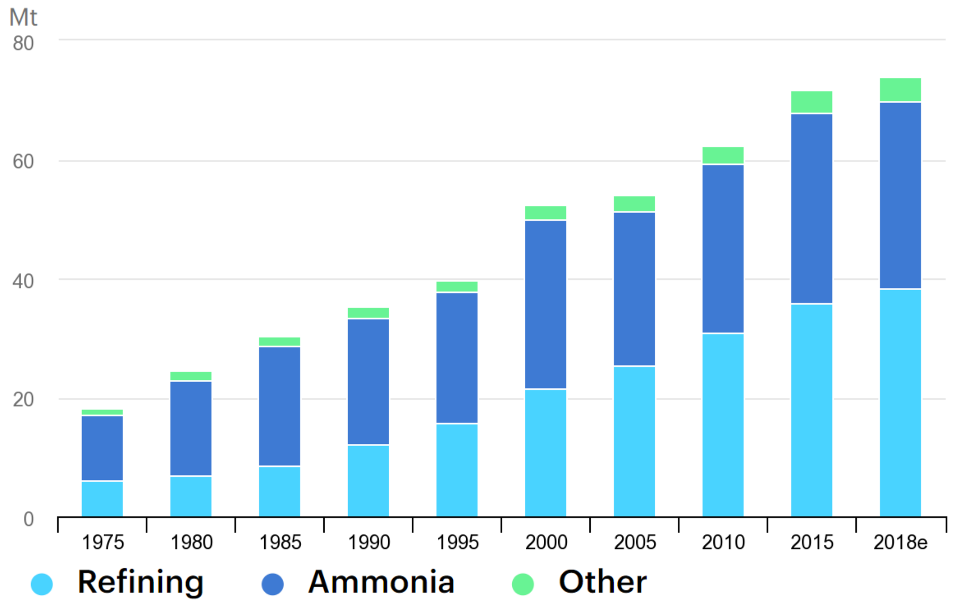

Figure 3: Global demand for pure hydrogen (Mt), 1975-2018. Adapted from Source: IEA (2019), The Future of Hydrogen, all rights reserved. (https://www.iea.org/data-and-statistics/charts/global-demand-for-pure-hydrogen-1975-2018).

Hydrogen has a gravimetric energy density of 143 MJ kg^{-1}, which is more than three times higher than gasoline (Table 1, column 2). Nonetheless, it has a very low volumetric energy density especially in gas phase (Table 1, column 3). For this reason, hydrogen must be compressed or in liquid state to supply enough energy density, but its liquefaction is an expensive energy consuming process[37,38]. On the other hand, this material has some appealing quality such as the lowest flashpoint and the highest octane number that make it an attractive fuel (Table 1, columns 4 and 5). The former indicates the temperature at which a compound in the presence of an ignition source produces enough vapour to form a flame at its surface[39]. Hence, the system required for ignition in hydrogen-based engine could be simpler than technologies based on other fuels. Moreover, it is expected to operate also in severe conditions[40]. The latter indicates the capability of a fuel to avoid a second undesired detonation inside the combustion chamber[41]. In addition to other benefits, hydrogen has a wide flammability range (Table 1, column 6) meaning a broad range opportunity to be employed as a fuel. Indeed, in order to be flammable, a mixture need to have a fuel concentration among the lower and the higher flammability level (LFL and HFL, respectively)[42]. In contrast, its wide flammability range and its ignition properties make hydrogen extremely difficult to store and to transport hindering the industrial application of this technology.

Table 1: Volumetric and gravimetric energy density, flash point of different fuels[40,42–46].

Fuel	*Energy per unit mass (MJ kg^{-1})*	*Energy per unit volume (MJ L^{-1})*	*Flash point (°C)*	*Octane number*	*Flammable range (%)*	*Auto-ignition temperature (°C)*
Hydrogen, liquid	143	10.1	-231	>130	4-75	585
Hydrogen, compressed	143	5.6	-231	>130	4-75	585
Hydrogen	143	0.0107	-231	>130	4-75	585
Methane	55.6	0.0378	-188	125	5.3-15	540
Natural gas	53.6	0.0364	-	-	-	-
LPG propane	49.6	25.3	-104	105	2.2-9.6	490
Gasoline	46.4	34.2	-45	87	1-7.6	246-280
Biodiesel	42.2	33	130	-	-	-
Diesel	45.4	34.6	62	30	0.6-5.5	210

1.1.1.1. Hydrogen based fuel cell systems

Fuel cells cleanly generate electrical energy in current directly from chemical energy of hydrogen, the fuel, emitting waste, hate and water[47]. This device is, in principle, similar to a battery but it does not necessitate recharging as long as fuel and oxidant are provided. If the fuel or the oxidant terminated, the fuel cell can be considered a battery. Indeed, in transportation application an hydrogen based fuel cell can last more before recharging or refuelling than a normal battery[48]. A fuel cell is composed by a porous anode (fuel electrode) and a cathode (oxidant electrode) placed at the side of a selectively conductive electrolyte layer. A catalyst oxidizes atomic hydrogen into H^+ and an electron. The proton goes through the electrolyte, while the electron generates a current that, after utilization, passes through the cathode producing O^{2-}. The oxygen anion and the hydrogen cation can bond and produce water[49]. The increasing interest in fuel cell technology is due to its clean and efficient conversion process. Moreover, all its components are compacted in a single unit cell avoiding noises and vibrations[49,50]. On the contrary, an industrial production and distribution need to solve problem related to the fuel supply, transportation and storage and the manufacturing costs[51–53]. Several types of fuel cells are currently under investigation and development, and some of them are available on the market:

- Proton Exchange or Polymer Electrolyte Membrane Fuel Cell (PEMFC)
- Alkaline Fuel Cell (AFC)
- Phosphoric Acid Fuel Cell (PAFC)
- Solid Oxide Fuel Cell (SOFC)
- Molten Carbonate Fuel Cell (MCFC)

Proton Exchange or Polymer Electrolyte Membrane Fuel Cell (PEMFC)

PEMFC is the most popular device in this field, in fact it was adopted by several automotive industries, such as Toyota (Mirai FCV), Honda (Clarity) and Hyundai (Tucson)[54]. In addition, the high current density generated, the rapid response time, the superior power density and the absence of dangerous emission and moving part make this technology appealing in different field, i.e. transport, building, electronics and portable devices[55,56]. The central component of PEMFC is the membrane electrode, composed by a polymer electrolyte membrane coated with active catalyst and inserted between the anode and the cathode. Because of the nature of the membrane, this fuel cell operates in the range of 60 – 80 °C. Hydrogen is fed in the anode where the hydrogen oxidation reaction (HOR) takes place splitting molecular hydrogen into protons and electrons. The electron generates electricity passing through the electric circuit. The oxygen charged at the cathode reacts in the oxygen reduction reaction (ORR) with the electrons and the hydrogen ion giving water[55,57,58]. The low operating temperature of this cell can be a disadvantage due to carbon monoxide derived from not pure hydrogen flow, which can poison the catalyst (typically platinum-based) reducing its activity[48]. A scheme of the component of PEMFC is shown in Figure 4.

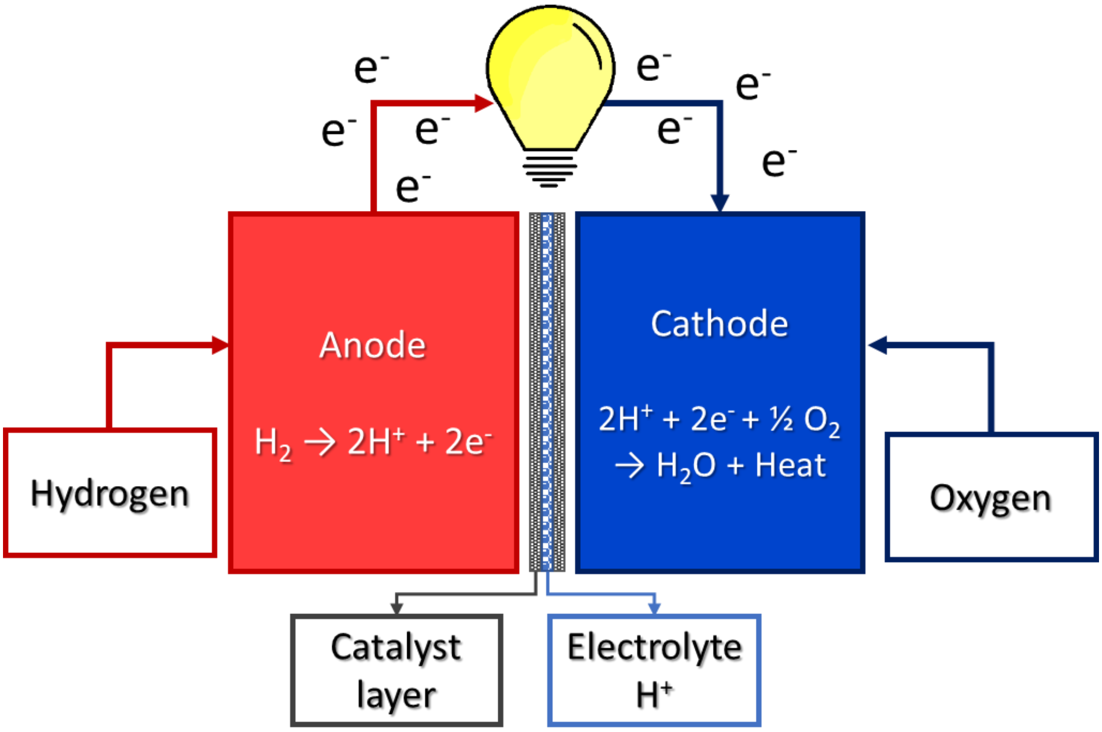

Figure 4: Scheme of the components of PEMFC and PAFC

Alkaline Fuel Cell (AFC)

This type of fuel cell was one of the first introduced and developed in 1960s and it was applied to provide on-board electricity in the NASA Apollo space programme[59]. This technology shows attractive features, i.e. excellent reaction kinetics which permits superior cell voltage (electrical efficiency) and, as a consequence, a lower noble metal-based catalyst quantity[60]. Alkaline fuel cell uses a liquid potassium hydroxide solution (KOH) as electrolyte. Hydrogen is fed at the anode and it reacts with the OH^- ions producing electrons and water. The oxygen at the cathode interacts with electrons and water yielding hydroxyl anions (Figure 5). One requirement of this fuel cell is the low CO_2 concentration. Carbon dioxide reacts with KOH and form K_2CO_3 and water. The formation of the carbonate decreases the number of ions at the anode and reduces the conductivity in the electrolyte modifying its composition. In consequence, terrestrial applications are hindered by the use of pure oxygen[60–62].

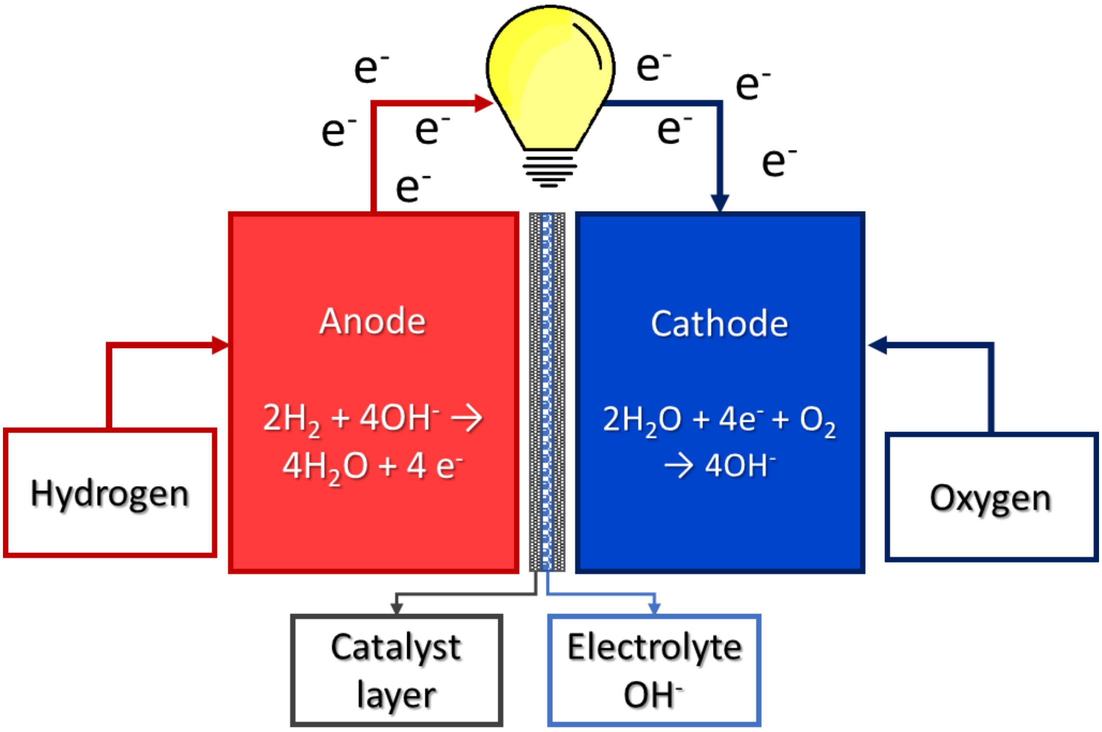

Figure 5: Scheme of the components of AFC

Phosphoric Acid Fuel Cell (PAFC)

Phosphoric acid fuel cell was the first technology of this type to be commercialized because of its high reliability and efficiency[63]. The electrochemical reaction of PAFC and PEMFC are identical (Figure 4), in fact hydrogen is fed to the anode to form H^+ and electrons. The electrolyte is mainly composed of phosphoric acid (H_3PO_4), which is a proton conductor, thermally and chemically stable and tolerant to carbon dioxide[64]. This fuel cell operates in a range of 150 – 200 °C, a compromise between increasing H_3PO_4 conductivity and cell life[65]. At the cathode, oxygen reacts with protons and electrons to give water. The conventional electrodes are composed of Pt supported on carbon black, and for this reason, carbon monoxide can poison the electrode and affect the overall performance of the cell[66]. Sulphur is another compound that can affect the anode forming H_2S which can be adsorbed by platinum[67]. Indeed, it is essential to maintain a low concentration of CO_2 and sulphur in the anode gas. In addition, also nitrogen concentration needs to be supervised: NH_3 can react with phosphoric acid reducing the efficiency of the electrochemical reactions[63].

Solid Oxide Fuel Cell (SOFC)

Solid oxide fuel cell offers the possibility to work at high temperature, from 500 °C to 1000 °C. As a consequence, natural gas can be used directly as a fuel and reformed in situ avoiding external systems[68]. The core of a SOFC consists in a dense oxygen anion electrolyte contained between the two porous electrodes (Figure 6). At the cathode the ORR takes place, i.e. oxygen consumes electrons forming oxide anions. Usually, the cathode electrode is composed of doped lanthanum manganite, which possess interesting features such as high electric conductivity, correct thermal expansion, compatibility with the electrolyte and sufficient porosity[69]. The O^{2-} ions formed at the cathode migrate through the electrolyte to the fuel electrode. As electrolyte yttria stabilized zirconia (YSZ) was successfully employed because of its ability to generate oxygen vacancies enhancing the conductivity[70,71]. At the anode, hydrogen (the fuel), is oxidized to produce water and electrons which can generate electricity passing through the circuit. Nickel can be employed as the fuel electrode because of the reducing condition, forming a skeleton of YSZ to prevent the sintering of the metal particles[69].

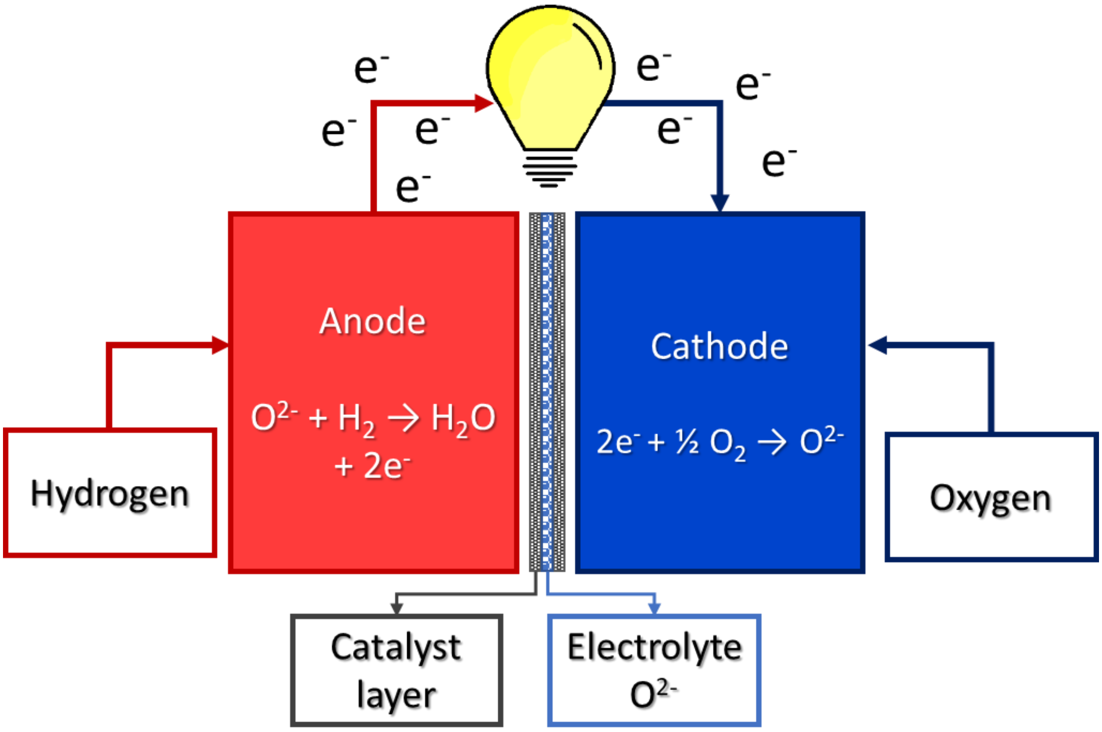

Figure 6: Scheme of the components of SOFC

Molten Carbonate Fuel Cell (MCFC)

This type of fuel cell operates in a narrow range at high temperature (≈ 650 °C) in order to reach sufficient conductivity and to have the possibility to employ low cost metals[72]. As seen for SOFC, the high temperature permits also the direct reform of natural gas and to have greater flexibility in the use of fuels. On the contrary, higher is the temperature lower is the life of the cell and corrosion stability. Nowadays, electrodes are based on nickel alloys at the anode and Ni-oxide at the cathode. The electrolyte is a molten carbonate salt mixture suspended in beta-alumina, which produces carbonate ions (CO_3^{2-}). At the cathode a mixture of oxygen and carbon dioxide yield CO_3^{2-}, that passes through the electrolyte to react with hydrogen at the anode forming CO_2 and electrons (Figure 7)[73,74].

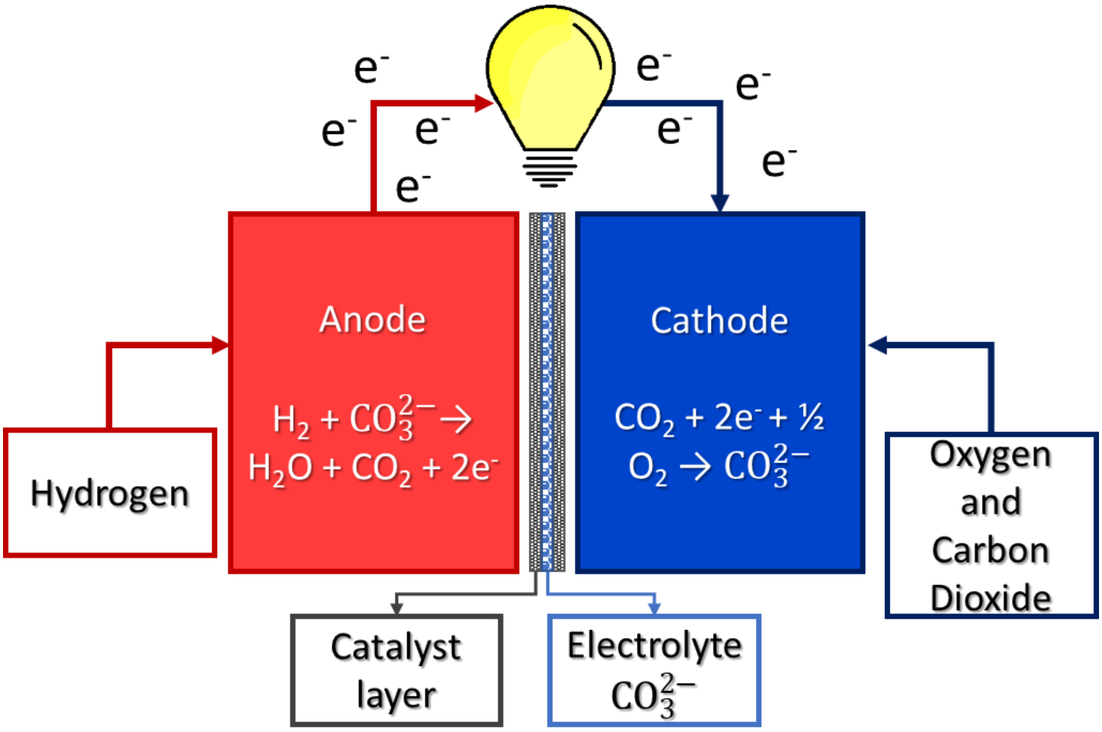

Figure 7: Scheme of the components of MCFC

In all these fuel cells, hydrogen produces clean energy and the by-product is water and heat. On the other hand, hydrogen must be obtained from a source, stored and transported because it is not naturally available as a gas and ready to be used. In the next section hydrogen production and storage technologies and its transportation will be discussed.

1.1.1.2. Hydrogen production

The future of a hydrogen-based economy reaching a zero-carbon emission target do not depend only on the “hydrogen to power phase” (the end use point), but most importantly on the production, storage and transportation of this energy source. Hydrogen can be produced from biomass, electricity, coal or natural gas. It is mostly produced from natural gas (70 million tonnes of hydrogen, MtH_2), accounting for around the 75 % of the global annual production. For coal is estimated the 23 % of hydrogen production[33]. The report on the future of hydrogen of the IEA for the 2019 G20[33] stated that production of hydrogen emitted CO_2 as Indonesia and UK together. Today, the processes that can produce this energy carrier are:

- Steam reforming
- Partial oxidation of refinery oil
- Coal gasification
- Electrolysis and biological methods

As a consequence, these technologies can be recognised as non-sustainable or environmentally friendly and energy intensive. Below is proposed a description of these methods.

Steam reforming

Natural gas reforming is the most developed technology for hydrogen production. In the U.S. today, the 95 % of hydrogen is produced using steam reforming in enormous plants[75]. Natural gas contains methane and its steam reforming is based on two main reactions: the reforming (Eq. 1) and the water gas shift reactions (Eq.2, WGS).

$$CH_4 + H_2O \rightarrow \mathrm{CO} + 3H_2 \qquad \Delta H = 206\ kJ\ mol^{-1} \quad (1)$$

$$CO + H_2O \rightarrow CO_2 + H_2 \qquad \Delta H = -41\ kJ\ mol^{-1} \quad (2)$$

Figure 8 shows a schematic diagram of the steam reforming process. The first step of the process is the desulphurization of the natural gas using a ZnO bed. Sulfur interact with nickel catalyst contained in the reforming unit, blocking the active sites and deactivating it[76]. An amount of hydrogen is then added to the mixture in order to catalytically form H_2S, which is eliminated in the sulfur removal unit (Eq. 3).

$$ZnO + H_2S \rightarrow ZnS + H_2O \quad (3)$$

After this step, a superheated steam is inserted and mixed with methane. Then, the mixture enters the reformer unit containing a $Ni/CaO/Al_2O_3$ catalyst. Next, the gas is cooled down from approximately 1100 K to about 540 K in order to flow in the WGS reactor. Here, Cu-based catalysts supported on alumina or zirconia converted steam and carbon monoxide in syngas (H_2 + CO). Now, the H_2 reach and CO poor syngas is cooled down in order to condense water and it moves to the absorber system. The H_2 – CO_2 mixture goes finally in the Pressure Swing Adsorption unit (PSA), where hydrogen is separated by molecular sieves in a cyclic process[77].

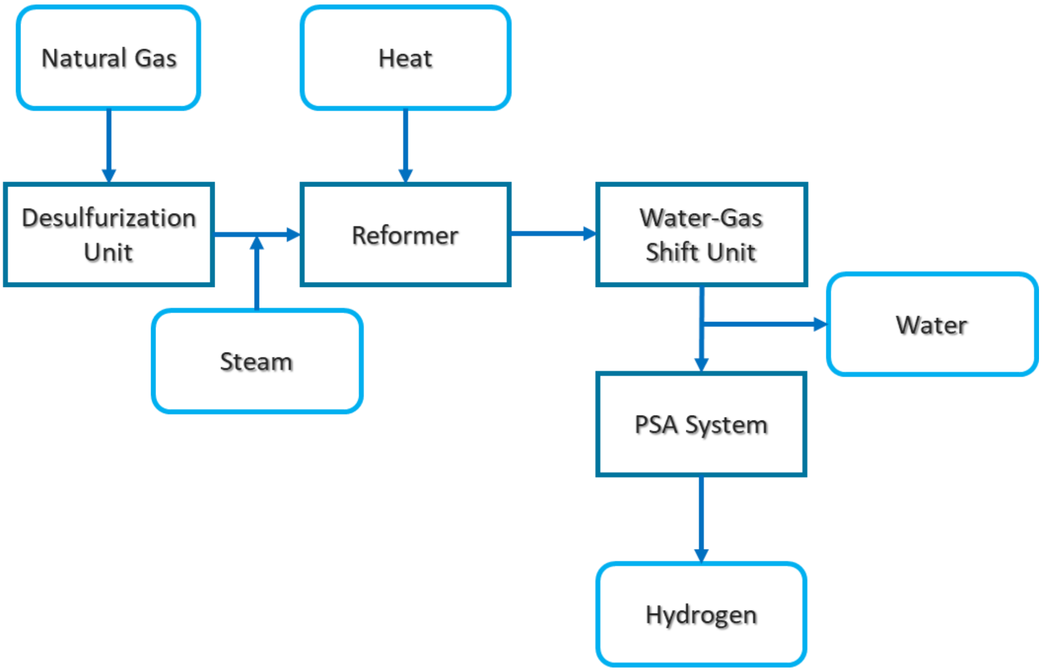

Figure 8: Scheme of the steam reforming process.

Partial oxidation (POX) of hydrocarbon

Hydrocarbon POX procedure possesses several advantageous features compared with other hydrogen production technologies such as the absence of an external feed like water, good response time and less sensitivity for fuel variation. This process can be either catalytic or catalyst-free and moreover, the reactor design is very simple and can be applied to almost all hydrocarbons (Figure 9)[78]. Here, pure methane, natural gas or hydrocarbons are heated in the presence of a stoichiometric amount of oxygen. The POX of hydrocarbons to syngas can occur without catalyst but at very high temperature, while using a catalyst the reaction temperature can be significantly reduced (Eq. 4).

$$C_nH_m + \frac{1}{2}nO_2 \rightarrow nCO + \frac{\mathrm{m}}{2}H_2 \tag{4}$$

Catalysts employed in this reaction are transition metal-based (Fe, Co and Ni), noble metal-based catalysts and perovskite oxides[79,80]. The strong disadvantage of this process is the production of carbon monoxide and carbon dioxide from fossil fuels (e.g. from C_8H_{18}: 12.35 kg CO_2 and 7.85 kg CO per kg of H_2[81]).

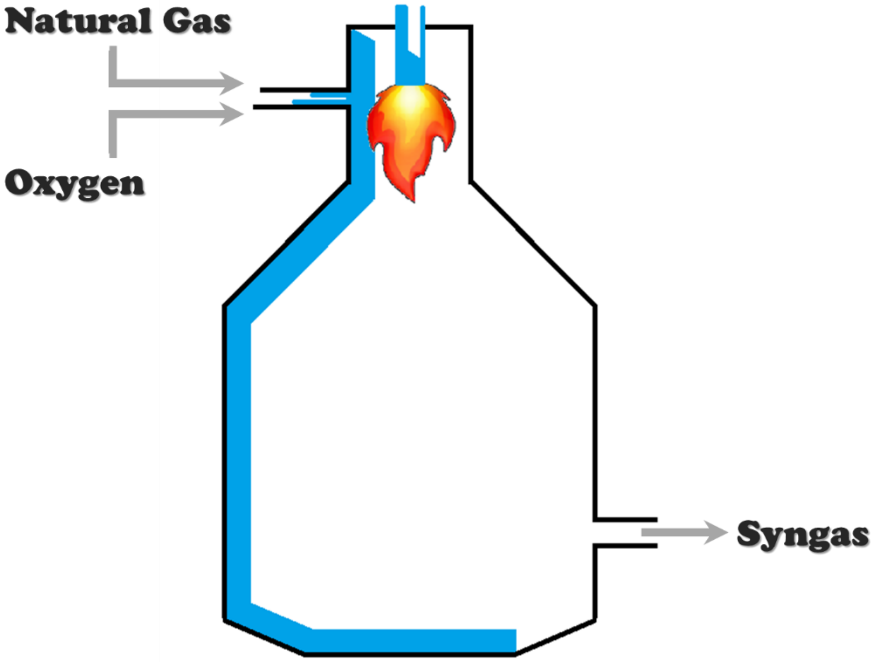

Figure 9: Schematic design of POX system.

Coal gasification

Gasification systems offer the opportunity to use all carbon-based feedstocks such as, coal, biomass, petroleum and wastes (Figure 10). The reaction of coal gasification to syngas (Eq. 5) is highly endothermic and a temperature upper to 1273 K is required to obtain an acceptable reaction rate.

$$C_nH_m + nH_2O \rightarrow nCO + \frac{m+n}{2}H_2 \qquad (5)$$

WGS reaction is exothermic and, in fact, it requires low temperature to produce CO_2. For this reason, after gasification the syngas is cooled down at approximately 673 K[82]. In the water gas shift unit, the syngas containing CO reacts with steam to obtain CO_2 and H_2. The hydrogen is further purified in a PSA unit[83]. In this process the environmentally dangerous product is carbon dioxide: from $CH_{0.8}$: 29.33 kg CO_2 per kg of H_2[81].

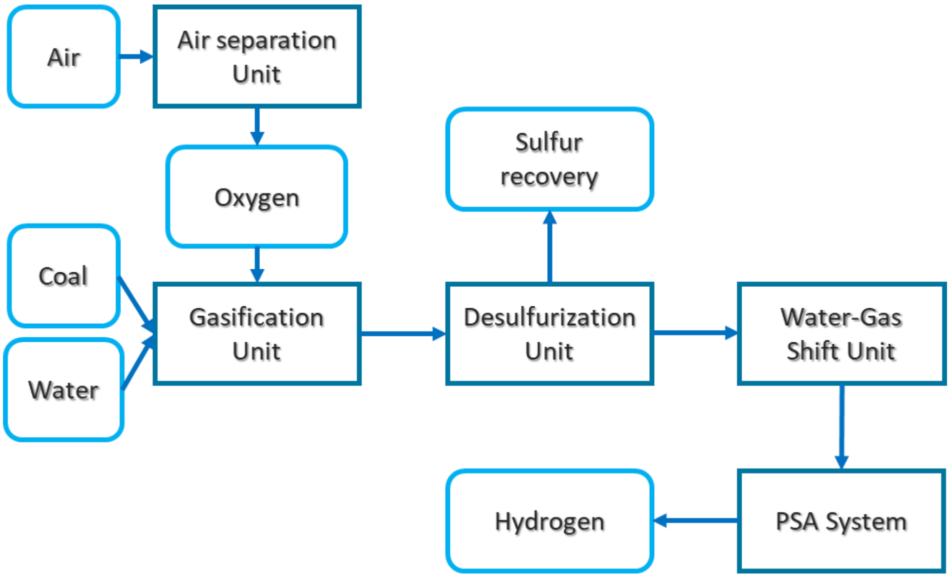

Figure 10: Schematic representation of a coal gasification plant.

Electrolysis

This process is the only considered to be environmentally friendly because it is not relying on fossil fuels if the energy employed in the electrolysis do not derived from non-renewable electricity. In addition, it produces very pure hydrogen (99.9 %) and it is applicable on small and large scales[81]. On the other hand, the large-scale implementation of this process is obstructed by the scarcity of active and stable electrocalysts. An efficient and long lifetime electrocatalyst is a crucial point to the development of water electrolysis on a large scale. Nowadays, different water electrolysis technologies are accessible for hydrogen production, such as alkaline, polymer-electrolyte membrane (PEM), solid oxide electrolyser (SOE). The different features and the principles of the various electrolysis technologies are showed in Figure 11 and Figure 12[84]. Nevertheless, in this process water is dissociated into hydrogen and oxygen under a direct current, according to Eq. 6 – 8.

$$H_2O \rightarrow \frac{1}{2}O_2 + 2H^+ + 2e^- \qquad \text{Anode (6)}$$

$$2H^+ + 2e^- \rightarrow H_2 \qquad \text{Cathode (7)}$$

$$H_2O \rightarrow \frac{1}{2}O_2 + H_2 \qquad \text{Overall (8)}$$

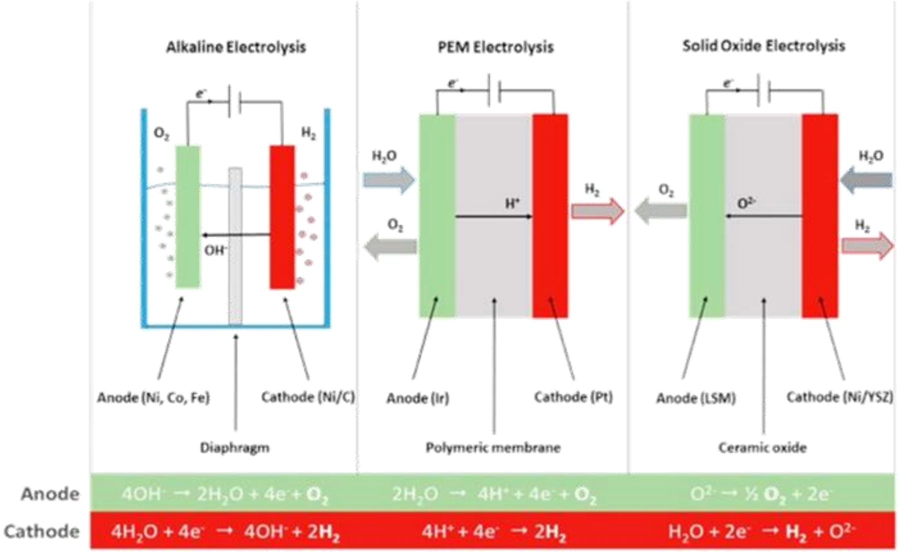

Figure 11: Operation principles of the main water electrolysis technologies. Reproduced from ref. [84]: F.M. Sapountzi et. al "Electrocatalysts for the generation of hydrogen, oxygen and synthesis gas" https://doi.org/10.1016/j.pecs.2016.09.001 with the permission of Elsevier.

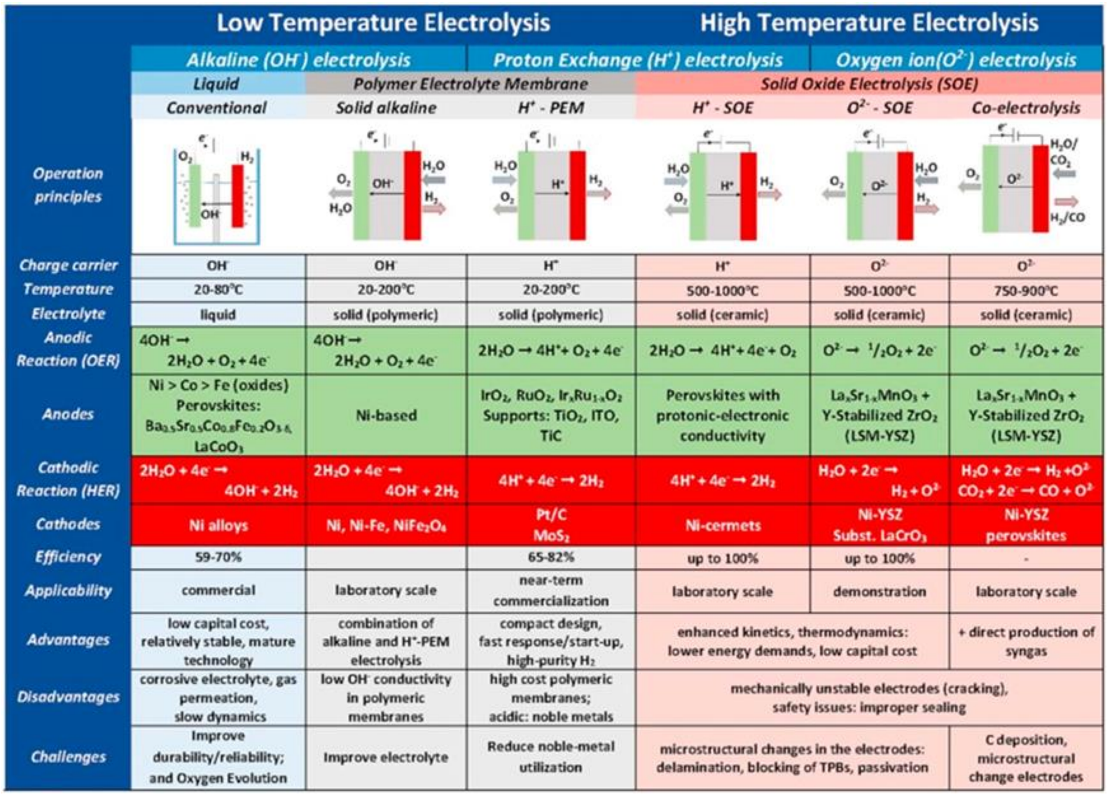

	Low Temperature Electrolysis			High Temperature Electrolysis		
	Alkaline (OH^-) electrolysis		Proton Exchange (H^+) electrolysis		Oxygen ion(O^{2-}) electrolysis	
	Liquid	Polymer Electrolyte Membrane		Solid Oxide Electrolysis (SOE)		
	Conventional	Solid alkaline	H^+ - PEM	H^+ - SOE	O^{2-} - SOE	Co-electrolysis
Operation principles						
Charge carrier	OH^-	OH^-	H^+	H^+	O^{2-}	O^{2-}
Temperature	20-80°C	20-200°C	20-200°C	500-1000°C	500-1000°C	750-900°C
Electrolyte	liquid	solid (polymeric)	solid (polymeric)	solid (ceramic)	solid (ceramic)	solid (ceramic)
Anodic Reaction (OER)	$4OH^- \rightarrow 2H_2O + O_2 + 4e^-$	$4OH^- \rightarrow 2H_2O + O_2 + 4e^-$	$2H_2O \rightarrow 4H^+ + O_2 + 4e^-$	$2H_2O \rightarrow 4H^+ + 4e^- + O_2$	$O^{2-} \rightarrow {}^1/_2 O_2 + 2e^-$	$O^{2-} \rightarrow {}^1/_2 O_2 + 2e^-$
Anodes	Ni > Co > Fe (oxides) Perovskites: $Ba_{0.5}Sr_{0.5}Co_{0.8}Fe_{0.2}O_{3-\delta}$, $LaCoO_3$	Ni-based	IrO_2, RuO_2, $Ir_xRu_{1-x}O_2$ Supports: TiO_2, ITO, TiC	Perovskites with protonic-electronic conductivity	$La_xSr_{1-x}MnO_3$ + Y-Stabilized ZrO_2 (LSM-YSZ)	$La_xSr_{1-x}MnO_3$ + Y-Stabilized ZrO_2 (LSM-YSZ)
Cathodic Reaction (HER)	$2H_2O + 4e^- \rightarrow 4OH^- + 2H_2$	$2H_2O + 4e^- \rightarrow 4OH^- + 2H_2$	$4H^+ + 4e^- \rightarrow 2H_2$	$4H^+ + 4e^- \rightarrow 2H_2$	$H_2O + 2e^- \rightarrow H_2 + O^{2-}$	$H_2O + 2e^- \rightarrow H_2 + O^{2-}$ $CO_2 + 2e^- \rightarrow CO + O^{2-}$
Cathodes	Ni alloys	Ni, Ni-Fe, $NiFe_2O_4$	Pt/C MoS_2	Ni-cermets	Ni-YSZ Subst. $LaCrO_3$	Ni-YSZ perovskites
Efficiency	59-70%		65-82%	up to 100%	up to 100%	-
Applicability	commercial	laboratory scale	near-term commercialization	laboratory scale	demonstration	laboratory scale
Advantages	low capital cost, relatively stable, mature technology	combination of alkaline and H^+-PEM electrolysis	compact design, fast response/start-up, high-purity H_2	enhanced kinetics, thermodynamics: lower energy demands, low capital cost		+ direct production of syngas
Disadvantages	corrosive electrolyte, gas permeation, slow dynamics	low OH^- conductivity in polymeric membranes	high cost polymeric membranes; acidic: noble metals	mechanically unstable electrodes (cracking), safety issues: improper sealing		
Challenges	Improve durability/reliability; and Oxygen Evolution	Improve electrolyte	Reduce noble-metal utilization	microstructural changes in the electrodes: delamination, blocking of TPBs, passivation		C deposition, microstructural change electrodes

Figure 12: Features of the main water electrolysis technologies. Reproduced from ref. [84]: F.M. Sapountzi et. al "Electrocatalysts for the generation of hydrogen, oxygen and synthesis gas" https://doi.org/10.1016/j.pecs.2016.09.001 with the permission of Elsevier.

In all these production methods, hydrogen is obtained as a gas and then, it needs to be transported or modified in order to be available for its final use.

1.1.1.3. Hydrogen storage and transportation

Transportation

Gaseous hydrogen requires transportation from the production point to refuelling station. For this reason, technical factors, safety, environmental impact and cost must be considered[85]. The utilization of pre-existing natural gas pipelines is the most economical way to transport hydrogen in its gas state, due to the high capital cost of these infrastructures[86–88]. Conversely, this can only be a temporary solution for hydrogen economy early stages. The majority of the high-pressure gas conduits are composed of ferric stainless steel, which is brittle to H_2[89]. Because of the high cost of installing new pipelines, transportation in trucks using tanks was considered. In this case hydrogen need to be stored in its compressed or liquefied form[86].

Compressed hydrogen storage

Production is not the only issue related to a hydrogen-based economy. Storage is a key factor of the development of its related technology, in particular for on-board prospective. Moreover, the hydrogen low energy density increases the challenge for its storage and transportation (Table 1, column 3). Compression from 20 to 100 MPa is the most widely employed method to store H_2[90]. The tanks used here are huge: Hyundai Tucson and Toyota Mirai possess tanks with volume of 140 L and 122 L and an autonomy of 500 and 426 km, respectively[86]. This can influence the public opinion negatively. Moreover, storage system security and low volumetric density are other difficulties in the development of compressed H_2 infrastructures[91,92]. This option can only be a starting point for commercialization.

Cryogenic hydrogen storage

Another possibility is hydrogen liquefaction, where it is maintained at a temperature below its boiling point (-253 °C). The technology applied is crucial in this case in order to maximize the efficiency of H_2 storage and minimize hydrogen boiling-off[86,90]. Indeed, the tanks are composed of an inner and an outer metallic wall separated using vacuum to reach thermal insulation that make it very expensive. Even if in this case the volumetric energy density of H_2 increases from $1.07\ 10^{-2}$ MJ L^{-1} to 10.1 MJ L^{-1} (Table 1), some disadvantages need to be solved. Among of all, hydrogen evaporate also in highly insulated containers and increases the pressure of the system causing safety concerns and energy losses. In addition, 30 to 35 % of the total energy of H_2 is employed for its liquefaction. Moreover, handling and transporting cryogenic hydrogen is difficult due to the need of special vacuum insulator hoses and tanks[93]. Because of these reasons, it is unlikely to use this technology in the future on vehicles.

Solid-state storage system

The conventional method to store hydrogen are not suitable for the future of hydrogen economy, because of their lack of efficiency and safety but also because they are bulky and expensive. In order to achieve a satisfying volumetric and gravimetric hydrogen capacity, in the last few years much attention was given to H_2 storage in solid state materials. In this system hydrogen is reversibly adsorbed and released either by physisorption or chemisorption. When molecular hydrogen interact with the surface of solid material by Van der Waals interactions physisorption is obtained. The materials employed are polymers, metal organic frameworks (MOFs), covalent organic frameworks (COFs), zeolites, activated carbon, nanofibers and nanotubes. This technique possesses rapid kinetics but also low hydrogen storage capacity at room temperature and pressure, i.e. high hydrogen storage capacities are possible only at extremely low temperature[94,95]. Chemisorption involves atomic hydrogen bonds with metals to form hydrides. In this process energy is needed to split the hydrogen bond in the molecule of interest. It is characterized by lower kinetics then physisorption and for this reason, the activation of the reactant increasing temperature or using a catalyst is required[92]. This method is safer than compressed or liquid hydrogen storage but metal hydrides tanks are very heavy and this is a problem for on-board application. The first stage of the formation of metal hydrides is the adsorption of hydrogen molecules into the material. Adding extra energy, molecular hydrogen dissociates into atomic hydrogen which diffuses into the bulk. An equal amount of energy needs to be given to the system in order to release hydrogen[95,96]. The typical hydrides employed are classified according to their stoichiometric formula, i.e. AB_5, AB_2, A_2B and AB. A denotes elements with high affinity for hydrogen (such as Ca, Ti, Y, Zr etc.) and B elements with low affinity for H_2 (such as Fe, Co, Cr, Ni, Mn)[95,97,98]. Most of the metal-hydrides present in the literature do not store large quantities of hydrogen and are characterized by slow kinetic and incapacity to operate at low temperature.

The need of solutions to transport and store hydrogen safely and efficiently make liquid-phase chemical hydrogen storage materials receiving much attention. These compounds include the hydrogen storage systems which are hydrogen-rich in their liquid form, such as hydrazine[99], formic acid[100], alcohols[101] or cyclic organic compounds[102]. Figure 13 shows a summary scheme of the possible methods and compounds to store and produce hydrogen.

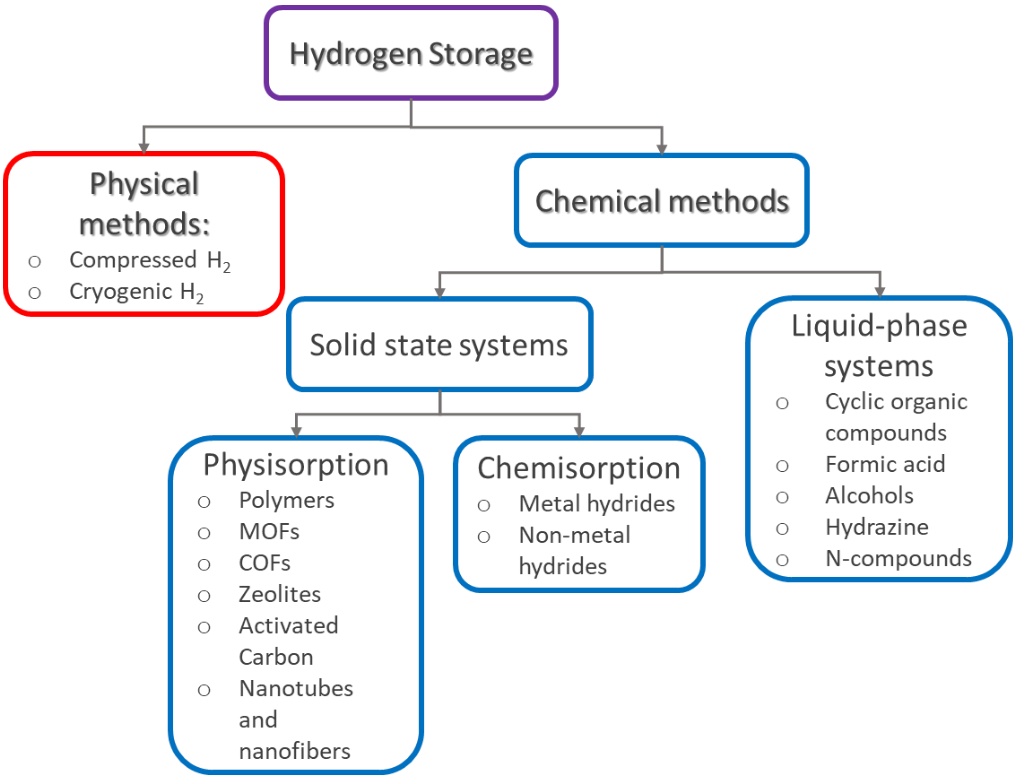

Figure 13: Hydrogen storage methods and possible compounds able to store and produce H_2.

An overview of the general aspects of renewable energy and hydrogen has been given. However, hydrogen is usually obtained by liquid-phase hydrogen carrier via heterogeneous catalysis. For this reason, in order to go more in-depth explaining reaction mechanism for hydrogen production, a general introduction of heterogeneous catalysis will be provided in the next section.

1.2. Heterogeneous catalysis

For the first time in 1835, the word "*catalyst*" was used by a Swedish chemist, J. J. Berzelius. New findings at the time could be rationally grouped in a one general concept: catalysis. Berzelius summarized this idea writing:

"It is, then, proved that several simple or compound bodies, soluble and insoluble, have the property of exercising on other bodies an action very different from chemical affinity.

By means of this action they produce, in these bodies, decompositions of their elements and different recombinations of these same elements to which they remain indifferent."[103]

With this statement he introduced the definition of "catalytic force", which is the force that can decompose bodies in a catalytic process. To rephrase it, a catalyst is a compound that is able to increase the reaction rate of a process without being consumed. At this moment in time, 80 % of the manufactured products involves catalysts in their production. Indeed, nearly 90 % of industrial processes in the word employ catalysts[104].

A catalyst allows to a reaction to proceed in milder condition or shorter time by decreasing the activation energy barrier (E_a) of a process (Figure 14). This modifies only the kinetic of the reaction, while thermodynamics remains unaffected.

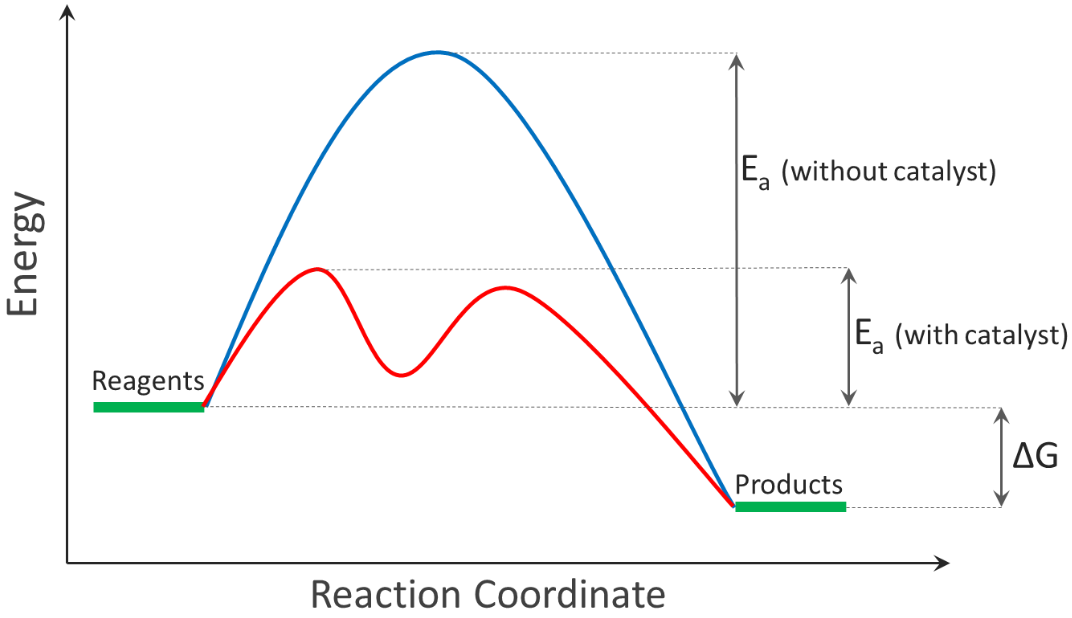

Figure 14: potential energy diagram for a reaction in presence of a catalyst (red) and in absence of a catalyst (blue). ΔG remained unchanged also after adding the catalyst.

Catalysts can be divided into three main groups, i.e. heterogeneous and homogeneous, depending on their chemical phase and enzyme catalysis. In the latter case, a biological molecule (enzyme) is employed as catalytic material[105,106]. This field of catalysis goes beyond the scope of this thesis.

In the first case the reactants and catalyst are in different phases, while for homogeneous systems reagents and catalyst are in the same phase.

Homogeneous catalysts are typically metal-organic complexes, where the metal is the active site which is coordinated with organic ligands. The oxidation state of the metal centre and the nature (hindrance and electronic properties) of the ligand dominate the chemistry of the material. Indeed, they can be easily tuned by changing the ligands and their interaction with the substrate can be simply controlled because of the localization of the active site and high chemical uniformity. On the other hand, homogeneous catalysts are part of only 20 % of industrial processes because of their recycle/separation problems and, as a consequence, economic disadvantage. Olefins hydroformylation, acetic acid synthesis and C-C couplings are few examples of industrial reaction that employed this type of materials[107].

Heterogeneous catalysts show several advantages such as the easier recovery and thermal stability, because of the absence of organic moieties. However, these systems are less active and selective due to the absence of a localized active site and the complexity of the chemistry involved because of the numerous interactions that take place on the material. Indeed, the first step of a heterogeneous catalytic process proceeds by the adsorption of the reactant species on the surface of the material. After the process itself the products need to be desorbed, the adsorption and desorption are usually the rate determining steps of the reaction because of the low availability of active centres on the surface[108]. This thesis is based on the use of heterogeneous systems, therefore in the next sections heterogeneous catalysis will be more extensively discussed.

1.2.1. Bulk catalysts

Heterogeneous or solid catalysts are usually grouped into supported and unsupported (bulk) materials. Bulk systems are divided into i) metals and metal alloys, ii) oxides and sulphides and iii) metal oxides, zeolites, clays and solid acid or bases[108]. Among them, metal oxides and mixed metal oxides are largely employed in industry, for example in ammonolysis, ammoxidation, dehydration of alcohols, dehydrogenation and oxidation processes[109].

Catalysts such as clays, zeolites, silica, alumina, phosphate, mixed oxide, ZnO, TiO_2 and ZrO_2 are part of this category of materials. The main industrial fields of application are acid-base reactions, oxidations and biomass conversion[110]. Metal oxides are generally formed by an oxide surface that terminates with oxide anions (O^{2-}), bonded to a metal cation (M^{n+}). Another important feature of the surface of the material is that the symmetry and coordination of M^{n+} cations is not equivalent to the bulk. In addition, their surface contains numerous and different defects, which are fundamental for the catalytic performance[111]. Because of the metal centre on the surface exhibits a low coordination number, it tends to interact more strongly with water by dissociating it according to Figure 15, and forming hydroxyls groups.

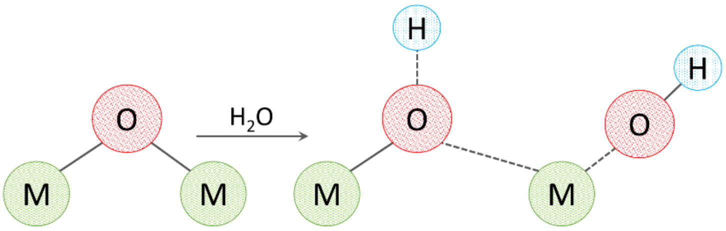

Figure 15: Schematic representation of the dissociation of water on the surface of a metal oxide.

Different defects can be present in metal oxides. Structural defects regarding the lattice of the catalyst and vacancies, interstitial atoms, impurities and dislocations are only few of the possible types. Metal oxides can also possess electronic defects, only if impurities are added. This type of extrinsic defects can introduce charge carriers in localised energy levels. If an electronic defect is inserted below the conduction band (CB), it has the ability to pump electrons in the CB forming an n-type semiconductor. On the other hand, a defect inserted near the valence band (VB) creates holes, which can accept electrons giving rise to p-type materials. For this reason, transport of defects, anions and conductivity should be considered in the case of solid metal oxide catalysts[108]. In the case of this type of materials, surface aggregates of atoms act as active sites. As an example, in oxidation reaction both the substrate and molecular oxygen must be activated. This means that surface active centres must possess the correct dimension to interact with the reactants. The reactive surface oxygen needs to be in domains with a defined number according to the stoichiometry of the reaction, in order to achieve high selectivity. Indeed, it was postulated that for the partial oxidation of propylene, the domain must contain between 2 and 5 adjacent O atoms in order to partially oxidize the substrate to acrolein[112]. With a surplus of oxygens only CO_2 and CO are produced, while completely isolated atoms could be inactive or produce allyl radicals, taking only an α-hydrogen[112]. The site isolation principle is illustrated in Figure 16 for butane oxidation over vanadyl phosphate material. Within the domains, oxygen can be easily exchanged but this is not true between domains because of oxygen diffusion barrier. This underlines the importance of the tuning of the surface in order to enhance the catalytic behaviour.

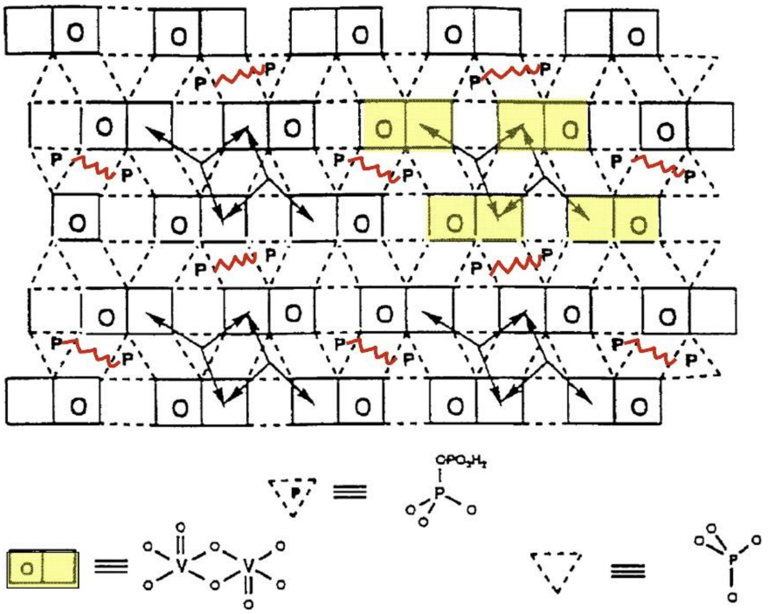

Figure 16: scheme for $(VO)_2P_2O_7$ surface structure. Black arrows indicate the pathways for surface oxygen mobility, while red connections represent the insulation due to P_2O_7 groups. Adapted from A. Pradyot et al. “A molecular level mechanism of n-butane oxidation to maleic anhydride over vanadyl pyrophosphate” https://doi.org/10.1007/BF00811368 with the permission of Springer Nature.

Regarding metals and alloys catalysts, metal gauzes or grids are usually employed in highly exothermic reactions in catalytic beds of small height. As an example, Ag grids are used in methane dehydrogenation and RhPt grids in the nitric acid process[113]. The surface area is a crucial parameter to determine the active sites and their availability during the reaction. These limitations can be surpassed by employing metallic nanoparticles deposited on high surface area materials called supports[114,115].

1.2.2. Supported metal nanoparticles (NPs)

Metal nanoparticles are defined as particles within the nanometric size range (between 1 and 100 nm). They can be composed by a single metal or two or more metals. In this case, if a metallic bond exists between the different metal species, NPs can be referred as alloys[116]. Bulk systems chemical and physical properties are independent from their size. Nevertheless, at the nanoscale, effects that change the properties of the material dependently on the size begin to dominate[117]. This behaviour is related in particular to the extreme increase of surface area/volume ratio and to the size-induced metal-insulator transition (quantum size effect)[117,118]. When a particle is larger than a micron, the number of metal atoms in the surface are outnumbered by the bulk atoms, while when the particle size is in the nanometric scale the portion of atoms at the surface became significant. Thus, the large surface area starts to dominate the physical-chemical properties of the material, meaning a substantial difference from the features of the bulk system. Figure 17 shows an example of the consequence of this fact in the melting temperature of gold nanoparticles. Indeed, the temperature increases with the diameter, meaning that more energy is required to break the metal-metal bond when an abundant fraction of highly coordinated atoms are present[117,119].

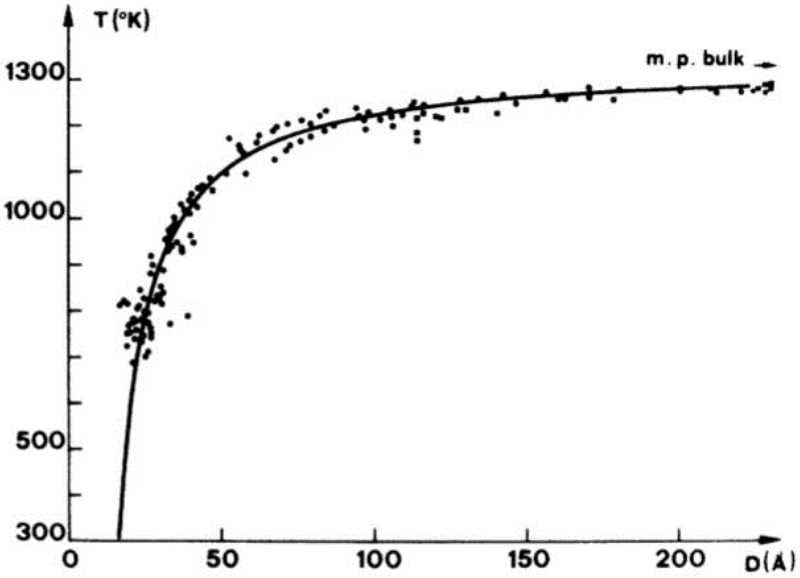

Figure 17: Dependence of melting point on the diameter of Au NPs. Reprinted from ref. [119]: P. Buffat et al. "Size effect on the melting temperature of gold particles" https://doi.org/10.1103/PhysRevA.13.2287 with the permission of the American Physical Society.

Therefore, quantum size effect is a deviation of electronic and optical features when the diameter of the material reaches the nanoscale. At the considered dimensions, valence and conduction bands are no more as the ones of metals but they assume discrete energy levels: as a consequence, the band gap of the material changes (Figure 18)[120].

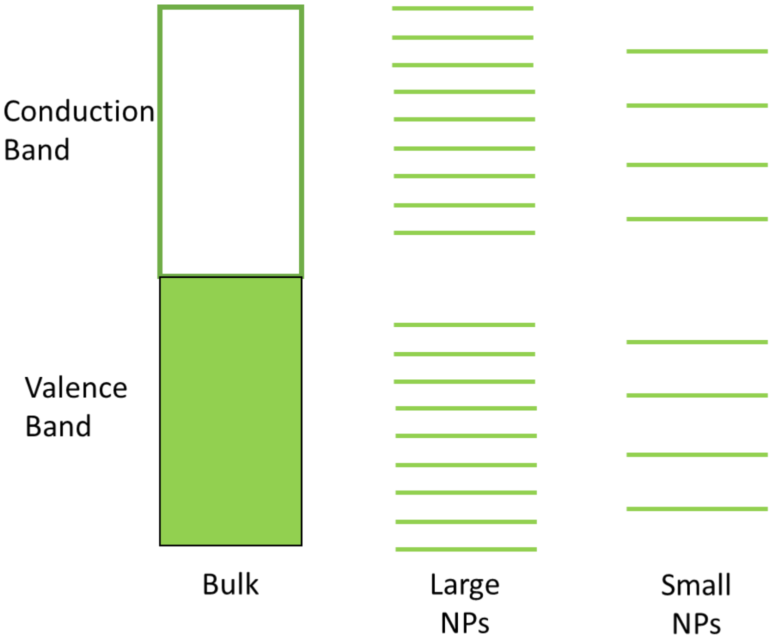

Figure 18: Scheme of the increase in bandgap with the decrease of dimensions. If NPs are sufficiently small, energy levels become discrete.

In catalysis NPs present several advantages due to their nature, in particular the increased number of active sites per unit area due to the surface/volume ratio and the superior zeta potential that decreases the possibility of their aggregation[121,122]. Metal NPs can be also obtained as colloidal solutions, which is a mixture where an insoluble substance (metal NPs) is microscopically dispersed into another substance (solvent)[123]. Colloidal metal nanoparticles can be used in their homogeneous form but also, they can be heterogenized using a support. Thus, the deposition of NPs avoids the problems related to the separation and purification discussed before but also bringing increased selectivity and activity to heterogeneous catalysts. Indeed, the size of metal NPs is of enormous importance in the final catalytic performance of the catalyst, and for this reason, particular attention is paid in their synthetic procedure. Indeed, Xiong et al.[124] have showed that manipulating the reduction kinetics of polyol synthetic process, selective triangular and hexagonal shaped Pd NPs can be obtained. Moreover, by a rapid reduction of the Pd precursor in presence of PVP cuboctahedral Pd NPs are generated (Figure 19).

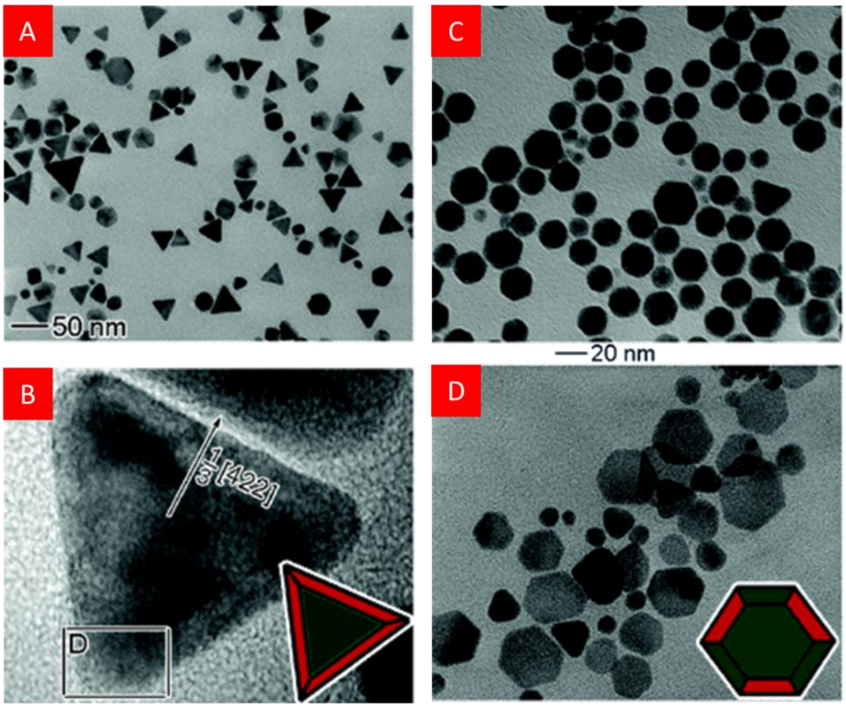

Figure 19: TEM images of Pd NPs with different morphology obtained by varying the reduction kinetics changing the amount of $FeCl_3$. Adapted with permission from ref. [124]: Y. Xiong et al. “Kinetically Controlled Synthesis of Triangular and Hexagonal Nanoplates of Palladium and Their SPR/SERS Properties” https://doi-org.pros2.lib.unimi.it/10.1021/ja056498s. Copyright 2005 American Chemical Society.

Size and shape are closely related to the catalyst surface which determine the catalytic activity. This is a consequence of the interaction between the substrate and the active site: metal NPs with different facet offers different binding configuration[125]. As an example, Tao and co-workers have demonstrated the dependence of the catalytic performance on the metal’s coordination number (CN) and so, on the number of edges and corners on the NP. They showed that Pt NPs with a size of 2.2 nm are composed by under-coordinated Pt atoms (CN=7), that are active in room temperature CO oxidation. On the other hand, Pt atoms with CN=9 exhibits no activity in this reaction[126].

Bratlie et al.[127] prepared cubic and cuboctahedral Pt NPs (Figure 20) and the effect on the shape was explored in benzene hydrogenation reaction. It was found that the two structures showed different selectivity for this reaction. Indeed, in the case of cuboctahedral NPs, both cyclohexane and cyclohexene were produced, while cubic particles only promoted the formation of cyclohexane. The difference was attributed to the different facets of the NPs: cuboctahedron consist of both (100) and (111), while cubic only of (100). Therefore, the diverse selectivity suggested that (100) facet favoured the cyclohexane production.

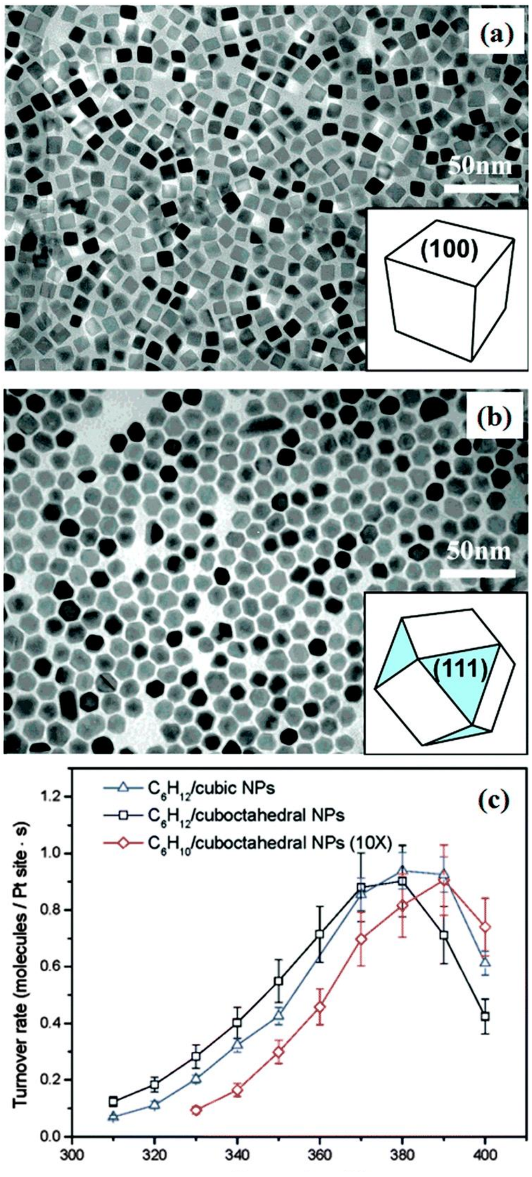

Figure 20: TEM images of a) cubic and b) cuboctahedral Pt NPs. C) Turnover rates of cyclohexane and cyclohexene formation on the two catalysts. Adapted with permission from ref. [127]: M. Bratlie et al. “Platinum Nanoparticle Shape Effects on Benzene Hydrogenation Selectivity” https://doi.org/10.1021/nl0716000. Copyright 2007 American Chemical Society.

In particular, Pd supported NPs are largely applied in hydrogenation and dehydrogenation reactions[128,129], which concern this Thesis.

1.2.2.1. Bimetallic NPs

Beside monometallic nanoparticles, bimetallic nanoparticles find large application. Here, two metals can be mixed forming a new material with unique properties which depend on the final structure ad composition. Different bimetallic structures can be produced depending on the synthetic methods and experimental parameters, and are grouped depending on their structure patterns[130] (core-shell, multi-shelled, segregated and random alloy; Figure 21). Core-shell structures are composed by one metal in the core encapsulated by another in the shell. It is possible to have more than one shell in the structure. In this case we talk about multi-shelled structures. Another type is the segregated alloyed structure. Here the two metals are isolated and only share one common surface. Conversely, when two metals are solid solution they are known as random alloys. Of all the structures, core-shell and random alloy showed the best performances for several reactions, from the alcohol oxidation[131,132] to cross-coupling reactions.

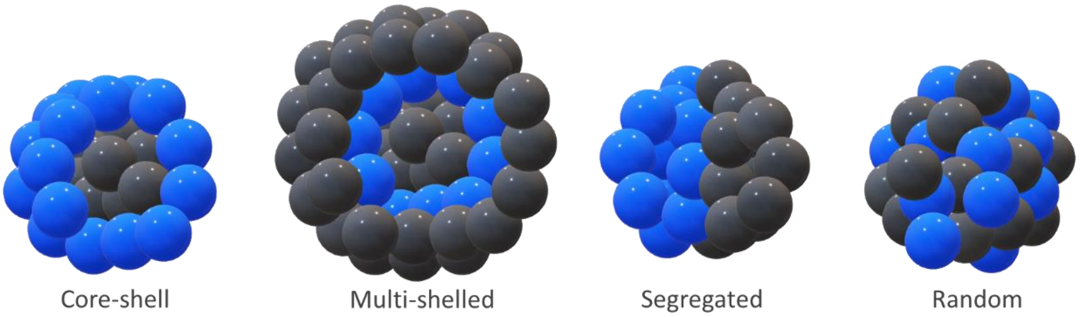

Figure 21: Schematic representation of the different bimetallic structures.

Among all, alloying is one of the most interesting method to modulate the catalytic properties of the material. In particular, two effects are responsible for its change in feature: the ligand and ensemble effects[130]. The first one is due to electronic interactions and for this reason it is also called electronic effect. The presence of a different metal causes a charge redistribution and a change in the d-band electronic structure. The latter, is due to geometric reasons and affects the lattice structure, i.e. metal-metal bond length and angle and the surface composition[133,134]. The different effects together are fundamental in enhancing the catalytic activity, stability and selectivity of a catalyst, but is very difficult to isolate them and exactly ascribe their contribution to the final result. In this field, density functional theory (DFT) is of great help to separate the effects by theoretical models[135,136].

1.2.3. Supported metal nanoparticles preparation

The synthetic procedure is one of the factors that strongly influence the properties of the NPs and so, of the catalyst. Physicists have predicted that NPs in the range of 1-10 nm possess electronic structure different from the bulk because of quantum size effect. This happens only if de Broglie wavelength of the valence electrons is of the same order of the particle itself[137]. Therefore, the control of the size and shape of nanoparticles and interplanar distances is of enormous importance to establish the activity of the catalyst. In the following section the most employed preparation method will be described, with a focus on sol-immobilization method which is the one used in this thesis work.

1.2.3.1. Co-precipitation

This method consists in the simultaneous precipitation of a soluble component with a macro-component by nucleation from a homogeneous solution after reaching the supersaturation condition of the solid. Co-precipitation produces extremely homogeneous distribution of the mixed components and a defined stoichiometry of precursors. The obtained material needs to be reduced or calcinated in order to activate the metallic phase, to eliminate the counterion of precursors and to create small and well mixed crystallites. Numerous different factors can affect the final product, e.g. temperature, pH, mixing sequence, solvent, additives, counterions and aging, making co-precipitation difficult to study and control. Moreover, this methodology requires high technology level and the difficult to control the quality of the precipitate during the precipitation step[116,138].

In this case, the support and the active phase are prepared simultaneously, while in the next methods of preparation the active phase (or its precursor) is uniformly added to a pre-synthesised support. All the following preparation techniques are ruled by nucleation and growth, interaction at the interphase and diffusive phenomena.

1.2.3.2. Impregnation

Impregnation is based on mixing the support with a solution of the metal precursor, which can fill the support's pores by capillarity. The metal does not strictly interact with the support: the interaction are hydrogen bonds, dipole-dipole interaction, London dispersion forces and van der Waals forces. Two type of impregnation procedure exists, depending on the quantity of solution used in the preparation. Indeed, in the dry procedure (called incipient-wetness), the volume of employed solution is calculated to coincide with the pore volume of the support. This method avoids the excess of precursor solution that can be deposited outside the pores, resulting in good particles dispersion. On the other hand, it is not possible to prepare catalysts with high metal loading, due to the solubility of the precursor in the amount of solvent needed. Conversely, in the wet or diffusional impregnation, in the first step the support is dispersed in the solvent and subsequently, mixed with a solution containing the precursor. In this way, the total volume used is higher than the pore volume of the material employed. In this case, the concentration gradient rules the diffusion of the solution into the pores. This method is largely employed because of its simplicity and good particle dispersion can be obtained on several porous supports. Nevertheless, heat treatment is needed in order to activate the metal phase and as a consequence, sintering can occur giving poor control on the particle size[139,140].

1.2.3.3. Chemical Vapour Deposition (CVD)

Chemical vapour deposition is largely employed to prepare 2D materials such as graphene, silicene and metal carbides. It can also be used to deposit nanoparticles on a selected support. A solid metal precursor is firstly heated in vacuum in order to be vaporized and then deposited on a solid material. Different technologies can be employed to vaporize the precursor, i.e. plasma, thermal laser, photolytic, fluidised-bed and microwave plasma. Immobilization and activation of the active phase can be obtained employing different chemical processes such as carbonisation, hydrolysis, sulfurization, pyrolysis, disproportionation, reduction, nitration and oxidation. The flexibility of the process allows to deposit numerous kinds of metal and non-metal on diverse supports. However, disadvantages are still present: precursors with high vapour pressure are needed. These chemicals and their decomposition by-products are usually very toxic and corrosive. A neutralization step is thus required, increasing the overall cost of the process[141–143].

1.2.3.4. Deposition-precipitation

In this method, the active phase is deposited by precipitation on the surface of dispersed support. A solution of the precursor is prepared and the nucleation over the support is started using a precipitating agent and specific reaction conditions. Varying the pH or the valence of the precursor and increasing the concentration of a metal complex are all conditions that can start the precipitation step. Differently from the co-precipitation method, here the limit of supersolubility of the bulk solution is not exceeded. However, this limit is surpassed at the solution-support interface where the nucleation barrier is decreased due to the strong metal-support interaction. In theory, high metal loading can be obtained using this technique due to the large volume of the starting solution. However, supports with relatively high surface area must be used in order to reach good particles dispersion, due to the necessity of a rapid diffusion of the precursor from the bulk to the interface.

1.2.3.5. Sol immobilization

Sol immobilization technique offers the great advantage of avoiding the activation step of the metal precursor after its deposition on the support. Herein, the active phase is pre-formed in the solution, and only after that, deposited on the support. This procedure prevents the changes in morphology, particle size and dispersion of the final catalyst, due to the calcination/reduction step. Metal nanoparticles are formed by adding a reducing agent to a solution of the metal salt or complex. In addition, a stabilizing agent is employed to prevent NPs agglomeration, which is a favourable process because of van der Waals attraction between them. This technique allows to control nanoparticle size and shape. In addition, virtually any support can be employed because the immobilization procedure only depends on the support's isoelectric point (IEP) and the nature of the stabiliser. Therefore, the pH and the protective agent largely influence the properties of the final material. A final step of washing is required to partially remove the protector from the active phase. It can hinders the interaction of the substrate with the metal during the reaction, decreasing the overall activity of the catalyst[144–147].

As said before, nucleation and growth are the two steps that define the production of a nanocrystals and for this reason they will be described below.

Nucleation

In the nucleation step, zero-valent nuclei are produced from a metal precursor using decomposition or reduction processes. A homogeneous nucleation is due to the uniform formation of nuclei in the liquid medium, with no presence of other crystalline species. If the metal precursor is in its zero-valent state, it decomposes and for this reason, the concentration of metal atoms in the solution increases, reaching the minimum supersaturation level. After that step, nuclei start to form by atoms aggregation (nucleation) and the concentration of dissolved metal atoms rapidly decreases under the supersaturation level, hindering any further nucleation. This process is named LaMer-type mechanism (Figure 22)[148]. If the precursor is positively charged, meaning that it is in a higher oxidation state than the metal atom, a reduction step is needed. It is not still disclosed if the precursor is reduced before or after the nucleation process. However, also in this case the formation of nuclei follows the LaMer-type mechanism[149].

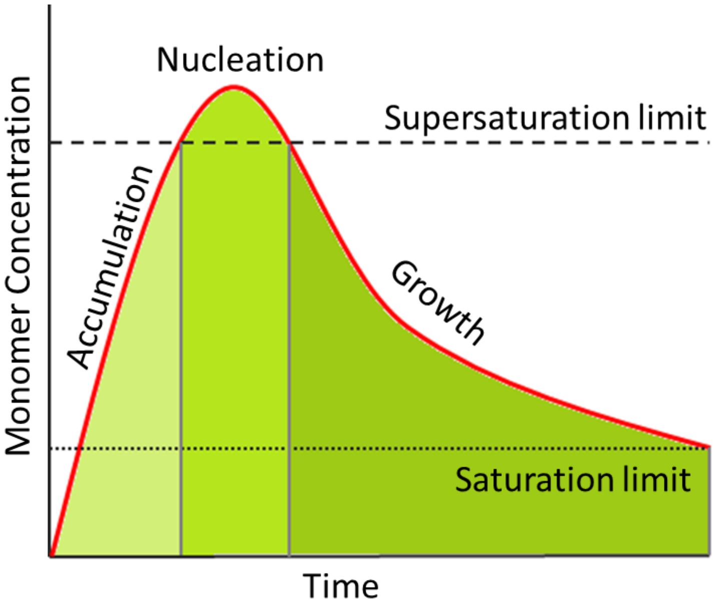

Figure 22: Different steps of nanoparticles formation following the LaMer-type mechanism: accumulation of atoms in the solution, nucleation in small clusters and subsequent growth to NPs.

The control of experimental conditions is of great importance in order to maintain reproducibility between different batches. Indeed, nucleation is extremely sensitive to stirring, impurities and temperature[150].

Growth

Nuclei are dynamic systems which are subjected to structural fluctuation, until a specific critical size. After that limit, fluctuations become too energetically costly and so, nuclei start to maintain a well-defined morphology forming structures called seeds. They can increase their size by addition of atoms still present in the solution. Two competitive forces energetically control the growth of seeds: i) the decrease of the bulk energy when the particle is growing and ii) the decrease of surface energy when an atom is re-dissoluted. In general, the first force dominates the equilibrium and leads to a continuous growth of nanocrystals. This process can be limited by the diffusion of the atoms from the solution to the seeds and the rate of atoms adsorption onto their surface[151].

However, coalescence and Ostwald ripening are other two processes that can push the growth of seeds. The first mechanism is driven by a minimization of the surface energy, merging two or more metallic atoms in larger NPs. The latter depends on the different solubility of clusters with different size. Herein, larger nanocrystals are less soluble and they can growth by deposition of nuclei derived from the more soluble smaller clusters due to their high surface energy. Both processes can broad the final average particle size if not fully limited during the growth step[152,153]. In addition, different nano-geometries can be formed during the overall step depending on the thermodynamic and the kinetic of the mechanism obtaining specific shapes requiring an accurate control over reaction parameters[149,150].

Indeed, the nature of the reducing and stabilizing agents, temperature, pH and metal precursor are all parameters that must be controlled in order to govern the features of the NPs (Figure 23).

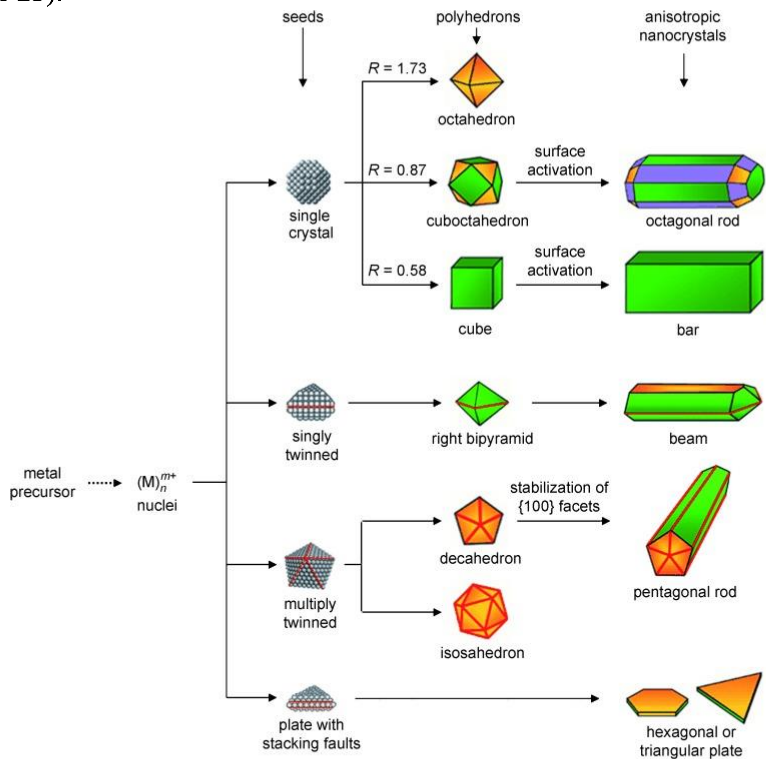

Figure 23: Different geometries produced with control of reaction parameters. Reprinted from ref. [149]: Y. Xia et al. "Shape-Controlled Synthesis of Metal Nanocrystals: Simple Chemistry Meets Complex Physics?" https://doi-org.pros2.lib.unimi.it/10.1002/anie.200802248 with the permission of John Wiley and Sons.

Reducing agent

Numerous reducing agents have been studied, but the most important and employed are sodium borohydride ($NaBH_4$)[144,146,154–156], hydrogen[157,158], hydrazine (N_2H_4)[159,160], ethanol[161], sodium citrate[162], ascorbic acid[163] and hydroxylamine[164]. Different factors influence the choice of the reducing agent depending on the desired NPs size, the stabilising agent and the temperature employed in the synthesis.

The reducing power of the agent can define the strength of the reduction. It can be described considering the standard reduction potential (E^0), which is the measure of the individual potential in standard state (concentration of 1 mol L^{-1}, temperature of 25 °C and pressure of 1 bar) against the standard hydrogen electrode. This is a simple descriptor, in fact lower is the E^0, higher is the reducing power and stronger is the reducing agent. Generally, chemicals with E^0 lower than – 0.5 V are considered strong reducing agent, while potential higher than – 0.5 V characterized the week reducing agents[165]. For example, $NaBH_4$ and hydrazine are strong agents, with a reduction potential of – 1.33 V and – 1.20 V, respectively[166,167]. The former is probably the most largely employed reducing agent for synthesising small and monodisperse nanoparticles because of the very low E^0. This allows an almost immediate reduction of the metal precursor, consuming all the metal producing nuclei and avoiding the growth step. Sodium borohydride is often added in excess and the BH_4^- ions can stabilize NPs by electrostatic repulsion. However, in acid water it hydrolyses to give Na_3BO_3 and H_2, making the stabilization effect only temporary and requiring a stabilizing agent to prevent agglomeration[165,168,169]. Hydrazine possesses a similar mechanism to the one previously explained, with a very rapid formation of nuclei and negligible growth[170]. As an example of week reducing agent, sodium citrate has a reduction potential of – 0.18 V. It is one of the oldest agents employed for preparing medium-large size gold nanoparticles. The relatively low E^0 permits a rapid nucleation mechanism without consuming all the precursor, leaving it available for the growth of nanocrystals. Citrate anions play also the role of stabilisers, adsorbing on the NPs surface and generating a negatively charged layer, which prevent further interaction[171,172].

The role of pH

Another important parameter to consider is the pH of the solution, in particular in aqueous medium. Numerous redox processes contain H^+ and OH^- specie and, for this reason, the pH can significantly affect the overall reaction. In addition, the variation of this parameter can largely influence the precursor degree of complexation and the reducing agent performance. Redox diagram can be used to disclose how the pH can affect the complexation in order to synthesise colloids with the desired properties (Figure 24)[173].

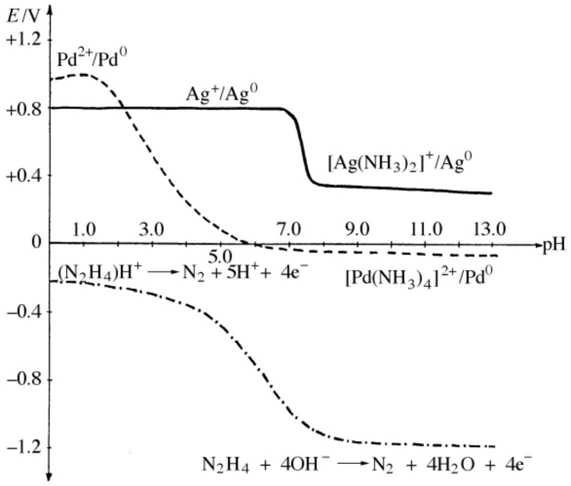

Figure 24: Influence of pH on common precursors and reducing agents. Reprinted from ref. [173]: D. V. Goia “Preparation and formation mechanisms of uniform metallic particles in homogeneous solutions” http://dx.doi.org/10.1039/B311076A with the permission of the Royal Society of Chemistry.

The role of temperature

Temperature of the reaction can have numerous effects on the final nature of NPs. Firstly, it affects the reaction potential and, for this reason, weak reducing agent are able to reduce most of the metal precursor at higher temperatures. Increasing temperature can also favour the metal precursor or stabilising agent dissolution, enhancing their solubility. Instead, high temperatures not only produce positive outcomes. In fact, it can also favour the kinetic of agglomeration process and sintering mechanism. This can result in an uncontrolled growth of the particle size and particle size distribution[174,175].

Stabilising agent

As mentioned before, the main role of stabilising agent is hindering nanoparticles agglomeration. A stabilisation by electrostatic effect is due to small molecules with a net charge. The interaction of these chemicals with the NPs generates an electric double layer that confers stabilization by repulsive Coulomb forces. Carboxylic acid, tetraalkylammonium and organosulfates are examples of electrostatic stabilisers[176]. On the other hand, the addition of bulky polymers that adsorb on the particle surface is called steric stabilisation. Are part of this category co-polymers, thiols and hydrogels[165].

In the last decades, the role of capping agents or stabilising agents have been extensively explored. It was observed that it is not only important in prevent nanoparticles aggregation, but also it has a strong influence in define activity, selectivity and stability of the final catalyst. Indeed, Villa and co-workers[145] have synthesised gold nanoparticles using three different stabilisers: polyvinyl alcohol (PVA, steric stabilisation), tetrakishydroxypropylphosphonium chloride (THPC, steric and electrostatic stabilisation) and citrate (electrostatic stabilisation). The obtained catalysts Au_{PVA}, Au_{THPC} and $Au_{citrate}$ were employed in the liquid-phase oxidation of glycerol. Au_{THPC} catalyst exhibited the highest activity, compared to the other two systems. This result can be explained by the particle size, in fact Au_{THPC} showed the lowest average diameter. However, sols had been aged for a week and tested again in the same condition. This test revealed that protecting agent play a fundamental role not only in preventing agglomeration, defining the particle size, but also in defining the activity of the final material because of the formed protective layer. Au NPs stabilised by PVA were able to maintain the initial particle size, while in Au_{THPC} system the particle grew due to coalescence forming big aggregates with the time. Indeed, stabilizing agents can poison the active phase limiting the accessibility to the metal surface, thus lowering the activity, but also can promote it enhancing yields and controlling the selectivity. Different studies have demonstrated that metal ligand interphase can influence activity, stability and selectivity due to different processes, i.e. charge transfer, selective blocking, chiral modification, steric hindrance and adsorption geometry[177]. For example, electron rich capping agents can donate electron to the metal surface and, as a consequence, favouring the adsorption of electron deficient substrates. This was proven by Zheng at al.[178] for the selective hydrogenation of nitroaromatic compounds. They modified Pt catalysts by using ethylenediamine, an electron-rich specie, leading to an enhanced selectivity to hydroxylamine. Herein, nitrobenzene is the electron deficient molecule, which efficiently interact with the catalyst to form hydroxylamine. The latter is an electron-rich product and so, it desorbs rapidly without being further hydrogenated. As said before, ligands can act as shield and can obstruct the interaction of the substrate with the metal phase. However, in some cases this capping agent shielding-effect can control the selectivity of a reaction. To be affected, a reaction has to be structure sensitive. This means that its different pathways are directly related with a specific active site of the metal NP, e.g. edge, corner or crystal planes, influencing the rate and the product distribution. Selecting a ligand which preferentially adsorb on a specific site, selectivity can be controlled. Indeed, Campisi and co-workers have demonstrated by DRIFTS-monitored CO adsorption, that PVA preferentially blocked the Pd(111) surface. This strongly affect the selectivity of benzyl alcohol oxidation reaction, inhibiting the decarbonylation pathway and favouring the formation of the aldehyde[179]. In addition, the capping agent can also control the substrate adsorption mode, again directing the final product distribution. This was confirmed by Fu et al.[180] who reported the selective hydrogenation of cinnamaldehyde. They employed amine-capped PtCo nanoparticles that give an unexpected chemoselectivity to cinnamyl alcohol. This was due to an inhibition of the flat mode adsorption onto the surface of the metal, preventing further hydrogenation of the C=C bond.

Another factor that largely influence the performance of the catalyst is the support because of the strong support-metal interaction.

1.2.3.6. The support

As mentioned before, metal NPs possess high surface energy and for this reason, they need to be stabilized. An effective strategy to avoid agglomeration is the deposition of a colloid on a selected support. This also improves the separation step of the catalyst, making easier the application, since unsupported nanoparticles are often difficult to reuse due to the small dimensions of the nanocrystals. Indeed, colloidal catalysts are generally named as quasi-homogeneous materials[181]. Consequently, a role of the support is to stabilize and immobilize metal nanoparticles, reducing their growth by agglomeration. In addition, these materials can also contribute to the overall performance of the catalyst by providing acid/base sites or through the metal-support interaction[182–187].

Metal oxides such as, CaO, MgO, TiO_2, NiO, WO_3, Nb_2O_5, CeO_2, ZrO_2 and Fe_2O_3 or SiO_2 and different types of Al_2O_3 and complex metal oxides (hydroxyapatites, zeolites, perovskites, hydrotalcites and clays) can be employed as supports. These materials are formed by a metal centre coordinated with oxygen atoms forming a stoichiometric compound and can be hydrated by interaction with water[111]. Most metal oxides are amphoteric and, therefore they can be polarized both negatively or positively. Hence, at the isoelectric point (IEP, pH value at which a generic molecule carries no net surface electrical charge), all charged are balanced giving a net zero charge. However, if the pH is higher that the IEP, the surface results negatively charged. On the contrary, if pH is lower than the IEP, the surface has a net positive charge. Then, metal nanoparticles can electrostatically interact with the support if opportunely polarised[188]. Nevertheless, some oxides, e.g. SiO_2 and MgO, possess a non-amphoteric behaviour, and in this case the material can only interact with positively or negatively charged systems. The IEP of these two materials are 1 and 12, respectively (Figure 25).

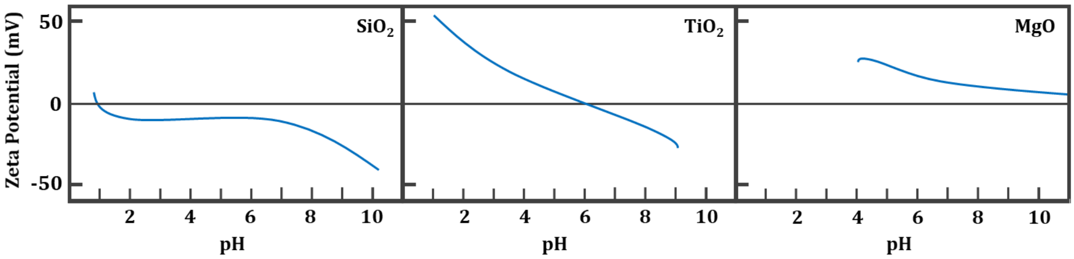

Figure 25: Representative images from the left of: acid, amphoteric and basic metal oxides and charge behaviour at different pH.

Another wide group of supports is carbonaceous materials. Indeed, they have the advantage to be easily modified through a variation of their structures, changing porosity and surface area or adding functional groups and topological defects. Combining these tuning possibilities leads to infinite modification possibilities to enhance metal support interaction but also to act as catalysts themselves, without metal[189–196]. A review of these materials will be given in the next section of the thesis.

1.3. Carbonaceous materials in catalysis

The catalytic properties of carbon materials, as support and catalyst, are mainly due to their surface features, which are consequences of the carbon atom nature. Carbon is the fourth most abundant element in the universe, and it is also a fundamental element in all life forms. The starting point of its chemistry is its tetravalent nature (four electrons available to form four chemical bonds), which confers the ability to form long chains by forming single C-C bonds but also to link with numerous other elements and so, explaining the variety of carbon-based compounds and its abundance in life. In addition, from its electronic configuration ($1s^2$ $2s^2$ $2p^2$), one 2s electron can be promoted to the p subshell forming the configuration $1s^2$ 2s $2p^3$. This promotion cost energy, which is usually compensated by the formation of stable bonds. They can be tetrahedral (sp^3) but also planar with three sp^2 hybridized covalent bonds and one p-orbital or linear (sp hybridization)[197].

1.3.1. Carbon allotropes

These numerous bond possibilities allow the formation of numerous allotropes, such as fullerene (zero-dimensional), carbon nanotubes and fibers (one-dimensional), graphene and graphite (two-dimensional and formed of only sp^2 hybridized carbons) and diamond (three-dimensional, sp^3 hybridized). Diamond and graphite are the traditional allotropes, which occur in nature. The others have been synthesised during the last decades and are indicated as synthetic carbon allotropes (SCA), although they are not real allotropes because in these compounds carbon also bonded heteroatoms[198]. The physic-chemical properties vary widely with the type of allotrope, and as a consequence, they all have different applications. Diamond possesses carbon atoms bonded tetrahedrally by sp^3 hybridization. It is transparent and hard, with a large band-gap between the valence and the conducting band[199]. Diamond can be found in nature but also synthesised by treating other allotropes, such as graphite at high pressure. In addition, it is an electrical insulator, the best natural thermal conductor and the hardest material (Figure 26)[199,200].

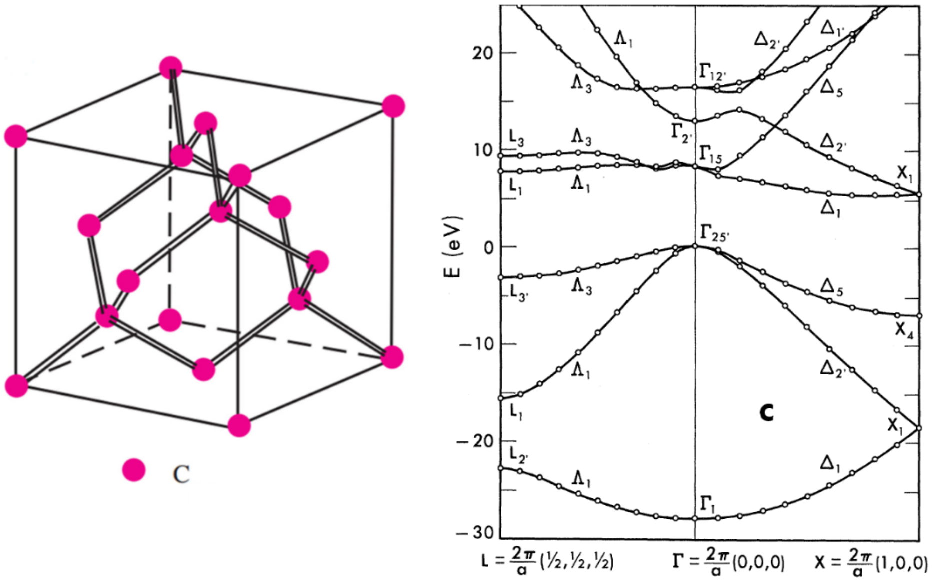

Figure 26: on the left: fcc structure of the diamond, on the right: diamond band structures. Reprinted from ref. [199]: W. Saslow et al. “Band Structure and Optical Properties of Diamond” https://doi-org.pros2.lib.unimi.it/10.1103/PhysRevLett.16.354 with the permission of the American Physical Society.

Diamond in its natural state is inert and it does not find any application, aside from exploiting its thermal conductivity and hardness[200]. However, it can be doped, especially with boron to produce a semi-metallic material, finding application in electronics. Boron possesses one electron less than carbon but similar radius, allowing easy incorporation in the diamond lattice as charge-acceptor and forming p-type semiconductor[201].

Diamond also finds many different applications when its particle size is in the nanoscale level (named nanodiamond, ND)[202]. NDs possess a complex structure of a diamond core and a graphitised carbon shell (Figure 27).

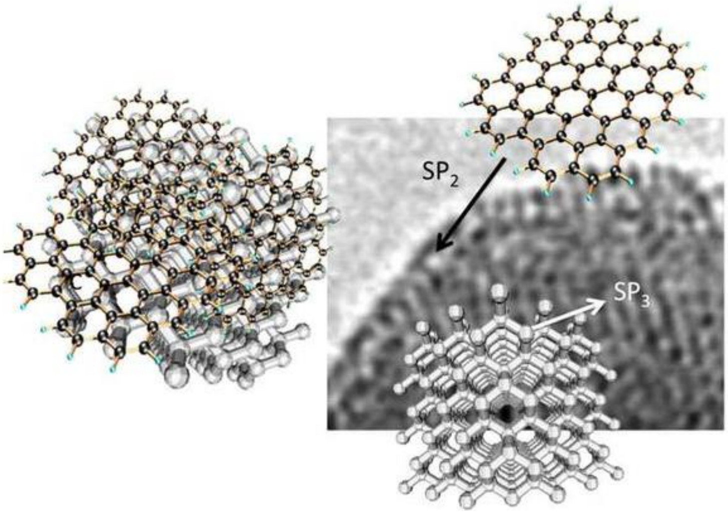

Figure 27: left: scheme of the structure of a nanodiamond; right: TEM image of a detonated nanodiamond structure, where it can be seen the external graphitic shell and the internal diamond core. Reprinted from ref. [211]: A. Apicella et al. “Hybrid Ceramo-Polymeric Nano-Diamond Composites” https://doi.org/10.3844/ajeassp.2018.766.782 with the permission of Science Publications.

Nanodiamonds can be applied in catalysis but also in sensors, optical computing, medicine and electrical energy storage due to their physical properties[202].

In catalysis, NDs are employed from the beginning of the 1990s because of their unique features, such as high thermal and chemical stability. Therefore, they can be applied in a wide range of reactions, such as dehydrogenation of propane[203] or butane[204], hydrogenation of C-C double and triple bonds[205,206], oxidative dehydrogenations[207], CO_2 reduction[208] and dechlorinations[209]. In addition, NDs have a small particle dimension and a relatively high surface area. They possess an average particle size between 4 and 8 nm. NDs large surface to volume ratio permits an higher surface reactivity than other carbons[207,210]. Indeed, nanodiamonds can be employed as support for metal NPs or as carbon-based catalysts because of their core-shell sp^2-sp^3 structure [211] that can be doped especially to form oxygen functional groups[212].

Differently from diamond, graphite is a semi metal and an electrical conductor. This is due to its layered structure, where in each layer carbon atoms are arranged in hexagonal rings. Above and below the planes, delocalized π-electrons are free to move conducting electricity along the layers. Isolating a single layer of graphite, a pure 2D structure can be obtained, named graphene (Figure 28). It attracted a lot of interest because of unique electrical properties, ambipolar electric field, high adsorption of white light, high surface area and elasticity[213]. These features are mainly due to the structure of the valence and the conducting bands that are in contact with each other[214].

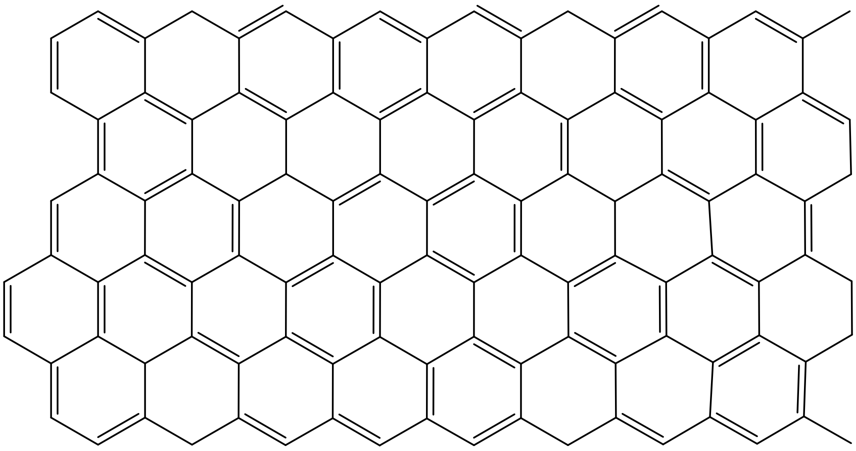

Figure 28: graphene layer composed by condensed benzene rings.

In catalysis graphite and its derivatives, such as graphene oxide (GO) and reduced graphene oxide (rGO), found numerous applications because of their chemical resistance and thermal stability. Moreover, depending on the type of atom involved, graphene shows a high adsorptivity on the top (T), hollow (H) and bridge (B) sites (Figure 29). Atoms can be adsorbed by physisorption (Cu, Ag and Au), or strong covalent interaction (Pt, Pd and Ni)[215]. This mainly depends on the properties of the adsorbate and the site. As an example, Cu, Ag and Au have a half-filled d-shell and they show long bond range. For this reason, they are expected to be physisorbed. In contrast, adatoms that have short bond distances, such as Pt, Pd and Ni form stronger covalent bonds with graphene layer, showing more resistance to migration[216,217].

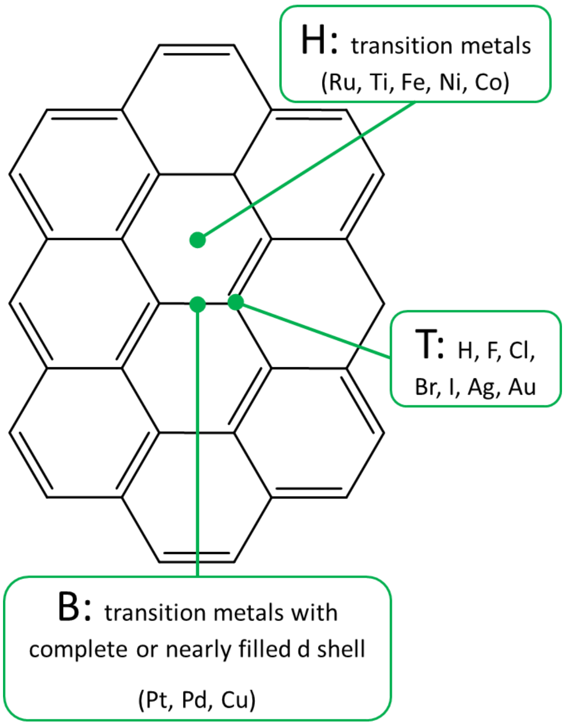

Figure 29: different adsorption sites of high symmetry and types of adatoms interacting with them.

Bare graphene is not very active as catalyst, due to its inactive π-conjugated system and for this reason, modification of its structure by adding heteroatoms or defect is needed. Effort have been made to use its oxidative derivates in catalysis, such as graphene oxide (GO), and reduced graphene oxide (rGO), but also adding different type of heteroatoms (P, B and N). These modifications can improve the catalytic properties in heterogeneous catalysis but lowering the conductivity and reducing the mobility of electrons by the introduction of defects[215,218].

Other allotropes can be derived from graphene such as fullerenes, nanotubes and nanofibers. Fullerene (C_{60} and C_{70}) structure corresponds to a closed C-atoms cage. This structure was predicted in 1970 and 15 years later, the existence of fullerenes was demonstrated experimentally[197]. The C_{60} molecule is formed by 20 hexagonal faces and 12 pentagonal faces, producing a truncated icosahedron (Figure 30). The insertion of a five hexagonal faces ring in its equatorial plane forms a C_{70} molecule. Similar insertion produces high ordered fullerenes. C-C bonds can be either singular (1.46 Å) or double (1.40 Å) along the pentagonal edges or between adjacent hexagons, respectively.

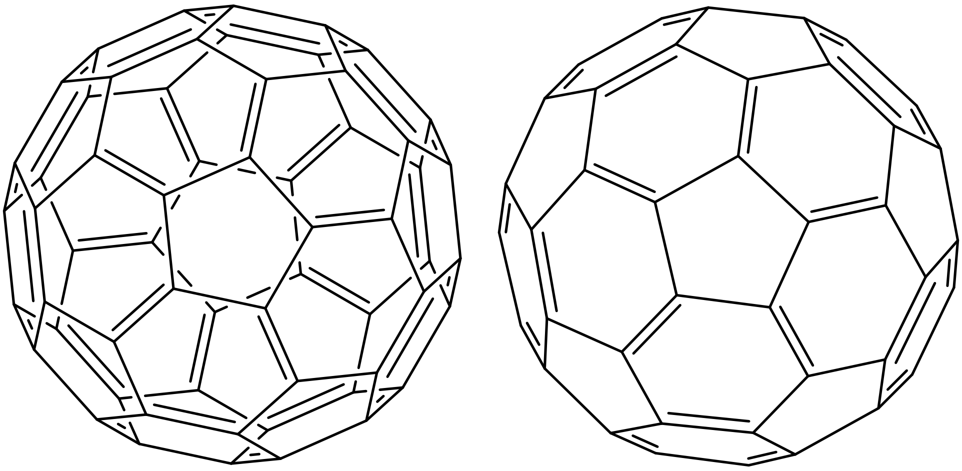

Figure 30: top (left) and side (right) views of a C_{60} fullerene.

Fullerenes can be doped with Rb, Cs, K and Co and employed as T_c-superconductors[219] or ferromagnets[220] and insulators[221]. In addition, it is utilized in polymer solar cells because of its strong acceptor properties[197]. Several are also the applications in catalysis. They can act as ligands in homogeneous catalysis, as support for metal NPs but also as catalysts themselves[222].

The insertion of numerous rings composed by hexagonal faces to a fullerene leads to the formation of carbon nanotubes (CNTs). They consist in a graphitic layer rolled up into a cylindrical shape. CNTs can have metallic or semiconductive behaviour depending on the arrangements of the hexagonal rings. They can be classified according to their rolling direction (helicity) as zig-zag and armchair (Figure 31).

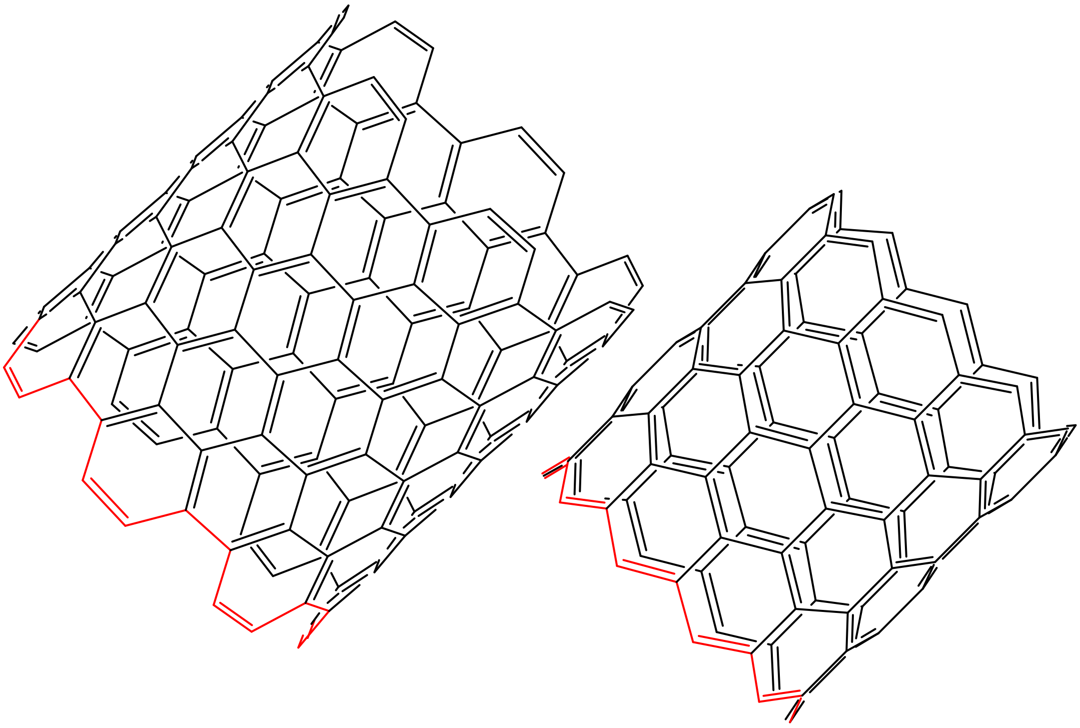

Figure 31: armchair (left) and zig-zag (right) carbon nanotubes.

Single-walled carbon nanotubes are composed of one cylindrical tube, while multi-walled carbon nanotubes are characterized by concentric cylindrical tubes (MWCNTs). They have a diameter typically of few nanometres, whereas the length can be of several centimetres[223]. A different allotrope which has curve sp^2 hybridization as fullerenes and CNTs is carbon nanofibers (CNFs). Despite this, the structure of CNFs is substantially different from the one of CNTs. In MWCNTs the different cylinders are axially aligned and formed mainly of hexagonal substructures. On the other hand, nanofibers are classified according to their graphene layer orientation, characterized by the angle (α) between graphene sheet and the fiber axis. CNFs with an angle between 0 and 90° are named fishbones, while with a $\alpha=0$ they are ribbon and correspond to nanotubes (Figure 32 b and c). In Figure 32 a are represented platelet nanostructures[224,225].

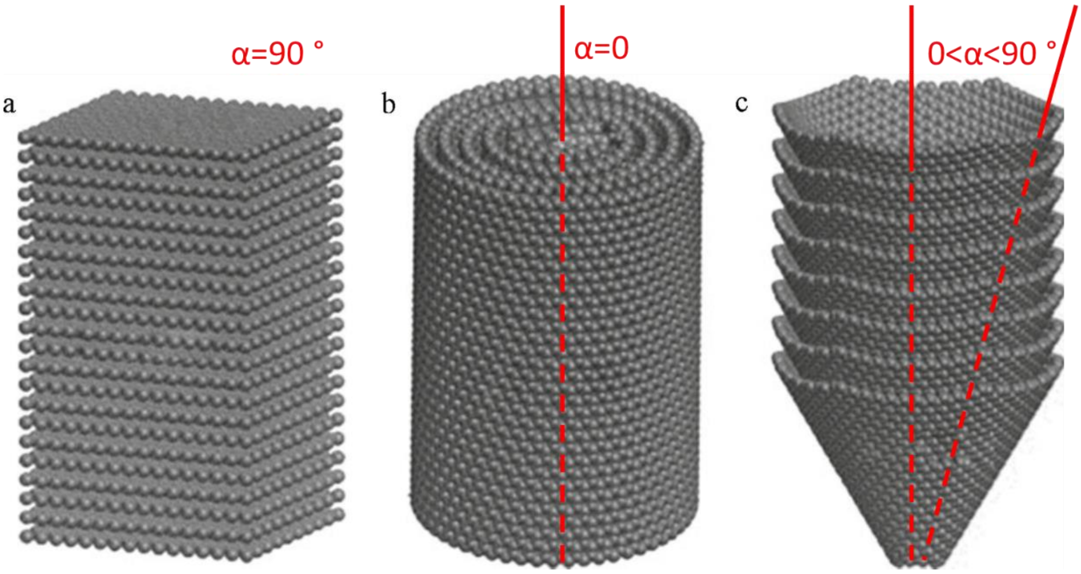

Figure 32: schematic representation of a) platelet, b) ribbon (CNTs) and c) fishbones carbon nanofibers. Adapted from ref. [224]: H. Y. Cheng et al. “Modelling of fishbone-type carbon nanofibers with cone-helix structures” https://doi.org/10.1016/j.carbon.2012.05.005 with the permission of Elsevier.

In addition, both simulations and experimental results have shown that fishbones CNFs can adopt two different topological structures: stacked-cup and cone-helix. The former is composed of discrete graphene cones periodically organised along the axis, while in the latter, graphite ribbons spiral along the axis. The different structure confers to CNFs different properties: fishbones with a cone-helix structure present improved thermal and electrical conductivity and superior mechanic strength than the stacked-cup counterparts[192,224,226].

CNTs and CNFs have been attracting a lot of attention in catalysis as catalyst or support since the first published report in 1994[227]. Numerous features make them interesting and attracting materials in this field, such as the large number of edges which provides anchoring sites for NPs and easily tuning possibilities by oxidation, ion doping by N and B and using confinement effect[192,228]. Moreover, they possess high surface area and large mesopores which can stabilise the active metal phase and unstable products. A fundamental feature of CNFs is the higher energetic diffusion barrier of metal atoms respect to the one on CNTs. As a consequence, metals on CNFs are more strongly anchored and then, more stable than on CNTs.[192].

All the allotropes described until here have ordinated structures, although amorphous materials exist. Indeed, amorphous carbon (aC) is a very reactive carbon which do not possess a crystalline structure, but it can present short range order. This structure is composed by a mixture of sp^3 and sp^2 hybridized carbon bonded in a random network configuration (Figure 33). Due to this fact, aC shows features intermediates between diamond and graphite: diamond like behaviour dominates the mechanical properties, while electrical characteristics are represented by the amount of sp^2 carbon. If the reactive dangling -bonds of amorphous carbon are saturated by hydrogen the material is named hydrogenated aC (H-aC), whereas if the allotrope is extremely dense of sp^3 hybridized carbon we talk about diamond-like carbon or tetrahedral amorphous carbon (ta-C). In the latter case, the structure can be seen as a random tetrahedral network with sporadic sp^2 bonds. The reactivity of this materials strictly depends on their structures, sp^2/sp^3 ratio and dangling bonds, which are strongly governed by the synthetic procedure. In other words, aC are unpredictable materials, which changes from batch to batch[229–231].

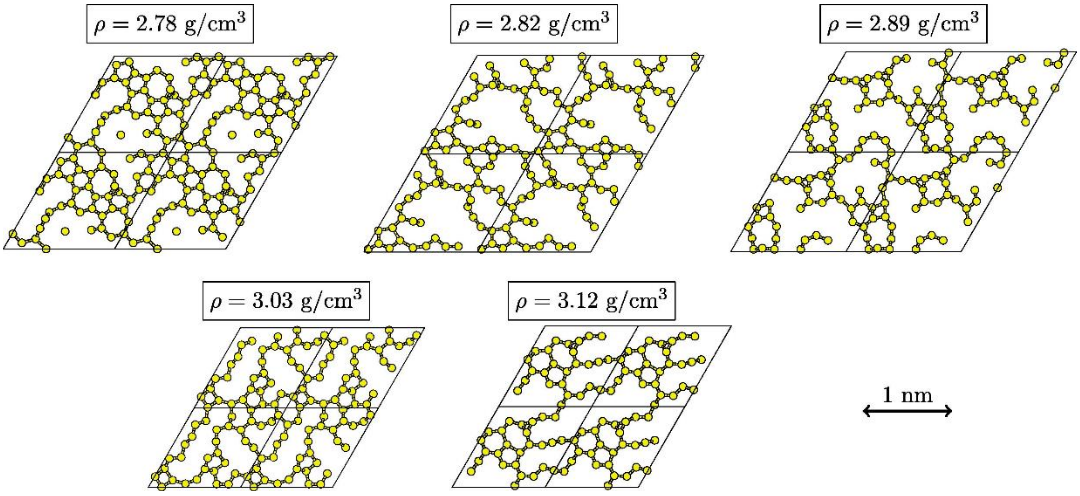

Figure 33: examples of obtained surface structures of amorphous carbon with different densities. Carbon is represented in yellow. Reprinted from Ref. [229]: M. A. Caro et al. "Atomic and electronic structure of tetrahedral amorphous carbon surfaces from density functional theory: Properties and simulation strategies" https://doi.org/10.1016/j.carbon.2014.06.060 with the permission of Elsevier.

Another class of amorphous carbon allotrope is glass-like carbon or glassy carbon (GC). This material is prepared by firing polymeric precursors (phenolic resins or furfuryl alcohol resins) in inert atmosphere. It possesses a number of different advantageous features, i.e. low density, high strength and hardness, resistance to corrosion and extreme impermeability to both liquid and gas. It is employed in the engineering of component used under extreme conditions, but also as electrode material for electrochemical reactions. Its structure consists of nearly 100 % sp^2 carbon bond. GC final morphology strongly depends on the temperature of the heat treatment and is divided into two main categories: the type-I GC obtained at temperatures lower 2000 °C, which is mainly composed of randomly disposed curved graphene layer fragments and the type-II GC produced at temperatures near 2500 °C, containing fullerene-like spheroids (FLS), connected by a disordered multilayer graphene (Figure 34). This material does not find application in liquid-phase catalysis[232–235].

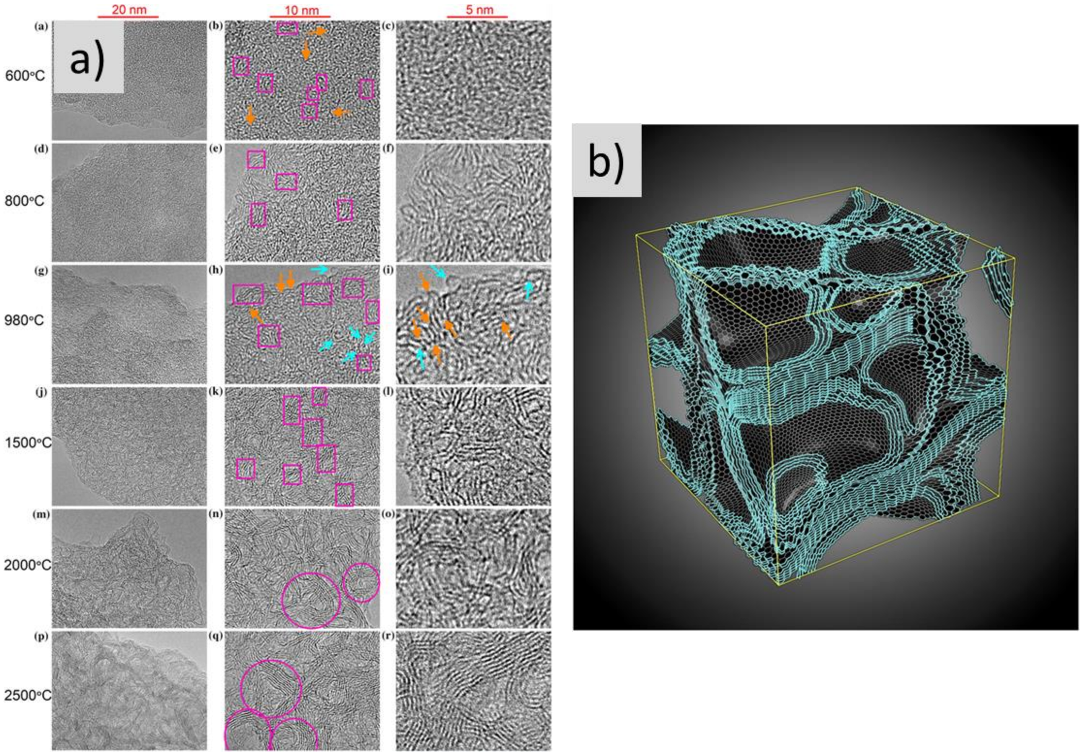

Figure 34: a) representative HRTEM images of different GC regions pyrolyzed at temperatures between 600 and 2500 °C. Rectangles indicates domains containing graphene and circles onion-like structures; b) reconstruction of FLSs connected by graphene layers in a type-II GC. Adapted from a) Ref. [232]: K. Jurkiewicz et al. "Evolution of glassy carbon under heat treatment: correlation structure–mechanical properties" https://doi.org/10.1007/s10853-017-1753-7 with the permission of Springer and b) Ref. [233]: Z. Zhao et al. "Nanoarchitectured materials composed of fullerene-like spheroids and disordered graphene layers with tunable mechanical properties" https://doi.org/10.1038/ncomms7212 with the permission of Springer Nature.

1.3.2. Modification of the surface structure of carbon materials

Carbon martials can be easily tuned by the introduction of heteroatoms and the addition of defects in their structure. These modifications can allow enhanced catalytic features as supports and as catalysts. An insight into the different type of defects and heteroatoms will be given in the next sub-section.

1.3.2.1. Defects

The different hybridization of carbon atoms in carbonaceous materials allows them to host different lattice defects because of reconstruction and rearrangements. Defects can be naturally contained in these materials but also con be inserted especially in the graphitized ones by chemical treatments or irradiation[215,218,236,237]. Graphene can be employed as a case of study to investigate the different defective structures valid also for other nanostructured carbon materials[218]. Indeed, sp^2-hybridized carbon atoms can form not only hexagons, but also different polygons, such as pentagons and heptagons, to form different structures and saturate the dangling carbons. These non-hexagonal rings can curve the graphene layer, depending on the symmetry of the polygons obtained. Even though with saturated bonds, these structures can be more reactive than pristine graphene, interacting and adsorbing other species due to the perturbation of π-electrons. In fact, different studies have shown that pristine graphene possess an inactive π-conjugated system, which is inert in the adsorption of molecules, although it can interact with atomic species (see section 1.3.1. and Figure 29)[238–240]. Defects in graphene can lead to infinite structures and morphologies. In the next sections only the simplest and most common ones, i.e. point defects, will be discussed

Point defects are zero-dimensional structures and vacancies and reconstructions are part of this group[241].

Single vacancy (SV)

Single vacancy is produced by removing one atom and it is the simplest defect in any material. SV has been observed experimentally by TEM (Figure 35 a)[242]. As it can be seen from Figure 35 b (red circles) the dangling bonds distort the structure decreasing the distance between each other toward the missing atom. This defect leads to an increase in the local density of states at Fermi energy, localized on the dangling carbons. The formation energy of this defect is relatively high (approximately 7 eV) because of the unsaturated bonds[241,243].

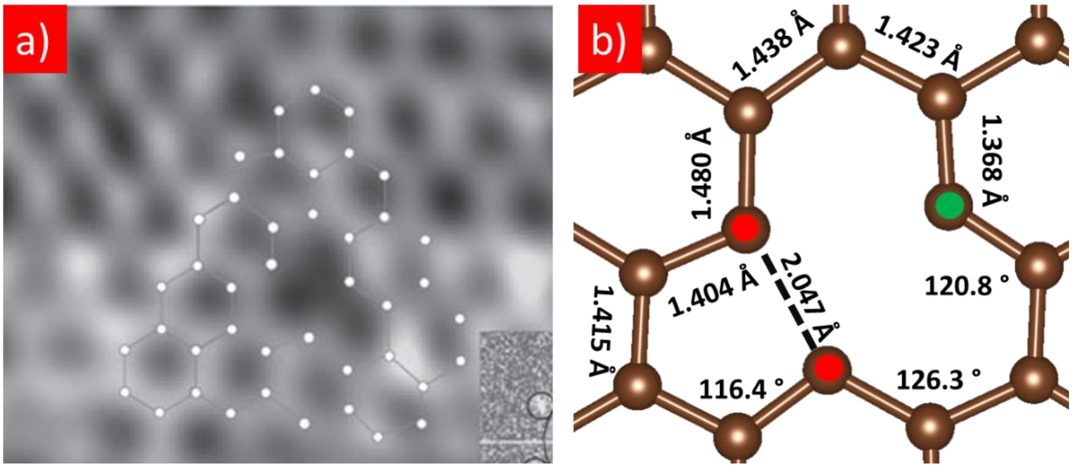

Figure 35: a) TEM image of a single vacancy defect in graphene. Adapted from Ref. [242]: M. H. Gass et al. "Free-standing graphene at atomic resolution" https://doi.org/10.1038/nnano.2008.280 with the permission of Springer Nature. b) Optimized SV structure. Circles are highlighting the dangling carbon, in red the distorted bonds.

Double vacancy (DV)

Double vacancy is obtained either by removing two neighbouring carbon atoms or for two SV coalescence. Also in this case, DV was observed by TEM (Figure 36 a)[242]. However, this defect does not possess dangling bonds, in fact the vacancy is fully reconstructed forming two pentagons and one octagon, instead of four hexagons (Figure 36 b). The formation energy of a DV is of the same order (near 7 eV) of a single vacancy. On the other hand, because two C atoms are now missing, the energy per missing atom is much lower than in SV. Indeed, double vacancy is thermodynamically favoured than single vacancy[241,243].

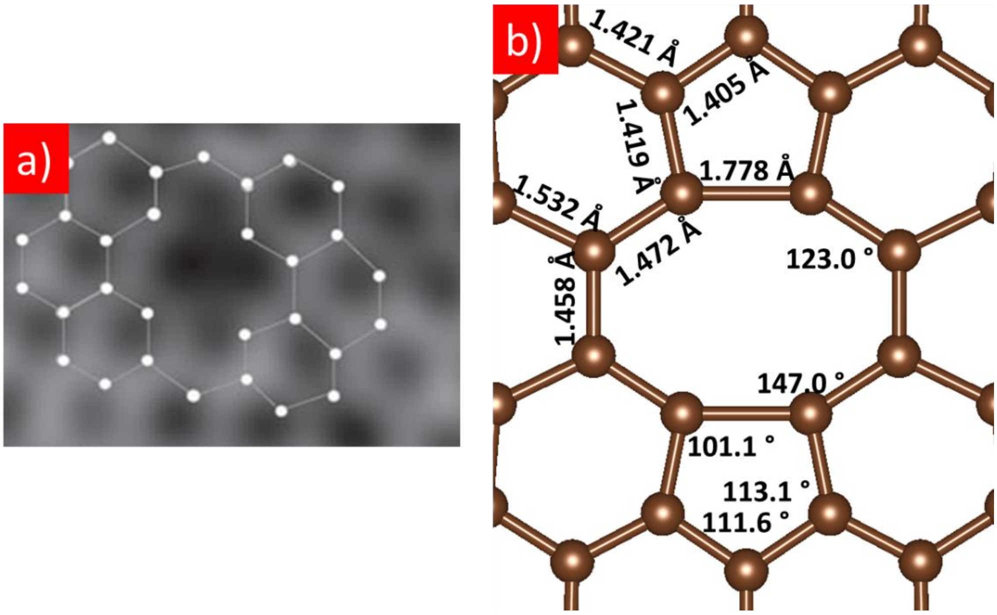

Figure 1: a) TEM image of a double vacancy defect in graphene. Adapted from Ref. [242]: M. H. Gass et al. “Free-standing graphene at atomic resolution” https://doi.org/10.1038/nnano.2008.280 with the permission of Springer Nature. b) Optimized DV structure.

Stone-Wales defects (SW)

Stone-Wales defects are formed by non-hexagonal rings produced by the rotation of C-C bonds. Three types of SW exist: one derived directly from pristine graphene, without any missing C atoms (SW1) and the others obtained from a double vacancy (SW2 and SW3).

In the former case, without removing or adding any atoms, one C-C bond rotates of 90° forming two pentagons and two heptagons from four hexagons (Figure 37)[244]. This defect has a formation energy of approximately 5 eV, which is very low in respect of the case of vacancies. Indeed, no dangling bonds are introduced and the same number of C atoms are retained in the transformation[241,243].

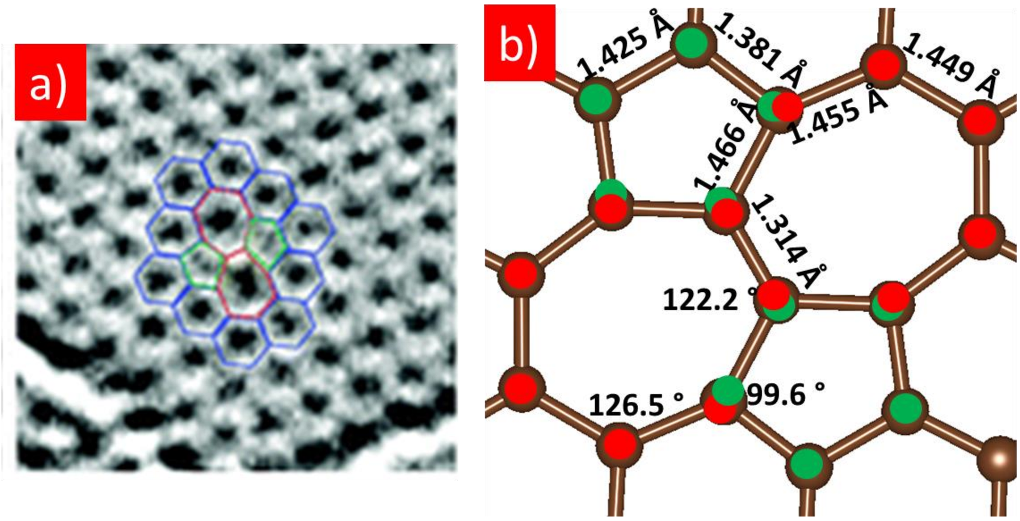

Figure 37: a) TEM image of a SW1 defect in graphene. Adapted from Ref. [244]: J. C. Meyer et al. “Direct Imaging of Lattice Atoms and Topological Defects in Graphene Membranes” https://doi.org/10.1021/nl801386m. Copyright 2008, American Chemical Society. b) Optimized SW1 structure. In red heptagons and in green pentagons.

DV is not the only structure obtained from a graphene with two missing C atoms. Analogously to the formation of SW1, SW2 can be formed by a rotation of 90° of one of the octagon bonds in DV, transforming it into three pentagons and three heptagons (Figure 38)[245]. The energy formation of this structure is approximately 6 eV (1 eV less than the formation energy of DV). Indeed, it is more favourable than the double vacancy defect[241,243].

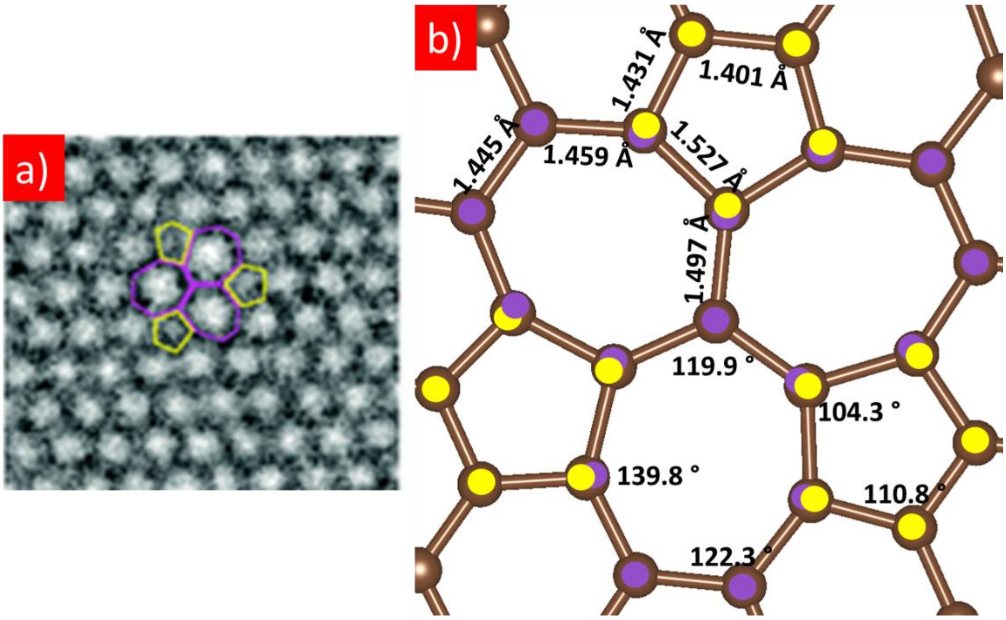

Figure 38: a) TEM image of a SW2 defect in graphene. Adapted from Ref. [245]: J. Kotakoski et al. “Stone-Wales-type transformations in carbon nanostructures driven by electron irradiation” https://link.aps.org/doi/10.1103/PhysRevB.83.245420. Copyright 2011, American Physical Society. b) Optimized SW2 structure. In purple heptagons and in yellow pentagons.

Rotating another bond, the SW3 defect can be obtained. It is formed by four heptagons and four pentagons with a hexagon in its centre[245] (Figure 39). Its formation energy has a value between the DV and SW2. Differently from SV, all this multiple vacancy structures cannot migrate, making them completely immobile in the graphene layer[241,243].

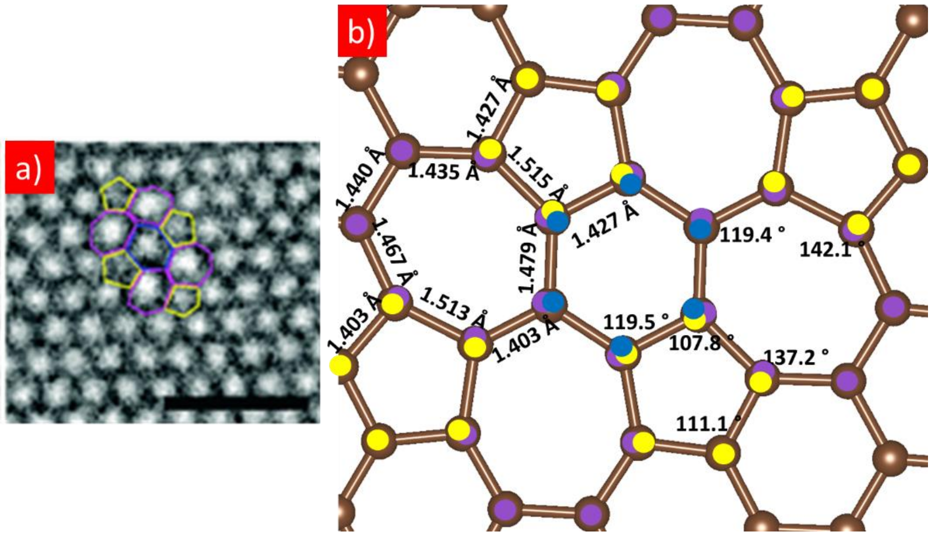

Figure 39: a) TEM image of a SW3 defect in graphene. Adapted from Ref. [245]: J. Kotakoski et al. "Stone-Wales-type transformations in carbon nanostructures driven by electron irradiation" https://link.aps.org/doi/10.1103/PhysRevB.83.245420. Copyright 2011, American Physical Society. b) Optimized SW3 structure. In purple heptagons, in blue the hexagon and in yellow pentagons.

Besides point-defects, heteroatoms can be easily inserted in carbonaceous material structures in order to modify their surface and to enhance the interaction with metallic species and molecules.

1.3.2.2. Introduction of heteroatoms in carbon materials

Carbon materials are composed by sp^3- and sp^2-hybridized carbon. The order and the planarity depend on the degree of graphitization. The arrangement of graphene sheets governs the physicochemical properties of these materials and their application. Indeed, their reactivity with molecules depends on their disordered fraction, i.e. imperfection and dangling bonds inside the structure or at their edge, which are the most active site. In the active sites, characterized by a high density of unpaired electrons, heteroatoms such as oxygen, nitrogen, phosphorous and boron can bond forming stable compounds[246–250]. The groups inserted are similar to the ones encountered in organic chemistry. Although the complexity of the carbon surface makes the features of these groups not fully predictable[251].

Oxygen functionalities

Oxygen functional groups are already present in the carbonaceous structure, and they strongly affect reactivity and activity of the carbon material. Oxygen can also be synthetically introduced by oxidation treatments. Oxidation of carbonaceous structure often allows further interaction with other groups such as nitrogen, but also can increase the hydrophilicity of the carbon surface. The typical oxygen containing functionalities are shown in Figure 40, such as carboxylic, phenolic, ketone and epoxides[251].

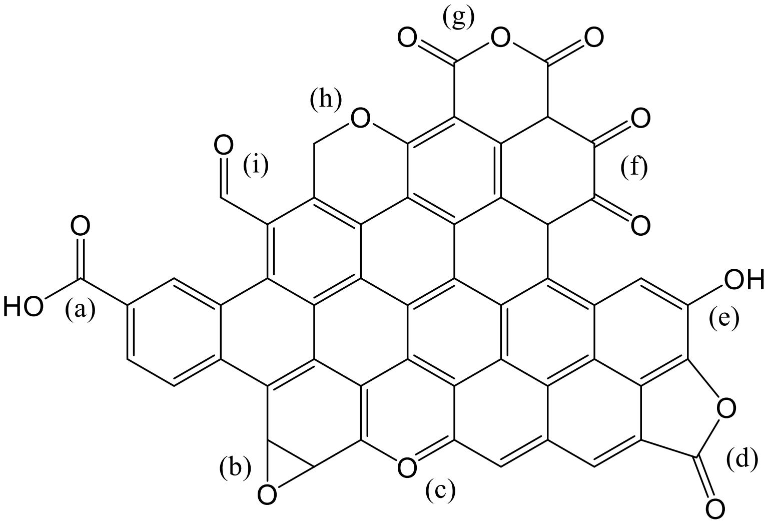

Figure 40: typical oxygen functional groups on carbon surface: a) carboxyl, b) epoxide, c) pyrone, d) lactone, e) hydroxyl, f) quinone, g) carboxylic anhydride, h) ether and i) carbonyl.

Usually, the addition of oxygen functional groups increases the acidity of the material. Acid groups are inserted by oxidative treatment in both liquid and gas-phase. In particular, in gas-phase treatment where oxygen, ozone or air are used at high temperatures (473-623 K), weak acidic groups, such as phenols, are predominantly introduced. Liquid-phase oxidation is normally performed using, nitric acid, hydrogen peroxide, sulfuric acid, potassium permanganate or sodium peroxydisulfide. Using strong oxidant such as, nitric acid or sodium peroxydisulfide leads to a surface mostly functionalised with carboxyl groups, while employing hydrogen peroxide produces a majority of phenols. Numerous oxidizing treatments are ended by washing the material with water, in order to remove the excess of oxidant or water-soluble products obtained in the process[252–255]. On the contrary, basic groups are obtained by reduction of the inserted oxygen groups or heating in inert atmosphere. The decomposition of the acid functionalities, i.e. carboxylic acid, lactone and phenols, results in active sites which are treated in air to form basic groups such as pyrones[251]. Here, the higher is the temperature the stronger is the effect of the oxidation. Indeed, Andrade and co-workers[256] have studied the effect of temperature in the oxidation treatment with HNO_3 of CNTs. Four different temperatures were selected (25, 75, 125 and 175 °C) and the amount of oxygen was analysed by EDS. It was found that the sample oxidised at 175 °C present the highest O amount. Moreover, it was showed that the type of acid doping changes with temperature. In particular, D’ Arsié et al.[257] doped a graphene monolayer with HNO_3 at different temperatures. At mild conditions (20 °C), graphene only adsorbed NO_3^- ions, which can easily desorb at low temperatures. On the contrary, increasing the temperature (52 °C) stable p-type doping was created. In addition, it was found in different studies that the concentration of different functional groups introduced changes with time. In particular, if the carbonaceous material is exposed for enough time to allow the reaction phenols, carbonyl and quinones groups can be converted into carboxylic functionalities[258,259].

Nitrogen functionalities

In the case of introducing N-functionalities, an N-rich precursor, such as carbazole, N-polymers, melamine or acridine, can be employed during carbon material synthesis. Moreover, nitrogen can be inserted onto the carbon surface by either liquid or gas post-treatments with nitrogen containing molecules. For example, ammonia is used in gas phase, at temperatures between 673 and 1273 K. In the liquid phase, compounds as carbazole, N-rich polymers, melamine and urea are employed and added to a suspension of the carbon in water or alcohol. The obtained material is then heated at temperatures between 673 and 1293 K. In order to increase the nitrogen content, pre-oxidised carbons can be used. In this case, the procedure results in the formation of chemical bonds between a basic nitrogen precursor and the O-containing carbon matrix[260–263]. The reactivity of the final material is determined by its acid or basic character, as in the case of oxygen. Treatments below 800 K involving amination and ammoxidation reactions, result in the production of lactams, amides and imides, which are slightly basics. On the contrary, employing higher temperatures leads to the conversion of the previously discussed groups into quaternary nitrogens, pyridines and pyrroles, increasing the basicity of the material and the surface polarity[251,260,262,264–267].
Indeed, the types of nitrogen functionalities added on the carbon matrix strongly depend on the treatment, i.e. precursors employed, chemical activity of the carbon surface and, among all, temperature of the heat treatment step, and they are summarized in Figure 41[251].

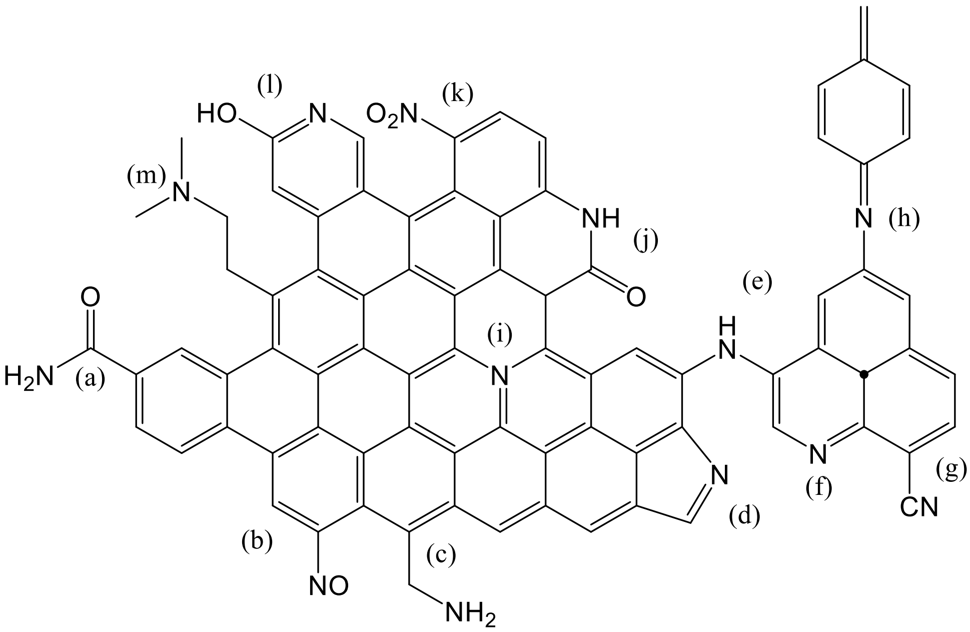

Figure 41: typical nitrogen functional groups on carbon surface: a) amide, b) nitro, c) amine, d) pyrrole, e) secondary amine, f) pyridine, g) nitrile, h) imine, i) quaternary amine, j) lactam, k) nitroso, l) pyridine and m) tertiary amine.

Boron functionalities

Boron atoms can be easily incorporated into the carbon lattice because of their size similar to the C ones, and substituted in both sp^2 and sp^3 configuration, forming BC_3 units[251]. The formed B-C bond possesses a length longer of the 0.5 % of the C-C bond, leading to disordered layers and obtaining p-types carbon materials because of the three valence electrons of boron. B-doped carbon materials can be directly produced by annealing treatment with $T < 1200$ °C, chemical vapour deposition (CVD) method, plasma etching, arc discharge and laser ablation[268–270]. In this case, the final materials have high crystallinity, but the excess of precursors (such as, BN, BCl_3, $C_9H_{18}BO_3$ or $C_6H_{15}BO_3$) usually forms different by-products, such as boron carbide, boron nitrate and boron particles affecting the obtained structure. In addition, these processes are expensive and complicated requiring high vacuum conditions[251,268–270]. Another option is the postgrowth substitution reaction, where the pre-formed carbon material interacts with the boron precursor (usually, boric acid or boron oxide) at high temperatures. Controlling temperature and reaction time, a uniform and controllable B distribution can be obtained. Employing O-containing precursors, weak B-O bonds can be formed, which can be eliminated and transformed in B-C bonds by increasing reaction time and temperature. The different bonding configurations of B doping in carbon materials are shown in Figure 42[271,272].

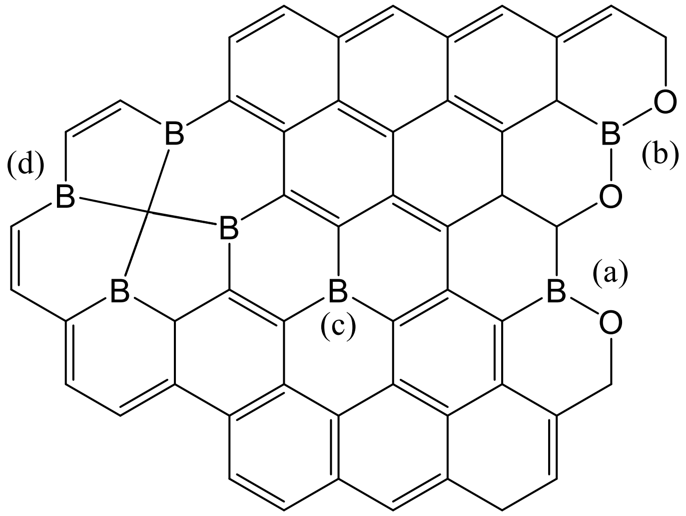

Figure 42: scheme of boron configuration on carbon surface: a) BC_2O, b) BCO_2, c) BC_3 and d) B_4C.

Phosphorous functionalities

Phosphorous functionalities can be incorporated into the carbonaceous structure by using phosphoric acid (H_3PO_4) in liquid and gas phase and forming acidic P-O based groups[251]. In addition, these functionalities possess the ability to strongly interact and to electronically modify metal atoms[273,274]. Usually mild conditions (liquid phase, 100 °C) are preferably employed among gas phase treatments (800 °C in argon atmosphere), obtaining functionalities attached at the surface by the formation of C-O-P bonds[251,275]. In this case, a mixture of HNO_3 and H_3PO_4 is used, firstly introducing O-functionalities, which act as anchoring sites for phosphorous[276,277]. The formed $-O-PO_3$ however, are not stable due to the easy breakage of -O-P bond leading to the loss of the functionality. For this reason, thermal treatment at temperatures between 400 °C and 600 °C are employed to transform these groups to the more stable $-PO_3$ ones, which contains the stronger -C-P bond, leading to enhanced stability of the functionalities[273,274]. Different phosphate-carbon complexes are shown in Figure 43.

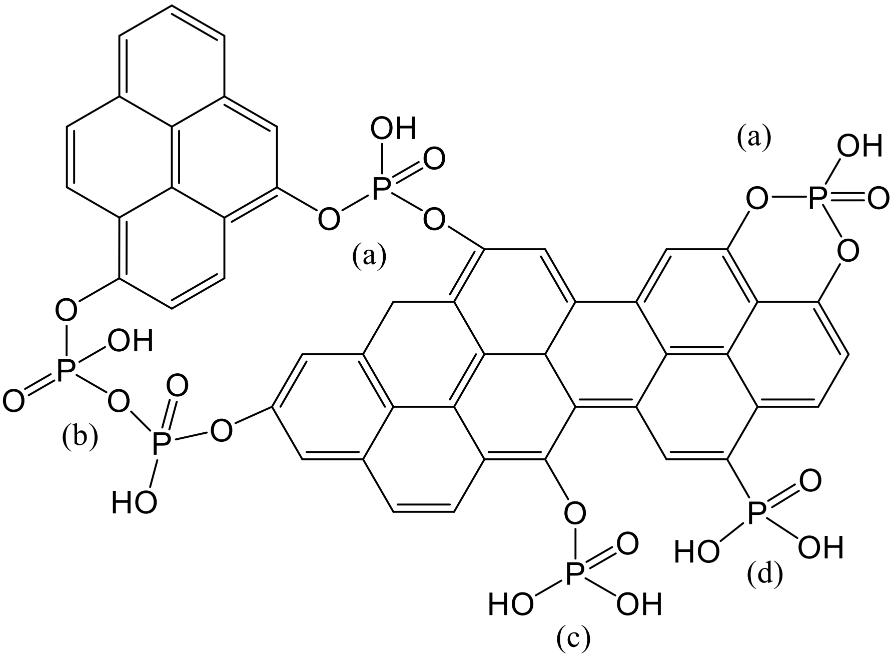

Figure 43: scheme of phosphorous functionalities on carbon surface: a) phospho-carbonaceous esters, b) pyrophosphate, c) -O-PO_3 group and d) -PO_3 group.

As reported above, due to the different features of carbonaceous materials and in particular the infinite number of modifications of their structure, they can be easily employed as support or as catalyst themselves. In the next sub-section an overview on the application of carbon in these two fields will be presented.

1.3.3. Carbon as catalyst support

Initially, carbon materials were employed as support mainly because the possibility to obtain enhanced dispersion of the active phase on their surface in respect to other materials, such as oxides, and moreover, in maintaining the crystallites separated avoiding their agglomeration. After metal-support interaction was investigated also for carbon materials, due to the strong interactions between the metal active phase and support depending on its physico-chemical properties (functional groups, defects and electronic features)[278], the concept of an “innocent” support was surpassed. Indeed, the morphology, shape and size of metal NPs depends also on the metal-support interaction, and these features influence the activity, selectivity and stability of the catalyst in the target reaction[279–281].

As an example, Alonso-Vante et al.[282] have demonstrated the strong interaction between Pt NPs and graphitic domains of two different carbonaceous materials, i.e. Vulcan XC-72 and MWCNTs. These domains, due to their electron storage ability of the π-π network can interact with the d-orbitals of the metal changing its electronic structure. Indeed, using DFT calculation and, in particular, Bader charge analysis they found and excess of negative charge at the top of the Pt cluster, identifying its polarization.

It was also observed an accumulation of negative charge at the metal-support interface. In this piece of work, defective graphene was chosen as support and, as a consequence of the electron deficiency of the material, a net flow of electron was identified from Pt cluster[283]. Moreover, Wang and co-workers[284] have showed that the different degree of graphitization of CNFs strongly affected the shape of the deposited Au NPs depending on the different interaction with the support. In particular, more ordered CNFs surface led to a binding of Au NPs through their {111} planes and, as a consequence, exhibiting more facet area (Figure 44 and 45). The differences in structure directly affect the catalytic performances in glycerol oxidation reaction.

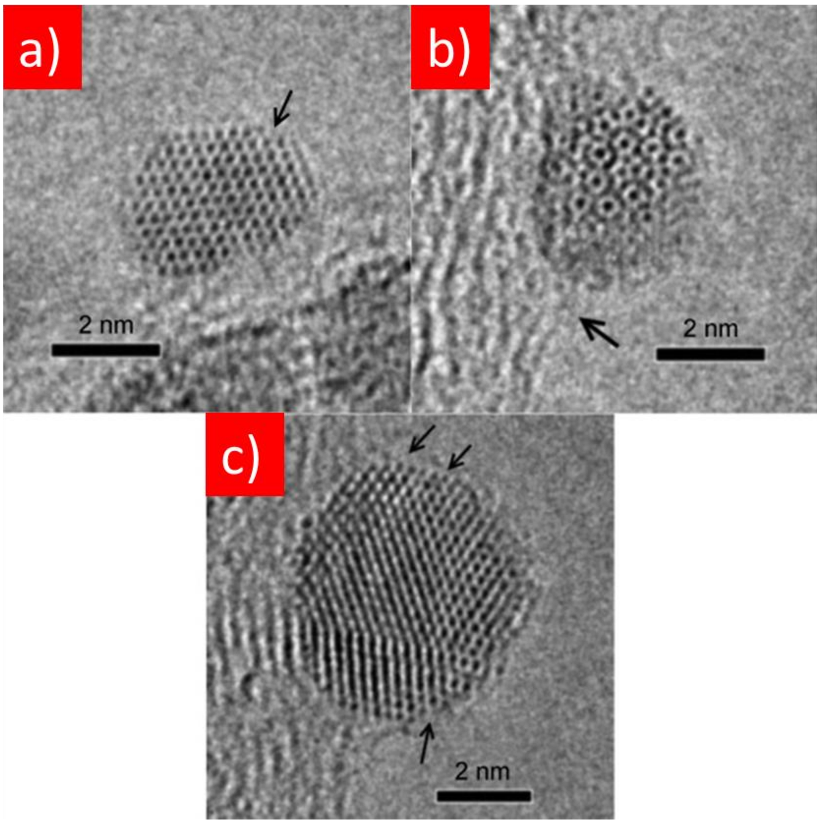

Figure 44: Aberration-corrected HRTEM images of Au NPs anchored on CNFs PS (low graphitization degree) with a) modified cuboctahedral configuration, b) icosahedral configuration showing interaction between particle and CNF surface, and c) surface carbon decoration with uncovered windows (each indicated by arrows). Adapted from Ref [284]: D. Wang et al. “Carbon-Supported Gold Nanocatalysts: Shape Effect in the Selective Glycerol Oxidation” https://doi-org.pros1.lib.unimi.it/10.1002/cctc.201200535 with the permission of John Wiley and Sons.

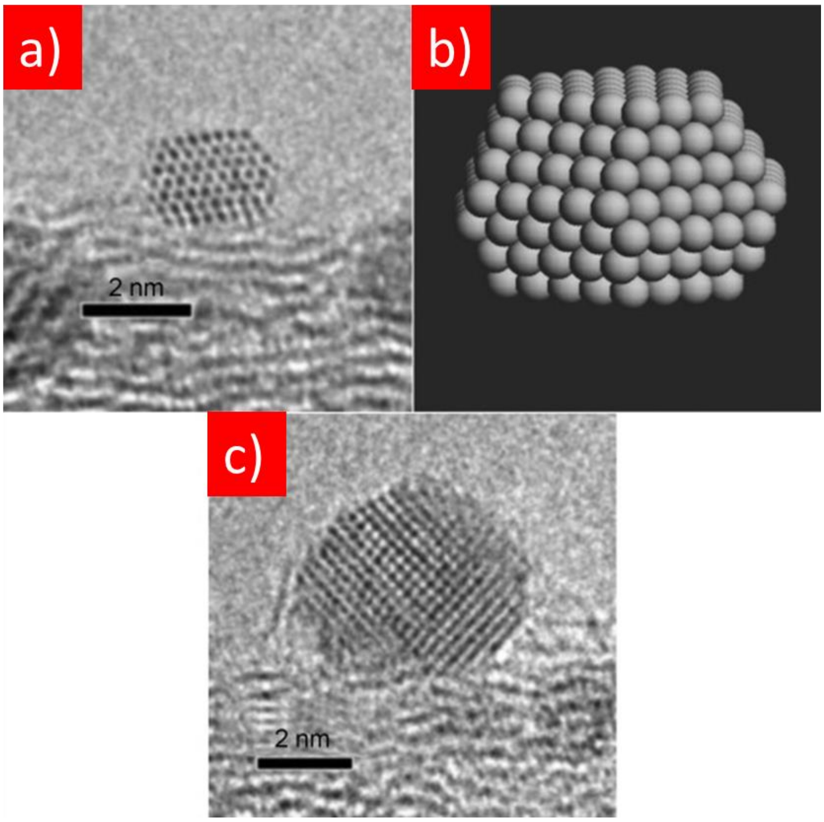

Figure 45: Aberration-corrected HRTEM images of Au NPs anchored on CNFs LHT (high graphitization degree). a) A representative 2–4 nm particle with (1 1 1) surface epitaxially parallel to the graphitic layer of CNF. b) Structure model derived from the image in part a. c) A larger particle with spherical shape showing carbon binding to the CNF surface. Adapted from Ref [284]: D. Wang et al. "Carbon-Supported Gold Nanocatalysts: Shape Effect in the Selective Glycerol Oxidation" https://doi-org.pros1.lib.unimi.it/10.1002/cctc.201200535 with the permission of John Wiley and Sons.

However, sp^2-based carbon materials are mostly hydrophobic and inert, offering a low number of sites to anchor metal NPs. In this case, the surface must be modified introducing defects and functional groups as described in the sub-sections above, increasing the possibility of metal-support interaction[285].

For example, Su and co-workers[286] studied the interaction of Pd NPs on oxygen and nitrogen modified carbon nanotubes (OCNTs and NCNTs, respectively). They observed a different interaction between Pd NPs and the support by using high-resolution TEM. By heating the samples to 600 °C, HRTEM images showed uniform metal nanoparticles dispersion on OCNTs encapsulated in carbon layer, while on NCNTs this was not observed (Figure 46). Moreover, by employing X-ray photoelectron spectroscopy (XPS) and temperature-programmed desorption (TPD) was found that Pd NPs interact differently with specific functionalities present on the CNTs surface. Indeed, acidic O groups are the preferred sites for anchoring metallic particles because of the lone pair around C=O, which can interact with the 4d Pd orbital, leading to a strong metal-support interaction. However, in NCNTs, these functionalities are employed in the formation of C-N bonds.

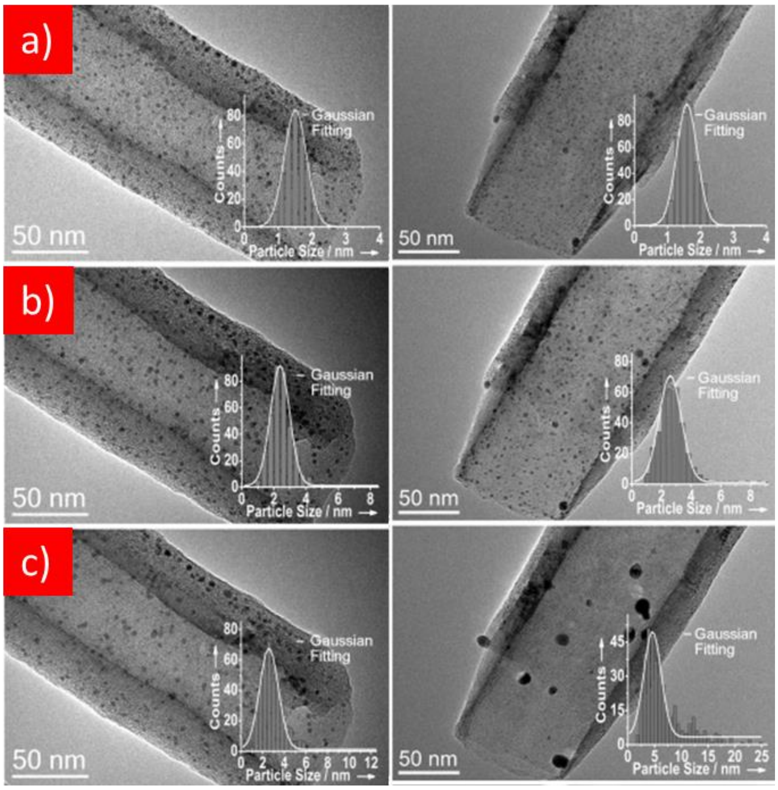

Figure 46: TEM images of Pd/OCNTs (left) and Pd/NCNTs (right) at a) room temperature, b) 330 °C and c) 600 °C. Adapted from Ref. [286]: D. S. Su et al. “Interaction between Palladium Nanoparticles and Surface-Modified Carbon Nanotubes: Role of Surface Functionalities” https://doi-org.pros1.lib.unimi.it/10.1002/cctc.201402272 with the permission of John Wiley and Sons.

The amount and type of functionalities also affect the electronic properties of the supported nanoparticles. As an example, Yu et al.[287] demonstrated that nitrogen doped carbon nanotubes tuned the electronic properties of supported Pt NPs. In fact, they showed that Pt anchored on NCNTs is more electron rich than Pt immobilised on pristine CNTs. They discovered by using XPS, TEM and Raman that graphitic nitrogen plays a determinant role in donating electrons. This effect also strongly influenced the catalytic performance of the material boosting the aerobic oxidation of glycerol.

In conclusion, carbons are good support to tailor the size, dispersion, crystallinity and structure of metal NPs, by tuning the surface properties.

Carbon materials also attracted much attention in their use as catalysts, without adding a metal active phase. In the next sub-section carbon-based catalysis will be briefly reviewed.

1.3.4. Carbocatalysis

The term carbocatalysis was created about 10 years ago by Robert Schlögl and Dangsheng Su. Carbocatalysis involves metal-free carbon catalysed reactions and it deals with the physical-chemistry of carbon surface to discover the real active site in the reaction[288]. The definition of carbocatalysis underlines the importance of the absence of metals either in stoichiometric or trace (dopants) amount.

A first example of carbocatalysis was given by Rideal and Wright, who reported that the oxidation of oxalic acid could occur in the presence of charcoal[289]. Nevertheless, this did not attract attention until the Second World War, where the petrochemical industry rises rapidly leading to increased interest in hydrogenation and dehydrogenation processes. Indeed, in the 1960s some researchers observed that carbon can also be active for the oxidative dehydrogenation (ODH) of alkane, because some deposits of carbon (coking) on the surface of iron oxide still were active in the ethylbenzene ODH. In this case, quinoidic oxygen was proposed to be the active site[198,290,291]. In any case, the amorphous materials employed in the early studies were disordered and amorphous and they showed low oxidation resistance, activity and stability[292–294].

In the past decades, nanomaterials developed rapidly leading to the intensive study of nanocarbons such as, fullerenes, graphene, CNTs and CNFs. This fact also extended the application of carbocatalysis due to the enhanced catalytic properties of nanocarbons.

Carbon catalysts are widely employed, studied and evaluated in gas phase reaction, electrocatalysis and photocatalysis. Several reviews about these topics are reported elsewhere[292,295–300] and are beyond the scope of this thesis.

However, the application of carbocatalysis in liquid phase reactions has been reported only in recent years[301]. Because this type of reactions is carried out at lower temperatures compared to gas phase, it is unnecessary to have a robust catalyst, but the active sites must not react or change with the solvent under the reaction condition. In the case of liquid phase reactions, the modification of the carbon surface plays a fundamental role to enhance its catalytic features. The effect of functionalisation can be seen, for example, in the solubility of carbon materials. In particular, CNTs or CNFs are strongly hydrophobic, and for this reason they cannot be dispersed in aqueous solution. However, by adding oxygen functionalities, the surface properties can be shifted from hydrophobic to hydrophilic. In addition, the insertion of heteroatoms greatly influences the acidity or basicity of the carbon catalyst, also affecting its electronic properties. The tailoring of the physical chemical properties strongly determines the activity, selectivity and stability of the catalytic material[301].

As an example, the possibility to activate oxidants or reductants is significant for a wide range of liquid-phase heterogeneous catalytic reactions. In oxidation reactions, molecular oxygen plays a fundamental role. Different are the sites that can activate O_2 on a carbonaceous material: from defects to heteroatom, but also zig-zag and armchair edges. Indeed, the production of peroxide and superoxide is preferential on defects sites rather than on basal planes. Su et al.[302] have studied how the bond in oxygen molecule cleaves onto CNTs. They have demonstrated that oxygen interact preferentially with defects and edges forming epoxy groups and then carbonyl moieties. The material obtained by interaction of CNTs with molecular oxygen was then successfully employed in the oxidative dehydrogenation of propane. In addition to defects, heteroatoms can also activate molecular oxygen. In particular, Subramanian and co-workers[303] have investigated the pathway for aerobic oxidation of alcohols over nitrogen-doped graphene. Moreover, the formation of activated oxygen species (AOS) was also in deep studied. They found that N-doped graphene can form different AOS depending on the position of the N-specie (centre, edge-tertiary and edge-secondary, Figure 47).

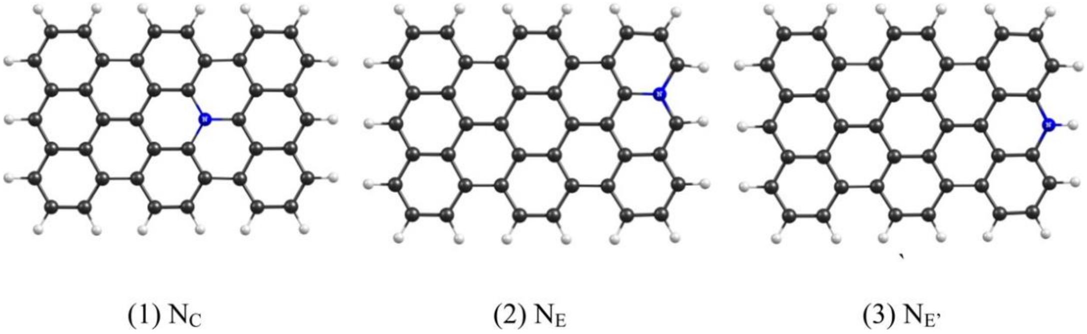

Figure 47: Different N-doped graphene geometries with N-doped ribbon at 1) centre, 2) edge-tertiary and 3) edge-secondary. Reprinted with permission from Ref. [303]: V. Subramanian et al. "Generalized Reaction Mechanism for the Selective Aerobic Oxidation of Aryl and Alkyl Alcohols over Nitrogen-Doped Graphene" https://doi.org/10.1021/acs.jpcc.5b07070. Copyright 2015, American Chemical Society.

Some possible options of oxygen activation by incorporated nitrogen are illustrated in Figure 48. All these mentioned AOS formed are reported to activate the O-H bond in alcohols and convert them to aldehyde, ketone or acids depending on the reaction mechanism.

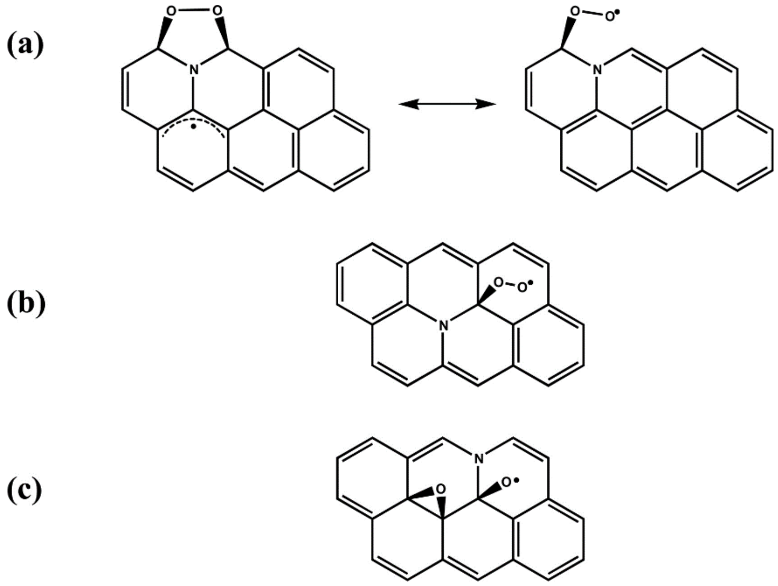

Figure 48: Schematic representation of formed activated oxygen species on different N-functionalities. Reprinted with permission from Ref. [303]: V. Subramanian et al. "Generalized Reaction Mechanism for the Selective Aerobic Oxidation of Aryl and Alkyl Alcohols over Nitrogen-Doped Graphene" https://doi.org/10.1021/acs.jpcc.5b07070. Copyright 2015, American Chemical Society.

As a consequence, carbocatalysts are widely employed in oxidation reactions[304,305]. For example, graphene-based carbocatalysts have shown activity in oxidation of benzyl alcohol to benzaldehyde. Herein, different mechanisms were proposed depending on the features of the material employed. In the case of graphene oxide, Bielawski et al.[306] showed a radical mechanism, started by a transfer of benzylic H atom of benzyl alcohol to the carbon surface. Then, epoxide groups underwent ring opening, resulting in the diol formation and dehydration (Figure 49). The reduced catalyst can be regenerated by using molecular oxygen.

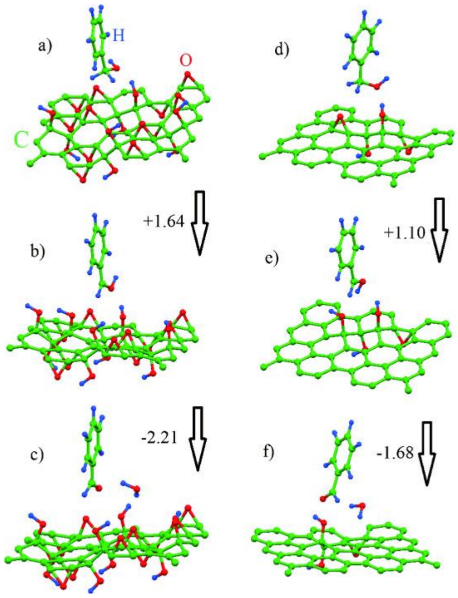

Figure 49: Optimized structures of initial (a,d), intermediate (b,e) and final (c,f) elementary steps of benzyl alcohol oxidation over GO with different epoxy and hydroxyl groups coverage (75 % for a-c and 12.5 % for d-f of carbon atoms are on the basal plan). Reprinted from Ref. [306]: C. W. Bielawski et al. “A Computational Investigation of the Catalytic Properties of Graphene Oxide: Exploring Mechanisms by using DFT Methods” https://doi-org.pros1.lib.unimi.it/10.1002/cctc.201200210 with the permission of John Wiley and Sons.

For P-doped carbocatalyst, He and co-workers proposed a non-radical reaction mechanism[307]. The condensation between the P=O moieties of the P-based functional group and alcohol was indicated as the first reaction step, followed by an H transfer which leads to the formation of the aldehyde (Figure 50). Also in this case, molecular oxygen is not involved directly in the reaction and the catalyst must be reactivated after the reaction.

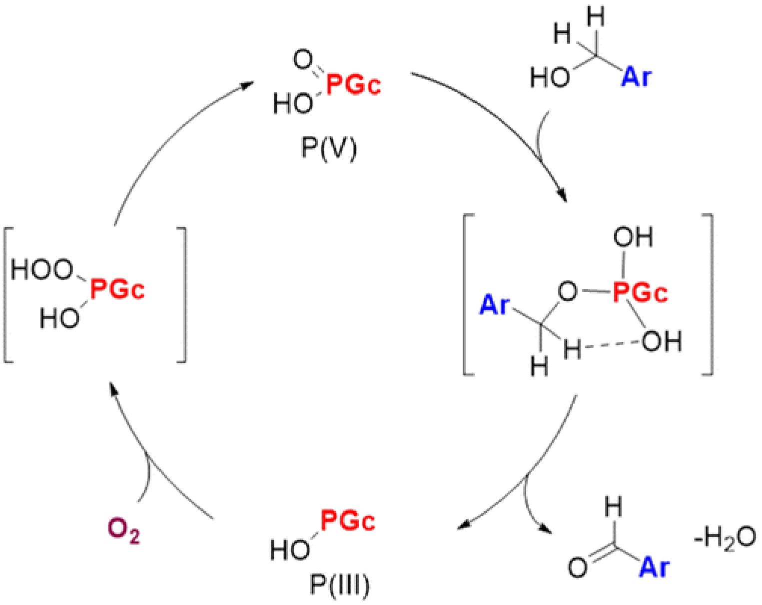

Figure 50: proposed mechanism of benzyl alcohol oxidation on P-doped graphene. The catalyst is regenerated by molecular oxygen. Reprinted from Ref. [307] with permission from H. He et al. “P-Doped Porous Carbon as Metal Free Catalysts for Selective Aerobic Oxidation with an Unexpected Mechanism” https://doi.org/10.1021/acsnano.5b07054. Copyright 2016, American Chemical Society.

Different is the mechanism in the case of N-doped carbon materials, where firstly molecular oxygen is activated with the formation of a peroxide radical. Then, this specie reacts with the alcohol substrate (Figure 51)[308].

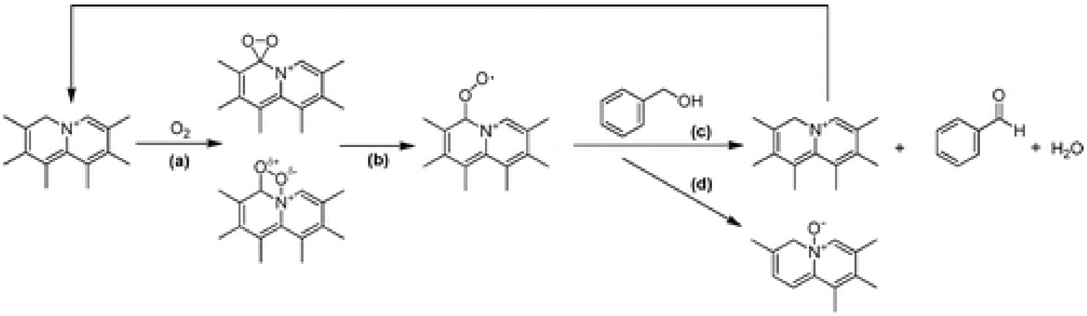

Figure 51: proposed mechanism for the formation of benzaldehyde over N-doped activated carbon catalyst in the presence of molecular oxygen. Reprinted from Ref. [308] with permission from M. Arai et al. "Nitrogen-Doped, Metal-Free Activated Carbon Catalysts for Aerobic Oxidation of Alcohols" https://doi.org/10.1021/acscatal.5b00375. Copyright 2015, American Chemical Society.

More difficult is the activation of hydrogen by carbocatalysts for hydrogenation reaction. Indeed in 2003, Schimmel et al.[309] investigated the adsorption of hydrogen onto different carbon materials, i.e. activated charcoal, carbon nanofibers and SWCNTs. They found that, at ambient temperature and pressure, the residence time of H_2 molecule is very short underling a negligible adsorption on carbon surface. All materials investigated showed no strong bond with hydrogen. In fact, their DFT calculation demonstrated that H_2 is very weakly bonded to a C-C aromatic bond. Thus, the possibility of a dissociation of the target molecule does not seem achievable.

The turning point in this field was the investigation of frustrated Lewis pairs (FLPs), which are combination of Lewis bases and acids that cannot recombine to form strong adducts because of electronic and steric factors[310]. In 2006, Stephan and co-workers[311] prepared by a reaction between tertiary phosphines $B(C_6F_5)_3$ a product with separated Lewis acid (boron) and bases (phosphorous). For the first time, an FLP compound have shown the peculiar ability to activate hydrogen molecule. In theory, FLPs can also exist in carbonaceous materials, by co-doping for example two different element in the carbon lattice. The finding of such material could extend carbon catalysis application also to hydrogenation reaction. The requirement is the insertion of a Lewis acid and a Lewis base at a short distance that can interact and activate molecular hydrogen forming two atomic species. Sun et al.[312] reported a DFT study where B and N doped bilayer graphene can effectively activate hydrogen through a successive activation of one hydrogen followed by the second one (Figure 52).

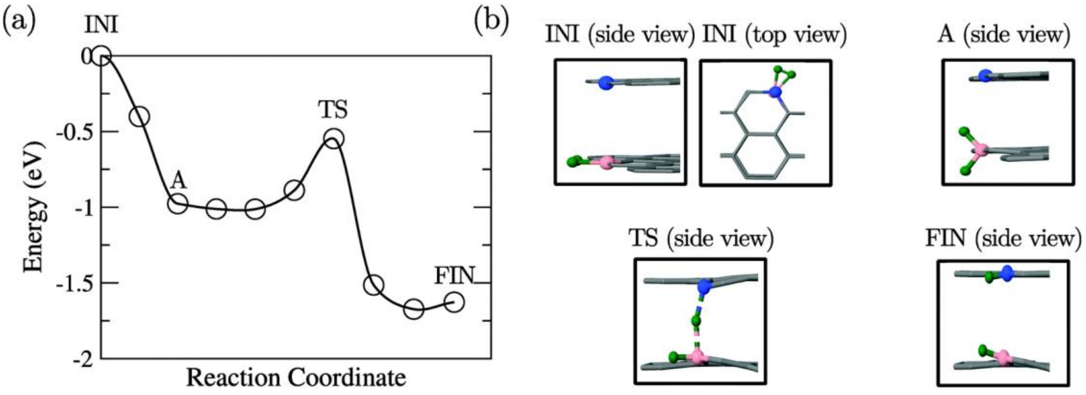

Figure 52: a) reaction pathway of molecular hydrogen activation on B and N doped graphene and b) most important structures found in the hydrogen activation pathway. Carbon is indicated in grey, boron in pink, nitrogen in blue and hydrogen in green. Reprinted from Ref. [312]: X. Sun et al. “Designing graphene as a new frustrated Lewis pair catalyst for hydrogen activation by co-doping” http://dx.doi.org/10.1039/C5CP07969A with the permission of the Royal Society of Chemistry.

However, carbon materials are not able to guarantee steric constrains and, as a consequence, to prevent the formation of a Lewis adduct. Until now, some groups reported some FLP carbonaceous materials but structures and mechanisms are not described, raising doubts about the reasons responsible of the activity of such materials. The research on this compounds is still at the beginning and more effort has to be made to rationalise and describe results[301,313,314].

However, reduction reactions can also be performed using carbon materials as catalyst, but using strong reductive agents different from molecular hydrogen. In particular, hydrazine can be employed, and until the 1980s it has been shown to be effective in the reduction of nitrobenzene and nitroarenes[301]. In order to understand the role of the different type of surface groups on graphene, model catalysts were employed (Figure 53), resulting in carbonyl group as the active site for nitroarenes reduction[315].

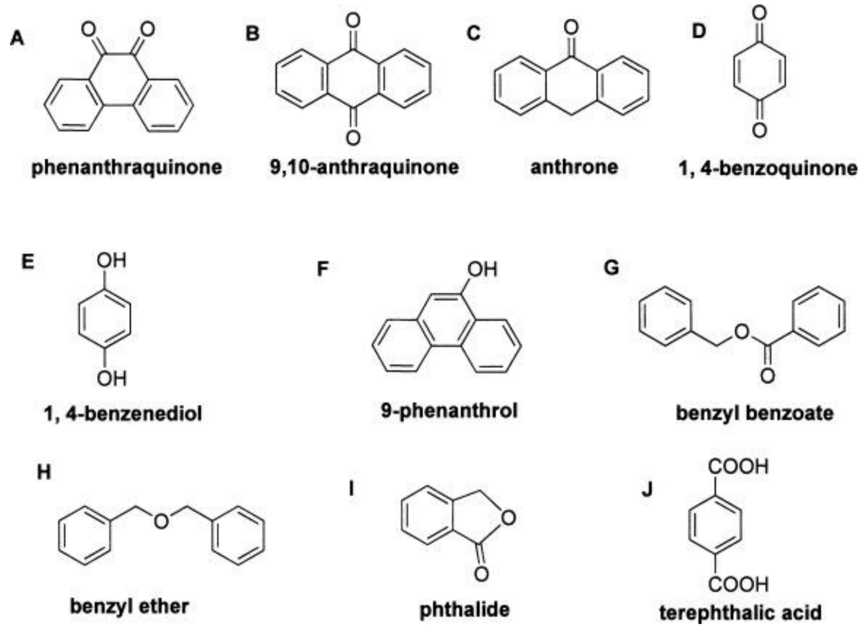

Figure 53: Structures of the model catalysts employed with different functional groups to mimic carbocatalysis. Reprinted from Ref. [315]: S. Wu et al. "Model Molecules with Oxygenated Groups Catalyze the Reduction of Nitrobenzene: Insight into Carbocatalysis" https://doi.org/10.1002/cctc.201402070 with the permission of John Wiley and Sons.

Hydrazine can be activated on this site, weakening the N-H bond. Then, the nitro group of the substrate can abstract the activated hydrogen from N_2H_4 molecule and be converted to a nitroso group, subsequently reduced to the amine (Figure 54)[315].

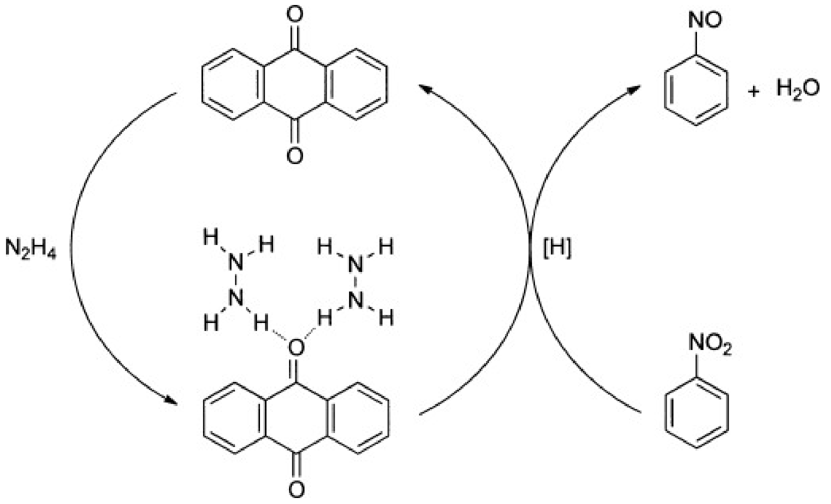

Figure 54: proposed mechanism for the formation of nitrosobenzene with anthraquinone used as a model catalyst in the presence of hydrazine. Reprinted from Ref. [315]: S. Wu et al. "Model Molecules with Oxygenated Groups Catalyze the Reduction of Nitrobenzene: Insight into Carbocatalysis" https://doi.org/10.1002/cctc.201402070 with the permission of John Wiley and Sons.

In conclusion, carbon materials can catalyse different liquid-phase reaction and they can be of fundamental importance in establish a more economic and green way to perform catalytic reactions. However, different issues need to be solved, such as the lower activity compared to the metal-based counterparts but also the low stability of functionalities during the reaction.

1.4. Liquid-phase chemical hydrogen storage materials

As reported in section 1.1.1.3, all the systems analysed for hydrogen storage show profound disadvantages that need to be solved before large-scale applications. In this context, liquid-phase chemical hydrogen storage materials, such as cyclic hydrocarbons, ammonia related compounds, formic acid, hydrazine hydrate and alcohols, can be the most plausible solution to solve transportation and storage issue related to hydrogen economy[316]. These chemicals can release hydrogen on-demand using a suitable catalyst and with high hydrogen generation rate. Moreover, liquid state is more suitable for storage and transportation employing the existing technologies[316]. At last, most of the liquid-state storage compounds can fulfil the target of hydrogen gravimetric capacity for storage systems (5.5 wt%, Table 2) imposed by the U.S. Department of Energy (DOE)[317]. They can store hydrogen reversibly or irreversibly. In the first case, these compounds can be hydrogenated and dehydrogenated at elevated temperatures maintaining their core structures avoiding the production of a new carrier for every cycle[102] (Figure 55).

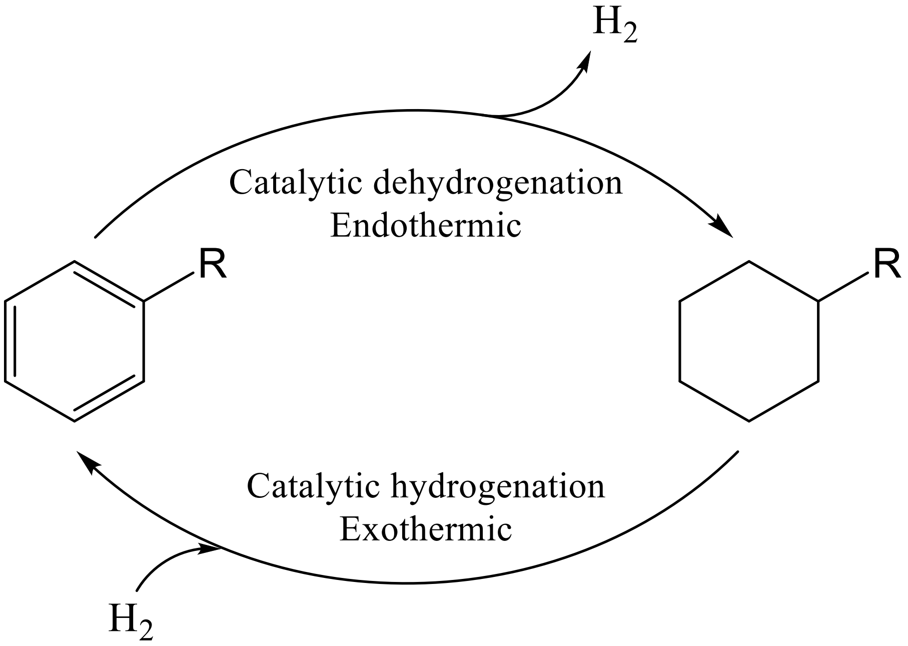

Figure 55: Schematic representation of reversible hydrogen carriers.

Cyclic hydrocarbons such as benzene, toluene and naphthalene or N-heterocyclic compounds such as N-ethylcarbazole, pyridines and quinolines are considered reversible liquid hydrogen carriers. Endothermic dehydrogenation is typically catalysed by noble-metal based catalysts between 150 and 400 °C[102,318–322]. The high temperature and the use of expensive noble metals may be a disadvantage for future prospective.

Other compounds, such as formic acid (FA), methanol (MeOH), hydrous hydrazine ($N_2H_4 \cdot H_2O$) and ammonia (NH_3), can store hydrogen irreversibly and they cannot be regenerated[102]. Nevertheless, if these carriers are produced from renewable sources, such as hydrogen and atmospheric CO_2 or N_2 the cycle is defined as "carbon-neutral", in contrast of fossil fuels[102,323–325]. Carbon neutrality means net-zero greenhouse gasses emission, and it is related in particular to CO_2. Indeed, in this case, the CO_2 or N_2 produced by the decomposition of these compounds are considered green because obtained from resources that are natural and renewable, such as biomass.

NH_3 decomposition is a promising candidate in the production of hydrogen and it was extensively studied because it yields carbon-free products, i.e. N_2 and H_2[326,327]. In addition, ammonia possesses an extremely high gravimetric hydrogen content of 17 wt%[326] and can be liquefied at -33 °C at 1 bar. On the other hand, Ru-based catalysts are the only materials active at a temperature below 500 °C[328].

Instead, $N_2H_4 \cdot H_2O$, which is an important nitrogen-hydrogen compound, presents all the benefits related to ammonia, but it can be decomposed at lower temperature. This carrier will be discussed in deep later.

MeOH decomposition was largely studied because of the high gravimetric hydrogen density (12.5 wt%)[326], but its industrial application is hindered by some drawbacks such as being a complicated process, the low storage safety and the hydrogen distribution after production. Until now, methanol reforming is the most attractive option to form hydrogen at temperatures around 200 – 300 °C. Pd, Ni and Cu-based catalysts are largely employed in this reaction but they deactivates because of coking and metal sintering[329].

FA possesses a lower gravimetric hydrogen content than MeOH (4.4 wt%), but a high volumetric hydrogen content of 53.4 g/L[330]. In addition, it can be decomposed around room temperature. This carrier will be reviewed in the next section.

Table 2: Gravimetric hydrogen content of different liquid-state carriers.

Liquid Carrier	*Hydrogen content (wt%)*	*Ref.*
Benzene	7.2	[102]
Carbazole	6.7	[102]
Pyridine	7.1	[102]
Pyrrole	5.6	[102]
Ammonia	17.8	[326]
Methanol	12.5	[326]
Formic acid	4.4	[330]
Hydrazine	12.5	[331]

Hydrous hydrazine	8.0	[332]

1.4.1. Formic Acid (FA)

Since 2010, formic acid has been attracting more and more attention as a liquid hydrogen carrier (Figure 56) not only for its high volumetric hydrogen capacity (53 g H_2/L) but, most importantly, because it is safe and non-toxic. Some liquid-state hydrogen storage materials, such as cyclic hydrocarbons, must be handled with extreme attention due to their violent reaction with oxidants, toxicity and risk of explosion[333]. On the contrary, FA is liquid and stable at room temperature and it possesses a narrow flammability range (18 – 57 v%), which is ideal for storage and transportation. In addition, formic acid selective dehydrogenation reaction produces environmentally benign gaseous products (CO_2/H_2)[333,334]. An important feature is the possibility to subsequently hydrogenate the carbon dioxide produced in FA dehydrogenation to regenerate it in a carbon-free emission process, producing formic acid[335].

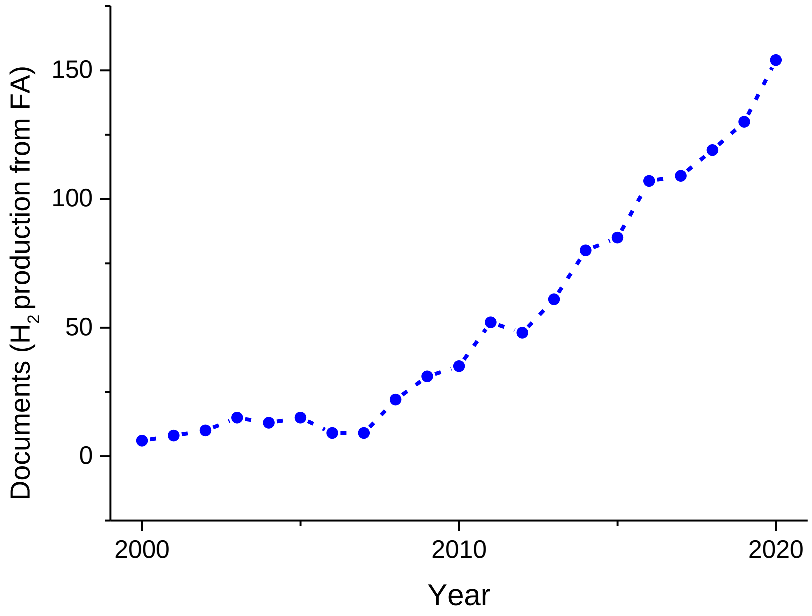

Figure 56: Published documents by year for “hydrogen production from formic acid”. Source Scopus.

1.4.1.1. Formic acid production

Formic acid is naturally produced by ants and bees of the genus Oxytrigona in their venom glands[336]. Nevertheless, it is a mixture of toxins and irritants, with FA as the predominant component. Formic acid is also present in some plants leave[337], fruits, honey and nettles[338,339]. Some speculations state that this compound is also present in the atmosphere due to forest emission. Moreover, FA is an intermediate in the human metabolism controlling the amount of methanol introduced in the organism[340–342]. Nowadays, industrial production of this chemical starts from fossil fuels, in a two-step reaction from MeOH and CO[343]. Notably, it can be also produced employing renewable sources, i.e. CO_2 and biomass, which is the best option to prevent and mitigate carbon emission.

Industrial Production - Methyl Formate Hydrolysis

Theoretically, the simplest process to produce formic acid is the reaction of CO with H_2O (Eq. 9). The drawback of this method is that below 150 °C the kinetic of this reaction is very slow and also at higher temperature, an enormous increase of the pressure is needed to produce FA in acceptable yields.

$$CO + H_2O \rightarrow HCOOH \tag{9}$$

To overcome this disadvantage, methyl formate is formed as an intermediate in the liquid-phase carbonylation of methanol catalysed by basic materials, i.e. $NaOCH_3$ or $KOCH_3$ (Eq. 10). After this step, the methyl formate is hydrolysed to give formic acid as the final product (Eq. 11). Different companies such as, BASF, Eastman Chemical Company and Kemira, utilizes this method varying the second reaction step[343,344].

$$CH_3OH + CO \rightarrow HCOOCH_3 \qquad \Delta H = -29.0\ kJ\ mol^{-1} \tag{10}$$

$$HCOOCH_3 \rightarrow \mathrm{HCOOH} + CH_3OH \qquad \Delta H = 16.3\ kJ\ mol^{-1} \tag{11}$$

Biomass conversion

Biomass can be converted into FA in several ways. One example is the conversion of cellulose into formic acid and levulinic acid passing through the production of glucose and 5-hydroxymethylfurfural (5-HMF). A combination of Lewis and Brønsted acids in catalytic amount is the most effective strategy to obtain enhanced yield (Figure 57)[345].

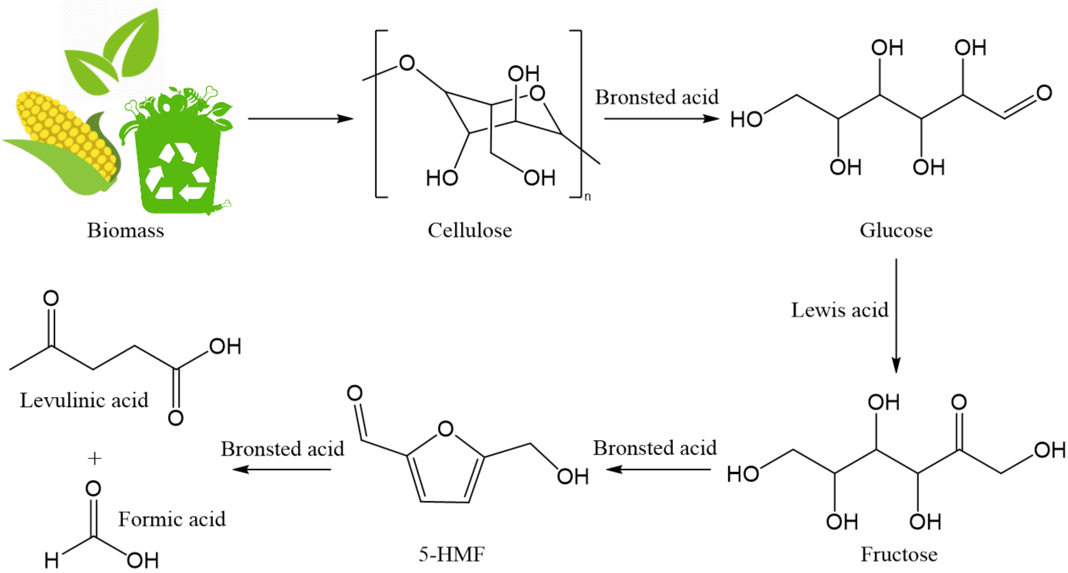

Figure 57: Reaction scheme of the conversion of biomass by acid hydrolysis into FA

Biomass can be also oxidized to produce FA. As an example, glucose can be converted into FA using H_2O_2 as an oxidant at room temperature and nearly ambient pressure in basic solution. Bases such as, NaOH and KOH can activate glucose conversion, while the oxidant favours FA formation acting on the oxidative glucose cleavage[346]. This process can also be catalysed using different substrates, an acid catalyst and an oxidant, i.e. O_2 (Table 3). Heteropoly acids (HPAs), are the most studied materials in this process. HPAs are a group of polyoxo compounds combining oxygen and hydrogen with metals, e.g. vanadium, tungsten or molybdenum, or with a non-metal, such as phosphorous or silicon[347].

Table 3: Different substrate, catalysts and oxidants employed in the catalytic oxidation of biomass to FA.

Substrate	*Catalyst*	*FA yield (%)*	*Oxidant*	*Ref.*
Glucose	$H_8PV_5Mo_7O_{40}$	85	O_2 (20 bar)	[348]
Cellulose	$H_4PVMo_{11}O_{40}$	68	O_2 (6 bar)	[349]
Sucrose	$H_8PV_5Mo_7O_{40}$	76	O_2 (20 bar)	[348]
Bagasse	$H_4PVMo_{11}O_{40}$	61	O_2 (6 bar)	[349]
Beech wood	$H_8PV_5Mo_7O_{40}$	61	O_2 (20 bar)	[348]
BM cellulose	$Co_{0.6}H_{3.8}PV_2Mo_{10}O_{40}$	66	$O_2 + N_2$ (20 bar)	[350]

CO_2 reduction

Using carbon dioxide to produce formic acid is attracting a lot of attention because of the sustainable carbon migration. CO_2 has to be reduced in the presence of a reductive agent because it is a relatively stable compound and its valorisation into chemical involves multiple electron transfer processes. The formation of FA from carbon dioxide using H_2 and water as reductants is the most favourable reaction in comparison to other products such as methane or methanol. However, the reaction is not thermodynamically favoured and for this reason, an inorganic base is frequently used as an additive to shift the equilibrium in favour of the hydrogenation[347]. Generally, carbon dioxide can be reduced with the assistance of a catalyst which is essential in conversion efficiency and FA selectivity. Ru and Ir-based homogeneous catalysts are successfully employed in this reaction[351,352]. Heterogeneous catalysts are also utilized in this context. In particular Pd, Au and Ru-based materials are efficient in this reaction[347,353]. In this case the support plays a crucial role in the catalytic behaviour of the material, resulting in higher activation of the substrate in presence of basic sites[354–357]. In addition, carbon dioxide can be reduced using photocatalysis and electrocatalysis, even though these processes produce FA in lower yield in respect to other methods[347,358,359].

1.4.1.2. Formic acid decomposition (FAD)

Formic acid decomposition occurs into two different pathways:

$$HCOOH \leftrightarrow H_2 + CO_2 \qquad \Delta G = -32.9\ kJ\ mol^{-1}, \Delta H = 31.2\ kJ\ mol^{-1} \quad (12)$$

$$HCOOH \leftrightarrow H_2O + CO \qquad \Delta G = -12.4\ kJ\ mol^{-1}, \Delta H = 29.2\ kJ\ mol^{-1} \quad (13)$$

The first reaction (Eq. 12), is the dehydrogenation pathway which produces hydrogen and carbon dioxide. H_2 can be directly feed as fuel in hydrogen-based fuel cells, while CO_2 can be used to regenerate FA (Figure 58).

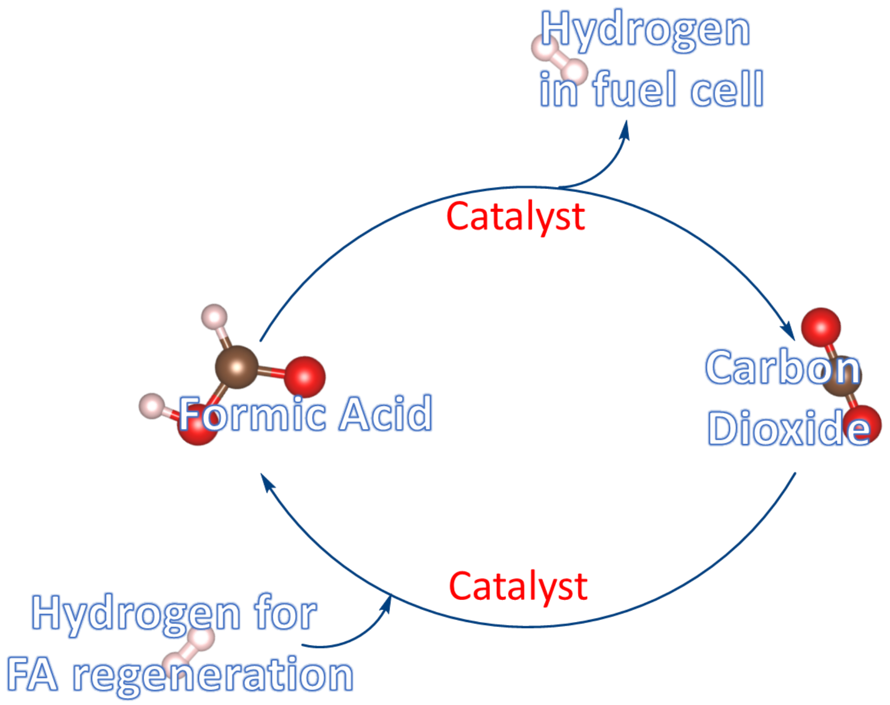

Figure 58: FA / CO_2 cycle for hydrogen production and FA regeneration.

The dehydration reaction (Eq. 13) forms water and CO and it should be avoided because of the problem related with the poisoning of the fuel cell electrode[48,129,342,360].

Formic acid can be easily decomposed utilizing homogeneous and heterogeneous catalyst. In order to selectively and quantitatively decompose FA, effort have to be made in finding the best material to boost its selectivity, conversion and stability. In the next section, some of the most performing heterogeneous and homogeneous catalysts are presented.

Homogeneous catalysts

Since the first report of Coffey in 1967 on Pt, Ru and Ir-based complexes for FAD[361], researches have focused their attention on the development of ruthenium and iridium-based homogeneous catalysts.

In general, two strategies are studied for selective dehydrogenation of FA. The first one is based on an acid-base reaction between a metal hydride (M-H) and formic acid to form a metal-formate intermediate and molecular hydrogen (Figure 59, Mechanism 1). Carbon dioxide is produced by β-hydride elimination (β-HE) of the formate ligand and the regeneration of the M-H species. In this type of mechanism, the potential risk is the interaction of the catalyst with water, which can decrease its activity. The second model is a typical oxidative addition (OA) – reductive elimination (RE) cycle (Figure 59, Mechanism

2). FA interacts with the reduced metal complex by OA process. The produced complex forms CO_2 by β-HE and gives a dihydride intermediate, which by RE, forms H_2. In this mechanism, the risk to produce CO increases because FA can bond to the reduced metal also with its C-H moiety, followed by decarbonylation reaction to form carbon monoxide[362].

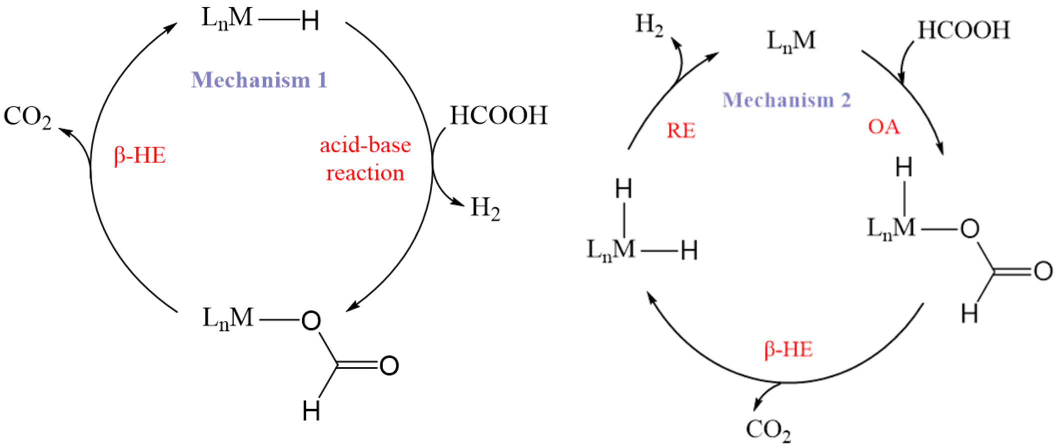

Figure 59: General proposed mechanism for hydrogen generation from formic acid.

For example, in 2008 Laurenczy and co-workers reported hydrophilic Ru-based catalysts obtained from the combination of the water-soluble ligand meta-trisulfonated triphenylphosphine (TPPTS) and either $[Ru(H_2O)_6]^{2+}$ or $RuCl_3$. A 90 – 95 % conversion of FA was reached using sodium formate as an additive at all the tested temperatures. On the other hand, the reaction rate rapidly decreased with the temperature (Figure 60)[363].

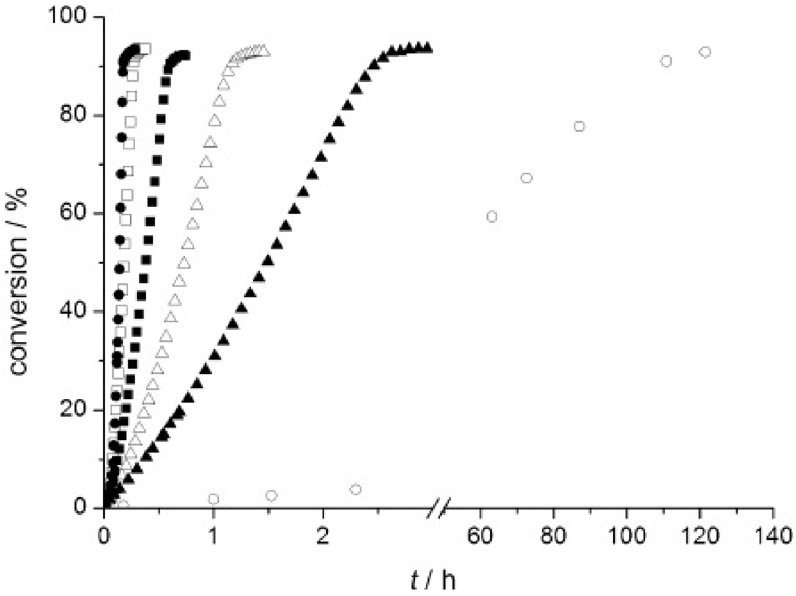

Figure 60: Effect of temperature on the decomposition of formic acid: 25 °C (○), 70 °C (▲), 80 °C (△), 90 °C (•), 100 °C (□), 120 °C. Reprinted from Ref. [363]: Laurenczy et al. “A Viable Hydrogen-Storage System Based On Selective Formic Acid Decomposition with a Ruthenium Catalyst” https://doi.org/10.1002/anie.200800320 with the permission of John Wiley and Sons.

The same group studied the effect of the ligand using a hydrophilic sulfonate aryl- and alkyl-ligands in a Ru(III) catalyst, obtaining excellent activity in FAD. The importance of the effect of basicity and hindrance of the ligand were confirmed to be the main parameters to consider in tuning the catalytic activity[364].

One year later, Beller at al. have efficiently generated hydrogen from FA at mild reaction conditions (40 °C) forming in situ a $[RuCl_2(benzene)]_2$/dppe (6 equivalent) complex. This catalyst showed high selectivity for hydrogen, promising stability and also a TON (turn over number) of approximately 260000[365]. More interestingly, the following publication reported how light can significantly improve the kinetic of the dehydrogenation reaction depending on the nature of the precursor and ligand employed. The proposed mechanism is shown in Figure 61[366].

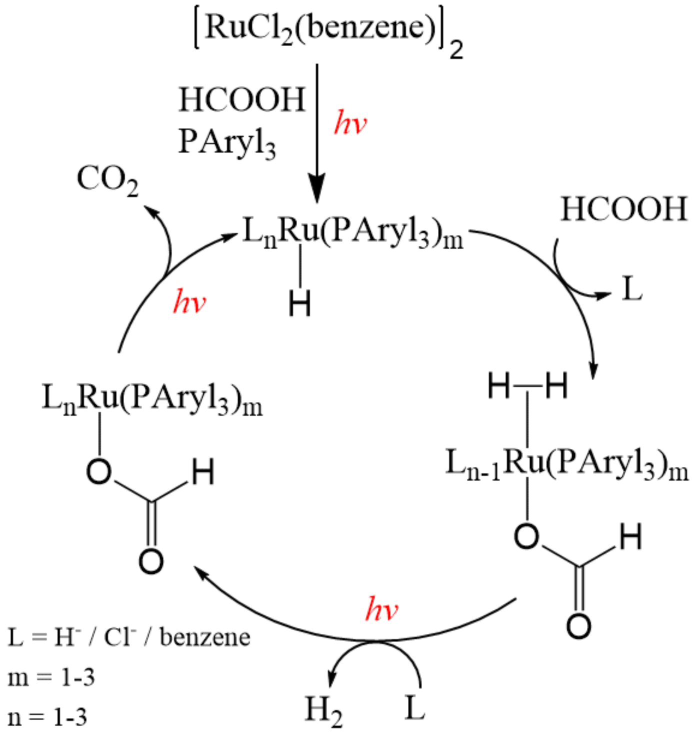

Figure 61: Proposed mechanism for the decomposition of FA using $[RuCl_2(benzene)]_2$ as catalyst and $PAryl_3$ as additive.

In 2016, Huang and co-workers developed a highly efficient and selective catalyst at 50 °C. This material is characterized by the presence of a dearomatized pyridine ligand and an imine arm. The presence of N-H bonds changes both thermodynamic stability toward water and kinetic behaviour of the catalyst. Moreover, the fact that the oxidation state of the Ru centre does not change during the reaction makes the catalyst highly selective to hydrogen formation, avoiding the production of CO[362]. The majority of the catalysts described here work in organic solvents. The hydrogen produced is always mixed with carbon dioxide and traces of solvents. In order to avoid their evaporation, ionic liquids are employed as reaction medium. Starting from Deng[367], a lot of different Ru-based amino-functionalised complexes were tested in ionic liquid, obtaining excellent results in term of selectivity and activity of the catalyst avoiding the problem of the solvent evaporation[330,368–370].

Ir-based catalysts are generally extremely efficient but, on the other hand they are more expensive than Ru-based systems[371]. In addition, Himeda reported that Ir-based catalysts are sensitive to the pH of the solution and the electronic effect due to the substitute in bipyridine ligand[372]. Xiao et al. investigated the NH functionality in an cyclometallated Ir(III) complex. They suggested that the NH moiety is fundamental in the selective formation of H_2 from FA by a mechanism of proton hopping[373]. This hypothesis was then confirmed by Ikariya, who worked on an Ir-complex obtained from N-triflyl-1,2-diphenylethylenediamine. This catalyst showed very high catalytic activity without base additives at ambient temperature[374].

Promising systems are shown in this discussion in terms of activity and selectivity of the catalysts. On the other hand, the separation of the catalyst from the reaction mixture, the use of harsh reaction condition and the usage of organic solvents hindered the utilization of homogeneous catalysts in industrial applications. The alternative and more attractive solution is employing heterogeneous catalysts, which can achieve high catalytic activity at low temperature and they can be used in water medium.

Heterogeneous catalysts

In 1911 for the first time, Sabatier starts to investigate the decomposition of FA in gas-phase over zinc oxide[375]. After Sabatier’s study, many heterogeneous systems have been tested in gas-phase FAD reaction[330,376,377], in particular metals (e.g. Zn, Cu, Ni, Pd and Ru)[378–381] and metal-oxides (e.g. MgO, ZrO_2 and SnO_2)[382–384]. Nevertheless, the reactions are carried out at high temperature ($T > 100$ °C), exceeding the FA boiling point and therefore, blocking their application in fuel cells. For this reason, the following researches focuses on the development of efficient heterogeneous materials for liquid-phase formic acid decomposition reaction at mild reaction conditions. In late 1970s, Williams et al. were able to decompose FA at room temperature using Pd/C as the catalyst[385]. Today, the common catalysts employed in liquid-phase formic acid decomposition are mainly based on Au, Pt and Pd[129,330,360]. Among all the material tested, Pd-based catalysts are considered the most promising because of their high selectivity and exceptional FA conversion achieved near room temperature[129,386], while Pt and Au based ones need higher temperatures (between 50 and 80 °C)[376]. As a consequence, effort have been made to optimize the performances of Pd-based materials for hydrogen production from formic acid optimizing the properties of the active phase[387–389] and tuning the support[390–393]. Regarding the metal active phase, numerous reports investigate the nature of the metal particles, i.e. electronic structure, size and shape in order to design the best catalyst in FAD reaction. For example, Nalvani-García and co-workers studied the relation between the Pd particle size and the activity of a Pd/C catalyst[394]. A series of Pd NPs with controlled size were synthesise using the polyol method and deposited over a carbonaceous support. Combining the experimental data with characterization, a volcano type relationship between the catalytic activity and NPs size was obtained, with the highest activity value at an average particle size of 3.9 nm. A mechanism for the FAD was also proposed (Figure 62). The reaction starts with the O-H bond dissociation and the formation of the palladium-formate intermediate. After that, the C-H bond breaks evolving CO_2 and producing the palladium-hydride species, which is the rate determining step. Finally, the recombination of the two atomic H evolves molecular hydrogen accompanied with the regeneration of the catalyst. In addition, the kinetic isotope effect (KIE) experiment was performed using deuterated formic acid and monitoring the progress of the reaction in order to examine more in deep the size sensitivity. Results obtained revealed that the optimal size accelerated the rate-determining C-H bond scission, underling the importance to perfectly control the particle size of the active phase. Other studies confirmed the size sensitivity for Pd NPs used in formic acid decomposition reaction[387,389,395]. All these reports confirmed the importance of the particle size control and, in particular, the volcano-type relationship between the activity of the catalyst and the proportion of low and high coordinated atoms in the nanoparticle structure.

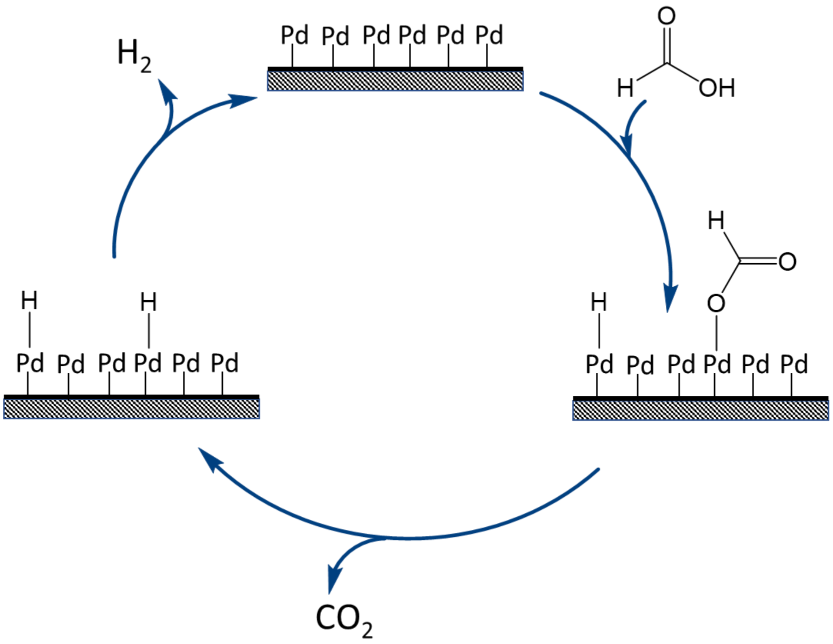

Figure 62: Proposed mechanism for FA decomposition over Pd NPs.

Another important result that can be noted comparing these different works, is the dependence of the maximum in the volcano-type plot on the used support. In particular, Jeon and Chung[396] employing acid functionalised support to deposit Pd NPs noticed the influence of their concentration on the activity of the catalyst. They concluded that the role of the support can be explained by considering two competitive factors. The first one is due to the recombination of the formate ion with a proton but also a delay in the deprotonation, while the second is the activation time of the catalyst in a basic solution by competitive adsorption between the formate and hydroxyl ions.

Indeed, numerous supports were investigated to anchor metal nanoparticles (NPs), such as silica[397,398], metal oxides[377], zeolites[399,400] and metal-organic frameworks (MOFs)[401,402]. Compared to these systems, carbon materials are the most versatile because of the facility to tune their surface modifying the porosity and introducing defects and heteroatoms[403–406]. These supports are of high interest in formic acid decomposition, not only because defects and functional groups can act as anchoring sites for NPs but also due to the possibility of inserting acid and basic functionalities which can help in the FAD mechanism. Indeed, Xu and co-workers[250] have successfully inserted boron-oxygen groups on carbon nanospheres (XC-72R). The support was then used to support ultrafine Pd nanoparticles. The obtained catalyst (Pd/OB-C1) showed enhanced activity (1963 h^{-1}) and selectivity to FA dehydrogenation compared to the Pd-based bare catalyst. The material exhibited also improved recyclability (no deactivation observed over 5 reaction runs). This effect is due to the ability of B-O groups to strongly interact with Pd, avoiding the leaching of NPs. In the same work, melamine precursor was added in the support preparation obtaining OB-C-N1 material. The Pd catalyst obtained showed superb activity (5354 h^{-1}) due to the increased B loading. Moreover, the N-functional group provided more basicity, favouring FA deprotonation leading to a selectivity of 100 % to hydrogen. Wang et al.[407] confirmed the role of the N-functional group, testing in FAD reaction Pd NPs supported on amino-functionalised hierarchically porous carbon (Pd/NHPC-NH_2). They also obtained enhanced activity (1265 h^{-1}), selectivity (100 % H_2) and durability due to the dual effect of amino-groups in stabilizing Pd NPs and acting as proton scavengers promoting O-H bond dissociation (Figure 63)[407,408]. Table 4 shows a comparison of different representative Pd-based catalysts supported on carbonaceous materials employed in the FAD reaction.

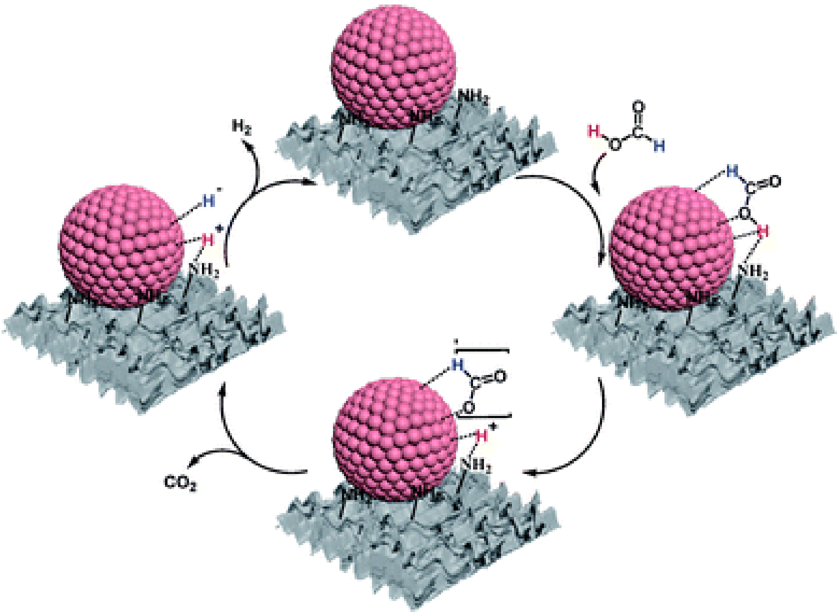

Figure 63: Proposed FAD reaction pathway over Pd/NHPC-NH_2. Reprinted from Ref. [407]: Z. Wang et al. “Pd nanoparticles anchored on amino-functionalized hierarchically porous carbon for efficient dehydrogenation of formic acid under ambient conditions” https://doi.org/10.1039/C9TA10196A with the permission of the Royal Society of Chemistry.

Table 4: Features of representative Pd-based catalysts supported on carbonaceous materials employed in the FAD reaction

Catalyst	*T (° C)*	*Initial Activity (h^{-1})*	*Ref.*
Pd/C	25	64	[409]
Pd/mpg-C_3N_4	25	144	[410]
Pd/C	25	304	[411]
Pd/B-C	25	1184	[411]
Pd/NMC-400	25	913	[412]
Pd/$CN_{0.25}$	25	752	[413]
Pd/C	25	835	[395]
Pd/C	30	228	[414]
Pd_{IMP}/CNF-HHT	30	563	[390]
Pd_{SI}/CNF-HHT	30	979	[390]
Pd/carbon black	30	1815	[389]
Pd-NC	45	645	[186]

Pd/C	50	7959	[415]
Pd/C nanospheres	60	7256	[416]
Pd/MSC-30	50	2623	[417]
Pd/N-MSC-30	60	8414	[393]
Pd/OB-C1	50	1963	[250]
Pd/OB-C-N1	50	5354	[250]
Pd/NHPC-NH_2	30	1265	[407]
Pd/NH_2-rGO	25	767	[408]

Another important factor to consider in order to tune the catalyst is the nature of the active site. It is well known that alloying one or more metals can affect the features of an heterogeneous catalyst, tailoring reactivity, stability and selectivity[401,402,418–424]. Inserting a second metal changes the coordination environment mainly because of two different mechanisms. The first one is the ligand or electronic effect, where the formation of an heteroatomic bond modifies the electronic configurations of the interacting metals resulting in a change of the surface chemical properties. Secondly, the geometry of a bimetallic structure is different from the monometallic one, e.g. average metal-metal bond length, resulting in a modification due to the strain of the lattice[425,426]. In formic acid decomposition reaction, the use of a second metal can mitigate the deactivation issues due to the leaching of Pd and the irreversible adsorption of intermediate species on the NPs surface[427,428]. In addition, the use of a non-noble metal in the multimetallic system is a strategy to reduce the cost of the catalyst without decrease its activity. Different Pd-based multimetallic catalysts have been employed in FAD reaction, e.g. PdAu[401,421,422,429,430], PdAg[402,422,423,431,432], PdCu[433], PdCuCr[434], PdAuNi[435] and PdAuCo[436].

Among them, PdAu bimetallic catalysts have attracted a lot of attention because of their superior activity and, in particular, stability. As an example, Liu and co-workers[437] have employed density functional theory (DFT) simulation to understand the effect of alloying gold to pure palladium. Pd_{55} and different $Pd_{55-x}Au_x$ clusters were optimized and the adsorption energy of the involved molecular species were calculated. They found that gold can weakly bond atomic hydrogen leading to an easier hydrogen production on bimetallic catalysts. Indeed, the k value for H recombination step on Pd_{55} is 3.0×10^{-7} s^{-1}, indicating the magnitude of the Pd-H interaction. On the contrary, on $Pd_{27}Au_{28}$ and $Pd_{22}Au_{33}$ clusters k values increase due to this weakened H adsorption on the catalyst surface (7.5×10^{-3} s^{-1} and 5.8×10^{2} s^{-1}, respectively). In 2019, Xing et al.[421] have prepared a series of PdAu/C catalysts via coprecipitation-reduction method and they were subsequently tested in room-temperature FAD reaction. They observed a dependence of the activity of the catalysts on the Pd(II)/Pd(0) ratio due to the incorporation and dissociation of molecular oxygen. Alloying Au to monometallic Pd/C catalyst the TOF value increased from 1539 h^{-1} to 2819, 3446, 5411 and 6634 h^{-1} for $Pd_{0.90}Au_{0.10}$, $Pd_{0.82}Au_{0.18}$, $Pd_{0.75}Au_{0.25}$ and $Pd_{0.69}Au_{0.31}$, respectively. Nevertheless, the TOF starts to decrease when the feed ratio of Au was further increased, i.e. for $Pd_{0.64}Au_{0.36}$ the TOF was 5473 h^{-1}. The introduction of gold in palladium lattice produces a lattice strain, favouring the formation of the PdO specie, resulting in an increased activity increasing Au content. In contrast to the strain effect, charge transfer from Au to Pd atoms (ligand effect) can decrease the capacity of Pd to dissociatively adsorb O_2, resulting in decreased activity when the ligand effect is dominant (Figure 64)[430].

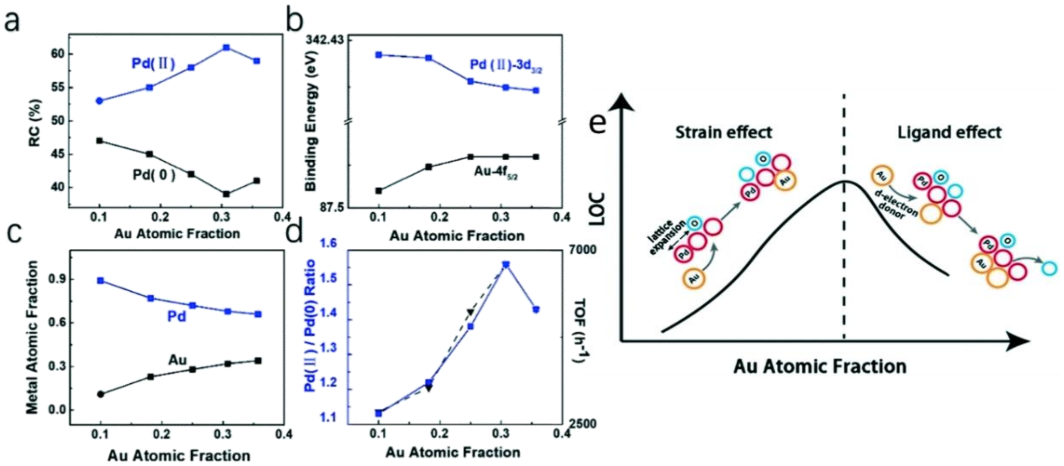

Figure 64: a) variation of the relative content of Pd(II) and Pd(0), b) dependence of the binding energies of Pd 3d and au 4f from XPS high resolution spectra, c) variation of Au and Pd atomic fraction on the surface of the catalysts, d) dependence of TOF and Pd(II)/Pd(0) surface ratio with Au atomic fraction and e) scheme of the volcano-type plot obtained related to the effect of gold on the capacity of Pd to bond with atomic oxygen. Adapted from Ref. [430]: Z. Xing "Optimizing the activity of Pd based catalysts towards room-temperature formic acid decomposition by Au alloying" http://dx.doi.org/10.1039/C8CY02402B with the permission of the Royal Society of Chemistry.

In order to deeply understand the influence of ensemble and ligand effect, Lee and co-workers employed a combination of experimental and computational investigation[438]. Firstly, they investigated the effect of the surface arrangement (ensemble) on the FAD kinetics by modelling four different PdAu(111) alloys changing surface and sub-surface arrangements. The different PdAu alloys were differenced by the first layer, i.e. pure palladium, triangular shaped Pd, linear Pd and mono Pd (Figure 65a). A pathway based on two sequential reactions was studied: i) $HCOOH^* \rightarrow HCOO^* + H^*$ and ii) $HCOO^* \rightarrow CO_2 + H_2$. The triangular shaped Pd surface showed the most favourable reaction energy and kinetic barriers because of the presence of three adjacent Pd atoms which stabilize the first transition state (TS1, Figure 65b).

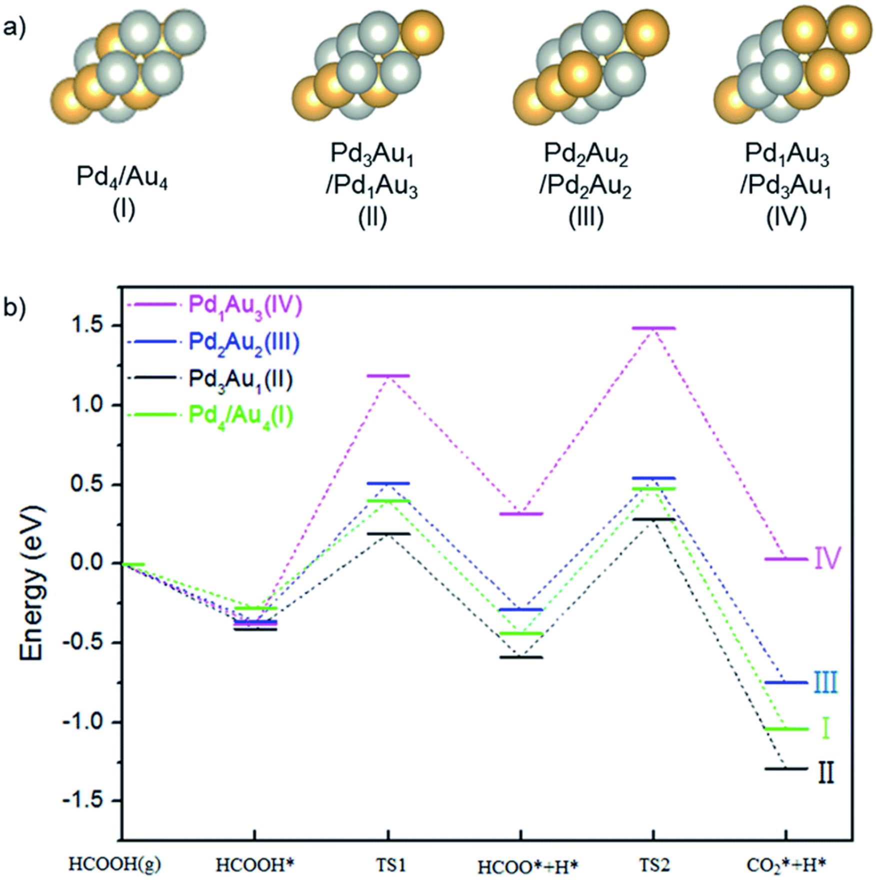

Figure 65: a) PdAu(111) modelled catalysts and b) calculated potential energy diagram of FA dehydrogenation reaction on the different modelled catalysts. Reprinted from Ref. [438]: J. H. Lee "Experimental and computational studies of formic acid dehydrogenation over PdAu: influence of ensemble and ligand effects on catalysis" https://doi.org/10.1039/C6TA03654F with the permission of the Royal Society of Chemistry.

Three different PdAu alloyed catalysts were then prepared and treated with different gasses (N_2 and CO) in order to change the amount of triangular Pd present on the surface. The catalysts showed an activity for FAD reaction that was proportional to the presence of 3-fold hollow site in the active phase of the catalyst. In addition, ligand effect was also considered in accelerating FA dehydrogenation because of the influence of Au contained in the sublayers of the metal phase. In order to study the contribution of this mechanism, $HCOO^-$ adsorption on the triangular Pd surface and on pure Pd in a bidentate mode were optimized. The PdAu surface showed a substantial reduction of binding energy compared to pure Pd surface due to PdAu interaction. In the presence of a Pd-rich surface the primary effect is the ensemble one, because the catalytically active metal (Pd) is diluted in a more inert one (Au). On the other hand, the existence of a gold dominant sub-surface increased the d electron density on the first layer reducing HCOO binding energy, also revealing the importance of ligand effect.

Other metals have a beneficial effect when alloyed with palladium. Indeed, Xing et al.[422] reported the synthesis of PdAu/C, PdAg/C and PdCu/C catalysts, which were used in FAD reaction at room temperature overcoming CO poisoning and producing high-pure hydrogen. PdCu/C material showed a very poor reaction rate, lower than the Pd/C one, while PdAu/C and PdAg/C showed enhanced activity (27 and 17 h^{-1}, respectively). They discovered that the introduction of these two metals can reduces the size of nanoparticles in the order Pd/C > PdAg/C > PdAu/C, explaining the better performance of PdAu/C. Moreover, the two alloyed catalysts possess longer life-time then pure palladium because CO cannot steadily be adsorbed on Ag and Au surfaces. According to other studies, the adsorption strength of CO follow the order Pd > Cu > Ag > Au[439]. Therefore, carbon monoxide poisoning was removed enhancing the stability of the catalysts. After this study, Tsang and co-workers[431] prepared Ag-Pd core-shell nanoparticles supported on carbonaceous material to enhance the hydrogen evolution from FA at room temperature. By atom probe tomography they confirmed the core-shell configuration of nanoparticles, with an Ag core of 8 nm coated by thin and continuous layers of Pd (between 1 and 10 Pd layers, Figure 66). They obtained a turnover frequency calculated on the Pd surface's site over the total Ag-Pd core shell of 125 h^{-1} at 20 °C, with a very small apparent activation energy of nearly 30 kJ mol^{-1}.

The enhanced catalytic properties of the catalyst were ascribed to the electronic promotion from the Ag core to the Pd shell. However, increasing the temperature up to 70 °C, more than 70 ppm of CO were produced due to a promotion of catalytic dehydration of FA and reverse WGS reaction, preventing the application of this catalyst in fuel cell technology.

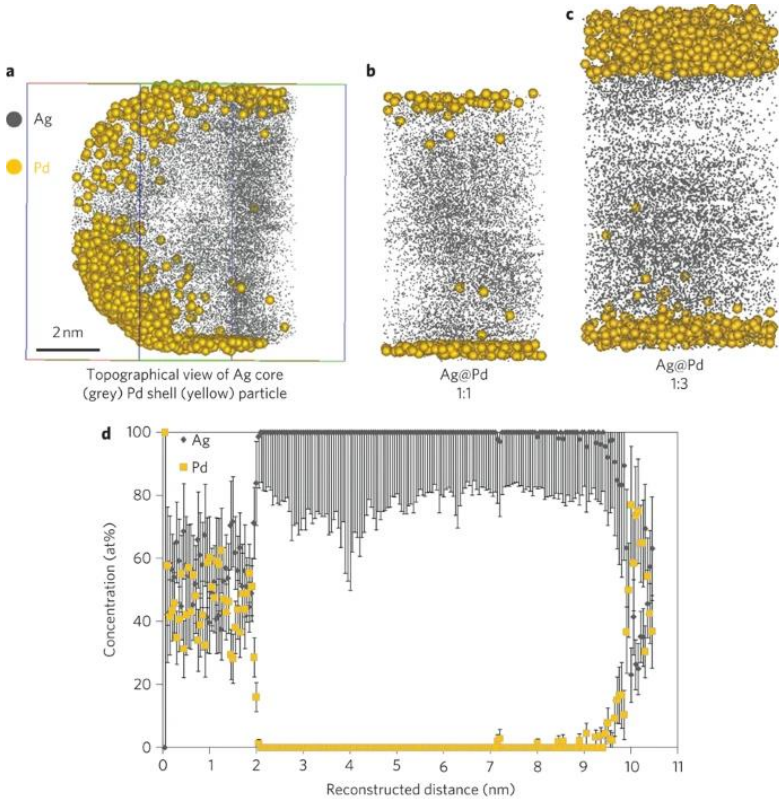

Figure 66: atom probe tomography results for Ag@Pd nanoparticles. Atom map a) of an individual Ag@Pd NP, b) showing the Ag@Pd NP shell thickness. d) Composition profile of a 1:3 Ag@Pd NP. Reprinted from Ref. [431]: S. C. E. Tsang et al. "Hydrogen production from formic acid decomposition at room temperature using a Ag–Pd core–shell nanocatalyst" https://doi.org/10.1038/nnano.2011.42 with the permission of Springer Nature.

In order to decrease the cost of the catalyst, Mori et al.[433] employed PdCu nanoparticles dispersed within a macroreticular basic resin with –N(CH_3)$_2$ functionalities in FAD reaction. Different PdCu molar ratios were prepared, tested and compared with the monometallic counterparts (Figure 67). Monometallic Cu catalyst is inactive in formic acid decomposition and almost all the bimetallic catalysts showed an activity superior to the monometallic materials with a maximum for $Pd_{50}Cu_{50}$/resin catalyst (Figure 67b). Moreover, this material exhibited considerably improved catalytic properties also compared to $Pd_{50}Au_{50}$/resin and $Pd_{50}Ag_{50}$/resin (Figure 67a). In addition, this catalytic system favourably suppressed CO formation (< 3 ppm) and it maintained its activity even after the durability tests due to the leaching inhibition.

Using kinetic isotope effect (KIE) experiment, they observed that the basic functionalities of the resin participated in the mechanism assisting the first O-H deprotonation step, forming a metal-formate species. The following step, is the β-hydride elimination to produce CO_2 and the metal-hydride ($M\text{-}H^-$). At last, the hydride species interacted with the previously formed $-^{+}HN(CH_3)_2$ group of the resin, forming molecular hydrogen. Furthermore, they concluded from the kinetic profile of Cu that Pd was the main active species in the reaction. Density functional theory was then used to elucidate the role of the $–N(CH_3)_2$ group and copper. The role of the basic functionality in the dissociation of the hydroxyl bond was confirmed and an electronic promotion from Cu to Pd was observed explaining the better activity of the $Pd_{50}Cu_{50}$/resin. Moreover, studying the adsorption energy of CO on Pd(111), Cu(111) and $Pd_{50}Cu_{50}$(111) optimized surfaces, an inhibition on the carbon monoxide adsorption on the bimetallic slab was detected, confirming the selectivity observed in the experimental studies, which is particularly desirable for PEMFCs.

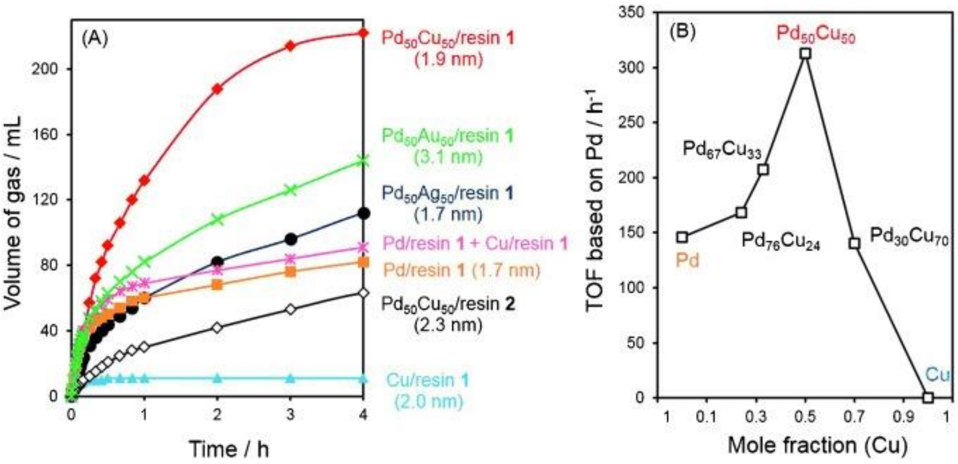

Figure 67: a) kinetics profiles of the different catalysts tested by Mori et al. b) Volcano-type plot obtained correlating the TOF values with the Cu molar fraction of different PdCu/resin catalysts. Reprinted from Ref. [433]: K. Mori et al. "Synergic Catalysis of PdCu Alloy Nanoparticles within a Macroreticular Basic Resin for Hydrogen Production from Formic Acid" https://doi.org/10.1002/chem.201501760 with the permission of John Wiley and Sons.

The same group also prepared on the same basic resin a trimetallic catalyst PdCuCr/resin, increasing the activity of the previously studied PdCu/resin catalyst[434]. KIE experiment revealed that Cr had a bifunctional role in this material. Firstly, surface chromium act as an anchor stabilizing the highly dispersed nanoparticles avoiding agglomeration and increasing the durability of the material. Moreover, the synergistic effect obtained by adding this metal boosted the C-H bond dissociation of the metal-formate intermediate because of the production of an electron-rich Pd active phase, favouring the rapid formation of molecular hydrogen.

The enhanced catalytic features of the other reported trimetallic catalysts, i.e. PdAuNi[435] and PdAuCo[436], are mainly ascribed to a combination of ligand and geometric effects.

As depicted here, in the last few decades effort have been made to improve catalytic condition, metal cost, durability and selectivity of the catalysts employed in formic acid decomposition reaction. On the other hand, for practical application prospective all these important features need to be further enhanced, in particular durability, control of the reaction kinetics and formation of by-products, all issues that the current research tries to overcome.

1.4.2. Hydrazine (N_2H_4)

Nitrogen-hydrogen compounds, such as ammonia, ammonia borane and hydrazine,[327] have attracted a lot of attention because of their ability to produce hydrogen without carbon sources emission, such as CO_2, which is dangerous for the environment and CO that poisons electrodes in PEMFCs[327,440]. Among all, hydrazine is one of the most promising N-H materials for hydrogen production because it is liquid in a width temperature range (between 1.4 to 113.5 °C) meaning that it can be easily transported at room temperature[441–444]. In addition, N_2H_4 possesses a high hydrogen content of 12.5 wt% [445]. On the other hand, handling hydrazine can be dangerous because of the risk of explosion associated at its hypergolic nature, in particular in presence of a metal[446]. This problem can be solved diluting N_2H_4 in an inert gas, for example argon[447] or using hydrous hydrazine ($N_2H_4 \cdot H_2O$), which is a safer derivate[448]. $N_2H_4 \cdot H_2O$ still contains 8 wt% of hydrogen and can be securely employed as a liquid hydrogen source, avoiding the problems related to storage and transportation[449,450].

1.4.2.1. Hydrazine production

Several methods are employed in order to produce hydrazine (usually obtained in its hydrated form), e.g. Raschig process using ammonia or urea and chloramines, Bayer process employing carbonyl compounds, the peroxide-ketazine process, urea-based process and electrochemical methods[451,452]. Nevertheless, only ammonia Raschig process, the urea-based method and the peroxide-ketazine process are the most employed in industry[451–453].

Raschig process

This process was discovered in 1907, and its key reaction is the oxidation of ammonia by the use of hypochlorite. It occurs in liquid phase involving three different reaction steps (Eq. 14).

$$NaOH + Cl_2 \rightarrow NaOCl + HCl \tag{14a}$$

$$NaOCl + NH_3 \rightarrow NH_2Cl + NaOH \tag{14b}$$

$$NH_2Cl + NH_3 + NaOH \rightarrow N_2H_4 \cdot H_2O + NaCl \tag{14c}$$

In this case, hydrazine is obtained in the hydrated form and to obtain anhydrous hydrazine reactive or extractive distillation methods need to be employed. Eq. 14a is the formation of sodium hypochlorite (NaOCl), which is obtained by inserting Cl_2 into a 30 % NaOH aqueous solution. In order to suppress the formation of sodium chlorate (NaO_3Cl), the reaction temperature is set below 30 °C, usually at 5 °C. In the second step of the process (Eq. 14b) a 5 to 15 % aqueous ammonia solution is added to NaOCl to produce chloramine (NH_2Cl). The reaction rate for the formation of NH_2Cl is relatively high compared to the formation of hydrazine (Eq. 14c), which is the rate determining step. In order to speed up this reaction a temperature between 130 °C and 150 °C and a pressure of 30 MPa are used. An excess of NH_3 is employed to minimize the hydrazine-chlorine decomposition. The product mixture is composed by the 1 % of hydrazine and 4 % of NaCl. Ammonia is condensed and concentrated in order to be recycled and the salt is separated from hydrazine hydrate using a forced-circulation salt evaporator[454,455]. Figure 68 shows a schematic representation of the Raschig process.

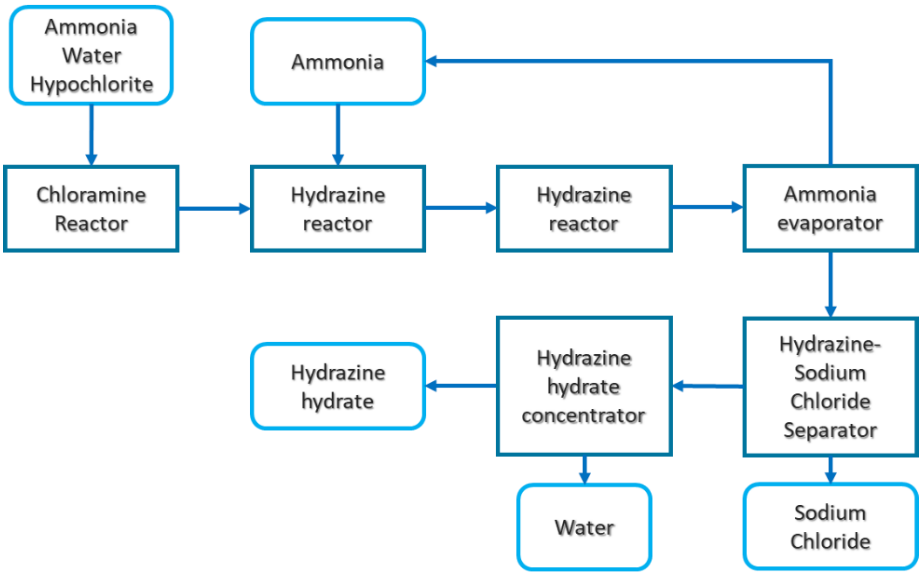

Figure 68: Schematic representation of the Raschig process for hydrazine production.

Hoffmann process (Urea-based Raschig process)

Eq.15 describes the overall reaction involved in the Hoffmann process.

$$CO(NH_2)_2 + NaOCl + 2NaOH \rightarrow N_2H_4{\cdot}H_2O + NaCl + Na_2CO_3 \tag{15}$$

Also in this case, an aqueous solution of sodium hydroxide interacts with chlorine to form NaOCl solution. Urea ($CO(NH_2)_2$) is inserted in the reactor as an aqueous solution adding steam in order to favour the endothermic dissolution, in a 1:4 ratio in respect to hypochlorite solution at a temperature of 100 °C. Crude product can be treated as in the Raschig process and it contains nearly 35 g of hydrazine/L. Compared with the Raschig one, Hoffmann process is more economical but only for low production levels. Indeed, it became obsolete due to the fast growth of plant size[453,454,456].

Urea-based process

In this process, amido compounds are nitrated and hydrogenated to give hydrazine. This process is composed by three reactions (Eq.16).

$$NH_2CONH_2 + HNO_3 \rightarrow NH_2CONHNO_2 + H_2O \tag{16a}$$

$$NH_2CONHNO_2 + 3H_2 \rightarrow NH_2CONHNH_2 + 2H_2O \tag{16b}$$

$$NH_2CONHNH_2 + NH_3 \rightarrow NH_2NH_2 + NH_2CONH_2 \tag{16c}$$

In the first step of the process (Eq.16a) nitrourea ($NH_2CONHNO_2$) and water are obtained from urea and nitric acid (HNO_3). Different amido compounds can be employed in this reaction, such as acetamide, benzamide and formamide and also diverse organic and inorganic nitrating agents. In Eq.16b $NH_2CONHNO_2$ is hydrogenated at temperature between 50 °C and 400 °C, with or without a catalyst. In the last step hydrazide ($NH_2CONHNH_2$) undergoes ammonolysis in a range of temperature of 90-150 °C producing hydrazine[451].

Kuhlmann Process (peroxide-ketazine process)

This process uses hydrogen peroxide (H_2O_2) as an oxidant, ammonia and a ketone to form an azine, which is further reduced to give hydrazine. This method has the significant advantage of not coproducing salts. In this respect this process can be considered green and of commercial significance. In the ketazine formation (Figure 69), H_2O_2 react with the oxaziridine produced by the reaction of ammonia with a ketone (typically methyl ethyl ketone because it is immiscible in the reaction mixture and can be easily separated). Usually, the reaction conditions are 50 °C and atmospheric pressure.

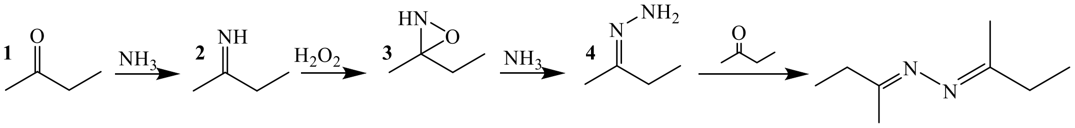

Figure 2: Scheme of the ketazine formation. 1) Imine is formed by condensation, 2) Imine oxidation to oxaziridine, 3) Hydrazone production from condensation of oxaziridine and 4) Hydrazone condensation with the ketone to produce ketazine.

The final step is the hydrolysis of ketazine (Figure 70). It needs to be pure because the production of hydrazine is acid-catalysed and the reactant must be separated from the initial ammonia-reach reaction mixture. The reaction is endothermic and, for this reason, it requires a pressure of 8 bar and a temperature of 130 °C at the top and 180 °C at the bottom of the column.

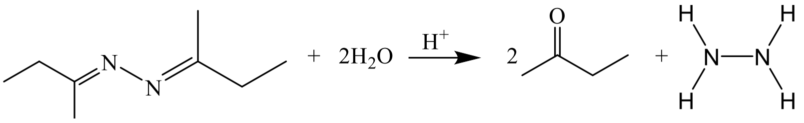

Figure 70: Ketazine hydrolysis to hydrazine.

A 30-45 % aqueous solution of hydrazine hydrate is obtained and the ketone is recycled[451,457].

A schematic representation of the process is shown in Figure 71.

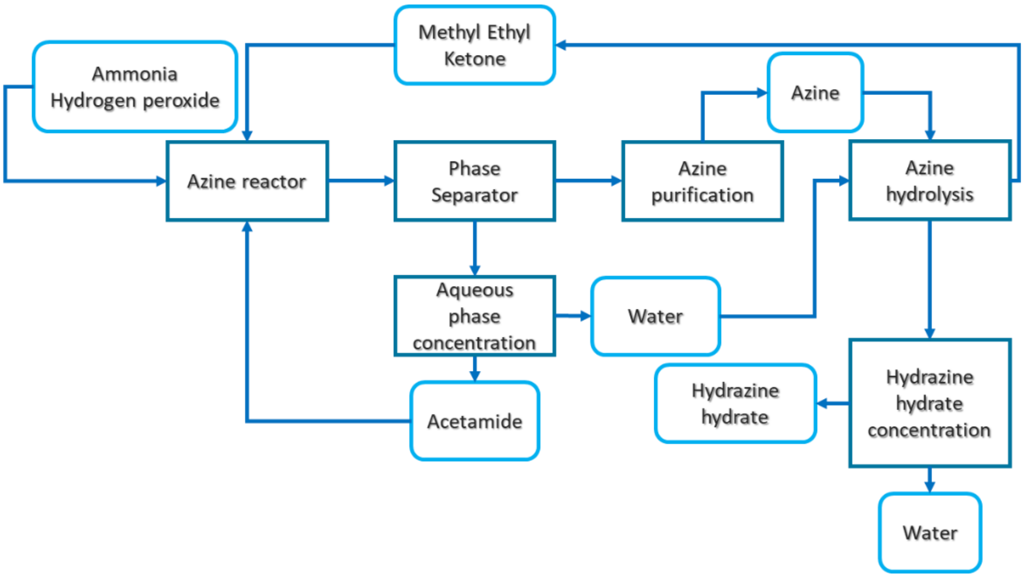

Figure 71: Schematic representation of the Kuhlmann process for hydrazine production.

1.4.2.2. Hydrazine decomposition

Hydrazine decomposition occurs into two different pathways[458–460]:

$$N_2H_4 \rightarrow N_2(g) + 2H_2\,(g) \qquad \Delta H = -95.4\,KJ.mol^{-1} \qquad (17)$$

$$3N_2H_4 \rightarrow N_2(g) + 4NH_3\,(g) \qquad \Delta H = -157.0\,KJ.mol^{-1} \qquad (18)$$

Eq. 17 represents the complete decomposition reaction, where molecular nitrogen and hydrogen are formed. Eq. 18 describes the incomplete decomposition pathway, which is thermodynamically favoured and produces ammonia and nitrogen. The produced ammonia can be subsequently dehydrogenated at high temperature to give nitrogen and hydrogen[328]. An efficient heterogeneous catalyst can be employed to selectively decompose hydrazine following Eq.17, such as Shell 405 (30 wt % Ir/Al_2O_3)[461,462]. During the decomposition process, the reaction chemical energy is transformed into kinetic energy, which can be employed. Indeed, hydrazine is used as a liquid propellant in aerospace application, artificial satellites and rockets[463,464]. Typically, during a catalytic decomposition reaction, N_2H_4 molecule adsorbs on the catalyst's surface. After this step, either N-N or N-H bond can be dissociated (Eq. 19 and 20, respectively). Thermodynamically, the N-N bond cleavage is favoured comparing their bond dissociation energies (BDE)[99,465]. The breakage of the N-N bond is the first step of the incomplete decomposition reaction, giving ammonia and nitrogen. Hence, the features of the catalyst employed are extremely important to boost N-H scission and to quench the formation of NH_3[447,466–468].

$$N_2H_4^* \rightarrow H_2N^* + H_2N^* \qquad BDE = 286.0\, KJ.mol^{-1} \quad (19)$$

$$N_2H_4^* \rightarrow H_3N_2^* + H^* \qquad BDE = 360.0\, KJ.mol^{-1} \quad (20)$$

Hydrazine can be replaced by its hydrated version ($N_2H_4 \cdot H_2O$) in order to reduce the risk in storage and transportation[449,450]. In order to evolve hydrogen from hydrazine hydrate on-demand, different unsupported and supported NPs were employed, especially based on Ir[448,469] and Rh[443,470] at first.

Unsupported monometallic NPs

Xu and co-workers[443] examined different unsupported metal nanoparticles (Rh, Ir, Ru, Co, Pd, Pt, Fe Ni and Cu) in hydrazine hydrate decomposition at room temperature (Figure 72). They found that among all, Rh NPs with an average particle size of 16 nm possesses a superior selectivity for complete $N_2H_4 \cdot H_2O$ decomposition of 43.8 %. On the contrary, Co, Ru and Ir showed a selectivity for H_2 of 7 %, exhibiting a preferential activation of the N-N bond and forming ammonia. In addition, Cu, Fe, Pt, Pd and Ni were found to be completely inactive in this reaction at mild condition, whereas they showed activity in gas-phase[447]. This result proved that the energy barrier for the decomposition of hydrazine is increased by the H_2O - N_2H_4 bond, influencing activity and selectivity of the catalysts.

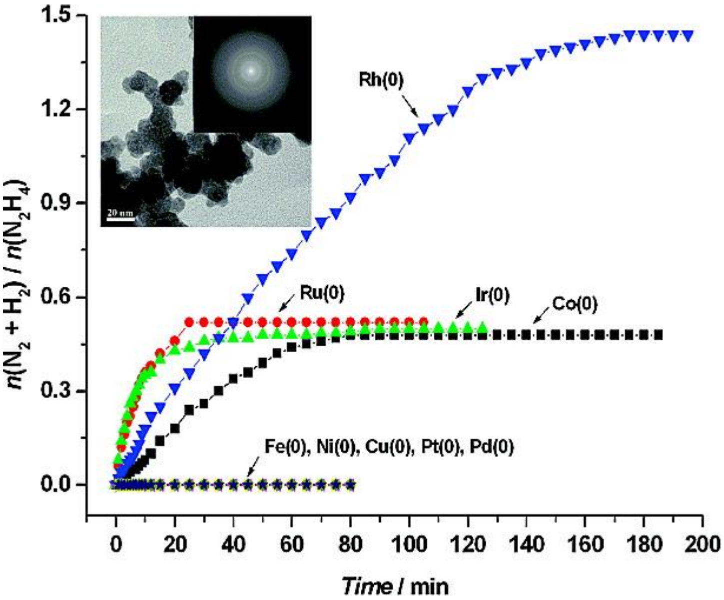

Figure 72: Decomposition of hydrous hydrazine vs time in aqueous solution using different metal NPs at room temperature. Inset: TEM image of Rh(0) NPs. Reprinted with permission from Ref. [443]: Q. Xu et al. "Room-Temperature Hydrogen Generation from Hydrous Hydrazine for Chemical Hydrogen Storage" https://doi-org.pros2.lib.unimi.it/10.1021/ja903869y. Copyright 2009 American Chemical Society.

In order to decrease the cost of the catalyst, the same authors have demonstrated that enhancing the temperature to 50 °C, unsupported Ni NPs can be active in hydrazine decomposition, showing 33 % selectivity to hydrogen[442].

In addition, the presence of sodium hydroxide (NaOH) as an additive in the reaction mixture can favour the formation of hydrogen instead of ammonia. In particular, Wang at al.[471] have studied the effect of NaOH on the selectivity of unsupported noble-metal free Ni NPs. It was seen that in the absence of NaOH, the selectivity to the complete hydrazine decomposition was only 64.5 %, whereas it reached 78.0 % adding a 0.25 M NaOH solution. Increasing its concentration to 0.5 M the selectivity to H_2 reached the 100 %, demonstrating its beneficial effect (Figure 73). NaOH have a bifunctional effect: i) OH^- ions suppress the formation of NH_3 and ii) they accelerate the rate-determining deprotonation step (Eq. 20) of hydrazine decomposition. In Table 5 are summarized the selectivity for H_2 of different unsupported monometallic NPs.

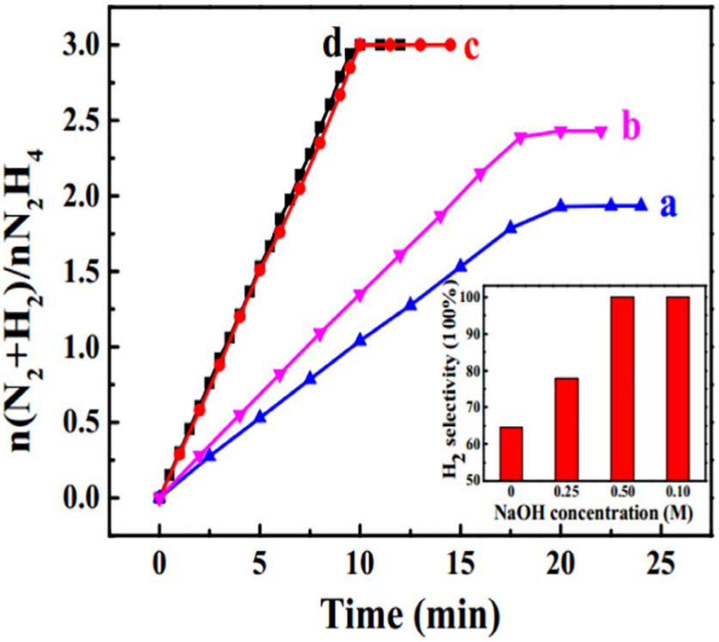

Figure 73: Decomposition of hydrous hydrazine vs time in aqueous solution with different NaOH concentration: a) absence of NaOH, b), c) and d) 0.25 M, 0.50 M and 1.00 M of NaOH, respectively. Inset: effect of NaOH concentration on the selectivity. Reprinted from Ref. [471]: H. Wang et al. “Facile synthesis of Ni nanoparticles from triangular $Ni(HCO_3)_2$ nanosheets as catalysts for hydrogen generation from hydrous hydrazine” https://doi.org/10.1016/j.catcom.2017.06.021 with permission of Elsevier.

Table 5: Hydrogen selectivity of different unsupported monometallic NPs in hydrous hydrazine decomposition.

Catalyst	*T (° C)*	*H_2 selectivity (%)*	*Ref.*
Rh	25	43.8	[443]

Rh	70	34.0	[443]
Pd	25	0	[443]
Ir	25	7	[443]
Pt	25	0	[443]
Ru	25	7	[443]
Co	25	7	[443]
Fe	25	0	[443]
Cu	25	0	[443]
Ni	25	0	[443]
Ni	50	33	[442]
Ni	70	64.5	[471]
Ni	70	100[a]	[471]

[a] Addition of NaOH

Unsupported bimetallic NPs

Alloying another metal to form bimetallic systems is an effective strategy to enhance the catalytic properties of the considered materials. Different bimetallic NPs have been used in this reaction with the purpose to tune the activity and the selectivity of the catalyst, i.e. bimetallic with i) two noble metals, ii) one noble and one non-noble metal and iii) two non-noble metals.

As an example, Xia and co-workers[472] prepared two different PdIr structures, core-shell octapods and alloyed nanocages. These catalysts were then tested in the decomposition of hydrous hydrazine at room temperature and compared with Pd nanocubes. Monometallic Pd exhibited no activity, confirming previous studies. On the contrary, the two bimetallic systems, in particular the nanocages showed enhanced activity and selectivity for H_2, i.e. 66 % for the nanocage and 29 % for the octapod. The difference was attributed to the diverse surface composition of the two structures. In the nanocage system, the presence of both Ir and Pd favoured the formation of heterometallic bonds, modifying the surface electronic structure of the nanocatalyst and boosting its activity and selectivity.

Among all the alloys with a non-noble metal, the systems based on nickel are the most used in hydrazine decomposition reaction. Indeed, Xu et al.[473] have successfully synthesised Ni_xRh_y alloyed nanocatalysts with different metal ratio. Figure 74 shows the strong dependence of hydrogen selectivity with Ni:Rh ratio. Even if monometallic Ni was inactive at room temperature and monometallic Rh possessed a low hydrogen selectivity, alloying the two metals strongly enhanced the catalytic properties of the material reaching the 100 % H_2 selectivity for Ni_1Rh_4. The physical mixing of Rh and Ni did not affect the general catalytic behaviour, indicating the necessity to have a Ni-Rh heteronuclear bond. The result is a modification of the nanocatalyst's surface and the interaction of the active phase (Rh) with N-N or N-H bonds.

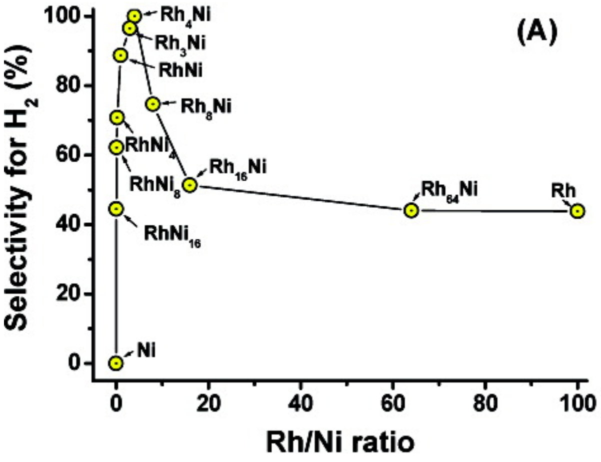

Figure 74: H_2 selectivity values vs RhNi ratio for room temperature hydrous hydrazine decomposition. Reprinted with permission of Ref. [473]: Q. Xu et al. "Complete Conversion of Hydrous Hydrazine to Hydrogen at Room Temperature for Chemical Hydrogen Storage" https://doi.org/10.1021/ja908037t. Copyright 2009, American Chemical Society.

Temperature plays a crucial role on the catalytic behaviour of the materials as observed for the monometallic nanocatalysts. Singh et al.[474] discovered that the materials with a high Rh content ($Rh_{95}Ni_5$ and $Rh_{90}Ni_{10}$) exhibited the same trend of monometallic Rh catalyst, i.e. decreasing of the H_2 selectivity by increasing the temperature from 25 to 70 °C. On the other hand, $Rh_{10}Ni_{90}$ showed an increase in selectivity from 28 % to 100 % enhancing the temperature to 50 °C. This system, which possess low Rh content but high performance, can be the starting point for a practical application. Because noble metals are extremely expensive, different noble-metal free Ni-based nanocatalysts were intensively studied in order to facilitate the potential industrial scale development of hydrous hydrazine as hydrogen carrier. Xu and co-workers[475] have synthesized and tested Ni_xFe_y NPs with different Ni and Fe ratio. All the prepared materials were inactive at room temperature and without a solution of NaOH 0.5 M. Enhancing the temperature to 50 °C without adding sodium hydroxide, the most performing catalyst (Ni:Fe = 1:1) showed 81 % selectivity for H_2, which was further improved to 100 % adding NaOH (Figure 75).

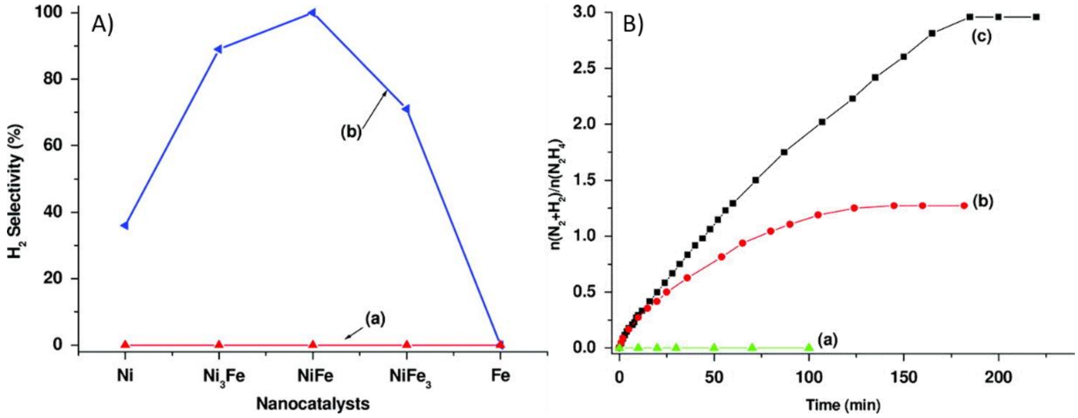

Figure 75: A) comparison of H_2 selectivity for the decomposition of hydrous hydrazine with NaOH 0.5 M at a) 298 K and b) 343 K. B) kinetic profile of a) Fe, b) Ni and c) NiFe for the decomposition of hydrous hydrazine at 343 K with NaOH 0.5 M. Reprinted with permission of Ref. [474]: A. K. Singh et al. "Noble-Metal-Free Bimetallic Nanoparticle-Catalyzed Selective Hydrogen Generation from Hydrous Hydrazine for Chemical Hydrogen Storage" https://doi-org.pros2.lib.unimi.it/10.1021/ja208475y. Copyright 2011, American Chemical Society.

Unsupported nanocatalysts may suffer of severe aggregation and agglomeration during the reaction. Therefore, they usually exhibit poor durability during several reaction runs because of the reduction of surface area and active sites. Immobilization of NPs on a support is a convenient strategy to reduce stability problems in catalytic performances and to enhance NPs dispersion. Furthermore, the use of specific material can enhance activity and selectivity of the catalyst due to synergistic effects between the active phase and the support.

Supported monometallic NPs

In the early stage of research noble monometallic supported nanoparticles were investigated, but they exhibited extremely poor activity and selectivity also at high temperature. For example, Zhang et al.[447] studied a series of group VIII metal NPs supported on SiO_2, e.g. 8wt%Ru/SiO_2, 8wt%Ir/SiO_2, 8wt%Rh/SiO_2, 8wt%Pd/SiO_2, 8wt%Pt/SiO_2 employing a fix bed reactor. All these catalysts completely decomposed hydrazine at temperature higher than 300 °C. When the temperature was reduced below this value, the H_2 production drastically decreased indicating that the preferential pathway is the incomplete hydrazine decomposition, forming ammonia. When temperature is increased to temperature upper to 300 °C, NH_3 is further decomposed to nitrogen and hydrogen indirectly boosting H_2 selectivity.

Lu and co-workers[476] used density functional theory (DFT) to study hydrazine decomposition over an Ir(111) surface. Different mechanisms were identified: i) intramolecular reaction between hydrazine molecules, ii) intramolecular reaction between amino groups co-adsorbed on the metal surface and iii) hydrazine dehydrogenation. Following the five different pathways found by the group a preferential initial N-N bond scission was identified leading to NH_3 and N_2 production (Figure 76) and confirming the results obtained in previous studies.

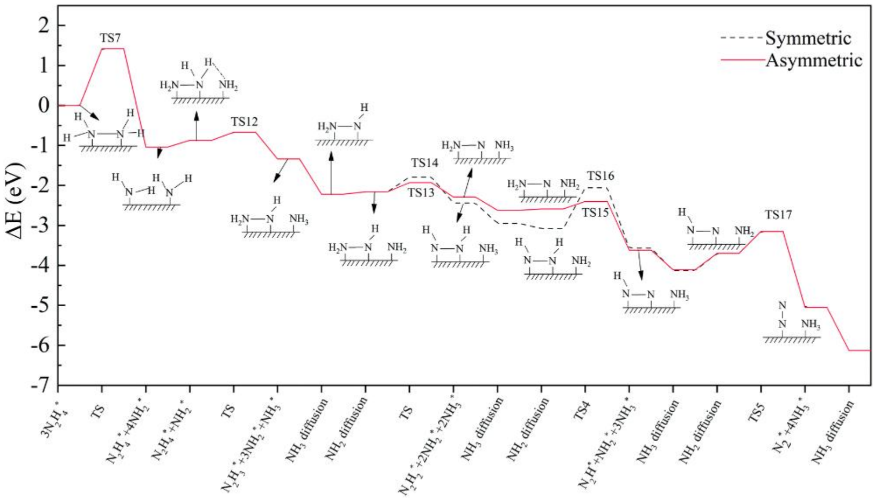

Figure 76: Energy profile for the intramolecular dehydrogenation of hydrazine assisted by co-adsorbed NH_2 over Ir(111) surface. Reprinted from Ref. [476]: X. Lu et al. "Mechanistic study of hydrazine decomposition on Ir(111)" https://doi.org/10.1039/C9CP06525C with the permission of the Royal Society of Chemistry.

More interest has been showed for the development of noble metal free catalysts, especially Ni-based ones[477–479]. The most used supports for these materials are large surface area metal oxides, because of their influence in catalytic activity through electronic effects. In particular He et al.[477] supported Ni NPs on CeO_2, ZrO_2, MgO and La_2O_3 oxides. Different types of Ni catalysts immobilised on cerium oxide were prepared using coprecipitation and impregnation methods obtaining Ni-xCeO_2 and Ni/CeO_2-IMP, respectively. Table 6 summarizes the different results obtained for the Ni/ CeO_2 catalysts.

Table 6: $N_2H_4 \cdot H_2O$ decomposition results for the different catalysts tested in Ref. [477].

Catalyst	*TOF (h^{-1})*	*H_2 selectivity (%)*
Ni	15.0	67
Ni-0.005CeO_2	32.4	84
Ni-0.025CeO_2	41.2	97
Ni-0.080CeO_2	51.6	99
Ni-0.233CeO_2	30.5	99

Ni-0.500CeO_2	26.0	99
Ni/CeO_2-IMP	15.0	65

From the characterization results the models of the highly active and selective Ni-0.080CeO_2 and for Ni/CeO_2-IMP were obtained and showed in Figure 77. In the first case, Ni was embedded by amorphous cerium oxide, which permitted the interaction between Ce and Ni and forming perturbated Ni specie ($Ni^{\delta+}$). This altered electronic structures lead to a facilitated N-H bond dissociation generating H_2 more efficiently.

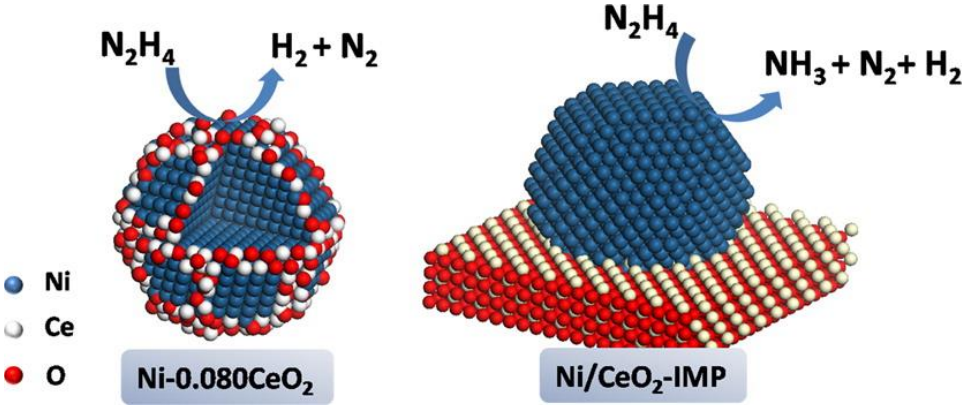

Figure 77: Structure models obtained from characterization of Ni-0.080CeO_2 and for Ni/CeO_2-IMP. Reprinted with permission from Ref. [477]: L. He et al. “Cerium-Oxide-Modified Nickel as a Non-Noble Metal Catalyst for Selective Decomposition of Hydrous Hydrazine to Hydrogen” https://doi.org/10.1021/acscatal.5b00143. Copyright 2015, American Chemical Society.

The promoting effect of oxides was also confirmed by the results obtained for Ni-ZrO_2, Ni-MgO and Ni-La_2O_3 catalysts where, all the different materials showed improved catalytic behaviour than pure Ni (Table 7).

Table 7: $N_2H_4 \cdot H_2O$ decomposition results for the different Ni-MO_x tested in Ref. [477]

Catalyst	*TOF (h^{-1})*	*H_2 selectivity (%)*
Ni	15.0	67
Ni-CeO_2	51.6	99
Ni-ZrO_2	47.1	95
Ni-MgO	26.5	90
Ni-La_2O_3	35.9	89

Moreover, Varma and co-workers[478] prepared a Ni/CeO_2 catalyst by using solution combustion method and varying the synthesis parameters. They discovered that the synthetic procedure influenced the final catalytic behaviour changing the physicochemical properties of the material, i.e. crystallinity, metal particle size, surface area and the formation of Ni-O-Ce bonds. The most performing catalyst, 6wt%Ni/CeO_2-HH-2 showed 100 % H_2 selectivity and a TOF of 34.0 h^{-1} at 50 °C. The activity of the material can be further improved increasing the reaction temperature: the reaction rate increased about 30-fold passing from 30 °C to 90 °C. On the other hand, when temperature was increased up to 70 °C the H_2 selectivity decreased to 93 % (90 °C) because of thermodynamic reasons (Figure 78).

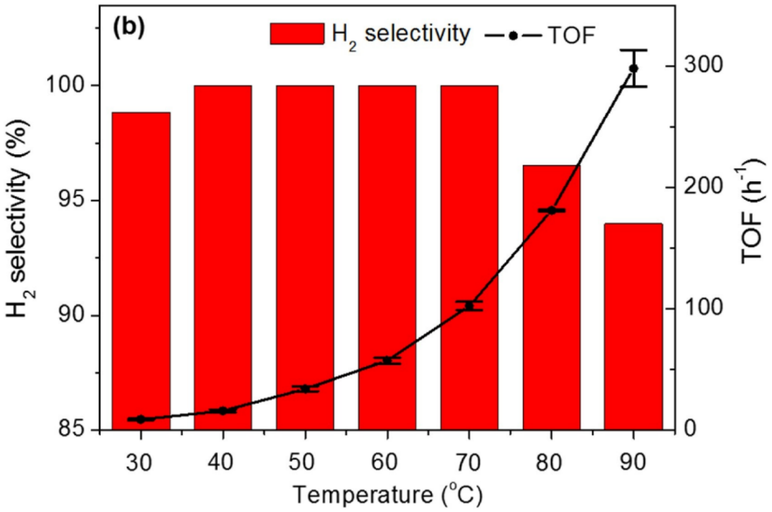

Figure 78: variation of selectivity and TOF changing the reaction temperature. Reprinted from Ref. [478]: A. Varma et al. “Hydrogen generation from hydrous hydrazine over Ni/CeO_2 catalysts prepared by solution combustion synthesis” https://doi.org/10.1016/j.apcatb.2017.08.053 with permission of Elsevier.

Other supports have been used to deposit Ni NPs. For instance, Guo et al.[479] have grown carbon nanotubes (CNTs) on Ni fibers (Ni-NFs) using chemical vapour deposition and obtaining the catalyst denoted as Ni-CNTs. In addition, they introduced hydroxyl groups on the CNTs surface employing a typical hydroxylation procedure, obtaining Ni-CNTs-OH material. This solution increased the wettability of the surface of CNTs as demonstrated by the different contact angles measured, i.e. 110.6 ° and 48.8 ° for CNTs and Ni-CNTs-OH (Figure 79a). Comparing the Ni-CNTs and Ni-CNTs-OH catalysts they could observed an increasing in the catalytic behaviour in particular on the reaction rate (TOF values of 9.3 h^{-1} and 19.4 h^{-1}, respectively) and durability (Figure 79b and c).

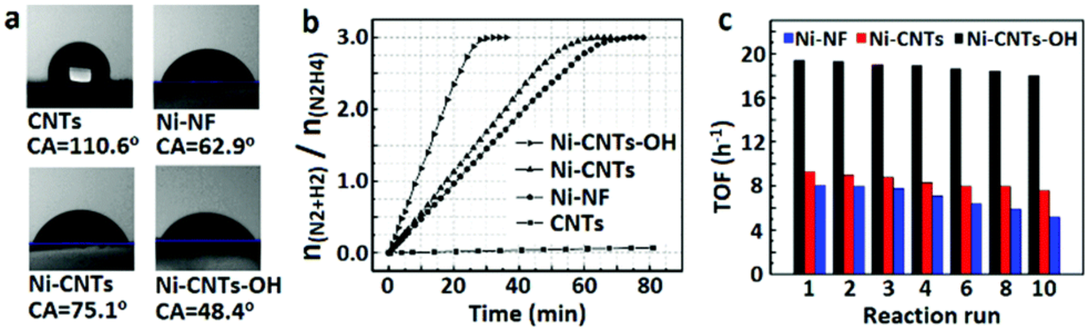

Figure 79: a) contact angles of the different materials, b) reaction kinetics at 333 K in 1.0 M NaOH aqueous solution and c) stability tests for hydrazine hydrate decomposition reaction. Reprinted from Ref. [479]: Z. Guo et al. "Anchoring carbon nanotubes and post-hydroxylation treatment enhanced Ni nanofiber catalysts towards efficient hydrous hydrazine decomposition for effective hydrogen generation" https://doi.org/10.1039/C9CC04559G with the permission of the Royal Society of Chemistry.

The effect of the basic environment was also disclosed by varying the concentration of NaOH in the reaction solution. In the absence of sodium hydroxide catalytic activity and selectivity are inefficient, while increasing the concentration to 0.6 M the catalytic performance significantly increased for all the reasons said before (suppressing the formation of NH_3 and promotion of the rate-determining step, Figure 80).

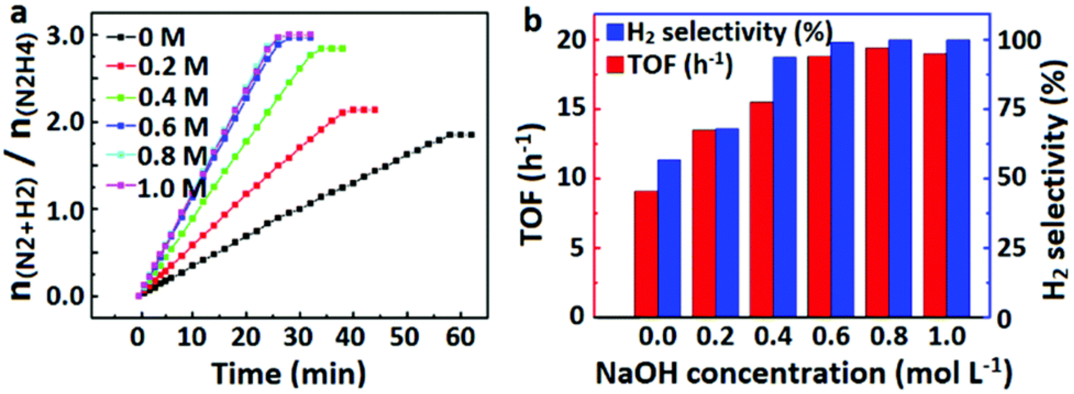

Figure 80: a) kinetic profiles of Ni-CNTs-OH catalyst in the presence of different NaOH concentrations and b) TOF values and H_2 selectivity at different NaOH amount. Reprinted from Ref. [479]: Z. Guo et al. "Anchoring carbon nanotubes and post-hydroxylation treatment enhanced Ni nanofiber catalysts towards efficient hydrous hydrazine decomposition for effective hydrogen generation" https://doi.org/10.1039/C9CC04559G with the permission of the Royal Society of Chemistry.

As previously mentioned, another strategy to improve the catalytic performance of a material is forming an alloyed structure using more than one metal.

Supported bimetallic NPs

Ni-based catalysts have been mostly alloyed with noble metals, such as Pt, Pd, Ir and Rh in order to maintain a lower cost of the material but enormously increased the catalytic properties.

Concerning RhNi catalysts, Zhang et al.[480] had successfully prepared a RhNi@graphene material using co-reduction method and graphene oxide (GO) as the initial support. This system was able to completely decompose hydrazine at room temperature in the presence of NaOH within 49 min of reaction, showing a 100 % H_2 selectivity. Herein, GO played a crucial role in dispersing RhNi NPs and to avoid their agglomeration due to its nature. GO possesses a hydrophobic basal plane and hydrophilic groups such as phenyl epoxides and hydroxyls, which can act as surfactants and anchor the NPs controlling their distribution during the synthesis of the catalyst. Moreover, using the same method, RhNi@Vulcan XC-72R was synthesised. By analysing the materials using SEM, TEM and XRD techniques they observed a similar size, distribution and crystallinity of the NPs but a lower activity for RhNi@Vulcan XC-72R catalyst, highlighting the synergistic effect between the active phase and the support. In addition, Liu and co-workers[481] used a different support, i.e. titanium carbide (MXene), to anchor RhNi NPs by one-step wet-chemical method obtaining RhNi/MXene catalyst. The chosen support is a graphene-like material transition-metal carbide, i.e. $Ti_3C_2(OH_xF_{1-x})_2$. The numerous functional groups of this system (Ti-OH and Ti-F) can stabilize the NPs during the reaction, improving the durability of the catalyst, but also improving its hydrophilicity. Among all the Rh_xNi_{1-x}/MXene catalysts investigated, $Rh_{0.8}Ni_{0.2}$/MXene showed the best catalytic activity at 50 °C with a selectivity for H_2 of 100 % (Figure 81). The excellent catalytic performances can be attributed to the RhNi NP size (2.8 nm) and their uniform dispersion on the support with the absence of aggregation. Moreover, the synergistic effect between the two metals alloyed can boost the surface electronic state improving the substrate-active phase interaction. Other supports were employed by the group, in particular GO, Al_2O_3, Vulcan XC-72R and multiwalled carbon nanotubes (MCNTs). The obtained catalysts were tested in the hydrazine decomposition in the same condition used for Rh_xNi_{1-x}/MXene showing lower catalytic performances. This behaviour can be attributed to the strong synergistic effect between the nanoparticles and the MXene. In addition, $Rh_{0.8}Ni_{0.2}$/MXene was also stable over six reaction runs confirming the expected enhanced durability due to the strong metal-support interaction.

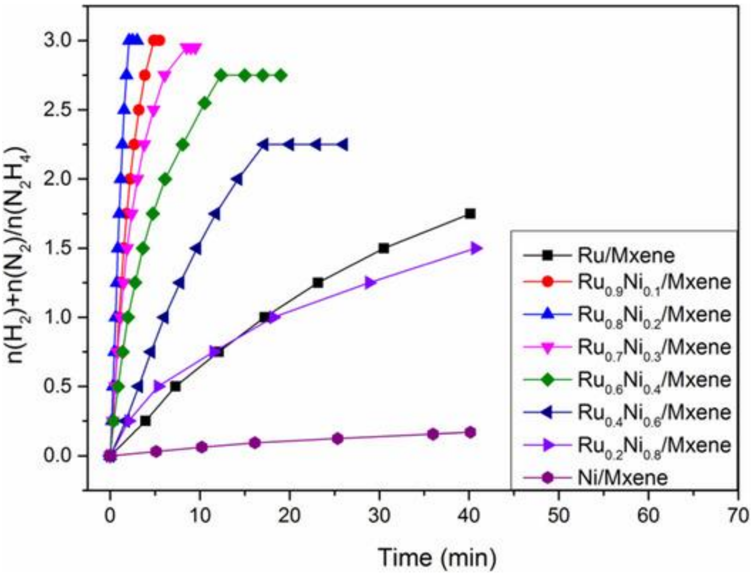

Figure 81: Time-course plots for H_2 production from hydrazine decomposition with RhNi/MXene catalysts with different RhNi ratio at 50 °C. Reprinted from Ref. [481]: T. Liu et al. "Highly Dispersed Bimetallic Nanoparticles Supported on Titanium Carbides for Remarkable Hydrogen Release from Hydrous Hydrazine" https://doi-org.pros2.lib.unimi.it/10.1002/cctc.201701633 with the permission of John Wiley and Sons.

NiIr nanoparticles with different metal ratio were encapsulated into the cavities of MIL-101 metal-organic frameworks (MOFs) by Cheng et al.[482] and applied in the hydrazine decomposition reaction. Similarly, the features of the support were fundamental in defining the final performances of the catalyst. MOFs possess a large surface area, chemical tunability but also high porosity with large pore size, which can be effective in the control of NPs shape and dispersion and avoiding agglomeration and metal leaching. In addition, the catalytic activity strongly depends on Ni/Ir molar ratio. From all the bimetallic catalyst, $Ni_{85}Ir_{15}$@MIL-101 showed the highest activity (464 h^{-1}) and 100 % hydrogen selectivity at 50 °C (Figure 82a). Also in this case, NiIr NPs were deposited on different supports, i.e. Al_2O_3, SiO_2 and carbon black and compared with $Ni_{85}Ir_{15}$@MIL-101 catalyst. All the material tested showed inferior catalytic activity, emphasising the dominant effect of MIL-101 in hydrogen production from hydrazine. Moreover, the limited window of pore size of this MOF prevented IrNi NPs to crossing the cavities avoiding durability problems. Indeed, $Ni_{85}Ir_{15}$@MIL-101 catalyst was found to be stable in activity and selectivity over five reaction runs. Another example of NiIr bimetallic catalyst was given by Wang and co-workers[483], who synthesised NiIr/CeO_2 catalyst. They confirmed the result obtained in the previous study, where a small amount of Ir can significantly enhance the catalytic properties in hydrogen generation from hydrazine. Indeed, Ni/CeO_2 showed high selectivity (96 %) and low reaction rate (14 h^{-1}), while when Ir was incorporated in Ni forming $Ni_{91}Ir_9$/CeO_2 catalyst the optimal catalytic performances were reached (Figure 82b). However, this catalyst slowly deactivates and, while maintaining the same selectivity value, the activity decreased to 58 h^{-1} after 15 cycles of reaction.

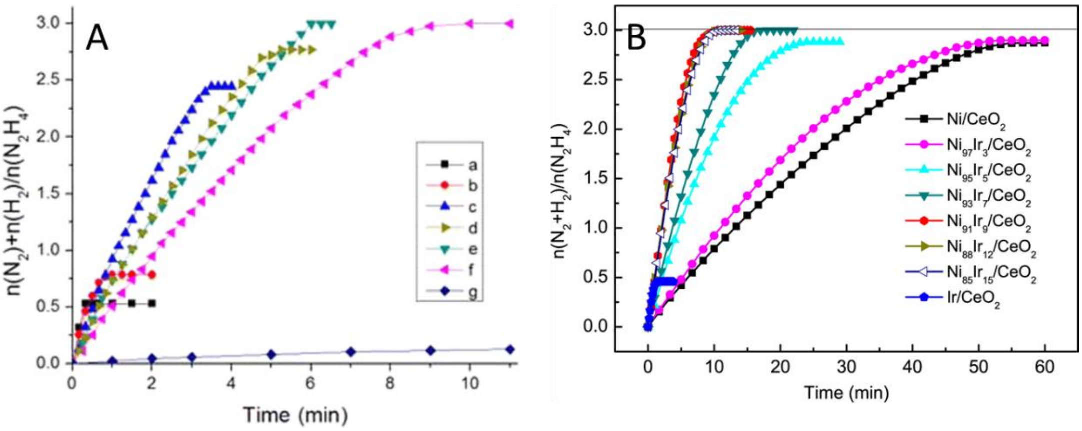

Figure 82: A) time plot for the decomposition of hydrous hydrazine at 50 °C with a) Ir@MIL-101, b) $Ni_{49}Ir_{51}$@MIL-101, c) $Ni_{71}Ir_{29}$@MIL-101, d) $Ni_{82}Ir_{18}$@MIL-10, e) $Ni_{85}Ir_{15}$@MIL-101, f) $Ni_{90}Ir_{10}$@MIL-101 and g) Ni@MIL-101. Adapted with permission from Ref. [482]: G. Cheng et al. "NiIr Nanoparticles Immobilized on the Pores of MIL-101 as Highly Efficient Catalyst toward Hydrogen Generation from Hydrous Hydrazine" https://doi.org/10.1021/acssuschemeng.5b00009. Copyright 2015, American Chemical Society. B) Time course profile for hydrazine decomposition reaction using $NiIr/CeO_2$ catalysts. Adapted from Ref. [483]: P. Wang et al. "Hydrogen generation from decomposition of hydrous hydrazine over $Ni-Ir/CeO_2$ catalyst" https://doi.org/10.1016/j.pnsc.2016.12.012 with the permission of Elsevier.

A recent study of Cao et al.[484] showed that also NiPd alloys can be effective in hydrazine decomposition. In this case reduced graphene oxide (rGO) was chosen as support and catalysts with different Pd/Ni molar ratios were prepared obtaining Pd_xNi_y/rGO materials. The monometallic counterparts exhibited poor catalytic activity, while the reaction rates of the bimetallic catalysts strongly depend on the Pd/Ni ratios. Among all, Pd_3Ni/rGO catalyst showed the best activity with a TOF at 50 °C with the addition of NaOH 0.5 M of 140 min^{-1} (8400 h^{-1}) and a 100 % selectivity for H_2 (Figure 83). It is clear that the improved catalytic properties were mainly due to the electronic and steric effects between the two metals. Nevertheless, this catalyst easily deactivates after three runs of reaction because of leaching of the metal (the metal loading decreased of the 28 % after three cycles).

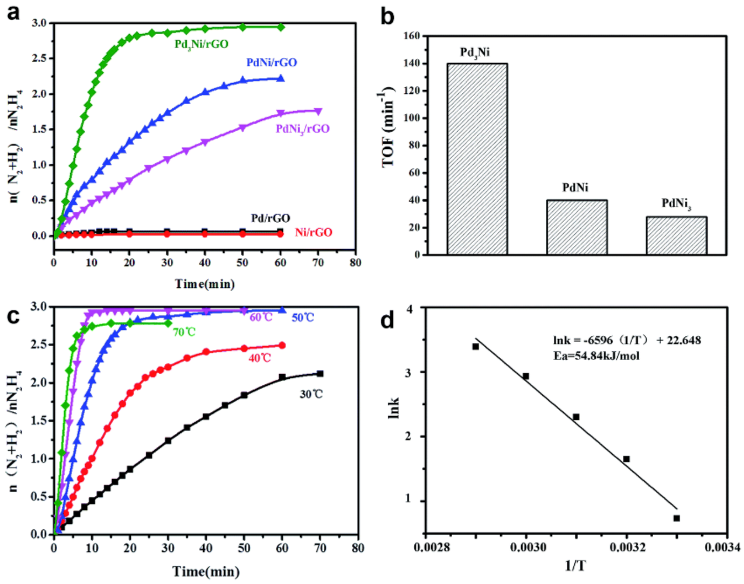

Figure 83: a) time course plot for hydrazine decomposition over PdNi/rGO catalysts, b) TOF, c) dependence of the reaction on the temperature and d) plot of ln k vs 1/T. Reprinted from Ref. [484]: R. Cao et al. "Pd–Ni nanoparticles supported on reduced graphene oxides as catalysts for hydrogen generation from hydrazine" https://doi.org/10.1039/C7RA04390B with the permission of the Royal Society of Chemistry.

Numerous different works reported the use of NiPt alloy with different supports to enhance the catalytic performance in hydrazine decomposition. Su and co-workers[485] deposited NiPt NPs within a MIL-101 functionalised by electro-donating groups NH_2 support obtaining Ni_xPt_y/MIL-101-NH_2 catalysts. $Ni_{0.8}Pt_{0.2}$/MIL-101-NH_2 was denoted as the best performing catalyst with a TOF value of 137 h^{-1} and 100 % H_2 selectivity (Figure 84a). NiPt NPs with molar ratio 0.8:0.2 were immobilized on different MOFs, i.e. bare MIL-101, MIL-101-SO_3H, MIL-101-NO_2, bare MOF-5 and MOF-5-NH_2, in order to study the effect of the support. All the prepared materials showed decreased activity and an increased particle size in respect to $Ni_{0.8}Pt_{0.2}$/MIL-101-NH_2. From these outcomes, it can be clearly seen that the pore size and the nature of the MOF support can largely influence the overall catalytic activity of the catalyst by modulating the particle size. In addition, the presence of basic functional groups was crucial in favouring the N-H bond scission in the first hydrazine decomposition step. Moreover, all the electron donating groups inserted can enrich the NiPt surface of electrons favouring the interaction of the active phase with hydrazine molecule. Regarding the durability of the material, the group could observe that selectivity remained unchanged after 5 reaction cycles, but also the presence of a slight decrease in catalytic activity due to partial agglomeration of NPs and oxidation of the NiPt surface. Another example of NiPt alloy was proposed by Luo et al.[486] where CeO_2 nanospheres was selected as support. They found that when Pt/Ni molar ratio is 1:1, a significantly enhanced catalytic activity was observed with a TOF value of 416 h^{-1} and 100 % hydrogen selectivity at 25 °C, underling the pivotal role of the Ni/Pt interaction (Figure 84b). Also for this specific alloy, an oxygen-rich titanium carbide MXenes was employed as support by Lu and co-workers[487]. Again, the effect of the support and the Ni/Pt molar ratio was evidenced. The optimized $Ni_{0.8}Pt_{0.2}/DT\text{-}T_3C_2T_x$ exhibited 100 % H_2 selectivity and an exceptional catalytic activity (TOF = 1220 h^{-1}, Figure 84c). From all these results, we can observe that Ni is the key element to decompose hydrazine, in fact the noble metals alone showed extremely low activities, while monometallic Ni can decompose hydrazine in most of the cases.

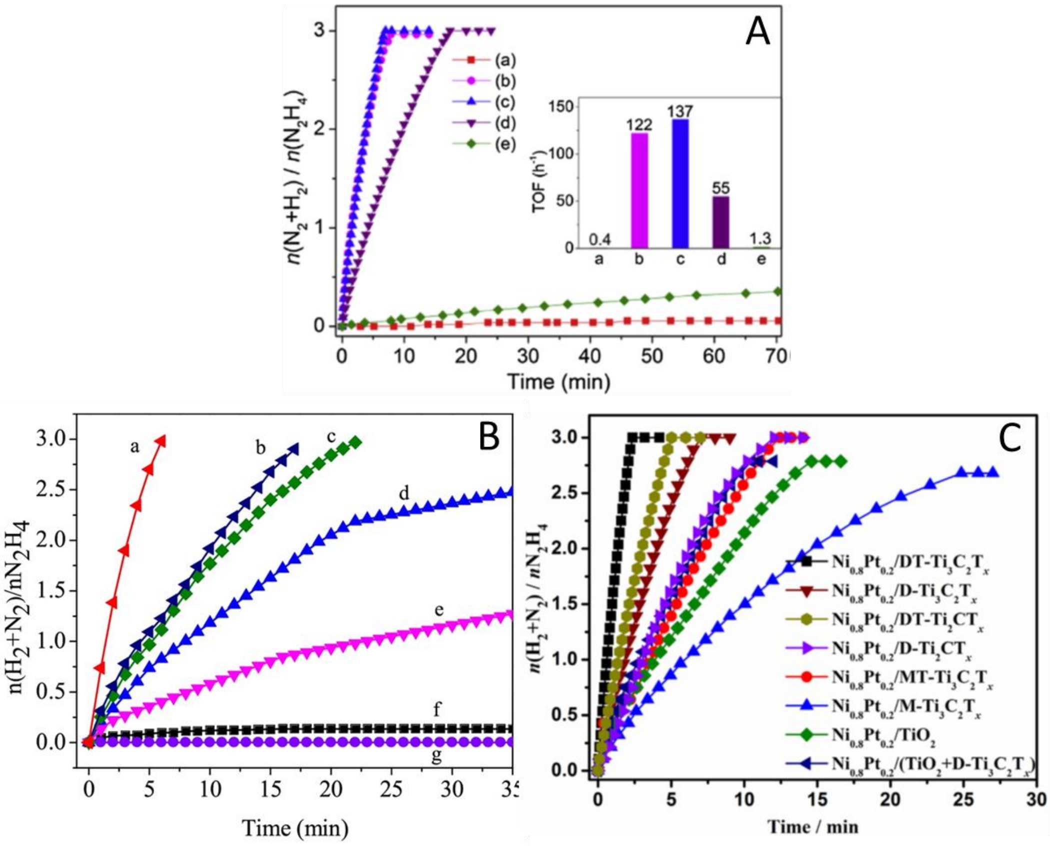

Figure 84: Time course plot for A) NiPt/MIL-101-NH_2 with different Ni/Pt molar ratios at 298 K: a) 0:1, b) 0.69:0.31, c) 0.8:0.2, d) 0.9:0.1 and e1:0 (Inset: TOF values of the catalysts). Adapted from Ref. [485]: H. Su et al. "Construction of bimetallic nanoparticles immobilized by porous functionalized metal-organic frameworks toward remarkably enhanced catalytic activity for the room-temperature complete conversion of hydrous hydrazine into hydrogen" https://doi.org/10.1016/j.ijhydene.2017.06.191 with permission from Elsevier. B) NiPt-CeO_2 with different Ni/Pt ratios at 298 K: a) 5:5, b) 7:3, c) 3:7, d) 1:9, e) 9:1, f) 10:0 and g) 0:10. Adapted from Ref. [486]: W. Luo et al. "NiPt nanoparticles supported on CeO_2 nanospheres for efficient catalytic hydrogen generation from alkaline solution of hydrazine" https://doi.org/10.1016/j.cclet.2018.11.010 with the permission of Elsevier. C) $Ni_{0.8}Pt_{0.2}$ on different supports at 323 K. Adapted from Ref. [487]: Z. H. Lu et al. "Monodispersed bimetallic nanoparticles anchored on TiO_2-decorated titanium carbide MXene for efficient hydrogen production from hydrazine in aqueous solution" https://doi.org/10.1016/j.renene.2020.04.047 with the permission of Elsevier.

More interestingly, various works reported the use of Fe to enhance the features of Ni-based catalysts. For example, Luo et al.[488] deposited NiFe NPs modified with different amount of CeO_x on reduced graphene oxide (rGO) using a co-reduction method. Ni_3Fe/rGO was firstly tested in order to clearly observe the role of cerium oxide addition. This catalyst showed poor activity and a hydrogen selectivity of only 74.5 %. Nonetheless, after doping activity and selectivity were significantly enhanced. Among all the catalysts, Ni_3Fe-$(CeO_x)_{0.15}$/rGO showed the highest catalytic activity (TOF = 126 h^{-1}) at 70 °C with NaOH 1 M and 100 % H_2 selectivity, evidencing a synergistic effect between Fe, Ni and Ce (Figure 85a). This fact was corroborated by X-ray photoelectron spectroscopy (XPS), where for both Ni 2p3/2 and Fe 2p peaks, a positive shift was observed, which was ascribed to a decrease electron density on the two metals and an increase of vacancies in their d-band. In addition, Ce^{3+} and Ce^{4+} peaks are both negatively shifted underling the strong electronic interaction between Fe, Ni and Ce. Indeed, varying the electronic configuration can change the surface nature of the catalyst, increasing the overall catalytic performance. On the other hand, during stability tests even if selectivity was retained, the catalyst slowly deactivates during 5 reaction runs. By performing transmission electron microscopy (TEM) on the used catalyst, a change in its morphology was detected, which can explain the durability test result. In the same year, Wen and co-workers[489] prepared NiFe nanoparticles, but in this case cerium oxide was employed as basic support for the active phase. It can be seen in Figure 85b that alloying Fe to Ni the catalytic activity and H_2 selectivity incredibly increased and all the bimetallic catalysts showed a superior reaction rate than the monometallic counterparts. Among all, $Ni_{0.6}Fe_{0.4}/CeO_2$ exhibited the optimal catalytic performance (more than 99 % H_2 selectivity and a TOF value of 5.37 h^{-1} at 50 °C). Also in his work, the role of CeO_2 was due to the high electron density of Ce^{3+}. It can act as a strong Lewis base facilitating the scission of N-H bond. Durability tests were then performed and a decreasing in both selectivity and activity was observed during 10 reaction cycles. This can be due to a slight agglomeration of NPs observed on the used catalyst.

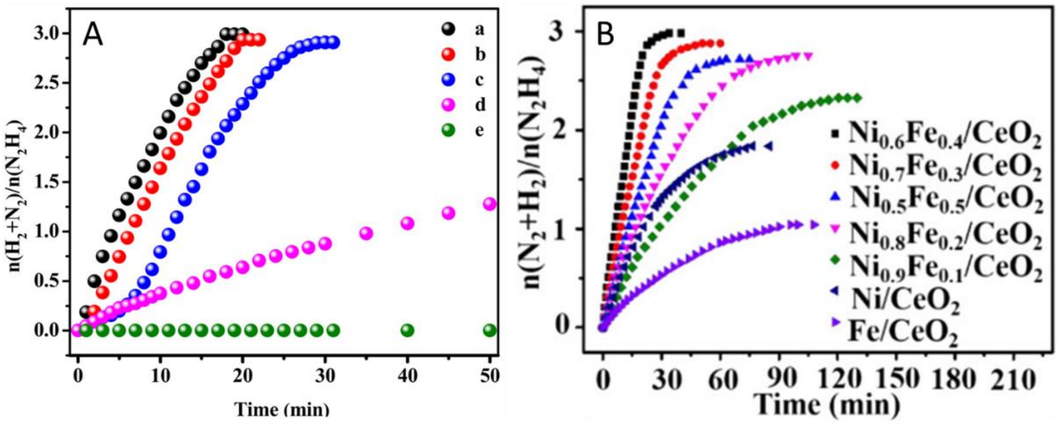

Figure 85: time course plot of A) $Ni_3Fe-CeO_x/rGO$ catalysts with different Ce content: a) 0.15, b) 0.1, c) 0.17 d) without CeO_x and e) CeO_x/rGO. Adapted from Ref. [488]: W. Luo et al. "CeOx-modified NiFe nanodendrits grown on rGO for efficient catalytic hydrogen generation from alkaline solution of hydrazine" https://doi.org/10.1016/j.ijhydene.2017.08.214 with the permission of Elsevier. B) 2D $NiFe/CeO_2$ catalysts with different Ni/Fe ratio. Adapted with permission from Ref. [489]: M. Wen et al. "2D $NiFe/CeO_2$ Basic-Site-Enhanced Catalyst via in-Situ Topotactic Reduction for Selectively Catalyzing the H_2 Generation from $N_2H_4 \cdot H_2O$" https://doi.org/10.1021/acsami.7b00652. Copyright 2017, American Chemical Society.

Table 8 summarizes the different activities, selectivity and conditions for the bimetallic supported catalysts treated in this section.

Table 8: Catalytic activities of different bimetallic supported catalysts used in hydrazine hydrate decomposition reaction.

Catalyst	*TOF (h^{-1})*	*H_2 selectivity (%)*	*Solvent*	*T (°C)*	*Ref*
$Rh_{4.4}Ni$@graphene	28	100	Aqueous NaOH	50 °C	[480]
$Rh_{0.8}Ni_{0.2}$/MXene	857	100	Aqueous NaOH	50 °C	[481]
$Ni_{85}Ir_{15}$@MIL-101	464	100	Aqueous NaOH	50 °C	[482]
$Ni_{91}Ir_9/CeO_2$	97	100	Aqueous NaOH	50 °C	[483]
Pd_3Ni/rGO	8400	100	Aqueous NaOH	50 °C	[484]
$Ni_{0.8}Pt_{0.2}$/MIL-101-NH_2	137	100	Aqueous NaOH	25 °C	[485]
$Ni_{0.8}Pt_{0.2}$/MIL-101-NH_2	676	100	Aqueous NaOH	50 °C	[485]
$Ni_5Pt_5-CeO_2$	416	100	Aqueous NaOH	25 °C	[486]
$Ni_{0.8}Pt_{0.2}/DT-T_3C_2T_x$	1220	100	Aqueous NaOH	50 °C	[487]
$Ni_3Fe-(CeO_x)_{0.15}/rGO$	126	100	Aqueous NaOH	70 °C	[488]
$Ni_3Fe-(CeO_x)_{0.15}/rGO$	57	100	Aqueous NaOH	55 °C	[488]

$Ni_{0.6}Fe_{0.4}/CeO_2$	6	>99	Water	50 °C	[489]

As depicted here, in the last few decades effort have been made to improve catalytic condition, metal cost, durability and selectivity of the catalysts employed in hydrazine hydrate decomposition reaction. On the other hand, for practical application prospective all these important features need to be further enhanced, in particular durability, control of the reaction kinetics and the cost of the material (from the support to the active phase). These are the main aims of the current research.

1.5. Aim of the Thesis

As addressed in the literature review, further investigations are required in order to improve the catalytic activity, stability and selectivity in formic acid decomposition reaction. The first part of my thesis will be dedicated to the design of new catalysts with the aim to improve the catalytic behaviour compared to existing Pd-based ones for formic acid selective decomposition reaction. In particular, the effect of the metal-support interaction and the geometrical and electronic effect in alloyed catalysts play a fundamental role to enhance the catalytic performance (Chapter 3-5).

Chapter 3 is devoted to study the metal-support interaction by doping with O and P functionalities the carbonaceous support.

The effect of the addition of a second metal to Pd is considered (Rh in Chapter 4 and Au in Chapter 5).

In addition, in order to decrease the cost and increase the environmental benignity of the catalyst, the application of metal-free carbon materials in the formic acid dehydrogenation is investigated (Chapter 6).

In the final chapter (Chapter 7), the above reported metal-free carbocatalysts are employed for the hydrazine hydrate dehydrogenation reaction, in order to produce H_2 without the presence of CO_2.

1.6. References

[1] IEA, *Key World Energy Statistics 2020*, **2020**.

[2] U.S. Energy Information Administration's (EIA), *International Energy Outlook 2019*, **2019**.

[3] European Commission, "Causes of climate change," can be found under https://ec.europa.eu/clima/change/causes_en, **2021**.

[4] United States EPA, "Climate Change Indicators," can be found under https://www.epa.gov/climate-indicators, **2021**.

[5] K. Rajeshwar, R. McConnell, K. Harrison, S. Licht, in (Eds.: K. Rajeshwar, R. McConnell, S. Licht), Springer New York, New York, NY, **2008**, pp. 1–18.

[6] European Commission, "Climate Action," can be found under https://ec.europa.eu/clima/change/causes_en, **n.d.**

[7] Organization of the Petroleum Exporting Countries, "OPEC," can be found under https://www.opec.org/opec_web/en/index.htm, **n.d.**

[8] IEA, Global Energy Review 2020, Paris, **2020**.

[9] IEA, Global Energy Review 2021, Paris, **2021**.

[10]N. L. Panwar, S. C. Kaushik, S. Kothari, *Renew. Sustain. Energy Rev.* **2011**, *15*, 1513–1524.

[11]A. Pareek, R. Dom, J. Gupta, J. Chandran, V. Adepu, P. H. Borse, *Mater. Sci. Energy Technol.* **2020**, *3*, 319–327.

[12] I. Yüksel, *Renew. Sustain. Energy Rev.* **2010**, *14*, 462–469.

[13] I. Kougias, G. Aggidis, F. Avellan, S. Deniz, U. Lundin, A. Moro, S. Muntean, D. Novara, J. I. Pérez-Díaz, E. Quaranta, P. Schild, N. Theodossiou, *Renew. Sustain. Energy Rev.* **2019**, *113*, 109257.

[14] D. Henner, REN21, RENEWABLES 2020 GLOBAL STATUS REPORT, **2020**.

[15]M. Shoaib, I. Siddiqui, S. Rehman, S. Khan, L. M. Alhems, *J. Clean. Prod.* **2019**, *216*, 346–360.

[16]B. Anand, R. Shankar, S. Murugavelh, W. Rivera, K. Midhun Prasad, R. Nagarajan, *Renew. Sustain. Energy Rev.* **2021**, *141*, 110787.

[17] G. K. Singh, *Energy* **2013**, *53*, 1–13.

[18] C. E. Chan-Thaw, A. Villa, *Appl. Sci.* **2018**, *8*, DOI 10.3390/app8020259.

[19]H. Chowdhury, B. Loganathan, I. Mustary, F. Alam, S. M. A. Mobin, in *Second Third Gener. Feed.* (Eds.: A. Basile, F.B.T.-S. and T.G. of F. Dalena), Elsevier, **2019**, pp. 323–344.

[20]A. Deneyer, T. Ennaert, B. F. Sels, *Curr. Opin. Green Sustain. Chem.* **2018**, *10*, 11–20.

[21] J. K. Saini, R. Saini, L. Tewari, *3 Biotech* **2015**, *5*, 337–353.

[22]Y. Dahman, K. Syed, S. Begum, P. Roy, B. Mohtasebi, in *Biomass, Biopolym. Mater. Bioenergy* (Eds.: D. Verma, E. Fortunati, S. Jain, X.B.T.-B. Zhang Biopolymer-Based Materials, and Bioenergy), Elsevier, **2019**, pp. 277–325.

[23]Bioenergy Technologies Office - U.S. Department of Energy, "Bioenergy Basics," can be found under https://www.energy.gov/eere/bioenergy/bioenergy-basics, **n.d.**

[24]M. C. Chiong, C. T. Chong, J.-H. Ng, S. S. Lam, M.-V. Tran, W. W. F. Chong, M. N. Mohd Jaafar, A. Valera-Medina, *Energy Convers. Manag.* **2018**, *173*, 640–658.

[25]C. Yang, R. Li, C. Cui, S. Liu, Q. Qiu, Y. Ding, Y. Wu, B. Zhang, *Green Chem.* **2016**, *18*, 3684–3699.

[26] A. Sonthalia, N. Kumar, *J. Energy Inst.* **2019**, *92*, 1–17.

[27] F. Long, W. Liu, X. Jiang, Q. Zhai, X. Cao, J. Jiang, J. Xu, *Renew. Sustain. Energy Rev.* **2021**, *148*, 111269.

[28]P. E. V de Miranda, in (Ed.: P.E.V.B.T.-S. and E. of H.-B.E.T. de Miranda), Academic Press, **2019**, pp. 1–38.

[29] M. Momirlan, T. N. Veziroglu, *Int. J. Hydrogen Energy* **2005**, *30*, 795–802.

[30] United States Congress, *Energy Policy Act 1992*, **1992**.

[31] US Department of Energy, *The Green Hydrogen Report*, **1995**.

[32] World Energy Council, *World Energy Issues Monitor*, **2017**.

[33] IEA, *The Future of Hydrogen*, Paris, **2019**.

[34] E4tech, The Fuel Cell Industry Review 2020, **2020**.

[35]I. Staffell, D. Scamman, A. Velazquez Abad, P. Balcombe, P. E. Dodds, P. Ekins, N. Shah, K. R. Ward, *Energy Environ. Sci.* **2019**, *12*, 463–491.

[36]A. Chapman, K. Itaoka, K. Hirose, F. T. Davidson, K. Nagasawa, A. C. Lloyd, M. E. Webber, Z. Kurban, S. Managi, T. Tamaki, M. C. Lewis, R. E. Hebner, Y. Fujii, *Int. J. Hydrogen Energy* **2019**, *44*, 6371–6382.

[37] D. Stolten, C. S. Remzi, N. Garland, *Fuel Cells: Data, Facts, and Figures*, Wiley-VCH, **2015**.

[38] M. Lehner, R. Tichler, H. Steinmüller, M. Koppe, *Power-to-Gas: Technology and Business Models*, Springer, Cham, **2014**.

[39] J. Skřínský, P. Dolníček, M. Skřínská, J. Marek, P. Lukešová, *Chem. Eng. Technol.* **2015**, *38*, 727–733.

[40] M. Mohon Roy, E. Tomita, N. Kawahara, Y. Harada, A. Sakane, *Int. J. Hydrogen Energy* **2009**, *34*, 7811–7822.

[41]Y. H. Teoh, H. G. How, K. H. Yu, H. G. Chuah, W. L. Yin, *J. Adv. Res. Fluid Mech. Therm. Sci.* **2020**, *45*, 22–34.

[42] K. Mazloomi, C. Gomes, *Renew. Sustain. Energy Rev.* **2012**, *16*, 3024–3033.

[43] G. R. Astbury, *Process Saf. Environ. Prot.* **2008**, *86*, 397–414.

[44]C. E. Grégoire Padró, F. Lau, *Advances in Hydrogen Energy*, Springer, Boston, MA, **2002**.

[45] R. K. Ahluwalia, J. K. Peng, *Int. J. Hydrogen Energy* **2009**, *34*, 5476–5487.

[46]P. Gandhidasan, A. Ertas, E. E. Anderson, *J. Energy Resour. Technol.* **1991**, *113*, 101–107.

[47]Hydrogen and Fuel Cell Technology Office - U.S. Department of Energy, “Fuel Cells,” can be found under https://www.energy.gov/eere/fuelcells/fuel-cells, **n.d.**

[48]M. C. Williams, in (Eds.: D. Shekhawat, J.J. Spivey, D.A.B.T.-F.C.T. for F.P. Berry), Elsevier, Amsterdam, **2011**, pp. 11–27.

[49] O. Z. Sharaf, M. F. Orhan, *Renew. Sustain. Energy Rev.* **2014**, *32*, 810–853.

[50]D. Shekhawat, D. A. Berry, J. J. Spivey, in (Eds.: D. Shekhawat, J.J. Spivey, D.A.B.T.-F.C.T. for F.P. Berry), Elsevier, Amsterdam, **2011**, pp. 1–9.

[51] J. W. Lim, D. G. Lee, *Compos. Struct.* **2013**, *95*, 557–563.

[52]A. Baroutaji, T. Wilberforce, M. Ramadan, A. G. Olabi, *Renew. Sustain. Energy Rev.* **2019**, *106*, 31–40.

[53] A. Alaswad, A. Baroutaji, H. Achour, J. Carton, A. Al Makky, A. G. Olabi, *Int. J. Hydrogen Energy* **2016**, *41*, 16499–16508.

[54]Y. Wang, D. F. Ruiz Diaz, K. S. Chen, Z. Wang, X. C. Adroher, *Mater. Today* **2020**, *32*, 178–203.

[55] Y. S. Kim, K.-S. Lee, *Polym. Rev.* **2015**, *55*, 330–370.

[56]A. Chandan, M. Hattenberger, A. El-kharouf, S. Du, A. Dhir, V. Self, B. G. Pollet, A. Ingram, W. Bujalski, *J. Power Sources* **2013**, *231*, 264–278.

[57]S. J. Peighambardoust, S. Rowshanzamir, M. Amjadi, *Int. J. Hydrogen Energy* **2010**, *35*, 9349–9384.

[58] A. Arshad, H. M. Ali, A. Habib, M. A. Bashir, M. Jabbal, Y. Yan, *Therm. Sci. Eng. Prog.* **2019**, *9*, 308–321.

[59] M. Warshay, P. R. Prokopius, *The Fuel Cell in Space: Yesterday, Today and Tomorrow*, Cleveland, Ohio, **1990**.

[60] G. Merle, M. Wessling, K. Nijmeijer, *J. Memb. Sci.* **2011**, *377*, 1–35.

[61] G. F. McLean, T. Niet, S. Prince-Richard, N. Djilali, *Int. J. Hydrogen Energy* **2002**, *27*, 507–526.

[62] P. Gouérec, L. Poletto, J. Denizot, E. Sanchez-Cortezon, J. H. Miners, *J. Power Sources* **2004**, *129*, 193–204.

[63]N. Sammes, R. Bove, K. Stahl, *Curr. Opin. Solid State Mater. Sci.* **2004**, *8*, 372–378.

[64] P. Stonehart, D. Wheeler, in (Eds.: B.E. Conway, C.G. Vayenas, R.E. White, M.E. Gamboa-Adelco), Springer US, Boston, MA, **2005**, pp. 373–424.

[65] U. Lucia, *Renew. Sustain. Energy Rev.* **2014**, *30*, 164–169.

[66] R.-H. Song, D. R. Shin, *Int. J. Hydrogen Energy* **2001**, *26*, 1259–1262.

[67] D. -T. Chin, P. D. Howard, *J. Electrochem. Soc.* **1986**, *133*, 2447–2450.

[68] N. Q. Minh, *Solid State Ionics* **2004**, *174*, 271–277.

[69] S. C. Singhal, *Solid State Ionics* **2000**, *135*, 305–313.

[70] R. M. DELL, A. HOOPER, in (Eds.: P. HAGENMULLER, W.B.T.-S.E. VAN GOOL), Academic Press, **1978**, pp. 291–312.

[71] S. P. S. Badwal, *Solid State Ionics* **2001**, *143*, 39–46.

[72] A. L. Dicks, Curr. Opin. Solid State Mater. Sci. **2004**, 8, 379–383.

[73] E. Antolini, *Appl. Energy* **2011**, *88*, 4274–4293.

[74] M. Bischoff, *J. Power Sources* **2006**, *160*, 842–845.

[75]Hydrogen and Fuel Cell Technologies Office **-** U.S. Department of Energy, "Hydrogen Production: Natural Gas Reforming," can be found under https://www.energy.gov/eere/fuelcells/hydrogen-production-natural-gas-reforming, **2021**.

[76] J. R. Rostrup-Nielsen, K. Pedersen, *J. Catal.* **1979**, *59*, 395–404.

[77] A. Carrara, A. Perdichizzi, G. Barigozzi, *Int. J. Hydrogen Energy* **2010**, *35*, 3499–3508.

[78] Z. Al-Hamamre, S. Voß, D. Trimis, *Int. J. Hydrogen Energy* **2009**, *34*, 827–832.

[79]S. Sengodan, R. Lan, J. Humphreys, D. Du, W. Xu, H. Wang, S. Tao, *Renew. Sustain. Energy Rev.* **2018**, *82*, 761–780.

[80]B. Meng, H. Zhang, Z. Zhao, X. Wang, Y. Jin, S. Liu, *Catal. Today* **2016**, *259*, 388–392.

[81] R. Kothari, D. Buddhi, R. L. Sawhney, *Renew. Sustain. Energy Rev.* **2008**, *12*, 553–563.

[82] S. Lin, M. Harada, Y. Suzuki, H. Hatano, *Fuel* **2002**, *81*, 2079–2085.

[83] C.-C. Cormos, F. Starr, E. Tzimas, S. Peteves, *Int. J. Hydrogen Energy* **2008**, *33*, 1286–1294.

[84] F. M. Sapountzi, J. M. Gracia, C. J. (Kees-J. Weststrate, H. O. A. Fredriksson, J. W. (Hans) Niemantsverdriet, *Prog. Energy Combust. Sci.* **2017**, *58*, 1–35.

[85]M. Qadrdan, Y. Saboohi, J. Shayegan, *Int. J. Hydrogen Energy* **2008**, *33*, 7314–7325.

[86]T. Sinigaglia, F. Lewiski, M. E. Santos Martins, J. C. Mairesse Siluk, *Int. J. Hydrogen Energy* **2017**, *42*, 24597–24611.

[87] S. Singh, S. Jain, V. PS, A. K. Tiwari, M. R. Nouni, J. K. Pandey, S. Goel, *Renew. Sustain. Energy Rev.* **2015**, *51*, 623–633.

[88]J. R. Fekete, J. W. Sowards, R. L. Amaro, *Int. J. Hydrogen Energy* **2015**, *40*, 10547–10558.

[89] C. Yang, J. Ogden, *Int. J. Hydrogen Energy* **2007**, *32*, 268–286.

[90]H. Barthelemy, M. Weber, F. Barbier, *Int. J. Hydrogen Energy* **2017**, *42*, 7254–7262.

[91] Y. S. H. Najjar, *Int. J. Hydrogen Energy* **2013**, *38*, 10716–10728.

[92] D. Pukazhselvan, V. Kumar, S. K. Singh, *Nano Energy* **2012**, *1*, 566–589.

[93] H. T. Hwang, A. Varma, *Curr. Opin. Chem. Eng.* **2014**, *5*, 42–48.

[94] K. C. Kim, *Int. J. Energy Res.* **2018**, *42*, 1455–1468.

[95] J. O. Abe, A. P. I. Popoola, E. Ajenifuja, O. M. Popoola, *Int. J. Hydrogen Energy* **2019**, *44*, 15072–15086.

[96] L. Zaluski, A. Zaluska, J. O. Ström-Olsen, *J. Alloys Compd.* **1997**, *253–254*, 70–79.

[97] V. Y. Zadorozhnyy, G. S. Milovzorov, S. N. Klyamkin, M. Y. Zadorozhnyy, D. V Strugova, M. V Gorshenkov, S. D. Kaloshkin, *Prog. Nat. Sci. Mater. Int.* **2017**, *27*, 149–155.

[98]Q. Lai, M. Paskevicius, D. A. Sheppard, C. E. Buckley, A. W. Thornton, M. R. Hill, Q. Gu, J. Mao, Z. Huang, H. K. Liu, Z. Guo, A. Banerjee, S. Chakraborty, R. Ahuja, K.-F. Aguey-Zinsou, *ChemSusChem* **2015**, *8*, 2789–2825.

[99] Y. Cheng, X. Wu, H. Xu, *Sustain. Energy Fuels* **2019**, *3*, 343–365.

[100] F. Sanchez, M. H. Alotaibi, D. Motta, C. E. Chan-Thaw, A. Rakotomahevitra, T. Tabanelli, A. Roldan, C. Hammond, Q. He, T. Davies, A. Villa, N. Dimitratos, *Sustain. Energy Fuels* **2018**, *2*, 2705–2716.

[101] M. Trincado, D. Banerjee, H. Grützmacher, *Energy Environ. Sci.* **2014**, *7*, 2464–2503.

[102]P. T. Aakko-Saksa, C. Cook, J. Kiviaho, T. Repo, *J. Power Sources* **2018**, *396*, 803–823.

[103] A. J. B. Robertson, *Platin. Met. Rev.* **1975**, *19*, 64–69.

[104] C. D. Millholland, “Industrial Uses Of Catalysts,” can be found under https://www.thermofisher.com/blog/materials/characterizing-the-effectiveness-of-industrial-catalysts/, **2021**.

[105] V. L. Arcus, M. W. Van Der Kamp, C. R. Pudney, A. J. Mulholland, *Curr. Opin. Struct. Biol.* **2020**, *65*, 96–101.

[106] G. Dedes, A. Karnaouri, E. Topakas, *Catalysts* **2020**, *10*, 743.

[107] A. F. Cotton, G. Wilkinson, C. A. Murillo, M. Bochmann, *Advanced Inorganic Chemistry*, Wiley, **1999**.

[108] J. C. Védrine, *Catalysts* **2017**, *7*, DOI 10.3390/catal7110341.

[109]H. Rase, HANDBOOK OF COMMERCIAL CATALYSTS - HETEROGENEOUS CATALYSTS, **2000**.

[110] J. C. Vedrine, Metal Oxides in Heterogeneous Catalysis, Elsevier, **2018**.

[111] C. Chizallet, G. Costentin, M. Che, F. Delbecq, P. Sautet, *J. Phys. Chem. B* **2006**, *110*, 15878–15886.

[112] R. K. Grasselli, *Catal. Today* **2014**, *238*, 10–27.

[113] E. V Ovchinnikova, N. V Vernikovskaya, A. G. Gribovskii, V. A. Chumachenko, *Chem. Eng. J.* **2021**, *409*, 128046.

[114] M. Sankar, Q. He, R. V Engel, M. A. Sainna, A. J. Logsdail, A. Roldan, D. J. Willock, N. Agarwal, C. J. Kiely, G. J. Hutchings, *Chem. Rev.* **2020**, *120*, 3890–3938.

[115] A. Martínez, G. Prieto, *Catal. Commun.* **2007**, *8*, 1479–1486.

[116] G. Ertl, H. Knözinger, J. Weitkamp, *Handbook of Heterogeneous Catalysis*, **2008**.

[117] W. P. Halperin, *Rev. Mod. Phys.* **1986**, *58*, 533–606.

[118] M. J. Ndolomingo, N. Bingwa, R. Meijboom, *J. Mater. Sci.* **2020**, *55*, 6195–6241.

[119] P. Buffat, J.-P. Borel, *Phys. Rev. A* **1976**, *13*, 2287–2298.

[120] S. V Nair, S. Sinha, K. C. Rustagi, *Phys. Rev. B* **1987**, *35*, 4098–4101.

[121] D. Astruc, F. Lu, J. R. Aranzaes, *Angew. Chemie Int. Ed.* **2005**, *44*, 7852–7872.

[122] F. Thielbeer, K. Donaldson, M. Bradley, *Bioconjug. Chem.* **2011**, *22*, 144–150.

[123] E. Matijevic, R. J. Good, *Surface and Colloid Science*, Springer Science & Business Media, **2012**.

[124] Y. Xiong, J. M. McLellan, J. Chen, Y. Yin, Z.-Y. Li, Y. Xia, *J. Am. Chem. Soc.* **2005**, *127*, 17118–17127.

[125] S. Cao, F. (Feng) Tao, Y. Tang, Y. Li, J. Yu, *Chem. Soc. Rev.* **2016**, *45*, 4747–4765.

[126] T. Feng, D. Sefa, W. Lin-Wang, L. Zhi, B. D. R., B. Hendrik, S. Miquel, S. G. A., *Science (80-.).* **2010**, *327*, 850–853.

[127] K. M. Bratlie, H. Lee, K. Komvopoulos, P. Yang, G. A. Somorjai, *Nano Lett.* **2007**, *7*, 3097–3101.

[128] X. Lan, T. Wang, *ACS Catal.* **2020**, *10*, 2764–2790.

[129] M. Navlani-García, K. Mori, D. Salinas-Torres, Y. Kuwahara, H. Yamashita, *Front. Mater.* **2019**, *6*, 1–18.

[130] F. Liao, T. W. B. Lo, S. C. E. Tsang, *ChemCatChem* **2015**, *7*, 1998–2014.

[131] G. L. Brett, P. J. Miedziak, D. W. Knight, S. H. Taylor, G. J. Hutchings, *Top. Catal.* **2014**, *57*, 723–729.

[132] N. Dimitratos, J. A. Lopez-Sanchez, J. M. Anthonykutty, G. Brett, A. F. Carley, R. C. Tiruvalam, A. A. Herzing, C. J. Kiely, D. W. Knight, G. J. Hutchings, *Phys. Chem. Chem. Phys.* **2009**, *11*, 4952–4961.

[133] R. Burch, *Acc. Chem. Res.* **1982**, *15*, 24–31.

[134] M. Chen, D. Kumar, C.-W. Yi, D. W. Goodman, *Science (80-.).* **2005**, *310*, 291–293.

[135] P. Liu, J. K. Nørskov, *Phys. Chem. Chem. Phys.* **2001**, *3*, 3814–3818.

[136] M. Cui, G. Johnson, Z. Zhang, S. Li, S. Hwang, X. Zhang, S. Zhang, *Nanoscale* **2020**, *12*, 14068–14075.

[137]C. Zeng, Y. Chen, K. Iida, K. Nobusada, K. Kirschbaum, K. J. Lambright, R. Jin, *J. Am. Chem. Soc.* **2016**, *138*, 3950–3953.

[138] A. P. LaGrow, M. O. Besenhard, A. Hodzic, A. Sergides, L. K. Bogart, A. Gavriilidis, N. T. K. Thanh, *Nanoscale* **2019**, *11*, 6620–6628.

[139] E. Marceau, X. Carrier, M. Che, O. Clause, C. Marcilly, *Handb. Heterog. Catal.* **2008**, 467–484.

[140] W.-C. Li, M. Comotti, F. Schüth, *J. Catal.* **2006**, *237*, 190–196.

[141]R. Atchudan, T. N. Jebakumar Immanuel Edison, S. Perumal, D. RanjithKumar, Y. R. Lee, *Int. J. Hydrogen Energy* **2019**, *44*, 2349–2360.

[142] K. B. K. Teo, S.-B. Lee, M. Chhowalla, V. Semet, V. T. Binh, O. Groening, M. Castignolles, A. Loiseau, G. Pirio, P. Legagneux, D. Pribat, D. G. Hasko, H. Ahmed, G. A. J. Amaratunga, W. I. Milne, *Nanotechnology* **2003**, *14*, 204–211.

[143]Y. B. Pottathara, Y. Grohens, V. Kokol, N. Kalarikkal, S. Thomas, in *Micro Nano Technol.* (Eds.: Y. Beeran Pottathara, S. Thomas, N. Kalarikkal, Y. Grohens, V.B.T.-N.S. Kokol), Elsevier, **2019**, pp. 1–25.

[144] L. Prati, A. Villa, *Catalysts* **2011**, *2*, 24–37.

[145] A. Villa, D. Wang, D. S. Su, L. Prati, *ChemCatChem* **2009**, *1*, 510–514.

[146]A. Villa, D. Wang, G. M. Veith, F. Vindigni, L. Prati, *Catal. Sci. Technol.* **2013**, *3*, 3036–3041.

[147] L. Prati, A. Villa, **2014**, *47*, 855–863.

[148] V. K. LaMer, R. H. Dinegar, *J. Am. Chem. Soc.* **1950**, *72*, 4847–4854.

[149]Y. Xia, Y. Xiong, B. Lim, S. E. Skrabalak, *Angew. Chemie Int. Ed.* **2009**, *48*, 60–103.

[150]Y. Wang, J. He, C. Liu, W. H. Chong, H. Chen, *Angew. Chemie Int. Ed.* **2015**, *54*, 2022–2051.

[151] T. Sugimoto, *Monodispersed Particles*, Elsevier, **2019**.

[152]H. Zheng, R. K. Smith, Y. Jun, C. Kisielowski, U. Dahmen, A. P. Alivisatos, *Science (80-.).* **2009**, *324*, 1309–1312.

[153] P. W. Voorhees, *J. Stat. Phys.* **1985**, *38*, 231–252.

[154] N. Dimitratos, F. Porta, L. Prati, A. Villa, *Catal. Letters* **2005**, *99*, 181–185.

[155]K. Alshammari, Y. Niu, R. E. Palmer, N. Dimitratos, *Philos. Trans. R. Soc. A Math. Phys. Eng. Sci.* **2020**, *378*, 20200057.

[156] L. Prati, A. Villa, C. Campione, P. Spontoni, *Top. Catal.* **2007**, *44*, 319–324.

[157]T. S. Ahmadi, Z. L. Wang, T. C. Green, A. Henglein, M. A. El-Sayed, *Science (80-.).* **1996**, *272*, 1924–1925.

[158] A. Henglein, *J. Phys. Chem. B* **2000**, *104*, 6683–6685.

[159] D. Burshtain, L. Zeiri, S. Efrima, *Langmuir* **1999**, *15*, 3050–3055.

[160] R. S. Underhill, G. Liu, *Chem. Mater.* **2000**, *12*, 3633–3641.

[161]S. Pathak, M. T. Greci, R. C. Kwong, K. Mercado, G. K. S. Prakash, G. A. Olah, M. E. Thompson, *Chem. Mater.* **2000**, *12*, 1985–1989.

[162] G. Frens, *Nat. Phys. Sci.* **1973**, *241*, 20–22.

[163] N. R. Jana, L. Gearheart, C. J. Murphy, *Chem. Mater.* **2001**, *13*, 2313–2322.

[164] K. R. Brown, D. G. Walter, M. J. Natan, *Chem. Mater.* **2000**, *12*, 306–313.

[165]A. D. Pomogailo, G. I. Dzhardimalieva, *Nanostructured Materials Preparation via Condensation Ways*, Springer, **2014**.

[166] D. V Goia, E. Matijević, *New J. Chem.* **1998**, *22*, 1203–1215.

[167] S. Saha, A. Pal, S. Kundu, S. Basu, T. Pal, *Langmuir* **2010**, *26*, 2885–2893.

[168] C. Deraedt, L. Salmon, S. Gatard, R. Ciganda, R. Hernandez, J. Ruiz, D. Astruc, *Chem. Commun.* **2014**, *50*, 14194–14196.

[169] H. Tsunoyama, N. Ichikuni, T. Tsukuda, *Langmuir* **2008**, *24*, 11327–11330.

[170] A. Krittayavathananon, P. Srimuk, S. Luanwuthi, M. Sawangphruk, *Anal. Chem.* **2014**, *86*, 12272–12278.

[171] M. Wuithschick, A. Birnbaum, S. Witte, M. Sztucki, U. Vainio, N. Pinna, K. Rademann, F. Emmerling, R. Kraehnert, J. Polte, *ACS Nano* **2015**, *9*, 7052–7071.

[172]J. Polte, T. T. Ahner, F. Delissen, S. Sokolov, F. Emmerling, A. F. Thünemann, R. Kraehnert, *J. Am. Chem. Soc.* **2010**, *132*, 1296–1301.

[173] D. V Goia, *J. Mater. Chem.* **2004**, *14*, 451.

[174] X. Liu, R. Huang, J. Zhu, *Chem. Mater.* **2008**, *20*, 192–197.

[175] J. Zhang, H. Liu, Z. Wang, N. Ming, *Adv. Funct. Mater.* **2007**, *17*, 3295–3303.

[176] I. Capek, *Noble Metal Nanoparticles*, Springer Japan, **2017**.

[177] S. Campisi, M. Schiavoni, C. E. Chan-Thaw, A. Villa, *Catalysts* **2016**, *6*, 1–21.

[178]G. Chen, C. Xu, X. Huang, J. Ye, L. Gu, G. Li, Z. Tang, B. Wu, H. Yang, Z. Zhao, Z. Zhou, G. Fu, N. Zheng, *Nat. Mater.* **2016**, *15*, 564–569.

[179] S. Campisi, D. Ferri, A. Villa, W. Wang, D. Wang, O. Kröcher, L. Prati, *J. Phys. Chem. C* **2016**, *120*, 14027–14033.

[180]B. Wu, H. Huang, J. Yang, N. Zheng, G. Fu, *Angew. Chemie Int. Ed.* **2012**, *51*, 3440–3443.

[181] L. Prati, A. Villa, *Acc. Chem. Res.* **2014**, *47*, 855–863.

[182] J. J. Liu, *ChemCatChem* **2011**, *3*, 934–948.

[183]P. Hu, Z. Huang, Z. Amghouz, M. Makkee, F. Xu, F. Kapteijn, A. Dikhtiarenko, Y. Chen, X. Gu, X. Tang, *Angew. Chemie Int. Ed.* **2014**, *53*, 3418–3421.

[184] B. Zhang, L. Shao, W. Zhang, X. Sun, X. Pan, D. S. Su, *ChemCatChem* **2014**, *6*, 2607–2612.

[185] B. Zhang, D. S. Su, *ChemCatChem* **2015**, *7*, 3639–3645.

[186]M. Jeon, D. J. Han, K.-S. Lee, S. H. Choi, J. Han, S. W. Nam, S. C. Jang, H. S. Park, C. W. Yoon, *Int. J. Hydrogen Energy* **2016**, *41*, 15453–15461.

[187]D. A. Bulushev, A. L. Chuvilin, V. I. Sobolev, S. G. Stolyarova, Y. V. Shubin, I. P. Asanov, A. V. Ishchenko, G. Magnani, M. Riccò, A. V. Okotrub, L. G. Bulusheva, *J. Mater. Chem. A* **2017**, *5*, 10574–10583.

[188] J. P. Brunelle, *Pure Appl. Chem.* **1978**, *50*, 1211–1229.

[189] R. Arrigo, M. Hävecker, S. Wrabetz, R. Blume, M. Lerch, J. McGregor, E. P. J. Parrott, J. A. Zeitler, L. F. Gladden, A. Knop-Gericke, R. Schlögl, D. S. Su, *J. Am. Chem. Soc.* **2010**, *132*, 9616–9630.

[190]Y. Park, J. Yoo, B. Lim, W. Kwon, S. W. Rhee, *J. Mater. Chem. A* **2016**, *4*, 11582–11603.

[191] I. Efremenko, M. Sheintuch, *J. Catal.* **2003**, *214*, 53–67.

[192] J. Zhu, A. Holmen, D. Chen, *ChemCatChem* **2013**, *5*, 378–401.

[193]A. Eckmann, A. Felten, A. Mishchenko, L. Britnell, R. Krupke, K. S. Novoselov, C. Casiraghi, *Nano Lett.* **2012**, *12*, 3925–3930.

[194]A. Primo, F. Neatu, M. Florea, V. Parvulescu, H. Garcia, *Nat. Commun.* **2014**, *5*, 1–9.

[195]N. Gupta, O. Khavryuchenko, A. Villa, D. Su, *ChemSusChem* **2017**, *10*, 3030–3034.

[196] C. Huang, C. Li, G. Shi, *Energy Environ. Sci.* **2012**, *5*, 8848–8868.

[197] M. Razeghi, *An Introd. to carbon Mater.* **2019**, DOI 10.1088/2053-2563/ab35d1.

[198]R. Schloegl, in *Adv. Catal.* (Eds.: B. Gates, F. Jentoft), Elsevier, **2013**, pp. 103–185.

[199] W. Saslow, T. K. Bergstresser, M. L. Cohen, *Phys. Rev. Lett.* **1966**, *16*, 354–356.

[200]Y. U. Peter, M. Cardona, *Fundamentals of Semiconductors: Physics and Materials Properties*, Springer Science & Business Media, **2010**.

[201]K. Muzyka, J. Sun, T. H. Fereja, Y. Lan, W. Zhang, G. Xu, *Anal. Methods* **2019**, *11*, 397–414.

[202]Y. Zhang, K. Y. Rhee, D. Hui, S. J. Park, *Compos. Part B Eng.* **2018**, *143*, 19–27.

[203]J. Liu, Y. Yue, H. Liu, Z. Da, C. Liu, A. Ma, J. Rong, D. Su, X. Bao, H. Zheng, *ACS Catal.* **2017**, *7*, 3349–3355.

[204] J. Zhang, X. Cai, K.-H. Wu, Y. Zhang, J. Wang, J. Diao, N. Wang, H. Liu, D. Su, *ChemCatChem* **2018**, *10*, 520–524.

[205]O. V Turova, E. V Starodubtseva, M. G. Vinogradov, V. I. Sokolov, N. V Abramova, A. Y. Vul, A. E. Alexenskiy, *Catal. Commun.* **2011**, *12*, 577–579.

[206]V. Campisciano, M. Gruttadauria, F. Giacalone, *ChemCatChem* **2019**, *11*, 90–133.

[207] J. Zhang, D. S. Su, R. Blume, R. Schlögl, R. Wang, X. Yang, A. Gajović, *Angew. Chemie Int. Ed.* **2010**, *49*, 8640–8644.

[208] L. Basso, M. Cazzanelli, M. Orlandi, A. Miotello, *Appl. Sci.* **2020**, *10*, DOI 10.3390/app10124094.

[209]E. A. Tveritinova, Y. N. Zhitnev, I. I. Kulakova, N. Cherkasov, K. I. Maslakov, E. A. Nesterova, A. S. Ivanov, S. V Savilov, V. V Lunin, *Appl. Surf. Sci.* **2015**, *355*, 74–81.

[210]J. Diao, Z. Feng, R. Huang, H. Liu, S. B. A. Hamid, D. S. Su, *ChemSusChem* **2016**, *9*, 662–666.

[211]A. Apicella, R. Aversa, F. I. T. Petrescu, *Am. J. Eng. Appl. Sci.* **2018**, *11*, 766–782.

[212]S. Navalón, A. Dhakshinamoorthy, M. Álvaro, H. García, *Chem. Mater.* **2020**, *32*, 4116–4143.

[213]C. N. R. et al. Rao, Supramolecular Chemistry of Fullerenes and Carbon Nanotubes Carbon Nanotube and Related Raman Spectroscopy in Graphene Related Systems Carbon Materials and Nanotechnology Carbon Nanomaterials Carbon Nanotubes and Related Structures, **2013**.

[214]T. Enoki, T. Ando, *Physics and Chemistry of Graphene*, Jenny Stanford Publishing, New York, NY, **2019**.

[215]Y. Yan, W. I. Shin, H. Chen, S. M. Lee, S. Manickam, S. Hanson, H. Zhao, E. Lester, T. Wu, C. H. Pang, *Carbon Lett.* **2021**, *31*, 177–199.

[216]L. Hu, X. Hu, X. Wu, C. Du, Y. Dai, J. Deng, *Phys. B Condens. Matter* **2010**, *405*, 3337–3341.

[217] K. Nakada, A. Ishii, *Solid State Commun.* **2011**, *151*, 13–16.

[218]A. Hashimoto, K. Suenaga, A. Gloter, K. Urita, S. Iijima, *Nature* **2004**, *430*, 870–873.

[219] S. Margadonna, K. Prassides, *J. Solid State Chem.* **2002**, *168*, 639–652.

[220]A. Mrzel, A. Omerzu, P. Umek, D. Mihailovic, Z. Jagličić, Z. Trontelj, *Chem. Phys. Lett.* **1998**, *298*, 329–334.

[221] B. Dang, J. Hu, Y. Zhou, J. He, *J. Phys. D. Appl. Phys.* **2017**, *50*, 455303.

[222] B. Coq, J. Marc Planeix, V. Brotons, *Appl. Catal. A Gen.* **1998**, *173*, 175–183.

[223] D. M. Guldi, N. Martin, *Carbon Nanotubes and Related Structures*, Wiley-VCH, **2010**.

[224] H.-Y. Cheng, Y.-A. Zhu, Z.-J. Sui, X.-G. Zhou, D. Chen, *Carbon N. Y.* **2012**, *50*, 4359–4372.

[225] D. Yadav, F. Amini, A. Ehrmann, *Eur. Polym. J.* **2020**, *138*, 109963.

[226] J. Vera-Agullo, H. Varela-Rizo, J. A. Conesa, C. Almansa, C. Merino, I. Martin-Gullon, *Carbon N. Y.* **2007**, *45*, 2751–2758.

[227]N. M. Rodriguez, M.-S. Kim, R. T. K. Baker, *J. Phys. Chem.* **1994**, *98*, 13108–13111.

[228] K. P. De Jong, J. W. Geus, *Catal. Rev.* **2000**, *42*, 481–510.

[229] M. A. Caro, R. Zoubkoff, O. Lopez-Acevedo, T. Laurila, *Carbon N. Y.* **2014**, *77*, 1168–1182.

[230]M. A. Caro, A. Aarva, V. L. Deringer, G. Csányi, T. Laurila, *Chem. Mater.* **2018**, *30*, 7446–7455.

[231]N. Marks, D. McKenzie, B. Pailthorpe, M. Bernasconi, M. Parrinello, *Phys. Rev. B - Condens. Matter Mater. Phys.* **1996**, *54*, 9703–9714.

[232] K. Jurkiewicz, M. Pawlyta, D. Zygadło, D. Chrobak, S. Duber, R. Wrzalik, A. Ratuszna, A. Burian, *J. Mater. Sci.* **2018**, *53*, 3509–3523.

[233]Z. Zhao, E. F. Wang, H. Yan, Y. Kono, B. Wen, L. Bai, F. Shi, J. Zhang, C. Kenney-Benson, C. Park, Y. Wang, G. Shen, *Nat. Commun.* **2015**, *6*, 6212.

[234]S. Sharma, C. N. Shyam Kumar, J. G. Korvink, C. Kübel, *Sci. Rep.* **2018**, *8*, 16282.

[235] S. Sharma, *Mater.* **2018**, *11*, DOI 10.3390/ma11101857.

[236] C. Carpenter, D. Maroudas, A. Ramasubramaniam, *Appl. Phys. Lett.* **2013**, *103*, 13102.

[237]S. H. M. Jafri, K. Carva, E. Widenkvist, T. Blom, B. Sanyal, J. Fransson, O. Eriksson, U. Jansson, H. Grennberg, O. Karis, R. A. Quinlan, B. C. Holloway, K. Leifer, *J. Phys. D. Appl. Phys.* **2010**, *43*, 45404.

[238] S. Yang, Z. Lan, H. Xu, G. Lei, W. Xie, Q. Gu, *J. Nanotechnol.* **2018**, *2018*, DOI 10.1155/2018/2031805.

[239] L. Ma, J. M. Zhang, K. W. Xu, V. Ji, *Appl. Surf. Sci.* **2015**, *343*, 121–127.

[240] X. Y. Liu, J. M. Zhang, K. W. Xu, V. Ji, *Appl. Surf. Sci.* **2014**, *313*, 405–410.

[241] F. Banhart, J. Kotakoski, A. V. Krasheninnikov, *ACS Nano* **2011**, *5*, 26–41.

[242] M. H. Gass, U. Bangert, A. L. Bleloch, P. Wang, R. R. Nair, A. K. Geim, *Nat. Nanotechnol.* **2008**, *3*, 676–681.

[243] I. Barlocco, S. Capelli, X. Lu, S. Tumiati, N. Dimitratos, A. Roldan, A. Villa, *Nanoscale* **2020**, *12*, 22768–22777.

[244]J. C. Meyer, C. Kisielowski, R. Erni, M. D. Rossell, M. F. Crommie, A. Zettl, *Nano Lett.* **2008**, *8*, 3582–3586.

[245] J. Kotakoski, J. C. Meyer, S. Kurasch, D. Santos-Cottin, U. Kaiser, A. V Krasheninnikov, *Phys. Rev. B* **2011**, *83*, 245420.

[246]W. Guo, S. Niu, X. Ji, W. Yu, T.-W. Lin, Y. Wu, Y. Li, L. Shao, *J. Nanoparticle Res.* **2018**, *20*, 180.

[247]X. Wang, N. Li, J. A. Webb, L. D. Pfefferle, G. L. Haller, *Appl. Catal. B Environ.* **2010**, *101*, 21–30.

[248]G.-H. Wang, Z. Cao, D. Gu, N. Pfänder, A.-C. Swertz, B. Spliethoff, H.-J. Bongard, C. Weidenthaler, W. Schmidt, R. Rinaldi, F. Schüth, *Angew. Chemie Int. Ed.* **2016**, *55*, 8850–8855.

[249]K. Yu, Y. Lin, J. C. Fan, Q. Li, P. Shi, Q. J. Xu, Y. L. Min, *Catalysts* **2019**, *9*, DOI 10.3390/catal9020114.

[250] S. Zhong, N. Tsumori, M. Kitta, Q. Xu, *Nano Res.* **2019**, *12*, 2966–2970.

[251] T. J. Bandosz, in *Carbon Mater. Catal.*, **2008**, pp. 45–92.

[252] N. Zhang, J. Xie, V. K. Varadan, *Smart Mater. Struct.* **2002**, *11*, 962–965.

[253]R. S. Ribeiro, A. M. T. Silva, J. L. Figueiredo, J. L. Faria, H. T. Gomes, *Carbon N. Y.* **2013**, *62*, 97–108.

[254] Z. Wu, C. U. Pittman, S. D. Gardner, *Carbon N. Y.* **1995**, *33*, 597–605.

[255] V. Z. Shemet, A. P. Pomytkin, V. S. Neshpor, *Carbon N. Y.* **1993**, *31*, 1–6.

[256]N. F. Andrade, D. S. T. Martinez, A. J. Paula, J. V Silveira, O. L. Alves, A. G. Souza Filho, *J. Nanoparticle Res.* **2013**, *15*, 1761.

[257]L. D'Arsié, S. Esconjauregui, R. S. Weatherup, X. Wu, W. E. Arter, H. Sugime, C. Cepek, J. Robertson, *RSC Adv.* **2016**, *6*, 113185–113192.

[258]D. C. Koningsberger, T. G. Ros, A. J. van Dillen, J. W. Geus, *Chem. A Eur. J.* **2002**, *8*, 1151–1162.

[259]R. R. N. Marques, B. F. Machado, J. L. Faria, A. M. T. Silva, *Carbon N. Y.* **2010**, *48*, 1515–1523.

[260] Y. El-Sayed, T. J. Bandosz, *Langmuir* **2005**, *21*, 1282–1289.

[261]A. Bagreev, J. A. Menendez, I. Dukhno, Y. Tarasenko, T. J. Bandosz, *Carbon N. Y.* **2005**, *43*, 208–210.

[262] S. Biniak, G. Szymański, J. Siedlewski, A. Świątkowski, *Carbon N. Y.* **1997**, *35*, 1799–1810.

[263] J. Lahaye, G. Nansé, A. Bagreev, V. Strelko, *Carbon N. Y.* **1999**, *37*, 585–590.

[264]L. Wachowski, J. W. Sobczak, M. Hofman, *Appl. Surf. Sci.* **2007**, *253*, 4456–4461.

[265]Q. Zhu, S. L. Money, A. E. Russell, K. M. Thomas, *Langmuir* **1997**, *13*, 2149–2157.

[266]J. R. Pels, F. Kapteijn, J. A. Moulijn, Q. Zhu, K. M. Thomas, *Carbon N. Y.* **1995**, *33*, 1641–1653.

[267]A. Rehman, M. Park, S.-J. Park, *Coatings* **2019**, *9*, DOI 10.3390/coatings9020103.

[268]F. H. Monteiro, D. G. Larrude, M. E. H. Maia da Costa, L. A. Terrazos, R. B. Capaz, F. L. Freire, *J. Phys. Chem. C* **2012**, *116*, 3281–3285.

[269] P. Ayala, M. H. Rümmeli, T. Gemming, E. Kauppinen, H. Kuzmany, T. Pichler, *Phys. status solidi* **2008**, *245*, 1935–1938.

[270]W. K. Hsu, S. Firth, P. Redlich, M. Terrones, H. Terrones, Y. Q. Zhu, N. Grobert, A. Schilder, R. J. H. Clark, H. W. Kroto, D. R. M. Walton, *J. Mater. Chem.* **2000**, *10*, 1425–1429.

[271]Y. Lin, Y. Zhu, B. Zhang, Y. A. Kim, M. Endo, D. S. Su, *J. Mater. Chem. A* **2015**, *3*, 21805–21814.

[272]W.-H. Chiang, G.-L. Chen, C.-Y. Hsieh, S.-C. Lo, *RSC Adv.* **2015**, *5*, 97579–97588.

[273]S. Campisi, S. Capelli, D. Motta, F. Trujillo, T. Davies, L. Prati, N. Dimitratos, A. Villa, *C* **2018**, *4*, 48.

[274]S. Campisi, F. Sanchez Trujillo, D. Motta, T. Davies, N. Dimitratos, A. Villa, *C* **2018**, *4*, 9.

[275]A. M. Puziy, O. I. Poddubnaya, B. Gawdzik, M. Sobiesiak, M. M. Tsyba, *Adsorpt. Sci. Technol.* **2007**, *25*, 531–542.

[276]L. Wang, X. Dong, H. Jiang, G. Li, M. Zhang, *Catal. Commun.* **2014**, *56*, 164–167.

[277]A. M. Puziy, O. I. Poddubnaya, B. Gawdzik, M. Sobiesiak, M. M. Tsyba, *Appl. Surf. Sci.* **2007**, *253*, 5736–5740.

[278] A. Schaetz, M. Zeltner, W. J. Stark, *ACS Catal.* **2012**, *2*, 1267–1284.

[279]R. Arrigo, S. Wrabetz, M. E. Schuster, D. Wang, A. Villa, D. Rosenthal, F. Girsgdies, G. Weinberg, L. Prati, R. Schlögl, *Phys. Chem. Chem. Phys.* **2012**, *14*, 10523–10532.

[280]B. Zhang, X. Ni, W. Zhang, L. Shao, Q. Zhang, F. Girgsdies, C. Liang, R. Schlögl, D. S. Su, *Chem. Commun.* **2011**, *47*, 10716–10718.

[281]X. Pan, B. Zhang, B. Zhong, J. Wang, D. S. Su, *Chem. Commun.* **2014**, *50*, 3856–3858.

[282]J. Ma, A. Habrioux, C. Morais, A. Lewera, W. Vogel, Y. Verde-Gómez, G. Ramos-Sanchez, P. B. Balbuena, N. Alonso-Vante, *ACS Catal.* **2013**, *3*, 1940–1950.

[283] D.-H. Lim, J. Wilcox, *J. Phys. Chem. C* **2012**, *116*, 3653–3660.

[284]D. Wang, A. Villa, D. Su, L. Prati, R. Schlögl, *ChemCatChem* **2013**, *5*, 2717–2723.

[285] B. Zhang, D. S. Su, *ChemCatChem* **2015**, *7*, 3639–3645.

[286] B. Zhang, L. Shao, W. Zhang, X. Sun, X. Pan, D. S. Su, *ChemCatChem* **2014**, *6*, 2607–2612.

[287] X. Ning, H. Yu, F. Peng, H. Wang, *J. Catal.* **2015**, *325*, 136–144.

[288] R. Schlögl, *J. Energy Chem.* **2021**, *61*, 219–227.

[289] E. K. Rideal, W. M. Wright, *J. Chem. Soc. Trans.* **1925**, *127*, 1347–1357.

[290] G. Emig, H. Hofmann, *J. Catal.* **1983**, *84*, 15–26.

[291] Y. Iwasawa, H. Nobe, S. Ogasawara, *J. Catal.* **1973**, *31*, 444–449.

[292] D. S. Su, J. Zhang, B. Frank, A. Thomas, X. Wang, J. Paraknowitsch, R. Schlögl, *ChemSusChem Chem. Sustain. Energy Mater.* **2010**, *3*, 169–180.

[293] G. Centi, S. Perathoner, D. S. Su, *Catal. Surv. from Asia* **2014**, *18*, 149–163.

[294] D. S. Su, S. Perathoner, G. Centi, *Chem. Rev.* **2013**, *113*, 5782–5816.

[295] M. Z. Rahman, K. Davey, S.-Z. Qiao, *J. Mater. Chem. A* **2018**, *6*, 1305–1322.

[296]L. Zhou, H. Zhang, H. Sun, S. Liu, M. O. Tade, S. Wang, W. Jin, *Catal. Sci. Technol.* **2016**, *6*, 7002–7023.

[297] L. Yang, Y. Zhao, S. Chen, Q. Wu, X. Wang, Z. Hu, *Chinese J. Catal.* **2013**, *34*, 1986–1991.

[298]J. Wang, H. Kong, J. Zhang, Y. Hao, Z. Shao, F. Ciucci, *Prog. Mater. Sci.* **2021**, *116*, 100717.

[299] S. Xiaoyan, W. Rui, S. U. Dangsheng, *Chinese J. Catal.* **2013**, *34*, 508–523.

[300] W. Qi, D. Su, *Acs Catal.* **2014**, *4*, 3212–3218.

[301]D. S. Su, G. Wen, S. Wu, F. Peng, R. Schlögl, *Angew. Chemie - Int. Ed.* **2017**, *56*, 936–964.

[302]R. Huang, J. Xu, J. Wang, X. Sun, W. Qi, C. Liang, D. S. Su, *Carbon N. Y.* **2016**, *96*, 631–640.

[303] V. S. Jeyaraj, M. Kamaraj, V. Subramanian, *J. Phys. Chem. C* **2015**, *119*, 26438–26450.

[304] X. Duan, H. Sun, S. Wang, *Acc. Chem. Res.* **2018**, *51*, 678–687.

[305]A. Villa, N. Dimitratos, *Metal-Free Functionalized Carbons in Catalysis*, The Royal Society Of Chemistry, **2018**.

[306] D. W. Boukhvalov, D. R. Dreyer, C. W. Bielawski, Y.-W. Son, *ChemCatChem* **2012**, *4*, 1844–1849.

[307]M. A. Patel, F. Luo, M. R. Khoshi, E. Rabie, Q. Zhang, C. R. Flach, R. Mendelsohn, E. Garfunkel, M. Szostak, H. He, *ACS Nano* **2016**, *10*, 2305–2315.

[308]H. Watanabe, S. Asano, S. Fujita, H. Yoshida, M. Arai, *ACS Catal.* **2015**, *5*, 2886–2894.

[309]H. G. Schimmel, G. J. Kearley, M. G. Nijkamp, C. T. Visser, K. P. de Jong, F. M. Mulder, *Chem. – A Eur. J.* **2003**, *9*, 4764–4770.

[310] D. W. Stephan, G. Erker, *Angew. Chemie Int. Ed.* **2015**, *54*, 6400–6441.

[311]G. C. Welch, R. R. S. Juan, J. D. Masuda, D. W. Stephan, *Science (80-.).* **2006**, *314*, 1124 LP – 1126.

[312]X. Sun, B. Li, T. Liu, J. Song, D. S. Su, *Phys. Chem. Chem. Phys.* **2016**, *18*, 11120–11124.

[313] M.-M. Trandafir, M. Florea, F. Neaţu, A. Primo, V. I. Parvulescu, H. García, *ChemSusChem* **2016**, *9*, 1565–1569.

[314] A. Primo, F. Neatu, M. Florea, V. Parvulescu, H. Garcia, *Nat. Commun.* **2014**, *5*, 5291.

[315] S. Wu, G. Wen, X. Liu, B. Zhong, D. S. Su, *ChemCatChem* **2014**, *6*, 1558–1561.

[316] C. Lang, Y. Jia, X. Yao, *Energy Storage Mater.* **2020**, *26*, 290–312.

[317]Hydrogen and Fuel Cell Technologies Office, “DOE Technical Targets for Onboard Hydrogen Storage for Light-Duty Vehicles,” can be found under https://www.energy.gov/eere/fuelcells/doe-technical-targets-onboard-hydrogen-storage-light-duty-vehicles, **2020**.

[318]T. Ichikawa, T. Matsuo, T. Tachikawa, T. Yamada, T. Yoshimura, M. Yoshimura, Y. Takagi, Y. Sawama, J. Sugiyama, Y. Monguchi, H. Sajiki, *ACS Sustain. Chem. Eng.* **2019**, *7*, 3052–3061.

[319] A. Kalenchuk, V. Bogdan, S. Dunaev, L. Kustov, *Fuel* **2020**, *280*, 118625.

[320]B. S. Shin, C. W. Yoon, S. K. Kwak, J. W. Kang, *Int. J. Hydrogen Energy* **2018**, *43*, 12158–12167.

[321]L. M. Kustov, A. L. Tarasov, O. A. Kirichenko, *Int. J. Hydrogen Energy* **2017**, *42*, 26723–26729.

[322] T. Shimbayashi, K. Fujita, *Tetrahedron* **2020**, *76*, 130946.

[323]B. Loges, A. Boddien, F. Gärtner, H. Junge, M. Beller, *Top. Catal.* **2010**, *53*, 902–914.

[324] T. Kobayashi, H. Takahashi, *Energy & Fuels* **2004**, *18*, 285–286.

[325] S. Saxena, S. Kumar, V. Drozd, *Int. J. Hydrogen Energy* **2011**, *36*, 4366–4369.

[326] M. Aziz, A. TriWijayanta, A. B. D. Nandiyanto, *Energies* **2020**, *13*, 1–25.

[327] R. Lan, J. T. S. Irvine, S. Tao, *Int. J. Hydrogen Energy* **2012**, *37*, 1482–1494.

[328]K. E. Lamb, M. D. Dolan, D. F. Kennedy, *Int. J. Hydrogen Energy* **2019**, *44*, 3580–3593.

[329] A. M. Ranjekar, G. D. Yadav, *Ind. Eng. Chem. Res.* **2021**, *60*, 89–113.

[330]X. Wang, Q. Meng, L. Gao, Z. Jin, J. Ge, C. Liu, W. Xing, *Int. J. Hydrogen Energy* **2018**, *43*, 7055–7071.

[331] M. K. Jana, U. Gupta, C. N. R. Rao, *Dalt. Trans.* **2016**, *45*, 15137–15141.

[332]Q. Yao, M. He, X. Hong, X. Chen, G. Feng, Z.-H. Lu, *Int. J. Hydrogen Energy* **2019**, *44*, 28430–28440.

[333] J. Eppinger, K.-W. Huang, *ACS Energy Lett.* **2017**, *2*, 188–195.

[334]N. Onishi, M. Iguchi, X. Yang, R. Kanega, H. Kawanami, Q. Xu, Y. Himeda, *Adv. Energy Mater.* **2019**, *9*, 1801275.

[335] S. Enthaler, J. von Langermann, T. Schmidt, *Energy Environ. Sci.* **2010**, *3*, 1207–1217.

[336]T. Brütsch, G. Jaffuel, A. Vallat, T. C. J. Turlings, M. Chapuisat, *Ecol. Evol.* **2017**, *7*, 2249–2254.

[337] N. E. TOLBERT, *J. Biol. Chem.* **1955**, *215*, 27–34.

[338] F. L. Shannon, *J. Ind. Eng. Chem.* **1912**, *4*, 526–528.

[339]I. Berregi, G. del Campo, R. Caracena, J. I. Miranda, *Talanta* **2007**, *72*, 1049–1053.

[340] K. E. McMartin, J. J. Ambre, T. R. Tephly, *Am. J. Med.* **1980**, *68*, 414–418.

[341] L. Crampton, "Formic Acid Dangers and Uses in Nature and in Humans," can be found under https://owlcation.com/stem/Formic-Acid-Dangers-and-Uses-in-Nature-and-in-Humans, **2021**.

[342]S. E. Sanni, P. A. Alaba, E. Okoro, M. Emetere, B. Oni, O. Agboola, A. O. Ndubuisi, *Sustain. Energy Technol. Assessments* **2021**, *45*, 101078.

[343] S. D. Sheet, *ICIS Chem. Bus.* **2017**, *1*, 1–12.

[344] A. K. Singh, S. Singh, A. Kumar, *Catal. Sci. Technol.* **2016**, *6*, 12–40.

[345]V. Choudhary, S. H. Mushrif, C. Ho, A. Anderko, V. Nikolakis, N. S. Marinkovic, A. I. Frenkel, S. I. Sandler, D. G. Vlachos, *J. Am. Chem. Soc.* **2013**, *135*, 3997–4006.

[346] C. Wang, X. Chen, M. Qi, J. Wu, G. Gözaydın, N. Yan, H. Zhong, F. Jin, *Green Chem.* **2019**, *21*, 6089–6096.

[347] X. Chen, Y. Liu, J. Wu, *Mol. Catal.* **2020**, *483*, 110716.

[348] J. Reichert, B. Brunner, A. Jess, P. Wasserscheid, J. Albert, *Energy Environ. Sci.* **2015**, *8*, 2985–2990.

[349] J. Zhang, M. Sun, X. Liu, Y. Han, *Catal. Today* **2014**, *233*, 77–82.

[350]N. V Gromov, O. P. Taran, I. V Delidovich, A. V Pestunov, Y. A. Rodikova, D. A. Yatsenko, E. G. Zhizhina, V. N. Parmon, *Catal. Today* **2016**, *278*, 74–81.

[351] S. Moret, P. J. Dyson, G. Laurenczy, *Nat. Commun.* **2014**, *5*, 4017.

[352]W.-H. Wang, J. F. Hull, J. T. Muckerman, E. Fujita, Y. Himeda, *Energy Environ. Sci.* **2012**, *5*, 7923–7926.

[353] D. A. Bulushev, J. R. H. Ross, *Catal. Rev.* **2018**, *60*, 566–593.

[354]G. A. Filonenko, W. L. Vrijburg, E. J. M. Hensen, E. A. Pidko, *J. Catal.* **2016**, *343*, 97–105.

[355]X. Lv, G. Lu, Z.-Q. Wang, Z.-N. Xu, G.-C. Guo, *ACS Catal.* **2017**, *7*, 4519–4526.

[356] K. Mori, T. Taga, H. Yamashita, *ACS Catal.* **2017**, *7*, 3147–3151.

[357] Z. Zhang, L. Zhang, S. Yao, X. Song, W. Huang, M. J. Hülsey, N. Yan, *J. Catal.* **2019**, *376*, 57–67.

[358] Y. Oh, X. Hu, *Chem. Soc. Rev.* **2013**, *42*, 2253–2261.

[359] X. Mao, T. A. Hatton, *Ind. Eng. Chem. Res.* **2015**, *54*, 4033–4042.

[360] L. Zhang, W. Wu, Z. Jiang, T. Fang, *Chem. Pap.* **2018**, *72*, 2121–2135.

[361] R. S. Coffey, *Chem. Commun.* **1967**, 923a-923a.

[362]Y. Pan, C. L. Pan, Y. Zhang, H. Li, S. Min, X. Guo, B. Zheng, H. Chen, A. Anders, Z. Lai, J. Zheng, K. W. Huang, *Chem. - An Asian J.* **2016**, *11*, 1357–1360.

[363]C. Fellay, P. J. Dyson, G. Laurenczy, *Angew. Chemie - Int. Ed.* **2008**, *47*, 3966–3968.

[364]W. Gan, C. Fellay, P. J. Dyson, G. Laurenczy, *J. Coord. Chem.* **2010**, *63*, 2685–2694.

[365] A. Boddien, B. Loges, H. Junge, F. Gärtner, J. R. Noyes, M. Beller, *Adv. Synth. Catal.* **2009**, *351*, 2517–2520.

[366] B. Loges, A. Boddien, H. Junge, J. R. Noyes, W. Baumann, M. Beller, *Chem. Commun.* **2009**, 4185–4187.

[367] X. Li, X. Ma, F. Shi, Y. Deng, *ChemSusChem* **2010**, *3*, 71–74.

[368]M. E. M. Berger, D. Assenbaum, N. Taccardi, E. Spiecker, P. Wasserscheid, *Green Chem.* **2011**, *13*, 1411–1415.

[369] A. Weilhard, M. I. Qadir, V. Sans, J. Dupont, *ACS Catal.* **2018**, *8*, 1628–1634.

[370] J. D. Scholten, M. H. G. Prechtl, J. Dupont, *ChemCatChem* **2010**, *2*, 1265–1270.

[371]C. Guan, D. D. Zhang, Y. Pan, M. Iguchi, M. J. Ajitha, J. Hu, H. Li, C. Yao, M. H. Huang, S. Min, J. Zheng, Y. Himeda, H. Kawanami, K. W. Huang, *Inorg. Chem.* **2017**, *56*, 438–445.

[372] Y. Himeda, *Green Chem.* **2009**, *11*, 2018–2022.

[373] J. H. Barnard, C. Wang, N. G. Berry, J. Xiao, *Chem. Sci.* **2013**, *4*, 1234–1244.

[374] A. Matsunami, Y. Kayaki, T. Ikariya, *Chem. – A Eur. J.* **2015**, *21*, 13513–13517.

[375] P. Sabatier, A. Maille, *Compt. Rendus* **1911**, *152*, 1212–1215.

[376] A. K. Singh, S. Singh, A. Kumar, *Catal. Sci. Technol.* **2016**, *6*, 12–40.

[377] Z. Li, Q. Xu, *Acc. Chem. Res.* **2017**, *50*, 1449–1458.

[378] N. Aas, Y. Li, M. Bowker, *J. Phys. Condens. Matter* **1991**, *3*, S281.

[379] Y. Sun, J. J. Vajo, C. Chan, W. H. Weinberg, **1988**.

[380] D. H. S. Ying, J. M. Robert, *J. Catal.* **1980**, *61*, 48–56.

[381] K. Hirota, K. Kuwata, Y. Nakai, *Bull. Chem. Soc. Jpn.* **1958**, *31*, 861–864.

[382] V. A. Gercher, D. F. Cox, *Surf. Sci.* **1994**, *312*, 106–114.

[383] P. A. Dilara, J. M. Vohs, *J. Phys. Chem.* **1993**, *97*, 12919–12923.

[384] X. D. Peng, M. A. Barteau, *Catal. Letters* **1990**, *7*, 395–402.

[385] R. Williams, R. S. Crandall, A. Bloom, *Appl. Phys. Lett.* **1978**, *33*, 381–383.

[386] N. He, Z. H. Li, *Phys. Chem. Chem. Phys.* **2016**, *18*, 10005–10017.

[387] M. Navlani-García, K. Mori, A. Nozaki, Y. Kuwahara, H. Yamashita, *ChemistrySelect* **2016**, *1*, 1879–1886.

[388]M. Navlani-García, M. Martis, D. Lozano-Castelló, D. Cazorla-Amorós, K. Mori, H. Yamashita, *Catal. Sci. Technol.* **2015**, *5*, 364–371.

[389]S. Zhang, B. Jiang, K. Jiang, W.-B. Cai, *ACS Appl. Mater. Interfaces* **2017**, *9*, 24678–24687.

[390] F. Sanchez, M. H. Alotaibi, D. Motta, C. E. Chan-Thaw, A. Rakotomahevitra, T. Tabanelli, A. Roldan, C. Hammond, Q. He, T. Davies, A. Villa, N. Dimitratos, *Sustain. Energy Fuels* **2018**, *2*, 2705–2716.

[391]S. S. Biswas, M. S. Tandrapadu, E. Abinaya, M. Eswaramoorthy, *Bull. Mater. Sci.* **2020**, *43*, 1–6.

[392]M. Farajzadeh, H. Alamgholiloo, F. Nasibipour, R. Banaei, S. Rostamnia, *Sci. Rep.* **2020**, *10*, 1–9.

[393]Z. Li, X. Yang, N. Tsumori, Z. Liu, Y. Himeda, T. Autrey, Q. Xu, *ACS Catal.* **2017**, *7*, 2720–2724.

[394] M. Navlani-García, K. Mori, A. Nozaki, Y. Kuwahara, H. Yamashita, *ChemistrySelect* **2016**, *1*, 1879–1886.

[395]J. Li, W. Chen, H. Zhao, X. Zheng, L. Wu, H. Pan, J. Zhu, Y. Chen, J. Lu, *J. Catal.* **2017**, *352*, 371–381.

[396] H. jin Jeon, Y. M. Chung, *Appl. Catal. B Environ.* **2017**, *210*, 212–222.

[397]M.-H. Jin, D. Oh, J.-H. Park, C.-B. Lee, S.-W. Lee, J.-S. Park, K.-Y. Lee, D.-W. Lee, *Sci. Rep.* **2016**, *6*, 33502.

[398] M.-H. Jin, J.-H. Park, D. Oh, J.-S. Park, K.-Y. Lee, D.-W. Lee, *Int. J. Hydrogen Energy* **2019**, *44*, 4737–4744.

[399]M. Navlani-García, M. Martis, D. Lozano-Castelló, D. Cazorla-Amorós, K. Mori, H. Yamashita, *Catal. Sci. Technol.* **2015**, *5*, 364–371.

[400]N. Wang, Q. Sun, R. Bai, X. Li, G. Guo, J. Yu, *J. Am. Chem. Soc.* **2016**, *138*, 7484–7487.

[401] J. M. Yan, Z. L. Wang, L. Gu, S. J. Li, H. L. Wang, W. T. Zheng, Q. Jiang, *Adv. Energy Mater.* **2015**, *5*, 10–15.

[402] H. Dai, N. Cao, L. Yang, J. Su, W. Luo, G. Cheng, *J. Mater. Chem. A* **2014**, *2*, 11060–11064.

[403]M. S. Shafeeyan, W. M. A. W. Daud, A. Houshmand, A. Arami-Niya, *Appl. Surf. Sci.* **2011**, *257*, 3936–3942.

[404] M. S. Shafeeyan, W. M. A. W. Daud, A. Houshmand, A. Shamiri, *J. Anal. Appl. Pyrolysis* **2010**, *89*, 143–151.

[405] W. M. A. W. Daud, A. H. Houshamnd, *J. Nat. Gas Chem.* **2010**, *19*, 267–279.

[406]H. Yu, F. Peng, J. Tan, X. Hu, H. Wang, J. Yang, W. Zheng, *Angew. Chemie - Int. Ed.* **2011**, *50*, 3978–3982.

[407]Z. Wang, C. Wang, S. Mao, Y. Gong, Y. Chen, Y. Wang, *J. Mater. Chem. A* **2019**, *7*, 25791–25795.

[408] X. Zhao, P. Dai, D. Xu, Z. Li, Q. Guo, *Int. J. Hydrogen Energy* **2020**, *45*, 30396–30403.

[409] Z.-L. Wang, J.-M. Yan, H.-L. Wang, Y. Ping, Q. Jiang, *Sci. Rep.* **2012**, *2*, 598.

[410] J. H. Lee, J. Ryu, J. Y. Kim, S.-W. Nam, J. H. Han, T.-H. Lim, S. Gautam, K. H. Chae, C. W. Yoon, *J. Mater. Chem. A* **2014**, *2*, 9490–9495.

[411] K. Jiang, K. Xu, S. Zou, W.-B. Cai, *J. Am. Chem. Soc.* **2014**, *136*, 4861–4864.

[412]J. Sun, H. Qiu, W. Cao, H. Fu, H. Wan, Z. Xu, S. Zheng, *ACS Sustain. Chem. Eng.* **2019**, *7*, 1963–1972.

[413]Q.-Y. Bi, J.-D. Lin, Y.-M. Liu, H.-Y. He, F.-Q. Huang, Y. Cao, *Angew. Chemie Int. Ed.* **2016**, *55*, 11849–11853.

[414] X. Wang, G.-W. Qi, C.-H. Tan, Y.-P. Li, J. Guo, X.-J. Pang, S.-Y. Zhang, *Int. J. Hydrogen Energy* **2014**, *39*, 837–843.

[415] J.-P. Zhou, J. Zhang, X.-H. Dai, X. Wang, S.-Y. Zhang, *Int. J. Hydrogen Energy* **2016**, *41*, 22059–22066.

[416] Q.-L. Zhu, N. Tsumori, Q. Xu, *J. Am. Chem. Soc.* **2015**, *137*, 11743–11748.

[417] Q.-L. Zhu, N. Tsumori, Q. Xu, *Chem. Sci.* **2014**, *5*, 195–199.

[418]J. H. Carter, S. Althahban, E. Nowicka, S. J. Freakley, D. J. Morgan, P. M. Shah, S. Golunski, C. J. Kiely, G. J. Hutchings, *ACS Catal.* **2016**, *6*, 6623–6633.

[419]N. Dimitratos, J. A. Lopez-Sanchez, D. Morgan, A. F. Carley, R. Tiruvalam, C. J. Kiely, D. Bethell, G. J. Hutchings, *Phys. Chem. Chem. Phys.* **2009**, *11*, 5142–5153.

[420]X. Zhu, Q. Guo, Y. Sun, S. Chen, J.-Q. Wang, M. Wu, W. Fu, Y. Tang, X. Duan, D. Chen, Y. Wan, *Nat. Commun.* **2019**, *10*, 1428.

[421]Z. Xing, Z. Guo, X. Chen, P. Zhang, W. Yang, *Catal. Sci. Technol.* **2019**, *9*, 588–592.

[422]X. Zhou, Y. Huang, W. Xing, C. Liu, J. Liao, T. Lu, *Chem. Commun.* **2008**, 3540–3542.

[423] K. Mori, M. Dojo, H. Yamashita, *ACS Catal.* **2013**, *3*, 1114–1119.

[424] J. Wang, W. Li, Y. Wen, L. Gu, Y. Zhang, *Adv. Energy Mater.* **2015**, *5*, 1–4.

[425] T. A. Maark, A. A. Peterson, *J. Phys. Chem. C* **2014**, *118*, 4275–4281.

[426]J. R. Kitchin, J. K. Nørskov, M. A. Barteau, J. G. Chen, *Phys. Rev. Lett.* **2004**, *93*, 4–7.

[427] F. Abild-Pedersen, M. P. Andersson, *Surf. Sci.* **2007**, *601*, 1747–1753.

[428]M. Mavrikakis, J. A. Herron, J. Scaranto, P. Ferrin, S. Li, *ACS Catal.* **2014**, *4*, 4434–4445.

[429] Y. Karatas, A. Bulut, M. Yurderi, I. E. Ertas, O. Alal, M. Gulcan, M. Celebi, H. Kivrak, M. Kaya, M. Zahmakiran, *Appl. Catal. B Environ.* **2016**, *180*, 586–595.

[430]Z. Xing, Z. Guo, X. Chen, P. Zhang, W. Yang, *Catal. Sci. Technol.* **2019**, *9*, 588–592.

[431] K. Tedsree, T. Li, S. Jones, C. W. A. Chan, K. M. K. Yu, P. A. J. Bagot, E. A. Marquis, G. D. W. Smith, S. C. E. Tsang, *Nat. Nanotechnol.* **2011**, *6*, 302–307.

[432]S. Zhang, Ö. Metin, D. Su, S. Sun, *Angew. Chemie - Int. Ed.* **2013**, *52*, 3681–3684.

[433]K. Mori, H. Tanaka, M. Dojo, K. Yoshizawa, H. Yamashita, *Chem. – A Eur. J.* **2015**, *21*, 12085–12092.

[434]K. Mori, K. Naka, S. Masuda, K. Miyawaki, H. Yamashita, *ChemCatChem* **2017**, *9*, 3456–3462.

[435]A. Bulut, M. Yurderi, M. Kaya, M. Aydemir, A. Baysal, F. Durap, M. Zahmakiran, *New J. Chem.* **2018**, *42*, 16103–16114.

[436]H. Kivrak, D. Atbas, O. Alal, M. S. Çögenli, A. Bayrakceken, S. O. Mert, O. Sahin, *Int. J. Hydrogen Energy* **2018**, *43*, 21886–21898.

[437]D. Liu, Z. Y. Gao, X. C. Wang, J. Zeng, Y. M. Li, *Appl. Surf. Sci.* **2017**, *426*, 194–205.

[438]J. H. Lee, J. Cho, M. Jeon, M. Ridwan, H. S. Park, S. H. Choi, S. W. Nam, J. Han, T. H. Lim, H. C. Ham, C. W. Yoon, *J. Mater. Chem. A* **2016**, *4*, 14141–14147.

[439] F. Abild-Pedersen, M. P. Andersson, *Surf. Sci.* **2007**, *601*, 1747–1753.

[440]L. Giorgi, A. Pozio, C. Bracchini, R. Giorgi, S. Turtù, *J. Appl. Electrochem.* **2001**, *31*, 325–334.

[441] S. K. Singh, Q. Xu, *J. Am. Chem. Soc.* **2009**, *131*, 18032–18033.

[442] S. K. Singh, Z. Lu, Q. Xu, *Eur. J. Inorg. Chem.* **2011**, *2011*, 2232–2237.

[443] K. S. Sanjay, X. B. Zhang, Q. Xu, *J. Am. Chem. Soc.* **2009**, *131*, 9894–9895.

[444]S. K. Singh, A. K. Singh, K. Aranishi, Q. Xu, *J. Am. Chem. Soc.* **2011**, *133*, 19638–19641.

[445] J. K. Norskov, C. H. Christensen, *Science (80-.).* **2006**, *312*, 1322 LP – 1323.

[446] Z. Zhang, S. Zhang, Q. Yao, X. Chen, Z.-H. Lu, *Inorg. Chem.* **2017**, *56*, 11938–11945.

[447] M. Zheng, R. Cheng, X. Chen, N. Li, L. Li, X. Wang, T. Zhang, *Int. J. Hydrogen Energy* **2005**, *30*, 1081–1089.

[448] S. J. Cho, J. Lee, Y. S. Lee, D. P. Kim, *Catal. Letters* **2006**, *109*, 181–186.

[449] H.-L. Jiang, S. K. Singh, J.-M. Yan, X.-B. Zhang, Q. Xu, *ChemSusChem* **2010**, *3*, 541–549.

[450] M. Yadav, Q. Xu, *Energy Environ. Sci.* **2012**, *5*, 9698–9725.

[451] P. Nikhitha, K. B. S. Saibabu, *Chem. Eng. Technol.* **2010**, *33*, 1543–1551.

[452] E. F. Rothgery, *Kirk-Othmer Encycl. Chem. Technol.* **2004**, DOI https://doi.org/10.1002/0471238961.0825041819030809.a01.pub2.

[453] G. R. Maxwell, *Synthetic Nitrogen Products*, Springer, Boston, MA, **2005**.

[454] H. Bünger, *Chemie Ing. Tech.* **1990**, *62*, 524.

[455] H. Hayashi, *Res. Chem. Intermed.* **1998**, *24*, 183–196.

[456] C. M. Cusano, The Hofmann Degradation of Oxamide and Urea, Union College - Schenectady, NY, **1955**.

[457] J.-P. Schirmann, P. Bourdauducq, *Ullmann's Encycl. Ind. Chem.* **2001**, DOI https://doi.org/10.1002/14356007.a13_177.

[458] J. P. Contour, G. Pannetier, *J. Catal.* **1972**, *24*, 434–445.

[459] R. Maurel, J. C. Menezo, *J. Catal.* **1978**, *51*, 293–295.

[460] P.-X. Zhang, Y.-G. Wang, Y.-Q. Huang, T. Zhang, G.-S. Wu, J. Li, *Catal. today* **2011**, *165*, 80–88.

[461] S. E. Wood, J. T. Bryant, *Prod. R&D* **1973**, *12*, 117–122.

[462]T. G. Soares Neto, A. J. G. Cobo, G. M. Cruz, *Appl. Catal. A Gen.* **2003**, *250*, 331–340.

[463] M. Pravica, L. Bai, Y. Liu, *Chem. Phys. Lett.* **2013**, *555*, 115–118.

[464] A. S. Shteinberg, in (Ed.: A.S. Shteinberg), Springer Berlin Heidelberg, Berlin, Heidelberg, **2008**, pp. 173–198.

[465] S. K. Singh, Q. Xu, *Catal. Sci. Technol.* **2013**, *3*, 1889–1900.

[466] A. K. Singh, M. Yadav, K. Aranishi, Q. Xu, *Int. J. Hydrogen Energy* **2012**, *37*, 18915–18919.

[467] L. Zhou, X. Luo, L. Xu, C. Wan, M. Ye, *Catalysts* **2020**, *10*, DOI 10.3390/catal10080930.

[468]L. He, B. Liang, L. Li, X. Yang, Y. Huang, A. Wang, X. Wang, T. Zhang, *Acs Catal.* **2015**, *5*, 1623–1628.

[469]Y. B. Jang, T. H. Kim, M. H. Sun, J. Lee, S. J. Cho, *Catal. Today* **2009**, *146*, 196–201.

[470] X. Du, P. Cai, W. Luo, G. Cheng, *Int. J. Hydrogen Energy* **2017**, *42*, 6137–6143.

[471] H. Wang, L. Wu, Y. Wang, X. Li, Y. Wang, *Catal. Commun.* **2017**, *100*, 33–37.

[472]M. Liu, Y. Zheng, S. Xie, N. Li, N. Lu, J. Wang, M. J. Kim, L. Guo, Y. Xia, *Phys. Chem. Chem. Phys.* **2013**, *15*, 11822–11829.

[473] S. K. Singh, Q. Xu, *J. Am. Chem. Soc.* **2009**, *131*, 18032–18033.

[474] A. K. Singh, M. Yadav, K. Aranishi, Q. Xu, *Int. J. Hydrogen Energy* **2012**, *37*, 18915–18919.

[475]S. K. Singh, A. K. Singh, K. Aranishi, Q. Xu, *J. Am. Chem. Soc.* **2011**, *133*, 19638–19641.

[476] X. Lu, S. Francis, D. Motta, N. Dimitratos, A. Roldan, *Phys. Chem. Chem. Phys.* **2020**, *22*, 3883–3896.

[477]L. He, B. Liang, L. Li, X. Yang, Y. Huang, A. Wang, X. Wang, T. Zhang, *ACS Catal.* **2015**, *5*, 1623–1628.

[478] W. Kang, A. Varma, *Appl. Catal. B Environ.* **2018**, *220*, 409–416.

[479]P. Yang, L. Yang, Q. Gao, Q. Luo, X. Zhao, X. Mai, Q. Fu, M. Dong, J. Wang, Y. Hao, R. Yang, X. Lai, S. Wu, Q. Shao, T. Ding, J. Lin, Z. Guo, *Chem. Commun.* **2019**, *55*, 9011–9014.

[480] J. Wang, X.-B. Zhang, Z.-L. Wang, L.-M. Wang, Y. Zhang, *Energy Environ. Sci.* **2012**, *5*, 6885.

[481]T. Liu, Q. Wang, J. Yuan, X. Zhao, G. Gao, *ChemCatChem* **2018**, *10*, 2200–2204.

[482]P. Zhao, N. Cao, J. Su, W. Luo, G. Cheng, *ACS Sustain. Chem. Eng.* **2015**, *3*, 1086–1093.

[483] H. Dai, Y. Zhong, P. Wang, *Prog. Nat. Sci. Mater. Int.* **2017**, *27*, 121–125.

[484] Y. Chen, L. Wang, Y. Zhai, H. Chen, Y. Dou, J. Li, H. Zheng, R. Cao, *RSC Adv.* **2017**, *7*, 32310–32315.

[485] P. Liu, X. Gu, Y. Wu, J. Cheng, H. Su, *Int. J. Hydrogen Energy* **2017**, *42*, 19096–19105.

[486] Y. Men, J. Su, X. Wang, P. Cai, G. Cheng, W. Luo, *Chinese Chem. Lett.* **2019**, *30*, 634–637.

[487] F. Guo, H. Zou, Q. Yao, B. Huang, Z. H. Lu, *Renew. Energy* **2020**, *155*, 1293–1301.

[488] Y. Men, X. Du, G. Cheng, W. Luo, *Int. J. Hydrogen Energy* **2017**, *42*, 27165–27173.

[489] D. Wu, M. Wen, C. Gu, Q. Wu, *ACS Appl. Mater. Interfaces* **2017**, *9*, 16103–16108.

[490] Z. Xing, P. Zhang, X. Chen, Z. Guo, W. Yang, *Catal. Sci. Technol.* **2019**, *9*, 588–592.

2. EXPERIMENTAL, METHODS AND CHARACTERIZATION

This chapter describes the techniques and materials employed in this thesis, for catalysts preparation, tests and products analysis. An introduction about the methods used in the density functional theory (DFT) studies and the basic principles of characterization techniques are also presented here. In addition, a list of used chemicals and equations are subsequently showed.

2.1. List of chemicals

The chemicals employed in all the experiments of this thesis are listed in Table 1 with their purity and suppliers.

Table 1: list of employed chemicals in this thesis.

Substance	*Formula / short name*	*Supplier*	*Purity (%)*
Pyrolytically stripped CNFs	CNFs-PS	Applied Science Company	n.a.
Low-heat treated CNFs	CNFs-LHT	Applied Science Company	n.a.
High-heat treated CNFs	CNFs-HHT	Applied Science Company	n.a.
Graphite	PG	Johnson Matthey	n.a.
Graphite oxide	GO	Sixth Element Company	n.a.
Nitric acid	HNO_3	Sigma-Aldrich	65
Phosphoric acid	H_3PO_4	Sigma-Aldrich	≥99
Hydrochloric acid	HCl	Sigma-Aldrich	37 (wt)
Sodium hydroxide	NaOH	Sigma-Aldrich	≥98
Sodium borohydride	$NaBH_4$	Sigma-Aldrich	99.99
Sulfuric acid	H_2SO_4	Sigma-Aldrich	95-98

Ethanol	EtOH	Sigma-Aldrich	≥95
Sodium tetrachloropalladate (II)	Na_2PdCl_4	Sigma-Aldrich	99.99
Sodium tetrachloroaurate(III) dihydrate	$NaAuCl_4{\cdot}2H_2O$	Sigma-Aldrich	99.99
Rhodium (II) acetate	$[Rh(CO_2CH_3)_2]_2$	Alfa Aesar	99.99
Formic Acid	HCOOH	Sigma-Aldrich	≥95
Hydrazine hydrate	$NH_2NH_2 \cdot H_2O$	Sigma-Aldrich	98
4- dimethylaminobenzaldehyde	4-DMAB	Sigma-Aldrich	98

2.2. Equations

Conversion (x_a):

$$x_a\ (\%) = \frac{[S]_{initial} - [S]_a}{[S]_{initial}} \tag{1}$$

Where $[S]_{initial}$ and $[S]_a$ are the concentrations of the substrate at the initial and the selected time a, respectively.

Activity:

$$Activity\ (h^{-1}) = \frac{mol\ S_{converted}}{mol\ M \cdot t} \tag{2}$$

Where *mol* $S_{converted}$ are the converted moles of the substrate, *mol M* the total moles of metal and *t* the selected time.

The remaining equations, referred to a specific part of the thesis, will be deeply discussed and presented appropriately.

2.3. Support functionalisation

In this thesis, carbon nanofibers CNFs were used as support in Chapters 3 to 5 and as catalyst in Chapters 6 and 7. Three different types of CNFs were employed in this study:

- Pyrolytically stripped (PS) CNFs: they are produced by pyrolytically stripping, which removes the superficial polyaromatic hydrocarbons.
- Low-heat treated (LHT) CNFs: they are produced by treating the fibers at 1500 °C. This treatment carbonises the traces of carbon deposited for chemical vapour deposition onto the surface of the fibers.
- High-heat treated (HHT) CNFs: they are produced by treating the fibers at 3000 °C obtaining the higher degree of graphitization[1].

2.3.1. HHT-CNFs functionalisation

HHT-CNFs were functionalised adding oxygen and phosphorous groups by liquid phase acid treatment.

In a standard 2 g preparation procedure of oxygen functionalised HHT-CNFs (O-HHT), the desired amount of HHT-CNFs was added at 100 mL of HNO_3 (65 wt%) in a round bottom flask placed in a heating system reflux condenser. After 1 h at 100 °C the solid was filtered and washed with 5 L of water in order to remove the acid in excess. The washed material was then dried in oven at 80 °C.

Phosphorous functionalised HHT-CNFs (P-HHT) were obtained employing the same heating system reflux condenser as O-HHT. In this case, 2 g of HHT-CNFs were added to 100 mL solution of HNO_3 (65 wt%) and H_3PO_4 (≥99 wt%) 1:1 vol/vol mixture. After 1 h at 100 °C, the solid was filtered, washed with 5 L of water and dried in oven at 80 °C. The resulting material was then calcinated at 400 °C for 4 h in a tubular furnace in static air conditions, obtaining the final product P-HHT. A schematic representation of the functionalisation procedure is shown in Figure 1.

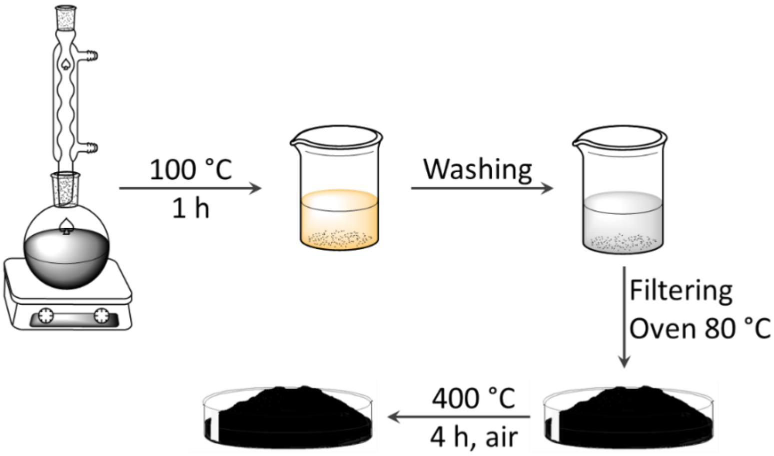

Figure 1: Schematic representation of P-HHT preparation by acid functionalisation.

2.4. Catalyst synthesis

2.4.1. Preparation of monometallic catalysts by sol-immobilisation

The following procedure applies to the synthesis of 1 g of all monometallic catalysts (1 wt%) on bare or functionalised HHT-CNFs.

In a typical sol-immobilization procedure[2] (Figure 2), a solution of the precursor salt (Table 2, columns 2 and 3) was added to the selected amount of milliQ H_2O (Table 2, column 4) in order to prepare the catalyst. Then, the capping agent PVA (M/PVA = 1/0.5) was inserted. After this step, the appropriate amount of freshly prepared aqueous solution of $NaBH_4$ (M/NaBH4 = 1/8 mol/mol) was added to the mixture at once and the instantaneous formation of metallic colloid was proved by the change in colour dependent on the nature of the metal.

After 15 to 30 minutes (Table 2, column 5) under vigorous stirring, 1 g of the support was added in order to anchor the colloidal NPs. By the addition of sulfuric acid (H_2SO_4), the suspension was acidified until pH 2 and stirred for 30 minutes to guarantee the total immobilisation of NPs on the selected support[3]. The solid was then filtered, washed with 1 L of deionised water and dried in oven at 80 °C for 1 day obtaining the final catalytic materials.

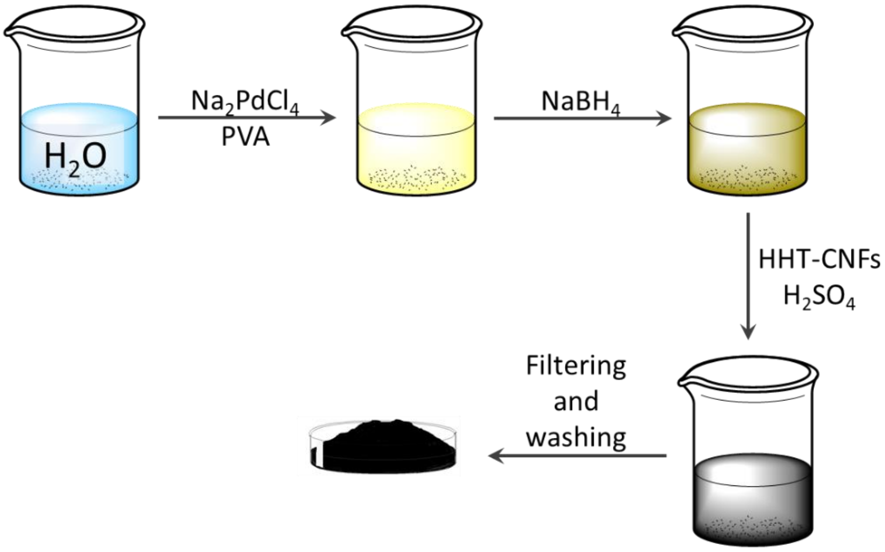

Figure 2: Schematic representation of sol-immobilisation method for preparing Pd@HHT catalyst.

Table 2: summary of the amount and type of metal precursor added and waiting time between the addition of the reducing agent and the support.

Metal	*Precursor*	*Moles of precursor employed (mol$_x$ 10^{-2})*	*Volume of water (L)*	*Waiting time for support addition (min)*
Pd	Na_2PdCl_4	9.40	0.1	30
Au	$NaAuCl_4{\cdot}2H_2O$	5.08	0.1	30
Rh*	$[Rh(CO_2CH_3)_2]_2$	9.72	1.0	15

* For Rh catalyst the precursor salt was added in a solution of H_2O/EtOH = 1/1 vol/vol

2.4.2. Preparation of bimetallic catalysts by sol-immobilisation

The following procedure applies to the synthesis of 1 g of 1 wt% bimetallic catalysts (Pd_xAu_y and Pd_xRh_y, with nominal x:y equal to 8:2, 6:4, 4:6 and 2:8). HHT-CNFs were selected as support.

The solution of the two precursor salts (Table 3) were added to a baker containing the selected amount of milliQ water (0.1 L for PdAu and 1 L for PdRh). Then, the capping agent PVA (M/PVA = 1/0.5) was inserted. Afterwards, the appropriate amount of freshly prepared aqueous solution of $NaBH_4$ (M/NaBH4 = 1/8 mol/mol) was added to the mixture at once and the instantaneous formation of metallic colloid was proved by the change in colour dependent on the nature of the metal. After 15 or 30 minutes (for PdRh and PdAu, respectively) under vigorous stirring, 1 g of the support was added in order to anchor the colloidal NPs. By the addition of sulfuric acid (H_2SO_4), the suspension was acidified until pH 2 and stirred for 30 minutes to guarantee the total immobilisation of NPs on the selected support[3]. The solid was then filtered, washed with 1 L of deionised water and dried in oven at 80 °C for 1 day obtaining the final catalytic materials.

Table 3: Summary of the amount and formula of precursors employed in the synthesis.

x:y ratio	*Precursor x*	*Precursor y*	*Moles of x employed (mol_x 10^{-2})*	*Moles of y employed (mol_y 10^{-2})*
Pd_8Au_2	Na_2PdCl_4	$NaAuCl_4 \cdot 2H_2O$	6.42	1.61
Pd_6Au_4	Na_2PdCl_4	$NaAuCl_4 \cdot 2H_2O$	4.21	2.80
Pd_4Au_6	Na_2PdCl_4	$NaAuCl_4 \cdot 2H_2O$	2.49	3.73
Pd_2Au_8	Na_2PdCl_4	$NaAuCl_4 \cdot 2H_2O$	1.12	4.47
Pd_8Rh_2*	Na_2PdCl_4	$[Rh(CO_2CH_3)_2]_2$	7.56	1.90
Pd_6Rh_4*	Na_2PdCl_4	$[Rh(CO_2CH_3)_2]_2$	5.72	3.80
Pd_4Rh_6*	Na_2PdCl_4	$[Rh(CO_2CH_3)_2]_2$	3.84	5.76
Pd_2Rh_8*	Na_2PdCl_4	$[Rh(CO_2CH_3)_2]_2$	1.94	7.72

* For Rh catalyst the precursor salt was added in a solution of H_2O/EtOH = 1/1 vol/vol

2.5. Catalyst characterization

In this section the different techniques employed in this thesis to characterise the catalysts produced will be introduced.

2.5.1. X-ray photoelectron spectroscopy (XPS)

X-ray photoelectron spectroscopy (XPS), which is also known as electron spectroscopy for chemical analysis (ESCA), is a powerful spectroscopic technique to characterize the composition and chemical state of solids with a high surface sensitivity. An important feature of this characterization technique is the possibility to detect every element of the periodic table with a detection limit behind 1%.

XPS is mainly based on the photoelectric effect (Figure 3, left). This principle defines the emission of an electron (referred as photoelectron) from the surface because of the irradiation by an electromagnetic source, e.g. X-rays. In general, the spectrum obtained contains both valence band and core-shell electrons. However, due to the quantity of information obtained by valence band electrons in a narrow region and the difficult analysis it is preferred to evaluate core-shell electrons. In this case, it is easy to distinguish the different elements present in the sample. The spectrum is composed by several narrow peaks on the continuous background. Narrow peaks are grouped into pure photoelectrons from the sample, satellite peaks and Auger electrons. The last ones derived from the emission of additional electrons. This emission is caused by electrons of the outer shell which try to fill the holes due to the emitted photoelectrons (Figure 3, right).

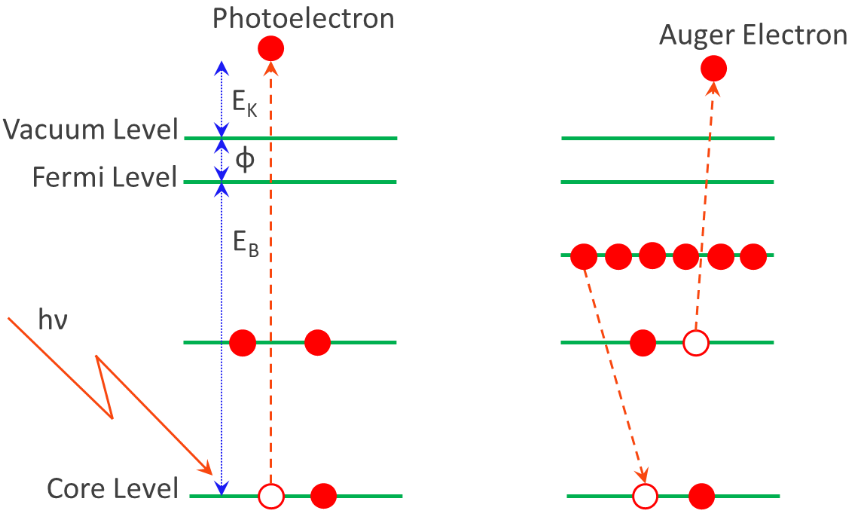

Figure 3: Photoelectric effect (left) and Auger electron emission (right).

The emission of an electron happens when the energy of a different photon is higher that the work function of the sample (electron binding energy). The quantity measured by the electron analyser is the kinetic energy (E_K) of the emitted photoelectrons. This energy is related with the binding energy of electron inside the atom (E_B), which is characteristic for every element through Eq. 3.

$$E_K = h\nu - E_B - \varphi_a \tag{3}$$

Where $h\nu$ is the energy of the incident photon and φ_a is the work function of the analyser, considered constant. This parameter can be artificially compensated, and for this reason the final binding energy can be calculated according to Eq. 4.

$$E_B = h\nu - E_K \tag{4}$$

E_B of a specific element also represent its local environment. Therefore, core-level photoelectrons are employed to identify the element, while small shifts in the E_B (chemical shift) can be determinant to distinguish its oxidation state. XPS can also be employed to quantitatively analyse elements on the sample, due to the proportional relation between the photoelectron peak intensity and the amount of the element. In this case, atomic sensitivity factors (ASF) need to be considered in order to consider the ability of each element to produce photoelectrons[4].

XPS is indicated as a surface sensitive method, which only analyse a thin layer of the outermost surface (between 1 to 10 nm). This is due to the inelastic scattering of low kinetic energy photoelectrons, loosing energy passing into the matter and never leaving the sample[5].

A schematic representation of a generic XPS spectrometer is presented in Figure 4. The excitation source, i.e. X-ray tube or synchrotron radiation, generates an X-ray beam, which is focused onto the sample surface by using electron lenses. Common sources are Mg and Al because of their X-ray strong intensity and narrow band width. The apparatus is maintained under ultra-high vacuum (UHV) with the aim of avoiding gas collisions of the emitted photoelectrons. After the emission, the emitted electrons enter the electron lenses which focus them to pass in the analyser. Here only photoelectrons with a specific energy can cross the electrostatic field created between the hemispheres. In conclusion, the electrons are multiplied and counted at the exit slit by the electron detection system[4].

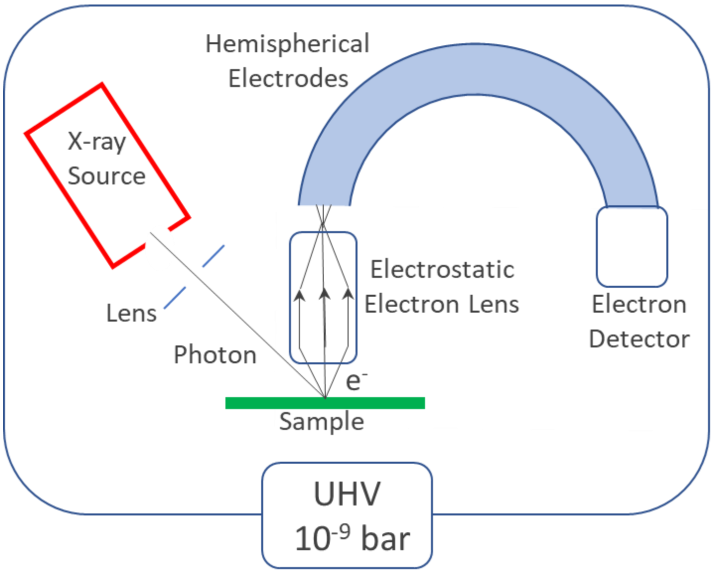

Figure 4: Schematic representation of the most important components of XPS instrument.

For this thesis, XPS experiment were carried out using a Thermo Scientific K-alpha+ spectrometer. Samples were analysed employing a monochromatic Al X-ray source operating at 72 W. Data were recorder at pass energy of 150 eV for survey spectra and 40 eV for high resolution scans, with 1 eV and 0.1 eV of step size, respectively. All data were then processed using CASAXPS, imposing Scofield sensitivity factors and -0.6 as energy exponent.

2.5.2. Electron microscopy (EM)

Electron microscopy is employed to observe objects that are smaller than 1 µm. In this case, optical microscopy is not able to produce images because of the long wavelength of visible light. The main difference between optical and electron microscopy is the source: in the first case it is visible light, while in the latter an electron beam, as suggested by the name[6]. As reported above, optical microscopy is affected by the diffraction limit, described as the limit beyond which it is impossible to resolve the object separate points because of diffraction phenomena. This effect became non-negligible when the object to be observed is of the same order of the wavelength. On the other hand, electrons possess a de Broglie wavelength smaller than 1 nm, depending on the applied accelerating voltage[7]. This special feature permits to achieve atomic resolution: for a 200 KeV transmission microscope an electron wavelength near 2.5 pm can be obtained[6].

Two types of EM are the most common: the scanning electron microscope (SEM)[8] and the transmission electron microscope (TEM)[6]. In TEM electrons are released from the sample surface by irradiation with the focused electron beam, employing electrons that can pass through the specimen. Figure 5 shows a generic TEM.

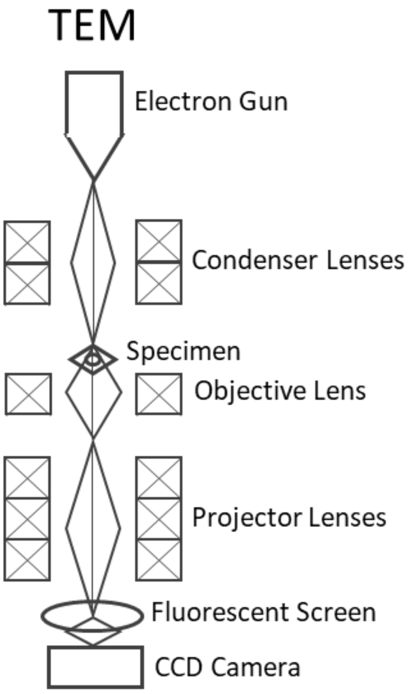

Figure 53: Schematic representation of the most important components of a TEM.

In transmission electron microscopy the electron gun generates the electron beam that is typically at higher acceleration than in SEM. Nevertheless, the condenser lenses focus the beam into a narrow direct flow of electrons that passes through the specimen. Then, the resulting beam is focused by the objective and projector lenses reaching finally either a fluorescent screen or a CCD camera detector.

In a *bright-field* TEM analysis the difference in width and density in the sample generates the contrast in the resulting image: an increasing in these parameters causes a darker image. However, when some electrons are diffracted by the sample an annular dark field (ADF) detector can detect the signal produced resulting in images. This method is the base of the so called *dark-field* analysis. The formation of these type of images do not depend on the density of the sample but on its specific crystallographic orientation.

In the scanning transmission electron microscope (STEM), the electron beam is focused in the selected and very thin spot (with a size between 0.05 and 0.2 nm) and scanned over the sample in a raster illumination system. Due to the beam's rastering, STEM can be coupled with other analytical techniques, such as the energy dispersive X-ray (EDX) and the annular dark-field imaging (ADF). EDX relies on X-rays emitted during the electron scanning, giving information about the composition of the sample since their energy is specific for every element of the periodic table. Indeed, EDX analysis is often coupled with STEM characterization[9].

In this thesis, two different types of TEM were employed. In collaboration with the Karlsruhe Institute of Technology (KIT) in Germany, high angle annular dark-field (HAADF) scanning transmission electron microscopy (STEM) and EDX analyses were used to characterise the catalysts discussed in Chapter 5. A Themis300 TEM from Thermofisher Scientific equipped with a Super-X-EDX and a probe aberration corrector detector was the microscope employed. ImageJ software was used to determine particle size distribution by fitting ellipsoidal shapes to metal NPs and considering more than 200 nanoparticles.

For the materials employed in Chapters 3 and 4, a double Cs aberration-corrected FEI Titan3 Themis 60-300 microscope equipped with a X-FEG gun, a monochromator and XEDS ChemiSTEM (consisting of 4-windowless SDD) detector was employed. Moreover, using HAADF detector we were able to record HR-STEM images. The visual quality of the XEDS mapping obtained were improved using Velox software. The metal particle size distribution was calculated based on the STEM-HAADF images considering the diameter of more than 150 metal NPs and using ImageJ software. Based on this data, the average particle diameter (d) was determined according to Eq. 5, where $n_i \geq 200$. Similarly, Eq.6 was employed to calculate the total metal dispersion (D). Here, N_S and N_t are the total number of surface metal atoms and the total number of atoms in the particle, respectively.

$$d = \frac{\sum n_i d_i}{\sum n_i} \tag{5}$$

$$D = \frac{N_S}{N_t} \tag{6}$$

2.5.3. Raman spectroscopy

Raman spectra are obtained by irradiating the sample with an energetic laser beam in the near IR and visible range. Different scattered photons can be emitted by the sample. In the case of inelastic light scattering, two different bands can be obtained in the spectrum: the molecule in the fundamental vibrational level ($\nu = 0$) can adsorb the photon from the source of energy $E_{ex} = h\nu_{ex}$ and, from a virtual exited state *j*, it emits a backscattered photon with lower energy ($E = h(\nu_{ex} - \nu_v)$), the so called Stokes scattering (Figure 6a). However, also molecules in an exited vibrational state can be promoted by interaction with the light emitted by the source, emitting backscattered photon with higher energy ($E = h(\nu_{ex} + \nu_v)$), derived from the anti-Stokes scattering (Figure 6b). Elastic scattering can also happen and an emission of a photon of energy E_{ex} can be observed. This radiation with $\nu = \nu_{ex}$ is called Rayleigh scattering (Figure 6c)[10].

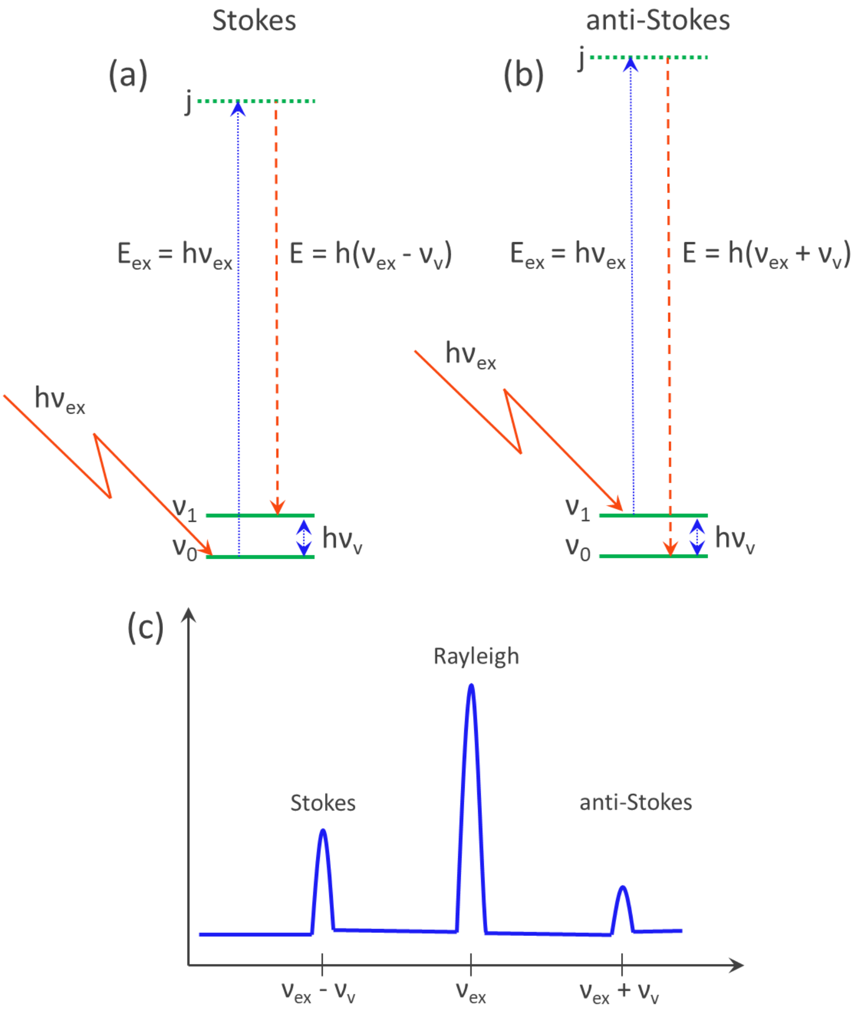

Figure 6: Different bands in Raman spectra. Raman scattering a) Stokes type and b) anti-Stokes type. c) Position of the different bands in a schematic Raman spectrum. Anti-Stokes scattering peak is less intense than Stokes scattering peak due to the inferior probability to found molecules in the first exited vibrational state. This probability increases with increasing the temperature of the experiment.

It is important to notice that a molecule, to be Raman active, needs to have bonds where their electric polarizability (α) varies with the bond length (r): $\partial\alpha/\partial r \neq 0$. Another selection rule state that Raman line are only corresponding to $\Delta\nu = \pm 1$; other lines can be observed, i.e. equivalent to $\Delta\nu = \pm 2$, but only in an attenuated version[11].

The main components of a Raman instrument are a laser source, the sample chamber and a spectrometer. The laser source is mandatory to obtain an intense Raman scattering: indeed, green and blue lasers are the most advantageous. The sample chamber depends on the nature of the sample. Typically, in a micro-Raman instrument for solid sample, it is collocated on a microscope plan. After selected the area and the focus, the sample can be excited by laser irradiation. Different types of Raman spectrometer are available nowadays depending on the application. They are mainly composed by a double grating to minimize the Rayleigh scattered radiation reaching the photomultiplier. A schematic of Raman instrumentation with the main components is shown in Figure 7[10].

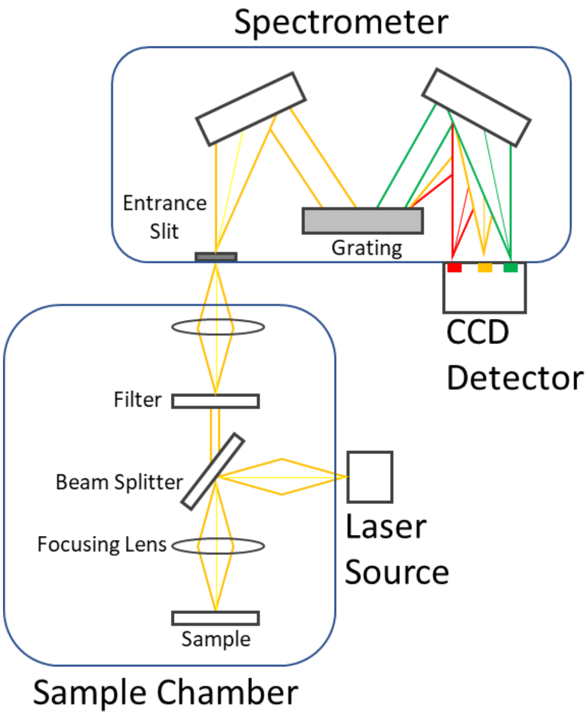

Figure 7: Schematic representation of the most important components of Raman instrument.

Raman spectroscopy is widely used to characterize carbon-based materials. In a typical spectrum of pristine graphite (PG), a sharp peak near 1580 cm^{-1} is observed (G band). The G band is a first order peak attributed to the E_{2g} mode (Figure 8a). Other set of peaks can be seen in the 2800-2600 cm^{-1} region, due to combination modes (second order, Figure 9, left). Here, two main peaks can be detected. The G'_2, which is sharp and at high frequency. On the contrary, the G'_1 is broad and at low frequency. When the system is defective, a new peak (D band) can be observed around 1350 cm^{-1} (Figure 9, right), due to the A_{1g} symmetry

(Figure 8b). This peak is usually forbidden in PG but it is active in presence of defects or substitutional heteroatoms. For this reason, the intensity ratio between the D and the G bands (I_D/I_G) can be used as an index of the degree of defectiveness in graphitized materials (Chapters 6 and 7)[4,12].

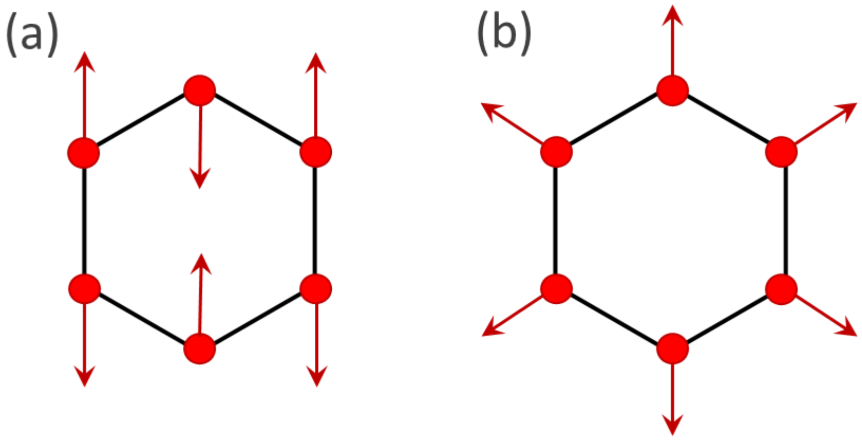

Figure 8: Schematic representation of vibrational a) E_{2g} mode (G band) and b) A_{1g} mode (D band).

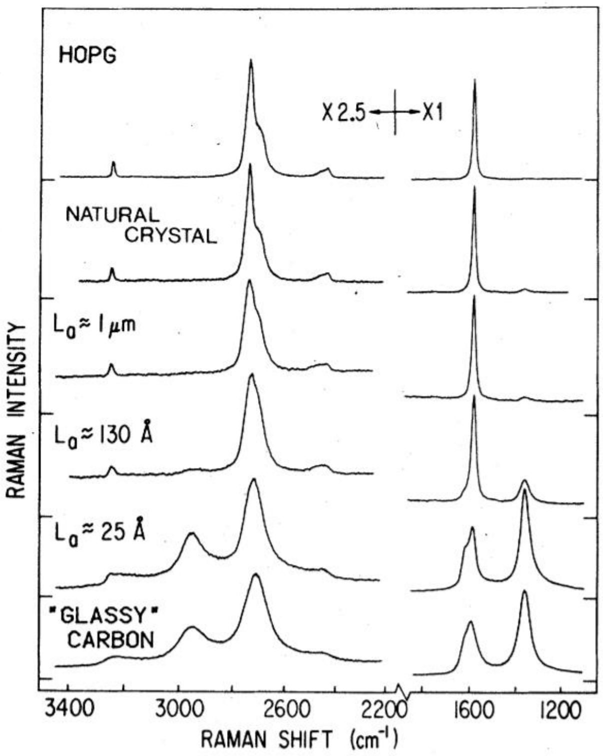

Figure 9: First (right) and second (left) order Raman spectra of different graphitized materials. From top to bottom: most ordered material (PG) to disordered. Reprinted from Ref. [12]: S. A. Solin et al. "First- and second-order Raman scattering from finite-size crystals of graphite" https://doi.org/10.1103/PhysRevB.20.392 with permission of the American Physical Society.

In this thesis, a micro-Raman spectrometer Horiba LabRam HR Evolution equipped with a green solid-state laser emitting at 532 nm was employed giving a spatial resolution of around

1 μm. The system was prepared with 300 lines per mm grating. A final laser power of 0.1 mW and an attenuation time of 300 s per two scans were used to obtain the final spectra.

2.5.4. Brunauer, Emmett and Teller (BET) method: obtaining the surface area

As reported above, carbon materials surface area is an important parameter to establish the final catalytic activity of the catalyst. In order to calculate that parameter, a gas can be adsorbed and condensed onto the material. Usually, nitrogen can be employed because its condensation temperature can be reached immerging the sample into liquid N_2. One of the most common method used to determine surface area was developed in 1938 by Stephen Brunauer, Paul H. Emmet and Edward Teller: the so-called BET method, from their surname's initials[13]. The BET equation derived from the Langmuir one (monolayer molecular adsorption) assuming that: i) the gas adsorbs in layer on a solid, ii) a vertical interaction between adsorption layers is negligible and iii) each layer can be studied applying the Langmuir model[14]. The obtained isotherm can be described by Eq. 7:

$$\frac{1}{\nu\left[\left(\frac{\rho}{\rho_0}\right)\right]} = \frac{c-1}{\nu_m\, c}\left(\frac{\rho}{\rho_0}\right) + \frac{1}{\nu_m\, c} \qquad (7)$$

Where the ν is the quantity of gas adsorbed, ν_m is the volume of gas adsorbed in the monolayer unit and ρ and ρ_0 are the equilibrium and saturation pressure of the adsorbate at the temperature of adsorption, respectively. It is worth to notice that c is the BET constant (Eq. 8), which is described by the enthalpy of adsorption of the first layer (E_1) and of the other layers (E_L).

$$c = e^{\frac{E_1 - E_L}{RT}} \qquad (8)$$

However, Eq. 7 is only valid for partial pressure (ρ/ρ_0) range of 0.05-0.35, where the resulting plot is linear. In this area, it is possible to calculate the quantity of adsorbed gas in the monolayer and the BET constant. Therefore, the surface area (A_S) can be obtained employing Eq. 9:

$$A_s = \left(\frac{\nu_m}{22414}\right) N_A\, \sigma \qquad (9)$$

Where N_A is the Avogadro number and σ the area covered by a single nitrogen molecule[15]. In this thesis, the surface area was determined using Quantachrome Autosorb instrument. Before starting the measurement, the sample was degassed for 3 h at 120 °C. All the surface areas were evaluated using the Brunauer-Emmett-Teller (BET) equation.

2.5.5. Inductively coupled plasma optical emission spectrometry (ICP-OES)

The inductively coupled plasma optical emission spectroscopy (ICP-OES) is a technique employed to determine chemical elements in a solution. In this thesis, this analysis was used to reveal the amount of metal in the filtered solution after the catalysts synthesis to establish the metal loading and to detect possible residual metals on carbocatalysts. This emission spectroscopy technique employs inductively coupled plasma to create ions and exited atoms, that emit peculiar electromagnetic radiations. In the ICP, a gas of ions (plasma), often argon, is produced by electric currents that are formed by electromagnetic induction (Figure 10). The plasma is sustained from electrical coils (MHz frequencies) by inductive coupling. The temperature of the source is maintained in the 6000-10000 K range. A Tesla unit ignites the Ar gas flowing through the torch creating a brief discharge arc and initiating the ionization process. The inelastic collision between ions and neutral argon particles generates a stable and high temperature plasma[16]. The peristaltic pump carries the sample into the nebulizer, where it is mixed with the carrier and introduced into the plasma flame. The nebulized sample molecules collide with ions in the plasma breaking their bonds and forming atomic ions, which can recombine emitting a characteristic radiation. Then, lenses are employed to focus the emitted light to the grating, where it is separated into different wavelengths and analysed by the optical spectrometer. Calibration lines are employed to perform quantitative analysis, thus the concentration can be directly obtained from the intensity of each line in the spectrum[10].

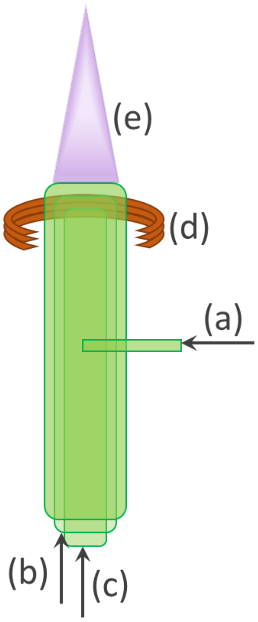

Figure 10: schematic representation of an ICP torch: a) cooling gas tangential to the outer tube, b) discharge gas flow (Ar), c) carrier with sample, d) induction coils and e) plasma torch.

In this thesis, the presence of possible metal traces on carbon materials, metal loading and metal leaching were evaluated by inductively coupled plasma optical emission spectroscopy using a Perking Elmer Optima 8000 emission spectrometer.

2.6. Catalytic tests

In this section the set-up employed in the different catalytic tests performed in this thesis will be described.

2.6.1. Formic acid decomposition (FAD) reaction

Formic acid decomposition (FAD) was performed in a batch reactor in order to collect kinetic data in a reproducible and accurate way.

In Figure 11 is shown a representative scheme and a photograph of the set-up employed for this reaction.

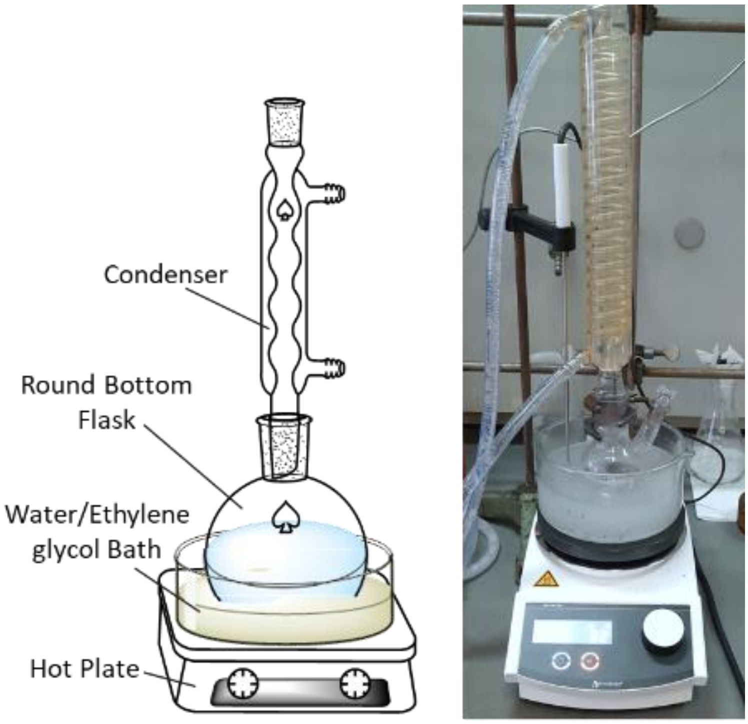

Figure 11: Representative scheme (left) and photograph (right) of the batch reactor set-up.

In this set-up, FAD reaction was performed in a 100 mL two-neck round-bottom flask placed in a water/ethylene glycol bath equipped with a reflux condenser and a magnetic stirrer. In all experiments, 10 mL of an HCOOH aqueous solution 0.5 M was inserted in the reactor and heated at a selected constant reaction temperature. This FA concentration was selected because in literature this value is commonly used and, thus, it facilitates the comparison with other catalytic systems. For metal-based systems (Pd-, PdAu- and PdRh-based), a pre-set temperature of 30 °C was chosen. This temperature allows measurement of kinetic profile near room temperature, which is required for portable fuel cells devices. It is slightly higher to ensure the reproducibility of the tests. Moreover, a substrate/metal molar ratio of 2000/1 was selected due to different factors. Firstly, this ratio permits to reach total FA conversion in 2 hours, allowing to perform several tests per day. In addition, the quantity of catalyst employed can be easily recovered to perform reusability tests. Moreover, in the study of Sanchez et al. on commercial Pd system and in the same conditions this parameter was optimized, showing that 2000/1 ratio avoids diffusion limitations[17]. In carbocatalysis tests, the temperature was increased to 80 °C, in order to better evaluate the different initial activity of every material. Moreover, the amount of catalyst selected was 10/1 in weight. This amount of catalyst permits us to work in kinetic regime but also to have significative difference in the performance of the different carbocatalysts. After the selected temperature was reached, the defined amount of catalyst was inserted in the FA solution and stirred at 1400 rpm.

The samples were withdrawn from the reactor periodically and the amount of residual FA was analysed by high performance liquid chromatography (HPLC) to follow the reaction progress. Each reaction was performed three times to ensure its reproducibility. The errors obtained was inferior to the one of the HPLC and, for this reason, the last one was employed to set the error bars. The initial activity was calculated at 5 minutes according to Eq. 2. Product analysis was performed employing the same set-up and reaction condition and connecting the reactor to an on-line micro-gas chromatograph (GC). HPLC and GC instruments will be explained in Sections 2.7.1 and 2.7.2, respectively.

Durability tests were performed on the most active systems in the same reaction condition but using as a reactor a 250 mL round-bottom flask with 25 mL of HCOOH aqueous solution 0.5 M. The catalyst was filtered and used in the next run without any further purification procedure.

2.6.2. Hydrazine hydrate decomposition reaction

Hydrazine decomposition reaction was performed in a batch reactor, showed in Figure 12.

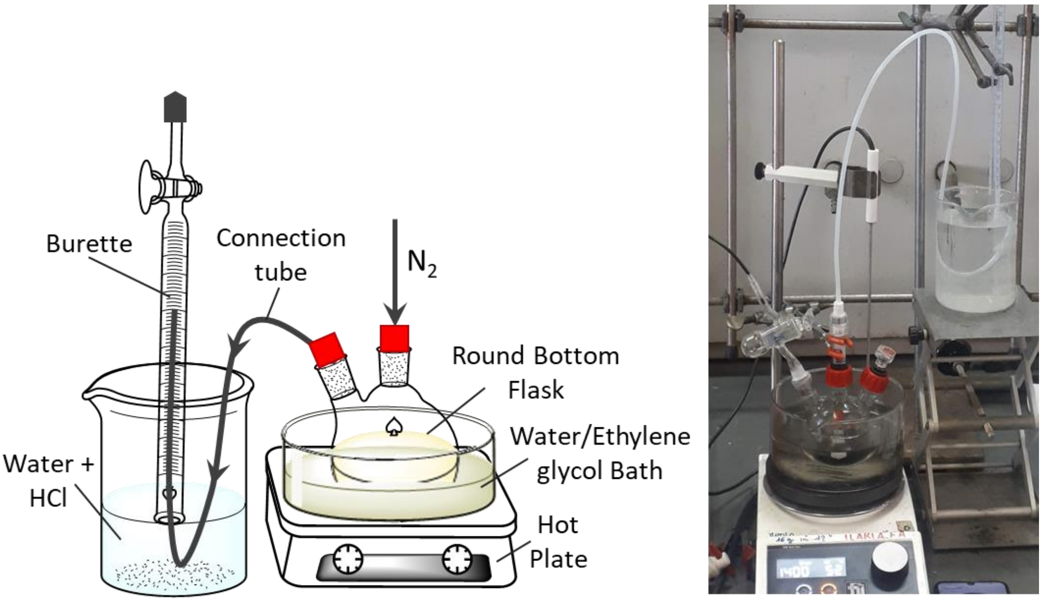

Figure 12: Representative scheme (left) and photograph (right) of the batch reactor set-up.

Hydrazine hydrate decomposition tests were conducted in a three-necked 50 mL round-bottom flask, with one neck connected with a burette employed for gas volume analysis (water displacement method) and another to N_2 (close during the reaction). It was placed in a water/ ethylene glycol bath and equipped with a magnetic stirrer. In normal conditions, 16 mL of a 0.5 M NaOH aqueous solution was heated at 50 °C adding the required amount of catalyst. The concentration of sodium hydroxide and the pre-set temperature was selected according to the previous studies[18,19], and also are the most used in literature. Once the temperature is reached, 600 μL of a 3.3 M hydrous hydrazine aqueous solution was added at once and the final mixture was stirred at 1400 rpm using a magnetic stirrer. The hydrazine hydrate/catalyst weight ratio was selected to be 15.7/1. Different amount of catalyst between 100 and 3 mg were tested, and 6.3 mg was selected to ensure the kinetic regime and to avoid diffusion limitations.

In order to study the kinetic profile of the reaction, two different tests at the same condition were performed. Firstly, the sample was withdrawn from the reactor periodically and hydrazine hydrate conversion was analysed using an UV-Vis spectrophotometer. In addition, a second test was carried out at the same conditions measuring the amount of gas evolved during 6 h of reaction and employing the water displacement method. The method employed for reactant and products analyses will be explained in Sections 2.7.3 and 2.7.4, respectively.

2.7. Analysis of reactants and products

In order to calculate the concentration of formic acid during the reaction high-performance liquid chromatography (HPLC) was employed. In addition, gaseous products (CO_2 and CO), were calculated using an on-line micro gas chromatograph (GC). In hydrazine hydrate decomposition reaction, the conversion of hydrazine was followed by UV-vis spectroscopy, while the evolution of gaseous products (H_2 and N_2) was calculated by water displacement method.

2.7.1. High-performance liquid chromatography (HPLC)

HPLC is a type of liquid chromatography employed to separate and identify a mixture of chemicals. In this technique, a solvent (mobile phase) carries the sample inside a chromatographic column filled with a solid adsorbent matrix (stationary phase). The main components of an HPLC are the mobile phase reservoir, a high-pressure pump, an injector, the column and the detectors. A representative scheme is shown in Figure 13.

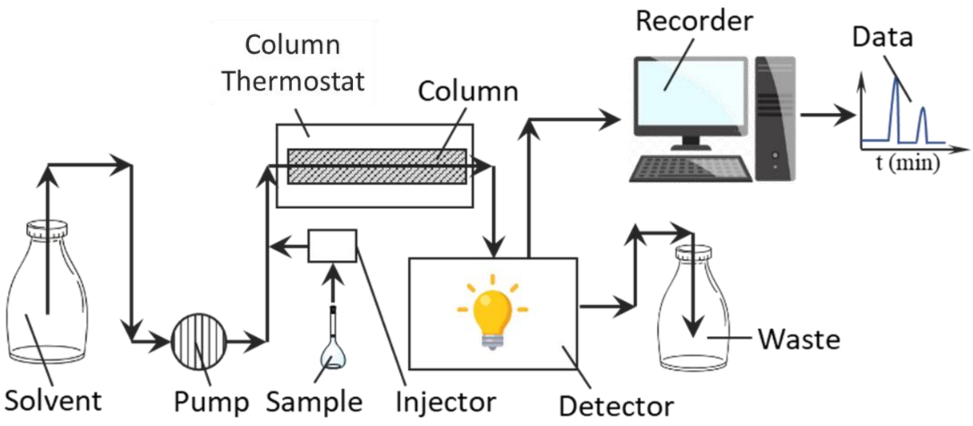

Figure 13: Schematic representation of an HPLC system.

In this system, the mixture of mobile phase and sample, inserted in the injector, is driven into the chromatographic column. Here, each component is separated due to its degree of interaction with the stationary phase. Because of the different interactions, the diverse compounds leave the column with different rates at diverse time, called retention time (t_R). It depends on different factors, such as the composition of the stationary phase and of the liquid phase and the chemistry of the analyte. The adsorbent of the column is typically granular and composed by solid particles, e.g. silica or polymers. The different components are then analysed by the detector, producing a signal that is proportional to the amount of the analyte at the end of the column[10].

The separation of the components of the reaction mixture can be reached by electrical charge, molecular size or polarity.

In the first case, the different attraction between the components on the sample and ions present on the stationary phase causes the separation. Analytes that don’t interact with the ions possess lower retention time, while the others are retained in the column (ion-exchange chromatography). In a size-exclusion chromatography, molecules are separated by molecular size. Indeed, the adsorbent is composed by inert and densely packed particles with small pores. Here, only the small molecules can penetrate the pores and thus, more time is required for them to elute, increasing their retention time. Larger molecules are excluded from the pores, leaving the column faster. The separation based on polarity can be in normal or reverse phase. In a normal phase chromatography, a polar stationary phase and a non-polar solvent are employed. Thus, the analyte that interact by its polar groups with the adsorbent is retained. Less polar molecules elute first, followed by other analytes in order of increasing polarity. In contrast, a non-polar stationary phase and an aqueous moderately polar solvent are employed in reverse phase chromatography. Indeed, in this case the most polar components elute first[10].

Detectors employed in this technique can be universal or selective. In the first case, the detector measures a physical property of the mobile phase, e.g. refraction index, dielectric constant or density. These detectors reveal the difference in the solvent response with and without the sample. Indeed, they can be used for all analytes but sensitivity is incredibly limited. Instead, selective detectors respond to a specific feature of the solute, e.g. UV absorption, fluorescence or diffusion current. The UV-visible detector is one of the most employed measuring the absorption of UV light at a specific wavelength[20]. In Figure 14 is represented a schematic design of a cell for measuring the UV absorption.

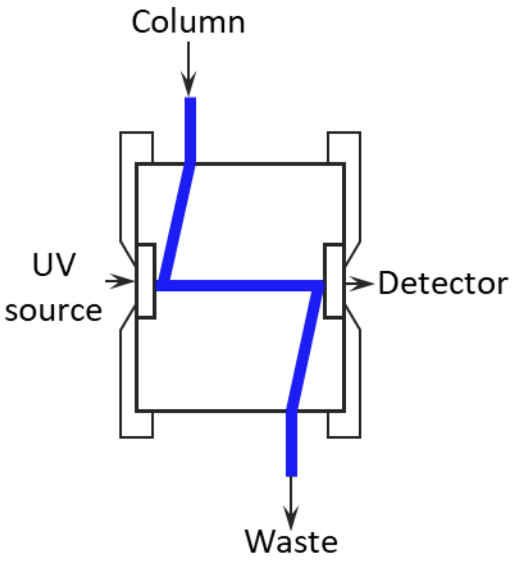

Figure 14: UV-vis adsorption cell for HPLC.

In this thesis, FA conversion was analysed using HPLC. In particular, an H^+ chromatographic column was employed (Alltech OA- 10,308, 300 mm 7.8 mm) with an UV detector settled at 210 nm. Samples from the reaction mixture were withdrawn at 0, 5, 15, 30, 60, 90, 120 minutes of reaction. The solution for the analysis was prepared using 200 μL of the sample in 5 mL H_3PO_4 solution (0.1 wt%), which was also the eluent for the analysis. The isocratic eluent flow was set at 0.4 mL min^{-1}. Four formic acid solution were prepared in order to build the calibration line, obtaining the FA response factor for the instrument.

2.7.2. Gas chromatography (GC)

Gas chromatography (GC) is a method used to separate and analyse a gas mixture. As for HPLC, in GC the sample is injected, mixed with the mobile phase (carrier gas) and inserted in the chromatographic column, where it can interact with the stationary phase. The interaction between the stationary phase and the analyte defines the retention time of each component. The molecule that leaves the column is detected, obtaining a peak signal which possess an area proportional to the quantity of analyte. Different types of GCs are available, but all are mainly composed by a gas supply for the carrier (typically helium, nitrogen or a mixture of the two), an injector (inlet), an oven and the detector. A schematic representation is showed in Figure 15[21,22].

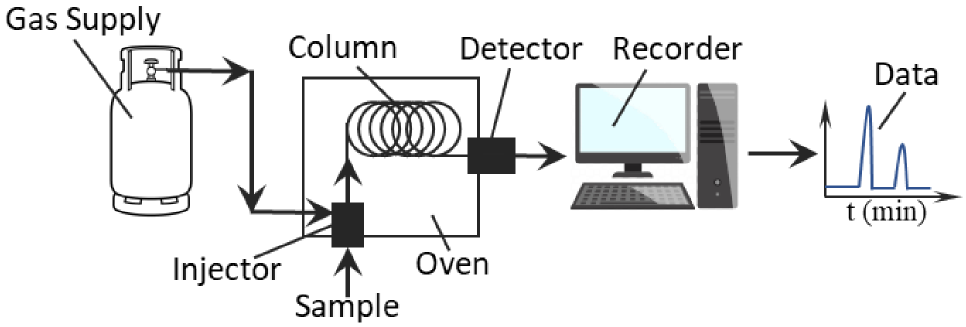

Figure 15: Schematic representation of a GC and its main components.

Different types of columns can be employed depending on the application and the mixture composition. The most common is a very thin (0.1-0.5 mm of internal diameter) and long (15-60 m) column, the so-called capillary column, where its interior surface is covered by the stationary phase. Finally, the separated compounds can reach the detector where they can be identified. The two detectors most employed are the thermal conductivity detector (TCD) and the flame ionization detector (FID). The former reveals changes in the thermal conductivity of the gas carrying the sample and the reference flow of gas carrier. The FID detects ions formed during the combustion of the compounds in a hydrogen flame. This type of detector is cheaper and more resistant but cannot detect CO, CO_2 and H_2[23,24], which are the products of FA decomposition reaction.

In this thesis, the gas phase obtained from FA decomposition reaction was analysed by an Agilent 3000 A online micro-GC. In particular, it was equipped with a TCD detector and two different columns: i) a molecular sieve module and ii) an OV-1 module with polydimethylsiloxilane as stationary phase. Calibration curves of CO and CO_2 were obtained using commercial standards.

2.7.3. Ultraviolet-Visible spectroscopy (UV-Vis)

UV-Vis spectroscopy analyses the adsorbed light in the UV-visible spectra region. In this technique, a photon is adsorbed by a molecule exiting an electron to a higher energy orbital. The instrument measures the power of light that interact with the sample (P), comparing it with the power of the source (P_0). The ratio between the two is expressed as transmittance (T). Usually, the absorbance (A, Eq. 10) is employed in order to have a direct correlation with the Lambert-Beer law[25,26]. This equation related the concentration of a chemical specie (C) with the absorbance measured by the instrument, according to Eq. 11.

$$A = ln\frac{P}{P_0} \tag{10}$$

$$A = \varepsilon_\lambda\, l\, C \tag{11}$$

In Eq. 11, l is the optical path length in cm and ε_λ is the molar attenuation coefficient or absorptivity, which is constant for a given substance at a given wave length (λ). The direct correlation between C and A fails at very high concentration, where other physical-chemical phenomena are present[27,28].

Figure 16 shows a schematic representation of a double beam UV-Vis spectrophotometer. The two different lamps provide the wavelength in the UV-Vis range. The wavelength is selected by the monochromator, and the light can reach the reference and the sample cuvettes. The transmitted light, then, passes through the detector that transform the photons received in electrical signal obtaining the final spectrum[10].

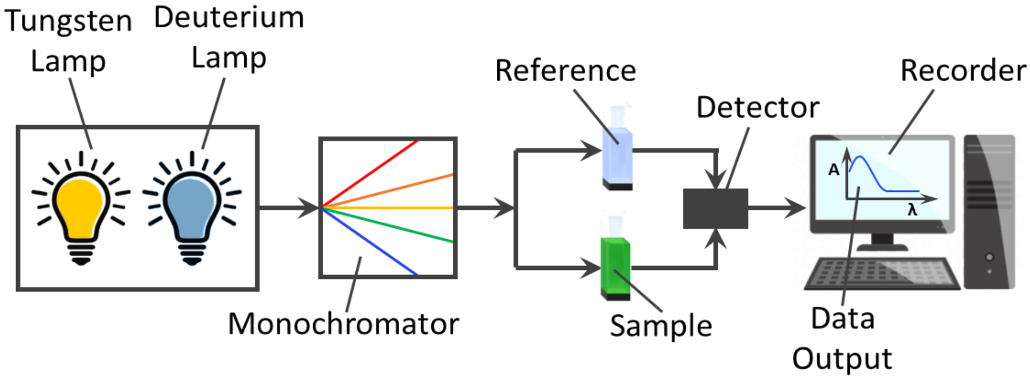

Figure 16: Schematic representation of an UV-Vis spectrophotometer.

In this thesis, hydrous hydrazine conversion was analysed employing a Jasco V-730 Spectrophotometer, with a 1 cm quartz cell. Samples from the reaction mixture were withdrawn at 0, 0.5, 1, 5, 10, 15, 30, 45, 60, 90, 120, 150, 180, 210, 240, 270, 300, 330 and 360 minutes of reaction. The analytical method was based on the reaction between $N_2H_4 \cdot H_2O$ with 4-dimethylaminobenzaldehyde (4-DMAB) in dilute hydrochloric acid according to Figure 17. Hydrous hydrazine quantitatively reacts with 4-DMAB giving a p-quinone structure, which adsorbs at 456 nm[29,30]. The concentration of $N_2H_4 \cdot H_2O$ was calculated using the Lambert-Beer law and calculating ε_λ by preparing four different substrate solutions and obtaining the calibration line.

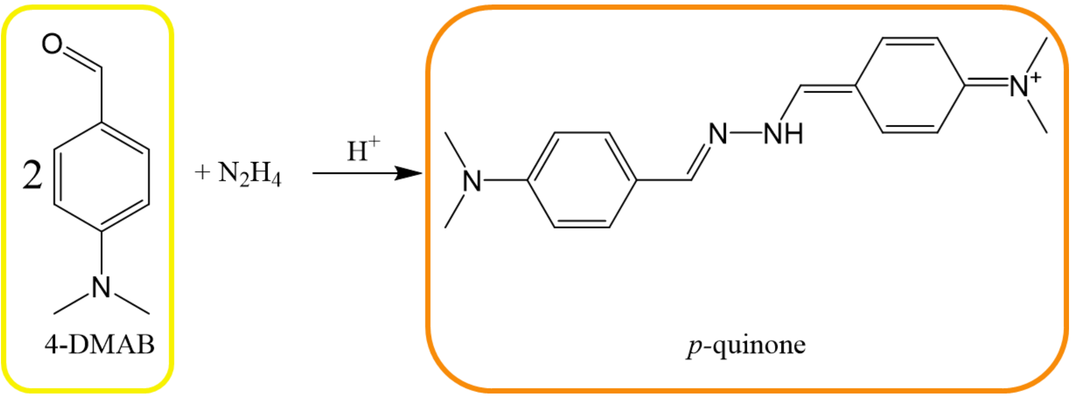

Figure 17: Reaction of 4-DMAB and hydrazine to give the yellow-orange p-quinone.

2.7.4. Water displacement method

Water displacement method is employed to calculate the amount of gas produced during a reaction. It is based on the concept that an object, submerged by a liquid, occupies a volume of liquid equal to the volume of the object. In the case of gasses produced in the reaction, it is possible to connect the reactor with a tube which is fed under a burette, filled with water and placed upside-down in a beaker containing H_2O (see reaction set-up in section 2.6.2). The gas phase produced in the reaction can exit from the tube and displacing the water in the burette, where the volume is marked (Figure 18).

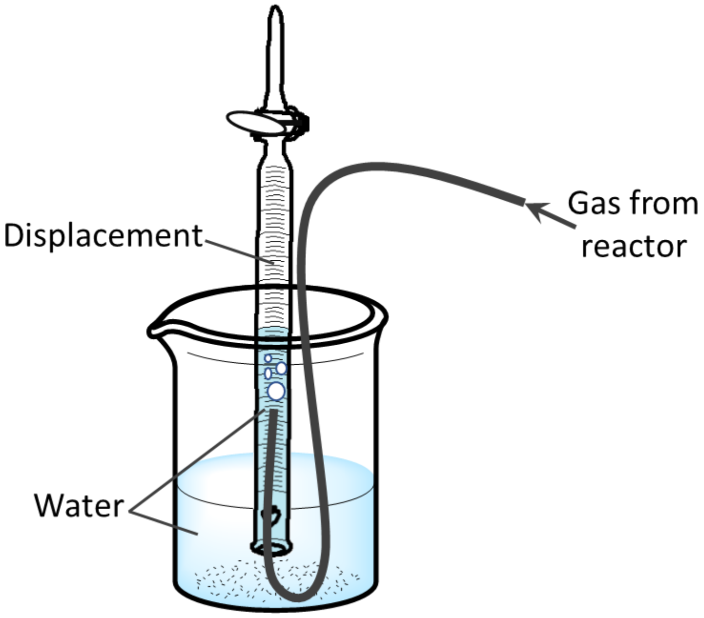

Figure 18: Representation of the water displacement method.

In this thesis, the gas product released from hydrazine hydrate decomposition were allowed to pass to a trap containing a 0.05 M HCl aqueous solution before to enter the burette. Employing this technique, the NH_3 produced, if any, could be removed measuring only the amount of N_2 and H_2 molecules. From the volume obtained ($V_{N_2+H_2}$), the total moles of the gas phase ($n_{N_2+H_2}$) were calculated by Eq. 12.

$$PV_{N_2+H_2} = n_{N_2+H_2}RT \tag{12}$$

Where P and T are the pressure and temperature and R is the ideal gas constant.

The selectivity to hydrogen (x) was then calculated according to Eq. 13.

$$3NH_2NH_2 \rightarrow (1+2x)\,N_2 + 6x\,H_2 + 4(1-x)\,NH_3 \tag{13}$$

Considering the molar ratio (λ) between the total moles of gas and the moles of hydrazine hydrate expressed in Eq. 14, the selectivity can be obtained considering Eq. 15.

$$\lambda = \frac{n_{N_2+H_2}}{n_{N_2H_4}} \tag{14}$$

$$x = \frac{3\lambda-1}{8} \tag{15}$$

2.8. Computational methodology

2.8.1. Density functional theory (DFT)

The aim of computational chemistry is finding a solution to the Schrödinger equation (Eq. 16)[31].

$$i\hbar\frac{d}{dt}\Psi = \hat{H}\Psi \tag{16}$$

$$\hat{H} = \hat{T} + \hat{V} \tag{17}$$

In this equation, $\hat{H}$ is the Hamiltonian operator that describes the total energy (described in Eq.17, with $\hat{T}$ and $\hat{V}$ the kinetic and potential energy operators, respectively) and Ψ the wavefunction of the considered system.

If the Hamiltonian is not explicitly time-depending, Eq. 16 can be simplified into Eq. 18, which is an eigenvalue equation (time-independent Schrödinger equation)[32].

$$\hat{H}\psi = \epsilon\psi \tag{18}$$

This approximation only considers stationary waves that correspond to stationary states with an invariant probability amplitude. Here, ψ is the wave function (eigenstate) of the system and ϵ the ground-state energy. In addition, the Hamiltonian operator can be treated as two separated factors, i.e. nuclear and electronic motions. Quantum effects were considered only in the letter case, while the former can be treated classically. This leads to a factorization of $\hat{H}$, called the Born-Oppenheimer approximation (Eq. 19)[33].

$$\hat{H}(\vec{r};\vec{R}) = \hat{T}_e + \hat{V}_{ee} + \hat{V}_{eN} \tag{19}$$

Where $\hat{T}_e$ is the electronic kinetic energy operator, $\hat{V}_{ee}$ is the electron-electron potential energy operator and $\hat{V}_{eN}$ the electron-nuclei potential energy. In this approximation, the Hamiltonian depends explicitly on electron coordinates $\vec{r}$ and parametrically from nuclear coordinates $\vec{R}$. Due to this, each value of $\vec{R}$ brings to its set of eigenstates with its energy.

However, the electron-electron potential energy operator shows no analytical solution, and for this reason, the aim of modern computational techniques is finding solutions that approximate the exact wavefunction, describing the system. In fact, it can be demonstrated by the variation theorem that the energy of a system described employing an approximate wavefunction is an upper-bound of the unknowable exact one[32].

2.8.1.1. DFT and Hohenberg-Kohn functional

Density functional theory is based on two different mathematical theorems defined by Kohn and Hohenberg[34]. They state that the energy of the ground state from Schrödinger equation can be described as a unique functional of its electron density (ρ_0). The electron density function (ρ) is described by only three spatial variables (x, y, z), while the wavefunction depends on 4N variables (three spatial and one spin coordinates). Moreover, using an arbitrary electron density ($\tilde{\rho}$), variation theorem can be employed obtaining a relation similar to the wavefunction one: $E[\tilde{\rho}] \geq E[\rho_0]$. Indeed, the energy functional can be expressed in terms of the ground state electron density according to Eq. 20.

$$E[\rho_0] = T[\rho_0] + V_{ee}[\rho_0] + V_{eN}[\rho_0] \tag{20}$$

The combination of the kinetic energy and the electron-electron potential energy is known as the Hohenberg-Kohn functional (Eq. 21), where it is possible to obtain an analytical solution only for ideal homogeneous electron gas.

$$F_{HK}[\rho_0] = T[\rho_0] + V_{ee}[\rho_0] \tag{21}$$

2.8.1.2. Kohn Sham (KS) solution with one-electron approximation

In DFT, Kohn Sham (KS) approach is employed in order to obtain the electron density function solving a set of mono-electronic equations (Eq. 22) for a set of virtual orbitals called Kohn Sham orbitals (φ_i).

$$h_i^{KS}\varphi_i(\boldsymbol{r}) = \epsilon_i\varphi_i(\boldsymbol{r}) \tag{22}$$

In the described set of equations, the operators do not act on the wavefunction φ_i, but on its amplitude probability (Eq. 23). Then, the real system electron density can be optimized by comparing it with one obtained from the ideal homogeneous electron gas under the same potential (Eq. 24).

$$\rho[\boldsymbol{r}] = |\varphi|^2 \tag{23}$$

$$\Psi^{Exact} = \left|\varphi_1^{KS}\varphi_2^{KS} \dots \varphi_N^{KS}\right\rangle \tag{24}$$

Therefore, the set of KS equations (Eq. 22) is processed using self-consistent field (SCF) cycles. Here, the relations between energy eigenvalues and electron density are solved iteratively by employing the variational principle described above by the second Hohenberg

Kohn theorem. Indeed, it is possible to express the energy functional in Eq. 20 as a difference with the ideal system, according to Eq. 25[35].

$$E[\rho_0] = T[\rho_0] + V_{eN}[\rho_0] + J[\rho_0] + E_{XC}[\rho_0] \tag{25}$$

Where $T[\rho_0]$ and $V_{eN}[\rho_0]$ retained their physical meaning from Eq. 20, while $J[\rho_0]$ is the classical term of $V_{eN}[\rho_0]$ and $E_{XC}[\rho_0]$ (exchange correlation functional) encloses all the deviation from the ideal system. Theoretically, DFT can lead to an exact solution to Schrödinger equation only if the correct exchange correlation functional is known. Considering the computational cost, even though it is not possible to exactly know E_{XC}, DFT achieves the best accuracy among most of the modern computational methodology[36]. Indeed, DFT theories are based on finding improved expressions of $E_{XC}[\rho_0]$ to emulate $F_{HK}[\rho_0]$. As a consequence, the functional need to be selected in respect to the particular studied system[37].

2.8.1.3. Plane Wave DFT and Bloch's theorems

Bulk solids and surfaces are characterized by their intrinsic periodicity, which strongly affects electronic delocalization and the periodic ionic potential applied on each electron by nuclear lattice. In order to accurately describe these materials, periodicity effect need to be considered. In this case, Bravais lattices can be employed to describe in a simple way periodic structure. Here, solids are thought to be a set of points in the space having well defined symmetric properties. They are then described by a set of linearly independent vectors (basis vectors) across the space. Basis vectors identify the smallest portion of the crystal structure (base) that can be repeated in space. Due to this approach, a crystal structure can be expressed as the convolution result of the Bravais lattice (net) and the base[38]. Because the arrangement and interaction of atoms is periodic, the Schrödinger equation retains this feature, obtaining Eq. 26 that describes the potential $U(\boldsymbol{r})$ applied to each electron at each point.

$$U(\boldsymbol{r} + \boldsymbol{R}) = U(\boldsymbol{r}) \tag{26}$$

Where $\boldsymbol{R}$ is the translation of the lattice vector module describing the symmetry of the material. Because the potential applied to an electron is periodic, the wavefunction will also be. Indeed, Born von Karman periodic boundary conditions (BvK PBC) are used to assess the periodicity of ψ in a cubic Bravais lattice, obtaining Eq. 27[39].

$$\psi(\boldsymbol{r} + \boldsymbol{R}) = \psi(\boldsymbol{r}) \tag{27}$$

It is possible to demonstrate that only functional form that respect the periodic potential constrains is a complex exponential function. Thus, to describe electron behaviour the basis set employed can be selected as a plane wave. This function has the property to satisfy this requirement only if its periodicity meets the one of Bravais lattice.

Two equations constitute the Bloch theorem, which generalises BvK PBC to any Bravais lattice, relaxing the constrains to cubic meshes. The first one (Eq. 28), describe the wavefunction of electrons in a periodic potential and its periodicity in $\boldsymbol{R}$ translations considering the wave vector index (k). In the other equation (Eq. 29), the electron wavefunction is defined as a product between a plane wave (e^{ikr}) and a function having the periodicity of Bravais lattice ($u_{nk}(\mathbf{r})$).

$$\psi(\boldsymbol{r}+\boldsymbol{R}) = e^{ikr}\psi(\boldsymbol{r}) \tag{28}$$

$$\psi_{nk}(\boldsymbol{r}) = e^{ikr}u_{nk}(\boldsymbol{r}) \tag{29}$$

Because of Bloch theorem, a new eigenvalue equation can be solved in terms of periodic functions, according to Eq. 30.

$$h_k\, u_{nk}(\boldsymbol{r}) = \epsilon_n(k)\, u_{nk}(\boldsymbol{r}) \tag{30}$$

For a generic point of the reciprocal space (k), a discrete set of eigenvalues exists. Thus, the additional index n is needed to univocally identify the energy of the nth electron at the k point. If the mesh selected is sufficiently dense it is possible to obtain continuous ϵ_n(k) functions, called electronic bands. k parameter varies continuously within the reciprocal unit cell, called Brillouin zone, and at each instant it describes a set of n-functions values, leading to the traditional picture of the band structure in continuous materials[32,40]. Employing this procedure is formally equivalent to solve the time independent Schrödinger equation. Nevertheless, using periodic functions enable to limit the calculation to an elementary cell selected.

2.8.1.4. Pseudopotentials

The Bloch theorem implies that each couple of n and k values describe a single plane wave, which value varies on the whole unit cell. However, the variation of the atomic potential is not homogeneous. Indeed, considering variation within the atomic sphere region is generally more complex than regions outside the nucleus and accounts for a significant portion of the overall energy. When pure plane wave basis is employed, solutions for Kohn-Sham equations for core electrons lead to slow convergence and high computational cost. To solve this problem, pseudopotential approach can be used separating valence and core electrons[41]. The potential derived from the core electrons is substituted with a suitable pseudopotential that leads to the same solution of the Schrödinger equation. This method only explicitly considers valence electrons, limiting the accuracy of the calculation. Additional optimization of pure pseudopotentials involves the use of norm-conserving pseudopotentials, Ultra Soft Pseudo Potentials (USPP) and Projected Augmented-Wave (PAW) method[42–44].

2.8.1.5. Charge density

In order to explore the charge density ρ(**r**), integrations of valence electrons pseudo-wavefunctions over all possible wave vectors are required. The optimized process implied the use of a grid-based approach and a discrete set of *k* points, obtaining Eq. 31.

$$\rho(\boldsymbol{r}) = \int |\psi_k(\boldsymbol{r})|^2 d^3k \approx \sum_k |\psi_k(\boldsymbol{r})|^2 \qquad (31)$$

In this equation, theoretically an infinite number of wave vectors can be employed to define the pseudo-wavefunctions. In order to have an efficient calculation, the maximum value is set to $|k|^2$, generally referred to a corresponding cut-off energy $E_{cut} = \frac{\hbar^2}{2m}|k|^2$ [35].

2.8.2. Potential energy surfaces (PES)

The Born-Oppenheimer approximation (Eq. 19) allows to solve easily the Schrödinger equation due to the decoupling of electronic and nuclear motion. Therefore, the forces acting on the ionic framework can be calculated by classical electrostatic. Indeed, the Hamiltonian operator ($\hat{H}$) depends parametrically on nuclear forces. As a result, the derivative of the total energy (E) to a parameter (λ) relates with the expectation value of the derivative of $\hat{H}$ to λ, according to the Hellmann-Feynman theorem (Eq. 32)[45,46].

$$\frac{dE_\lambda}{d\lambda} = \langle \psi_\lambda \left| \frac{d\hat{H}_\lambda}{d\lambda} \right| \psi_\lambda \rangle \qquad (32)$$

In the case of ionic movement on potential energy surfaces (PES) obtained from the electronic Schrödinger equation, the parameter λ can be replaced with the nuclear coordinates ($\boldsymbol{R}$). This leads to the calculation of equilibrium geometries where all the Feynman forces acting upon the nuclei (due to other nuclei or electrons) are not included. In order to obtain accurate structures, PES must be efficiently explored and optimized[47].

2.8.2.1. Dispersion interactions

When the electronic energy of a specific ionic configuration is obtained from the ab initio DFT cycle, the PES analysis can be further improved to obtain a more accurate description of the system. In particular, dispersion interaction has been demonstrated to be relevant in surface science, especially studying surface reactivity[48,49]. Multipolar expansion of the interaction potential with multipole-induced long-range correlative interactions approach considers these effects, which cannot be easily introduced in DFT because of its intrinsic locality. Among the numerous solutions proposed, the most promising one is the DFT-D3 method optimized by Grimme and co-workers[50,51]. This method consists of a correction applied to the energies obtained from the SCF cycle of the Kohn-Sham equations ($E_{KS\text{-}DFT}$), knowing the energy eigenvalues. This procedure affects only PES results, not influencing the electron density obtained. Indeed, the energy of each point on the potential energy surface is obtained according to Eq. 33.

$$E_{DFT-D} = E_{KS-DFT} - E_D \qquad (33)$$

In this equation, E_D is the dispersion interaction contribution to the total energy. This correction is calculated employing a correlation that involves geometry-dependent dispersion coefficients, that can be considered as a sum of all atom pairs and triples in the system. To maintain the evaluation local, calculations are limited using a cut-off Van der Waals radius[51]. The considered approach allows a consistent description of dispersion interactions limiting the computation effort.

2.8.2.2. Geometry optimization

PES can be employed in order to find the most important configurations, i.e. global and local minima (most and relative stable configurations, respectively) and saddle points (transition states between stable configurations). Modern computational chemistry packages possess different optimization algorithms to locate minima adjacent the input geometry. The minima search is processed iteratively, bringing the system closer to the minimum. One of the most employed algorithms is the Generalized Newton-Raphson (GNR) where, for a general function $f(x)$, $\nabla f(x)$ and $\nabla^2 f(x)$ are considered. The minimum is identified through a convergence analysis of the first derivative and of the sign of the second derivative of the energy to the atom position. (Eq. 34)[52].

$$\frac{\partial E}{\partial x_i} = 0\,;\, \frac{\partial^2 E}{\partial x_i^2} > 0 \tag{34}$$

GNR approach requires the calculation of the Hessian matrix of the system, which lead to a more accurate calculation while increasing the computational cost. Due to the numerical and iterative nature of computational calculations, the convergences are considered verified selecting an arbitrary threshold value.

2.8.3. Bader quantum theory of atoms in molecules (QTAIM)

From the quantum physics, the linear combination of the atomic contributions leads to a molecular wavefunction that describes the considered system. The development of molecular orbitals delocalized throughout the molecule drives to the apparent loss of individual atomic properties (atomic charges). The aim of QTAIM is to divide the molecular space into interacting sub-systems, ensuring consistency with charge density properties $\rho(r)$ and the quantum wavefunction. The main problem that need to be overcome employing this method arises from the arbitrary partition of molecular charge in real space. In particular, it is possible to demonstrate that the Hamiltonian operator can lose one of its fundamental properties, the hermicity (Eq. 35)[53].

$$\langle\psi\middle|\hat{H}\psi\rangle = \langle\psi\hat{H}\middle|\psi\rangle \tag{35}$$

It can be verified that this property of the Hamiltonian operator is equivalent to the quantum density current vector flux $\vec{J}$, vanishing along the surface that delimits the system *S*, according to Eq. 36.

$$\oint \vec{J}\hat{n}\, dS = 0 \tag{36}$$

With $\hat{n}$ the normal vector to *S*. The Schrodinger time-dependent equation give the possibility to physically interpret a non-zero flux along the delimiting surface as a net variation in time of the charge density, $\rho(r)$, (Eq. 37)[54].

$$\oint \vec{J}\hat{n}\, dS = \int \frac{\partial \rho(r)}{\partial t} d\vec{r} \tag{37}$$

Similar to the Hellmann-Feynman theorem for nuclei, the forces acting on electrons can be obtained by the Ehrenfest first and second equations (Eq. 38 and 39, respectively).

$$\langle \hat{p} \rangle = \mathrm{m}\frac{\partial \langle \hat{r} \rangle}{\partial \mathrm{t}} \tag{38}$$

$$\langle \hat{F} \rangle = \mathrm{m}\frac{\partial^2 \langle \hat{r} \rangle}{\partial \mathrm{t}^2} \tag{39}$$

These equations are equivalent of classical equations of linear momentum and force but purely expressed in terms of quantum expectation values. It is known that a quantum system can be consider at equilibrium state when both Feynman and Ehrenfest forces are zero. Using the quantum virial theorem, it can be demonstrated that an arbitrary partition of $\rho(r)$ can bring non-zero forces, leading to incoherencies in energy definition and a non-zero $\vec{J}$ flux. As a consequence, this situation brings to non-equilibrium configurations[55]. Bader verified that non-arbitrary surfaces that are consistent with both isolated atoms and bound system corresponds to the zero-flux condition, described in Eq. 40.

$$\oint \nabla \rho(\vec{r})\hat{n}\, dS = 0 \tag{40}$$

These zero-flux surfaces (ZFS) lead to topological atoms and atomic basins delimited by the corresponding ZFSs. This method results in defining the total energy (E_{TOT}) of the system as the sum of the topological atom energies (E_i), retaining the individual atomic features (atomic charges), according to Eq. 41[56].

$$E_{TOT} = \textstyle\sum_N E_i \tag{41}$$

2.8.3.1. Bader QTAIM and Laplacian's topology

Charge density scalar field can be obtained by a topological analysis of critical points. To unveil this information, the Hessian matrix *H* of the system needs to be calculated (Eq. 42).

$$H=\begin{bmatrix}\frac{\partial^2\rho(r)}{\partial x^2} & \frac{\partial^2\rho(r)}{\partial x\partial y} & \frac{\partial^2\rho(r)}{\partial x\partial z}\\ \frac{\partial^2\rho(r)}{\partial y\partial x} & \frac{\partial^2\rho(r)}{\partial y^2} & \frac{\partial^2\rho(r)}{\partial y\partial z}\\ \frac{\partial^2\rho(r)}{\partial z\partial x} & \frac{\partial^2\rho(r)}{\partial z\partial y} & \frac{\partial^2\rho(r)}{\partial z^2}\end{bmatrix}\rightarrow H'=\begin{bmatrix}\frac{\partial^2\rho(r)}{\partial x^2} & 0 & 0\\ 0 & \frac{\partial^2\rho(r)}{\partial y^2} & 0\\ 0 & 0 & \frac{\partial^2\rho(r)}{\partial z^2}\end{bmatrix} \tag{42}$$

Where the derivatives matrix *H* can be diagonalized to *H'*. This structure emphasises the curvatures of the function along the three main directions. Indeed, as a consequence of the diagonalization, the three remaining values correspond to the *H* eigenvalues (λ_i), making possible to characterize the critical points of *ρ(r)*. Moreover, the trace of *H'* corresponds to the Laplacian operator applied on charge density $\nabla^2\rho(r)$, according to Eq. 43.

$$Tr(H')=\lambda_1+\lambda_2+\lambda_3=\frac{\partial^2\rho(r)}{\partial x^2}+\frac{\partial^2\rho(r)}{\partial y^2}+\frac{\partial^2\rho(r)}{\partial z^2} \tag{43}$$

This equation enables to perform the topological study of charge density scalar field by mapping $\nabla^2\rho(r)$ and to locate charge density curvatures in the space, i.e. accumulation and depletion (Eq. 44)[57].

$$\int \nabla^2\rho\, dV=\int \nabla\cdot(\nabla\rho)\, dV=\oint \nabla\rho\hat{n}\, dS \tag{44}$$

Herein, the total flux in a volume can be evaluated for a limit case of a point of coordinates $(x,y,z)=\vec{r}$. Usually, a function $L(\rho)=-\nabla^2\rho$ is employed. As a consequence, $L(\rho)>0$ $(\nabla^2\rho(r)<0)$ and $L(\rho)<0$ $(\nabla^2\rho(r)>0)$ stand for accumulation and depletion of charge, respectively. Due to this procedure, Bader discovered four different categories of critical points in charge density function, i.e. nuclear positions, bond critical points (BCP), ring critical points (RCP) and cage critical points (CCP). This method is widely employed because of its advantages, such as its coherence with isolated atoms and quantum interacting systems and the possibility of partition without introducing arbitrary terms. In addition, it possesses the possibility to have quantitative descriptors of chemical interaction, e.g. the Laplacian operator applied on charge density. On the other hand, Bader QTAIM is typically applied in the case of weak interaction[58].

2.8.4. Computational methods employed in this thesis

2.8.4.1. Chapter 3 – Enhancing activity, selectivity and stability of palladium catalysts in formic acid decomposition: Effect of support functionalization

As previously reported by Barlocco et al.[59], in Chapter 3 the Vienna ab-initio simulation package (VASP) was used to perform periodic plane-wave DFT calculations in a graphene supported Pd NP model[60,61]. The exchange-correlation was described by employing spin-polarized revised Perdew-Burke-Ernzerhof (rPBE) method of the generalized gradient approximation (GGA) with a plane-wave kinetic cutoff energy of 450 eV[62]. The projector augmented wave (PAW) represented non-spherical contributions to the core from the valence electrons' gradient corrections[63–65]. Long range interactions were included utilizing the DFT-D3 method of Grimme with the zero damping approach[50]. Furthermore, the solvent effect of water was also calculated by an implicit polarized continuum model (PCM), describing the interaction between a solute and solvent[66,67]. The optimized convergence threshold of electronic relaxation and internal forces were set to 10^{-7} eV and 0.01 eV/Å, respectively. A 0.2 $Å^{-1}$ k-spacing mesh was used to accurately define the Brillouin zone with a smearing broadening of 0.1 eV.

A simplified model of the experimental sample was employed in order to reduce the computational cost. Despite it, the model includes the interface between the carbon substrate and the Pd particle. The optimized lattice parameter of the graphene layer employed as support is 2.469 Å, which agrees with the experimental value (2.46 Å)[68]. All surfaces were represented by a p(8×8) supercell slab model to avoid the interaction between the defects. Layered graphene is an acceptable model for the large diameter and highly graphitized nanofibers used in the experiment. The extensive conformational study of the supported nanoparticle restricted its size to 15 atoms. To establish the most stable initial shape of the Pd_{15} cluster on pristine graphene, in addition to moieties that maximized the exposure of the most stable facets and those based on previous reports, an unbiased genetic algorithm (GA) was employed to explore almost 100 independent structures[69,70]. A 15 Å of vacuum perpendicular to the slab was added to avoid any interaction with periodic images

Clusters adhesion energy (E_{ADH}) was calculated as the difference between the combined system (cluster attached to the surface, E_{C+S}) and the isolated species (clusters, E_C and selected surface, E_S in gas phase with the same geometry as the combined model), as Eq. 45. Hence, E_{ADH} only accounts for the adhesion and not the reconstruction energy.

$$E_{ADH} = E_{C+S} - (E_C + E_S) \tag{45}$$

2.8.4.2. Chapter 5 – Disclosing the role of Gold on Palladium-Gold alloyed supported catalysts in formic acid decomposition

As previously reported by Barlocco et al.[71], in Chapter 5 periodic plane-wave density functional theory (DFT) calculations were performed using the Vienna ab initio simulation package (VASP).[61,72] The exchange-correlation was described by the spin-polarized revised Perdew-Burke-Ernzerhof (rPBE) method of the generalized gradient approximation (GGA) with a plane-wave kinetic cutoff energy of 450 eV.[62] Non-spherical contributions correlated to the gradient of the density are integrated in the projector augmented wave (PAW).[43,63,65] The long-range interaction was characterized by the DFT-D3 method of Grimme with zero-damping.[73] The solvent effect of water was also considered by an implicit polarized continuum model (PCM), which describes the interaction between a solute and solvent into the plane-wave DFT.[67,74] The optimized convergence threshold of internal forces and electronic relaxation was set to 0.01 eV/Å and 10^{-7} eV, respectively. A 0.2 $Å^{-1}$ k-spacing sampled the Brillouin zone with a smearing broadening of 0.1 eV.

The experimental catalysts were modelled by pristine carbon surface decorated with metallic nanoparticles maintaining an equivalent Au:Pd ratio. The optimized lattice parameter of supporting pristine graphene is 2.469 Å, which is in agreement with the benchmark value of 2.46 Å.[75] All surfaces were represented by a p(8×8) supercell slab model to avoid the interaction between the metal clusters. The expensive exploration of the supported nanoparticles' conformational morphology restricted their size to 15 metallic atoms. To determine the most stable initial shapes and the distribution of species within the NPs, we employed an unbiased genetic algorithm (GA) to explored up to 100 independent structures for each Pd, Au and AuPd clusters, besides moieties that maximized the exposure of the most stable facets, i.e., (111) and those based on previous reports.[69] We recognized that not all possible configurations were simulated, nevertheless, we proved during the presented research that these clusters are highly dynamic and their reactivity is not related directly to the rigid morphology of the global energy minima's structure.[70] We added 15 Å of vacuum perpendicular to the carbon slab to avoid any spurious interaction with periodic images. Dipole correction perpendicular to the surface was applied upon deposition of the NPs.

NPs' adhesion energy (E_{ADH}) was calculated according to Eq. 45. The molecular adsorption energy (E_{Ads}), which is equivalent to the desorption energy (E_{Des}) was defined as the difference between the combined system ($E_{Combined}$) and the isolated species, i.e. the desorbed molecular species (E_M) and the cluster (E_{C+S}) in the same geometry as the last combined models, as described in Eq. 46. The final cluster after the desorption step is considered to spontaneously reconstruct to the initial state. The reaction energy (E_R) is defined as the total energy difference between the final (final adsorbate-NP/C, E_F) and the initial states (initial adsorbate-NP/C, E_I), according to Eq. 47.

$$E_{Ads} = E_{Combined} - (E_{C+S} + E_M) \tag{46}$$

$$E_R = E_F - E_I \tag{47}$$

2.8.4.3. Chapter 6 – Role of defects in carbon materials during metal-free formic acid decomposition

As previously reported by Barlocco et al.[76], in Chapter 6 periodic plane-wave density functional theory (DFT) calculations were performed using the Vienna ab-initio simulation package (VASP)[77,78]. We employed generalised gradient approximation by Perdew–Burke–Ernzerhof functional revised for solids[79] and a kinetic energy of 450 eV to expand the planewaves of the Kohn–Sham valence states[80]. All the calculations include the long-range dispersion correction approach by Grimme[51,81], which is an improvement on pure DFT to evaluate molecular interactions[18,82–84]. We included also the implicit solvation model as implemented in VASPsol describing the bulk water effect of electrostatics, cavitation, and dispersion on the FA interaction with the C-materials[67,85]. The optimization thresholds were 10^{-5} eV and 0.01 eV/Å for electronic and ionic forces relaxation, respectively. The Brillouin zone was sampled by Γ-centre k-point mesh generated through a Monkhorst–Pack grid of 5 × 5 × 1 k-points, which ensures no Pulay stress [86]. In order to improve the convergence of the Brillouin-zone integrations, the partial occupancies were determined using the first order Methfessel–Paxton method corrections smearing with a set width for all calculations of 0.1 eV.

Carbon materials were represented by a single layer slab models of a 6 x 6 pristine supercell containing the different defects: single vacancy (SV), double vacancy (DV) and three different Stone Wales defects (SW1, SW2, SW3). The supercell was in a hexagonal lattice with the unit cell vectors a and b in the surface plane and c perpendicular to the graphene plane; a and b were optimized at 14.8199 Å. We added a vacuum width of 15 Å (c), which is large enough to avoid spurious periodic interactions.

In order to compare the formation energy of the defective surfaces with the energy of pristine graphene, I described the difference in energy ΔE as in Eq. 48.

$$\Delta E = E_S - n\,E_c \tag{48}$$

Where E_S is the energy of the considered surface, n the number of carbon atoms in it and E_c is the energy of the single carbon atom in the hexagonal lattices of graphene. The adsorption energy (E_{Ads}) and the reaction energy (E_R) were defined as in Eq. 46 and 47, respectively.

2.8.4.4. Chapter 7 – Hydrazine selective decomposition over metal-free carbonaceous materials

In Chapter 7, periodic plane-wave density functional theory (DFT) calculations were carried out using the Vienna Ab-initio Simulation Package (VASP)[77,78]. The generalized gradient approximation from the revised Perdew-Burke-Ernzerhof approximation (RPBE)[62] has been used to take into account the correlation-exchange electronic contributions, with a kinetic energy cutoff of 500 eV chosen for the expansion of the Kohn–Sham valence states plane-waves[80]. All the calculations includes the long-range dispersion correction approach by Grimme from DFT-D3 methods[87,88], an improvement on pure DFT to evaluate molecular interactions[18,82–84]. We also included the implicit solvation model as implemented in VASPsol[67,85], where solvent is considered as a polarizable continuum dielectric bath. The optimization thresholds for electronic and ionic forces relaxation were respectively 10^{-5} eV and 0.02 eV/Å. For Brillouin zone sampling, a Γ-centred k-point mesh generated through Monkhorst–Pack method of dimensions 5 × 5 × 1 in order to avoid Pulay stress[86]. To improve the convergence of the Brillouin-zone, a first order Methfessel–Paxton method has been used with an energetic width value of 0.2 eV.

All carbon-based materials were modeled starting from a single layer slab of a 6 x 6 pristine graphene supercell and introduced different defects: single vacancy (SV), double vacancy (DV) and three different Stone Wales defects (SW1, SW2, SW3)[76]. The supercell is in a hexagonal crystalline system with unit cell vectors *a* and *b* lying in surface plane and perpendicular to *c* axis. Both, *a* and *b*, were optimized at 14.8 Å, in well agreement with experimental values obtained by Transmission Electron Aberration-corrected Microscope (TEAM)[89]. We introduced a polarizable continuum dielectric bath of ~16 Å perpendicular to the C-surface in order to avoid spurious periodic interactions.

Computational characterization of the surfaces was performed using the Bader analysis as implemented by Henkelmann et al.[90]. A fast convergence of charges with respect to the Fast Fourier Transform grid was obtained employing the Grid Method by Yu[91], which quadratically converges charge values with respect to mesh size. A grid of 370 x 370 x 390 points was applied in order to optimize memory usage and precision of the calculations. These values were obtained converging two equivalent carbon charges in pristine graphene. Charge density local curvatures, local accumulations and depletions were evaluated to disclose the ability of every inequivalent surface site to adsorb and decompose hydrazine. The optimized parameters obtained from the Grid method were employed in a Laplacian topological analysis[57]. The AIM-UC Bader Analysis Toolkit implemented by David Vega et al.[92] was applied on a total electron density obtained combining the valence charge data and the core charges, resulting in Laplacian of charge density map, which allowed to analyze Bond Critical Points (BCP). Before adsorbing the hydrazine molecule, a systematic study on all possible active sites was performed using NH_3 as a probe molecule and considering both dissociative and non-dissociative adsorption modes. The molecular adsorption energy (E_{Ads}) was defined as the difference between the combined system and the isolated species, according to Eq. 46. The reaction energy (E_R) of each N_2H_4 dissociation elementary step was described in Eq. 47.

Hydrogen diffusion calculations were performed on the single vacancy (SV) system, which proved to be the most active defect in this study. A hydrogen atom was placed in the desired position where only its *z* coordinate could relax during the optimization calculation. All carbon atoms were allowed to relax except two of them sufficiently far from the active site to avoid rotations or translations of the considered surface as a whole [92]. The hydrogen diffusion energy (E_D) was calculated as the energy difference between atomic hydrogen within the vacancy, in the most stable configuration, and diffused atomic hydrogen structures.

2.9. References

[1]Applied Sciences, “Pyrograf Products,” can be found under https://apsci.com/pyrograf-products/, **n.d.**

[2]S. Campisi, D. Ferri, A. Villa, W. Wang, D. Wang, O. Kröcher, L. Prati, *J. Phys. Chem. C* **2016**, *120*, 14027–14033.

[3]A. Villa, D. Wang, N. Dimitratos, D. Su, V. Trevisan, L. Prati, *Catal. Today* **2010**, *150*, 8–15.

[4] A. Villa, N. Dimitratos, *Metal-Free Functionalized Carbons in Catalysis*, The Royal Society Of Chemistry, **2018**.

[5] J. F. Watts, J. Wolstenholme, *An Introduction to Surface Analysis by XPS and AES*, John Wiley & Sons, **2019**.

[6]C. B. Carter, D. B. Williams, Transmission Electron Microscopy: Diffraction, Imaging, and Spectrometry, Springer, **2016**.

[7] L. De Broglie, **1924**.

[8] J. I. Goldstein, D. E. Newbury, J. R. Michael, N. W. M. Ritchie, J. H. J. Scott, D. C. Joy, *Scanning Electron Microscopy and X-Ray Microanalysis*, Springer, **2017**.

[9] S. J. Pennycook, P. D. Nellist, *Scanning Transmission Electron Microscopy: Imaging and Analysis*, Springer Science & Business Media, **2011**.

[10]D. A. Skoog, F. J. Holler, S. R. Crouch, *Principles of Instrumental Analysis*, Cengage Learning, **2017**.

[11] K. Maaz, *Raman Spectroscopy and Applications*, BoD–Books On Demand, **2017**.

[12] R. J. Nemanich, S. A. Solin, *Phys. Rev. B* **1979**, *20*, 392–401.

[13] S. Brunauer, P. H. Emmett, E. Teller, *J. Am. Chem. Soc.* **1938**, *60*, 309–319.

[14] K. S. W. Sing, *Adv. Colloid Interface Sci.* **1998**, *76–77*, 3–11.

[15]M. Jaroniec, M. Kruk, A. Sayari, in *Mesoporous Mol. Sieves 1998* (Eds.: L. Bonneviot, F. Béland, C. Danumah, S. Giasson, S.B.T.-S. in S.S. and C. Kaliaguine), Elsevier, **1998**, pp. 325–332.

[16] M. Thompson, *Handbook of Inductively Coupled Plasma Spectrometry*, Springer Science & Business Media, **2012**.

[17]F. Sanchez, D. Motta, A. Roldan, C. Hammond, A. Villa, N. Dimitratos, *Top. Catal.* **2018**, *61*, 254–266.

[18]X. Lu, S. Francis, D. Motta, N. Dimitratos, A. Roldan, *Phys. Chem. Chem. Phys.* **2020**, *22*, 3883–3896.

[19] D. Motta, I. Barlocco, S. Bellomi, A. Villa, N. Dimitratos, *Nanomaterials* **2021**, *11*, 1340.

[20] M. Swartz, J. Liq. Chromatogr. Relat. Technol. **2010**, 33, 1130–1150.

[21] R. L. Grob, E. F. Barry, *Modern Practice of Gas Chromatography*, John Wiley & Sons, **2004**.

[22]H. M. McNair, J. M. Miller, N. H. Snow, *Basic Gas Chromatography*, John Wiley & Sons, **2019**.

[23] J. G. K. Sevcik, *Detectors in Gas Chromatography*, Elsevier, **2011**.

[24] R. P. W. Scott, Libr. Sci. LLC available online http//www. Chromatogr. org/2/contents. html **2003**.

[25] Beer, *Ann. Phys.* **1852**, *162*, 78–88.

[26] J.-H. Lambert, JH Lambert,... Photometria, Sive de Mensura et Gradibus Luminis, Colorum et Umbrae, Sumptibus Viduae E. Klett, **1760**.

[27] W. Mäntele, E. Deniz, **2017**.

[28] G. Zaccanti, P. Bruscaglioni, *J. Mod. Opt.* **1988**, *35*, 229–242.

[29] C. Gojon, B. Dureault, *J. Nucl. Sci. Technol.* **1996**, *33*, 731–735.

[30] W. D. Basson, J. F. Van Staden, *Analyst* **1978**, *103*, 998–1001.

[31] E. Schrödinger, *Phys. Rev.* **1926**, *28*, 1049.

[32] D. J. Griffiths, Introduzione Alla Meccanica Quantistica, CEA, **2005**.

[33] M. Born, R. Oppenheimer, *Ann. Phys.* **1927**, *389*, 457–484.

[34] W. K. P.Hohenberg, *Phys. Rev. B* **1964**, DOI 10.1007/BF01198136.

[35] E. Engel, R. M. Dreizler, *Density Functional Theory*, Springer, **2013**.

[36] G. E. Tao, J., Perdew, J. P., Staroverov, V. N. & Scuseria, **2003**, 91, 3–6.

[37]G. I. Csonka, J. P. Perdew, A. Ruzsinszky, P. H. T. Philipsen, S. Lebègue, J. Paier, O. A. Vydrov, J. G. Ángyán, *Phys. Rev. B - Condens. Matter Mater. Phys.* **2009**, *79*, 1–14.

[38]L. D. LANDAU, A. I. AKHIEZER, E. M. LIFSHITZ, in (Eds.: L.D. LANDAU, A.I. AKHIEZER, E.M.B.T.-G.P. LIFSHITZ), Pergamon, Oxford, **1967**, pp. 115–143.

[39] N. W. Ashcroft, N. D. Mermin, **1976**.

[40] C. Kittel, P. McEuen, P. McEuen, *Introduction to Solid State Physics*, Wiley New York, **1996**.

[41] W. E. Pickett, *Comput. Phys. Reports* **1989**, *9*, 115–197.

[42] P. E. Blöchl, *Phys. Rev. B* **1994**, *50*, 17953.

[43] G. Kresse, D. Joubert, *Phys. Rev. B* **1999**, *59*, 1758–1775.

[44] D. Vanderbilt, *Phys. Rev. B* **1990**, *41*, 7892.

[45] P. Politzer, J. S. Murray, *J. Mol. Model.* **2018**, *24*, 266.

[46] R. P. Feynman, *Phys. Rev.* **1939**, *56*, 340–343.

[47] D. Sholl, J. A. Steckel, *Density Functional Theory: A Practical Introduction*, John Wiley & Sons, **2011**.

[48]N. Marom, A. Tkatchenko, M. Rossi, V. V Gobre, O. Hod, M. Scheffler, L. Kronik, *J. Chem. Theory Comput.* **2011**, *7*, 3944–3951.

[49] R. H. Bradley, R. Daley, F. Le Goff, *Carbon N. Y.* **2002**, *40*, 1173–1179.

[50] S. Grimme, S. Ehrlich, L. Goerigk, *J. Comput. Chem.* **2011**, *32*, 1456–1465.

[51] S. Grimme, J. Antony, S. Ehrlich, H. Krieg, *J. Chem. Phys.* **2010**, *132*, DOI 10.1063/1.3382344.

[52] R. McGill, P. Kenneth, *Aiaa J.* **1964**, *2*, 1761–1766.

[53]E. Sanville, S. D. Kenny, R. Smith, G. Henkelman, *J. Comput. Chem.* **2007**, *28*, 899–908.

[54] W. Tang, E. Sanville, G. Henkelman, *J. Phys. Condens. Matter* **2009**, *21*, 84204.

[55] B. C. Hall, *Quantum Theory for Mathematicians*, Springer, **2013**.

[56]R. Bader, J. Findlay, T. M. Knowlton, in *Circ. Fluid. Bed Technol.*, Elsevier, **1988**, pp. 123–137.

[57] P. L. A. Popelier, *Coord. Chem. Rev.* **2000**, *197*, 169–189.

[58] C. R. Wick, T. Clark, *J. Mol. Model.* **2018**, *24*, 1–9.

[59]I. Barlocco, S. Bellomi, J. J. Delgado, X. Chen, L. Prati, N. Dimitratos, A. Roldan, A. Villa, *Catal. Today* **2021**, DOI 10.1016/j.cattod.2021.07.005.

[60] G. Kresse, J. Furthmüller, *Comput. Mater. Sci.* **1996**, *6*, 15–50.

[61] T. Bučko, J. Hafner, S. Lebègue, J. G. Ángyán, *J. Phys. Chem. A* **2010**, *114*, 11814–11824.

[62] B. Hammer, L. B. Hansen, J. K. Nørskov, *Phys. Rev. B* **1999**, *59*, 7413–7421.

[63] J. P. Perdew, K. Burke, M. Ernzerhof, *Phys. Rev. Lett.* **1996**, *77*, 3865–3868.

[64] G. Kresse, D. Joubert, *Phys. Rev. B* **1999**, *59*, 1758–1775.

[65] P. E. Blöchl, O. Jepsen, O. K. Andersen, *Phys. Rev. B* **1994**, *49*, 16223–16233.

[66]K. Mathew, V. S. C. Kolluru, S. Mula, S. N. Steinmann, R. G. Hennig, *J. Chem. Phys.* **2019**, *151*, 234101.

[67] K. Mathew, R. Sundararaman, K. Letchworth-Weaver, T. A. Arias, R. G. Hennig, *J. Chem. Phys.* **2014**, *140*, DOI 10.1063/1.4865107.

[68] A. K. Geim, *Science (80-.).* **2009**, *324*, 1530 LP – 1534.

[69] R. L. Johnston, *Dalt. Trans.* **2003**, 4193–4207.

[70]G. Sun, J. T. Fuller, A. N. Alexandrova, P. Sautet, *ACS Catal.* **2021**, *11*, 1877–1885.

[71]I. Barlocco, S. Capelli, X. Lu, S. Bellomi, X. Huang, D. Wang, L. Prati, N. Dimitratos, A. Roldan, A. Villa, *ChemCatChem* **2021**, *n/a*, DOI https://doi.org/10.1002/cctc.202100886.

[72] G. Kresse, J. Furthmüller, *Comput. Mater. Sci.* **1996**, *6*, 15–50.

[73] S. Grimme, S. Ehrlich, L. Goerigk, *J. Comput. Chem.* **2011**, *32*, 1456–1465.

[74]K. Mathew, V. S. C. Kolluru, S. Mula, S. N. Steinmann, R. G. Hennig, *J. Chem. Phys.* **2019**, *151*, 234101.

[75] A. K. Geim, *Science (80-.).* **2009**, *324*, 1530 LP – 1534.

[76] I. Barlocco, S. Capelli, X. Lu, S. Tumiati, N. Dimitratos, A. Roldan, A. Villa, *Nanoscale* **2020**, 22768–22777.

[77] G. Kresse, J. Furthmüller, *Phys. Rev. B - Condens. Matter Mater. Phys.* **1996**, *54*, 11169–11186.

[78] G. Kresse, *J. Non. Cryst. Solids* **1995**, *192–193*, 222–229.

[79] J. P. Perdew, A. Ruzsinszky, G. I. Csonka, O. A. Vydrov, G. E. Scuseria, L. A. Constantin, X. Zhou, K. Burke, **2007**, *136406*, 1–4.

[80] N. D. Mermin, *Phys. Rev.* **1965**, *137*, 1–3.

[81] S. Fias, S. Van Damme, P. Bultinck, ... *Comput. Chem.* **2008**, *29*, 358–366.

[82]H. Fang, A. Roldan, C. Tian, Y. Zheng, X. Duan, K. Chen, L. Ye, S. Leoni, Y. Yuan, *J. Catal.* **2019**, *369*, 283–295.

[83]E. Nowicka, S. Althahban, T. D. Leah, G. Shaw, D. Morgan, C. J. Kiely, A. Roldan, G. J. Hutchings, *Sci. Technol. Adv. Mater.* **2019**, *20*, 367–378.

[84] M. G. Quesne, A. Roldan, N. H. De Leeuw, C. R. A. Catlow, *Phys. Chem. Chem. Phys.* **2019**, *21*, 10750–10760.

[85] R. Sundararaman, K. Schwarz, *J. Chem. Phys.* **2017**, *146*, DOI 10.1063/1.4976971.

[86] J. D. Pack, H. J. Monkhorst, *Phys. Rev. B* **1977**, *16*, 1748–1749.

[87] R. Sure, J. Antony, S. Grimme, *J. Phys. Chem. B* **2014**, *118*, 3431–3440.

[88]S. Ehrlich, J. Moellmann, W. Reckien, T. Bredow, S. Grimme, *ChemPhysChem* **2011**, *12*, 3414–3420.

[89] Y. W. Tan, H. L. Stormer, P. Kim, K. S. Novoselov, M. L. Cohen, S. G. Louie, X. Wang, L. Zhang, S. Lee, H. Dai, Y. Kobayashi, K. Fukui, M. Fujita, G. Dresselhaus, M. S. Dresselhaus, M. A. Pimenta, B. R. A. Neves, A. Jorio, Y. Zhang, M. Mailman, P. M. Ajayan, S. K. Nayak, C. H. Park, Y. W. Son, S. P. Lu, S. Piscanec, A. C. Ferrari, G. Dobrik, P. Lambin, A. Oberlin, T. Solid, K. Suenaga, S. Iijima, P. Hermet, V. Meunier, L. Henrard, D. Gunlycke, C. T. White, S. Chen, B. I. Yakobson, S. Gradecak, *Science (80-.).* **2009**, *323*, 1705–1708.

[90] G. Henkelman, A. Arnaldsson, H. Jónsson, *Comput. Mater. Sci.* **2006**, *36*, 354–360.

[91] M. Yu, D. R. Trinkle, *J. Chem. Phys.* **2011**, *134*, 1–8.

[92] D. Vega, D. Almeida, *J. Comput. Methods Sci. Eng.* **2014**, *14*, 131–136.

3. ENHANCING ACTIVITY, SELECTIVITY AND STABILITY OF PALLADIUM CATALYSTS IN FORMIC ACID DECOMPOSITION: EFFECT OF SUPPORT FUNCTIONALIZATION

The results discussed in this Chapter were previously reported in my work, published on *Catal. Today* **2021**, *382*, 61–70 (https://doi.org/10.1016/j.cattod.2021.07.005)[1].

3.1. Introduction

3.1.1. Palladium NPs interacting with P- and O-based functionalities

The advantages of modifying the support to strongly enhance the catalytic properties of Pd-based catalysts, especially in formic acid decomposition (FAD) reaction were thoroughly reviewed in Sections 1.3.3. and 1.4.1.2. Indeed, a strong metal-support interaction prevents Ostwald ripening, migration and coalescence of the nanoparticles, increasing the stability and durability of the material[2,3]. In addition, selecting carbon as support can enable an exceptionally versatile modification of its structure, changing its electronic and geometric properties by inserting heteroatoms (Section 1.3.)[4–7].

In this study, high heat-treated carbon nanofibers (HHT-CNFs) were selected as support according to the investigation of Sanchez et al.[8]. They demonstrated that HHT-CNFs can efficiently enhanced the activity of Pd catalyst in FAD reaction because of the presence of smaller and homogeneously dispersed Pd nanoparticles, compared with less graphitised CNFs, i.e. CNFs-PS (pyrolytically stripped) and CNFs-LHT (low heat treated). In addition, Campisi end co-workers[9] have reported that HHT-CNFs can be easily functionalised without undergoing morphological modification, comparing to other low-graphitised carbon materials.

In order to more deeply investigate the electronic and structural effects of heteroatoms on Pd supported on CNFs, oxygen and phosphorous groups were introduced. Indeed, it was reported that oxygen as a dopant affects the charge transfer between carbon and metal NPs, enhancing the electron density of the neighbouring carbon atoms and, as a consequence, increasing the back-donation from C to metal atoms[10]. In addition, Zhang and co-workers[11] reported that the lone pair around acidic O functionalities (e.g. carboxylic acids and anhydrides) interacts with 4d and 5s Pd orbitals, strengthening the metal-support interaction and avoiding agglomeration and leaching. Phosphorous was selected due to its low electronegativity and large size. Moreover, Xin et al.[12] have disclosed the effect of P-doping by XPS technique, concluding that it influences the electronic properties of Pd and, in particular, a donation of electrons from Pd to P. This effect indicates a strong interaction between the P-doped support and the Pd active phase. Indeed, Chen et al.[13] have employed a P-doped graphene to support Pd NPs, increasing the fraction of Pd^{2+}compared to bare graphene. This catalyst showed outstanding activity in the formation of 2,5-furandicarboxylic acid from 5-hydroxylmethylfurfural. In addition, Li et al.[14] have deposited Pd NPs on a phosphorous-carbon framework and successfully used the catalyst in the hydrogenation of nitroarene. The increased activity and stability were attributed again to electronic effects and, specifically, to the formation of electron rich Pd-P species, resulting from the electron transfer from C to P atoms. However, the deposition of oxygen and phosphorous functionalities for FAD reaction remains challenging.

3.1.2. Aim and objectives of the Chapter

In this work, palladium NPs were deposited on oxygen and phosphorous functionalised HHT-CNFs. In order to disclose the relation between structure of the material and its catalytic behaviour the catalysts were characterised by transmission electron microscopy (HR-TEM, STEM-HAADF and STEM-EDX) and X-ray photoelectron spectroscopy (XPS). In addition, to in depth investigate the surface-Pd interaction and to reveal the connection between catalytic properties and functionalities, density functional theory (DFT) simulations was carried out studying the interaction between Pd_{15} cluster and different functionalised support surfaces.

3.2. Results

As previously reported by Barlocco et al.[1], two different O and P functionalised high-heat treated carbon nanofibers (HHT-CNFs) were prepared, i.e. O-HHT and P-HHT. The P functionalised non-carbonized catalyst was not prepared as previous studies of our group demonstrated that a heat treatment above 400 °C favours the formation of direct C-P bond instead of the more unstable C-O-P bond[15]. C-O-P bond leads to P-leaching from the carbonaceous surface, hence, decreasing the stability of the catalyst[9]. The support functionalization procedure did not affect the surface area (37 ± 0.9, 36± 1.3 and 36 ± 2.1 $m^2\ g^{-1}$ for HHT-CNFs, O-HHT-CNFs and P-HHT-CNFs, respectively). The prepared HHT-CNTs were used as support for palladium nanoparticles via sol immobilization technique, using PVA as capping agent and $NaBH_4$ as reducing agent.

3.2.1. Catalyst characterisation

3.2.1.1. XPS results

XPS analyses were performed to analyse oxygen and phosphorous functionalities introduced on the CNF surfaces and to determine Pd oxidation state as well as its content at the surface (Figure 1 and Figure 2, Table 1). The oxidative treatment with HNO_3 increased the oxygen content from 0.9% of HHT to 7.77% for O-HHT. After the functionalization with a mixture of H_3PO_4 and HNO_3, 4.83% of O and 1.39% of P where detected on the surface of the carbon material. Pd samples showed that after O and P functionalization Pd exposure increased 1wt%Pd@P-HHT (1.57%)> 1wt%Pd@O-HHT (1.14%)> 1wt%Pd@HHT (0.77%) (Table 1)[16]. It is worth to note that P content on 1wt%Pd@P-HHT (0.56%) decreased compared to P-HHT (1.39%), whereas oxygen content is similar. On the contrary, O content on 1wt%Pd@O-HHT (6.48%) decreased compared to O-HHT (7.77%). As no P and O leaching was found, we can assess that Pd is preferentially deposited on O (for 1%Pd@O-HHT) and P functionalities (1wt%Pd@P-HHT). Table 1 summarizes the chemical species observed on the surface and their concentration. Peak assignments were made according to phosphorylated carbons[17] and to oxidize carbon nanotubes[18]. In the O1s region, three main oxygen groups were identified. BE of 531.2-531.4 eV can be assigned to a carbon-oxygen double bond and to P=O and P-O species, the signal around 533 eV to C-O, C-O-C, P-O-C and the signal at 534 eV can be assigned to carboxylic species.

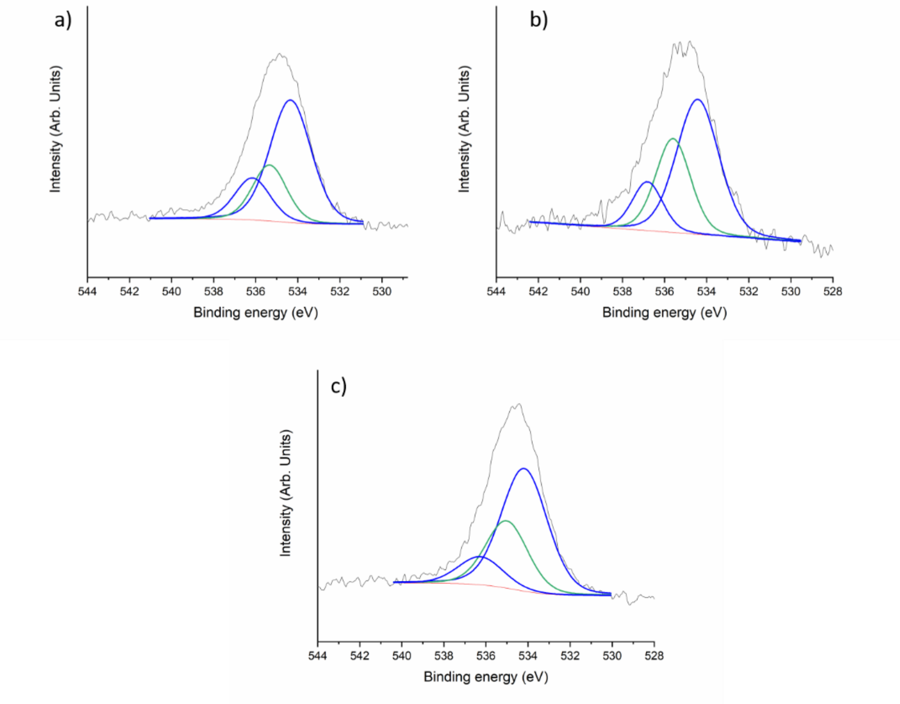

Figure 1: High resolution XPS spectra of O 1s for a) Pd@HHT, b) Pd@O-HHT and c) Pd@P-HHT.

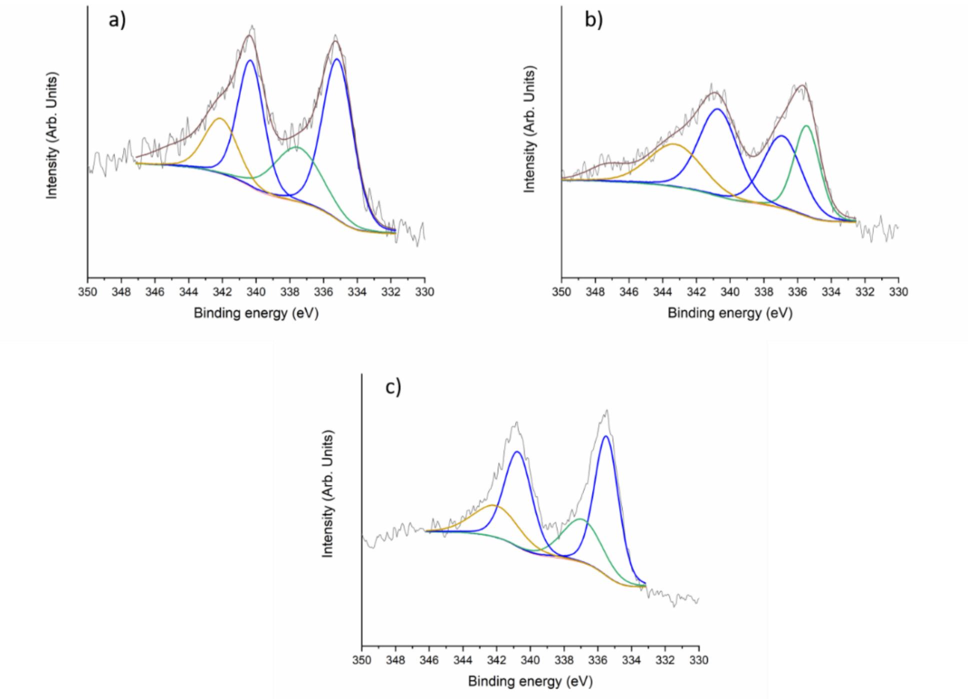

Figure 2: High resolution XPS spectra of Pd 3d for a) Pd@HHT, b) Pd@O-HHT and c) Pd@P-HHT.

Table 1: Results of O, P and Pd high resolution (HR) spectra.

Sample		*O 1s*			*P 1s*	*Pd 3d*		*Atomic ratio (%)*
		C=O, P=O, P-O	C-O, C-O-C, P-O-C	COOH	C-O-PO_3, C-P	Pd^{2+}	Pd^0	C-O-P-Pd
HHT	BE	531.2	533.0	534.1	-	-	-	99.1-0.9-0.0-0.0
	Atom %	*50.4*	*48.4*	*1.2*				
O-HHT	BE	531.3	532.9	533.9	-	-	-	92.2-77.8-0.0-0.0
	Atom %	*54.8*	*35.3*	*8.5*	-	-	-	
P-HHT	BE	531.4	533.0	534.2	134.2	-	-	93.5-4.8-1.4-0.0
	Atom %	*61.3*	*33.2*	*5.5*	*100*			
Pd@HHT	BE	531.3	533.2	534.3	-	336.4	335.0	96.5-2.7-0.0-0.8
	Atom %	*49.8*	*49.2*	*1.0*		*38.5*	*61.5*	
Pd@O-HHT	BE	531.2	533.0	534.2	-	336.8	335.0	92.1-6.5-0.0-1.1
	Atom %	*56.3*	*33.4*	*10.7*	-	*43.5*	*56.5*	
Pd@P-HHT	BE	531.4	532.8	534.4	133.9	336.5	334.8	93.1-4.7-0.6-1.6
	Atom %	*58.5*	*27.0*	*14.5*	*100*	*22.9*	*77.1*	

3.2.1.2.TEM-STEM results

Figure 3 shows representative STEM images of the Pd catalysts in its fresh state, as well as the particle size distribution. We can observe that Pd nanoparticles are, in general, homogenously distributed on the carbon nanotube surface, although some agglomerations are observed. The average particle size decreases from 3 nm to 2.3 nm when the treated supports are used. If we consider the particle size distribution, we can observe that the 1wt%Pd@HHT exhibits a nearly unimodal distribution centred at 3 nm. When palladium is supported on P-HHT and O-HHT supports, the fraction of particles smaller than 2 nm dramatically increase and a bimodal particle size distribution is obtained. These small particles slightly increase the dispersion of the Pd nanoparticles from 36% up to 42%.

On the other hand, the composition of the samples was analysed by acquiring STEM-EDS mappings. Figure 4 includes a statistical relevant mapping obtained for sample 1wt%Pd@P-

HHT. We clearly can observe the presence of P in the carbon nanotube, although the phosphorous content in some areas is below the detection limit. The EDS spectrum of isolated particles A and B in the image, shows the fact that some particles are in intimal contact with P, but not all of them. This can be related with the bimodal particle size distribution observed in these samples.

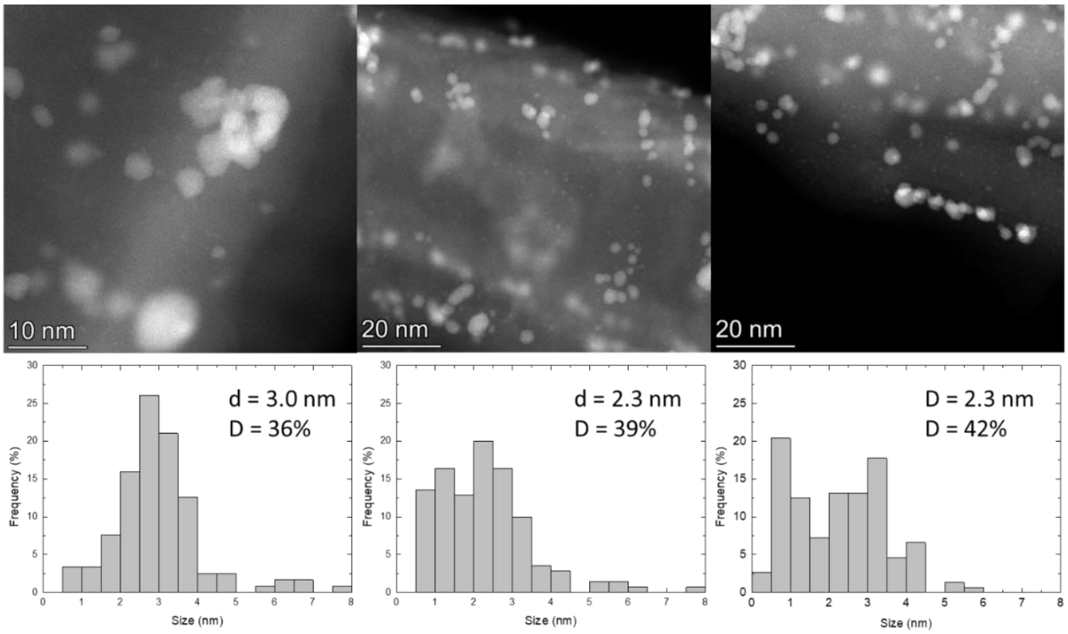

Figure 3: Representative HR-STEM images (top) and particle size distribution (bottom) of 1wt%Pd@HHT (left) 1wt%Pd@O-HHT (middle) and 1wt%Pd@P-HHT (right).

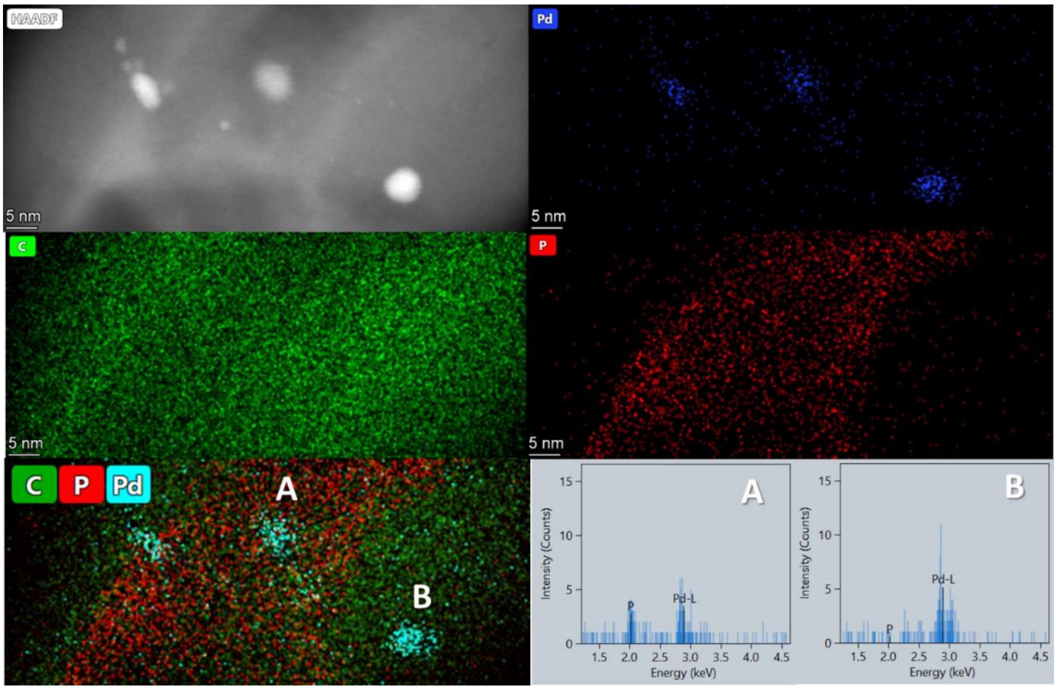

Figure 4: STEM-EDS element mapping analysis of sample 1wt%Pd@P-HHT. EDS spectra of selected nanoparticles are also included.

3.2.2. Catalytic activity

The catalytic performance of Pd NPs deposited on the functionalised supports, i.e. 1wt%Pd@P-HHT and 1wt%Pd@O-HHT, was evaluated in liquid-phase formic acid decomposition and compared with 1wt%Pd@HHT. 1wt%Pd@O-HHT showed an activity superior to 1wt%Pd@HHT, i.e. 1485 h^{-1} and 979 h^{-1}, respectively. On the other hand, 1wt%Pd@P-HHT exhibited a similar activity (899 h^{-1}). These activity's values are comparable with the majority of the catalysts present in literature (Table 2). Kinetic profiles for the three catalysts were examined after 2 h of reaction (Figure 5). A similar reaction profile was obtained for both functionalised catalysts, showing also no signs of deactivation. An exceptionally high conversion (85 and 70 %) for the two functionalised catalysts was achieved. Considering the conversion at 2h of reaction and XPS and TEM analyses results it was possible to correlate the properties of the catalysts with their catalytic behaviour. The higher conversion of 1wt%Pd@P-HHT and 1wt%Pd@O-HHT compared 1wt%Pd-HHT to can be attributed to the smaller Pd particles and the higher particles dispersion observed by HR-TEM in the functionalised materials (from 3.0 nm for the non-functionalised material to 2.3 nm for 1wt%Pd@P-HHT and 1wt%Pd@O-HHT). In addition, XPS showed an increase in Pd exposure for the two functionalised materials (from 0.77% for 1wt%Pd@HHT to 1.57% for 1wt%Pd@P-HHT and 1.14% for 1wt%Pd@O-HHT), which in turn led to an increase in the surface's active sites. The direct participation of the support in the activity of the catalysts can be excluded. The bare supports were tested in FAD reaction at the same reaction condition, but no conversion was observed.

Table 2: Comparison of the activity of different Pd-based catalysts (SF: Sodium formate).

Catalyst	*T (°C)*	*Reagent*	*Initial Activity (h^{-1})*	*Ref.*
Pd@P-HHT	30	Formic acid (0.5 M)	899	This work
Pd@O-HHT	30	Formic acid (0.5 M)	1485	This work
Pd/HHT	30	Formic acid (0.5 M)	979	[19]
Pd-MnO_x/SiO_2-NH_2	20	Formic acid (0.265 M)	140	[20]
Pd/rGO-AP	50	Formic Acid (10 M)	477	[21]
Pd@SBA-15/DTC	25	Formic acid (2.0 M)	1952	[22]
Pd/resin	75	HCOOH/HCOONa = 9/1	820	[23]
Pd-MnO_x/NH_2-KIE-6	25	Formic Acid (0.5 M)	541	[24]
Pd(2wt%)-MnOx(Mn basis 4wt%)/NH_2-KIE6-c	25	Formic Acid (0.5 M)	593	[25]
Pd/NMC-400	25	Formic Acid (1 M)	913	[26]
Pd/NMC-500	25	Formic Acid (1 M)	680	[26]
Pd/NMC-600	25	Formic Acid (1 M)	642	[26]
Pd/NMC-700	25	Formic Acid (1 M)	469	[26]
5 wt% Pd/C	30	Formic Acid (0.5 M)	1136	[27]

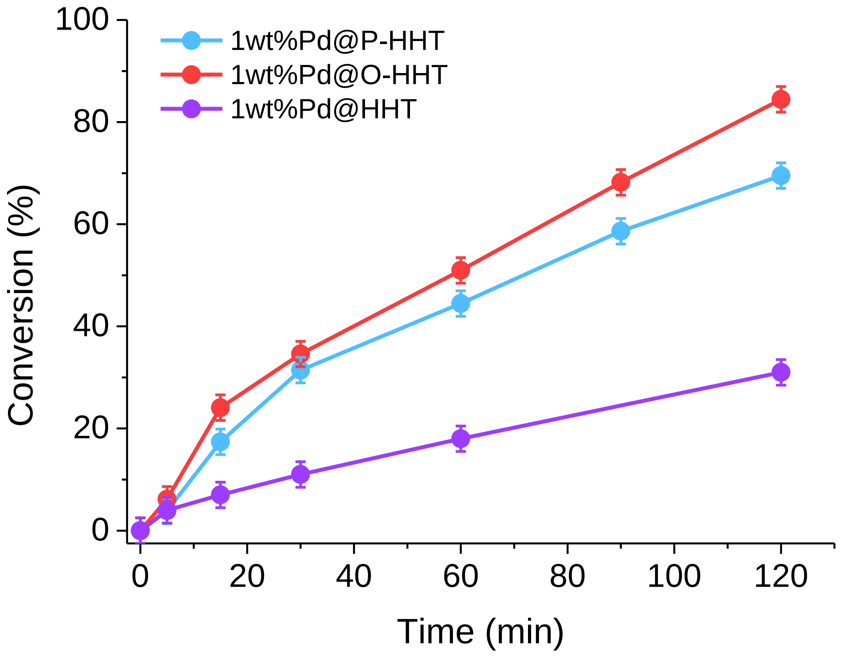

Figure 5: Kinetic profile of 1wt%Pd@P-HHT (light blue), 1wt%Pd@O-HHT (red) and 1wt%Pd@HHT (violet) catalysts for formic acid dehydrogenation.

A crucial feature of the catalysts to be implemented at large scale is the durability of the catalyst. We performed recycling tests on the three systems after 2 h of reaction. Stability tests were performed by filtering the catalyst without any further purification treatment. According to the previous studies, Pd catalysts rapidly deactivates after the first run (Figure 6 a)[27]. Such behaviour can be assigned to sintering and CO poisoning of NPs. Indeed, the average particle size increased from 3.0 to 4.7 nm during 9 hours of experiment, while carbon monoxide occupied the active sites[28,29]. The two Pd-based catalysts supported on functionalised CNFs exhibit remarkable stability up to six cycles of reaction, 12 h of reaction (Figure 6 b-c). The initial increasing in activity observed for Pd@O-HHT and Pd@P-HHT catalysts can be assigned to the desorption of PVA from the Pd NPs which blocked active sites, as previously demonstrated[30]. From XPS analysis a decrease in phosphorous and oxygen exposure in P-HHT and O-HHT after Pd deposition was detected, suggesting the preferential deposition of the metal on P and O functionalities. This result was also confirmed by STEM-EDS analysis on Pd@P-HHT catalyst, where some Pd NPs appear in contact with P (Figure 4). This data can explain the superior durability of the functionalised catalysts thanks to the electronic interaction between Pd and functional groups. Moreover, in order to establish the selectivity of the catalysts, the gaseous products obtained were analysed after 30 minutes of reaction connecting the reactor to a micro-GC. The non-functionalised 1wt%Pd@HHT showed a 55% selectivity for the dehydrogenation pathway, while the two functionalised materials, 1wt%Pd@O-HHT and 1wt%Pd@P-HHT, showed an increased selectivity of 75% and 65%, respectively, which remained practically constant during the six consecutive experiments, Figure 6. A reduction in the CO production for 1wt%Pd@O-HHT and 1wt%Pd@P-HHT can also explain the excellent stability observed for these two catalysts. Moreover, in this case HR-TEM analysis showed similar particle size before and after stability tests.

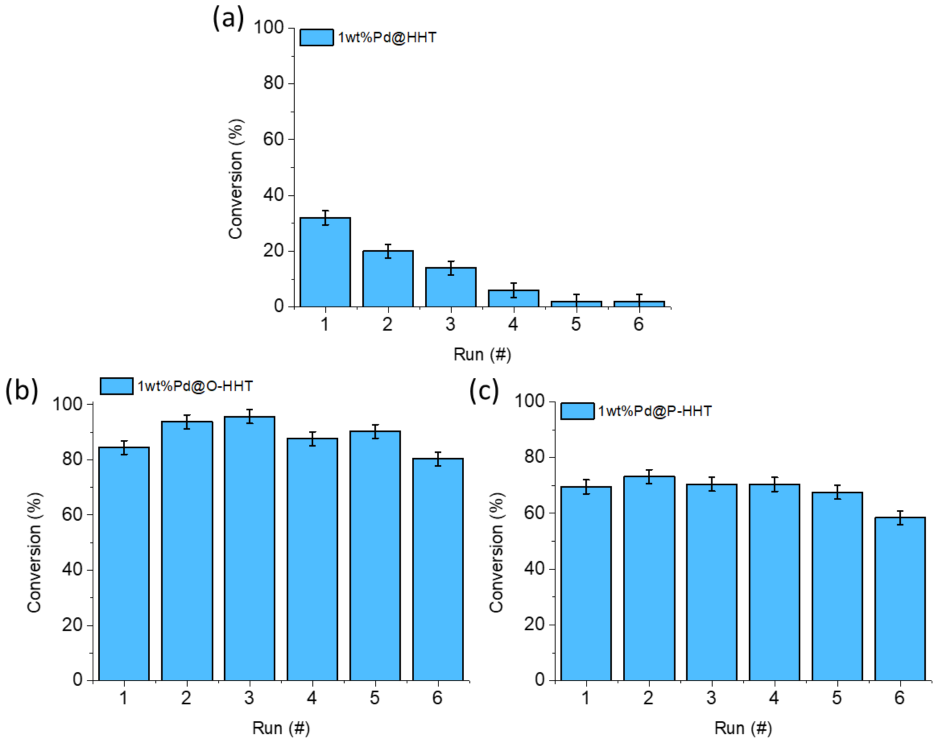

Figure 6: Recycling tests of a) Pd@HHT, b) Pd@O-HHT and c) Pd@P-HHT for formic acid dehydrogenation.

3.2.3. DFT results

DFT studies were performed in order to disclose the role of the different O and P functionalization on stabilising the Pd NPs. Danis demonstrated that, among all, SV is the most reactive defect towards the addition of an heteroatoms functional group[31]. Based on the typical functional groups found on the carbon surface after a standard functionalization procedure[10,15,32,33], five different functionalization groups were anchored on the SV, i.e. carboxyl (G_COOH), hydroxyl (G_OH), carbonyl (G_CO) and phosphate (G_PO_3H) groups (Figure 7).

The Pd_{15} cluster was brought near the defective part of the surfaces and relaxed until convergence of the interatomic forces. The optimised structures are represented in Figure 8, and different adhesion energies (E_{ADH}) summarised in Table 3. For every surface, the cluster-support adhesion is negative indicating and exothermic and favourable process driven by the minimisation of cluster area[34]. All functionalised surfaces showed an E_{ADH} between 1.649 and 0.465 eV lower than the pristine graphene, proving an increased stability of Pd atoms upon functionalisation of the surfaces. In particular, oxygen groups displayed stronger interaction with Pd cluster, confirming the observed increased stability of the Pd@O-HHT catalyst (Figure 6 b). Furthermore, the E_{ADH} seems to be related to the catalytic activity through Eq. 1, excluding any CO poisoning through pathway 2.

$$\mathrm{FAD}_{\mathrm{Conversion}} = \frac{\Delta \mathrm{E}_{ADH}}{E_{ADH}^{GP}} \cdot \mathrm{FAD}_{\mathrm{Conversion}}^{\mathrm{PG}} + \mathrm{FAD}_{\mathrm{Conversion}}^{\mathrm{PG}} \qquad (1)$$

The E_{ADH} of the O-functionalise catalysts is ~50% lower than the one of PG, which, added to PG relative FAD conversion (55%), leads to a rough Pd@O-HHT conversion of ~82%. In the case of Pd@P-HHT, its E_{ADH} is ~25% lower than on PG, which relative conversion adds 14% to the PG one (55%) resulting in 69%, very close to the 65% conversion determined experimentally. The variation between the experimentally FAD conversion and the one from Eq. 1 may be attributed, in principle, to CO poisoning. However, more results are needed to prove such relation and also to consider poisoning and difference in active sites.

Table 3: Adhesion energies (E_{ADH}) of the Pd cluster on the bare and functionalised surfaces.

System	E_{ADH} *(eV)*
Pd/PG	-2.029
Pd/G_COOH	-3.028
Pd/G_OH	-3.023
Pd/G_CO	-3.678
Pd/G_PO3H	-2.494

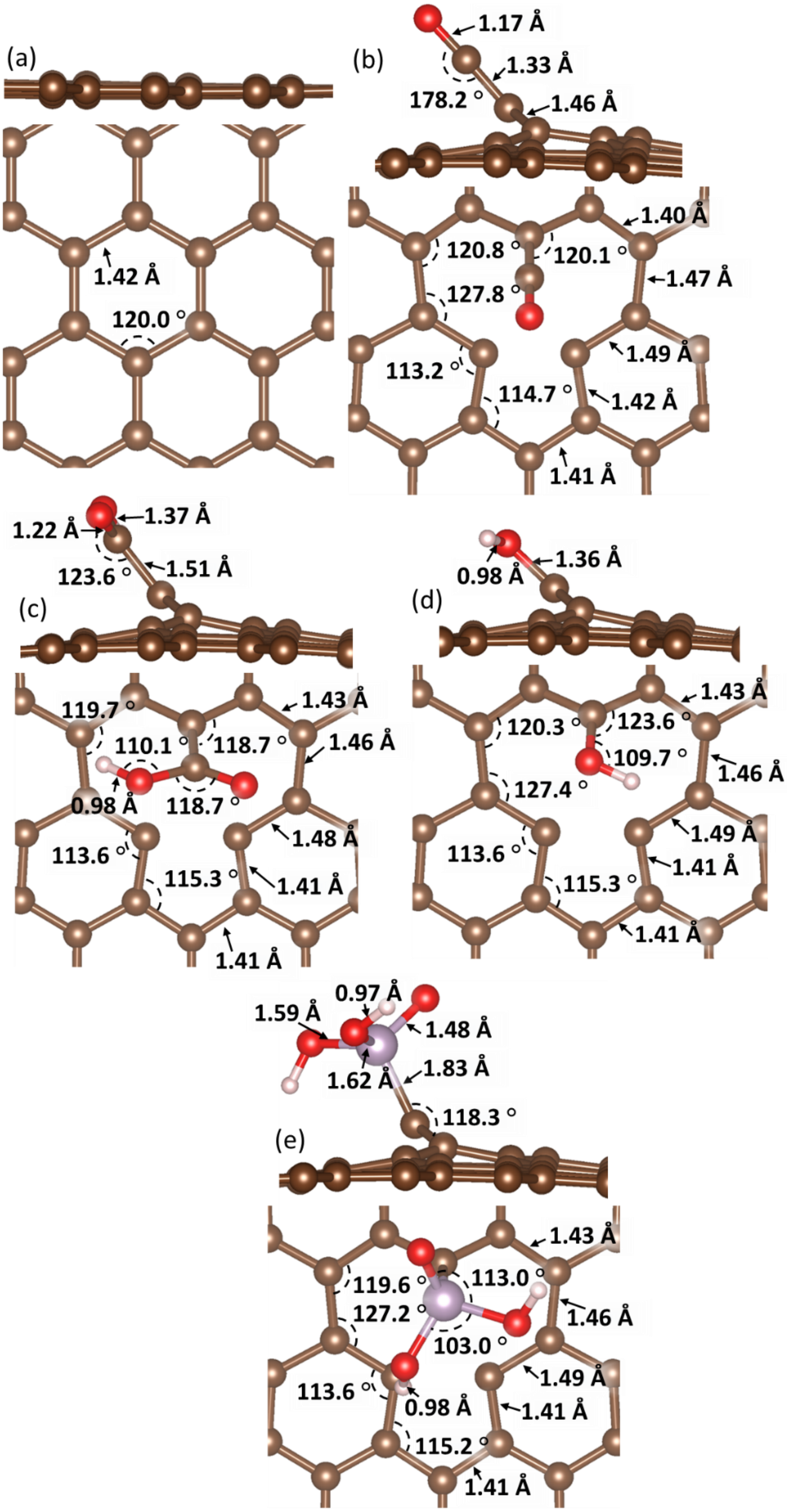

Figure 7: Side and top views of the optimized surfaces a) pristine graphene (PG), b) carbonyl doped SV graphene (G_CO), c) carboxyl doped SV graphene (G_COOH), d) hydroxyl doped SV graphene (G_OH) and e) phosphate doped SV graphene (G_PO3H). Inset shows the distances (Å) and angles (°) of interest. Carbon atoms are represented in brown, oxygen in red, hydrogen in white and phosphorous in violet.

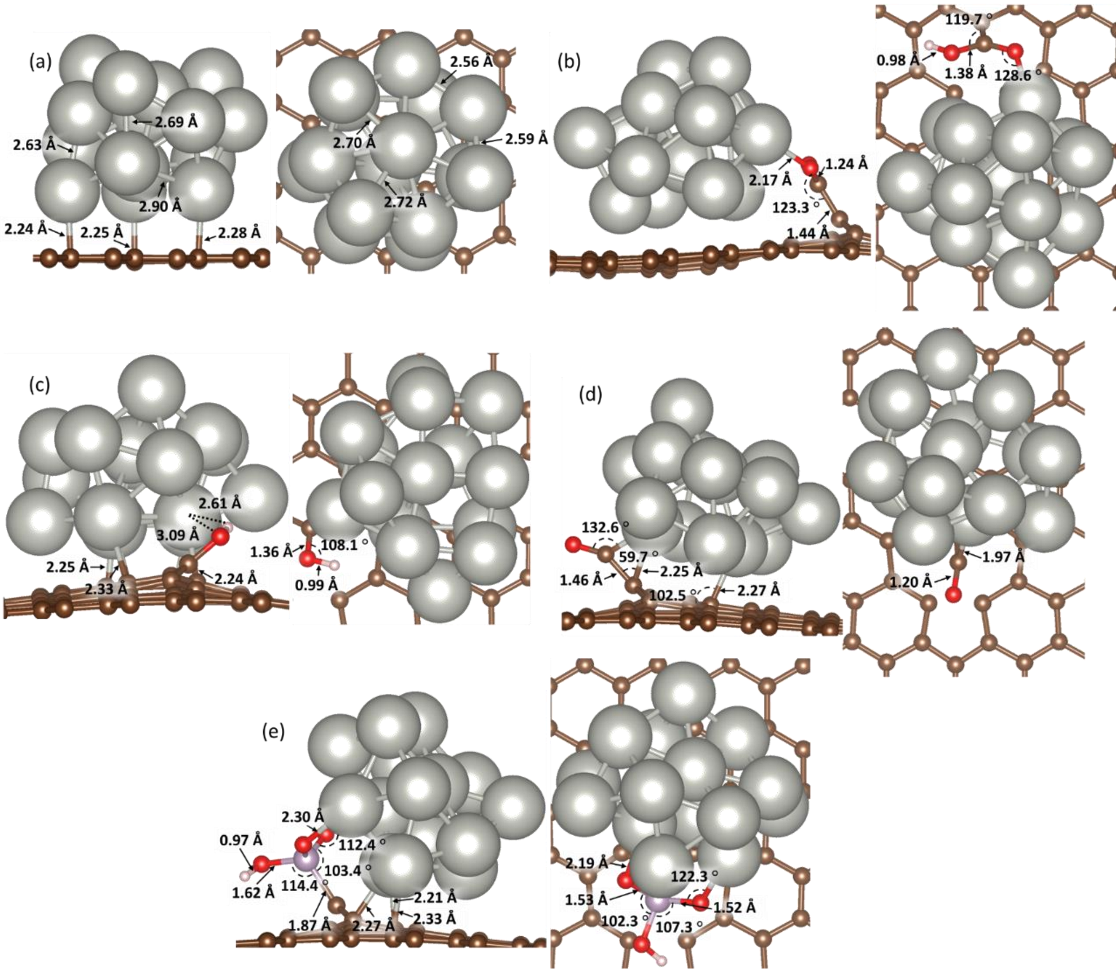

Figure 8: Side and top views of the optimized structures of Pd_{15} cluster on a) pristine graphene (PG), b) carboxyl doped SV graphene (G_COOH), c) hydroxyl doped SV graphene (G_OH), d) carbonyl doped SV graphene (G_CO) and e) phosphate doped SV graphene (G_PO3H). Inset shows the distances (Å) and angles (°) of interest. Carbon atoms are represented in brown, palladium in silver, oxygen in red, hydrogen in white and phosphorous in violet.

3.3. Conclusions

A combination of DFT and experimental data were employed to investigate and understand the support-metal interaction of Pd NPs deposited on oxygen and phosphorous functionalised high-heat treated carbon nanofibers for the formic acid decomposition reaction. After the acid functionalisation of the support using HNO_3 and H_3PO_4, the Pd particle depositions were carried out using sol-immobilization method leading to 1wt%Pd@O-HHT and 1wt%Pd@P-HHT catalysts. Theses catalysts obtained were characterized using TEM and XPS analyses. The kinetic profiles evidenced an increasing of conversion after two hours for both the functionalised systems respect the bare HHT standard. This enhanced catalytic behaviour can be assessed to an interaction between the metal and the functional group on the support confirmed by XPS and TEM analyses. Furthermore, an inhibition of the dehydration pathway was obtained for the functionalised materials. An excellent durability was observed in both systems during six consecutive runs, avoiding the leaching of Pd as observed for 1wt%Pd@HHT. These results were supported by a systematic DFT study of the Pd adhesion energies on different O and P functionalised surfaces shedding light to the stabilisation effect of the functional groups on Pd clusters. All functionalised surfaces showed stronger stabilisation of the Pd cluster than on the pristine graphene model confirming an increased stability of Pd nanoparticles. In particular, oxygenated supports displayed a stronger interaction with Pd validating the observed increased stability of the 1wt%Pd@O-HHT catalyst.

3.4. References

[1] I. Barlocco, S. Bellomi, J. J. Delgado, X. Chen, L. Prati, N. Dimitratos, A. Roldan, A. Villa, *Catal. Today* **2021**, *382*, 61–70.

[2]S. B. Simonsen, I. Chorkendorff, S. Dahl, M. Skoglundh, J. Sehested, S. Helveg, *J. Am. Chem. Soc.* **2010**, *132*, 7968–7975.

[3] S. R. Challa, A. T. Delariva, T. W. Hansen, S. Helveg, J. Sehested, P. L. Hansen, F. Garzon, A. K. Datye, *J. Am. Chem. Soc.* **2011**, *133*, 20672–20675.

[4]X. Wang, G. Sun, P. Routh, D.-H. Kim, W. Huang, P. Chen, *Chem. Soc. Rev.* **2014**, *43*, 7067–7098.

[5] A. A.-N. Mohammad Saleh Shafeeyan, Wan Mohd Ashri Wan Daud, Amirhossein Houshmand, *Appl. Surf. Sci.* **2011**, *257*, 3936–3942.

[6] M. S. Shafeeyan, W. M. A. W. Daud, A. Houshmand, A. Shamiri, *J. Anal. Appl. Pyrolysis* **2010**, *89*, 143–151.

[7] W. M. A. W. Daud, A. H. Houshamnd, *J. Nat. Gas Chem.* **2010**, *19*, 267–279.

[8] F. Sanchez, M. H. Alotaibi, D. Motta, C. E. Chan-Thaw, A. Rakotomahevitra, T. Tabanelli, A. Roldan, C. Hammond, Q. He, T. Davies, A. Villa, N. Dimitratos, *Sustain. Energy Fuels* **2018**, *2*, 2705–2716.

[9]S. Campisi, F. Sanchez Trujillo, D. Motta, T. Davies, N. Dimitratos, A. Villa, *C* **2018**, *4*, 9.

[10] S. Campisi, S. Capelli, D. Motta, F. Trujillo, T. Davies, L. Prati, N. Dimitratos, A. Villa, *C* **2018**, *4*, 48.

[11] B. Zhang, L. Shao, W. Zhang, X. Sun, X. Pan, D. S. Su, *ChemCatChem* **2014**, *6*, 2607–2612.

[12]Z. Xin, S. Wang, J. Wang, X. Huang, X. Ji, Y. Yao, L. Shao, *Electrochem. commun.* **2016**, *67*, 26–30.

[13]C. Chen, X. Li, L. Wang, T. Liang, L. Wang, Y. Zhang, J. Zhang, *ACS Sustain. Chem. Eng.* **2017**, *5*, 11300–11306.

[14]C. Lu, M. Wang, Z. Feng, Y. Qi, F. Feng, L. Ma, Q. Zhang, X. Li, *Catal. Sci. Technol.* **2017**, *7*, 1581–1589.

[15] X. Wu, L. R. Radovic, *Carbon N. Y.* **2006**, *44*, 141–151.

[16] A. Villa, D. Wang, C. E. Chan-Thaw, S. Campisi, G. M. Veith, L. Prati, *Catal. Sci. Technol.* **2016**, *6*, 598–601.

[17] J. Bedia, J. M. Rosas, J. Márquez, J. Rodríguez-Mirasol, T. Cordero, *Carbon N. Y.* **2009**, *47*, 286–294.

[18]S. Kundu, Y. Wang, W. Xia, M. Muhler, *J. Phys. Chem. C* **2008**, *112*, 16869–16878.

[19] F. Sanchez, M. H. Alotaibi, D. Motta, C. E. Chan-Thaw, A. Rakotomahevitra, T. Tabanelli, A. Roldan, C. Hammond, Q. He, T. Davies, A. Villa, N. Dimitratos, *Sustain. Energy Fuels* **2018**, *2*, 2705–2716.

[20] A. Bulut, M. Yurderi, Y. Karatas, M. Zahmakiran, H. Kivrak, M. Gulcan, M. Kaya, *Appl. Catal. B Environ.* **2015**, *164*, 324–333.

[21] S. S. Biswas, M. S. Tandrapadu, E. Abinaya, M. Eswaramoorthy, *Bull. Mater. Sci.* **2020**, *43*, 1–6.

[22] M. Farajzadeh, H. Alamgholiloo, F. Nasibipour, R. Banaei, S. Rostamnia, *Sci. Rep.* **2020**, *10*, 1–9.

[23] K. Mori, M. Dojo, H. Yamashita, *ACS Catal.* **2013**, *3*, 1114–1119.

[24]D.-W. Lee, M.-H. Jin, J. C. Park, C.-B. Lee, D. Oh, S.-W. Lee, J.-W. Park, J.-S. Park, *Sci. Rep.* **2015**, *5*, 15931.

[25]M.-H. Jin, D. Oh, J.-H. Park, C.-B. Lee, S.-W. Lee, J.-S. Park, K.-Y. Lee, D.-W. Lee, *Sci. Rep.* **2016**, *6*, 33502.

[26] J. Sun, H. Qiu, W. Cao, H. Fu, H. Wan, Z. Xu, S. Zheng, *ACS Sustain. Chem. Eng.* **2019**, *7*, 1963–1972.

[27]F. Sanchez, D. Motta, A. Roldan, C. Hammond, A. Villa, N. Dimitratos, *Top. Catal.* **2018**, *61*, 254–266.

[28] F. Abild-Pedersen, M. P. Andersson, *Surf. Sci.* **2007**, *601*, 1747–1753.

[29]H. Sakai, T. Nakajima, N. Yoshida, S. Kishimoto, *React. Kinet. Catal. Lett.* **1982**, *19*, 297–301.

[30] S. Campisi, C. E. Chan-Thaw, D. Wang, A. Villa, L. Prati, *Catal. Today* **2016**, *278*, 91–96.

[31] P. A. Denis, F. Iribarne, *J. Phys. Chem. C* **2013**, *117*, 19048–19055.

[32] I. Barlocco, S. Capelli, X. Lu, S. Tumiati, N. Dimitratos, A. Roldan, A. Villa, *Nanoscale* **2020**, *12*, 22768–22777.

[33] R. Arrigo, M. Hävecker, S. Wrabetz, R. Blume, M. Lerch, J. McGregor, E. P. J. Parrott, J. A. Zeitler, L. F. Gladden, A. Knop-Gericke, R. Schlögl, D. S. Su, *J. Am. Chem. Soc.* **2010**, *132*, 9616–9630.

[34] L. Ratke, P. W. Voorhees, *Growth and Coarsening : Ostwald Ripening in Material Processing*, Springer Berlin Heidelberg, **2002**.

4. SYNTHESIS OF PALLADIUM-RHODIUM BIMETALLIC NANOPARTICLES FOR FORMIC ACID DEHYDROGENATION

The results discussed in this Chapter were previously reported in my work, published on *J. Energy Chem.* **2020**, *52*, 301–309 (https://doi.org/10.1016/j.jechem.2020.04.031)[1].

4.1. Introduction

4.1.1. Rhodium and palladium-rhodium alloys in heterogeneous catalysis

The beneficial effect of alloying two different metals in order to obtain bimetallic nanoparticles, especially in formic acid decomposition (FAD) reaction, was widely explained in Sections 1.2.2.1. and 1.4.1.2. Indeed, noble metals alloyed nanoparticles (NPs) are fundamental for several and essential industrial processes due to their higher activity and stability in respect to non-noble transition metals[2,3]. In this chapter the advantage of alloying Rh to Pd will be presented.

Rhodium is employed in many catalytic reactions such as the C-H activation[4]. It was reported that alloying Rh to Pd it is possible to enhance the catalytic properties of pure palladium in different reactions, e.g. hydrogenation of cyclohexene[5], oxidation of o-phenylenediamine[6] and ethanol steam reforming[7]. However, the Pd-Rh system is barely investigated because it is difficult to obtain well-defined bimetallic Pd-Rh structure. Indeed, Pd and Rh are immiscible at the thermal equilibrium in bulk state over the whole composition range, therefore the alloy is in a segregated state at room temperature[8]. For this reason, alloys formed by these two metals have been obtained only in a metastable state by quenching the mixture at extremely high temperature, above 1000 K[9]. In the last decade, it was reported that Pd-Rh alloyed system can be obtained at low temperature, mixing the two metal at the atomic level, using a polyols method where poly(N-vinyl-2-pyrrolidone) (PVP) acts as stabilizer and ethylene glycol as reducer[5,10].

It was also disclosed by Ham and co-workers[11] by using theoretical calculations that the addition of Rh to Pd increases the activity of pure Pd in the formic acid dehydrogenation, enhancing the selectivity to H_2 and avoiding the formation of CO, which acts as poison for Pd catalysts. This beneficial effect is due to a contraction of the Pd-Pd distance and the increase in the electron density in surface Pd atoms compared to pure Pd[11].

4.1.2. Aims and objectives of the chapter

In this work, Pd-Rh nanoparticles were prepared immobilising preformed metal NPs with an alloy structure via sol-immobilisation[12]. Polyvinyl alcohol (PVA) and $NaBH_4$ were used as protecting agent and reducing agent, respectively. We choose highly graphitized carbon nanofibers (HHT) as support. Indeed, it has been recently reported that the utilization of these materials can improve the catalytic activity of supported Pd nanoparticles compared to other carbonaceous supports[13]. The synthesized catalysts were tested in the decomposition of formic acid to produce hydrogen in liquid phase at mild reaction conditions. The structure of the catalysts before and after reaction was carefully studied by means of electron microscopy. The most active catalysts were then tested in the liquid-phase hydrogenation of muconic acid, a process that can yield bio adipic acid, a compound widely used as monomer in polyamides and polyesters syntheses[14]. Muconic acid hydrogenation was performed in presence of formic acid as hydrogen donor.

4.2. Results

As previously reported by Barlocco et al.[1], Pd_xRh_y/HHT bimetallic catalysts with different Pd:Rh atomic ratio, and the corresponding Pd and Rh monometallic ones were prepared by sol immobilization method using polyvinyl alcohol (PVA) as protective agent. Compared to the classical preparation method[13] where pure water is used as solvent, a mixture of ethanol and water was used due to the low solubility of $[Rh(CO_2CH_3)_2]_2$ in water.

4.2.1. Catalyst characterisation

4.2.1.1. TEM-STEM results

The catalysts were characterized at the sub-nanometric scale by transmission electron microscopy. TEM image of the monometallic Pd/HHT was reported elsewhere[13] and a STEM image of Rh/HHT is reported in Figure 1.

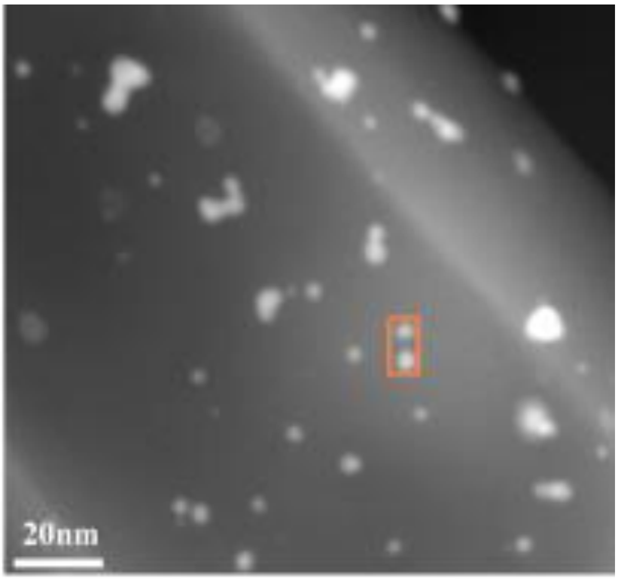

Figure 1: STEM image of monometallic Rh catalyst.

Both monometallic catalysts showed a similar average particle size of 3.2 and 3.5 nm, respectively (Table 1) with particles well dispersed on the surface of the carbon nanofibers.

Table 1: Nominal and calculated Pd-Rh molar ratio and average particle size for the Pd_x-Rh_y catalysts.

Catalyst	*Nominal Pd-Rh molar ratio*	*Calculated Pd-Rh molar ratio (EDX-TEM)*	*Calculated Pd-Rh molar ratio (ICP)*	*Average particle size (nm)*
Pd	-	-	-	3.2 ± 0.8
Pd used	-	-	-	4.5±1.3
Pd_8Rh_2	80:20	90:10	87:13	2.9±0.9
Pd_8Rh_2 used	80:20	95:5	93:7	4.5±1.0
Pd_6Rh_4	60:40	69:31	73:27	2.5±0.6
Pd_6Rh_4 used	60:40	81:19	84:16	3.0±0.7
Pd_4Rh_6	40:60	49:51	47:53	3.4±1.3
Pd_2Rh_8	20:80	40:60	38:62	2.6±0.7
Rh	-	-	-	3.5±1.1

Figure 2 to Figure 5 show representative results obtained by STEM and the investigation of the Pd-Rh bimetallic systems. The catalysts show a similar average particle size in the range of 2.5-3.2 nm, Table 1, with a narrow particle size distribution, as shown in Figures 1c-4c. STEM-XEDS analysis was performed on individual particles to analyse their composition (Figure 2 to Figure 5, Table 1). Line profiles of single particles are also included to illustrate the formation of bimetallic nanoparticles. Regarding sample Pd_2Rh_8, (Figure 2) an average particle size of 2.6 nm was obtained, although some big agglomeration of tiny crystallites was found in the sample (Figure 6). Interestingly, the particles included in these agglomerations have a low content of Rh (< 10%) or even they are pure Pd (Figure 6 b). The small particles are always made of both Rh and Pd, with a Pd-Rh ratio different from particle to particle and average Pd-Rh molar ratio of 40:60 (Table 1, Figure 2 b).

Pd_4Rh_6 consists of particles with an average particle size of 3.2 nm (Table 1), with a broader particle distribution, (Figure 3). All the particles analysed were bimetallic with an average molar ratio of 49:51 (Pd:Rh), which indicates an enrichment of Pd, if we compare it with the nominal composition (40:60). This composition also varies from particle to particle, (Figure 3 b). In addition, in this case, large aggregates were observed (Figure 7 a) with a lower content of Rh (Pd-Rh ratio of 79:21) in comparison with the one obtained for the small particles (Figure 7 b).

Particles with an average size of 2.5 nm were found for Pd_6Rh_4 catalyst (Table 1), with the presence of large aggregations of particles (Figure 8). STEM-XEDS analysis (Figure 4) confirms the presence of Pd-Rh bimetallic particles with an average molar ratio of 69:31, which again show a higher Pd content that what it was expected. Moreover, for this sample the Pd-Rh relative content varies from particle to particle (Figure 4 b).

Pd_8Rh_2 shows highly and homogeneously dispersed metal nanoparticles with an average size of 2.9 nm and no aggregates were observed (Figure 5). Particles exhibit an enrichment of Pd, with an average Pd:Rh atomic ratio of 90:10, which it is also higher than the nominal one of 80:20. STEM-XEDS analysis performed on individual particles demonstrated that almost all the particles were Pd-Rh bimetallic, although the content of Rh is lower than the nominal one in all the prepared catalysts. Additionally, monometallic Rh and Pd particles were not observed. In order to demonstrate the formation of the bimetallic nanoparticles, EDS line profiles of isolated nanoparticles are included in Figure 2 to Figure 5. In all the analysed nanoparticles, we can observe the signals of Rh and Pd inside of the individual particles. Although the presence of very small particle with size of 2-6 nm complicated the analysis, the obtained line profiles may indicate a relatively homogenous distribution of both metal and that there is not any preferential distribution of the elements such core-shell structure. To understand the discrepancy between nominal and calculated Pd:Rh atomic ratio, we utilized the inductively coupled plasma optical emission spectroscopy (ICP-OES) to analyse the metal loading of the synthesised catalysts (Table 1). The analysis performed on the filtrated solution, after the immobilization of the metal colloid on the carbon nanofibers, revealed the presence of Rh in solution. The same problem has been detected for the monometallic Rh catalyst which shows a calculated loading of 0.91% instead of the nominal one of 1%.

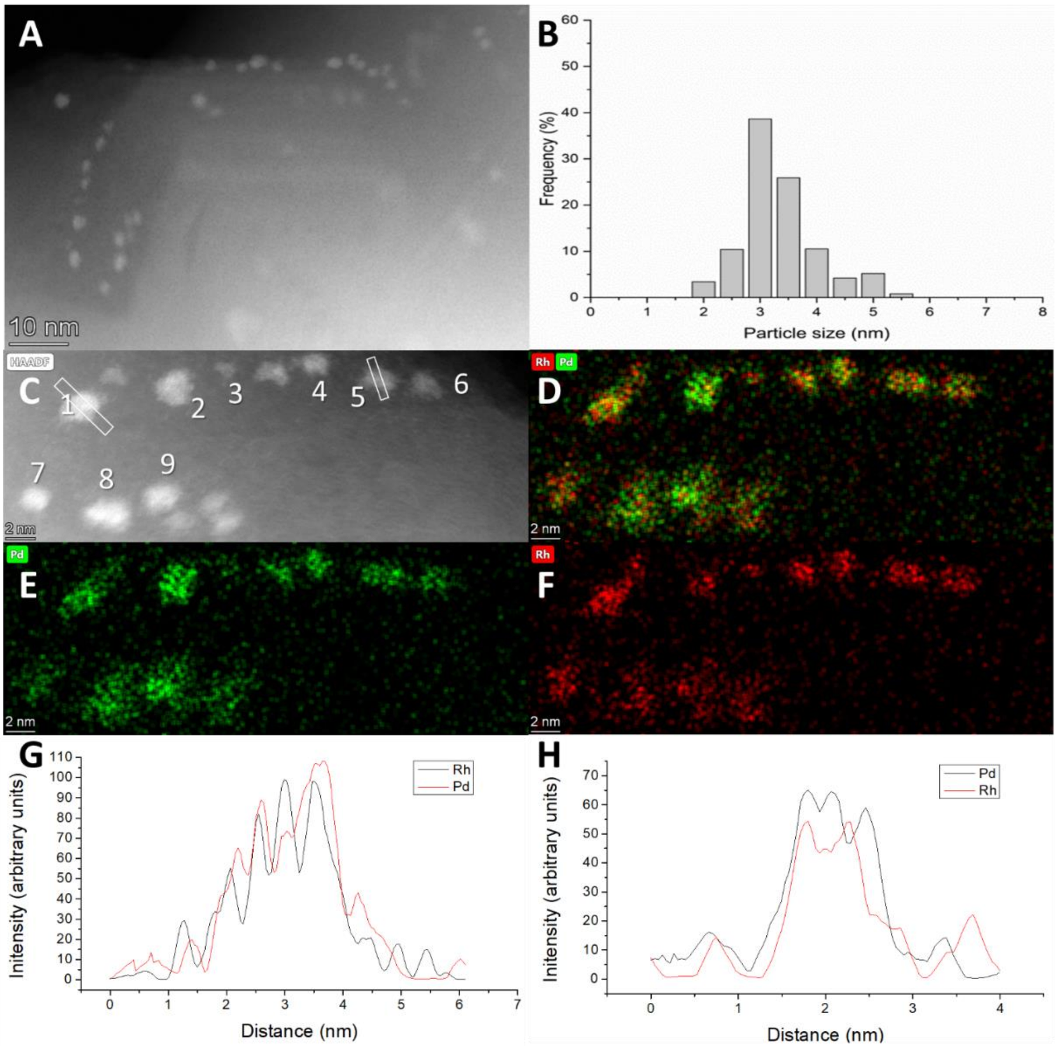

Figure 2: A) STEM-HAADF image of Pd_2Rh_8 catalyst, B) particle size distribution, C-F) STEM-XEDS of single nanoparticles (Pd-Rh atomic ratio: 1) 75:25, 2) 71:29 3) 20:80 4) 63:27 5) 52:48 6) 60:40 7) 62:38 8) 81:19 9) 29:71) and G-H) Line profile of the particle 1 and 5 respectively.

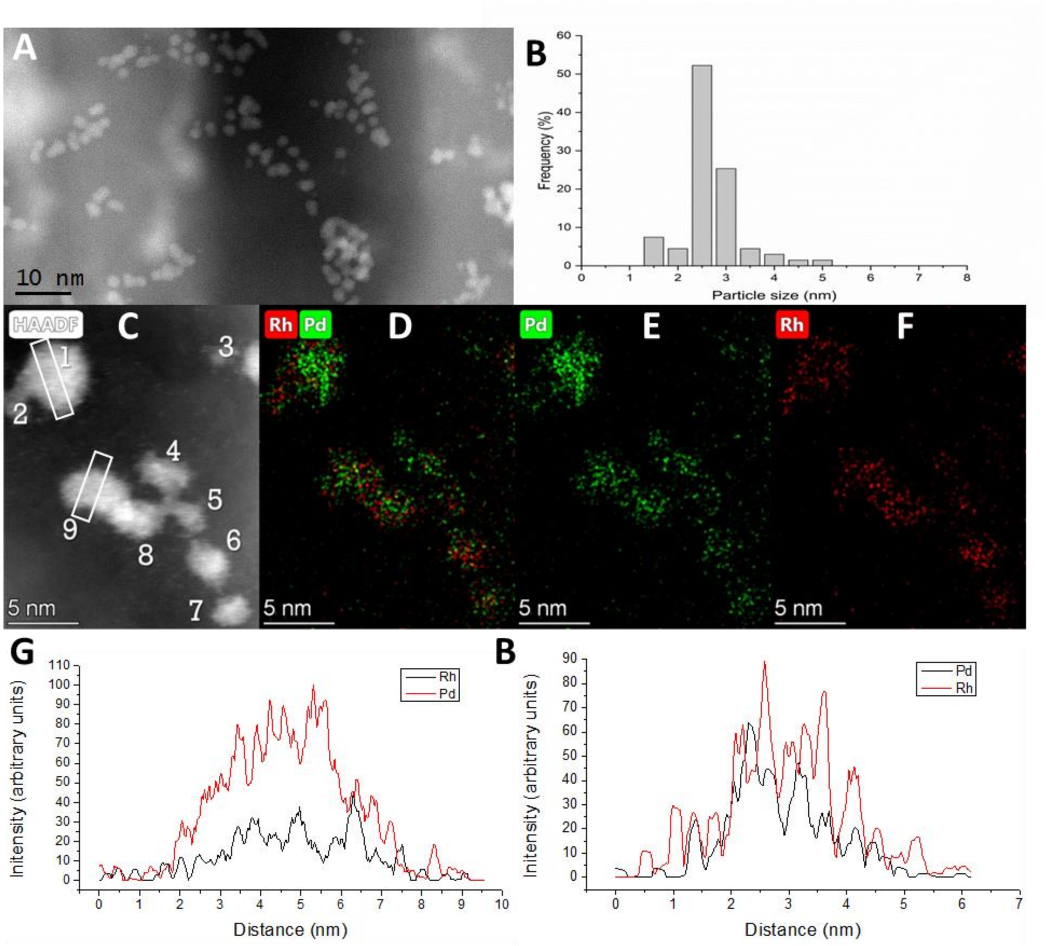

Figure 3: A) STEM-HAADF image of Pd_4Rh_6 catalyst, B) particle size distribution, C-F) STEM-XEDS of single nanoparticles (Pd-Rh atomic ratio: 1) 67:33, 2) 40:60, 3) 28:72, 4) 15:85, 5) 60:40, 6) 75:25, 7) 57:43, 8) 59:41, 9) 53:47) and G-H) Line profile of the particle 1 and 9 respectively.

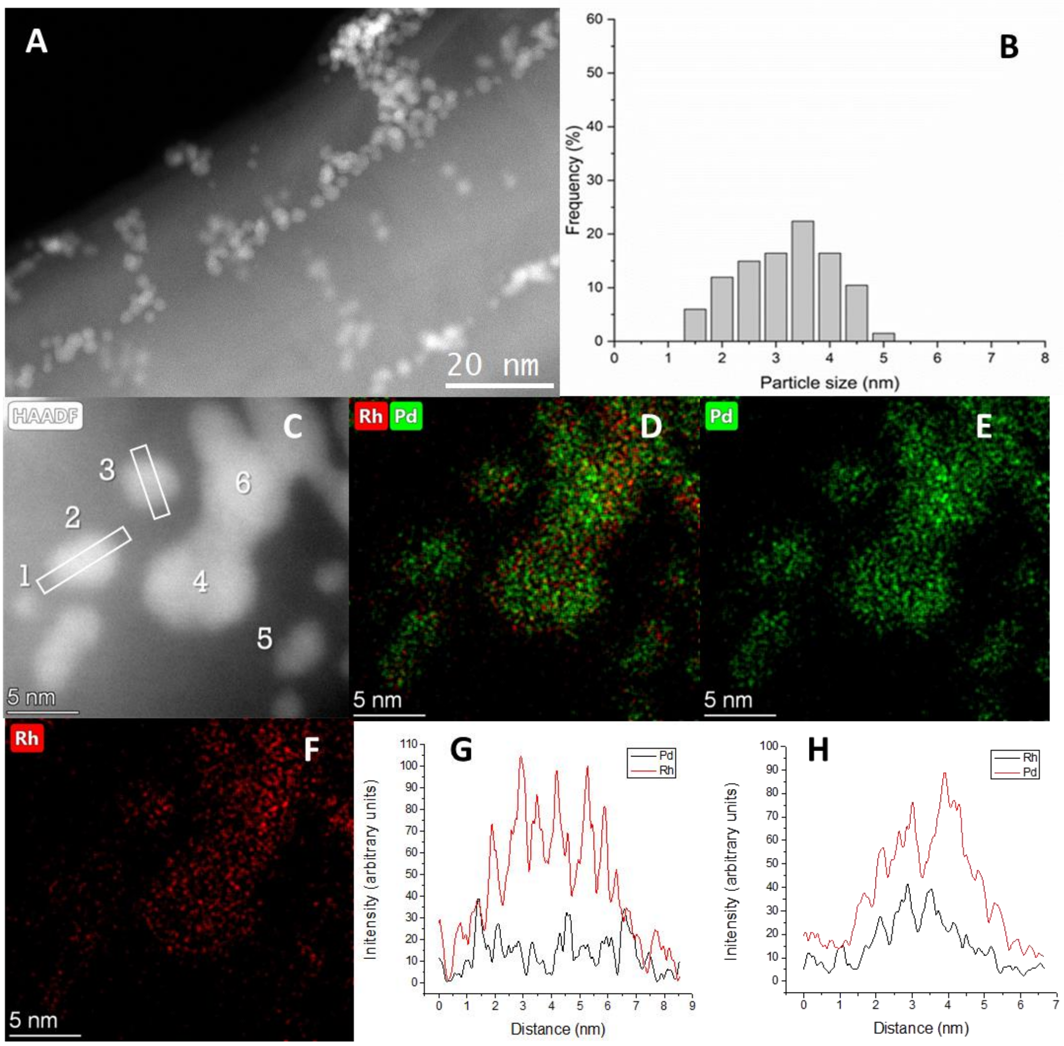

Figure 4: A) STEM-HAADF image of Pd_6Rh_4 catalyst, B) particle size distribution, C-F) STEM-XEDS of single nanoparticles (Pd-Rh atomic ratio: 1) 40:60, 2) 62:38, 3) 89:11, 4) 75:25, 5) 67:33, 6) 62:38) and G-H) Line profile of the particle 2 and 3 respectively.

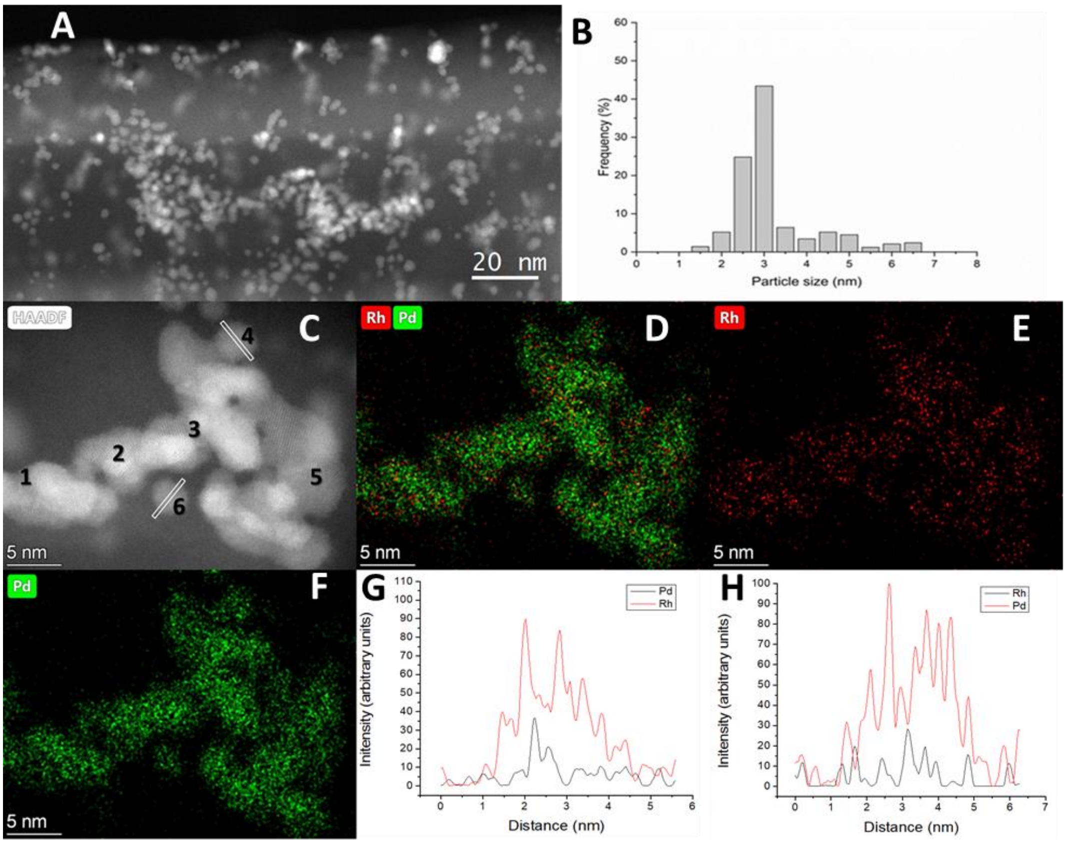

Figure 5: A) STEM-HAADF image of Pd_8Rh_2 catalyst, B) particle size distribution, C-F) STEM-XEDS of single nanoparticles (Pd-Rh atomic ratio: 1) 92:8, 2) 82:18, 3) 99:1, 4) 90:10, 5) 89:11) and G-H) Line profile of the particle 4 and 6 respectively.

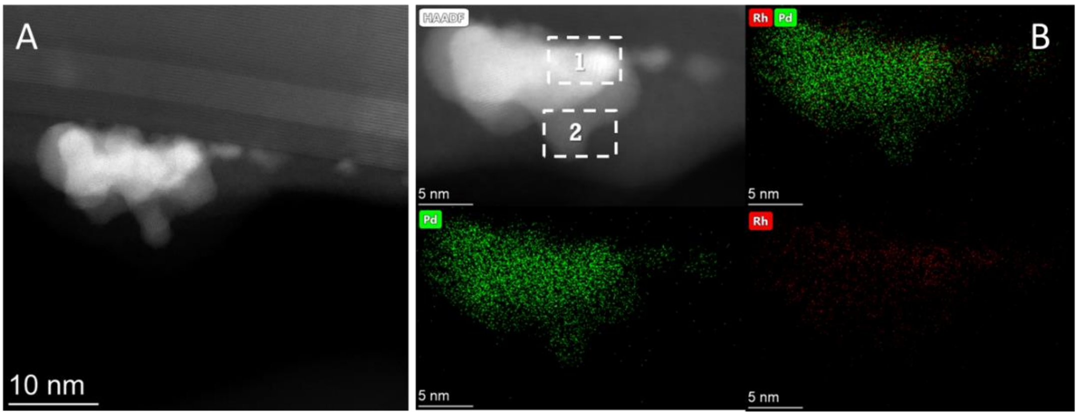

Figure 6: A) STEM images of Pd_2Rh_8 showing large aggregates of crystallites and B) STEM-XEDS analysis of a large aggregate ((Pd-Rh ratio: 1) 27:74, 2) 30:70).

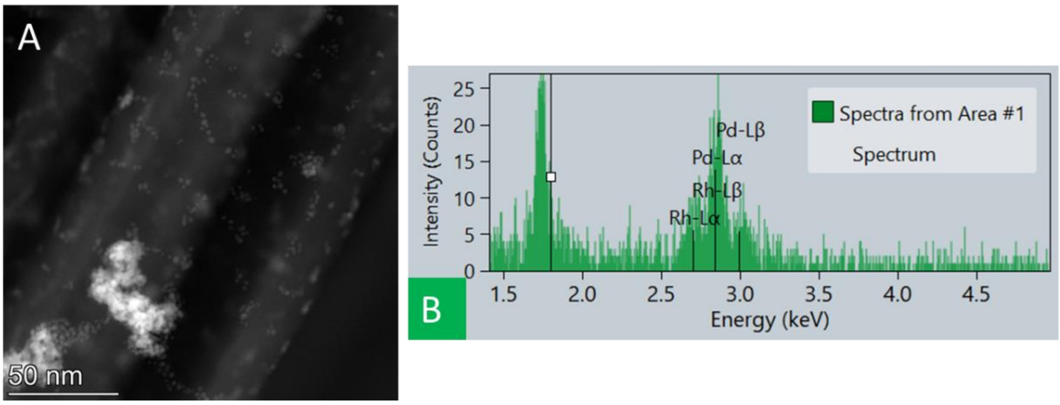

Figure 7: A) STEM images of Pd_4Rh_6 showing a large aggregation of particles and B) the corresponding EDX spectra showing an enrichment of Pd (Pd:Rh ratio of 79:21).

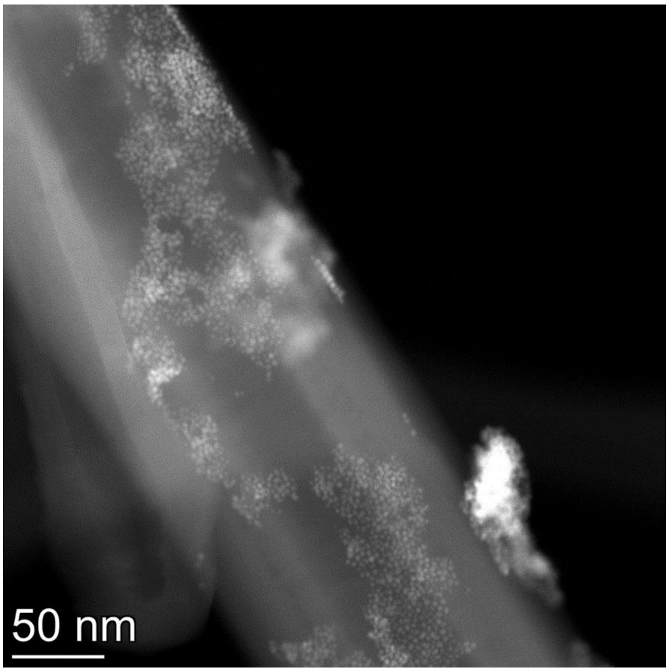

Figure 8: STEM images of Pd_6Rh_4 showing isolated large aggregation of particles.

4.2.2. Catalytic activity

4.2.2.1. Formic acid dehydrogenation reaction

The catalytic performance of the Pd-Rh catalysts was evaluated in the liquid-phase decomposition of formic acid as a model reaction for hydrogen generation (Reaction conditions: 0.5 M HCOOH in water, 30 °C, stirring rate of 1400 rpm, substrate/metal molar ratio of 2000). The decomposition of formic acid follows two main pathways: (i) dehydrogenation ($HCOOH \rightarrow CO_2 + H_2$, $\Delta G = -48.4\ kJ\ mol^{-1}$) and (ii) dehydration ($HCOOH \rightarrow CO + H_2O$, $\Delta G = -28.5\ kJ\ mol^{-1}$). The reaction conditions, in particular stirring rate and substrate/metal molar ratio were optimised in previous reports, in order that the reaction is taking place in chemical kinetic regime[13]. Figure 9 presents the catalytic activity of the catalysts prepared by varying the Pd-Rh atomic ratio. To better correlate the effect of the metal ratio and the activity, the calculated Pd-Rh instead of the nominal molar ratio will be now considered. The activity is expressed as mol of formic acid reacted per total mol of metal per hour and calculated after 5 minutes of reaction. The highest initial activity was obtained using $Pd_{90}Rh_{10}$ (1793 h^{-1}), followed by monometallic Pd and $Pd_{69}Rh_{31}$ which showed similar results (979 and 921 h^{-1}, respectively). Increasing the Rh content, the activity progressively decreased and the monometallic Rh showed very low activity (Figure 9). However, this trend was not followed by $Pd_{40}Rh_{60}$ which showed an activity two times higher (696 h^{-1}) than $Pd_{48}Rh_{52}$ (341 h^{-1}). We could not find the reason to fully justify the observed catalytic trend. Indeed, the two catalysts showed similar bimetallic structure, even the particle size is slightly larger for $Pd_{48}Rh_{52}$ (3.4 nm) than the other bimetallic catalysts (2.4-2.9 nm, Table 1). In general, the influence of particle size in catalyst activity for this series of catalysts seem to be negligible compared to that of Pd-Rh composition.

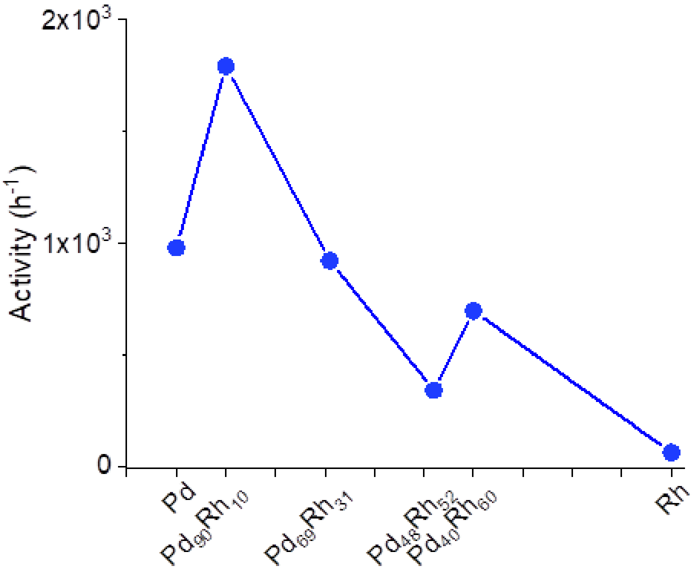

Figure 9: Activity vs Pd-Rh ratio in the formic acid dehydrogenation.

Table 2 presents a comparison of the activity of various Pd based bimetallic catalysts for the liquid phase dehydrogenation of formic acid under mild conditions. $Pd_{90}Rh_{10}$ shows an activity better of most of the catalysts presented in the literature. Figure 10 showed similar reaction profiles for all the catalysts and no evident deactivation phenomena seem to be present. $Pd_{90}Rh_{10}$ showed the highest conversion after 2h of reaction (81%). Interestingly $Pd_{69}Rh_{31}$, despite showing a similar initial activity than monometallic Pd, showed a higher conversion after 2h than this latter one (54 and 28%, respectively, Figure 10). The products detected in the gas phase were mainly CO_2 and H_2 with presence of CO under the detection limit of the instrument (5 ppm) for the bimetallic systems and of 12 ppm for the monometallic Pd catalyst. Therefore, these catalysts can be used for the production of H_2 in fuel cells, since

CO is the main issue for chemical poisoning in the case of using hydrogen fuel cells for the generation of energy and it is important to be kept below 10 ppm level.

Table 2: Comparison of catalytic activity of Pd-based bimetallic catalysts for the liquid phase dehydrogenation of formic acid under mild conditions.

Catalyst	*T (ºC)*	*Reagent*	*TOF (h^{-1})*		*Ref.*
			Initial	2 h	
$Pd_{90}Rh_{10}$/HHT	30	Formic acid (0.5 M)	1793		This work
$Pd_{69}Rh_{31}$/HHT	30	Formic acid (0.5 M)	921		This work
Pd/HHT	30	Formic acid (0.5 M)	979		This work
Pd/C	21	Formic acid (1.33 M)	18	15	[15]
	30		48	28	
$Au_{41}Pd_{59}$/C	50	Formic acid (1 M)	230		[16]
Ag@Pd (1:1)	35	Formic acid		156	[17]
Ag/Pd alloy (1:1)	20			144	[17]
$Ag_{42}Pd_{58}$	50	Formic acid (1 M)	382		[18]
Pd-MnO_x/SiO_2-NH_2	20	Formic acid (0.265 M)	140		[19]
	50		1300		
$Ag_{0.1}Pd_{0.9}$/rGO	25	Formic acid	105		[20]
PdNiAg/C	50	Formic acid (0.175 M)	85		[21]
$Pd_{50}Cu_{50}$/resin	75	HCOOH/HCOONa=9:1	810		[22]
20 wt% PdAu/C–CeO_2	102	9.94 M formic acid–3.33 M sodium formate solution	832		[23]

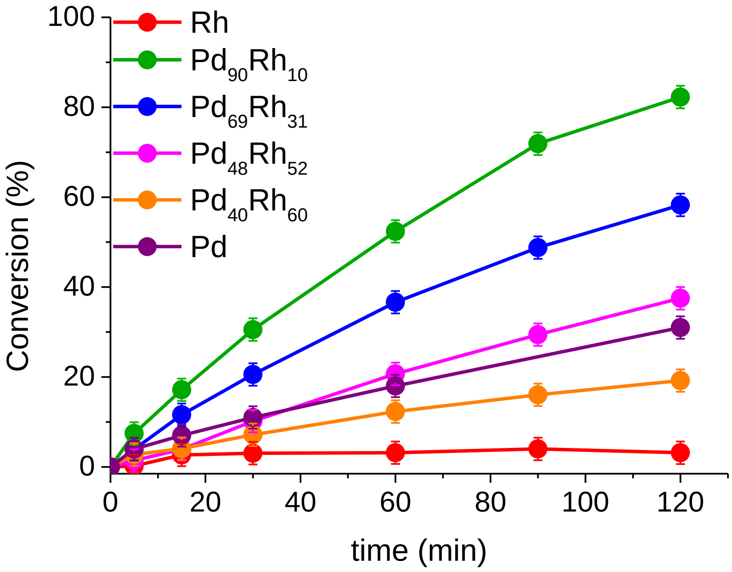

Figure 10: Reaction profiles for Pd-Rh catalysts in the formic acid dehydrogenation.

Stability tests have been performed using $Pd_{90}Rh_{10}$, $Pd_{69}Rh_{31}$, the catalysts presenting the highest conversion after 2 h and compared to the Pd monometallic one (Figure 11). Recycling experiments were carried out by filtering and using the catalyst in the next run without any further purification. Palladium catalyst rapidly deactivated after the first run, in agreement with previous studies[13] (Figure 11 a). Agglomeration and coalescence of the particles was observed, and the average particle size increased from 3.0 to 4.7 nm (Table 1).

ICP analysis performed on the filtrated solution revealed the leaching of 5% of Pd during the reaction. Moreover, Pd active sites can be poisoned by the CO produced (11-15 ppm, in the different cycles). It is well known, indeed, that CO can poison Pd catalysts even when present at ppm level[24]. A similar trend was observed for $Pd_{90}Rh_{10}$, the most active catalyst (Figure 11 b). STEM analysis evidenced the coalescence of the particles with growing of the average particle size from 2.9 to 4.5 nm (Figure 12). The STEM-XEDS analysis showed an enrichment in Pd of the particles, which have an average composition of 95:5 with the presence of segregated monometallic Pd particles (Table 1). ICP results demonstrated that this is due to the partial leaching of Rh in the reaction solution, whereas no leaching of Pd was observed. On the contrary, $Pd_{69}Rh_{31}$ showed a good stability during the 6 cycles (Figure 11 c). STEM analysis of the used catalyst evidenced a limited growing of the average particle size from 2.5 to 3.0 nm (Table 1). The analysis of the atomic composition of the single nanoparticles showed an enrichment in Pd with a Pd-Rh atomic ratio of 81:19 (Figure 13), due to the leaching of Rh in the solution. The high stability might be attributed to a catalyst with a Pd-Rh composition similar to the most active ones. The higher activity of the new phase is offset by the leaching of metal in the solution, and the conversion was constant during the 6 cycles. The partial Rh leaching observed for the bimetallic catalysts can be due to the fact that Pd-Rh structures are not stable upon hydrogen absorption/desorption, leading to a partial segregation of the two metals [9,25]. Probably, segregated Rh is more prone to leaching than when alloyed.

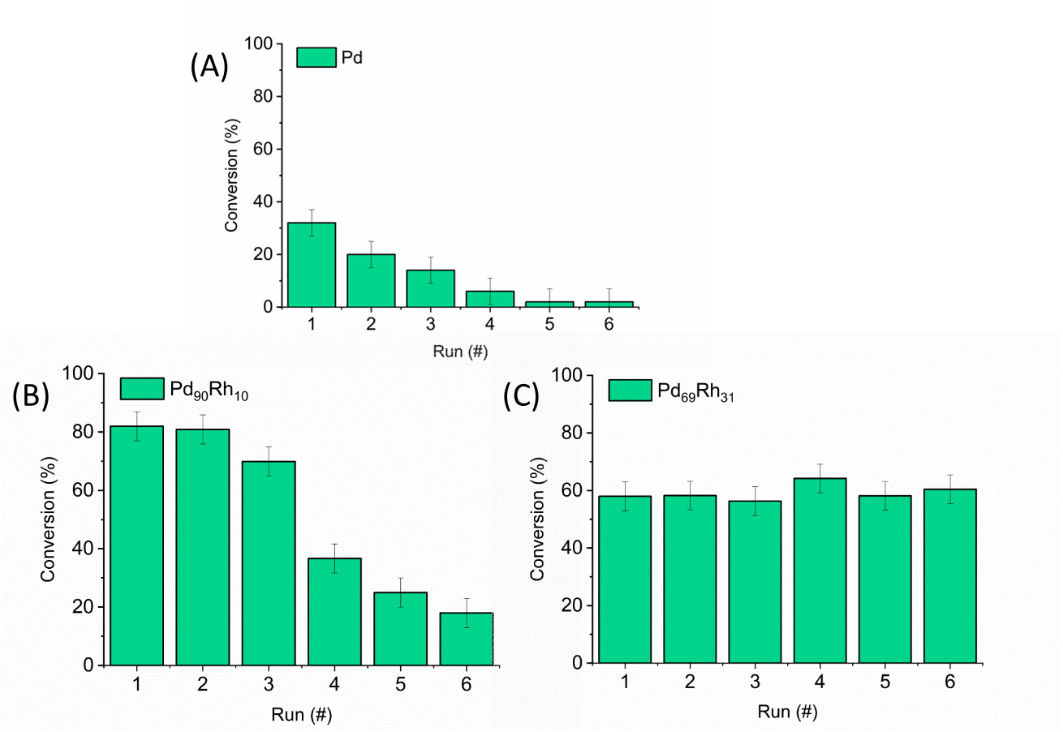

Figure 11: Recycling tests for a) monometallic Pd, b) $Pd_{90}Rh_{10}$ and c) $Pd_{69}Rh_{31}$.

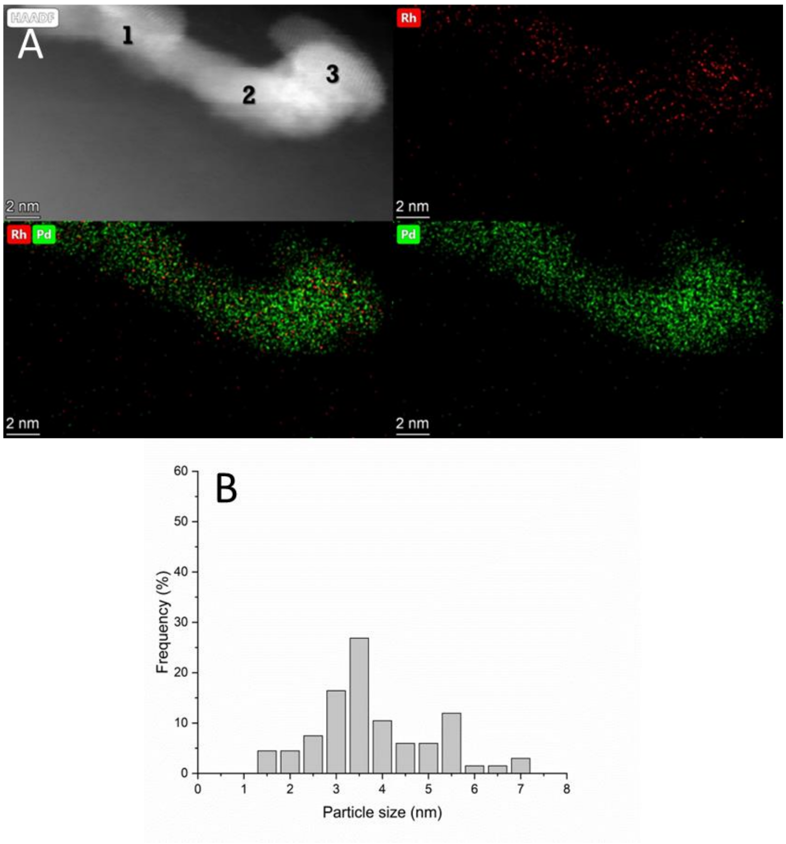

Figure 12: a) STEM-HAADF image, STEM-XEDS of single nanoparticles and b) particle size distribution of $Pd_{90}Rh_{10}$ used catalyst.

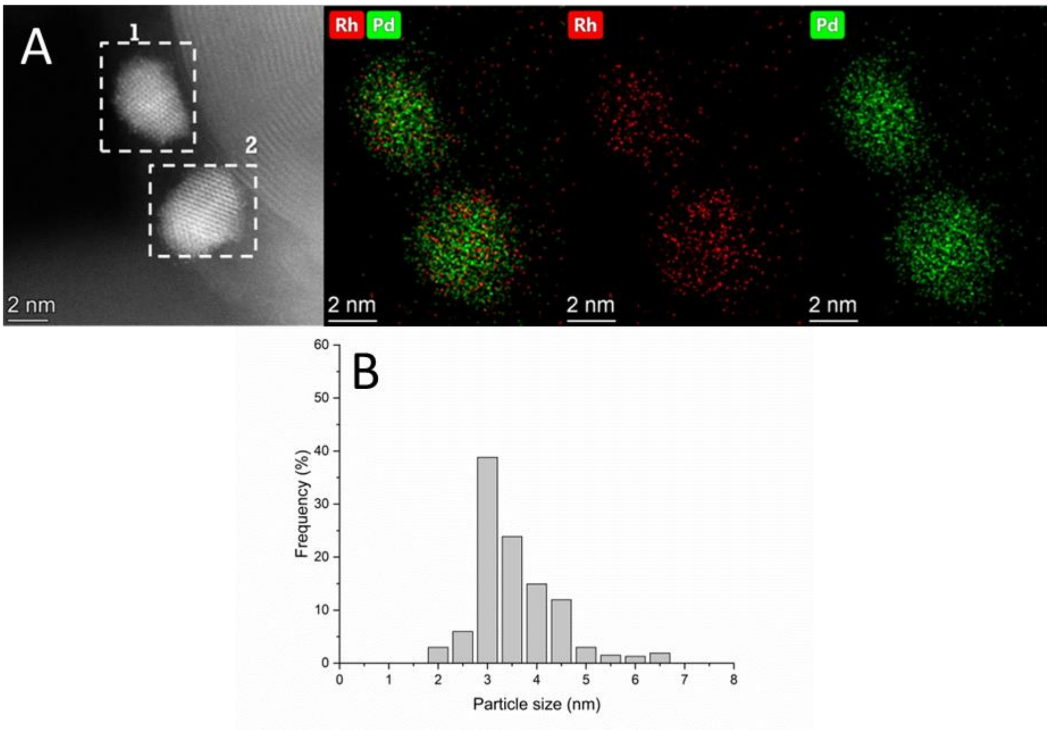

Figure 13: a) STEM-HAADF image, STEM-XEDS of single nanoparticles and b) particle size distribution of $Pd_{69}Rh_{31}$ used catalyst.

4.2.2.2. Muconic acid *in-situ* hydrogenation

Numerous chemical industries are nowadays developing processes based on renewable sources, such as the production of bio-adipic acid[26]. Adipic acid (AA) is widely used as monomer in polyamides and polyesters syntheses[14]. Nowadays, the totality of commercialised AA is derived from oil of the benzene fraction, raising environmental and safety concerns[27]. One of the most appealing route to produce this monomer is based on the use of *cis*,*cis*-(2Z,4Z)muconic acid (MA) as a starting material, which can be obtained either from lignin and lignocellulose[28], one of the most abundant renewable material. This reaction proceeds in two-steps as it was recently shown[29]. In the first one, monounsaturated acids are produced ((2E)-hexenedioic acid and (3E)-hexenedioic acid), followed by the hydrogenation of the second C=C bond to obtain adipic acid (Scheme 1). Pd and Pt based catalysts have been successfully employed in this reaction, using molecular H_2[29,30]. Nevertheless, Pd ones showed the best activity at mild condition (50 °C and 1 bar of H_2)[31]. In addition, it was reported that formic acid (FA) can be employed as H-donor at mild reaction conditions, enabling the possibility to generate hydrogen *in-situ* to perform hydrogenation reactions[29,32].

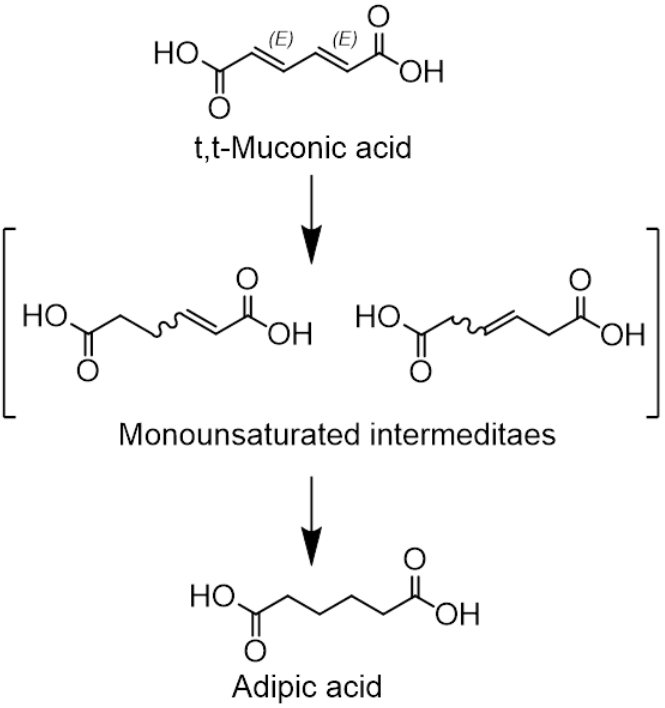

Scheme 1: Two step conversion of muconic acid into bio-adipic acid.

In this work we utilized formic acid for the upgrade of muconic acid (MA) to adipic acid (AA). Therefore, we combine the ability of Pd catalyst to generate hydrogen from formic acid (H-source) and at the same time to activate H_2 under mild conditions to hydrogenate muconic acid to bio-adipic acid. Muconic acid hydrogenation was performed under similar reaction conditions utilized for the dehydrogenation of formic acid (Reaction conditions: 0.007 M MA in water, MA/Formic acid ratio of 1/4 (mol/mol), 30 °C, stirring rate of 1400 rpm, substrate/metal molar ratio of 200). The two most active bimetallic catalysts, $Pd_{90}Rh_{10}$ and $Pd_{69}Rh_{31}$ were compared to monometallic Pd. In Figure 14 it is plotted the concentration of the reactant MA, the mono unsaturated intermediates and adipic acid as a function of reaction time. All the catalysts were highly active in the first step, almost quantitatively converting MA to the intermediates after 1h of reaction. However only the two bimetallic catalysts were able to convert the intermediates to adipic acid, in particular in the case of $Pd_{69}Rh_{31}$. The lower activity of Pd can be attributed to the lower activity and stability in the generation of hydrogen from formic acid compared to bimetallic counterparts. However, it can be observed that after 2h of reaction the concentration of the products remains stable. Future studies will be performed to improve the catalytic performance of the present catalysts and to understand the reason of deactivation in the muconic acid hydrogenation in presence of formic acid as hydrogen donor.

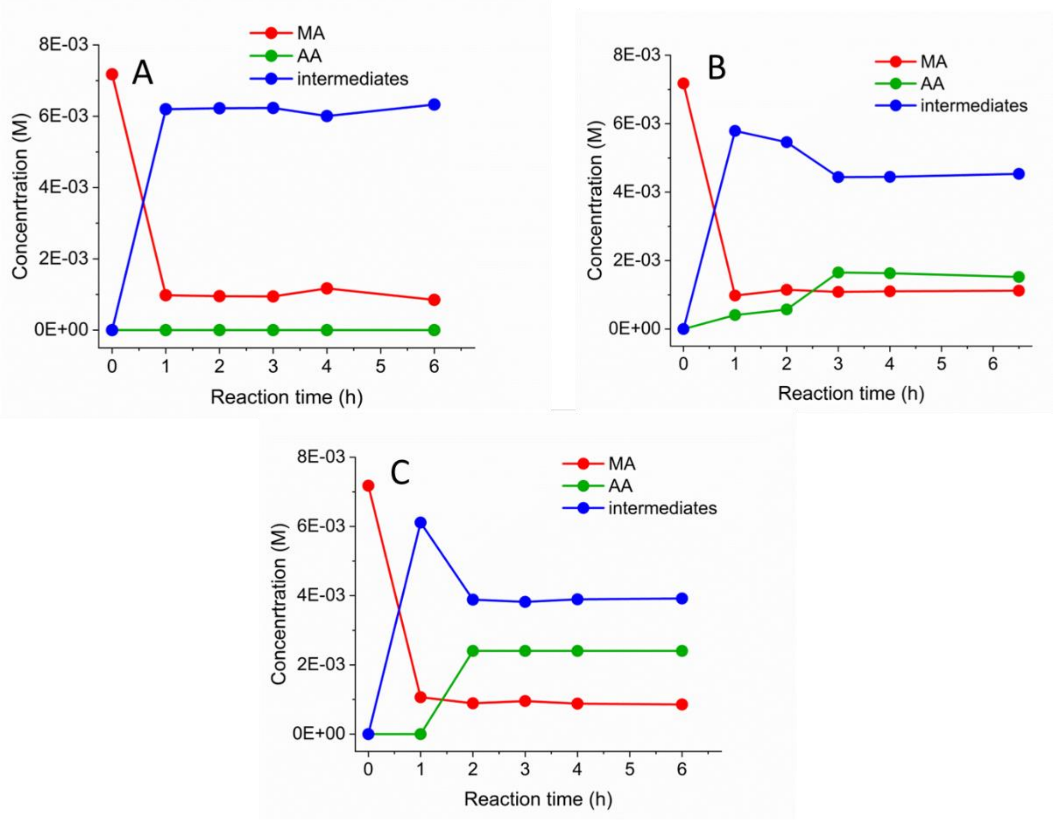

Figure 14: Activity of a) monometallic Pd, b) $Pd_{90}Rh_{10}$ and c) $Pd_{69}Rh_{31}$ catalysts in the muconic acid hydrogenation using formic acid as hydrogen donor.

4.3. Conclusions

A series of preformed colloidal Pd_xRh_y nanoparticles and the corresponding monometallic supported Pd and Rh nanoparticles were prepared by sol immobilization method and deposited on highly graphitized carbon nanofibers (HHT). Using this technique, it was reported for the first time, the ability to prepare preformed bimetallic random alloyed Pd-Rh nanoparticles with average particle size in the range of 2-4 nm even at low temperature as confirmed by STEM-HAADF and STEM-XEDS analyses. However, the composition of the particles is not homogeneous from particle to particle and a general enrichment in Pd was observed compared to the nominal Pd-Rh ratio. These results were attributed to the unsuccessful quantitative immobilization of Rh, as evidenced by ICP analysis. Bimetallic catalysts showed good activity in the dehydrogenation of formic acid in liquid phase, in particular for Pd-rich bimetallic systems ($Pd_{90}Rh_{10}$ and $Pd_{69}Rh_{31}$). Comparing the product analysis of liquid and gas phase products, we concluded that the major reaction pathway towards the production of CO_2 and H_2 was obtained for all the catalysts, with minor formation of CO in the range of 5-15 ppm. However, in the case of monometallic Pd, traces of CO (11-15 ppm) were observed. A good stability during 6 consecutive runs was observed for $Pd_{69}Rh_{31}$ compared to monometallic Pd which rapidly deactivate. The low stability of this latter one was attributed to the growing of particle size due to coalescence of the particle, partial Pd leaching and presence of CO which acts as poison for Pd-based catalysts. Furthermore, monometallic Pd, $Pd_{90}Rh_{10}$ and $Pd_{69}Rh_{31}$ were tested in the muconic acid hydrogenation using formic acid as hydrogen donor, under mild conditions. The catalysts showed good activity for the first step of the reaction, towards the production of monounsaturated products. Only in the case of using bimetallic catalysts the second step of the reaction towards the formation of adipic acid was enhanced.

4.4. References

[1]I. Barlocco, S. Capelli, E. Zanella, X. Chen, J. J. Delgado, A. Roldan, N. Dimitratos, A. Villa, *J. Energy Chem.* **2020**, *52*, 301–309.

[2] M. Besson, P. Gallezot, C. Pinel, *Chem. Rev.* **2014**, *114*, 1827–1870.

[3] T. Mallat, A. Baiker, *Chem. Rev.* **2004**, *104*, 3037–3058.

[4] D. A. Colby, R. G. Bergman, J. A. Ellman, *Chem. Rev.* **2010**, *110*, 624–655.

[5] G. W. Piburn, H. Li, P. Kunal, G. Henkelman, S. M. Humphrey, *ChemCatChem* **2018**, *10*, 329–333.

[6]W. Ye, S. Kou, X. Guo, F. Xie, H. Sun, H. Lu, J. Yang, *Nanoscale* **2015**, *7*, 9558–9562.

[7] L. Soler, A. Casanovas, J. Ryan, I. Angurell, C. Escudero, V. Pérez-Dieste, J. Llorca, *ACS Catal.* **2019**, *9*, 3641–3647.

[8] S. N. Tripathi, S. R. Bharadwqj, *J. Phase Equilibria* **1994**, *15*, 208–212.

[9] H. Noh, J. D. Clewley, T. B. Flanagan, A. P. Craft, *J. Alloys Compd.* **1996**, *240*, 235–248.

[10]H. Kobayashi, H. Morita, M. Yamauchi, R. Ikeda, H. Kitagawa, Y. Kubota, K. Kato, M. Takata, S. Toh, S. Matsumura, *J. Am. Chem. Soc.* **2012**, *134*, 12390–12393.

[11] J. Cho, S. Lee, S. P. Yoon, J. Han, S. W. Nam, K. Y. Lee, H. C. Ham, *ACS Catal.* **2017**, *7*, 2553–2562.

[12] L. Prati, A. Villa, *Acc. Chem. Res.* **2014**, *47*, 855–863.

[13] F. Sanchez, M. H. Alotaibi, D. Motta, C. E. Chan-Thaw, A. Rakotomahevitra, T. Tabanelli, A. Roldan, C. Hammond, Q. He, T. Davies, A. Villa, N. Dimitratos, *Sustain. Energy Fuels* **2018**, *2*, 2705–2716.

[14] J. P. Oppenheim, G. L. Dickerson, *Kirk-Othmer Encycl. Chem. Technol.* **2003**, DOI https://doi.org/10.1002/0471238961.0104091604012209.a01.pub2.

[15]C. Hu, J. K. Pulleri, S. W. Ting, K. Y. Chan, *Int. J. Hydrogen Energy* **2014**, *39*, 381–390.

[16] Ö. Metin, X. Sun, S. Sun, *Nanoscale* **2013**, *5*, 910–912.

[17] K. Tedsree, T. Li, S. Jones, C. W. A. Chan, K. M. K. Yu, P. A. J. Bagot, E. A. Marquis, G. D. W. Smith, S. C. E. Tsang, *Nat. Nanotechnol.* **2011**, *6*, 302–307.

[18] S. Zhang, Ö. Metin, D. Su, S. Sun, *Angew. Chemie - Int. Ed.* **2013**, *52*, 3681–3684.

[19] A. Bulut, M. Yurderi, Y. Karatas, M. Zahmakiran, H. Kivrak, M. Gulcan, M. Kaya, *Appl. Catal. B Environ.* **2015**, *164*, 324–333.

[20]V. Mazumder, M. Chi, M. N. Mankin, Y. Liu, Ö. Metin, D. Sun, K. L. More, S. Sun, *Nano Lett.* **2012**, *12*, 1102–1106.

[21]M. Yurderi, A. Bulut, M. Zahmakiran, M. Kaya, *Appl. Catal. B Environ.* **2014**, *160–161*, 514–524.

[22]K. Mori, H. Tanaka, M. Dojo, K. Yoshizawa, H. Yamashita, *Chem. – A Eur. J.* **2015**, *21*, 12085–12092.

[23] X. Zhou, Y. Huang, W. Xing, C. Liu, J. Liao, T. Lu, *Chem. Commun.* **2008**, 3540–3542.

[24]H. Sakai, T. Nakajima, N. Yoshida, S. Kishimoto, *React. Kinet. Catal. Lett.* **1982**, *19*, 297–301.

[25] H. Noh, T. B. Flanagan, B. Cerundolo, A. Craft, *Scr. Metall. Mater.* **1991**, *25*, 225–230.

[26] T. Beardslee, S. Picataggio, *Lipid Technol.* **2012**, *24*, 223–225.

[27] W. Niu, K. M. Draths, J. W. Frost, *Biotechnol. Prog.* **2002**, *18*, 201–211.

[28] D. R. Vardon, M. A. Franden, C. W. Johnson, E. M. Karp, M. T. Guarnieri, J. G. Linger, M. J. Salm, T. J. Strathmann, G. T. Beckham, *Energy Environ. Sci.* **2015**, *8*, 617–628.

[29] S. Capelli, D. Motta, C. Evangelisti, N. Dimitratos, L. Prati, C. Pirola, A. Villa, *ChemCatChem* **2019**, *11*, 3075–3084.

[30] S. Capelli, A. Rosengart, A. Villa, A. Citterio, A. Di Michele, C. L. Bianchi, L. Prati, C. Pirola, *Appl. Catal. B Environ.* **2017**, *218*, 220–229.

[31] S. Capelli, D. Motta, C. Evangelisti, N. Dimitratos, L. Prati, C. Pirola, A. Villa, *Nanomater.* **2020**, *10*, DOI 10.3390/nano10030505.

[32] J. E. Matthiesen, J. M. Carraher, M. Vasiliu, D. A. Dixon, J.-P. Tessonnier, *ACS Sustain. Chem. Eng.* **2016**, *4*, 3575–3585.

5. DISCLOSING THE ROLE OF GOLD ON PALLADIUM-GOLD ALLOYED SUPPORTED CATALYSTS IN FORMIC ACID DECOMPOSITION

The results discussed in this Chapter with the permission of John Wiley and Sons were previously reported in my work, published on *ChemCatChem* **2021**, *13*, 4210–4222 (https://doi.org/10.1002/cctc.202100886)[1].

5.1. Introduction

5.1.1. Palladium-gold alloys for formic acid decomposition reaction

In Sections 1.2.2.1. and 1.4.1.2, it has been shown that the introduction of a second metal, especially gold, can overcome the problems related with the stability and the selectivity of Pd-based catalysts in FAD reaction[2–4]. In particular, Xing et al.[5] have discovered that, unlike Pd/C catalyst, PdAu/C is able to inhibit the formation of CO, avoiding the problem of the poisoning. In addition, they found that an initial increasing in the amount of gold causes the strain effect, promoting lattice expansion. At higher Au/Pd ratios, the activity is controlled by the electronic effect, due to the electron transfer from Au to Pd[5]. Indeed, the optimized activity and stability is the result of a suitable balance between the internal lattice strain and the synergistic effects[6,7]. Furthermore, Li et al.[8] studied Pd_{55} and $Pd_xAu_{(55-x)}$ clusters via density functional theory (DFT). They discovered that gold can weakly bond atomic hydrogen leading to an easier hydrogen production on bimetallic catalysts. Yoon and co-workers[3] combined experimental and DFT techniques in order to disclose the synergistic and ensemble effects of gold in PdAu bimetallic catalysts. Different PdAu(111) modelled alloys were prepared and the importance of these two factors on the catalytic activity in FA decomposition (FAD) reaction was confirmed. Karatas et al.[9] have shown the enhanced stability of PdAu nanoparticles (NPs) against leaching and agglomeration when supported on MnO_x, providing a superior efficiency for the FA dehydrogenation reaction. Nevertheless, a detailed study on the interaction between PdAu clusters and carbonaceous surface is still missing. Moreover, the rationalization between the role of bulk and interfacial metal atoms in the catalytic activity in formic acid decomposition reaction has not been reached. Indeed, it is well known that the interaction between support and active phase is fundamental in the catalyst behaviour. Additionally, a detailed mechanistic investigation on the effect of the addition of gold to palladium not only on the activity, but also on selectivity and stability of these bimetallic catalysts was not reported yet.

5.1.2. Aim and objectives of the Chapter

In this chapter, to study the effect of Au on the activity, selectivity and stability of Pd based catalysts, a combination of DFT and experimental studies was employed. 15 atoms clusters of Pd, Au and PdAu were modelled on a graphene surface from the bulk and superficial analyses results obtained, in order to precisely establish the principles of their performance. Therefore, experimental and theoretical details on the enhanced catalytic performance of PdAu bimetallic catalysts in the FAD process under mild reaction conditions are reported. Activity, selectivity and stability tests were done using Pd-Au bimetallic catalysts with different Pd/Au molar ratios supported on high heat treated (HHT) carbon nanofibers. The combination of simulations and experiments permitted us to disclose the beneficial effect of the second metal concerning the superior activity, selectivity and stability of the bimetallic systems.

5.2. Results

As previously reported by Barlocco and co-workers[1], bimetallic catalysts with different Pd:Au molar ratio and their monometallic counterparts were prepared via sol-immobilization technique, using PVA as capping agent and $NaBH_4$ as reducing agent. Fresh and used catalysts were then characterized employing transmission electron microscopy (TEM) and X-ray photoelectron spectroscopy (XPS) in order to establish a correlation between the morphology of the materials and their catalytic activity.

5.2.1. Catalyst characterisation

5.2.1.1. TEM-STEM results

TEM analyses were performed in order to investigate the structures of the materials, i.e. average particle size, particle size distribution and bulk gold-palladium atomic ratio. Monometallic (1%Pd@HHT and 1%Au@HHT) and bimetallic (1%Pd_xAu_y@HHT) catalysts were characterized at the sub-nanometric scale by TEM. 1%Pd@HHT shows an average particle size of 3.9 nm (Table 1)[10]. All bimetallic catalysts appear to have a similar average particle size, between 2.9 and 4 nm (Table 1), with a narrow particle size distribution (Figure 1 b to Figure 4 b). Figure 1 to Figure 4 show the representative results of STEM and EDX analysis on the single NPs for Pd_xAu_y bimetallic systems. The NPs are well dispersed on the support. By STEM-EDS spectrum imaging, we evaluated the amount of Pd and Au on individual metal NPs and observed a good agreement between the nominal and the actual atomic ratio for all the bimetallic catalysts, except for Pd_2Au_8 catalyst (Table 1). For this catalyst, the Au/Pd atomic ratio calculated by EDX is higher than the nominal one, in fact, Au/Pd_{EDX} (8.70/1.30) ratio is equal to 6.69 while Au/Pd_{nom} (8/2) corresponds to 4 (Table 1, row 6). This discrepancy can be attributed to the presence of some segregated palladium nanoparticles. STEM-HAADF images and STEM-EDS maps of single nanoparticles suggested that the catalysts consist in Au-Pd alloyed systems (Figure 1 to Figure 4).

Table 1: Results of TEM-EDX analysis.

Catalyst	*Nominal Pd:Au molar ratio*	*Pd:Au molar ratio (EDX-TEM)*	*Au/Pd_{nom}*	*Au/Pd_{EDX}*	*Average particle size (nm)*
Pd	-	-	-	-	3.9 ± 1.2
Pd_8Au_2	8.00 : 2.00	8.35 : 1.65	0.25	0.20	3.5 ± 0.9
Pd_6Au_4	6.00 : 4.00	5.86 : 4.14	0.67	0.71	2.9 ± 0.7
Pd_4Au_6	4.00 : 6.00	4.46 : 5.54	1.50	1.24	4.0 ± 0.8
Pd_2Au_8	2.00 : 8.00	1.30 : 8.70	4.00	6.69	3.1 ± 0.6
Au	-	-			3.4 ± 1.2
Pd_8Au_2 used	8.00 : 2.00	8.06 : 1.94	0.25	0.24	3.9 ± 1.1
Pd_6Au_4 used	6.00 : 4.00	5.83 : 4.17	0.67	0.70	3.1 ± 0.8

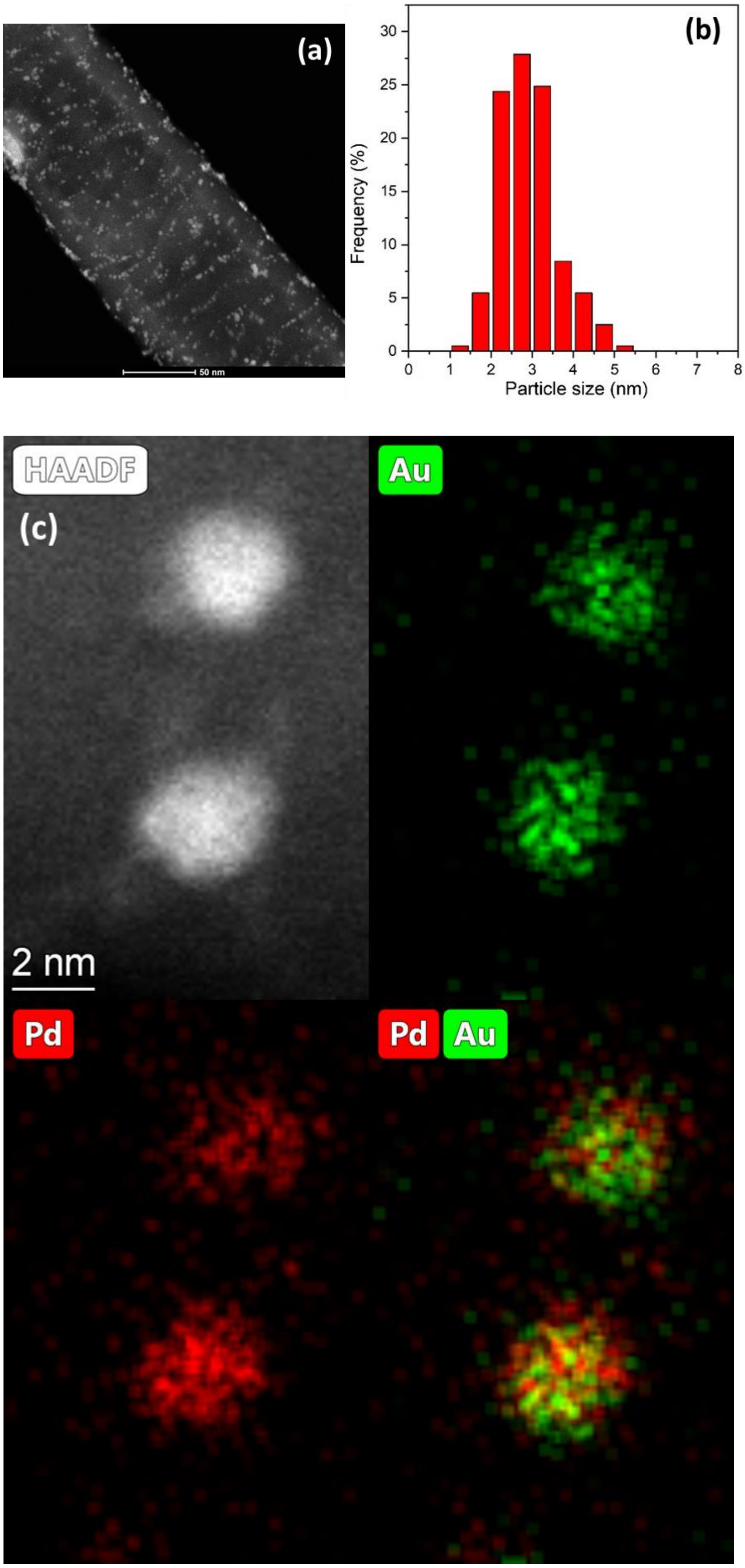

Figure 1: a) STEM-HAADF image of 1%Pd_6Au_4@HHT catalyst, b) particle size distribution and c) STEM-EDS maps of single nanoparticles.

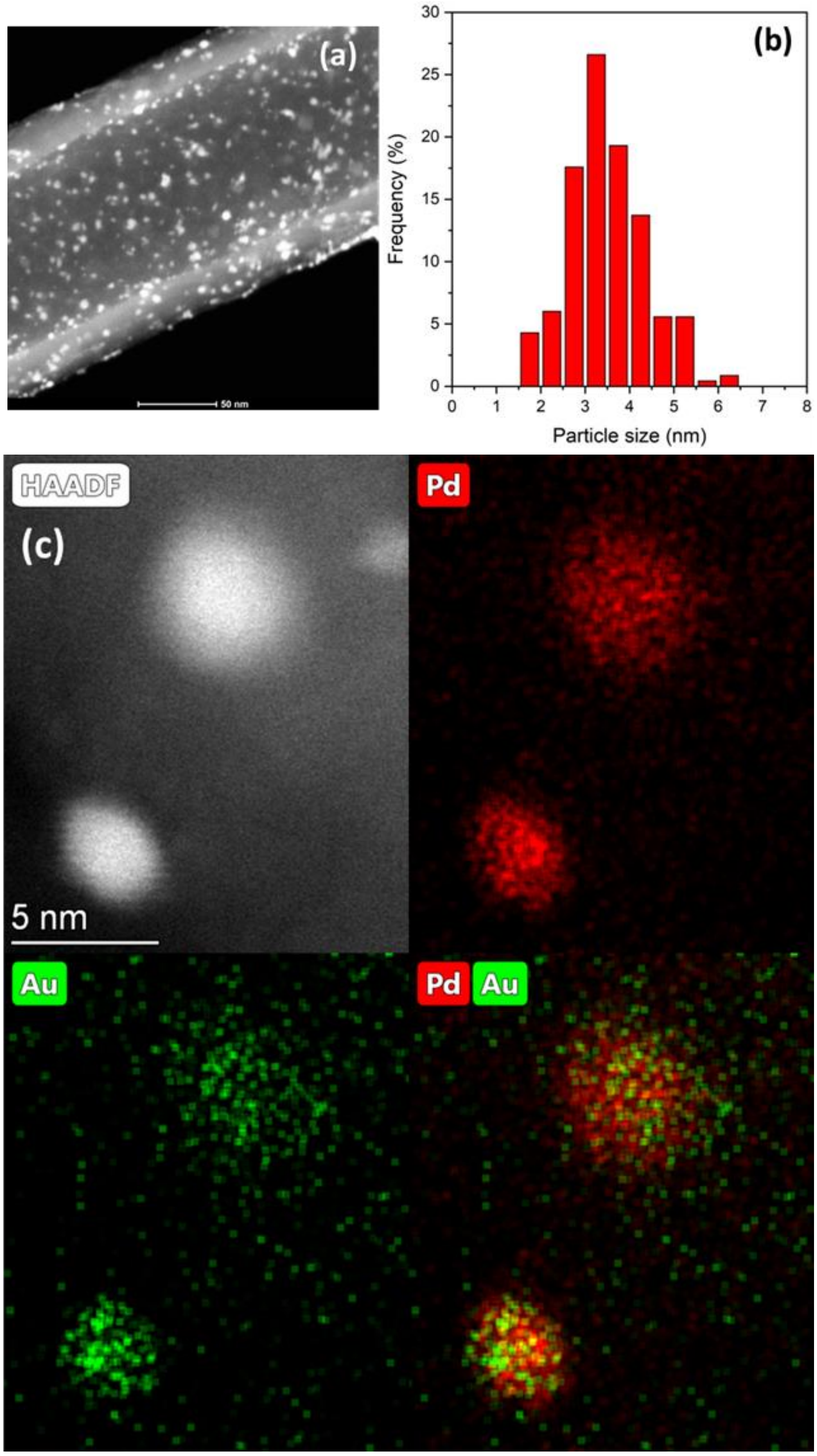

Figure 2: a) STEM-HAADF image of 1%Pd_8Au_2@HHT catalyst, b) particle size distribution and c) STEM-EDS maps of single nanoparticles.

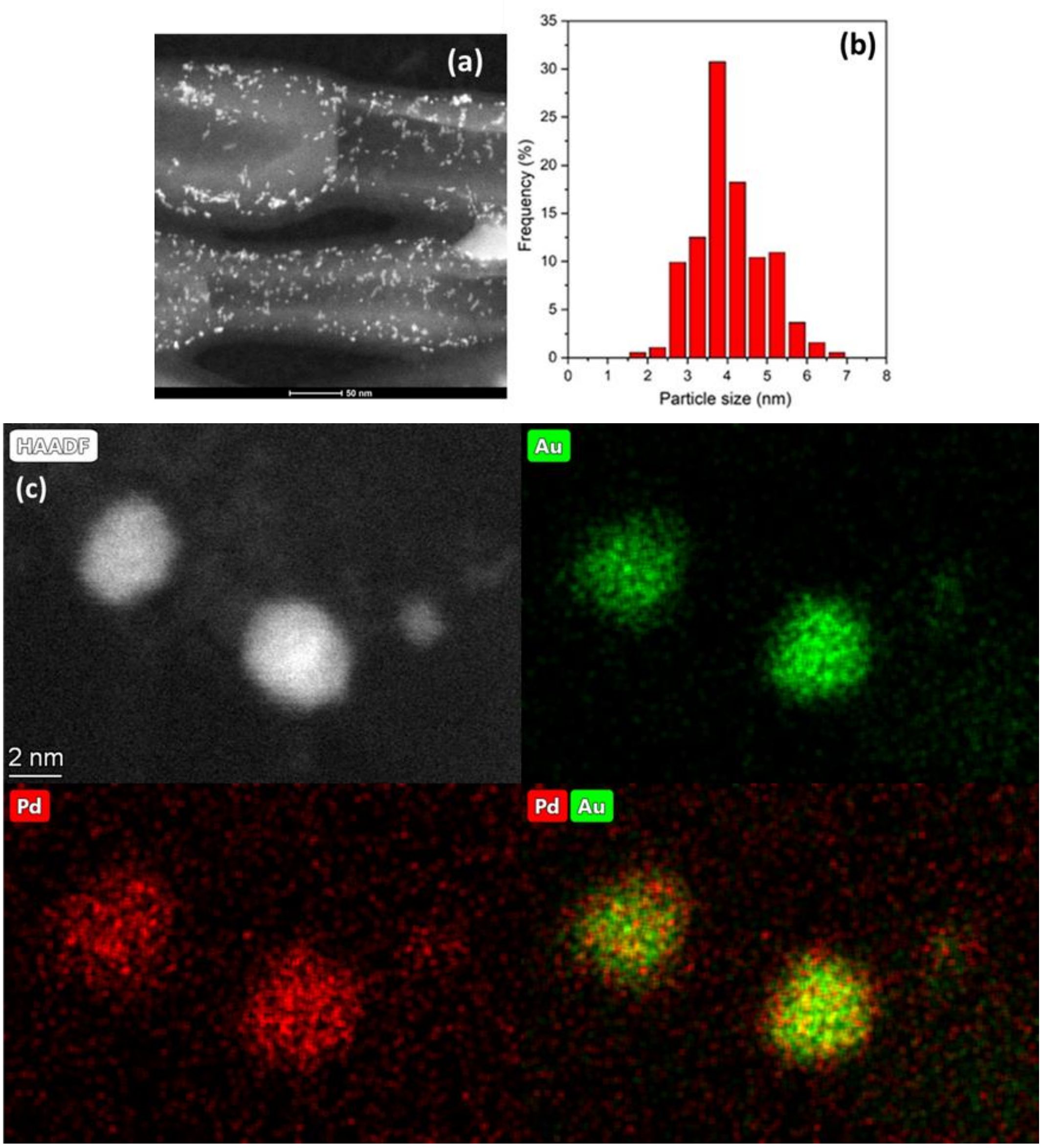

Figure 3: a) STEM-HAADF image of 1%Pd_4Au_6@HHT catalyst, b) particle size distribution and c) STEM-EDS maps of single nanoparticles.

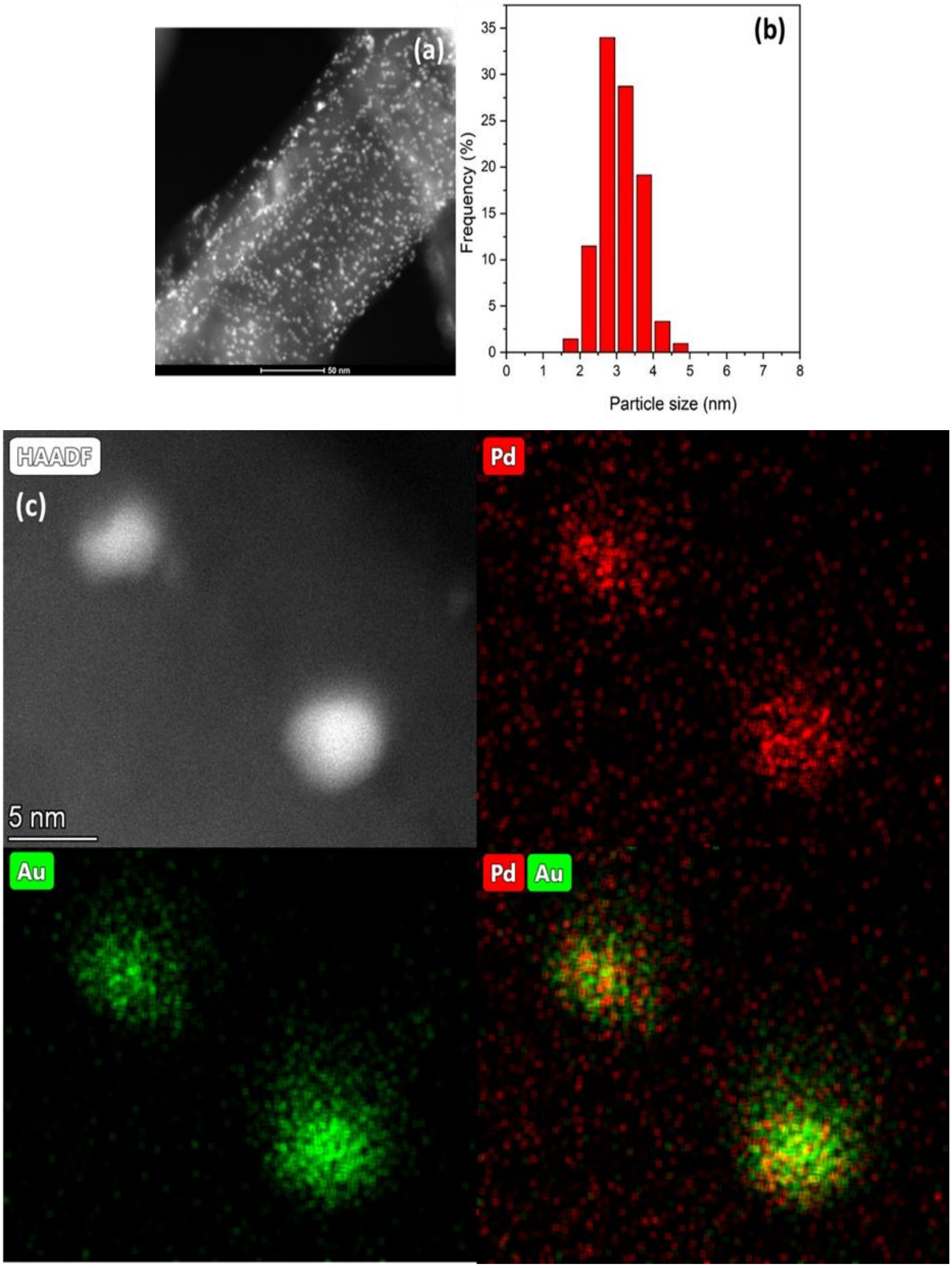

Figure 4: a) STEM-HAADF image of 1%Pd_2Au_8@HHT catalyst, b) particle size distribution and c) STEM-EDS maps of single nanoparticles.

5.2.1.2. XPS results

In order to obtain information of the surface composition (e.g., oxidation state, superficial atomicity, and exposed gold-palladium ratio), X-ray photoelectron spectroscopy was performed. From the survey spectra obtained by XPS analysis, we detected 4 main species: C 1s (284.24-284.59 eV), O 1s (532.24-32.59 eV), Au 4f (83.31-84.24 eV), and Pd 3d (335.40-337.59 eV). The Au/Pd surface atomic ratio measured by XPS is lower than the corresponding bulk Au/Pd measured by EDX, which may suggest surface enrichment of Pd atoms on the bimetallic nanoparticles (Table 2). This outcome confirms the result obtained using TEM analysis, which previously shows an enrichment of Pd on the surface.

The high-resolution spectra of Au 4f (Figure 5) and Pd 3d (Figure 6) were deconvoluted. Au 4f shows two main species, which were assigned to Au^0 and $Au^{\delta+}$. The peaks at 84.11-84.32 eV and 85.30-85.62 eV were ascribed to Au^0 and $Au^{\delta+}$, respectively (Table 3, Column 3 and 4). The higher is the amount of Pd used during the catalyst synthesis, the lower is the amount of Au^0. This phenomenon can be attributed to the transfer of electron from gold to palladium, as it has been shown in reference[11]. In particular, the higher the amount of gold, the higher the Au^0 amount meaning a transfer of electron from gold to palladium. In the high-resolution spectra of Pd 3d, three different peaks were detected. Two main species were identified: Pd^0 and Pd^{II} in a B.E. range of 335.50-336.70 eV and 337.00-338.60 eV, respectively. Moreover, a satellite peak of Pd was found between 342.30 eV and 348.11 eV. From the relative area value of the Pd species the Pd^0/Pd^{II} ratio was calculated (Table 3, Column 10). Furthermore, a decrease in the binding energy of the Pd^0 peak (ΔB.E. between 1.1 -1.2 eV) in bimetallic catalysts was observed. This modification of B.E. can be attributed to an electronic interaction between the two metals, in particular to a donation of electron from gold to palladium[11].

Table 2: Results of survey spectra.

Sample		*C1s*	*O1s*	*Au4f*	*Pd3d*	*Au/Pd_{nom}*	*Au/Pd_{XPS}*	*Au/Pd_{EDX}*
Pd	BE	284.59	532.50	-	337.6	-	-	-
	Atom %	*92.12*	*7.24*	-	*0.57*			
Pd_8Au_2	BE	284.24	532.24	84.24	336.2	0.25	0.11	0.20
	Atom %	*91.18*	*7.30*	*0.14*	*1.31*			
Pd_6Au_4	BE	284.40	532.40	83.40	335.4	0.67	0.60	0.71
	Atom %	*95.50*	*3.50*	*0.39*	*0.65*			
Pd_4Au_6	BE	284.32	532.32	84.32	335.5	1.50	1.07	1.24
	Atom %	*96.20*	*3.10*	*0.32*	*0.30*			
Pd_2Au_8	BE	284.50	532.50	83.50	335.5	4.00	2.86	6.69
	Atom %	*98.33*	*1.40*	*0.20*	*0.07*			
Au	BE	284.31	532.31	83.31	-	-	-	-
	Atom %	*97.80*	*2.10*	*0.10*	-			
Pd_8Au_2 used	BE	284.30	532.30	83.30	337.3	0.25	0.13	0.24
	Atom %	*94.97*	*4.85*	*0.02*	*0.16*			
Pd_6Au_4 used	BE	285.51	532.51	83.51	335.5	0.67	0.50	0.70
	Atom %	*97.29*	*2.47*	*0.08*	*0.16*			

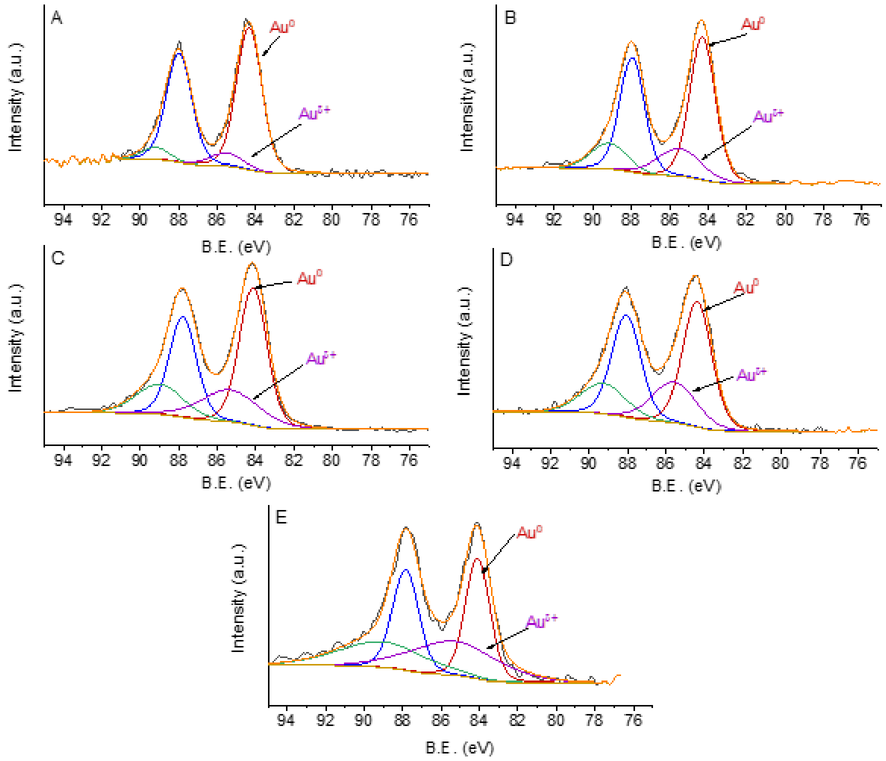

Figure 5: HR spectra of Au 4f of A) Au@HHT, B) Pd_2Au_8@HHT, C) Pd_4Au_6@HHT, D) Pd_6Au_4@HHT and E) Pd_8Au_2@HHT.

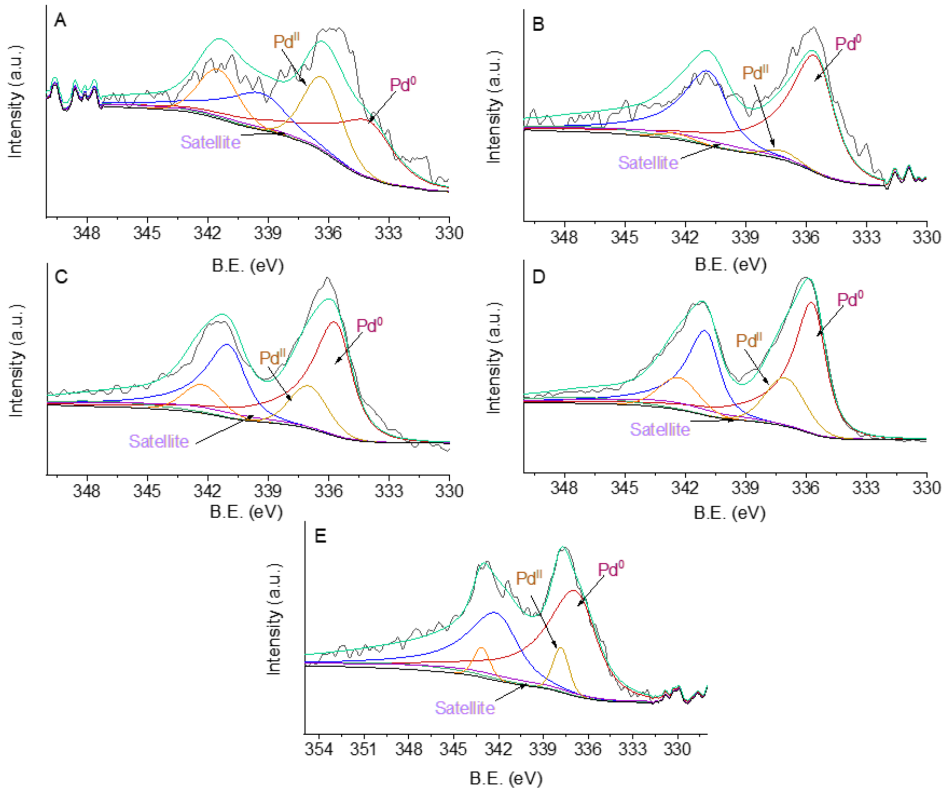

Figure 6: HR spectra of Pd 3d of A) Pd_2Au_8@HHT, B) Pd_4Au_6@HHT, C) Pd_6Au_4@HHT, D) Pd_8Au_2@HHT and E) Pd@HHT.

Table 3: Results of high resolution XPS spectra.

		Au 4f			**Pd 3d**			
Sample		*Au^0*	*$Au^{\delta+}$*	*$Au^0/Au^{\delta+}$*	*Pd^0*	*Pd^{II}*	*Pd_{Sat}*	*Pd^0/Pd^{II}*
Pd	BE	-	-	-	336.70	337.80	348.11	10.16
	Atom %	-	-		*80.68*	*7.94*	*11.38*	
Pd_8Au_2	BE	84.11	85.31	1.03	335.60	337.10	347.10	3.14
	Atom %	*50.77*	*49.23*		*68.52*	*21.82*	*9.66*	
Pd_6Au_4	BE	84.32	85.62	2.11	335.60	337.00	342.50	3.57
	Atom %	*67.80*	32.20		*67.05*	*18.77*	*14.18*	
Pd_4Au_6	BE	84.15	85.30	2.09	335.50	337.20	342.30	4.75
	Atom %	*67.66*	*32.34*		*79.99*	*16.84*	*3.17*	
Pd_2Au_8	BE	84.21	85.45	3.17	335.50	337.20	342.30	2.10
	Atom %	*76.04*	*23.96*		*61.85*	*29.43*	*8.71*	
Au	BE	84.22	85.60	9.10	-	-	-	-
	Atom %	*90.10*	*9.90*		-	-	-	
Pd_8Au_2 used	BE	83.84	85.04	1.36	335.68	338.00	347.03	2.46
	Atom %	*57.57*	*42.43*		*64.60*	*26.29*	*9.11*	
Pd_6Au_4 used	BE	84.12	85.31	1.78	335.29	337.00	342.14	5.74
	Atom %	*64.04*	*35.96*		*76.03*	*13.26*	*10.71*	

5.2.2. Catalytic activity

The catalytic performance of PdAu bimetallic catalysts were tested for the FAD reaction, a model reaction for hydrogen generation. The optimized conditions are 30 °C and 1400 rpm using a solution 0.5 M of FA in water and a FA/metal molar ratio of 2000/1. Reaction conditions (metal:substrate ratio, stirring rate) are optimized in order to assess the kinetic regime of the reaction[12]. In Figure 7, the catalytic activity at different Pd-Au atomic ratio is shown. The activity is calculated as mol of FA reacted on total mol of metal (Au+Pd) per hour (considering the conversion at 5 minutes of reaction).

Monometallic Au exhibited an extremely low activity in FA decomposition (633 h^{-1}) confirming the results of Z. Zhao et al.[13], while monometallic 1%Pd@HHT showed an activity of 979 h^{-1}. All the bimetallic catalysts displayed an activity superior to the two monometallic counterparts, except for 1%Pd_2Au_8@HHT (878 h^{-1}). The highest initial activity was observed for 1%Pd_6Au_4@HHT (3539 h^{-1}) followed by 1%Pd_4Au_6@HHT (1983 h^{-1}) and 1%Pd_8Au_2@HHT (1502 h^{-1}). Correlating the initial activity and Au:Pd ratio calculated from XPS and TEM-EDX analyses, we were able to correlate the surface properties of the catalysts with their catalytic behaviour. A Volcano plot was obtained from such correlation for exposed and bulk Pd (Table 2 and Figure 7). Furthermore, the activity increases with the amount of Au until a maximum for 1%Pd_6Au_4@HHT. It was reported in the literature that a PdAu alloy with this metal atomic ratio possesses a perfect balance between the lattice and the ligand effect[4,5]. In addition, these four catalysts showed an activity for this reaction higher than most of the catalysts present in the literature (Table 4).

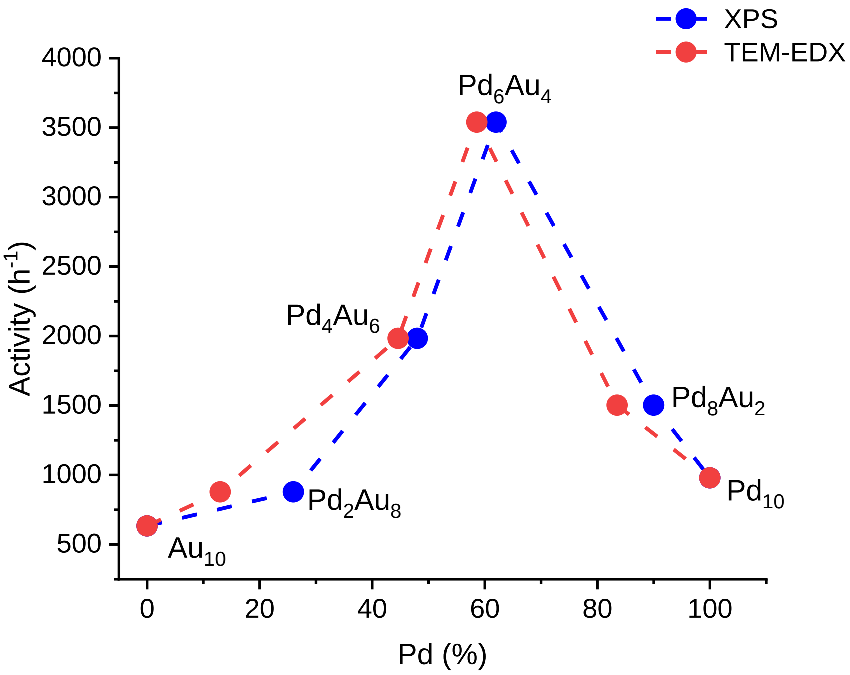

Figure 74: Dependence of the FAD initial activity on the different Pd:Au atomic ratio calculated from XPS (exposed, blue) and TEM-EDX (bulk, red) analyses.

Table 4: Comparison of the activity of different Pd-based bimetallic catalysts.

Catalyst	*T (°C)*	*Reagent*	*TOF (h^{-1})*		*Ref.*
			Initial	2 h	
Pd_6Au_4/HHT	30	Formic acid (0.5 M)	3539		This work
Pd_4Au_6/HHT	30	Formic acid (0.5 M)	1983		This work
Pd_8Au_2/HHT	30	Formic acid (0.5 M)	1502		
Pd/HHT	30	Formic acid (0.5 M)	979		This work
Pd/C	21	Formic acid (1.33 M)	18	15	[14]
	30		48	28	
$Au_{41}Pd_{59}$/C	50	Formic acid (1 M)	230		[15]
Ag@Pd (1:1)	35	Formic acid		156	[16]
Ag/Pd alloy (1:1)	20			144	[16]
$Ag_{42}Pd_{58}$	50	Formic acid (1 M)	382		[17]
Pd-MnO_x/SiO_2-NH_2	20	Formic acid (0.265 M)	140		[18]
	50		1300		
$Ag_{0.1}Pd_{0.9}$/rGO	25	Formic acid	105		[19]
PdNiAg/C	50	Formic acid (0.175 M)	85		[20]
$Pd_{50}Cu_{50}$/resin	75	HCOOH/HCOONa=9:1	810		[21]
20 wt% PdAu/C–CeO_2	102	9.94 M formic acid–3.33 M sodium formate solution	832		[22]
300 sc% Pd-on-Au/C	23	Formic acid (1 M)	123		[13]
$Pd_{90}Rh_{10}$/HHT	30	Formic acid (0.5 M)	1793		[23]
$Pd_{69}Rh_{31}$/HHT	30	Formic acid (0.5 M)	921		[23]
Au_2Pd_3@(P)N-C	30	Formic acid	5400		[3]

Considering the FA conversion at 2 h of reaction, 1%Pd_4Au_6@HHT exhibited the best performance after 2 h of reaction (FAD of 73%), while Au the worst one (FAD <10%) (Figure 8). Despite the initial activity of 1%Pd_8Au_2@HHT was about 2.5 times lower than the one of 1%Pd_4Au_6@HHT, these two catalysts showed a similar conversion from 30 min of reaction and 1%Pd_8Au_2@HHT reached a FAD conversion of 68%.

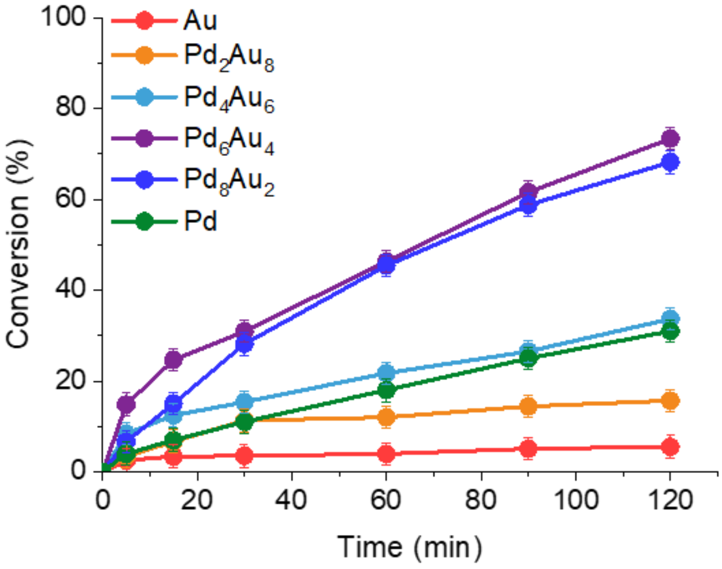

Figure 8: Conversion as a function of reaction time of the different 1%Pd_xAu_y@HHT catalysts for the liquid phase dehydrogenation reaction of FA under mild conditions.

In order to determine the selectivity of the reaction, the gas phase was analysed connecting the reactor with an on-line micro-GC to evaluate the CO/CO_2 ratio. The product detected in the gas phase at 2 h of reaction for the alloyed bimetallic catalysts was only CO_2 without the presence of CO, showing a selectivity >99% for H_2, while 1%Pd@HHT catalyst exhibited 77% selectivity to this product. The high selectivity of the systems can permit the application of the considered bimetallic catalysts in hydrogen fuel cell. Indeed, carbon monoxide is the main issue for the development of this technology and it has to be lower than 10 ppm[24].

An extremely important feature of a catalyst is the durability to be industrially attractive. For this reason, stability tests were performed on catalysts that showed the best conversion at 2 h (1%Pd_6Au_4@HHT and 1%Pd_8Au_2@HHT). The obtained results were compared with the monometallic palladium (Figure 9). Recycling tests were performed by filtering the catalyst without any further treatment. According to previous studies, palladium catalyst quickly deactivates after the first run (Figure 9 a)[25]. This deactivation is probably due to coalescence and agglomeration of the particles, in fact the average particle size increase from 3.0 to 4.7 nm. In addition, the poor selectivity of the monometallic Pd catalysts generated CO thus poisoning the Pd active sites[26,27]. On the contrary, the catalysts that show the highest conversion at 2 h, i.e. 1%Pd_6Au_4@HHT and 1%Pd_8Au_2@HHT, exhibit a good stability up to 6 cycles of reaction (Figure 9 b-c). The initial increase in the conversion trend can be due to the partial removal of PVA used during NPs synthesis, which can block some active sites[28], or the partial reduction of oxidized Pd, present in the fresh catalyst, during the reaction (Table 3). Moreover, GC analyses showed that also selectivity remained constant.

To elucidate the reasons for the enhanced stability observed for the bimetallic catalysts, STEM analysis performed on the used 1%Pd_8Au_2@HHT and 1%Pd_6Au_4@HHT (Figure 10 and Figure 11) did not show significant modifications of the catalyst morphology. The 1%Pd_8Au_2@HHT fresh catalyst has a mean particle size of 3.5 nm, while the used one 3.9 nm. The analysis performed on 1%Pd_6Au_4@HHT shows a mild increment of particle size from 2.9 to 3.1 nm for the fresh and used catalysts, respectively (Figure 10). Moreover, comparing the Au/Pd atomic ratio of fresh and use catalyst (Table 2, row 5-6 and 8-9), no substantial changes were observed hence, confirming the results in stability and selectivity over more runs.

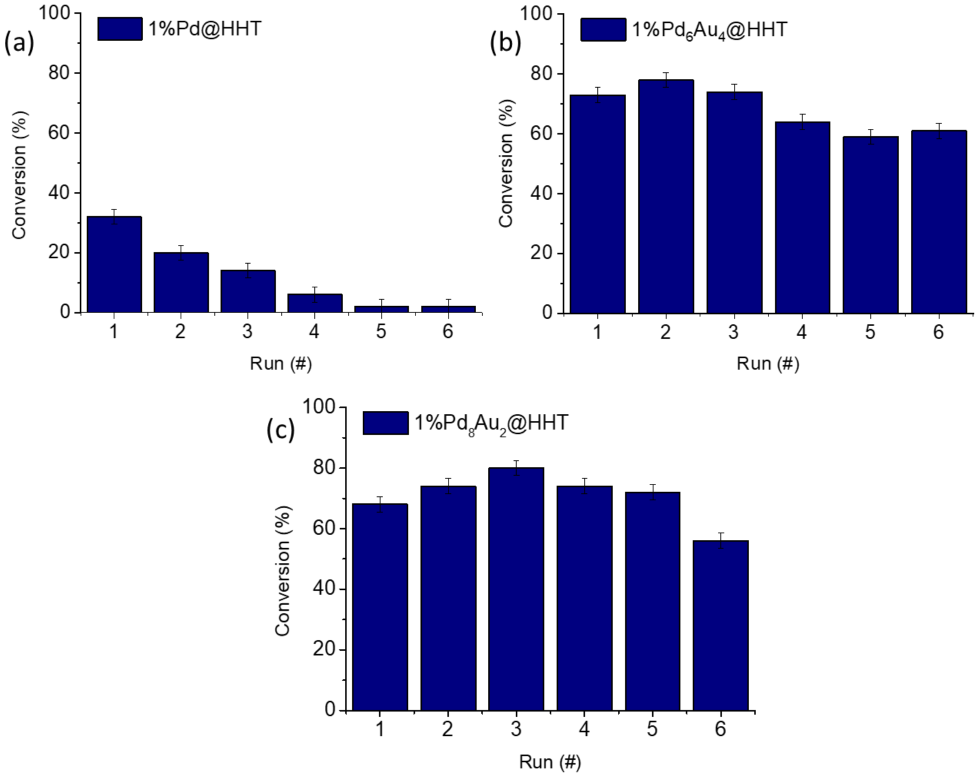

Figure 9: Recycling tests a) monometallic 1%Pd@HHT b) $1\%Pd_6Au_4$@HHT c) $1\%Pd_8Au_2$@HHT.

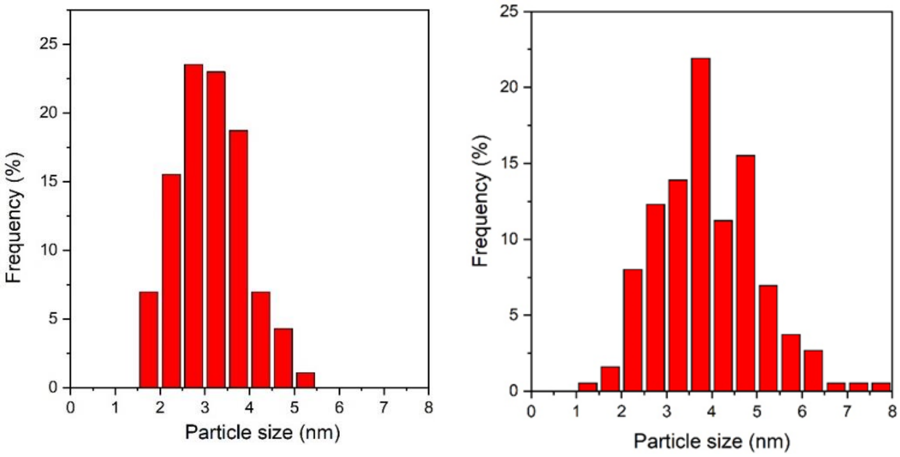

Figure 10: Average particle size distribution of a) used $1\%Pd_6Au_4$@HHT and b) used $1\%Pd_8Au_2$@HHT.

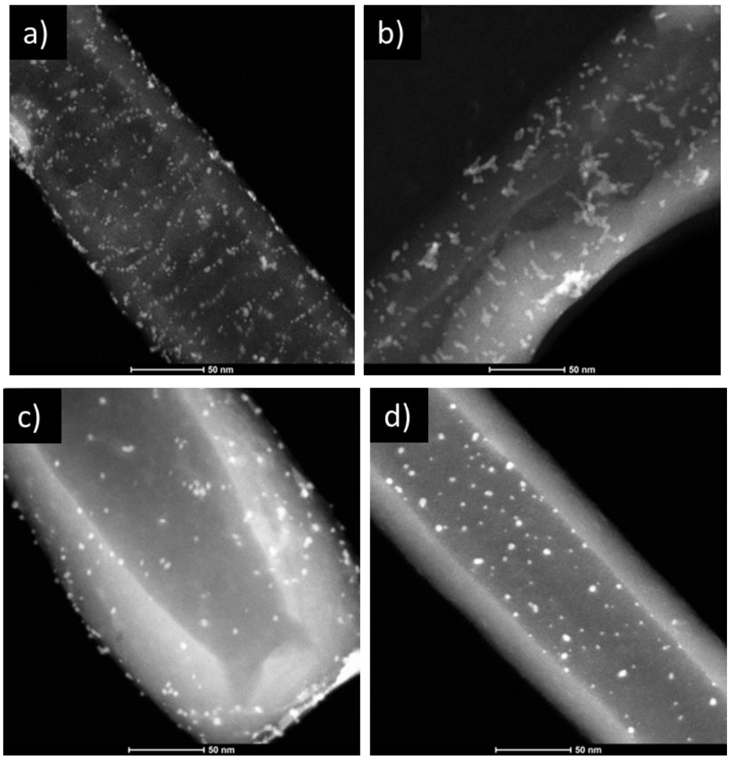

Figure 11: STEM-HAADF images of a) 1%Pd_6Au_4@HHT fresh b) 1%Pd_6Au_4@HHT used c) 1%Pd_8Au_2@HHT fresh and d) 1%Pd_8Au_2@HHT used.

5.2.3. DFT study

DFT studies were performed in order to elucidate the superior resistance to sinter and catalytic behaviour of our bimetallic catalysts compared to the monometallic ones (activity and selectivity towards H_2). For this reason, two monometallic (Au_{15}, Pd_{15}; Figure 12 a-b) and one bimetallic (Pd_9Au_6; Figure 12 c) clusters on graphitic surfaces were optimized. Pd_9Au_6 is equivalent in Au/Pd atomic ratio of the most promising catalyst, Pd_6Au_4 in line with the results obtained from TEM-EDX analyses. Nanoparticles are dynamic systems that rapidly change their local atomic structure, chemical state and crystallinity under operating condition[29–32]. We considered clusters' reconstruction energies in both initial (FA adsorption) and final (products desorption) steps to ensure comparability between the energy profiles. Indeed, small NPs are fluxionable[33] and present a relatively large number of low-energy-lying configurations interconvertible under the reaction conditions considered[34].

In order to select the most active site for FA adsorption, CO was selected as a probe molecule. CO is a non-desirable intermediate in the HCOOH decomposition mechanism and therefore, simulations will inform the worst-case scenario, i.e., active sites avid for CO adsorption. We adopted this approach to avoid undertaking reaction mechanisms simulations on all possible sites. Instead, carbon monoxide was brought to all non-equivalent adsorption sites on the clusters and the whole system was relaxed. Carbon monoxide prefers bonding on the metal atoms rather than at the interface between the cluster and the support. This may be attributed to the interaction of the O-lone pair electrons with the inactive π-conjugation of the support[35]. Then, formic acid was brought and relaxed on the most favorable CO adsorption site with diverse orientations. We selected the most stable adsorption configurations of each structure to perform the subsequent FA decomposition reaction steps. Every elementary step was analysed, resulting in the energy profile in Figure 13. Au is not able to chemically bind FA, in accordance with the poor catalytic activity showed in our experimental results (Figure 7 and Figure 8), therefore it is not included in Figure 13.

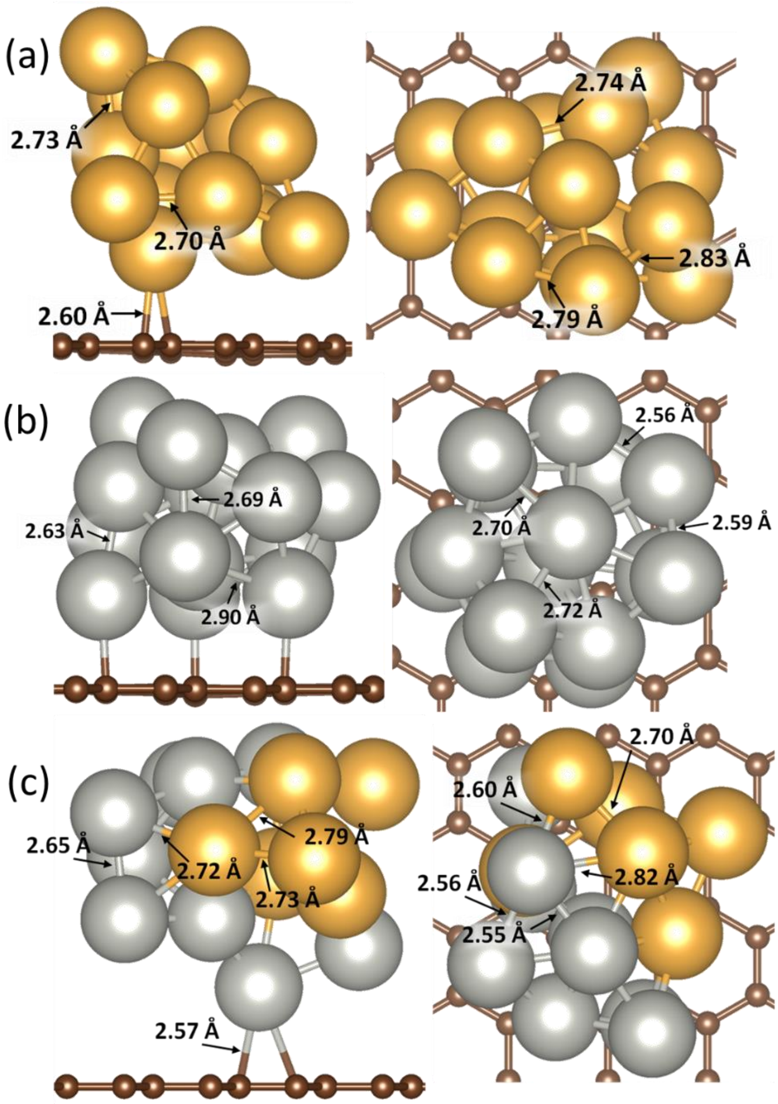

Figure 12: Side and top views of (a) Au_{15} optimized cluster, (b) Pd_{15} optimized cluster and (c) Pd_9Au_6 optimized cluster. Inset shows the distances (Å) of interest. Carbon atoms are represented in brown, gold atoms in gold and palladium in silver.

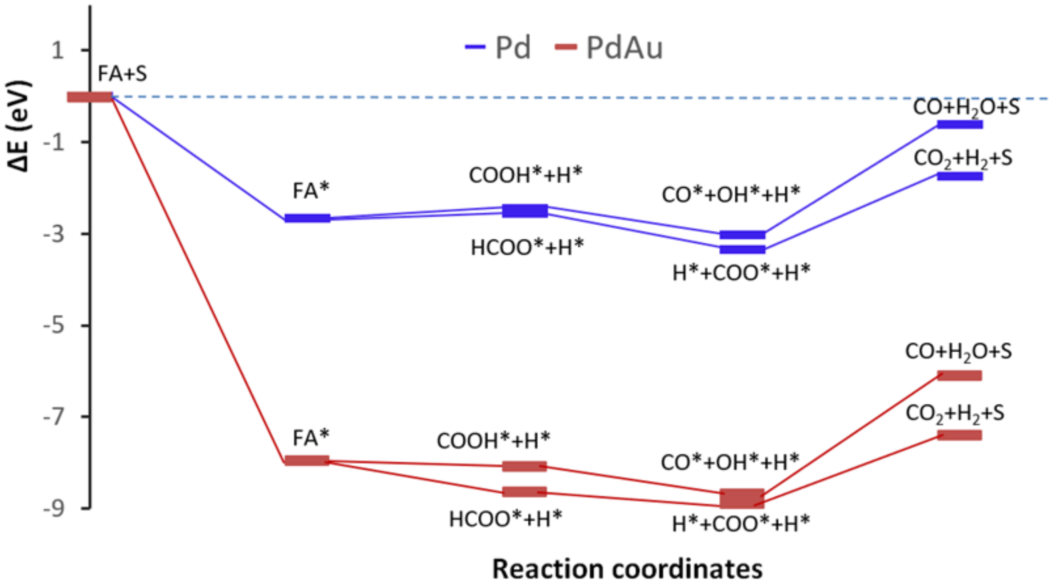

Figure 13: Energy profile for the different pathways of formic acid decomposition on Pd$_{15}$ (blue) and Pd$_9$Au$_6$ (red) clusters. The energy of the initial state FA + S was calculated as the energy of the initial cluster structure (S) and the energy of formic acid (FA) isolated. Final state S is the reconstructed structure. The final S can reconstruct to the initial S spontaneously. * indicates the adsorbed species.

The adsorption of FA is exothermic for both Pd and Pd$_9$Au$_6$, showing a total energy (E$_{tot}$) of -2.669 and -7.935 eV, respectively (Figure 14 a and 12 a). These values can be divided into two different contributions: the first one derives from the reconstruction of the metal atoms during the interaction of the NP with FA (E$_{Rec}$), while the second one describes the adsorption of the substrate (E$_{Ads}$) on the reconstructed cluster. The extremely negative value of energy found for Pd$_9$Au$_6$ was mainly due to the NP reconstruction upon FA adsorption, where the metal atoms reached a more stable conformation (E$_{Rec}$= -6.775 eV). A different behaviour was found for monometallic Pd. The contributions of the reconstruction energy and the adsorption energy are similar (E$_{Rec}$= -1.043 eV). This ability of the bimetallic NP to stabilize FA can also explain the superior reactivity and durability of the bimetallic catalysts, in particular, the 1%Pd$_6$Au$_4$@HHT catalyst showed in the experimental results, i.e. activity of 3539 h^{-1}, conversion of 73% after 2h and an excellent stability over 6 runs of reaction.

Following the Pd pathway, two different intermediates can be observed. The first and less stable one is obtained from the cleavage of C-H bond forming COOH* intermediate (E$_R$=0.208 eV, Figure 14 b), while the second intermediate, HCOO*, shows an E$_R$ of 0.112 eV (Figure 14 d). The two intermediates can now decompose following two different pathways forming carbon dioxide and hydrogen or leading to co-adsorbed carbon monoxide and hydroxyl. Both pathways are exothermic, although the formation of carbon dioxide is favoured by an E$_R$ of -0.791 eV (Figure 14 e) that is 0.227 eV lower than the second path (Figure 14 c). These competitive pathways confirm the presence of both carbon monoxide and carbon dioxide observed in the experimental tests.

The formation of HCOO* and COOH* intermediates on Pd_9Au_6 is exothermic (-0.688 eV and -0.128 eV, respectively; Figure 15 b-d). We also observe that the most stable species is also HCOO* but, on this catalyst, the difference with COOH* is 0.560 eV, which already eases the competition towards HCOO*. Considering again both possible pathways in the following decomposition step, the favourite route is the formation of carbon dioxide and atomic hydrogen adsorbed on the surface (E_R=-0.271 eV, Figure 15 e) differing from the undesired pathway of 0.230 eV (Figure 15 c). The releasing of the molecular species from the surface of the catalyst is for both pathways endothermic but, in the case of carbon dioxide and hydrogen the energy barrier is lower (E_B=1.511 eV), whereas for carbon monoxide and water the energy gap to overcome is 2.582 eV. The energy difference between the preferred CO_2 path and the one forming CO explains the selectivity between monometallic Pd catalyst and the bimetallic Pd_9Au_6 systems. This result is in agreement with the DFT study of J. Cho et al. where the importance of the second metal effect in a core shell structure is highlighted. It was claimed that adding a second metal, such as Au, as core of a core-shell Pd structure can enhance the rate of this reaction and also suppress the dehydration pathway[2].

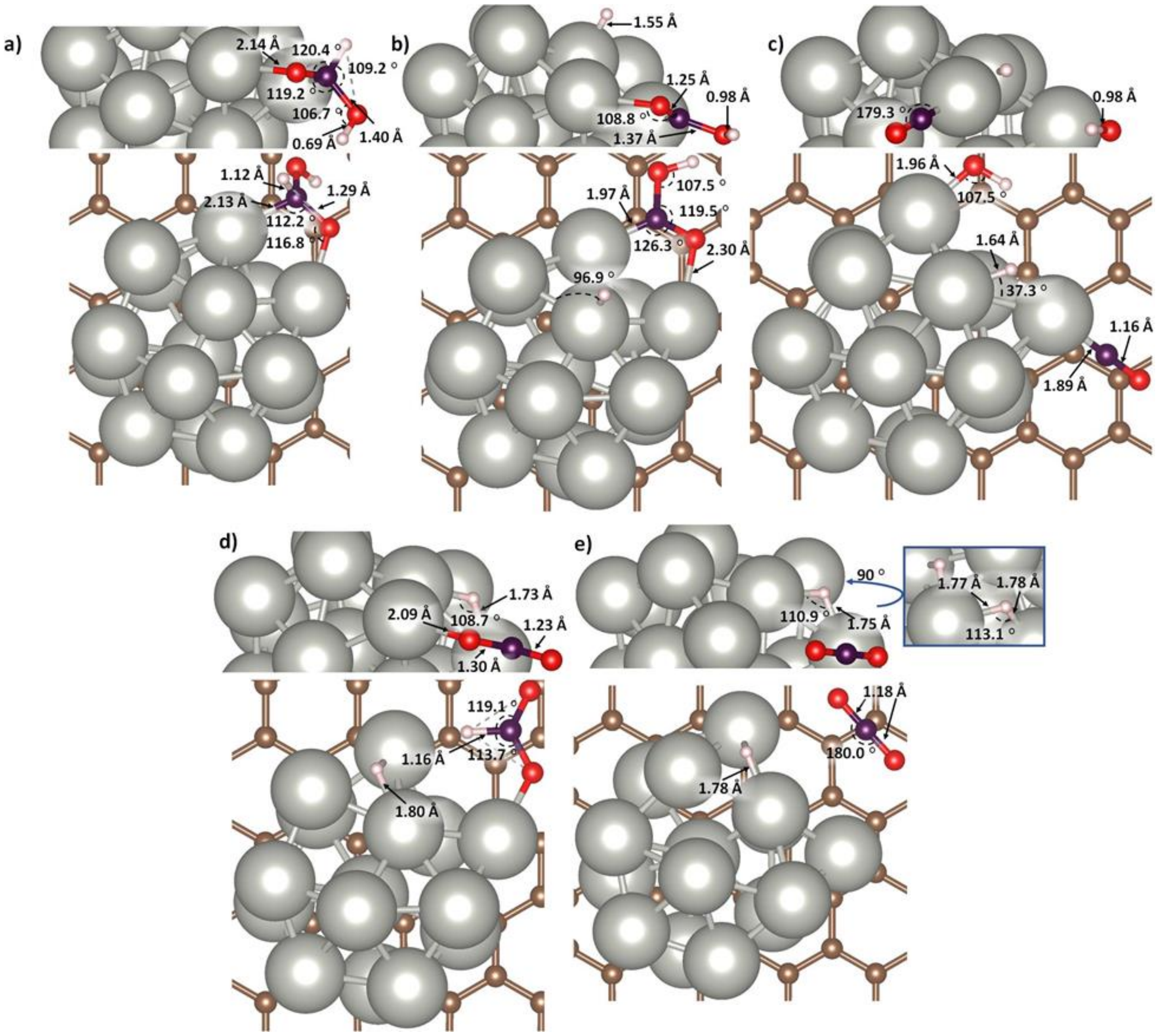

Figure 14: Top and side views of the optimized elementary steps on Pd_{15} cluster; (a) FA adsorbed on the cluster, (b) COOH and H adsorbed after the dissociation of the C-H bond, (c) CO, H and OH adsorbed after the dissociation of the C-OH bond, (d) HCOO and H adsorbed after the dissociation of the O-H bond and (e) H and H adsorbed on the cluster after the dissociation of C-H bond. CO2 is more stable in gas phase than adsorbed. The inset in this figure is referred to a rotation of 90 ° on the z axis showing the second H adsorbed on the Pd. Inset shows the distances and angles of interest. Carbon atoms are represented in brown, palladium in silver, oxygen in red, hydrogen in white and the carbon atoms of formic acid in purple.

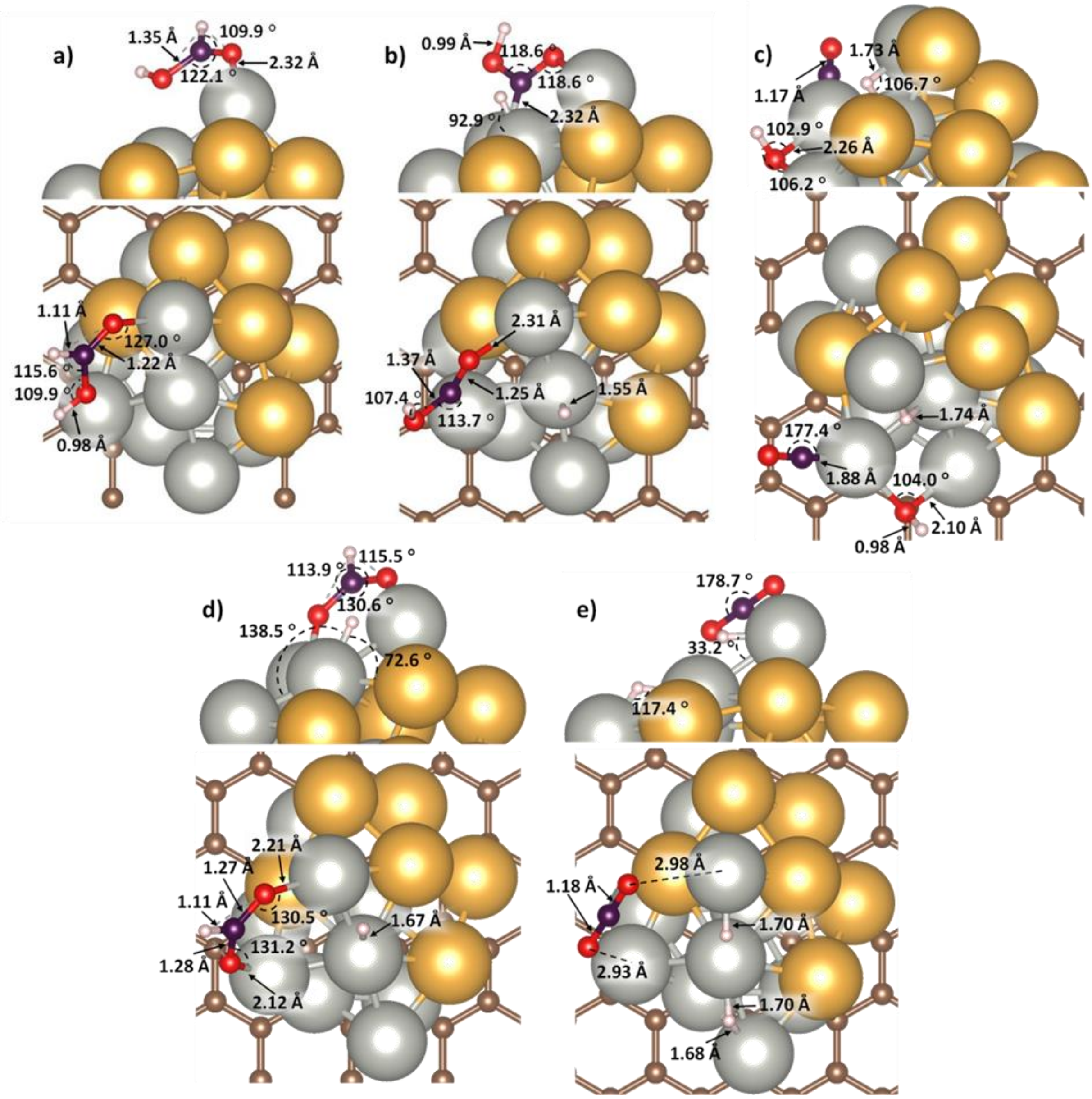

Figure 15: Top and side views of the optimized elementary steps on Pd_9Au_6 cluster; (a) FA adsorbed on the cluster, (b) COOH and H adsorbed after the dissociation of the C-H bond, (c) CO, H and OH adsorbed after the dissociation of the C-OH bond, (d) HCOO and H adsorbed after the dissociation of the O-H bond and (e) H and H adsorbed on the cluster after the dissociation of C-H bond. CO_2 is more stable in gas phase than adsorbed. Insets show distances and angles of interest. Carbon atoms are represented in brown, gold atoms in gold, palladium in silver, oxygen in red, hydrogen in white and the carbon atoms of formic acid in purple.

In order to reveal the selectivity, reactivity and superior stability of Au_6Pd_9 supported nanoparticles, we investigated the electronic structure of all the three supported systems on graphene. We calculated the partial charge density of the supported clusters from the gas phase with the same morphology. Upon adhesion, the electron density rearranges as shown from the electron density depletion (blue) and gain (yellow) iso-surfaces in Figure 16. In Au system, the arrangement places the electrons at the core of the nanoparticle as previously observed[36]. The Pd nanoparticle localizes its electron density away from the surface while on Au_6Pd_9 the electron density is relocated at the interface between the nanoparticle and the support. This suggests a stronger interaction with the support in the bimetallic system in full agreement with the results obtained in the experimental part, where the bimetallic catalysts showed a durability superior than monometallics.

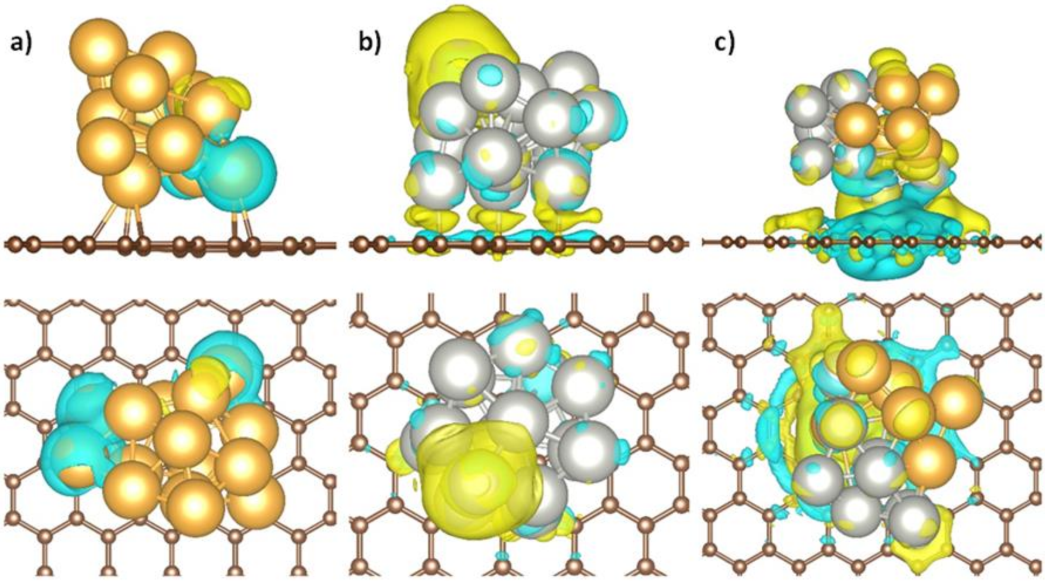

Figure 16: Side and top view of the partial charge density analysis upon: a) Au_{15}, b) Pd_{15} and c) Au_6Pd_9. Yellow and blue iso-surfaces denote gain and depletion of electron density. Gold, silver and khaki spheres represent gold, palladium and carbon, respectively.

5.3. Conclusion

In conclusion, this work combines DFT and experimental data to disclose the role of gold in enhancing activity, selectivity and stability of palladium catalyst during the formic acid decomposition. PdAu catalysts were synthesised using sol-immobilization technique with a systematic variation of Au to Pd molar ratio, obtaining in the majority cases an alloy with an enrichment of palladium on the surface confirmed by XPS, STEM-HAADF and STEM-XEDS analyses. The activity plot showed a typical volcano trend with a maximum for 1%Pd_6Au_4@HHT catalyst (3539 h^{-1}). An increasing in conversion at 2 h of reaction is observed for most of the bimetallic systems, in particular for 1%Pd_6Au_4@HHT and 1%Pd_8Au_2@HHT (73% and 68%, respectively). Moreover, an inhibition of the dehydration pathway was observed for gold-containing catalysts. 1%Pd_6Au_4@HHT and 1%Pd_8Au_2@HHT also showed an excellent stability during six consecutive runs, whereas 1%Pd@HHT rapidly deactivates because of leaching, coalescence and CO-poisoning. DFT models of Pd_{15}, Au_{15} and Pd_9Au_6 clusters were then employed to better understand the beneficial effect of gold observed in the experimental results. While Au_{15} was not able to interact with FA, Pd_{15} and Pd_9Au_6 could exothermically adsorb the substrate according to our observations. Nonetheless, the Pd_9Au_6 catalyst showed a more exothermic adsorption of formic acid than Pd_{15}, confirming the superior activity of the bimetallic system. Moreover, considering the pathways observed for both systems, the Pd_9Au_6 favourite route was the formation of carbon dioxide and hydrogen, while Pd_{15} can follow both the dehydrogenation and dehydration pathways, in agreement with the analyses performed on the products. Additionally, as far as we know this is the first study demonstrating a stronger interaction between the bimetallic system and the support confirming the excellent durability results observed in the experimental part, using the analysis of the electronic structures of the different modelled clusters. These results demonstrate that alloying Pd with Au facilitates the synthesis of active, highly selective and durable catalysts for the sustainable formation of hydrogen from formic acid decomposition at mild conditions.

5.4. References

[1]I. Barlocco, S. Capelli, X. Lu, S. Bellomi, X. Huang, D. Wang, L. Prati, N. Dimitratos, A. Roldan, A. Villa, *ChemCatChem* **2021**, *13*, 4210–4222.

[2]J. Cho, S. Lee, S. P. Yoon, J. Han, S. W. Nam, K. Y. Lee, H. C. Ham, *ACS Catal.* **2017**, *7*, 2553–2562.

[3]J. H. Lee, J. Cho, M. Jeon, M. Ridwan, H. S. Park, S. H. Choi, S. W. Nam, J. Han, T. H. Lim, H. C. Ham, C. W. Yoon, *J. Mater. Chem. A* **2016**, *4*, 14141–14147.

[4] Q. Wang, L. Chen, Z. Liu, N. Tsumori, M. Kitta, Q. Xu, *Adv. Funct. Mater.* **2019**, *29*, 1–7.

[5] Z. Xing, Z. Guo, X. Chen, P. Zhang, W. Yang, *Catal. Sci. Technol.* **2019**, *9*, 588–592.

[6] Q. Lv, Q. Meng, W. Liu, N. Sun, K. Jiang, L. Ma, Z. Peng, W. Cai, C. Liu, J. Ge, L. Liu, W. Xing, *J. Phys. Chem. C* **2018**, *122*, 2081–2088.

[7] J. H. Carter, S. Althahban, E. Nowicka, S. J. Freakley, D. J. Morgan, P. M. Shah, S. Golunski, C. J. Kiely, G. J. Hutchings, *ACS Catal.* **2016**, *6*, 6623–6633.

[8]D. Liu, Z. Y. Gao, X. C. Wang, J. Zeng, Y. M. Li, *Appl. Surf. Sci.* **2017**, *426*, 194–205.

[9]Y. Karatas, A. Bulut, M. Yurderi, I. E. Ertas, O. Alal, M. Gulcan, M. Celebi, H. Kivrak, M. Kaya, M. Zahmakiran, *Appl. Catal. B Environ.* **2016**, *180*, 586–595.

[10]F. Sanchez, D. Motta, L. Bocelli, S. Albonetti, A. Roldan, C. Hammond, A. Villa, N. Dimitratos, *C* **2018**, *4*, 26.

[11]X. Zhu, Q. Guo, Y. Sun, S. Chen, J.-Q. Wang, M. Wu, W. Fu, Y. Tang, X. Duan, D. Chen, Y. Wan, *Nat. Commun.* **2019**, *10*, 1428.

[12] F. Sanchez, M. H. Alotaibi, D. Motta, C. E. Chan-Thaw, A. Rakotomahevitra, T. Tabanelli, A. Roldan, C. Hammond, Q. He, T. Davies, A. Villa, N. Dimitratos, *Sustain. Energy Fuels* **2018**, *2*, 2705–2716.

[13] Z. Zhao, K. N. Heck, P. Limpornpipat, H. Qian, J. T. Miller, M. S. Wong, *Catal. Today* **2019**, *330*, 24–31.

[14]C. Hu, J. K. Pulleri, S. W. Ting, K. Y. Chan, *Int. J. Hydrogen Energy* **2014**, *39*, 381–390.

[15] Ö. Metin, X. Sun, S. Sun, *Nanoscale* **2013**, *5*, 910–912.

[16] K. Tedsree, T. Li, S. Jones, C. W. A. Chan, K. M. K. Yu, P. A. J. Bagot, E. A. Marquis, G. D. W. Smith, S. C. E. Tsang, *Nat. Nanotechnol.* **2011**, *6*, 302–307.

[17] S. Zhang, Ö. Metin, D. Su, S. Sun, *Angew. Chemie - Int. Ed.* **2013**, *52*, 3681–3684.

[18] A. Bulut, M. Yurderi, Y. Karatas, M. Zahmakiran, H. Kivrak, M. Gulcan, M. Kaya, *Appl. Catal. B Environ.* **2015**, *164*, 324–333.

[19]V. Mazumder, M. Chi, M. N. Mankin, Y. Liu, Ö. Metin, D. Sun, K. L. More, S. Sun, *Nano Lett.* **2012**, *12*, 1102–1106.

[20]M. Yurderi, A. Bulut, M. Zahmakiran, M. Kaya, *Appl. Catal. B Environ.* **2014**, *160–161*, 514–524.

[21]K. Mori, H. Tanaka, M. Dojo, K. Yoshizawa, H. Yamashita, *Chem. – A Eur. J.* **2015**, *21*, 12085–12092.

[22] X. Zhou, Y. Huang, W. Xing, C. Liu, J. Liao, T. Lu, *Chem. Commun.* **2008**, 3540–3542.

[23]I. Barlocco, S. Capelli, E. Zanella, X. Chen, J. J. Delgado, A. Roldan, N. Dimitratos, A. Villa, *J. Energy Chem.* **2020**, *52*, 301–309.

[24] D. Mellmann, P. Sponholz, H. Junge, M. Beller, *Chem. Soc. Rev.* **2016**, *45*, 3954–3988.

[25]F. Sanchez, D. Motta, A. Roldan, C. Hammond, A. Villa, N. Dimitratos, *Top. Catal.* **2018**, *61*, 254–266.

[26]H. Sakai, T. Nakajima, N. Yoshida, S. Kishimoto, *React. Kinet. Catal. Lett.* **1982**, *19*, 297–301.

[27] F. Abild-Pedersen, M. P. Andersson, *Surf. Sci.* **2007**, *601*, 1747–1753.

[28] S. Campisi, C. E. Chan-Thaw, D. Wang, A. Villa, L. Prati, *Catal. Today* **2016**, *278*, 91–96.

[29] A. Bergmann, B. Roldan Cuenya, *ACS Catal.* **2019**, *9*, 10020–10043.

[30] C. Chizallet, P. Raybaud, *Catal. Sci. Technol.* **2014**, *4*, 2797–2813.

[31]S. W. Chee, J. M. Arce-Ramos, W. Li, A. Genest, U. Mirsaidov, *Nat. Commun.* **2020**, *11*, 2133.

[32] J. Dean, M. G. Taylor, G. Mpourmpakis, *Sci. Adv.* **2019**, *5*, eaax5101.

[33]A. S. Crampton, M. D. Rötzer, C. J. Ridge, F. F. Schweinberger, U. Heiz, B. Yoon, U. Landman, *Nat. Commun.* **2016**, *7*, 10389.

[34] H. Zhai, A. N. Alexandrova, *J. Phys. Chem. Lett.* **2018**, *9*, 1696–1702.

[35] I. Barlocco, S. Capelli, X. Lu, S. Tumiati, N. Dimitratos, A. Roldan, A. Villa, *Nanoscale* **2020**, *12*, 22768–22777.

[36] A. Roldán, J. M. Ricart, F. Illas, G. Pacchioni, *Phys. Chem. Chem. Phys.* **2010**, *12,* 10723–10729.

6. ROLE OF DEFECTS IN CARBON MATERIALS DURING METAL-FREE FORMIC ACID DEHYDROGENATION

The results discussed in this Chapter with the permission of the Royal Society of Chemistry were previously reported in my work, published on *Nanoscale* **2020**, *12*, 22768–22777 (https://doi.org/10.1039/D0NR05774F)[1].

6.1. Introduction

6.1.1. Defects in metal-free carbocatalysts

Metal based catalysts have been employed in different dehydrogenation reactions due to their good activity, selectivity and stability[2–6]. However, to enhance the overall sustainability of the process, metal free analogues have been considered[7–9]. Among all, carbon-based catalysts are attracting significant attention in reducing the use of metals (Section 1.3.4.) in different heterogeneous gas phase[10–12] and liquid phase[13,14] reactions, in electrocatalytic[15] and photocatalytic[16] processes.

Moreover, the advantages to employ carbon materials were extensively reviewed in Section 1.3. In particular, combining the presence of heteroatoms (e.g. O, N, P and B; Section 1.3.2.2.) and intrinsic topological defects (i.e. vacancies and non-hexagonal rings; Section 1.3.2.1.) leads to several tuning possibilities to influence the carbocatalyst's activity[17–20].

For example, Qiu and co-workers showed that the amount of defects in different activated carbons is correlated with their activity in acetylene hydrochlorination reaction[21]. In addition, Jia et al. reported that defects obtained by removing heteroatoms are effective in oxygen reduction reaction (ORR), oxygen evolution reaction (OER) and hydrogen evolution reaction (HER)[22].

6.1.2. Aim and objectives of the Chapter

Herein, I studied the role of the defects in four different commercial carbon materials, i.e. graphite (GP), graphite oxide (GO), and two carbon nanofibers (CNFs) with different graphitization degrees (PR24-PS and PR24-LHT) in the formic acid dehydrogenation (FAD) in liquid phase under mild reaction conditions. Theoretical studies were then performed to rationalize the activity of the diverse topological defects in adsorbing and decomposing FA.

6.2. Results

As previously reported by Barlocco et al.[1], a systematic study combining experiments and computational simulation on FA adsorption and decomposition on different graphitic structures was carried out to understand the role of the defects present in carbocatalysts in this reaction. The catalysts were tested in the liquid phase formic acid decomposition reaction (80 °C, 1400 rpm and FA/catalyst: 10/1 wt/wt) and characterized by X-Ray photoelectron spectroscopy (XPS), Brunauer-Emmett-Teller (BET) method, inductively coupled plasma optical emission spectroscopy (ICP-OES) and Raman spectroscopy.

6.2.1. Catalytic activity and characterization

Carbocatalysts were pre-treated with a solution of HCl 0.1 M to remove possible impurities and confirmed the absence of metal impurities using ICP- OES. I measured the initial catalytic activity after 5 minutes of reaction and I observed that the most active catalysts were GO and PR24-PS with a FA conversion of 28.5 and 27.5%, respectively, followed by PR24-LHT (13.9%) and GP (3%). However, beyond the 5 minutes of reaction, all the catalysts suffered a strong deactivation (Figure 1). Analysis of the gases evolved revealed that the reaction mainly follows the dehydrogenation pathway with a selectivity of 70-75% to $H_2 + CO_2$ and to $CO + H_2O$ of 25-30% for all systems[23].

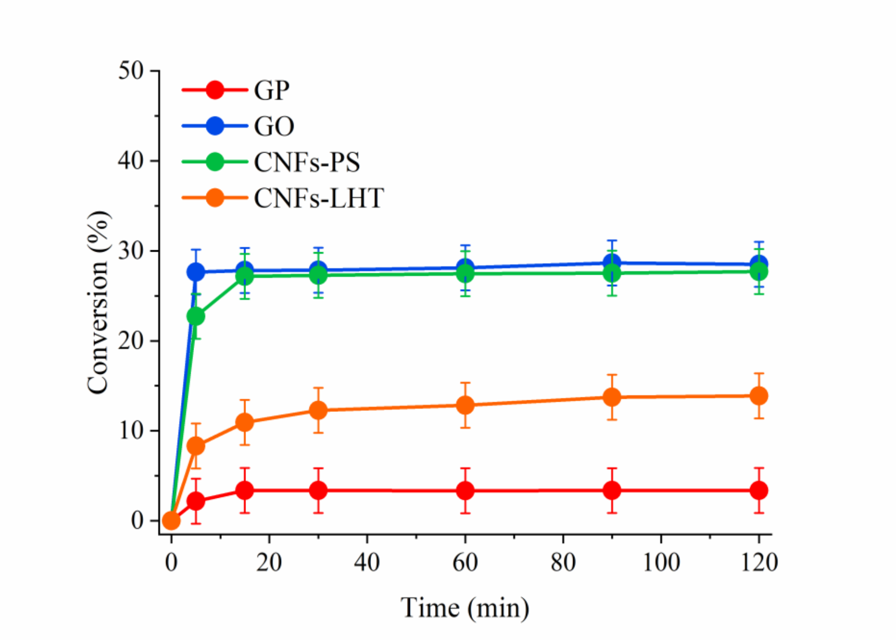

Figure 1: Conversion trend for the formic acid decomposition reaction for the different carbonaceous materials: Graphite (GP), graphite oxide (GO) and CNFs PR24-PS and PR24-LHT.To ensure reproducibility, the experiments were repeated three times (experimental error ± 2.5 %).

To identify the active sites of these catalysts and rationalize their deactivation, I characterized their structure and surface properties using BET, Raman spectroscopy and XPS. Graphite and graphite oxides show a surface area of 14 and 12 $m^2 g^{-1}$, respectively, whereas PR24-PS and PR24-LHT presented a higher surface area (43 and 38 $m^2 g^{-1}$, respectively) (Table 1). Raman spectroscopy was used to investigate the graphitization degree of carbon materials. Raman spectra show two bands at around 1600 cm^{-1} (G band) and 1350 cm^{-1} (D band) which are characteristic carbonaceous materials[24]. The G band is generated by the C=C stretching vibrations in the graphite lattice and it is related to structurally ordered graphite domains[24]. The D band corresponds to the A_{1g} mode, which is forbidden according to the selection rules in graphite, but it is activated in the presence of structural defects or in plane substitutional heteroatoms[24]. Hence, I used the ratio of the integral intensities of D and G bands (I_D/I_G) as an index of the defectiveness of the graphite layers (Table 1). All carbon materials studied in this work present both D and G Raman bands (Figure 2) with the following I_D/I_G ratio: GO (1.64)> PR24-PS (1.54)> PR24-LHT (0.60) > GP (0.09). To be notice the dramatic effect on CNFs I_D/I_G ratio respect the annealing temperature (700 °C and 1500 °C for PR24-PS and PR24-LHT, respectively).

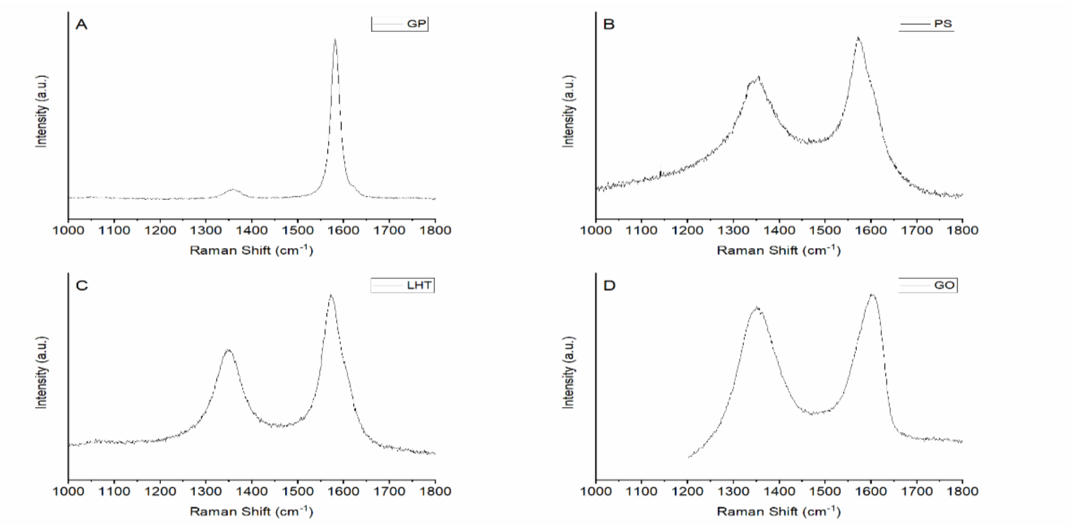

Figure 2: Raman spectra of a) pristine graphene, b) PS-CNFs, c) LHT-CNFs and d) graphene oxide.

I employed XPS to record the survey and the high-resolution (HR) spectra of C1s species. Survey spectra revealed the presence of both C and O element, while no N or S were detected. From HR C1s spectra an evaluation of the relative concentration of C-C sp^3 and C=C sp^2 species in the different materials was performed (Figure 3 and Table 2). The component at approximately 284.4 eV can be attributed to the presence of sp2-hybridised carbon species, whereas the one at 285 eV indicates the presence of sp3- hybridized carbon species.[25] XPS-HR C1s spectra confirmed a high graphitization degree in the case of GP, where carbon is mainly present in the sp^2 form, whereas a combination of sp^2 and sp^3 is present for the other carbonaceous materials with a sp^2/sp^3 ratio of 7.00 , 4.00 and 0.03 for PR24-LHT, PR24-PS and GO, respectively (Table 1). XPS survey analysis revealed a higher oxygen content for GO (O/C of 0.45), while the carbon nanofibers displayed an O/C ratio of about 0.1. On the contrary, GP contained a very low amount of oxygen, as expected for highly graphitized materials (Table 1). The deconvolution of the O1s signal identified four main oxygen groups and the peak assignment has been made following the literature:[26] (i) O-(C=O*)-$C_{aliphatic}$ at a binding energy (E_B) of 532 eV, (ii) O-C-O/C-O-C at E_B= 533 eV, (iii) O*-(C=O)-$C_{aliphatic}$ at E_B= 534 eV to and (iv) H_2O at BE= 537 eV (Figure 4 and Table 3).

Oxygen is mainly presented in the form of O-(C=O*)-$C_{aliphatic}$ on the surface of GP, PR24-PS and PR24-LHT (92%, 75.20% and 74.12%, respectively), and in the form of O-C-O/C-O-C (77.29%) in GO sample (Table 3).

Table 1: Carbon catalysts characteristics derived from BET, Raman and XPS analysis and their initial (5 minutes of reaction) catalytic activity towards the FA decomposition.

Catalyst	*Surface area (m^2 g^{-1})*	*Raman (I_D/I_G)*	*XPS*		*Conversion (%)*
			sp^2/sp^3	*O/C*	
GP	14	0.09	-	0.02	3.0
PR24-PS	43	1.54	4.00	0.13	27.5
PR24-LHT	38	0.60	7.00	0.09	13.9
GO	12	1.64	0.03	0.45	28.5

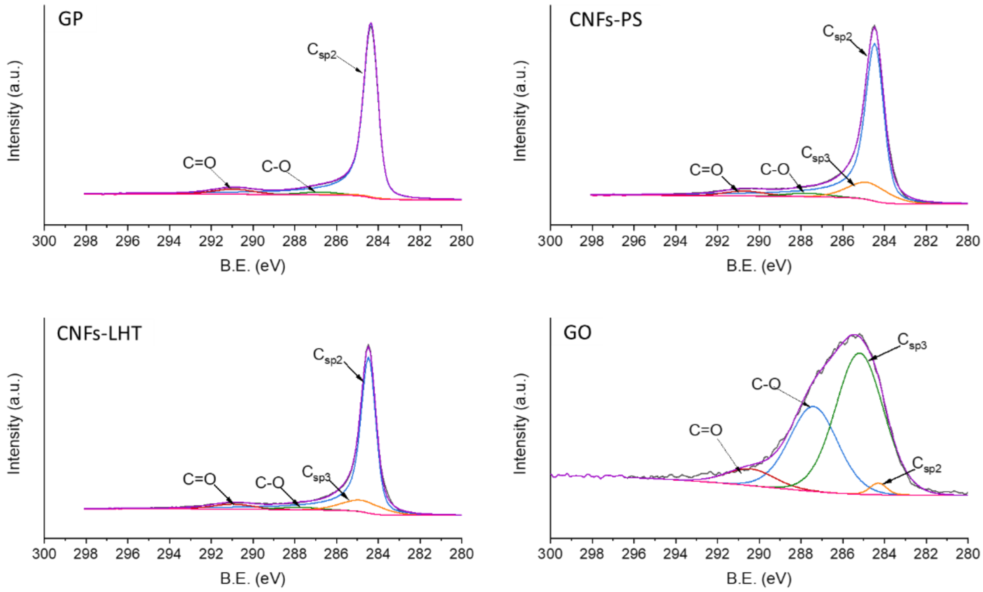

Figure 3: Deconvolution of C 1s HR spectra of the different catalyst.

Table 2: Atomic % of the different C species detected after C 1s HR spectra deconvolution.

Sample		*C=C*	*C-C*	*C-O*	*C=O*
PR24-PS	BE	284.4	284.9	287.2	290.0
	Atom %	*75.8*	*18.2*	*3.7*	*1.8*
PR24-LHT	BE	284.5	284.9	287.4	290.1
	Atom %	*83.8*	*12.0*	*2.6*	*1.6*
GO	BE	284.3	285.2	287.4	290.4
	Atom %	*1.7*	*57.1*	*34.4*	*6.8*

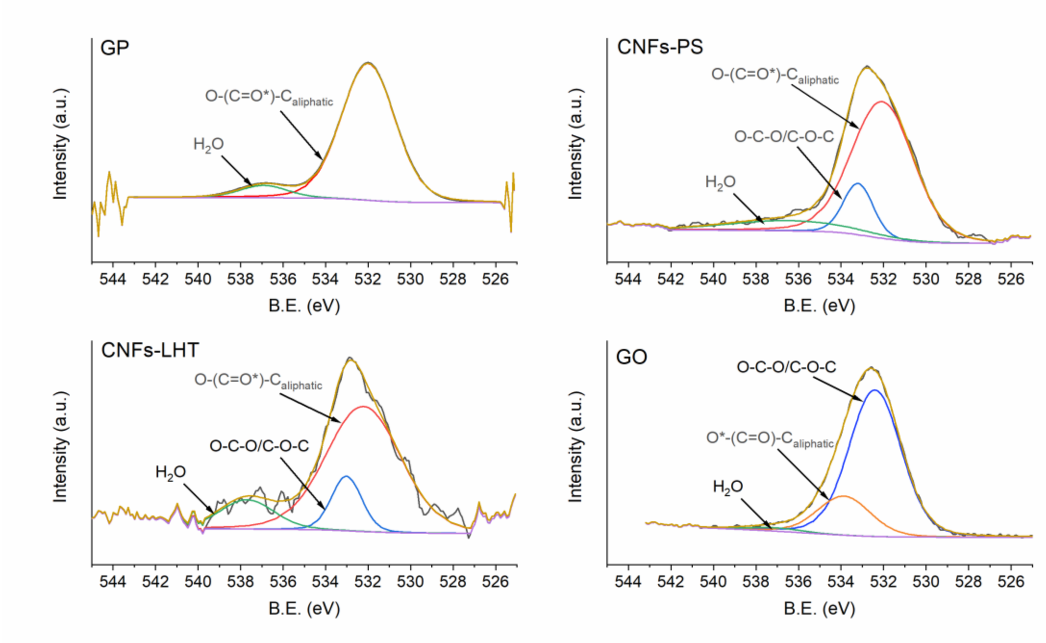

Figure 4: Deconvolution of O 1s HR spectra of the different catalyst.

Table 3: Atomic % of the different O species detected after O 1s HR spectra deconvolution.

Sample		*O-(C=O*)-*$C_{aliphatic}$	*O-C-O/C-O-C*	*O*-(C=O)-*$C_{aliphatic}$	H_2O
GP	BE	532.0	-	-	536.9
	Atom %	*92.5*	-	-	*7.5*
PR24-PS	BE	532.0	533.2	-	536.5
	Atom %	*75.2*	*13.5*	-	*11.3*
PR24-LHT	BE	532.2	533.0	-	537.6
	Atom %	*74.1*	*13.2*	-	*12.7*
GO	BE	-	532.6	533.9	537.1
	Atom %	-	*77.3*	*20.9*	*1.8*

We plotted the FA conversion as a function of the I_D/I_G ratio, the O/C ratio, and the different oxygen groups to identify their relationship and rationalize the activity of the carbon materials with their defectiveness and the presence of oxygen functional groups (Figure 5). We found a linear relationship between the FA conversion and the I_D/I_G ratio ($R^2 = 0.99$), whereas there is not a direct correlation of the activity with the oxygen groups present on the surface (Figure 6).

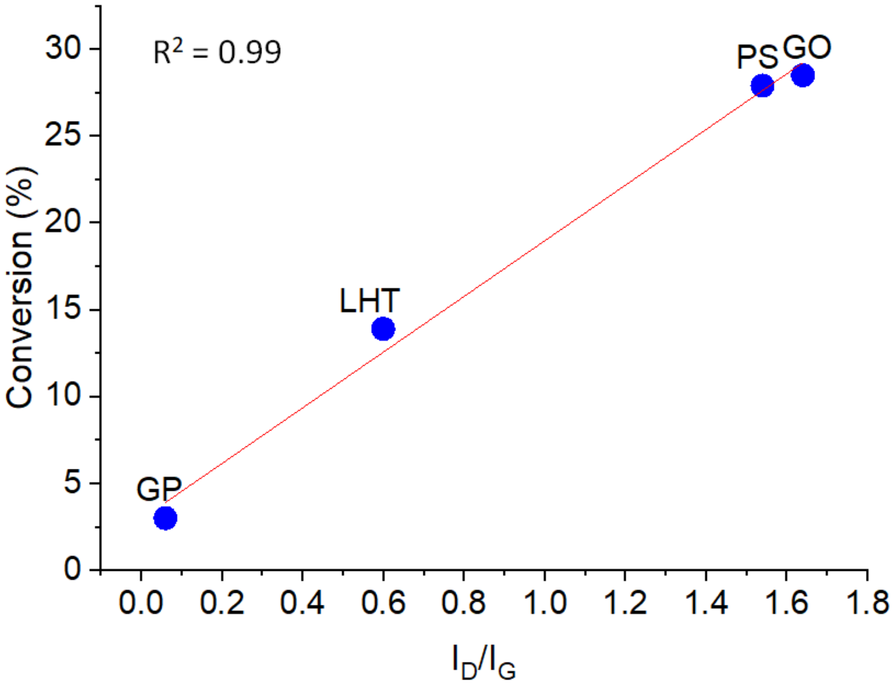

Figure 5: Linear correlation of conversion vs I_D/I_G.

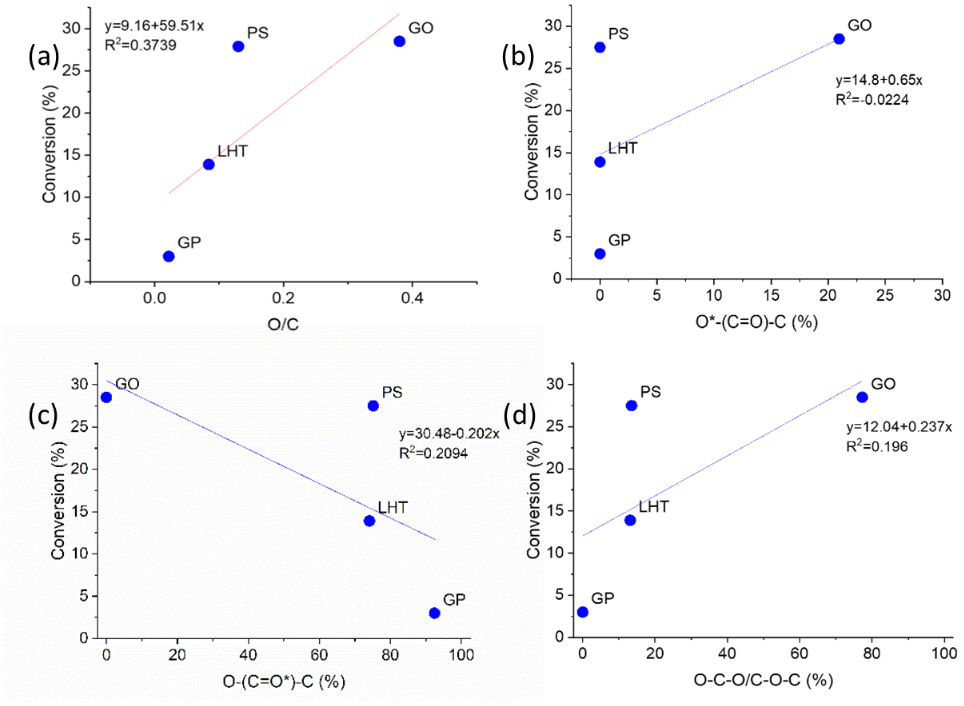

Figure 6: Linear correlation of conversion vs: a) O/C, b) O*-(C=O)-C, c) O-(C=O*)-C and d) O-C-O/C-O-C.

6.2.2. DFT study

6.2.2.1. Graphitic structures

The correlation between the previous characterization results and the FA decomposition activity suggests that the defects on the graphitic matrix participate in the mechanism for activation of formic acid, such as vacancies and Stone Wales defects rather than the oxygen groups as previously suggested by Raman and conversion correlations. I performed a systematic computer simulations study based on density functional theory to shed light on the FA decomposition and catalysts deactivation mechanisms.

Six different graphitic surfaces were modelled according to the reported defects in literature[27] (Figure 7): pristine graphite, Single Vacancy (SV), Double Vacancy (DV) and three different Stone Wales defects (SW1, SW2, SW3).

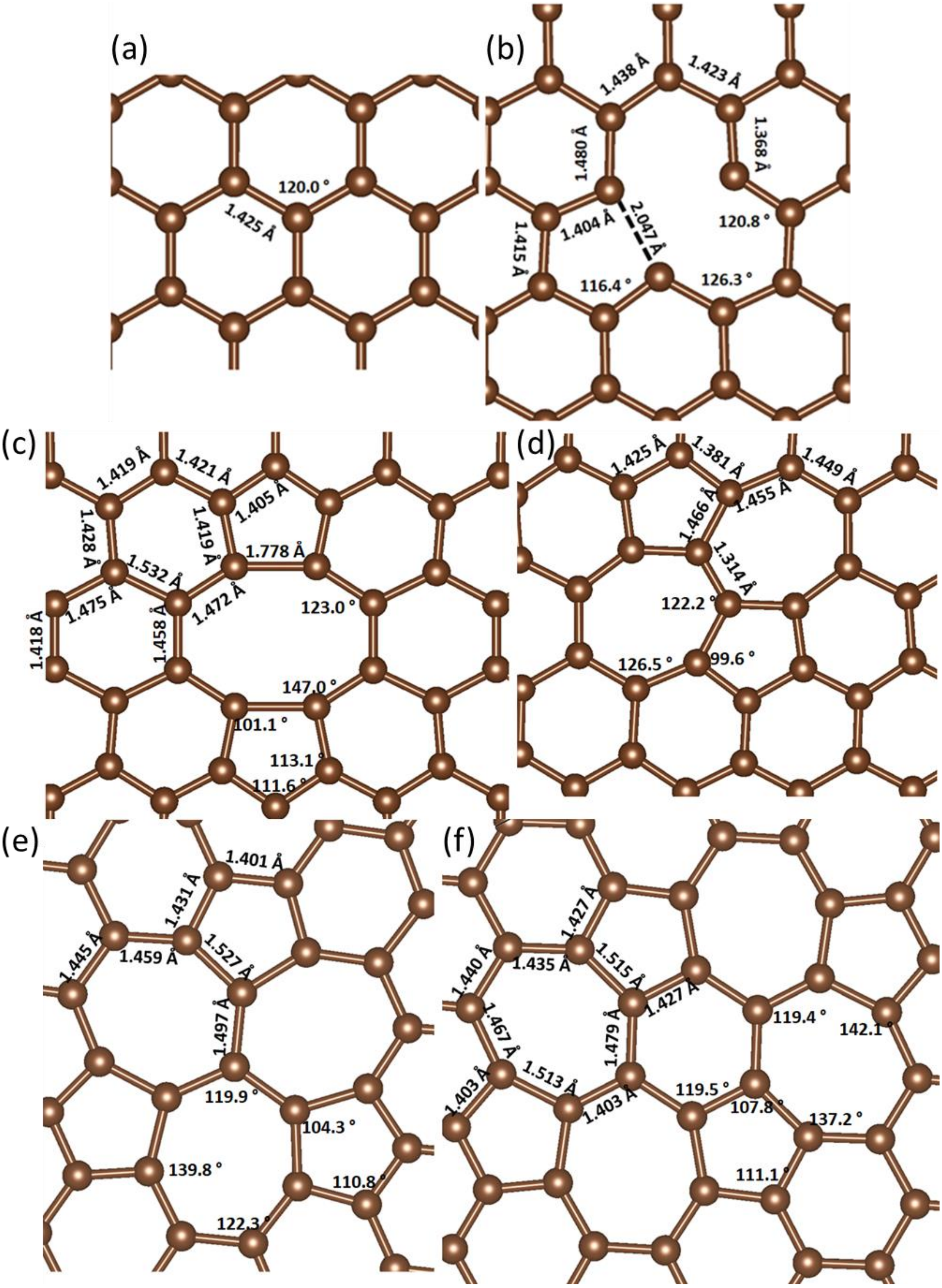

Figure 7: Top view of the optimized graphitic surfaces: a) pristine graphene b) SV c) DV d) SW1 e) SW2 f) SW3. Inset, distances (Å) and angles (°) of interest. Carbon atoms are brown.

SV and DV were prepared by removing respectively one and two neighbouring carbon atoms from pristine graphene and re-optimizing the structure at fixed supercell lattice. Similarly, SW1 was found rotating a C-C bond of 90° from pristine graphene, while SW2 was obtained rotating a bond of 90° from DV, and SW3 rotating a second different bond of 90° from SW2[28]. The flexibility of the honeycomb lattice allows its reconstruction to minimize dangling bonds thus providing further stability, e.g. forming non-hexagonal rings. In the DV defect, the optimization leads to an octagon and two pentagons. The SW1 is a point defect where four hexagons (without C-vacancies) are transformed into two pentagons and two heptagons. The octagon present in the DV structure transforms it into the SW2 surface composed by three pentagons and three heptagons, while SW3 contains four pentagons, one hexagon and four heptagons. The presence of these defects forces the rearrangement of C electronic structure which also influences the catalytic properties and the stability of the material. All the surfaces show a positive relative energy meaning that they are less thermodynamically favorable than pristine graphene (Table 4). In agreement with previous experiments, our result confirms that the formation energies of SV and DV are near 7.5 eV[29,30] while the one of SW1 is around 5 eV[31,32] compared to pristine graphene. SW2 and SW3 are more stable than DV as an even number of missing carbon atoms permits a full reconstruction of the bonds decreasing the dangling bonds[33], which also agrees with the study by Lee *et al*.[34] In agreement with my results, it has also been reported that the reconstruction energy of DV forming SW2 is about 1 eV lower than the one of DV, and that the energy of SW3 lies between the two energies of DV and SW2[29,30].

Table 4: Relative energies of the different graphitic surfaces.

Surface	*ΔE (eV)*
Graphene (G)	0.00
Single vacancy (SV)	+7.22
Double vacancy (DV)	+7.17
Stone-Wales defect (SW1)	+4.89
Stone-Wales defect (SW2)	+5.71
Stone-Wales defect (SW3)	+6.70

6.2.2.2. Formic acid adsorption

I brought the formic acid to non-equivalent surface sites on different orientations and relaxed the structure leading to different adsorption modes. I selected the most stable adsorption configurations of each surface to carry on the subsequent FA decomposition reaction steps (Figure 8).

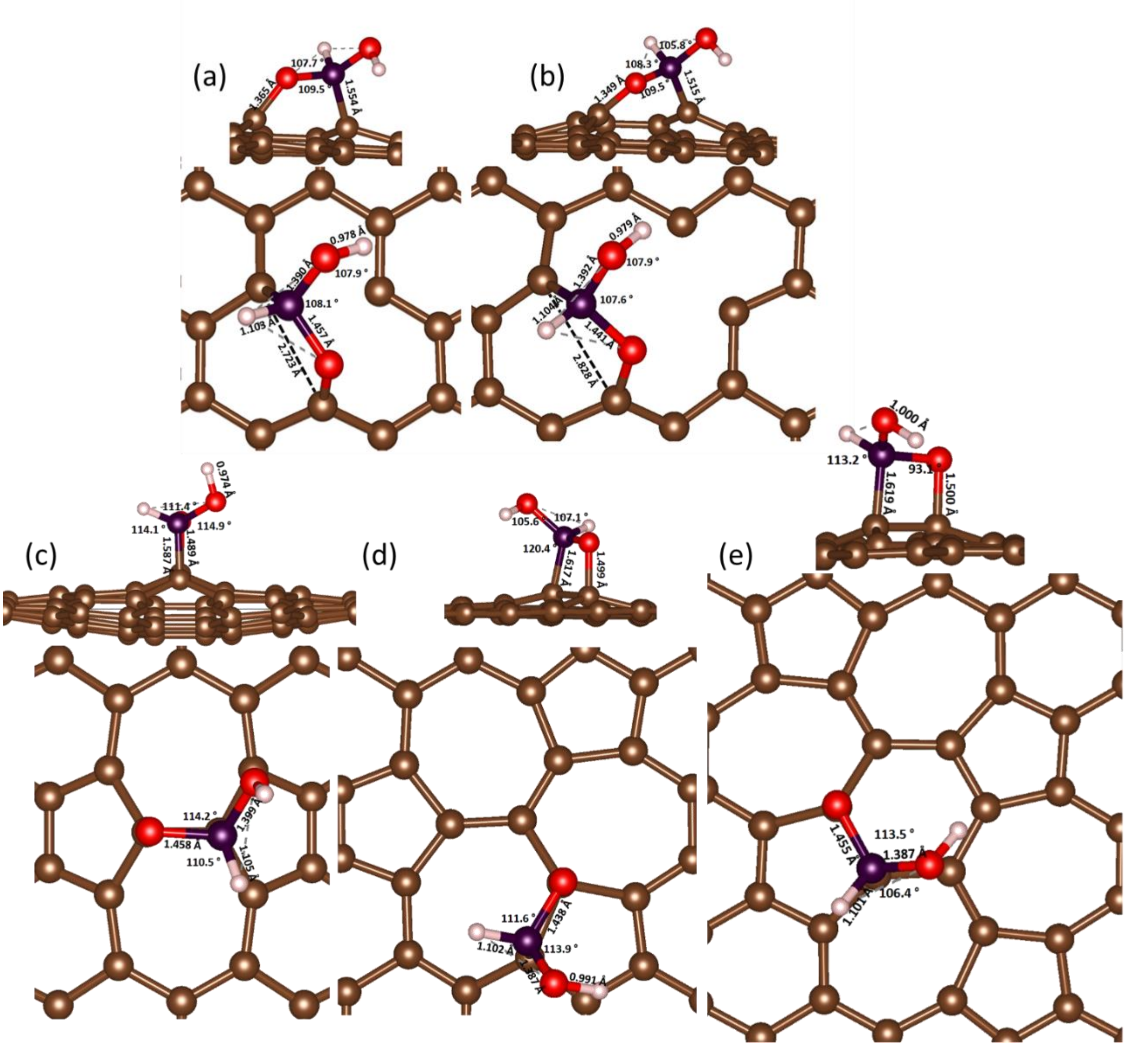

Figure 8: Top and side view of the most favourable FA configuration on the different surfaces; a) FA/SV b) FA/DV c) FA/SW1 d) FA/SW2 e) FA/SW3. Inset, distances (Å) and angles (°) of interest. Carbon atom is labelled in brown, oxygen in red, hydrogen in white and carbon atom of formic acid in purple.

In accordance with previous studies, pristine graphene has an inactive π-conjugation, which is not sensitive in the adsorption of molecules[35–37]. In fact, the pristine graphene is not capable to chemically bind molecular formic acid on its surface. Another possible way to adsorb FA is through a dissociative adsorption (DA), i.e. where the bond between H and C (or O) breaks forming a new bond with the surface. This pathway was shown by Solymosi when FA adsorbs on Pt-based catalyst forming formate species[38]. Nevertheless, graphene remains incapable to adsorb dissociated FA.

Wang *et al.* demonstrated that by increasing the amount of defects in the graphene surface, the activity towards the activation of peroxymonosulfate is enhanced due to the unconfined π-electrons[39]. I summarized the adsorption energies (E_{ADS}) on the defective structures in Table 5 and only SV and DV have a favourable (exothermic) interaction with FA.

Table 5: Dissociative and molecular adsorption energies (E_{ADS}) formic acid on the defective graphene surfaces.

Surface	*E_{ADS} molecular (eV)*	*E_{ADS} dissociative (eV)*	
		(HCOO+H*)*	*(*COOH+H*)*
Single vacancy (SV)	-2.71	-	-3.42
Double vacancy (DV)	-1.29	-	+0.20
Stone-Wales defect (SW1)	+0.46	+0.59	-0.42
Stone-Wales defect (SW2)	+0.62	+1.19	+0.54
Stone-Wales defect (SW3)	+0.81	+0.96	+0.83

The molecular adsorption of FA on SV and DV slightly distorts the graphitic structure: the distance between two carbon atoms increases of 0.676 Å and 1.051 Å, respectively (Figure 8 a and b). Indeed, it has been demonstrated that SV defect has great affinity with different functional groups, e.g. CO[40] and O in peroxymonosulfate leading to the O-O cleavage[39]. Xu *et al*. proved that DV are also reactive (compared with pristine graphene) upon its exposure to different DNA bases[41]. Contrarily, the SW surfaces showed only FA physisorption. I then considered the dissociative adsorption pathway on SW structures and found that SW1 is the only SW structure able to provide an exothermic adsorption site upon C-H bond scission (Figure 9 a). Instead, SW2 and SW3 showed endothermic adsorptions (Table 5). The dissociative adsorption of FA on SV and DV surfaces was also considered. On the first surface, it leads to one stable structure where COOH and H are adsorbed on the surface giving a reaction energy of -3.42 eV (Figure 9 b), which can be considered as the subsequent dehydrogenation step in the reaction pathway. On the contrary, for the DV system the structure obtained gave an endothermic E_B of +0.20 eV denoting this pathway unlikely.

To confirm that the activity does not depend on the oxygen groups present on the carbon surface, different type of oxygen functionalities on pristine graphene were optimized. in accordance with XPS analysis (Table 2 and Table 3). We evaluated epoxides, hydroxyl and oxygen incorporated in the graphene structure (Figure 10), but we didn’t find any exothermic adsorption of FA demonstrating that these types of functionalities are not active for the FA decomposition reaction.

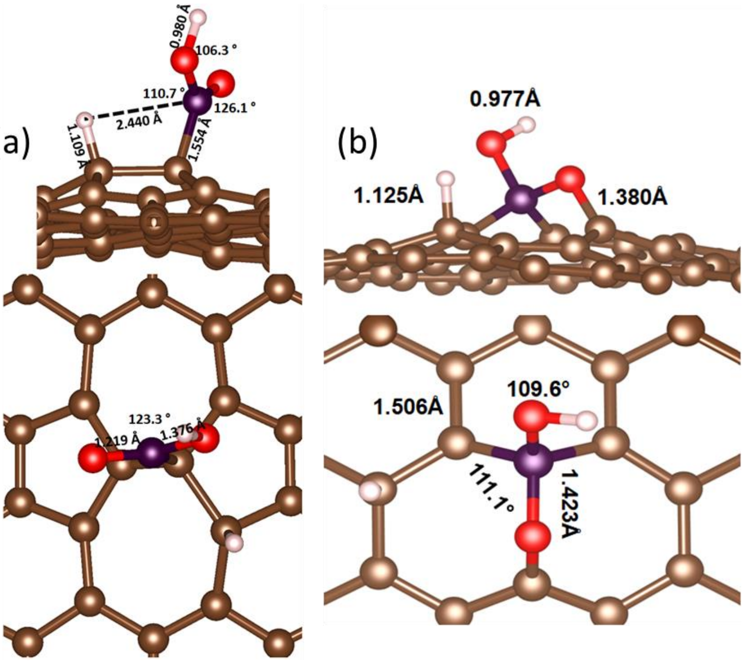

Figure 9: Top and side view of a) Dissociative adsorption of formic acid on SW1 and b) COOH and H adsorbed on SV when C-H bond is broken. Inset, distances (Å) and angles (°) of interest. Carbon atom is labelled in brown, oxygen in red, hydrogen in white and carbon atom of formic acid in purple.

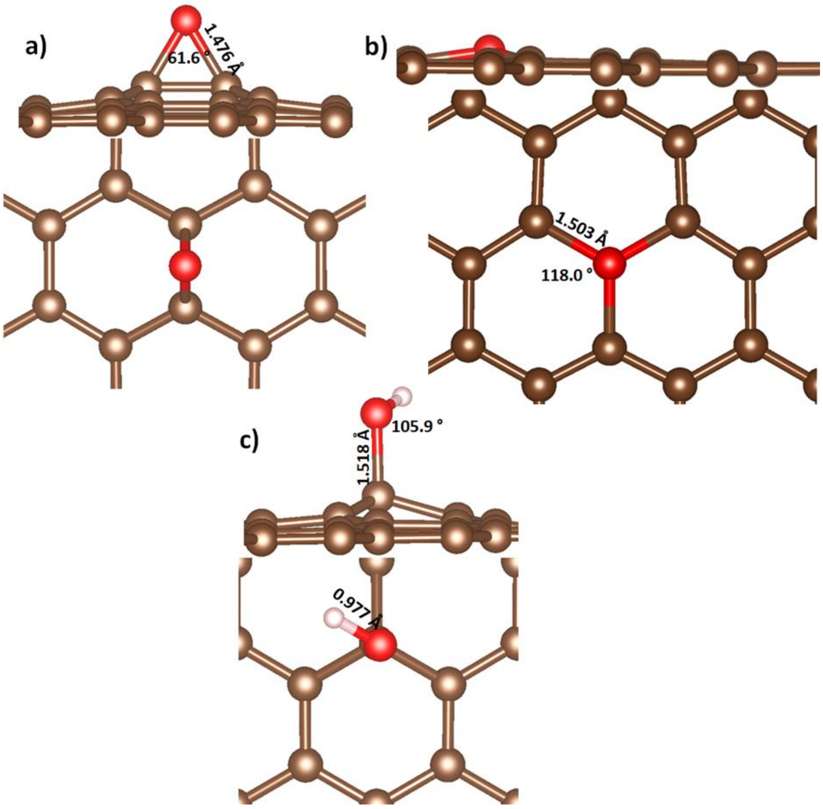

Figure 10: Top and side view of graphene with O-functionalities: a) epoxide b) O incorporated in the surface c) hydroxyl. Inset, distances (Å) and angles (°) of interest. Carbon atom is labelled in brown, oxygen in red and hydrogen in white.

6.2.2.3. Formic acid decomposition

The decomposition of molecularly adsorbed FA on SV and DV was studied considering both dehydrogenation and dehydration reaction pathways leading to carboxyl (COOH*) and formate (HCOO*) intermediates, respectively[4]. Thus, I proceeded by considering the C-H bond scission and comparing its reaction energy with the one for O-H bond scission on SV and DV surfaces.

Single Vacancy (SV) system

The dissociation of the C-H bond leads to a co-adsorption of COOH and H (Figure 9b), which are stabilised by the SV structure giving a reaction energy (E_R) of -0.71 eV. While the co-adsorbed hydrogen was considered to migrate across the graphitic structure, the following reaction elementary step proceeds through the scission of the O-H or the C-OH bond. Both pathways showed a strong endothermic profile of +6.67 and +3.30 eV, respectively (Figure 11a and b). In any case, the OH and H co-adsorbed on the surface may recombine forming H_2O (E_R = -6.22 eV, Figure 11c) leaving CO strongly bound to the surface (E_B = -6.71 eV), whose adsorption poisons the SV active sites.

FA may undergo through the dehydrogenation pathway on the defective surface, which leads to the adsorption of H, O and HCO (E_R = -1.12, Figure 11d) through the hydroxymethylene intermediate, HCOH (E_R = -0.88 eV, Figure 11e). Indeed, when FA is adsorbed on the SV site, the carbonyl C-O bond length increased of 0.22 Å compared to the gas phase structure (dC-O= 1.24 Å), making the breakage of C-O bond possible. Considering the structure in Figure 11d, only carbon monoxide can be produced (E_R = -0.42 eV) yielding the structure in Figure 11f, where the oxygen remains bound on the surface.

The recombination of adsorbed hydrogen would yield H_2 gas, however, the desorption of molecular H_2 unlikely occurs at low coverages as the desorption energy is quite endothermic (+1.85 eV). Figure 12 depicts the corresponding energy profiles of FA decomposition through the COOH and HCOH intermediates on the SV structure.

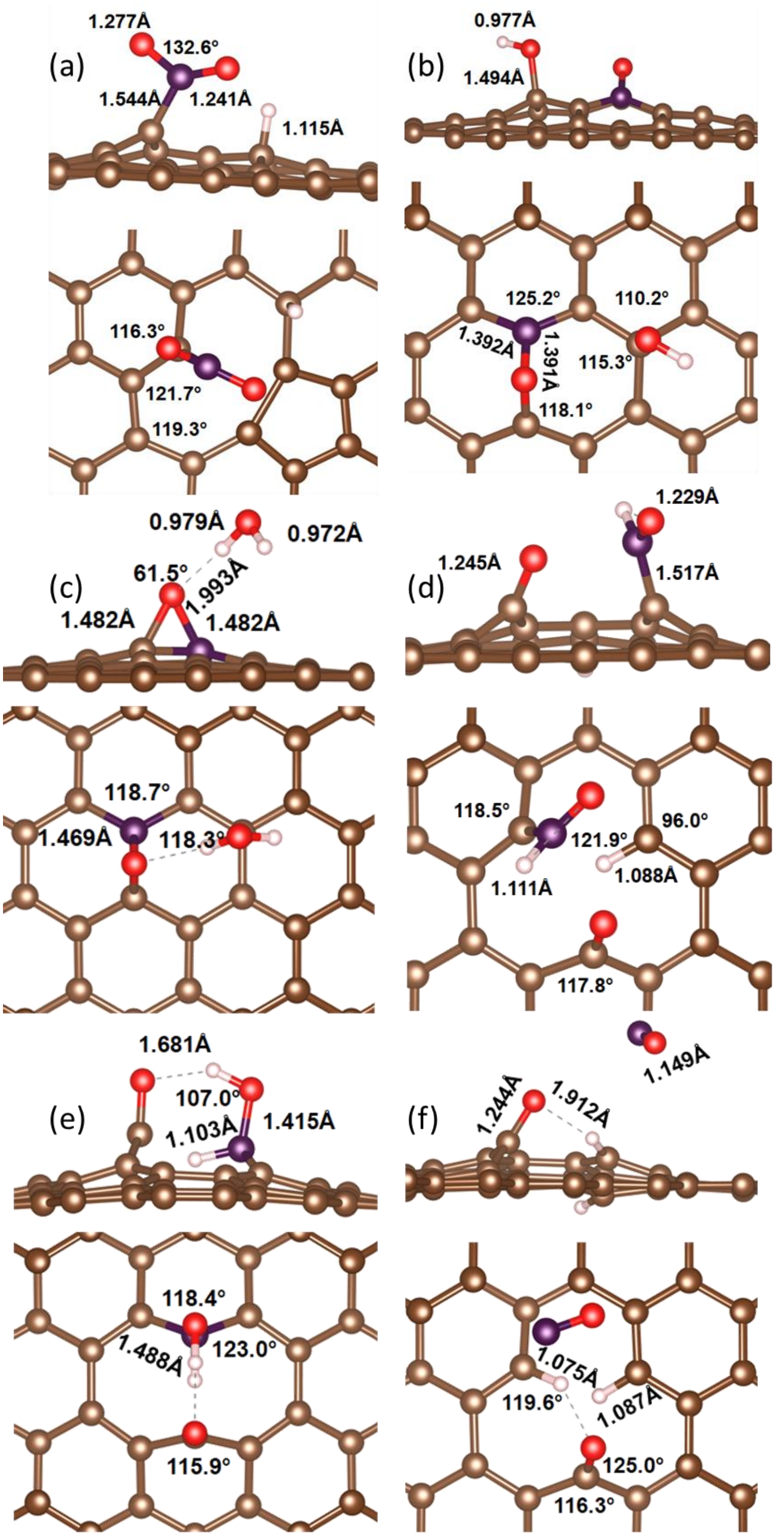

Figure 11: Top and side view of a) COO and H adsorbed on SV; only one hydrogen is considered in this step because the H adsorbed on the surface migrates in another site, b) CO and OH adsorbed on SV; only one hydrogen is considered in this step because the H adsorbed on the surface migrates in another site, c) CO and H_2O adsorbed on the surface; water is more stable in gas phase than adsorbed, d) structure obtained taking out the H from the OH group. The carbonyl and the hydroxyl bonds broke, e) the intermediate structure; breakage of the C-O bond before the O-H one and f) releasing of carbon monoxide from the surface. Inset, distances (Å) and angles (°) of interest. Carbon atom is labelled in brown, oxygen in red, hydrogen in white and carbon atom of formic acid in purple.

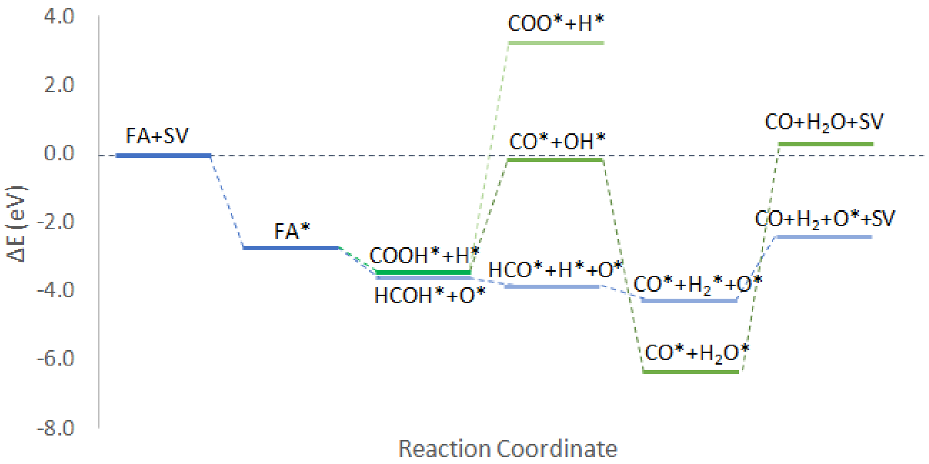

Figure 12: Energy profile for the different pathways of Formic Acid decomposition on SV structure. * indicates adsorbed species.

Double Vacancy (DV) system

Similar to SV, FA adsorption on the DV site gives an increasing of the C-O bond length of 0.20 Å compared to the gas phase structure (dC-O = 1.24 Å). The dissociation of C-H bond on the DV is an endothermic process (E_R = +1.49 eV) and therefore unlikely to proceed. (Figure 13 a). However, the hydroxylmethylene (Figure 13 b) intermediate sits only at +0.60 eV from the adsorbed HCOOH. The dehydrogenation to HCO is strongly driven by an E_R = -2.00 eV (Figure 13c). Considering both possible decomposition pathways, the favourite route is through the hydroxylmethylene specie followed by a highly endothermic (E_R = 4.51 eV) scission of C-H bond leading to adsorbed CO and H_2 (Figure 13d). These species are strongly bound to the dangling bonds of the surface thus poisoning the active sites. Figure 14 shows the corresponding energy profiles of FA decomposition through COOH and HCOH intermediates on the DV structure.

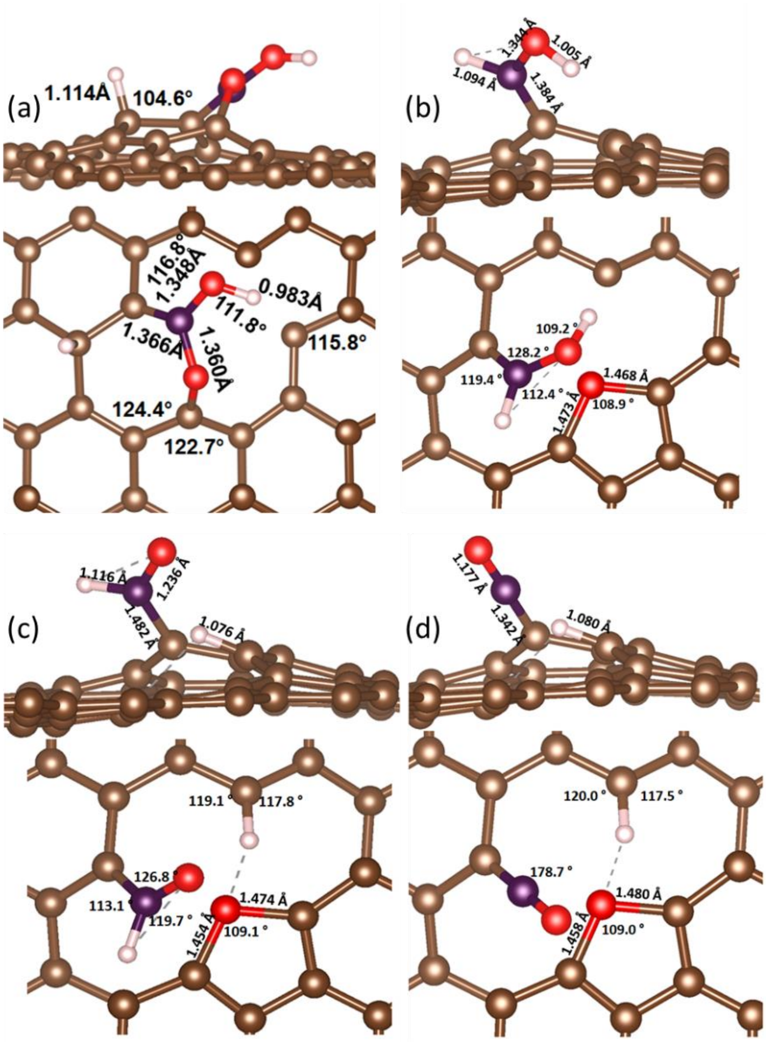

Figure 13: Top and side view of a) the breakage of C-H bond of FA on Double Vacancy system; COOH and H adsorbed on the surface, b) the intermediate structure; breakage of C-O bond, c) the structure obtained taking out the H from the OH group. The carbonyl and the hydroxyl bonds broke and d) the breakage of the C-H bond. Inset, distances (Å) and angles (°) of interest. Carbon atom is labelled in brown, oxygen in red, hydrogen in white and carbon atom of formic acid in purple.

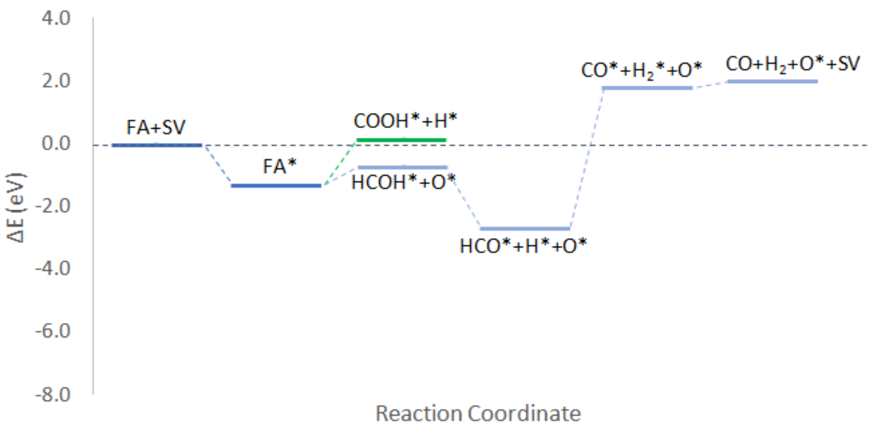

Figure 14: profile for the different pathways of Formic Acid decomposition on DV structure. * indicates adsorbed species.

Stone-Wales (SW1) system

The dissociative adsorption of FA on the first Stone Wales (SW1) defect leads to a favourable co-adsorption of COOH and H (E_R = -0.42 eV, Figure 10 a), while the breakage of the hydroxyl bond is endothermic (E_R = +0.59 eV) (Table 5). In this case the reaction energy is endothermic, E_R = 5.53 eV (Figure 15 a). Following the carboxylic intermediate we investigated the scission of C-OH bond to CO and OH co-adsorbed on the surface, and breaking of the O-H bond (Figure 15 b). Both processes are highly endothermic as seen in the energy profile of Figure 16.

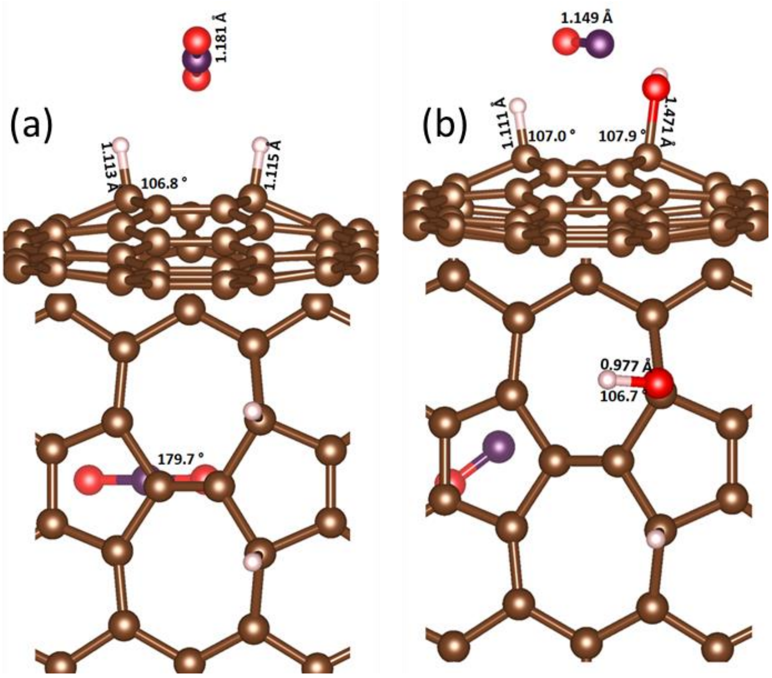

Figure 15: Top and side view of a) the breakage of the O-H bond and b) the breakage of C-OH bond. Inset, distances (Å) and angles (°) of interest. Carbon atom is labelled in brown, oxygen in red, hydrogen in white and carbon atom of formic acid in purple.

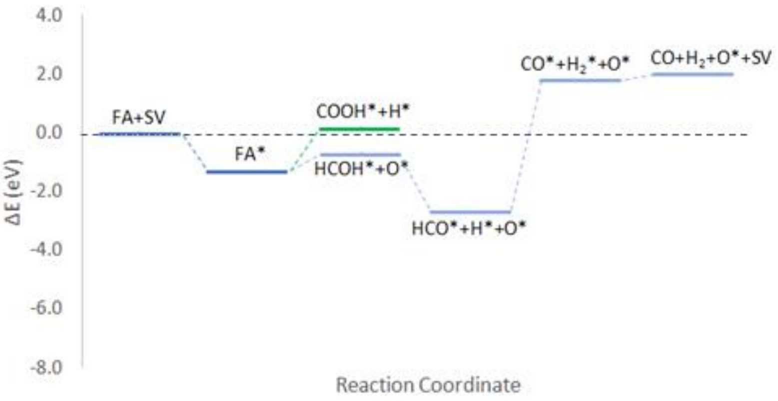

Figure 16: Profile for the different pathways of Formic Acid decomposition on SW1 structure. * indicates adsorbed species.

6.3. Conclusions

I have carried out a systematic investigation on graphitic defects as active sites using formic acid as a probe molecule. Different metal-free catalysts based on graphitic structures (Pristine graphene, graphene oxide, PS carbon nanofibers and LHT carbon) were experimentally tested and their structure analyzed by BET, XPS and Raman spectroscopies. I found a correlation between the FA conversion and the number of defects presented in the catalysts. In particular, the FA decomposition increases by increasing the defectiveness of the material, i.e. in the order GO > PR24-PS > PR24-LHT > GP. This result was confirmed by both XPS and Raman techniques. Plotting the conversion vs. I_D/I_G ratio and vs. the amount of different oxygen groups displayed on the surface, I found a linear correlation between conversion and defects ($R^2 = 0.99$), but no direct correlation with oxygen groups was established. I am, then, able to ascribe the activity of the materials to the defects and not to the presence of oxygen functional groups. In order to understand the rule of the different type of defects, we investigated the decomposition of formic acid using DFT models of pristine graphene and different defective graphene surfaces, e.g. single and double vacancy, and different Stone-Wales defects. I demonstrated that not all defects act as active centres to adsorb and decompose formic acid. The activity is mainly due to the single vacancy defect because it is the only system able to decompose formic acid to gaseous molecules, thus recycling the active site. Two different pathways were found, one passing through the carboxyl species and the other one through a hydroxymethylene intermediate. In both cases, I obtained the saturation of the active site because of CO and atomic hydrogen irreversible adsorption. For the double vacancy structure, the hydroxymethylene pathway can be compared with the one of the single vacancy defects, while for the Stone-Wales no active sites were found able to decompose the FA molecule. Different types of oxygen functionalities (e.g. epoxide, oxygen incorporated in the structure and hydroxyl) were investigated, but they did not show any activity in the adsorption of FA, confirming the experimental results where no direct correlation between oxygen groups and catalytic behaviour was observed. When the vacancies are completely saturated, the catalyst deactivates explaining the experimental observations after 5 minutes of reaction. In conclusion, a first insight into the role of the defects present on carbon material in the FA dehydrogenation and dehydration was provided.

6.4. References

[1]I. Barlocco, S. Capelli, X. Lu, S. Tumiati, N. Dimitratos, A. Roldan, A. Villa, *Nanoscale* **2020**, *12*, 22768–22777.

[2] C. Li, J. B. Baek, *ACS Omega* **2020**, *5*, 31–40.

[3]X. Zhou, Y. Huang, W. Xing, C. Liu, J. Liao, T. Lu, *Chem. Commun.* **2008**, 3540–3542.

[4] J. A. Herron, J. Scaranto, P. Ferrin, S. Li, M. Mavrikakis, *ACS Catal.* **2014**, *4*, 4434–4445.

[5] Y. Cheng, X. Wu, H. Xu, *Sustain. Energy Fuels* **2019**, *3*, 343–365.

[6] B. Yin, E. Zhao, X. Hua, K. Wang, W. Wang, G. Li, T. Liu, *New J. Chem.* **2020**, *44*, 2011–2015.

[7] N. Gupta, O. Khavryuchenko, A. Villa, D. Su, *ChemSusChem* **2017**, *10*, 3030–3034.

[8] P. Veerakumar, P. Thanasekaran, T. Subburaj, K.-C. Lin, *C* **2018**, *4*, 54.

[9] M. M. Titirici, M. Antonietti, *Chem. Soc. Rev.* **2010**, *39*, 103–116.

[10] G. Mestl, N. I. Maksimova, N. Keller, V. V. Roddatis, R. Schlögl, *Angew. Chemie - Int. Ed.* **2001**, *40*, 2066–2068.

[11] P. N. Optics, N. York, **2008**, *322*, 73–78.

[12] J. Zhang, D. S. Su, R. Blume, R. Schlögl, R. Wang, X. Yang, A. Gajović, *Angew. Chemie - Int. Ed.* **2010**, *49*, 8640–8644.

[13] D. R. Dreyer, H. P. Jia, C. W. Bielawski, *Angew. Chemie - Int. Ed.* **2010**, *49*, 6813–6816.

[14]M. A. Patel, F. Luo, M. R. Khoshi, E. Rabie, Q. Zhang, C. R. Flach, R. Mendelsohn, E. Garfunkel, M. Szostak, H. He, *ACS Nano* **2016**, *10*, 2305–2315.

[15]D. R. Paul, W. J. Koros, R. Y. F. Liu, Y. S. Hu, E. Baer, A. Hiltner, H. D. Keith, R. Y. F. Liu, A. Hiltner, E. Baer, R. E. Cohen, A. Bellare, R. J. Albalak, W. Hu, G. Reiter, **2009**, *323*.

[16] J. Xu, L. Zhang, R. Shi, Y. Zhu, *J. Mater. Chem. A* **2013**, *1*, 14766–14772.

[17]Y. Jiang, L. Yang, T. Sun, J. Zhao, Z. Lyu, O. Zhuo, X. Wang, Q. Wu, J. Ma, Z. Hu, *ACS Catal.* **2015**, *5*, 6707–6712.

[18] C. Tang, H. F. Wang, X. Chen, B. Q. Li, T. Z. Hou, B. Zhang, Q. Zhang, M. M. Titirici, F. Wei, *Adv. Mater.* **2016**, *28*, 7030.

[19]L. Tao, Q. Wang, S. Dou, Z. Ma, J. Huo, S. Wang, L. Dai, *Chem. Commun.* **2016**, *52*, 2764–2767.

[20]Q. Xiang, W. Yin, Y. Liu, D. Yu, X. Wang, S. Li, C. Chen, *J. Mater. Chem. A* **2017**, *5*, 24314–24320.

[21]Y. Qiu, S. Ali, G. Lan, H. Tong, J. Fan, H. Liu, B. Li, W. Han, H. Tang, H. Liu, Y. Li, *Carbon N. Y.* **2019**, *146*, 406–412.

[22]Y. Jia, L. Zhang, A. Du, G. Gao, J. Chen, X. Yan, C. L. Brown, X. Yao, *Adv. Mater.* **2016**, *28*, 9532–9538.

[23]L. P. L. Gonçalves, D. B. Christensen, M. Meledina, L. M. Salonen, D. Y. Petrovykh, E. Carbó-Argibay, J. P. S. Sousa, O. S. G. P. Soares, M. F. R. Pereira, S. Kegnæs, Y. V. Kolen’Ko, *Catal. Sci. Technol.* **2020**, *10*, 1991–1995.

[24] F. Tuinstra, J. L. Koenig, *J. Chem. Phys.* **1970**, *53*, 1126–1130.

[25]F. Y. Xie, W. G. Xie, L. Gong, W. H. Zhang, S. H. Chen, Q. Z. Zhang, J. Chen, *Surf. Interface Anal.* **2010**, *42*, 1514–1518.

[26] G. Beamson, D. Briggs, **1992**, p. Appendices 3.1 and 3.2.

[27]T. Xu, L. Sun, Defects Adv. Electron. Mater. Nov. Low Dimens. Struct. **2018**, 5, 137–160.

[28] F. Banhart, J. Kotakoski, A. V. Krasheninnikov, *ACS Nano* **2011**, *5*, 26–41.

[29] A. V. Krasheninnikov, P. O. Lehtinen, A. S. Foster, R. M. Nieminen, *Chem. Phys. Lett.* **2006**, *418*, 132–136.

[30] A. El-Barbary, H. Telling, P. Ewels, I. Heggie, R. Briddon, *Phys. Rev. B - Condens. Matter Mater. Phys.* **2003**, *68*, 1–7.

[31]J. Ma, D. Alfè, A. Michaelides, E. Wang, *Phys. Rev. B - Condens. Matter Mater. Phys.* **2009**, *80*, 1–4.

[32]L. Li, S. Reich, J. Robertson, *Phys. Rev. B - Condens. Matter Mater. Phys.* **2005**, *72*, 1–10.

[33]D. Borisova, V. Antonov, A. Proykova, *Int. J. Quantum Chem.* **2013**, *113*, 786–791.

[34]G. Do Lee, C. Z. Wang, E. Yoon, N. M. Hwang, D. Y. Kim, K. M. Ho, *Phys. Rev. Lett.* **2005**, *95*, 1–4.

[35] L. Ma, J. M. Zhang, K. W. Xu, V. Ji, *Appl. Surf. Sci.* **2015**, *343*, 121–127.

[36] X. Y. Liu, J. M. Zhang, K. W. Xu, V. Ji, *Appl. Surf. Sci.* **2014**, *313*, 405–410.

[37] S. Yang, Z. Lan, H. Xu, G. Lei, W. Xie, Q. Gu, *J. Nanotechnol.* **2018**, *2018*, DOI 10.1155/2018/2031805.

[38] F. Solymosi, Á. Koós, N. Liliom, I. Ugrai, *J. Catal.* **2011**, *279*, 213–219.

[39]X. Duan, H. Sun, Z. Ao, L. Zhou, G. Wang, S. Wang, *Carbon N. Y.* **2016**, *107*, 371–378.

[40]S. Yang, G. Lei, H. Xu, B. Xu, H. Li, Z. Lan, Z. Wang, H. Gu, *Appl. Surf. Sci.* **2019**, *480*, 205–211.

[41] Z. Xu, B. R. Meher, D. Eustache, Y. Wang, *J. Mol. Graph. Model.* **2014**, *47*, 8–17.

7. HYDRAZINE SELECTIVE DECOMPOSITION OVER METAL-FREE CARBONACEOUS MATERIALS

7.1. Introduction

7.1.1. Metal-free catalysts in hydrazine hydrate decomposition reaction

Hydrazine hydrate ($N_2H_4 \cdot H_2O$) decomposition reaction was widely reviewed in Section 1.4.2.2. Indeed, supported and unsupported Ir[1,2], Rh[3,4], and Ni-based[5–7] metal nanoparticles (NPs) are extensively employed in this process, producing H_2 with high selectivity and activity. However, employing metal increases the cost and decreases the sustainability of the overall process. Indeed, carbon-based catalysts can be a key alternative to overcome these problems (Section 1.3.4.).

The decomposition of hydrazine (N_2H_4) over metal-free catalysts has only been reported on g-Si_3C, which is able to adsorb N_2H_4 in its *anti*-configuration and decompose it into N_2 and NH_3[8].

As previously reported in Chapter 6, carbon-based materials can be effective in the generation of H_2 from formic acid (FA). In particular, single-vacancy defect showed a superior activity in the adsorption and decomposition of FA than oxygen functionalities and other topological defects[9].

7.1.2. Aim and objectives of the Chapter

In this work, I studied the catalytic activity of different carbonaceous materials, i.e. graphite and two types of carbon nanofibers with different graphitization degree (PR24-PS and PR24-HHT), in liquid phase hydrazine hydrate decomposition in order to investigate the activity of defects in its decomposition. Indeed, my previous study on formic acid[9] (Chapter 6), have demonstrated the activity of defects and in particular single vacancy, in adsorbing and activating the substrate. Moreover, the effect of the presence of a base was evaluated by testing the materials with or without NaOH. A systematic density functional theory (DFT) study on hydrazine was then employed to rationalise the role of defects in adsorbing and decomposing it.

7.2. Results

A systematic study combining experiments and computational simulation on hydrazine adsorption and decomposition on different graphitic structures was carried out to unveil the role of defects on the catalytic performance.

The reaction conditions were optimized to assess the reaction kinetic regime and to establish the correct amount of catalyst to be used. The catalysts were then tested at 50 °C and 1400 rpm, using 600 µL of a hydrazine solution 3.3 M in 16 mL of NaOH 0.5 M and a $N_2H_4 \cdot H_2O$:catalyst weight ratio of 15.7:1. To ensure reproducibility, all the experiments were repeated three times. Moreover, the materials were characterised by Raman spectroscopy and inductively coupled plasma optical emission spectroscopy (ICP-OES).

7.2.1. Catalytic activity and characterisation

Carbocatalysts were firstly analysed by ICP-OES to ensure the absence of possible metallic impurities. Then, they were tested in hydrazine hydrate decomposition reaction. Figure 1 shows the different kinetic profiles for 6 h of reaction. CNFs-PS exhibited the highest conversion at 6 h (94 %), whereas CNFs-HHT and graphite showed similar conversion (71 % and 65 %, respectively) (Table 1, column 4). On the most active material, CNFs-PS, H_2 selectivity was calculated using water displacement method and 89 % selectivity for the complete hydrazine decomposition reaction was determined.

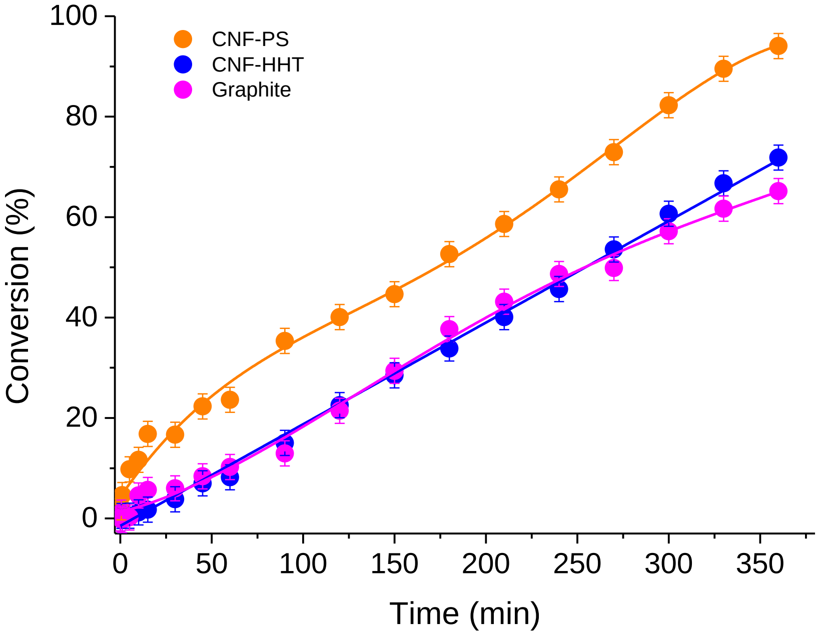

Figure 1: Conversion trend for the hydrazine decomposition reaction for the different carbonaceous materials: Graphite (violet), CNFs PR24-PS (orange) and PR24-HHT (blue).

In order to rationalize these results in terms of structural properties, I characterized all the catalysts using Raman spectroscopy. This technique allows to investigate the graphitization degree of carbon materials measuring the two bands at around 1600 cm^{-1} (G band) and 1350 cm^{-1} (D band)[10]. The G band is generated by the C=C stretching vibrations in the graphite lattice, and it is related to structurally ordered graphite domains. The D band corresponds to the A_{1g} mode, which is forbidden according to the selection rules in graphite, but active in the presence of structural defects or in plane substitutional heteroatoms[10]. All carbon materials studied in this work present both D and G Raman bands with the following I_D/I_G ratio: CNF-PS (1.54) > Graphite (0.20) > CNFs-HHT (0.11) (Table 1 and Figure 2).

Table 1: Raman characteristics of carbon catalysts, their initial catalytic activity (15 minutes of reaction) and final conversion towards hydrazine decomposition (6 h).

Catalyst	*Raman* *(I_D/I_G)*	*Activity at 15 min* *($mg^{-1}min^{-1}*10^{2}$)*	*Conversion at 6h* *(%)*
GP	0.20	6	65
PR24-PS	1.54	18	94
PR24-HHT	0.11	1.9	71

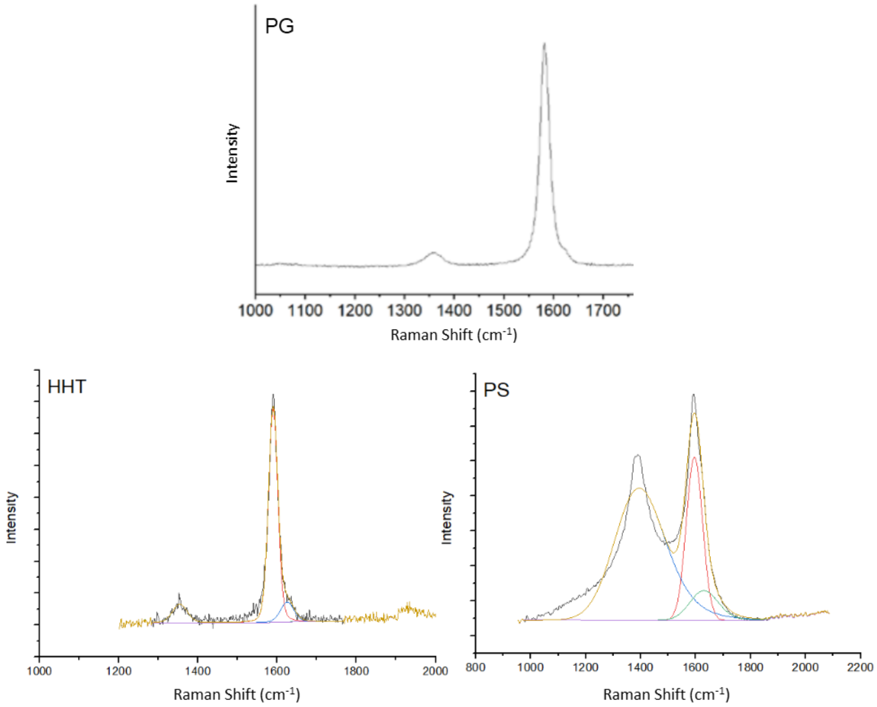

Figure 2: Raman spectra of graphite (top), PR24-HHT (bottom left) and PR24-PS (bottom right).

To unveil the effect of NaOH in the reaction environment, the most active material (CNFs-PS) was tested at the same experimental conditions, in the absence of NaOH, but with distilled water as solvent. From the comparison between the reaction profiles showed in Figure 3, it appears clear that the presence of NaOH affects not only the selectivity of the reaction, but also its kinetics[11,12]. Indeed, the catalyst tested at the same conditions with NaOH exhibited about 70% of hydrous hydrazine conversion at 4 h of reaction, while the same material tested in water presented a 15 % conversion.

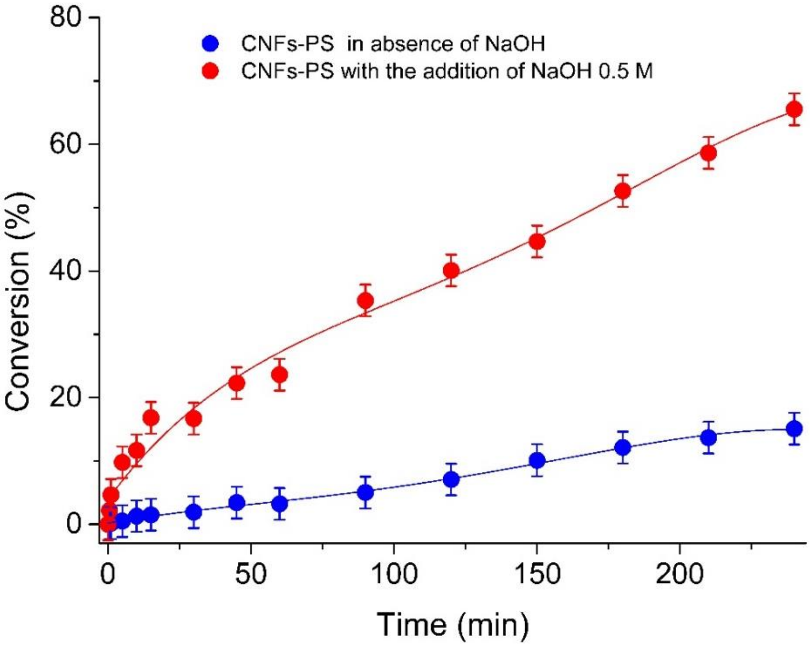

Figure 3: Comparison of conversion trend for hydrazine decomposition in a different reaction environment. Alkaline aqueous solvent (red) and distilled water (blue).

7.2.2. DFT study

Systematic DFT simulations were performed to elucidate the roles of carbon defects in hydrazine activation and decomposition and explain the presented experimental results. Six different graphitic surfaces were modelled: pristine graphite (PG), single vacancy (SV), double vacancy (DV) and three different Stone-Wales defects (SW, VSW1, VSW2) represented in Figure 4.

7.2.2.1. Hydrazine adsorption

Prior to proceed with the adsorptions, we performed an evaluation of charge density at Bond Critical Points (BCP)[13] to estimate the potential active sites of the different optimized surfaces (Figure 5). As previously shown, only sites presenting distortions in the graphene π-system are able to interact favourably with adsorbates[14]. The obtained electron densities measured on the defects are summarised in Table 2. It was observed that only SV and DV are potential catalysts candidates to bind N_2H_4 as these two structures contain dangling C-atoms lacking electron density[9]. This result, underling the localization of the catalytic site on both SV and DV.

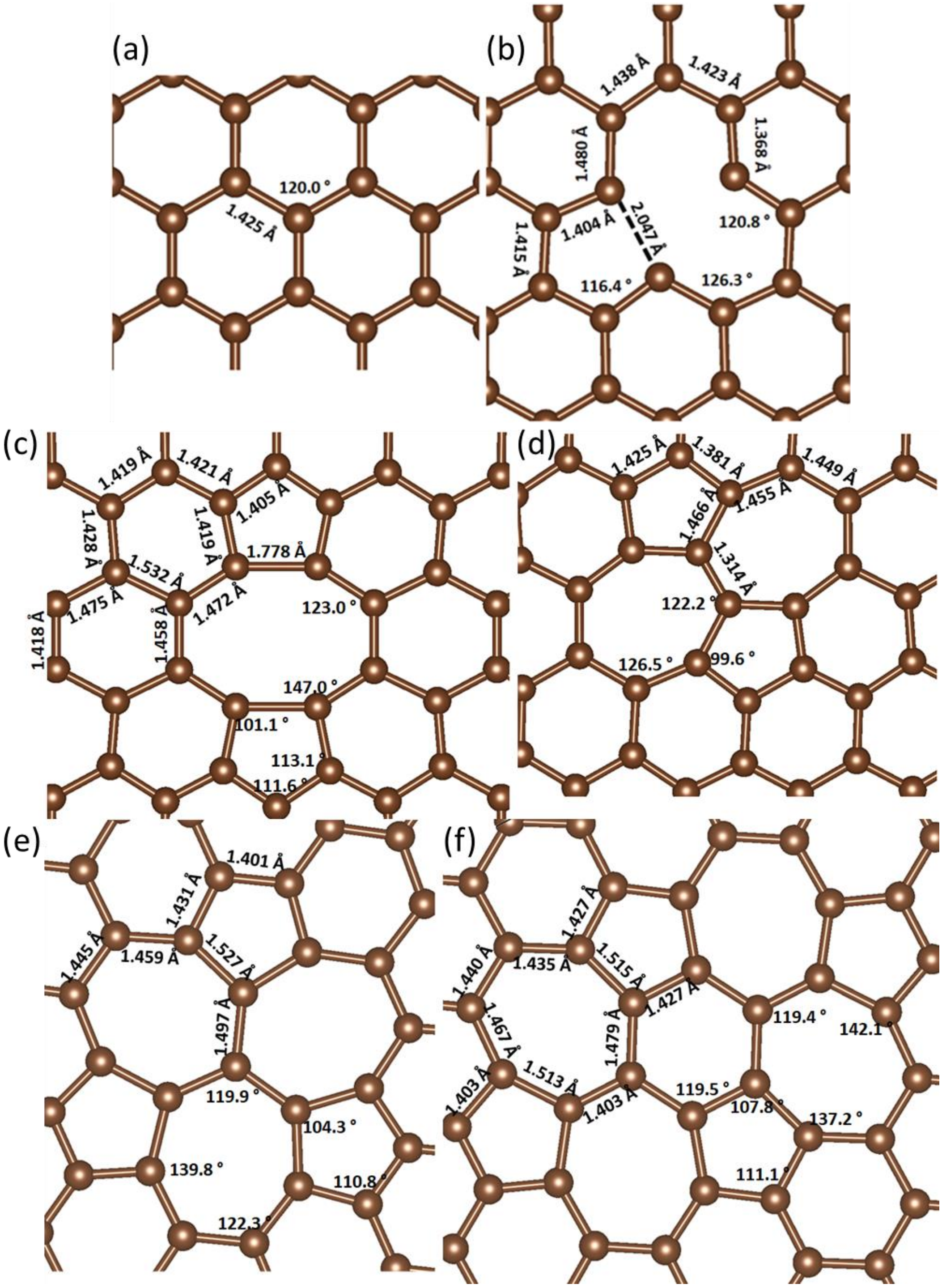

Figure 4: Top view of the optimized graphitic surfaces: a) pristine graphene b) SV c) DV d) SW e) VSW1 f) VSW2. Inset, distances (Å) and angles (°) of interest. Carbon atoms are brown.

Table 2: Charge density at Bond Critical Points of the potential active sites.

Surface Site	$\rho(\vec{r}_{BCP})\ \left(\frac{e^-}{Å^3}\right)$
Graphene (G)	2.03
Single vacancy (SV)	0.587
Double vacancy (DV)	0.974 and 0.979
Stone-Wales defect (SW)	1.863 – 2.589
Stone-Wales defect (VSW1)	1.628 – 2.156
Stone-Wales defect (VSW2)	1.602 – 2.134

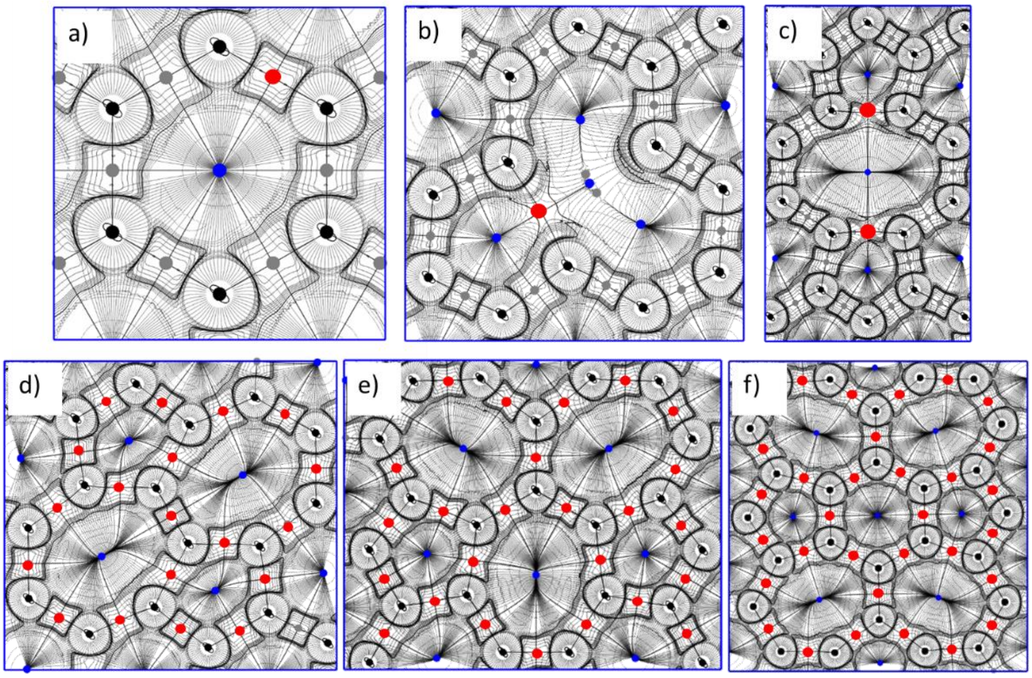

Figure 5: Charge density Laplacian analysis iso-surfaces plot of: a) PG, b) SV, c) DV, d) SW, e) VSW1 and f) VSW2. Red circle indicates the evaluation site for $\rho(\vec{r}_{BCP})$, black circles indicate nuclear charge density maxima, grey Bond Critical Points and blue Ring Critical Points.

I validated the assumptions regarding the active sites by using ammonia (NH_3) as a probe molecule. It was brought near non-equivalent active sites and the system relaxed. In line with previous studies, the graphitic areas possess an inactive π-conjugation, not sensitive to adsorption of molecules[14–17]. Only single vacancies showed a favourable (exothermic) interaction with ammonia, indicating that a $\rho(\vec{r}_{BCP})$ smaller than 0.6 $\frac{e^-}{Å^3}$ defines the active sites on carbon surfaces. Combining the Laplacian of charge density analysis and the performed tests with NH_3, we were able to identify C_3, $C_{3'}$ and C_7 in the single vacancy system as possible active sites (Figure 6).

Then, hydrazine was placed and relaxed on such sites with different initial orientations. Molecule dissociative adsorption[18,19] was also considered, i.e. breaking the N-H or N-N bonds while forming a new one with the surface, similar to previous works on metal surfaces. The least stable N_2H_4 adsorption configuration is the anti-single linked (*a-SL*) configuration where hydrazine bonded C_3 (Figure 6 a). When the molecule is bonded to two active sites in a bridge configuration, it may adopt the cis-bridged (*cB-H*) configuration driving the N-H dissociation (Figure 6 b) or the cis-bridged (*cB-N*) structure resulting in the N-N bond scission (Figure 6 c). It can be seen from the adsorption energies inserted in Figure 6 that the resulting stability increases following the sequence a-SL < cB-N < cB-H. Zheng et al. investigated the same adsorption process on metal-free SiC_3 siligraphene resulting in the following stability sequence: cis-N_2H_4 < gauche-N_2H_4 < anti-N_2H_4[8]. In addition, mechanistic studies performed on metal surfaces, such as Ir[20], Cu[21], Ni[22–24] and Pt[25], are consistent with the siligraphene trends. In this study, a gauche adsorbed configuration was not obtained from structural optimizations, which shows C behaves differently to SiC_3 siligraphene and metals. Unlike in these studies, the different adsorption modes on defective graphene are driven by the lack of electron density. Hence, the *a*-SL structure only saturates one dangling carbon atom showing a week adsorption energy (E_{ADS} = -0.78 eV), whereas when two or more dangling bonds are saturated (cB-N and cB-H, respectively), the species are more strongly bonded to the surface.

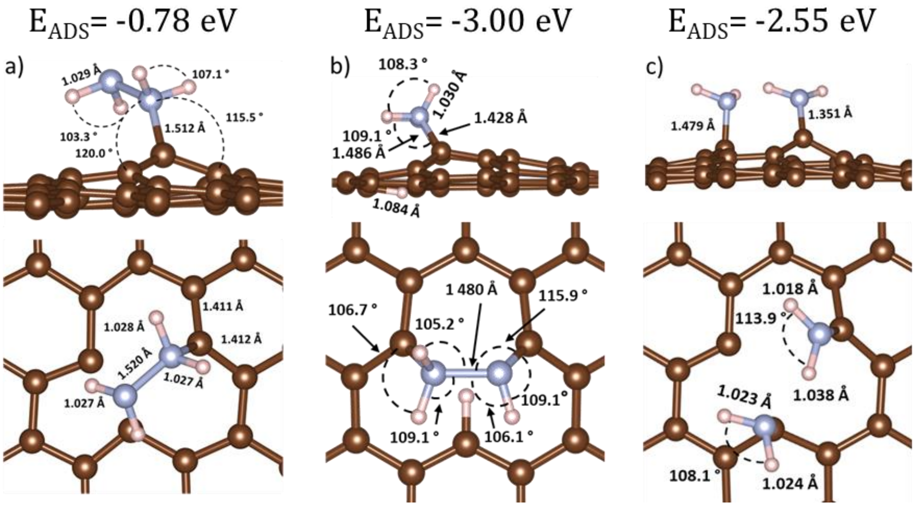

Figure 6: Top and side view of the most favourable Hydrazine configurations: a) a-SL b) cB-H c) cB-N. Inset are the adsorption energies (E_{ADS}) and the main distances (Å) and angles (°) of interest. Carbon atom is labelled in brown, nitrogen in blue and hydrogen in white.

7.2.2.2. Hydrazine decomposition

I considered two symmetric and one asymmetric dehydrogenations, and incomplete decomposition pathways based on previous reports[26–28]. However, only the most stable routes to the formation of H_2 and NH_3 was analysed in detail. The cB-H was the most stable adsorption configuration and the first step for the complete hydrazine reforming ($N_2H_4 \rightarrow N_2 + 2H_2$), whereas the cB-N was the first step towards an incomplete hydrazine decomposition ($3N_2H_4 \rightarrow\ N_2\ +\ 4NH_3$) (Figure 6 b and c, respectively). The difference in energy between the N-H and the N-N dissociative adsorptions indicated that the hydrogen production pathway was the preferable one ($\Delta E_{(NN\text{-}NH)}$ = 0.450 eV). Indeed, once the N-H bond was broken and the C_3-H bond was formed, the reaction pathway leaded towards the hydrogen production.

To proceed with dehydrogenation reaction mechanisms over continuous surfaces, e.g. graphene and metal slabs, we could consider a negligible activation energy for the migration of the dissociated H adatoms similar to the spill on metal catalysts[29]. However, the SV is a point defect, and the active site is isolated from adjacent dangling bonds. Thus, two different hydrogen production pathways were tested (Figure 7). The first one, SWC-Decomposition (symmetric non-directional solvent complete decomposition, Figure 7), simulated the absence of an alkaline aqueous medium and the H species needed to overcome a non-negligible diffusion energy barrier to free the active site. Hence, I investigated the H migration along three different paths (Figure 8) in similar fashion to previous studies[30–32]. For the most favourable migration pathway (Figure 9), I obtained a diffusion energy barrier (E_D) of 3.48 eV in polarizable continuum background, which did not provide a realistic directional solvation in aqueous solutions[31] (Figure 10). According to the simulations, two H atoms occupying nearest neighbour dangling carbon sites had an endothermic reaction energy (E_R = 2.90 eV) to form H_2 (Figure 11). However, the experiments were performed in solution, which surrounded H* with an arranged (dipole) solvation shell promoting the H diffusion through the solution as well as the H_2 evolution through the Heyrovsky mechanism[33]. Thus, I considered the desorption from C_3 negligible in comparison with the energy required to dissociate and form N-H and N-N bonds. The second mechanism tested for the release of C_3, SAC-Decomposition (symmetric alkaline complete decomposition, Figure 7), did not involve diffusion and recombination but the formation of water with the OH^- groups. Indeed, sodium hydroxide could interact and promote the reactivation of the C site to proceed with the dehydrogenation steps.

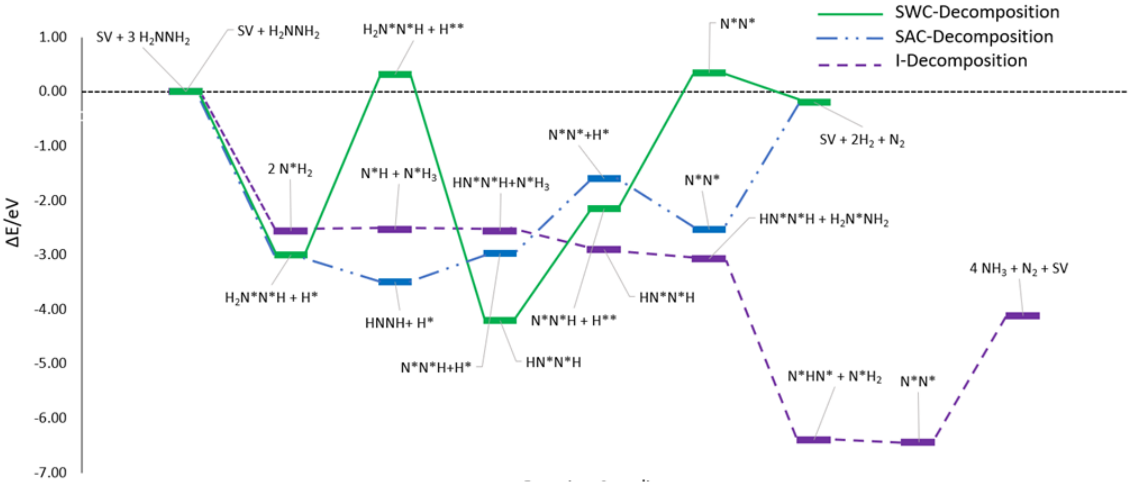

Figure 7: Energy profiles for hydrazine decomposition pathways. Purple line indicates the incomplete decomposition pathway leading to NH_3(I-decomposition), blue and green lines indicate the two possibilities of symmetric dehydrogenation with NaOH and water (respectively SAC- and SWC- decomposition. In the SWC-Decomposition pathway H** indicates diffused atomic hydrogen species, a single * is used to indicate which atom is adsorbed on surface active sites.

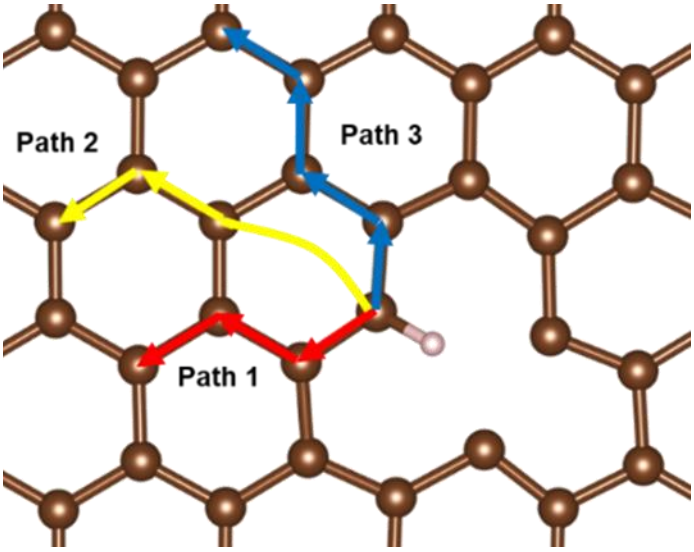

Figure 8: Out of vacancy atomic hydrogen diffusion pathways.

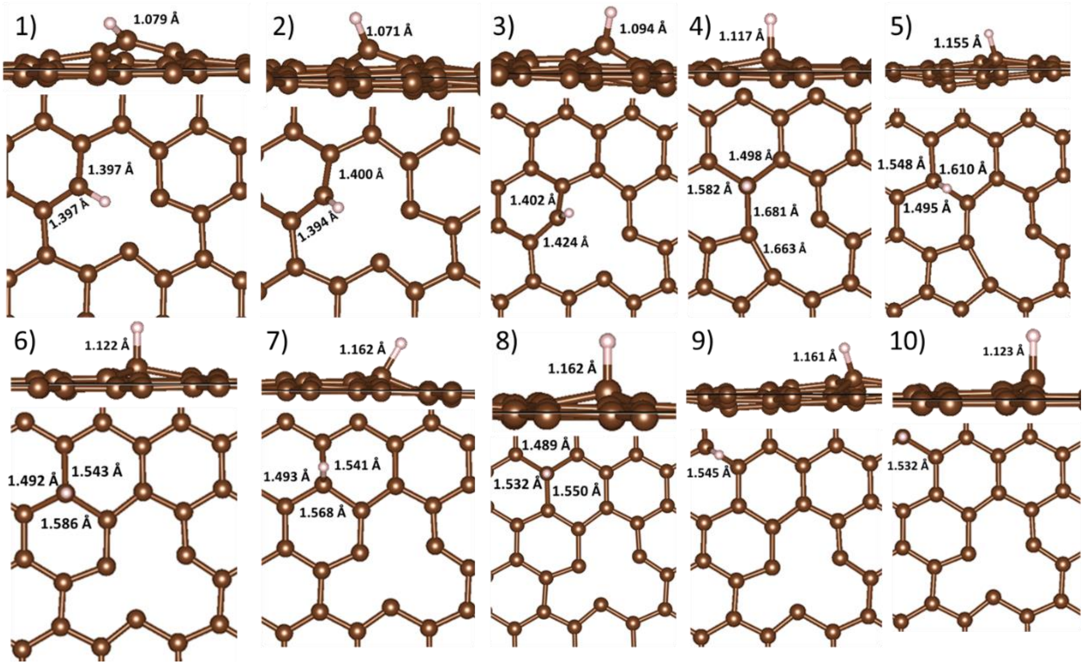

Figure 9: Top and side view of the most favourable steps of hydrogen diffusion process. Inset, distances (Å) and angles (°) of interest. Carbon atom is labelled in brown and hydrogen in white.

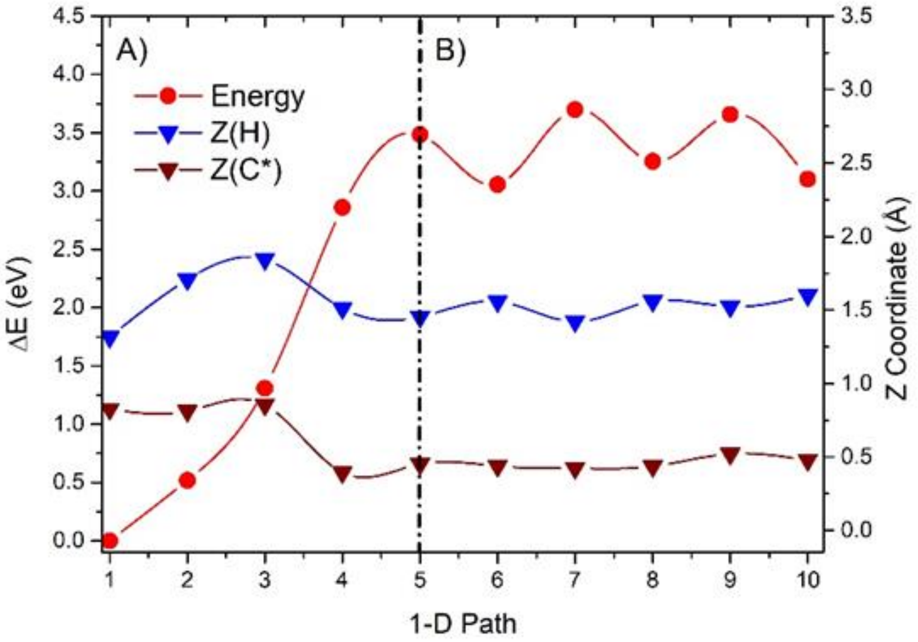

Figure 10: Hydrogen diffusion on SV system. A, left side) Vacancy influence B, right side) Graphene-like behaviour. Red profile: hydrogen diffusion energy profile. Blue profile: H z-coordinate fluctuations. Brown profile: C atom bonded with H z-coordinate fluctuations.

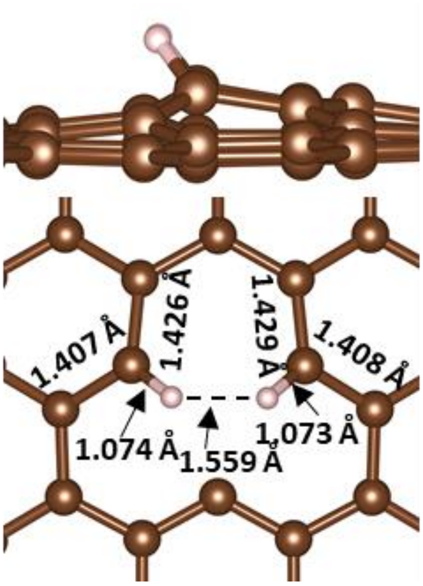

Figure 11: Hydrogen recombination on SV system. Inset, distances (Å) and angles (°) of interest. Carbon atom is labelled in brown and hydrogen in white.

SWC H_2 production

Considering the diffusion and recombination of atomic hydrogen and thus the absence of NaOH, SWC-Decomposition pathway was tested. The first dehydrogenation on cB-H structure, common to both SAC and SWC pathways, presented an increment in the N centres sp^3 character and the N-N bond stretches by about 0.03 Å, while the N-H stretching was negligible. The C_3-N and C_7-N bonds equilibrium lengths were not symmetric and differed by 0.058 Å. In addition, the initial SV site changed its structure to accommodate the adsorbed species (Figure 12 a and Figure 14 a). In the following step along the SWC pathway, the adsorbed $H_2N^*N^*H$ intermediate may take three different dehydrogenation pathways: two symmetric and one asymmetric (Figure 7). Among all symmetric decomposition pathways, SWC was the most favourable one, and for this reason, it will be the only one considered (Figure 7, SWC-decomposition). Upon diffusion on the co-adsorbed H (Figure 12b, E_R = 3.319 eV, the intermediate HNNH (Figure 12 c) showed a N-N bond contraction of 0.037 Å and a reduction of the C_3-N and C_7-N bond lengths (0.094 Å and 0.005 Å, respectively). The superior stability of the adsorbed HN^*N^*H compared to the asymmetric counterpart, $H_2N^*N^*$ ($\Delta E_{\text{Asymm--Symm}}$ = 0.739 eV, Figure 13) could be related to the higher symmetry of the structure. The energy needed to overcome the H_2 in-vacancy recombination energy leads to an endothermic step (E_R = 1.066 eV). The subsequent step proceeded through the scission of another N-H bond (Figure 12 d). The dehydrogenated N centre assumed a sp^2 hybridization, i.e., planar configuration. The structure obtained was exceptionally exothermic due to an overall dangling carbons saturation (E_R of -3.625 eV). Nonetheless, the contribution of E_D (+3.48 eV) slightly increased the reaction energy. In the final structure (Figure 12 e, E_R =+2.50 eV), N-N bond showed an additional contraction indicating an increasing sp hybridization, typical of molecular N_2, which spontaneously evolved from the surface freeing the active site (E_R = -0.19 eV).

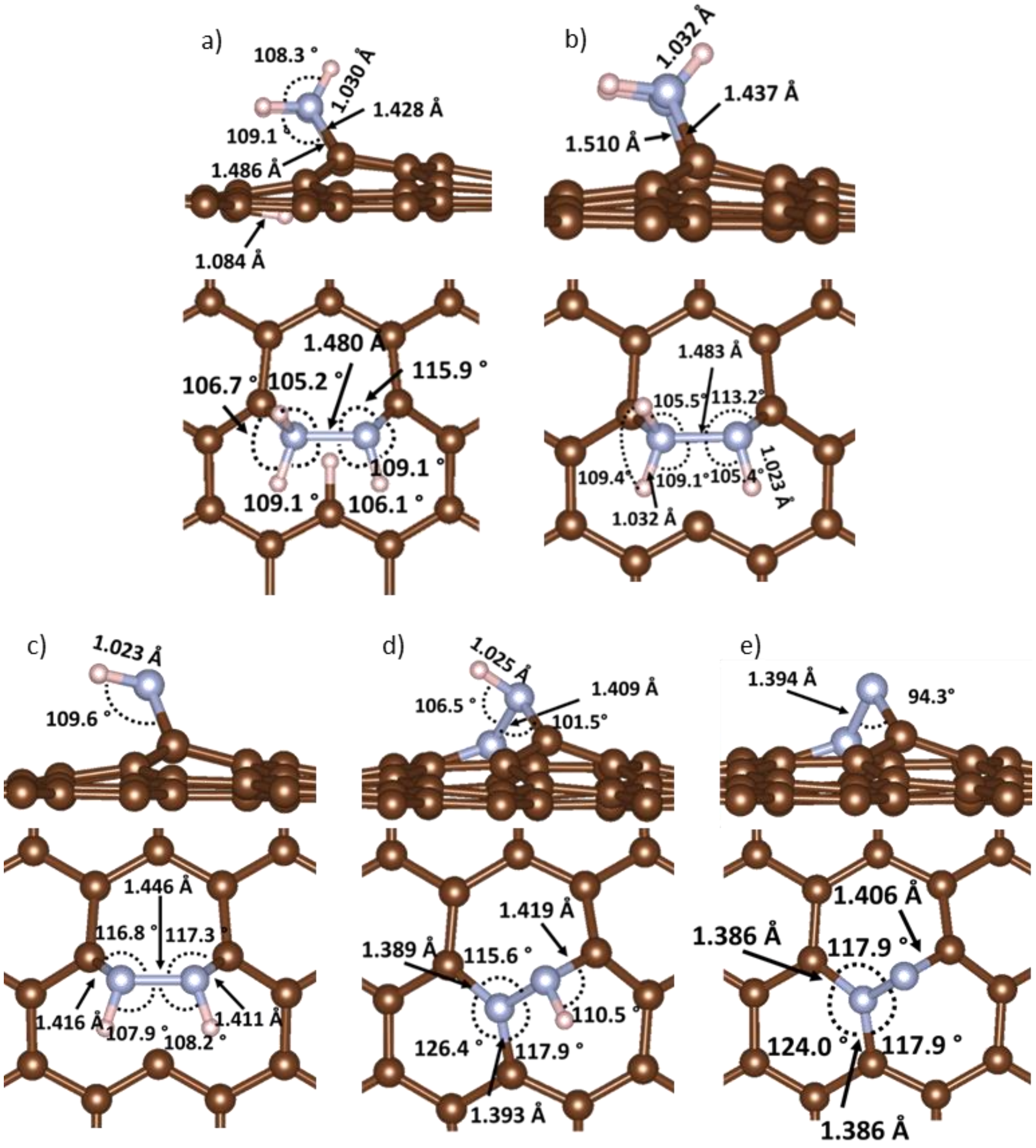

Figure 12: Top and side view of the most favourable hydrazine configurations for H_2 production in water: a) Dissociative adsorption step N*H_2N*H + H*, b) Hydrogen diffusion step N*H_2N*H + H**, c) second dehydrogenation step and H_2 evolution, N*HN* H, d) third dehydrogenation step with diffusion, N*N* H + H** and e) last dehydrogenation step, H_2 and N_2 evolution, N*N*. Inset, distances (Å) and angles (°) of interest. Carbon atoms are labelled in brown, nitrogen in blue and hydrogen in white.

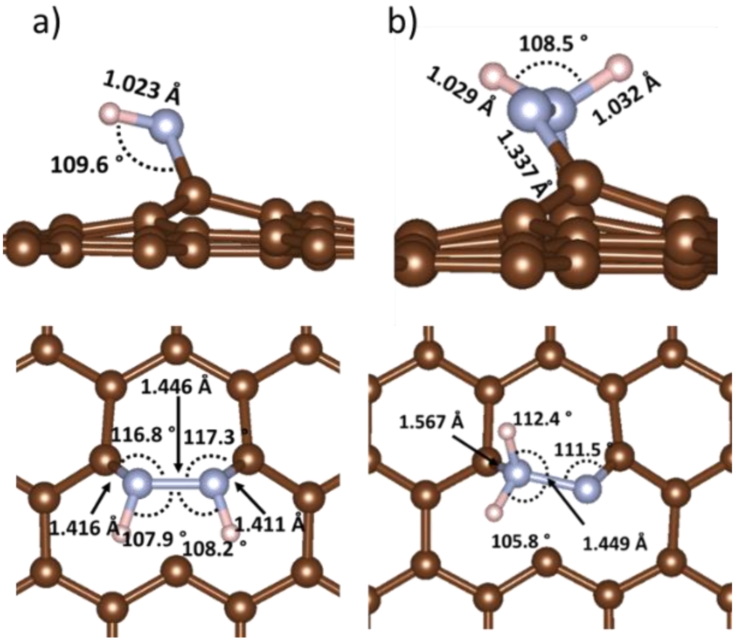

Figure 13: Top and side view of second de-hydrogenation step: a) Symmetric decomposition and b) Asymmetric decomposition. Inset are distances (Å) and angles (°) of interest. Carbon atom is labelled in brown, nitrogen in blue and hydrogen in white. $\Delta E_{Asymm--Symm} = 0.739$ eV.

SAC H_2 production

Here, in contrast to SWC-decomposition pathway, the presence of NaOH is considered disregarding the H recombination-diffusion steps. In this case, OH- can interact with the adsorbed atomic hydrogen, freeing the active site and leading to next dehydrogenation step. The presence of NaOH as alkaline medium (SAC) leaded to a more favourable dehydrogenation pathway (Figure 7). Figure 14 shows the SAC-Decomposition mechanism where, in each step, the dangling bonds were completely saturated increasing its stability. The dissociative adsorption step (Figure 14 a) was followed by a further hydrogen extraction (Figure 14 b, $E_R = -0.491$ eV) due to the interaction with OH^- ions, which presented an exothermic behaviour. Differently from the SWC, the formation of a C_3-H bond influenced both structures and energies ($\Delta E_{SWC-SAC} = 3.810$ eV, Figure 12 b and Figure 14 b). The N-H and C-N bonds were more contracted, in particular the C-N bonds respectively by 0.018 and 0.045 Å, while the N-H bonds by 0.004 and 0.013 Å. In the subsequent step (Figure 14 c, $E_R = 0.525$ eV), further dehydrogenation was performed with the *in-situ* evolution of a molecular hydrogen specie. The C-N bond related to the bare N centre contracted by 0.085 Å, while either N-N or N-H bonds did not show any variation. Moreover, it is possible to observe that the bare N centre tilted towards the C_3-H. Overall, the step is slightly endothermic, due to the breakage of the N-H bond. Subsequently (Figure 14 d), the bare N centre bonded to C_3 and a scission of the N-H bond occurred and the atomic H bonded to a non-active C atom ($E_R = +1.377$ eV). Indeed, from Figure 14 d it is possible to observe that the structure was deformed in order to bond the H atoms. The structure of the last dehydrogenation step (Figure 14 e) was completely equivalent to the one described in the SWC mechanism (Figure 12 e). Nonetheless, from the energetic point view, the difference was mainly related to H_2 evolution. Indeed, in the SWC mechanism it was necessary to overcome the energetic barrier deriving from the in-vacancy recombination of two diffused H atoms (E_R = 2.900 eV, Figure 11). Here, the hydrogen evolution did not require any recombination, leading to an exothermic step (E_R = -0.937 eV). In the last step, N_2 evolution was endothermic and required overcoming an energetic barrier of 2.328 eV.

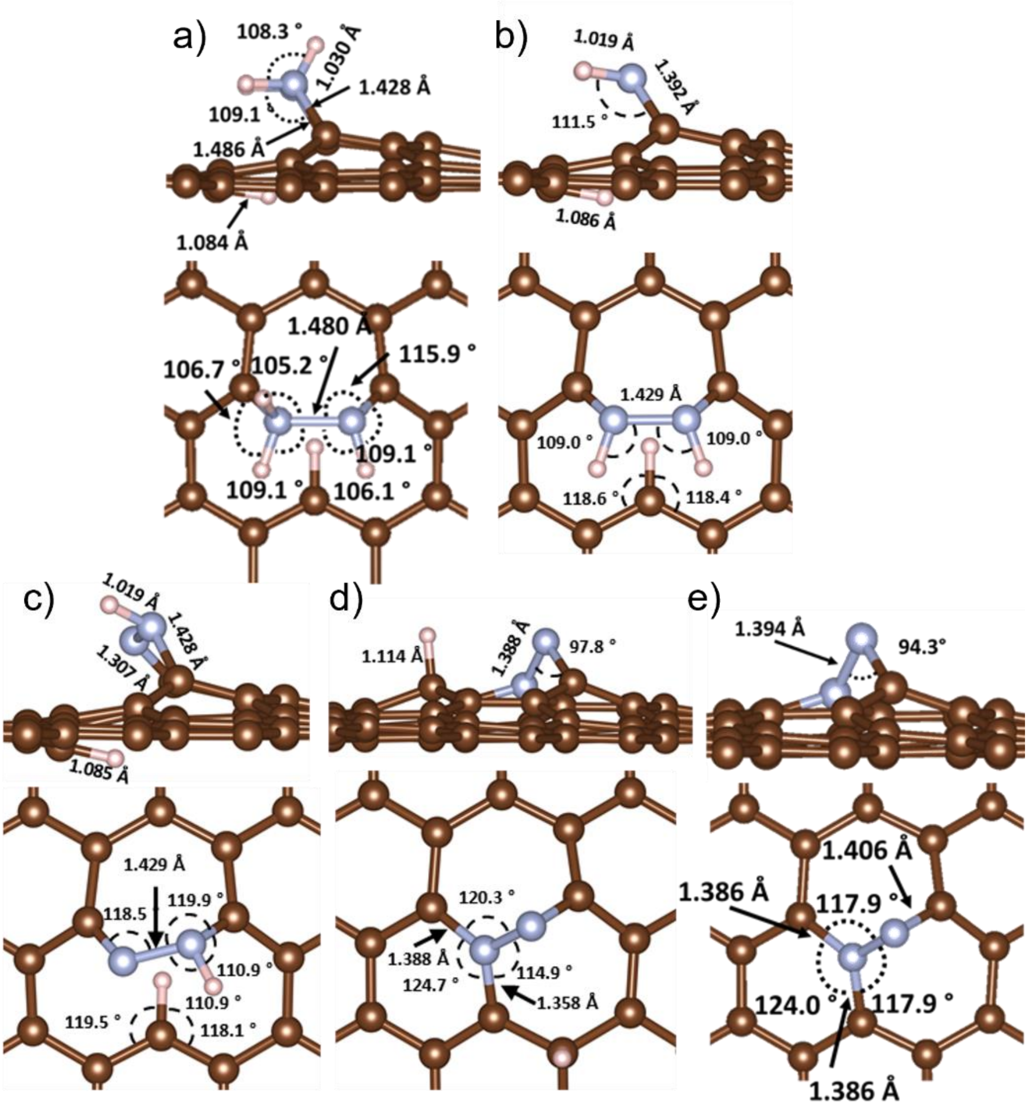

Figure 14: Top and side view of the most favourable hydrazine configurations for H_2 production in presence of aqueous NaOH: a) Dissociative adsorption step $N^*H_2N^*H + H^*$, b) Dehydrogenation step: $N^*HN^*H + H^*$, c) second dehydrogenation step and H_2 evolution, N^*N^* H + H*, d) third dehydrogenation step, $N^*N^* + H^*$ and e) last dehydrogenation step, H_2 and N_2 evolution, N^*N^*. Inset, distances (Å) and angles (°) of interest. Carbon atoms are labelled in brown, nitrogen in blue and hydrogen in white.

NH_3 production

Hydrazine can be also decomposed into NH_3 and N_2 through the incomplete decomposition pathway (I-Decomposition), where three N_2H_4 molecules are involved. The first step of NH_3 production (Figure 15 a) involved the breakage of N-N bond upon adsorption, forming the cB-N structure (E_{ADS} = - 2.55 eV). The two adsorbed NH_2 lied on the dangling carbons with sp^3-like configuration. The following elementary step consisted in a hydrogen transfer, involving the two $N*H_2$, followed by the NH_3 evolution. As can be seen from the structure in Figure 15 b, the remaining N*H tilted toward vacancy centre. A contraction of the free dangling carbons (C_3-$C_{3'}$) distance is then observed, leading to a slightly endothermic process (E_R = + 0.018 eV). To close the catalytic cycle, a subsequent hydrazine adsorption bridging between the available active sites was considered (Figure 15 c). The initial N*H took two hydrogen atoms from the second N_2H_4 in a concerted mechanism upon its adsorption, leading to the formation of HN*N*H + $N*H_3$. This step showed an overall exothermic energy (E_R = - 0.019 eV), along with the following NH_3 exothermic evolution process, leading HN*N*H on the SV (Figure 15 d, E_R = - 0.35 eV). In the subsequent elementary step, a third hydrazine could exothermically co-adsorb on the under-coordinated carbon sites C_7 (E_R = -0.163 eV, Figure 15 e). In this position, the third hydrazine molecule interacted with an H of the adsorbed HN*N*H yielding a NH_3 molecule (Figure 15 e). The structure obtained is energetically favourable (E_R = -3.33 eV, Figure 15 f) and the H-free N bridged between two carbon sites with a sp^2 hybridization. Instead, the C_7 atom was saturated connecting two N atom, showing a conventional sp^3 geometry. The interaction between $N*H_2$ and the H located on the bridged HN*N* leaded to the evolution of the last NH_3 (Figure 15 f, E_R = -0.05 eV). The resulting N_2 was anchored on the carbon lattice (E_R = +2.32 eV) analogously to the SAC hydrogen production pathway.

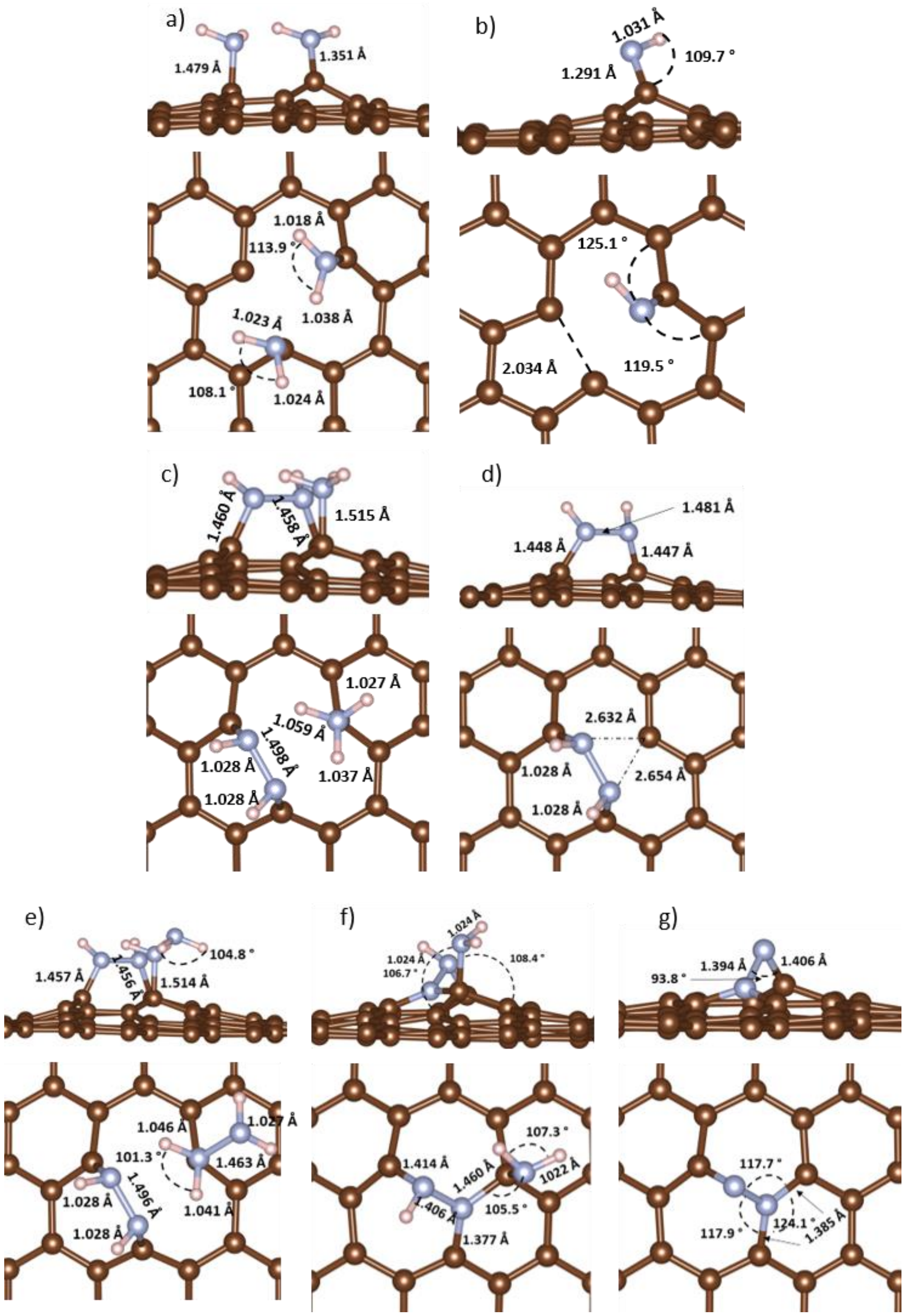

Figure 15: Top and side view of the most favourable Hydrazine configurations for NH_3 production: a) N-N bond breakage step, 2 N^*H_2, b) First NH_3 evolution step, N*H, c) Second Hydrazine adsorption step, N*HN*H + N^*H_3 , d) Second NH_3 evolution step, N*HN*H, e) Third Hydrazine linkage step**,** N*HN*H + $N^*H_2NH_2$**,** f) Third NH_3 evolution step, N*HN* + N^*H_2 and g) Fourth NH_3 and N_2 evolution step, N*N*. Inset, distances (Å) and angles (°) of interest. Carbon atom is labelled in brown, nitrogen in blue and hydrogen in white.

Rationalizing the results obtained combining experimental and DFT study the activity and the selectivity of the most performing material (PR24-PS) can be explained. In particular, SV defect showed an exothermic adsorption energy to our substrate, indicating that it is the only defect which participates in the reaction. CNFs-PS is the catalyst with the higher defectiveness degree, leading to the observed enhanced activity in the experimental results. Moreover, the investigation on the two complete dehydrogenation pathways (SWC- and SAC-Decomposition) can explain the difference in the reaction rate changing the pH. Indeed, in absence of NaOH the adsorbed atomic hydrogen needs to overcome the energetic barrier due to its diffusion and recombination, whereas in alkaline environment the OH^- ions can interact with H*, freeing the active site and leading to next dehydrogenation step. Confirming that, a selectivity for H_2 of the 89 % at 94 % of conversion was found testing CNFs-PS in presence of NaOH. Considering the initial dissociative adsorption, the first step of the dehydrogenation pathway is the more favourable (dissociation of the N-H bond, -3.00 eV) than the scission of the N-N bond (-2.55 eV) which lead to NH_3 as product. This first reaction step is crucial to define the reaction mechanisms and the computational results fully agree with the ones obtained in the experiments.

7.3. Conclusions

In this study, different metal-free carbonaceous materials, i.e. CNFs PS, CNFs HHT and graphite were tested in hydrazine hydrate decomposition reaction for the first time. In addition, a systematic density functional theory (DFT) study on N_2H_4 adsorption and decomposition mechanism was then employed to understand the role of the defects paving the pathway to the development of new and efficient carbocatalysts to be used in this reaction. A conversion of 94 %, 71 % and 65 % was observed after 6 h of reaction for CNFs PS, CNFs HHT and graphite, respectively. For the best of our knowledge, this is the first work reported in literature, which shows the ability of metal-free carbonaceous materials to decompose hydrazine hydrate. Moreover, a selectivity for H_2 of the 89 % at 94 % of conversion was found testing CNFs-PS. The materials were also analysed using ICP and Raman spectroscopy. A correlation between the numbers of defects present in the catalysts and the initial activity of the hydrazine decomposition reaction was found. In particular, initial activity increases increasing the number of defects, i.e. CNFs-PS > CNFs-HHT > graphite. Correlating the I_D/I_G ratio obtained by Raman spectroscopy and the initial activity, a linear correlation was found. In addition, CNFs PS were also tested in absence of alkaline medium to understand the effect of NaOH. The catalyst showed a conversion (15 % conversion at 4 h) lower than in presence of NaOH (70 % conversion at 4 h).

In order to understand the effect of the defects on the decomposition of hydrazine, different surfaces were modelled using DFT calculation, i.e. pristine graphene, single and double vacancies, and different Stone–Wales defects. According to our previous studies, only SV showed an exothermic adsorption energy to the considered substrate, indicating that it is the only defect, which participates in the reaction. Two symmetrical and one asymmetrical dehydrogenation pathways were found, but only the most favourable (symmetric hydrazine dehydrogenation) was considered in the discussion. On the most stable hydrogen production pathway, the effect of the alkaline medium was elucidated through calculations concerning the diffusion and recombination of atomic hydrogen. Indeed, the presence of NaOH helps extracting H species without additional energetic barriers, as opposed to the calculations performed in polarizable continuum medium. In addition, an incomplete decomposition pathway forming N_2 and NH_3 was studied and compared with the dehydrogenation one. Considering the initial dissociative adsorption, the first step of the dehydrogenation pathway is the more favourable (dissociation of the N-H bond, -3.00 eV) than the scission of the N-N bond (-2.55 eV) which lead to NH_3 as product. This first reaction step is crucial to define the reaction mechanisms and the computational results fully agree with the ones obtained in the experiments. Moreover, comparing two different hydrogen production pathways (with and without diffusion and recombination), I confirmed that the presence of sodium hydroxide in the experimental reaction environment can modify the energy gap between the two pathways, leading to a selectivity to H_2 near 90 %. Overall, this work provides a complete insight of hydrazine decomposition over intrinsic elementary defects of metal-free carbonaceous catalysts. Finally, these results can be used as a raw model for the synthesis of carbocatalysts with enhanced features for the liquid phase hydrazine decomposition reaction, focusing on widening the $\Delta E_{(NN—NH)}$ energy gap.

7.4. References

[1] Y. B. Jang, T. H. Kim, M. H. Sun, J. Lee, S. J. Cho, Catal. Today 2009, 146, 196–201.
[2] S. J. Cho, J. Lee, Y. S. Lee, D. P. Kim, Catal. Letters 2006, 109, 181–186.
[3] X. Du, P. Cai, W. Luo, G. Cheng, Int. J. Hydrogen Energy 2017, 42, 6137–6143.
[4] S. K. Singh, X.-B. Zhang, Q. Xu, J. Am. Chem. Soc. 2009, 131, 9894–9895.
[5] Z. Zhang, S. Zhang, Q. Yao, X. Chen, Z.-H. Lu, Inorg. Chem. 2017, 56, 11938–11945.
[6] L. He, B. Liang, Y. Huang, T. Zhang, Natl. Sci. Rev. 2018, 5, 356–364.
[7] S. K. Singh, Z. Lu, Q. Xu, Eur. J. Inorg. Chem. 2011, 2011, 2232–2237.
[8] F. Zheng, H. Dong, Y. Ji, Y. Li, Appl. Surf. Sci. 2019, 469, 316–324.
[9] I. Barlocco, S. Capelli, X. Lu, S. Tumiati, N. Dimitratos, A. Roldan, A. Villa, Nanoscale 2020, 12, 22768–22777.
[10] F. Tuinstra, J. L. Koenig, J. Chem. Phys. 1970, 53, 1126–1130.
[11] J. Wang, X.-B. Zhang, Z.-L. Wang, L.-M. Wang, Y. Zhang, Energy Environ. Sci. 2012, 5, 6885.
[12] S. K. Singh, A. K. Singh, K. Aranishi, Q. Xu, J. Am. Chem. Soc. 2011, 133, 19638–19641.
[13] C. R. Wick, T. Clark, J. Mol. Model. 2018, 24, 1–9.
[14] X. Lu, A. Roldan, J. Phys. Chem. C 2021, DOI 10.1021/acs.jpcc.1c03996.
[15] L. Ma, J. M. Zhang, K. W. Xu, V. Ji, Appl. Surf. Sci. 2015, 343, 121–127.
[16] X. Y. Liu, J. M. Zhang, K. W. Xu, V. Ji, Appl. Surf. Sci. 2014, 313, 405–410.
[17] S. Yang, Z. Lan, H. Xu, G. Lei, W. Xie, Q. Gu, J. Nanotechnol. 2018, 2018, DOI 10.1155/2018/2031805.
[18] D. C. de Oliveira, W. O. Silva, M. Chatenet, F. H. B. Lima, Appl. Catal. B Environ. 2017, 201, 22–28.
[19] B. Luo, T. Wu, L. Zhang, F. Diao, Y. Zhang, L. Ci, J. Ulstrup, J. Zhang, P. Si, Electrochim. Acta 2019, 317, 449–458.
[20] X. Lu, S. Francis, D. Motta, N. Dimitratos, A. Roldan, Phys. Chem. Chem. Phys. 2020, 22, 3883–3896.
[21] S. S. Tafreshi, A. Roldan, N. H. de Leeuw, Phys. Chem. Chem. Phys. 2015, 17, 21533–21546.
[22] M. K. Agusta, H. Kasai, Surf. Sci. 2012, 606, 766–771.
[23] H. Yin, Y.-P. Qiu, H. Dai, L.-Y. Gan, H.-B. Dai, P. Wang, J. Phys. Chem. C 2018, 122, 5443–5451.
[24] M. K. Agusta, M. David, H. Nakanishi, H. Kasai, Surf. Sci. 2010, 604, 245–251.
[25] M. K. Agusta, W. A. Diño, M. David, H. Nakanishi, H. Kasai, Surf. Sci. 2011, 605, 1347–1353.

[26] J. P. Contour, G. Pannetier, J. Catal. 1972, 24, 434–445.

[27] R. Maurel, J. C. Menezo, J. Catal. 1978, 51, 293–295.

[28]P.-X. Zhang, Y.-G. Wang, Y.-Q. Huang, T. Zhang, G.-S. Wu, J. Li, Catal. today 2011, 165, 80–88.

[29] D. Zhao, D. Lü, Y. Zang, X. Zhao, Prog. Chem. 1997, 9, 759–788.

[30]C. P. Herrero, R. Ramírez, Phys. Rev. B - Condens. Matter Mater. Phys. 2009, 79, 1–8.

[31] Y. Lei, S. A. Shevlin, W. Zhu, Z. X. Guo, Phys. Rev. B - Condens. Matter Mater. Phys. 2008, 77, 1–8.

[32] L. Chen, A. C. Cooper, G. P. Pez, H. Cheng, J. Phys. Chem. C 2007, 111, 18995–19000.

[33] E. Skúlason, V. Tripkovic, M. E. Björketun, S. Gudmundsdóttir, G. Karlberg, J. Rossmeisl, T. Bligaard, H. Jónsson, J. K. Nørskov, J. Phys. Chem. C 2010, 114, 18182–18197.

8. CONCLUSIONS AND FUTURE WORKS

Benign and sustainable alternative energy sources are needed to mitigate the increasing dependence on fossil fuels and their high environmental impact. Hydrogen is recognised as an efficient alternative energy carrier because of its high energy density and innocuous products upon utilisation. Despite this, its direct use is hindered due to the shortage of economically and sage hydrogen storage technologies and, therefore, alternative methods to store and transport it is of paramount importance. Among all, liquid-phase hydrogen carriers are one of the most promising alternatives because of the high hydrogen content, mild decomposition conditions and availability. These chemicals can release hydrogen on-demand using a suitable catalyst and with high hydrogen generation rate. Moreover, liquid state is more suitable for storage and transportation employing the existing technologies. Among them, formic acid (FA) and hydrazine hydrate ($N_2H_4 \cdot H_2O$) are two of the most auspicious candidates.

Different are the issues to solve in order to efficiently employ these chemicals in our energy transition. In particular, efficient carbon-based heterogeneous systems can effectively make enormous difference in the production of hydrogen from liquid carriers. Indeed, metal-based catalysts and especially Pd-based ones offer enhanced activity also at room temperature, but selectivity and stability need to be improved to be industrially applicable. In addition, carbon materials have the advantage of being easily tuned through variation in their structure, for example, changing the surface area and porosity and adding functional groups or generating topological defects. Moreover, their stability in liquid phase reactions makes them auspicious candidates in catalytic processes.

For these reasons, the aim of my thesis is to design new catalytic systems in order to limit or avoid these problems.

In Chapters 3-6 this thesis focused on formic acid (FA) selective decomposition reaction. Indeed, FA is non-toxic compound that can be obtained from catalytic conversion of lignocellulose and possesses a high hydrogen content (4.4 wt% of H_2).

In the last few years, scientists have been increased their attention on the design of selective heterogeneous catalysts able to convert FA into H_2. These materials have the advantage to be easily recovered from the reaction mixture and reused. Different metals have been used to decompose formic acid at mild conditions (temperature lower than 50 °C and atmospheric pressure) such as Cu, Au, Ag, Pd.

Pd/C catalysts have been deeply studied due to their ability to obtain hydrogen from FA decomposition even at room temperature. Unfortunately, Pd catalysts are not fully selective toward the dehydrogenation pathway and they produce CO in a large extent. The high affinity with CO, that blocks the active sites, results in a rapid deactivation, limiting its industrial application. For these reasons, the aim of these four Chapters describes the design of catalysts with better performance in terms of activity, selectivity and durability compared to the existing Pd-based catalysts acting on both support and active phase adding a second metal.

It has been shown that metal-support interaction plays a fundamental role in modify the behaviour of the catalytic material. An efficient interaction between support and NPs can also prevent their migration, coalescence and Ostwald ripening, increasing the stability of the catalyst. In particular, carbon surface structural features strongly influence the metal-support interaction. The introduction of heteroatoms, e.g. O, N, B and P, in carbon materials' honeycomb lattice structure can increase the activity and the stability of the catalyst changing its electronic features. Indeed, ***Chapter 3*** started with the deposition of Pd nanoparticles (NPs) on oxygen and phosphorous functionalised carbon nanofibers (CNFs) by sol immobilization method leading to 1wt%Pd@O-HHT and 1wt%Pd@P-HHT catalysts. A combination of DFT and experimental data were employed to investigate and understand the support-metal interaction. The catalysts obtained were characterized using TEM and XPS analyses. The kinetic profiles evidenced an increasing of conversion after two hours for both the functionalised systems respect the bare HHT standard. This enhanced catalytic behaviour can be assessed to an interaction between the metal and the functional groups on the support confirmed by XPS and TEM analyses. Furthermore, an inhibition of the dehydration pathway was obtained for the functionalised materials. An excellent durability was observed in both systems during six consecutive runs, avoiding the leaching of Pd as observed for 1wt%Pd@HHT. These results were supported by a systematic DFT study of the Pd adhesion energies on different O and P functionalised surfaces shedding light to the stabilisation effect of the functional groups on Pd clusters. All functionalised surfaces showed stronger stabilisation of the Pd cluster than on the pristine graphene model confirming an increased stability of Pd nanoparticles. In particular, oxygenated supports displayed a stronger interaction with Pd validating the observed increased stability of the 1wt%Pd@O-HHT catalyst.

A different strategy to modify the catalytic properties of a material is the introduction of a second metal to form an alloy structure. This is due to two different effects: the formation of new electronic states (ligand effect) and the strain of the lattice (steric effects). Indeed, Chapter 4 and 5 focused on the investigation of the catalytic behaviour of two different alloys: Pd_xAu_y and Pd_xRh_y. In ***Chapter 4***, rhodium was chosen because it was recently demonstrated by using theoretical calculations that the addition of Rh to Pd enhance the activity of pure Pd in the formic acid dehydrogenation, enhancing the selectivity to H_2 and avoiding the formation of CO which acts as poison for Pd catalysts. The beneficial effect obtained by introducing Rh to Pd was attributed to a contraction of the Pd-Pd distance and the increase in the electron density in surface Pd atoms compared to pure Pd. It is worth to underline that the PdRh systems are barely studied. The problem is that it is difficult to obtain well-defined bimetallic Pd-Rh structure. In fact, Pd and Rh are immiscible at the thermal equilibrium bulk state over the whole composition range, therefore the alloy is in a segregated state at room temperature. Indeed, PdRh alloyed NPs and the monometallic counterparts were preformed and supported on HHT by sol immobilization method. PdRh NPs had an average particle size in the range of 2-4 nm even at low temperature as confirmed by STEM-HAADF and STEM-XEDS analyses. However, the composition of the particles is not homogeneous from particle to particle and a general enrichment in Pd was observed compared to the nominal Pd-Rh ratio. These results were attributed to the unsuccessful quantitative immobilization of Rh, as evidenced by ICP analysis. Bimetallic catalysts showed good activity in the dehydrogenation of formic acid in liquid phase, in particular for Pd-rich bimetallic systems ($Pd_{90}Rh_{10}$ and $Pd_{69}Rh_{31}$). Comparing the product analysis of liquid and gas phase products, we concluded that the major reaction pathway towards the production of CO_2 and H_2 was obtained for all the catalysts, with minor formation of CO in the range of 5-15 ppm. However, in the case of monometallic Pd, traces of CO (11-15 ppm) were observed. A good stability during 6 consecutive runs was observed for $Pd_{69}Rh_{31}$ compared to monometallic Pd which rapidly deactivate. The low stability of this latter one was attributed to the growing of particle size due to coalescence of the particle, partial Pd leaching and presence of CO which acts as poison for Pd-based catalysts. Furthermore, monometallic Pd, $Pd_{90}Rh_{10}$ and $Pd_{69}Rh_{31}$ were tested in the muconic acid hydrogenation using formic acid as hydrogen donor, under mild conditions. The catalysts showed good activity for the first step of the reaction, towards the production of monounsaturated products. Only in the case of using bimetallic catalysts the second step of the reaction towards the formation of adipic acid was enhanced.

On the other hand, in ***Chapter 5*** Au was selected because it is able to overcome the selectivity problem generating ultrapure hydrogen. This work combines DFT and experimental data to disclose the role of gold in enhancing activity, selectivity and stability of palladium catalyst during the formic acid decomposition. PdAu catalysts were synthesised using sol-immobilization technique with a systematic variation of Au to Pd molar ratio, obtaining in the majority cases an alloy with an enrichment of palladium on the surface confirmed by XPS, STEM-HAADF and STEM-XEDS analyses. The activity plot showed a typical volcano trend with a maximum for $1\%Pd_6Au_4@HHT$ catalyst (3539 h^{-1}). An increasing in conversion at 2 h of reaction is observed for most of the bimetallic systems, in particular for $1\%Pd_6Au_4@HHT$ and $1\%Pd_8Au_2@HHT$ (73% and 68%, respectively). Moreover, an inhibition of the dehydration pathway was observed for gold-containing catalysts. $1\%Pd_6Au_4@HHT$ and $1\%Pd_8Au_2@HHT$ also showed an excellent stability during six consecutive runs, whereas 1%Pd@HHT rapidly deactivates because of leaching, coalescence and CO-poisoning. DFT models of Pd_{15}, Au_{15} and Pd_9Au_6 clusters were then employed to better understand the beneficial effect of gold observed in the experimental results. While Au_{15} was not able to interact with FA, Pd_{15} and Pd_9Au_6 could exothermically adsorb the substrate according to our observations. Nonetheless, the Pd_9Au_6 catalyst showed a more exothermic adsorption of formic acid than Pd_{15}, confirming the superior activity of the bimetallic system. Moreover, considering the pathways observed for both systems, the Pd_9Au_6 favourite route was the formation of carbon dioxide and hydrogen, while Pd_{15} can follow both the dehydrogenation and dehydration pathways, in agreement with the analyses performed on the products. Additionally, this study demonstrated a stronger interaction between the bimetallic system and the support confirming the excellent durability results observed in the experimental part, using the analysis of the electronic structures of the different modelled clusters. These results demonstrate that alloying Pd with Au facilitates the synthesis of active, highly selective and durable catalysts for the sustainable formation of hydrogen from formic acid decomposition at mild conditions.

Moreover, to increase the overall sustainability of the process and decrease the cost of the final materials, metal-free catalysts were also tested in FA decomposition. These results were described in ***Chapter 6***. Indeed, carbon-based catalysts are attracting significant attention to reduce the use of metals in heterogeneous catalytic reactions. In addition to heteroatoms, carbon materials can also be tuned by generating topological defects. Different studies have demonstrated that the presence of intrinsic defects in carbon materials can be active in different catalytic reactions. In order to demonstrate the activity of the different defects in FA dehydrogenation, I carried out a systematic investigation on graphitic defects as active sites. Indeed, different metal-free catalysts based on graphitic structures (Pristine graphene GP, graphene oxide GO, PS and LHT carbon nanofibers PR24-PS and PR24-LHT) were experimentally tested and their structure analyzed by BET, XPS and Raman spectroscopies. After 5 minutes of reaction, all the catalysts deactivate, showing a final conversion of 3 % for GP, 14 % for PR24-LHT, 27 % for PR24-PS and 28 % for GO. I found a correlation between the FA conversion and the number of defects presented in the catalysts. In particular, the FA decomposition increases by increasing the defectiveness of the material, i.e. in the order GO > PR24-PS > PR24-LHT > GP. This result was confirmed by both XPS and Raman techniques. Plotting the conversion vs. I_D/I_G ratio and vs. the amount of different oxygen groups displayed on the surface, we found a linear correlation between conversion and defects ($R^2 = 0.99$), but no direct correlation with oxygen groups was established. I was, then, able to ascribe the activity of the materials to the defects and not to the presence of oxygen functional groups. In order to understand the role of the different type of defects, I investigated the decomposition of formic acid using DFT models of pristine graphene and different defective graphene surfaces, e.g. single and double vacancy, and different Stone-Wales defects. I demonstrated that not all defects act as active centers to adsorb and decompose formic acid. The activity is mainly due to the single vacancy defect because it is the only system able to decompose formic acid to gaseous molecules, thus recycling the active site. Two different pathways were found, one passing through the carboxyl species and the other one through a hydroxymethylene intermediate. In both cases, I obtained the saturation of the active site because of CO and atomic hydrogen irreversible adsorption. For the double vacancy structure, the hydroxymethylene pathway can be compared with the one of the single vacancy defects, while for the Stone-Wales no active sites were found able to decompose the FA molecule. Different types of oxygen functionalities (e.g. epoxide, oxygen incorporated in the structure and hydroxyl) were investigated, but they did not show any activity in the adsorption of FA, confirming the experimental results where no direct correlation between oxygen groups and catalytic behavior was observed. When the vacancies are completely saturated, the catalyst deactivates explaining the experimental deactivation after 5 minutes of reaction. In conclusion, a first insight into the role of the defects present on carbon material in the FA dehydrogenation and dehydration was provided.

A further step in the development of a fully sustainable hydrogen economy is to investigate H_2 production from carbon-free liquid-phase hydrogen carriers, hence avoiding undesired emissions, e.g. CO_2, and species damaging the catalysts, e.g. CO poisoning Pt/C electrodes in proton exchange membrane fuel cells (PEMFCs). Indeed, Hydrazine (N_2H_4) can be employed as hydrogen carrier because it is liquid at T < 114 °C (1 atm) and can be easily transported. Moreover, N_2H_4 possesses a hydrogen content of 12.5 wt% and decomposes into a mixture of ammonia, hydrogen and nitrogen in the presence of catalysts such as Shell 405 (30 wt % Ir/Al_2O_3). The production of NH_3 is the thermodynamically favoured reaction and it needs to be avoided. Because of its hypergolic nature, the risk of explosion is one of the most serious problem related to handling hydrazine, especially in the presence of a metal that may catalyse its decomposition. One solution can be the dilution of N_2H_4 in water, forming hydrous hydrazine ($N_2H_4 \cdot H_2O$), which can be particularly important as a liquid hydrogen source. Hydrous hydrazine still contains 7.9 wt % of hydrogen, avoiding all the issues related to H_2 storage and transportation. The development of a catalyst capable to exothermically react with $N_2H_4 \cdot H_2O$ and selectively decompose it into hydrogen is key for a H_2-based economy. In order to generate hydrogen in a controlled manner and on-demand, different supported and unsupported metal NPs have been investigated. At first, noble metals such as Ir and Rh perform well as reforming catalyst. Nevertheless, due to the cost and synergetic catalytic properties, Ni was introduced as second metal providing superior activity and selectivity. The addition of an alkali medium (NaOH solution) can enhance the selectivity and the rate of the reaction. Despite the excellent activity, selectivity and stability of metal-based catalysts, employing metals is raising reservations about the overall sustainability of hydrogen production reactions. Moreover, the decomposition of hydrazine on a metal-free carbon-based catalyst has been reported only on g-Si_3C and only by DFT studies.

Indeed, the metal-free carbon-based catalysts employed in Chapter 6, were also tested in hydrazine decomposition reaction and the results were exposed in ***Chapter 7***. Different metal-free carbonaceous materials, i.e. CNFs PS, CNFs HHT and graphite were tested in hydrazine hydrate decomposition reaction for the first time. In addition, a systematic density functional theory (DFT) study on N_2H_4 adsorption and decomposition mechanism was then employed to understand the role of the defects paving the pathway to the development of new and efficient carbocatalysts to be used in this reaction. A conversion of 94 %, 71 % and 65 % was observed after 6 h of reaction for CNFs PS, CNFs HHT and graphite, respectively. Moreover, a selectivity for H_2 of the 89 % at 94 % of conversion was found testing CNFs-PS. The materials were also analysed using ICP and Raman spectroscopy. A correlation between the numbers of defects present in the catalysts and the initial activity of the hydrazine decomposition reaction was found. In particular, initial activity increases increasing the number of defects, i.e. CNFs-PS > CNFs-HHT > graphite. Correlating the I_D/I_G ratio obtained by Raman spectroscopy and the initial activity, a linear correlation was found. In addition, CNFs PS were also tested in absence of alkaline medium to understand the effect of NaOH. The catalyst showed a conversion (15 % conversion at 4 h) lower than in presence of NaOH (70 % conversion at 4 h).

In order to understand the effect of the defects on the decomposition of hydrazine, different surfaces were modelled using DFT calculation, i.e. pristine graphene, single and double vacancies, and different Stone–Wales defects. According to our previous studies, only SV showed an exothermic adsorption energy to our substrate, indicating that it is the only defect, which participates in the reaction. Two symmetrical and one asymmetrical dehydrogenation pathways were found, but only the most favourable (symmetric hydrazine dehydrogenation) was considered in our discussion. On the most stable hydrogen production pathway, the effect of the alkaline medium was elucidated through calculations concerning the diffusion and recombination of atomic hydrogen. Indeed, the presence of NaOH helps extracting H species without additional energetic barriers, as opposed to the calculations performed in polarizable continuum medium. In addition, an incomplete decomposition pathway forming N_2 and NH_3 was studied and compared with the dehydrogenation one. Considering the initial dissociative adsorption, the first step of the dehydrogenation pathway is the more favourable (dissociation of the N-H bond, -3.00 eV) than the scission of the N-N bond (-2.55 eV) which lead to NH_3 as product. This first reaction step is crucial to define the reaction mechanisms and the computational results fully agree with the ones obtained in the experiments.

Moreover, comparing two different hydrogen production pathways (with and without diffusion and recombination), I confirmed that the presence of sodium hydroxide in the experimental reaction environment can modify the energy gap between the two pathways, leading to a selectivity to H_2 near 90 %. Overall, this work provides a complete insight of hydrazine decomposition over intrinsic elementary defects of metal-free carbonaceous catalysts. Finally, these results can be used as a raw model for the synthesis of carbocatalysts with enhanced features for the liquid phase hydrazine decomposition reaction, focusing on widening the $\Delta E_{NN—NH}$ energy gap.

Further studies on both formic acid and hydrazine hydrate will concern the investigation of different functionalisation on metal-free carbon materials, e.g. O, N, B, S and P. Functionalisations will be introduced on both pristine and defective materials in order to study the different functional groups inserted. Indeed, it is reported that this modification induces changes in the electronic properties of the material, making doped metal-free catalysts very successfully employed in different kind of reactions, e.g. oxidations[1,2].

Moreover, as previously reported in Section 1.3.2.2. the use of different methodologies to modify the structure can permit the selective introduction of functional groups either acid and basic, which can act differently on the substrate modifying activity, selectivity and stability of the carbocatalyst.

The first further step in hydrazine hydrate decomposition study will be focused on oxygen functionalities. As widely discussed in Section 1.3.2.2., the addition of O-based groups can increase the acidity of the material and its hydrophilicity leading to enhanced catalytic properties. For example, Pereira and co-workers[3] have shown the presence of a linear correlation between the activity of the carbon catalyst for the oxidative dehydrogenation of ethylbenzene and the amount of carbonyl and quinone groups. Moreover, different studies have pointed out that the amounts and types of surface functional groups strongly influenced not only the activity but also the reaction mechanism of carbon materials[4,5].

Regarding formic acid metal-free decomposition, the results exposed in Chapter 6 showed that oxygen functional groups, i.e. epoxide, oxygen incorporated in the structure and hydroxyl, were not active in interacting and decomposing FA. For this reason, future works will be focused in particular in the introduction of N and P functionalities.

Indeed, Gao and co-workers have shown that the introduction of nitrogen in graphene caused high charge and spin density in the adjacent *ortho* carbon, promoting the activation of oxygen species[6]. Moreover, Gupta et al. have demonstrated that N-containing carbon nanotubes are active in the conversion of glycerol to dihydroxyacetone. They also proved that surface pyridinic groups are the catalytically active specie in this reaction[7]. Phosphorous possesses the same number of valence electrons as N, and for this reason P-doped carbon materials are also electron rich[8]. However, the polarity of the C-P bond is opposite to the one of C-N bond, making P slightly positive and C partially negative[9]. In addition, another effect of P-doping can be due to the additional vacant 3d orbital. All these effects make P-doped carbon materials interesting metal-free catalysts[10]. Indeed, Patel et al. have demonstrated that this material can be employed as an effective selective carbocatalyst for aerobic oxidation of benzylic alcohols[10].

Raman spectroscopy will be also employed to quantify and locate the type of defects, in particular single vacancy, and heteroatoms. Eckmann et al. have shown that Raman spectroscopy is a powerful technique to quantify the type of defects in graphene. Indeed, by analyzing the intensity ratio between the two Raman-forbidden bands (D and D') they were able to prove the nature of defects. In particular, vacancy-like defects exhibited an $I_D/I_{D'}$ of approximatively 7[11]. In addition, it was demonstrated that the presence of heteroatoms can blue-shift the D and G bands[12,13].

Once individuated the most performing material for the metal-free decomposition of formic acid and hydrazine, the attention will be moved on in-situ one-step hydrogenation reaction. As previously reported in Section 1.3.4., reduction reaction can also be performed using carbon materials as catalyst but using strong reductive agents different from molecular hydrogen. For instance, in Chapter 4 the hydrogen produced from formic acid was employed in the in-situ conversion of muconic acid to adipic acid, showing increased activity in this reaction[14]. Moreover, hydrazine can be employed as a strong reductive agent, and until the 1980s it have been shown to be effective in the reduction of nitrobenzene and nitroarenes[15]. Indeed, Wu and co-workers showed that carbonyl and hydroxyl groups on carbon materials can activate hydrazine, which can hydrogenate nitrobenzene[16]. However, literature still lacks specific and systematic studies on carbon-based metal-free catalyst on in-situ hydrogenation reactions. In addition, direct hydrogenation reaction for the valorisation of biomass derived compounds, e.g. vanillin, can be a useful practical application of these dehydrogenation reactions to obtain value added chemicals.

Finally, the investigation of other carbon-free liquid-phase hydrogen carriers, e.g. ammonia, will be another step of this research. Indeed, NH_3 decomposition is a promising candidate in the production of hydrogen and it was extensively studied because it yields carbon-free products, i.e. N_2 and H_2[17,18]. In addition, ammonia possesses an extremely high gravimetric hydrogen content of 17 wt%[17] and can be liquefied at -33 °C at 1 bar. On the other hand, Ru-based catalysts are the only materials active at a temperature below 500 °C[19]. The study of this process at mild reaction condition and in liquid phase can permit its industrial application.

8.1. References

[1] H. P. Jia, D. R. Dreyer, C. W. Bielawski, Tetrahedron 2011, 67, 4431–4434.

[2] J. Long, X. Xie, J. Xu, Q. Gu, L. Chen, X. Wang, ACS Catal. 2012, 2, 622–631.

[3] M. F. R. Pereira, J. J. M. Orfao, J. L. Figueiredo, Appl. Catal. A Gen. 1999, 184, 153–160.

[4] B. F. Machado, M. Oubenali, M. R. Axet, T. T. Nguyen, M. Tunckol, M. Girleanu, O. Ersen, I. C. Gerber, P. Serp, J. Catal. 2014, 309, 185–198.

[5] Z. Sui, J. Zhou, Y. Dai, W. Yuan, Catal. today 2005, 106, 90–94.

[6] Y. Gao, G. Hu, J. Zhong, Z. Shi, Y. Zhu, D. S. Su, J. Wang, X. Bao, D. Ma, Angew. Chemie - Int. Ed. 2013, 52, 2109–2113.

[7] N. Gupta, O. Khavryuchenko, A. Villa, D. Su, ChemSusChem 2017, 10, 3030–3034.

[8] S. Some, J. Kim, K. Lee, A. Kulkarni, Y. Yoon, S. Lee, T. Kim, H. Lee, Adv. Mater. 2012, 24, 5481–5486.

[9] X. Zhang, Z. Lu, Z. Fu, Y. Tang, D. Ma, Z. Yang, J. Power Sources 2015, 276, 222–229.

[10]M. A. Patel, F. Luo, M. R. Khoshi, E. Rabie, Q. Zhang, C. R. Flach, R. Mendelsohn, E. Garfunkel, M. Szostak, H. He, ACS Nano 2016, 10, 2305–2315.

[11]A. Eckmann, A. Felten, A. Mishchenko, L. Britnell, R. Krupke, K. S. Novoselov, C. Casiraghi, Nano Lett. 2012, 12, 3925–3930.

[12]K. N. Kudin, B. Ozbas, H. C. Schniepp, R. K. Prud'homme, I. A. Aksay, R. Car, Nano Lett. 2008, 8, 36–41.

[13] H. Murphy, P. Papakonstantinou, T. I. T. Okpalugo, J. Vac. Sci. Technol. B Microelectron. Nanom. Struct. Process. Meas. Phenom. 2006, 24, 715–720.

[14]I. Barlocco, S. Capelli, E. Zanella, X. Chen, J. J. Delgado, A. Roldan, N. Dimitratos, A. Villa, J. Energy Chem. 2020, 52, 301–309.

[15] D. S. Su, G. Wen, S. Wu, F. Peng, R. Schlögl, Angew. Chemie - Int. Ed. 2017, 56, 936–964.

[16] S. Wu, G. Wen, X. Liu, B. Zhong, D. S. Su, ChemCatChem 2014, 6, 1558–1561.

[17] M. Aziz, A. TriWijayanta, A. B. D. Nandiyanto, Energies 2020, 13, 1–25.

[18] R. Lan, J. T. S. Irvine, S. Tao, Int. J. Hydrogen Energy 2012, 37, 1482–1494.

[19] K. E. Lamb, M. D. Dolan, D. F. Kennedy, Int. J. Hydrogen Energy 2019, 44, 3580–3593.